Synthesis, Characterisation, and Solid-State Properties of Substituted Ni-Co and Ni-Mn Ferrites and Their Applications

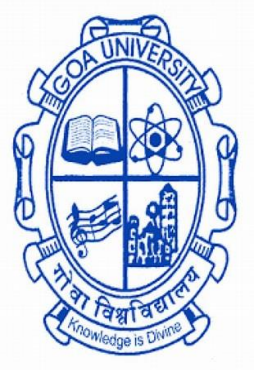
A THESIS SUBMITTED IN PARTIAL FULFILLMENT FOR THE DEGREE OF

DOCTOR OF PHILOSOPHY

in subject Chemistry

IN THE SCHOOL OF CHEMICAL SCIENCES

GOA UNIVERSITY



By

Ms. Sanjali Navelkar

School of Chemical Science, Goa University,

Goa

AUGUST 2025

DECLARATION

I, Sanjali Navelkar hereby declare that this thesis represents work which has been carried out by me and that it has not been submitted, either in part or full, to any other University or Institution for the award of any research degree.

Place: Taleigao Plateau.
Date:

Ms. Sanjali Navelkar
Research Scholar
School of Chemical Sciences
Goa- University

CERTIFICATE

I hereby certify that the above Declaration of the candidate, Sanjali Navelkar is true and the work was carried out under my supervision.

Prof. V. M. S. Verenkar
School of Chemical Sciences,
Goa University

Acknowledgment

I would like to express my deepest gratitude to all those who have supported me throughout the journey of completing this thesis.

First and foremost, I am profoundly thankful to my guide, Prof. V. M. S. Verenkar, for their invaluable guidance, patience, and encouragement. Their insight and expertise were instrumental in shaping the direction and quality of my work.

I also extend my sincere appreciation to the DRC members of the committee and my subject experts, Prof. Sunder Dhuri and Dr. Rohan Kunkaliker, for their thoughtful feedback and constructive suggestions. I would also like to thank the Vice Deans (Dr. Bidhan Sinkre and Dr. Digamber Porob) for their regular help and support. I am grateful to my teachers, Prof. V.S. Nadkarni (former Dean of SCS), Prof. R.N. Shirsat, Prof. B.R. Shrinivasan, and all the other members and teachers of the School of Chemical Sciences.

My special thanks to my group mates, Dr. Prajoti Gauns Dessai, Dr. Seneca Costa, Sonam Kumari, Mangala Sawal, Mansi Ugvekar, Upma Gaonkar, Priyanka Modak, Mr. Pritesh Khobrekar, and Ms. Namrata Kumari.

I am also grateful to all my other colleagues, research scholars, peers, teaching, and non-teaching staff in the School of Chemical Sciences, whose support and discussions made this experience all the more enriching.

I would like to acknowledge the Goa University for the research scholarship and the Department of Science and Technology, DST-PURSE, for providing the financial support that made this research possible.

To my family and friends, thank you for your unwavering support, patience, and understanding throughout this journey. Your belief in me has been a source of strength during the most challenging moments. My heartfelt gratitude goes to my parents, whose unconditional love, prayers, and unwavering belief in me have been my greatest source of strength. Their sacrifices, patience, and constant support have laid the foundation for everything I have achieved.

Finally, I dedicate this thesis to my parents and my husband, who inspired my love of learning, whose constant encouragement and love have been the foundation of my academic pursuits.

CONTENT

CHAPTER 1: Introduction and Literature Review

1.1 Introduction……...1

1.1.1 History of ferrites……...……....1

1.1.2 Crystal structure of ferrites.....……3

1.1.3 Classification of spinels ferrites depending on their magnetic properties……...…...5

1.1.4 Magnetic properties of ferrites……6

1.1.5 Magnetic hysteresis……7

1.1.6 Electrical and Dielectric Properties……8

1.2 Literature Review……...……..9

1.2.1 Literature review on Methods of preparation…….…….…….9

1.2.1.1 Literature Review on Combustion Method…….....9

1.2.1.2 Literature review on Precursor -combustion method….....12

1.2.2 Literature review on Ni-Co-Zn and Ni-Mn-Zn ferrites..……..……..14

1.2.2.1 Literature Review of Ni-Co-Zn Ferrites…….14

1.2.2.2 Literature Review of Ni-Mn-Zn Ferrites…….……23

1.2.3 Literature review on Applications of Ferrites……..27

1.2.3.1 Literature Review of Gas Sensing……...27

1.2.3.2 Literature Review of Electrochemical Properties……33

1.2.3.3 Literature Review of Ferrites as an Anti-microbial Agent……..35

1.3 Aim and Objective……..……38

CHAPTER 2: Experimental protocols and characterisation techniques

2.1 Introduction ……..53

2.2 Experimental Procedure……53

2.2.1 Synthesis using Precursor combustion method……..53

2.2.2 Synthesis using combustion technique……..……..…54

2.3 Annealing Process……..55

2.3.1 Pellet formation……..…55

2.3.2 Pre-sintering process...……...55

2.3.3 Sintering process……....56

2.4 Characterisation Techniques……...……..56

2.4.1 Chemical Analysis…….56

2.4.2 Thermal studies……..…56

2.4.3 X-Ray Diffraction study……..……..…….....57

2.4.4 Infrared spectroscopy studies……59

2.4.5 Raman Spectroscopy Technique…….…...59

2.4.6 X-ray photoelectron spectroscopy……...…...60

2.4.7 Microstructural studies…….…..60

2.4.8 BET Surface area study……..61

2.4.9 Resistivity……..…….....61

2.4.10 AC Susceptibility……...62

2.4.11 Vibrating Sample Magnetometer …….……62

2.4.12 Dielectric study…….……...63

2.4.13 Permeability study……....63

2.5 Gas sensing studies…….64

2.5.1 Fabrication of thick films…….65

2.5.2 Test system and gas sensing measurements…….65

2.6 Electrochemical studies…….64

2.6.1 Fabrication of electrodes……..66

2.6.2 Electrochemical measurements……67

2.7 Antibacterial Studies.…… 67

CHAPTER 3: A comparative study of 'as prepared' and 'sintered' $Ni_{0.6}Co_{0.4}Zn_xFe_2O_4$(x=0.0-0.6) ferrites and their applications

3.1 Introduction……73

3.2 Synthesis of Zn-doped Ni-Co ferrites $Ni_{0.6}Co_{0.4}Zn_xFe_2O_4$(x=0.0-0.6) by precursor combustion method……74

3.3 Characterisation of $Ni_{0.6-x}Co_{0.4}Zn_xFe_2(C_4H_2O_4)_3.6N_2H_4$ (x=0.0,0.1,0.2,0.3,0.4,0.5,0.6) precursor……74

3.3.1 CHNS Analysis……..75

3.3.2 Infrared spectroscopy…….76

3.3.3 TG/DTA analysis……..79

3.3.4 Isothermal mass loss study/ Total mass loss study……...84

3.3.5 Hydrazine estimation and Total mass loss study……..85

3.4 Characterisation of 'as prepared' and 'sintered' $Ni_{0.6}Co_{0.4}Zn_xFe_2O_4$(x=0.0-0.6)…….87

3.4.1 Phase purity and elemental analysis……..87

3.4.1.1 Powder X-ray Diffraction…….…….87

3.4.1.2 Elemental analysis…….……90

3.4.2 Morphological studies……....91

3.4.2.1 Scanning Electron Microscopy……..…91

3.4.2.2 Transmission Electron Microscopy……..…….... 95

3.4.3 Surface Area Studies (BET Analysis)……...…....96

3.4.4 Raman studies…….....98

3.4.5 X-ray Photoelectron Spectroscopic studies (XPS Analysis) ……...101

3.5 Solid-State studies……...111

3.5.1 DC Electrical Resistivity…… ….111

3.5.2 Magnetisation study (Vibrating sample magnetometer) ...…… .114

3.5.3 AC Susceptibility…….123

3.5.4 Dielectric study……126

3.5.4.1 Dielectric constant versus frequency……...…127

3.5.4.2 Dielectric properties versus temperature……..……128

3.5.4.3 Dielectric properties of ‘sintered’ ferrites……...……..131

3.5.4.4 Dielectric properties concerning temperature of ‘sintered’ ferrites.…132

3.5.5 Initial Permeability Study……135

3.6 Applications of Ferrites…….140

3.6.1 Gas Sensing applications of ‘as prepared’ $Ni_{0.6}Co_{0.4}Zn_xFe_2O_4$(x=0.0, 0.1, 0.2, 0.3, 0.4, 0.5, 0.6)ferrites…….……..140

3.6.2 Selection of optimum temperature for gas sensing studies…….143

3.6.3 % Response at variable x concentration……. 143

3.6.4 Gas Sensing Mechanism…….146

3.6.5 Working Principle of Metal Oxide Sensors……147

3.7 Electrochemical Application……..…148

3.7.1 Electrochemical studies of $Ni_{0.6-x}Co_{0.4}Zn_xFe_2O_4$ (x=0.0, 0.1, 0.2, 0.3, 0.4, 0.5,0.6) ferrites……148

3.8 Antibacterial Application……..…154

3.9 Summary……...…158

CHAPTER 4: A comparative study of 'as-prepared' and 'sintered' $Ni_{0.6-x}Mn_{0.4}Zn_xFe_2O_4$ (x= 0.0, 0.1, 0.2, 0.3, 0.4, 0.5, 0.6) ferrites and their applications

4.1 Introduction……..…...……...…169

4.2 Optimization study of $Ni_{0.3}Zn_{0.3}Mn_{0.4}Fe_2O_4$ ferrites...……..……169

4.3 Synthesis of ferrite $Ni_{0.6-x}Mn_{0.4}Zn_xFe_2O_4$ (x=0.0, 0.1, 0.2, 0.3, 0.4, 0.5, 0.6) ferrites via combustion method using hexamine as the fuel…….……...177

4.4 Characterisation of 'as prepared' and 'sintered' $Ni_{0.6-x}Mn_{0.4}Zn_xFe_2O_4$ (x=0.0, 0.1, 0.2, 0.3,0.4,0.5, 0.6) ferrites……176

4.4.1 Powder X-ray Diffraction Studies...…….177

4.4.2 Chemical Analysis……...….181

4.4.3 Infrared Spectroscopy……..……182

4.4.4 Morphological studies……..184

4.4.4.1 High Resolution Transmission Electron Microscopy (HR-TEM)....184

4.4.4.2 Scanning Electron Microscopy (SEM)…….……187

4.4.5 Surface Area Studies (BET Analysis) ……...…..189

4.4.6 Raman spectroscopy.…….....190

4.4.7 X-ray Photoelectron Spectroscopy……...193

4.5 Solid-State properties of ‘as prepared’ and ‘sintered’ $Ni_{0.6-x}Mn_{0.4}Zn_xFe_2O_4$ (x=0.0, 0.1,0.2, 0.3, 0.4, 0.5, 0.6) ferrites……...203

4.5.1 DC Electrical Resistivity……..203

4.5.2 AC Susceptibility studies…….207

4.5.3 Magnetisation study (Vibrating sample magnetometer)……..210

4.5.4 Dielectric study……220

4.5.4.1 Dielectric study with respect to frequency of ‘as prepared’ and ‘sintered’ $Ni_{0.6-x}Mn_{0.4}Zn_xFe_2O_4$ (x= 0.0, 0.1, 0.2, 0.3, 0.4, 0.5, 0.6) ferrites…..220

4.5.4.2 Dielectric study with respect to temperature of ‘as prepared’ and ‘sintered’ $Ni_{0.6-x}Mn_{0.4}Zn_xFe_2O_4$ (x= 0.0, 0.1, 0.2, 0.3, 0.4, 0.5, 0.6) ferrites…..223

4.5.5 Initial Permeability ……..……224

4.6 Gas sensing Application……230

4.6.1 Gas Sensing application of ‘as prepared’ $Ni_{0.6-x}Mn_{0.4}Zn_xFe_2O_4$ (x=0.0, 0.1, 0.2, 0.3, 0.4, 0.5, 0.6)ferrites ……..……230

4.6.2 Selection of optimum temperature for gas sensing studies……..230

4.6.3 % Response at variable x concentration……...231

4.6.4 Gas Sensing Mechanism for reducing gas……...237

4.7 Electrochemical performance……. ...239

4.7.1 Electrochemical performance of $Ni_{0.6-x}Mn_{0.4}Zn_xFe_2O_4$ (x=0.0, 0.1, 0.2, 0.3, 0.4, 0.5,0.6) ferrites……...…….……239

4.8 Antibacterial studies……...……..…245

4.9 Summary…….250

CHAPTER 5: Summary & Conclusion

5.1 Summary of the Thesis……..260

5.2 Conclusion…….270

Appendix I: Publications

Appendix II: Conferences, workshops, seminars attended

List of Tables

CHAPTER 3

3.1 The theoretical and experimental percentages of C, H, and N in $Ni_{0.6-x}Co_{0.4}Zn_xFe_2(C_4H_20_4)_3.6N_2H_4$ (x=0.0, -0.6) precursors……..…….....75

3.2 IR peak position of various organic moieties for all the $Ni_{0.6-x}Co_{0.4}Zn_xFe_2(C_4H_20_4)_3.6N_2H_4$ (x=0.0,0.1,0.2,0.3,0.4,0.5,0.6) precursors….79

3.3 The TG/DTA/DTG data of $Ni_{0.6-x}Co_{0.4}Zn_xFe_2(C_4H_20_4)_3.6N_2H_4$ (x=0.0,0.1,0.2,0.3,0.4,0.5,0.6) precursors…….....81

3.4 Isothermal mass loss and simultaneous hydrazine study of $Ni_{0.6-x}Co_{0.4}Zn_xFe_2(C_4H_2O_4)_3.6N_2H_4$ (x=0.0,0.1,0.2,0.3,0.4,0.5,0.6) precursors……...85

3.5 Hydrazine estimation and total mass loss study of $Ni_{0.6-x}Co_{0.4}Zn_xFe_2(C_4H_2O_4)_3.6N_2$ (x=0.0,0.1,0.2,0.3,0.4,0.5,0.6) precursors……86

3.6 Lattice constant (a), Unit cell (V), the crystallite size (D), x-ray density (dx), bulk density (dm), and porosity% (P) of 'as prepared' and 'sintered' $Ni_{0.6}Co_{0.4}Zn_xFe_2O_4$ (x=0.0, 0.1, 0.2, 0.3, 0.4, 0.5, 0.6) ferrites…….……90

3.7 Theoretical and experimental percentages of Ni^{2+}, Co^{2+}, Zn^{2+}, and Fe^{3+} present in 'as prepared' $Ni_{0.6-x}Co_{0.4}Zn_xFe_2O_4$ (x=0.0-0.1, 0.2, 0.3, 0.4, 0.5, 0.6) ferrites……91

3.8 The values of Raman active modes of 'as prepared'$Ni_{0.6-x}Co_{0.4}Zn_xFe_2O_4$ (x=0.0, 0.1, 0.2, 0.3, 0.4, 0.5,0.6) ferrites…...……..……...100

3.9 The values of the Raman active modes of 'sintered'$Ni_{0.6-x}Co_{0.4}Zn_xFe_2O_4$ (x=0.0, 0.1, 0.2, 0.3, 0.4, 0.5,0.6) ferrites……101

3.10 Binding energies of $Fe^{3+}2p_{3/2}$ and $2p_{1/2}$ along with their satellite peaks obtained from the XPS study of 'as prepared'$Ni_{0.6-x}Co_{0.4}Zn_xFe_2O_4$ (x= 0.0- 0.6) ferrites.103

3.11 Binding energies of $Zn^{2+}2p_{3/2}$, $2p_{1/2,}$ and O1s along with their satellite peaks obtained from the XPS study of 'as prepared'$Ni_{0.6-x}Co_{0.4}Zn_xFe_2O_4$ (x= 0.0- 0.6) ferrites…… .103

3.12 Binding energies of $Ni^{2+}2p_{3/2}$ along with their satellite peaks obtained from the

XPS study of 'as prepared' $Ni_{0.6-x}Co_{0.4}Zn_xFe_2O_4$ (x= 0.0- 0.6) ferrites……...108

3.13 Binding energies of $Co^{2+}2p_{3/2}$ and $2p_{1/2}$ along with their satellite peaks obtained from the XPS study of 'as prepared' $Ni_{0.6-x}Co_{0.4}Zn_xFe_2O_4$ (x= 0.0- 0.6) ferrites……....110

3.14 M_s, H_c, M_r, and T_B obtained from the MH and MT plots of 'as prepared' and 'sintered' $Ni_{0.6-x}Co_{0.4}Zn_xFe_2O_4$ (x=0.0, 0.1, 0.2, 0.3, 0.4, 0.5, 0.6) ferrites at RT, 60 K and a constant field of 250, 500 and 1000Oe……120

3.15 'T_c' of 'as prepared' and 'sintered' $Ni_{0.6}Co_{0.4}Zn_xFe_2O_4$(x=0.0, 0.1, 0.2, 0.3, 0.4,0.5 0.6) ferrites……..125

3.16 The Curie Temperature (T_c) of 'sintered' $Ni_{0.6-x}Co_{0.4}Zn_xFe_2O_4$ (x=0.0, 0.1, 0.2, 0.3, 0.4, 0.5, 0.6) evaluated from AC susceptibility and Initial permeability studies……..……139

3.17 Specific capacitance of as-prepared $Ni_{0.6}Co_{0.4}Zn_xFe_2O_4$(x=0.0, 0.1, 0.2, 0.3, 0.4, 0.5, 0.6) ferrites at a variable scan rate and current density of 1A/g, and R_s…..151

CHAPTER 4

4.1 Metal nitrate: fuel ratio, Lattice constants, Average crystallite size, Saturation magnetization, Coercivity, Remanence, and Curie temperature. …….170

4.2 Lattice constant (a), Unit cell (V), the crystallite size (D), x-ray density (dx), bulk density (dm), and porosity% (P) of 'as prepared' and 'sintered' $Ni_{0.6-x}Mn_{0.4}Zn_xFe_2O_4$(x=0.0, 0.1, 0.2, 0.3, 0.4, 0.5, 0.6) ferrites……..……180

4.3 Theoretical and experimental percentages of 'as prepared' $Ni_{0.6-x}Mn_{0.4}Zn_xFe_2O_4$ (x=0.0, 0.1, 0.2, 0.3, 0.4, 0.5, 0.6) ferrites…….181

4.4 IR data of 'as prepared' and 'sintered' $Ni_{0.6-x}Mn_{0.4}Zn_xFe_2O_4$ (x=0.0, 0.1, 0.2, 0.3, 0.4, 0.5,0.6) ferrites…….....184

4.5 The Raman active modes of 'as prepared' $Ni_{0.6-x}Mn_{0.4}Zn_xFe_2O_4$ (x=0.0, 0.1, 0.2, 0.3, 0.4, 0.5,0.6)ferrites…….……192

4.6 The Raman active modes of 'sintered' $Ni_{0.\ x}Mn_{0.4}Zn_xFe_2O_4$ (x=0.0, 0.1, 0.2,

0.3, 0.4, 0.5,0.6) ferrites……193

4.7 Binding energies of $Mn^{2+}2p_{3/2}$ and $2p_{1/2}$ along with their satellite peaks……..196

4.8 Binding energies of $Zn^{2+}2p_{3/2}$, $2p_{1/2}$ and O1s ……196

4.9 Binding energies of $Ni^{2+}2p_{3/2}$ and $Ni^{2+}2p_{1/2}$ along with their satellite peaks…….199

4.10 Binding energies of $Fe^{3+}2p_{3/2}$ and $2p_{1/2}$ along with their satellite peaks……..…..201

4.11 'Tc' of 'as prepared' and 'sintered' $Ni_{0.6-x}Mn_{0.4}Zn_xFe_2O_4$ (x=0.0-0.6)ferrites…..209

4.12 M_s, H_c, M_r, and T_B of 'as prepared' and 'sintered' $Ni_{0.6-x}Mn_{0.4}Zn_xFe_2O_4$ (x=0.0, 0.1, 0.2, 0.3, 0.4, 0.5, 0.6) ferrites at 300 K, 60K, 250, 500, 1000Oe……..……219

4.13 The Curie temperature (T_c) of 'sintered' $Ni_{0.6-x}Mn_{0.4}Zn_xFe_2O_4$ (x=0.0, 0.1, 0.2, 0.3, 0.4, 0.5, 0.6) ferrites evaluated from AC susceptibility and Initial permeability studies and Anisotropy constant……229

4.14 Specific capacitance of 'as prepared' $Ni_{0.6-x}Mn_{0.4}Zn_xFe_2O_4$ (x=0.0, 0.1, 0.2, 0.3, 0.4,0.5, 0.6) ferrites at variable scan rate.…….241

4.15 Specific capacitance via galvanic charge/ discharge study of 'as prepared' $Ni_{0.6-x}Mn_{0.4}Zn_xFe_2O_4$ (x=0.0, 0.1, 0.2, 0.3, 0.4, 0.5, 0.6) ferrites at a current density of 1A g^{-1}……..…….....244

List of Figures

CHAPTER 1

1.1 Spinel structure of ferrite unit cell……4

1.2 Hysteresis curve ……7

CHAPTER 2

2.1 Gas sensing setup used for sensing measurement…….....64

2.2 Schematic representation of electrochemical performance using cyclic voltametry……...……67

CHAPTER 3

3.1 IR spectra of $Ni_{0.6-x}Co_{0.4}Zn_xFe_2(C_4H_20_4)_3.6N_2H_4$ (x=0.0,0.1,0.2,0.3,0.4,0.5,0.6) precursor isothermally heated from RT- 140^oC…….……77

3.2 IR spectra of $Ni_{0.6-x}Co_{0.4}Zn_xFe_2(C_4H_20_4)_3.6N_2H_4$ (x=0.0,0.1,0.2,0.3,0.4,0.5,0.6) precursor isothermally heated from from 180^oC- As-burnt……....78

3.3 TG-DTA-DTG curves of $Ni_{0.6-x}Co_{0.4}Zn_xFe_2(C_4H_20_4)_3.6N_2H_4$ (x=(0.0=a, 0.1=b, 0.2=c, 0.3=d, 0.4=e, 0.5=f, 0.6=g) precursors…….....84

3.4 a. X-ray diffraction patterns of ‘as prepared’ $Ni_{0.6}Co_{0.4}Zn_xFe_2O_4$(x=0.0, 0.1, 0.2,0.3 0.4,0.5,0.6)……..88

3.4 b. Plot of Intensity versus 2theta for (311) plane‘as prepared’ $Ni_{0.6}Co_{0.4}Zn_xFe_2O_4$(x=0.0, 0.1, 0.2,0.3,0.4,0.5,0.6) ferrites……...88

3.5 The X-ray diffraction patterns of ‘sintered’ $Ni_{0.6}Co_{0.4}Zn_xFe_2O_4$(x=0.0, 0.1, 0.2, 0.3, 0.4, 0.5, 0.6) ferrites……89

3.6 (a-g) SEM images along with EDX patterns of ‘as prepared’ $Ni_{0.6-x}Co_{0.4}Zn_xFe_2O_4$ (x=0.0, 0.1, 0.2, 0.3, 0.4,0.5,0.6) ferrites…….....92-93

3.7 (a-g) SEM images of ‘sintered’ $Ni_{0.6-x}Co_{0.4}Zn_xFe_2O_4$ (x=0.0, 0.1, 0.2, 0.3, 0.4, 0.5,0.6) ferrites……..94

3.8 (a-g) TEM images alongside SAED patterns and histogram of ‘as prepared’ $Ni_{0.6-x}Co_{0.4}Zn_xFe_2O_4$ (x=0.0, 0.1, 0.2, 0.3, 0.4, 0.5,0.6) ferrites……...…….95

3.9 BET surface area curves for ‘as prepared’ $Ni_{0.6-x}Co_{0.4}Zn_xFe_2O_4$ (x=0.0,

0.1, 0.2, 0.3, 0.4, 0.5,0.6) ferrites……...97

3.10 The Raman spectra of 'as prepared' $Ni_{0.6-x}Co_{0.4}Zn_xFe_2O_4$ (x=0.0, 0.1, 0.2, 0.3, 0.4, 0.5, 0.6) ferrites……...……..99

3.11 The Raman spectra of 'sintered' $Ni_{0.6-x}Co_{0.4}Zn_xFe_2O_4$ (x=0.0, 0.1, 0.2, 0.3,0.4,0.5,0.6) ferrites……..……..100

3.12 The full scan spectrum of 'as prepared' $Ni_{0.6}Co_{0.4}Zn_xFe_2O_4$(x=0.0, 0.1, 0.2, 0.3, 0.4, 0.5, 0.6) ferrites……...…….102

3.13 The deconvoluted XPS data of Fe 2p for all the 'as prepared' $Ni_{0.6}Co_{0.4}Zn_xFe_2O_4$ (x=0.0, 0.1, 0.2, 0.3, 0.4, 0.5, 0.6) ferrites……...……104

3.14 The deconvoluted XPS data of Zn 2p for all the 'as prepared' $Ni_{0.6}Co_{0.4}Zn_xFe_2O_4$ (x=0.0, 0.1, 0.2, 0.3, 0.4, 0.5, 0.6) ferrites..…….105

3.15 The deconvoluted XPS data of O 1s for all the 'as prepared' $Ni_{0.6}Co_{0.4}Zn_xFe_2O_4$ (x=0.0, 0.1, 0.2, 0.3, 0.4, 0.5, 0.6) ferrites……...106

3.16 The deconvoluted XPS data of Ni for all the 'as prepared' $Ni_{0.6}Co_{0.4}Zn_xFe_2O_4$ (x=0.0, 0.1, 0.2, 0.3, 0.4, 0.5, 0.6) ferrites……...107

3.17 The deconvoluted XPS data of Co for all the 'as prepared' $Ni_{0.6}Co_{0.4}Zn_xFe_2O_4$ (x=0.0, 0.1, 0.2, 0.3, 0.4, 0.5, 0.6) ferrites……...108

3.18 a: Plots of log resistivity vs. 1/T*1000 during heating cycle for 'as prepared' $Ni_{0.6-x}Co_{0.4}Zn_xFe_2O_4$ (x=0.0-0.6)ferrites…….....112

b: Plots of log resistivity vs. 1/T*1000 during cooling cycle for 'as prepared' $Ni_{0.6-x}Co_{0.4}Zn_xFe_2O_4$ (x=0.0-0.6) ferrites……..…..112

3.19 a: Plots of log resistivity vs. 1/T*1000 during heating cycle for 'sintered' $Ni_{0.6-x}Co_{0.4}Zn_xFe_2O_4$ (x=0.0-0.6) ferrites……... ……114

b: Plots of log resistivity vs. 1/T*1000 during cooling cycle for 'sintered' $Ni_{0.6-x}Co_{0.4}Zn_xFe_2O_4$ (x=0.0-0.6) ferrites……114

3.20 The plot of magnetic moment vs. magnetic field of 'as prepared' $Ni_{0.6-x}Co_{0.4}Zn_xFe_2O_4$ (x=0.0, 0.1, 0.2, 0.3, 0.4, 0.5,0.6) ferrites measured at RT…...116

3.21 The plot of magnetic moment vs. magnetic field of 'as prepared' $Ni_{0.6-}$

$_xCo_{0.4}Zn_xFe_2O_4$ (x=0.0, 0.1, 0.2, 0.3,0.4, 0.5, 0.6) ferrites measured at 60K…..116

3.22 The plot of magnetic moment v/s magnetic field of 'sintered' $Ni_{0.6-x}Co_{0.4}Zn_xFe_2O_4$ (x=0.0, 0.1, 0.2, 0.3, 0.4, 0.5,0.6) ferrites measured at RT……....117

3.23 The plot of magnetic moment v/s magnetic field of 'sintered' $Ni_{0.6-x}Co_{0.4}Zn_xFe_2O_4$ (x=0.0, 0.1, 0.2, 0.3, 0.4, 0.5,0.6) ferrites measured at 60K……117

3.24 MT plots (FC and ZFC curves) of 'as prepared' $Ni_{0.6-x}Co_{0.4}Zn_xFe_2O_4$ (x=0.0, 0.1, 0.2, 0.3, 0.4, 0.5, 0.6) ferrites at 1000,500 &250 Oe……...121

3.25 MT plots (FC and ZFC) curves of 'sintered' $Ni_{0.6}Co_{0.4}Zn_xFe_2O_4$(x=0.0, 0.1, 0.2, 0.3, 0.4, 0.5, 0.6)ferrites at 1000,500 &250 Oe…….…..122

3.26 AC susceptibility plots of 'as prepared' $Ni_{0.6-x}Co_{0.4}Zn_xFe_2O_4$ (x=0.0-0.6) ferrites……...……...125

3.27 AC susceptibility plots of 'sintered' $Ni_{0.6-x}Co_{0.4}Zn_xFe_2O_4$ (x=0.0-0.6)ferrites…126

3.28 a: The plot of Dielectric constant vs. Log Frequency at RT for 'as prepared' $Ni_{0.6-x}Co_{0.4}Zn_xFe_2O_4$ (x=0.0-0.6) ferrites…….129

3.28 b**:** The plot of Dielectric Loss vs. Log Frequency at RT for 'as prepared' $Ni_{0.6-x}Co_{0.4}Zn_xFe_2O_4$(x=0.0-0.6) ferrites……..129

3.29 a: The plot of Dielectric Constant vs. Temperature for 'as prepared' $Ni_{0.6-x}Co_{0.4}Zn_xFe_2O_4$ (x=0.0-0.6) ferrites at 1 kHz ……..…...130

3.29 a: The plot of Dielectric Loss vs. Temperature for 'as prepared' $Ni_{0.6-x}Co_{0.4}Zn_xFe_2O_4$ (x=0.0-0.6) ferrites at 1 kHz ……..…...130

3.30 a: The plot of Dielectric Constant vs. Temperature for 'as prepared' $Ni_{0.6-x}Co_{0.4}Zn_xFe_2O_4$ (x=0.0-0.6) ferrites at 1MHz……..131

3.30 b:The plot of Dielectric loss vs. Temperature for 'as prepared' $Ni_{0.6-x}Co_{0.4}Zn_xFe_2O_4$ (x=0.0-0.6) ferrites at 1MHz…….131

3.31 a: The plot of Dielectric constant vs. Log frequency of 'sintered' $Ni_{0.6-x}Co_{0.4}Zn_xFe_2O_4$ (x=0.0-0.6) ferrites..……...…….…..132

3.32 b:The plot of Dielectric Loss vs. Log Frequency of 'sintered' $Ni_{0.6-x}Co_{0.4}Zn_xFe_2O_4$

(x=0.0-0.6) ferrites…… .132

3.33 a:The plot of Dielectric Constant vs. Temperature for 'sintered' $Ni_{0.6-x}Co_{0.4}Zn_xFe_2O_4$ (x=0.0-0.6) ferrites at 1 kHz……..134

3.33 b: The plot of Dielectric Loss vs. Temperature for 'sintered' $Ni_{0.6-x}Co_{0.4}Zn_xFe_2O_4$ (x=0.0-0.6) ferrites at 1 kHz……134

3.34 a: The plot of Dielectric Constant vs. Temperature for 'sintered' $Ni_{0.6-x}Co_{0.4}Zn_xFe_2O_4$ (x=0.0-0.6) ferrites at 1MHz ……..134

3.34 b: The plot of Dielectric Loss vs. Temperature for 'sintered' $Ni_{0.6-x}Co_{0.4}Zn_xFe_2O_4$ (x=0.0-0.6) ferrites at 1MHz ……..134

3.35 a: The plot of Initial Permeability vs Log Frequency of 'sintered' $Ni_{0.6-x}Co_{0.4}Zn_xFe_2O_4$ (x=0.0, 0.1, 0.2, 0.3, 0.4, 0.5, 0.6) ferrites…….137

3.35 b: The plot of Tan δ vs Log Frequency of 'sintered' $Ni_{0.6-x}Co_{0.4}Zn_xFe_2O_4$ (x=0.0, 0.1, 0.2, 0.3, 0.4, 0.5, 0.6) ferrites……137

3.36 a: The plot of Initial Permeability vs Temperature of 'sintered' $Ni_{0.6-x}Co_{0.4}Zn_xFe_2O_4$ (x=0.0, 0.1, 0.2, 0.3, 0.4, 0.5, 0.6) ferrites……138

3.36 b: The plot of Tan δ vs Temperature of 'sintered' $Ni_{0.6-x}Co_{0.4}Zn_xFe_2O_4$ (x=0.0, 0.1, 0.2, 0.3, 0.4, 0.5, 0.6) ferrites……138

3.37 Temperature dependent sensor response of 'as prepared' $Ni_{0.6-x}Co_{0.4}Zn_xFe_2O_4$ (x=0.0, 0.1, 0.2, 0.3, 0.4, 0.5, 0.6) ferrites ……..142

3.38 The plot of % response vs time of $Ni_{0.6-x}Co_{0.4}Zn_xFe_2O_4$ (x= 0.3) ferrite for A:NO_x, B:NH_3, and C:Cl_2 at RT……..142

3.39 The plot of % Response vs. composition of $Ni_{0.6-x}Co_{0.4}Zn_xFe_2O_4$ (x=0.0, 0.1, 0.2, 0.3, 0.4, 0.5, 0.6) ferrites towards NO_x gas…….143

3.40 A: The plot of % Response vs. Compositions of 'as prepared' $Ni_{0.6-x}Co_{0.4}Zn_xFe_2O_4$ (x=0.0, 0.1, 0.2, 0.3, 0.4, 0.5, 0.6) ferrites for Cl_2 gas…….144

B: The plot of % Response vs. Time of 'as prepared' $Ni_{0.6-x}Co_{0.4}Zn_xFe_2O_4$ (x = 0.5) ferrites for Cl_2 gas at RT …….144

3.41 A: The plot of resistance vs. Time for sample x=0.3, B: Plot of % Response vs.

Time for sample x=0.3, C: % Response vs. Composition for LPG, D: % Response vs. Increasing concentration in gas, x=0.0, E: Plot of % Response vs. Time to test the reproducibility studies of sample x=0.6…….....145

3.42 The plot of % response vs. composition (x) of 'as prepared' $Ni_{0.6-x}Co_{0.4}Zn_xFe_2O_4$ (x=0.0, 0.1, 0.2, 0.3, 0.4, 0.5, 0.6) ferrites for NH_3 gas at 100 °C using 100 ppm of test gas……..…146

3.43 The plot of specific capacitance versus scan rate of 'as prepared' $Ni_{0.6-x}Co_{0.4}Zn_xFe_2O_4$(x=0.0, 0.1, 0.2, 0.3, 0.4, 0.5,0.6) ferrites……150

3.44 a:CV Plots of 'as prepared' $Ni_{0.6-x}Co_{0.4}Zn_xFe_2O_4$ (x=0.0, 0.1, 0.2, 0.3, 0.4, 0.5,0.6) ferrites…….....152

3.44 b: The galvanic charge/discharge plots of **'**as prepared' $Ni_{0.6-x}Co_{0.4}Zn_xFe_2O_4$ (x=0.0, 0.1, 0.2, 0.3, 0.4, 0.5, 0.6) ferrites……...153

3.44 c: The Nyquist plot of **'**as prepared' $Ni_{0.6-x}Co_{0.4}Zn_xFe_2O_4$ (x=0.0, 0.1, 0.2, 0.3, 0.4, 0.5, 0.6) ferrites……153

3.45 Graph showing the effect of two different concentrations of $Ni_{0.6-x}Co_{0.4}Zn_xFe_2O_4$ (x=0.0, 0.1, 0.2, 0.3, 0.4, 0.5,0.6) ferrites on percentage survival of *Staphylococcus aureus*…….…….....155

3.46 Antibacterial activity of $Ni_{0.6-x}Co_{0.4}Zn_xFe_2O_4$ (x=0.0, 0.1, 0.2, 0.3, 0.4, 0.5,0.6) and control at (Conc: 1000 µg/mL) on percentage survival of *Staphylococcus aureus*…….....156

3.47 Antibacterial activity of $Ni_{0.6-x}Co_{0.4}Zn_xFe_2O_4$ (x=0.0, 0.1, 0.2, 0.3, 0.4, 0.5,0.6) and control at (Conc: 500 µg/mL) on percentage survival of *Staphylococcus aureus.*…….....157

CHAPTER 4

4.1 The powder XRD patterns of $Ni_{0.3}Mn_{0.4}Zn_{0.3}Fe_2O_4$ at different metal nitrate: fuel ratios…….……....171

4.2 Plot of lattice constant and crystallite size as a function of metal nitrate: fuel ratio……..172

4.3 a:IR spectra of $Ni_{0.3}Mn_{0.4}Zn_{0.3}Fe_2O_4$ ferrite with different metal nitrate: fuel ratios (1-5)……..172

4.3 b:IR spectra of $Ni_{0.3}Mn_{0.4}Zn_{0.3}Fe_2O_4$ ferrite with different metal nitrate: fuel ratios (6-10)……...….173

4.4 The plot of magnetic moment versus magnetic field of $Ni_{0.3}Mn_{0.4}Zn_{0.3}Fe_2O_4$ with different metal: fuel ratio……..173

4.5 The plot of normalized AC susceptibility as a function of temperature of $Ni_{0.3}Mn_{0.4}Zn_{0.3}Fe_2O_4$ with different metal: fuel ratios……..174

4.6 The plot of saturation magnetization and Curie temperature as a function of temperature of $Ni_{0.3}Mn_{0.4}Zn_{0.3}Fe_2O_4$ ferrite with different metal: fuel ratios. ….174

4.7 a: plot of dielectric constant versus log frequency and b: dielectric loss versus log frequency for samples with different metal: fuel ratios……..….175

4.8 a: The plot of log resistivity v/s 1/T * 1000 of $Ni_{0.3}Mn_{0.4}Zn_{0.3}Fe_2O_4$ from (1-5) samples and b: 6-10 samples with different metal nitrate: fuel ratio……176

4.9 The powder XRD patterns of 'as prepared' $Ni_{0.6-x}Mn_{0.4}Zn_xFe_2O_4$ (x=0.0, 0.1, 0.2, 0.3, 0.4, 0.5, 0.6) ferrites ……..178

4.10 The 311 peaks of 'as prepared' $Ni_{0.6-x}Mn_{0.4}Zn_xFe_2O_4$ (x=0.0, 0.1, 0.2, 0.3, 0.4, 0.5, 0.6) ferrites……...……....178

4.11 Powder X-ray diffraction pattern of $Ni_{0.3}Mn_{0.4}Zn_{0.3}Fe_2O_4$ ferrite at different sintering temperatures: 1000 °C for 10 h, 1050 °C for 5 h, 1050 °C for 10 h, and 1100 °C for 10 h.…….…….179

4.12 The powder XRD patterns of 'sintered' $Ni_{0.6-x}Mn_{0.4}Zn_xFe_2O_4$ (x=0.0, 0.1, 0.2, 0.3, 0.4, 0.5, 0.6) ferrites…….179

4.13 IR spectra of 'as prepared' $Ni_{0.6-x}Mn_{0.4}Zn_xFe_2O_4$ (x=0.0, 0.1, 0.2, 0.3, 0.4, 0.5,0.6) ferrites……..183

4.14 IR spectra of 'sintered' $Ni_{0.6-x}Mn_{0.4}Zn_xFe_2O_4$ (x=0.0, 0.1, 0.2, 0.3, 0.4, 0.5, 0.6) ferrites……...183

4.15 HRTEM images, SAED pattern and histogram of 'as prepared'

$Ni_{0.6-x}Mn_{0.4}Zn_xFe_2O_4$ (x=0.0, 0.1, 0.2, 0.3, 0.4, 0.5,0.6) ferrites……186

4.16 a: SEM images of $Ni_{0.6-x}Mn_{0.4}Zn_xFe_2O_4$ (x=0.0, 0.1, 0.2, 0.3, 0.4, 0.5,0.6) ferrites ……..…...187

4.16 b: EDX images of $Ni_{0.6-x}Mn_{0.4}Zn_xFe_2O_4$ (x=0.0, 0.1, 0.2, 0.3, 0.4, 0.5,0.6) ferrites……..188

4.17 The N_2 isotherm of 'as prepared' $Ni_{0.6-x}Mn_{0.4}Zn_xFe_2O_4$ (x=0.0, 0.1, 0.2, 0.3, 0.4, 0.5,0.6) ferrites…….……....189

4.18 Raman spectra of 'as prepared' $Ni_{0.6-x}Mn_{0.4}Zn_xFe_2O_4$ (x=0.0, 0.1, 0.2, 0.3, 0.4, 0.5,0.6) ferrites.……191

4.19 Raman spectra of 'sintered' $Ni_{0.6-x}Mn_{0.4}Zn_xFe_2O_4$ (x=0.0, 0.1, 0.2, 0.3, 0.4, 0.5,0.6) ferrites……192

4.20 Full scan spectra of 'as prepared' $Ni_{0.6-x}Mn_{0.4}Zn_xFe_2O_4$ (x=0.0, 0.1, 0.2, 0.3, 0.4, 0.5, 0.6) ferrites…….……..194

4.21 The deconvoluted XPS spectra of Mn for all the 'as prepared' $Ni_{0.6-x}Mn_{0.4}Zn_xFe_2O_4$ (x=0.0, 0.1, 0.2, 0.3, 0.4, 0.5, 0.6) ferrites……195

4.22 The deconvoluted XPS spectra of Zn 2p for all the 'as prepared' $Ni_{0.6-x}Mn_{0.4}Zn_xFe_2O_4$ (x=0.0, 0.1, 0.2, 0.3, 0.4, 0.5, 0.6) ferrites……..197

4.23 The deconvoluted XPS spectra of O 1s for all the 'as prepared' $Ni_{0.6-x}Mn_{0.4}Zn_xFe_2O_4$(x=0.0, 0.1, 0.2, 0.3, 0.4, 0.5, 0.6) ferrites …….198

4.24 The deconvoluted XPS spectra of Ni 2p for all the 'as prepared' $Ni_{0.6-x}Mn_{0.4}Zn_xFe_2O_4$ (x=0.0, 0.1, 0.2, 0.3, 0.4, 0.5, 0.6) ferrites……200

4.25 The deconvoluted XPS spectra of Fe 2p for all the 'as prepared' $Ni_{0.6-x}Mn_{0.4}Zn_xFe_2O_4$ (x=0.0, 0.1, 0.2, 0.3, 0.4, 0.5, 0.6) ferrites……202

4.26 a: Plots of log resistivity vs. 1/T during heating and cooling for 'as prepared' $Ni_{0.6-x}Mn_{0.4}Zn_xFe_2O_4$ (x=0.0, 0.1, 0.2, 0.3, 0.4, 0.5, 0.6) ferrites……..204

b: Plots of log resistivity vs. 1/T during heating and cooling for 'sintered' $Ni_{0.6-x}Mn_{0.4}Zn_xFe_2O_4$ (x=0.0, 0.1, 0.2, 0.3, 0.4, 0.5, 0.6) ferrites…….206

4.27 a: AC susceptibility plots of 'as prepared' $Ni_{0.6-x}Mn_{0.4}Zn_xFe_2O_4$ (x=0.0-0.6) ferrites…….208
b: AC susceptibility plots of 'sintered' $Ni_{0.6-x}Mn_{0.4}Zn_xFe_2O_4$ (x=0.0-0.6) ferrites…….209
4.28 a: The plot of magnetization versus magnetic field of 'as prepared' $Ni_{0.6-x}Mn_{0.4}Zn_xFe_2O_4$ (x=0.0, 0.1, 0.2, 0.3, 0.4, 0.5, 0.6) ferrite at 300K..……210
b: The plot of magnetization versus magnetic field of 'as prepared' $Ni_{0.6-x}Mn_{0.4}Zn_xFe_2O_4$ (x=0.0, 0.1, 0.2, 0.3, 0.4, 0.5, 0.6) ferrite at 60 K ……211
4.29 a: The plot of magnetization versus magnetic field of 'sintered' $Ni_{0.6-x}Mn_{0.4}Zn_xFe_2O_4$ (x=0.0, 0.1, 0.2, 0.3, 0.4, 0.5, 0.6) ferrites at 300K…….214
b: The plot of magnetization versus magnetic field of 'sintered' $Ni_{0.6-x}Mn_{0.4}Zn_xFe_2O_4$ (x=0.0, 0.1, 0.2, 0.3, 0.4, 0.5,0.6) ferrites measured at 60K……...……214
4.30 Zero field cooled and field cooled curves of 'as-prepared' $Ni_{0.6-x}Mn_{0.4}Zn_xFe_2O_4$ (x=0.0, 0.1, 0.2, 0.3, 0.4, 0.5, 0.6) ferrites at 1000,500 &250 Oe…….....217
4.31 Zero field cooled and field cooled curves of 'sintered' $Ni_{0.6-x}Mn_{0.4}Zn_xFe_2O_4$ (x=0.0, 0.1, 0.2, 0.3, 0.4, 0.5, 0.6) ferrites at 1000,500 &250 Oe…….……218
4.32 a: Dielectric constant vs. Log frequency of 'as prepared' $Ni_{0.6-x}Mn_{0.4}Zn_xFe_2O_4$ (x=0.0-0.6) ferrites…….....221
b: Dielectric loss vs. Log frequency of 'as prepared' $Ni_{0.6-x}Mn_{0.4}Zn_xFe_2O_4$ (x=0.0-0.6) ferrites…….....221
4.33 a: Dielectric constant vs. Log frequency of 'sintered' $Ni_{0.6-x}Mn_{0.4}Zn_xFe_2O_4$ (x=0.0-0.6) ferrites……..…….....221
b: Dielectric loss vs. Log frequency of 'sintered' $Ni_{0.6-x}Mn_{0.4}Zn_xFe_2O_4$ (x=0.0-0.6) ferrites…….....221
4.34 a: Dielectric constant vs. Temperature at 1kHz for 'as prepared' $Ni_{0.6-x}Mn_{0.4}Zn_xFe_2O_4$ (x=0.0-0.6) ferrites…….……..222
b: Dielectric loss vs. Temperature at 1kHz for 'as prepared' $Ni_{0.6-x}Mn_{0.4}Zn_xFe_2O_4$ (x=0.0-0.6) ferrites…….....222

c: Dielectric constant vs. Temperature at 1MHz for 'as prepared' $Ni_{0.6-x}Mn_{0.4}Zn_xFe_2O_4$ (x=0.0-0.6) ferrites ……..…….223

d: Dielectric loss vs. temperature at 1MHz for 'as prepared' $Ni_{0.6-x}Mn_{0.4}Zn_xFe_2O_4$ (x=0.0-0.6) ferrites……...223

4.35 a: Dielectric constant vs. Temperature at 1kHz for 'sintered' $Ni_{0.6-x}Mn_{0.4}Zn_xFe_2O_4$ (x=0.0-0.6) ferrites…….…..…223

b: Dielectric loss vs. Temperature at 1kHz for 'sintered' $Ni_{0.6-x}Mn_{0.4}Zn_xFe_2O_4$ (x=0.0-0.6) ferrites…….....223

c: Dielectric constant vs. Temperature at 1MHz for 'sintered' $Ni_{0.6-x}Mn_{0.4}Zn_xFe_2O_4$ (x=0.0-0.6) ferrites……..……224

d: Dielectric loss vs. temperature at 1MHz for 'sintered' $Ni_{0.6-x}Mn_{0.4}Zn_xFe_2O_4$ (x=0.0-0.6) ferrites……..224

4.36 a: Initial permeability vs Log frequency of 'sintered' $Ni_{0.6-x}Mn_{0.4}Zn_xFe_2O_4$ (x= 0.0, 0.1, 0.2, 0.3, 0.4, 0.5, 0.6) ferrites……..…226

4.36 b: Tan δ vs Log frequency of 'sintered' $Ni_{0.6-x}Mn_{0.4}Zn_xFe_2O_4$ (x=0.0, 0.1, 0.2, 0.3, 0.4,0.5, 0.6) ferrites……226

4.37 a: Initial permeability vs Temperature of 'sintered' $Ni_{0.6-x}Mn_{0.4}Zn_xFe_2O_4$ (x=0.0, 0.1,0.2, 0.3, 0.4, 0.5, 0.6) ferrites……...228

4.37 b: Tan δ vs Temperature of 'sintered' $Ni_{0.6-x}Mn_{0.4}Zn_xFe_2O_4$ (x=0.0, 0.1, 0.2, 0.3, 0.4, 0.5, 0.6) ferrites……228

4.38 Gas sensing study of 'as prepared'$Ni_{0.3}Mn_{0.4}Zn_{0.3}Fe_2O_4$ at variable temperatures against oxidizing and reducing gases…….……232

4.39 A: % Response vs. composition of 'as prepared'$Ni_{0.6-x}Mn_{0.4}Zn_xFe_2O_4$ (x=0.0-0.6) ferrites at RT for LPG gas

B: % Response vs. Time for sample x=0.0 at RT for LPG gas, C: Plot of resistance vs. Time for sample x=0.0 at RT for LPG gas……..….233

4.40 a: The reproducibility plot of sample x=0.4, b:The reproducibility plot of sample x=0.6 …….234

4.40 c: CO_2-TPD profile of $Ni_{0.6-x}Mn_{0.4}Zn_xFe_2O_4$ (x=0.0, 0.3,0.6) ferrites……..……..236

d: NH_3-TPD profile of$Ni_{0.6-x}Mn_{0.4}Zn_xFe_2O_4$ (x=0.0, 0.3,0.6) ferrites……....237

4.41 Plot of specific capacitance versus scan rate of 'as prepared' $Ni_{0.6-x}Mn_{0.4}Zn_xFe_2O_4$ (x=0.0, 0.1, 0.2, 0.3, 0.4, 0.5,0.6) …….239

4.42 a:CV Plots of 'as prepared' $Ni_{0.6-x}Mn_{0.4}Zn_xFe_2O_4$ (x=0.0, 0.1, 0.2, 0.3, 0.4, 0.5, 0.6) ferrites……240

b: Galvanic charge/ discharge plots of 'as prepared' $Ni_{0.6-x}Mn_{0.4}Zn_xFe_2O_4$ (x=0.0, 0.1, 0.2, 0.3, 0.4, 0.5, 0.6) ferrites at current density of 1A g^{-1}…….242

c: The Nyquist plot of 'as prepared' $Ni_{0.6-x}Mn_{0.4}Zn_xFe_2O_4$ (x=0.0, 0.1, 0.2, 0.3, 0.4, 0.5, 0.6) ferrites……..243

4.43 Graph showing the effect of two different concentrations of $Ni_{0.6-x}Mn_{0.4}Zn_xFe_2O_4$ (x=0.0, 0.1, 0.2, 0.3, 0.4, 0.5, 0.6) ferrites on the percentage survival of *Staphylococcus aureus*……..……..247

4.44 Antibacterial activity of $Ni_{0.6-x}Mn_{0.4}Zn_xFe_2O_4$ (x=0.0, 0.1, 0.2, 0.3, 0.4, 0.5, 0.6) ferrites and control at (Conc: 500 µg/mL) on percentage survival of *Staphylococcus aureus*…….248

4.45 Antibacterial activity of $Ni_{0.6-x}Mn_{0.4}Zn_xFe_2O_4$ (x=0.0, 0.1, 0.2, 0.3, 0.4, 0.5,0.6) ferrites and control at (Conc: 1000 µg/mL) on percentage survival of *Staphylococcus aureus*…….248

Chapter 1

Introduction and Literature Review

1.1 Introduction

Nanotechnology has gained importance as it offers excellent materials with the potential to produce products with enhanced performance. Nanomaterials are a class of compounds having dimensions between 1 and 100 nm. Ferrites are one of the materials that come under the category of nanomaterials. Ferrum means iron in Latin, from which the word ferrite has been introduced. Their magnetic nature categorizes them as ferrimagnetic compounds. The properties that make ferrite an outstanding material are its extensive surface area and nano size, with ease of tuning as required. The ferrites are stable even at temperatures higher than 500 °C and have outstanding magnetic, optical, and electrical properties. Their properties change from nanoparticles to bulk. These materials are suitable for various purposes including its use as sensors and catalysts [1-5]. The properties of ferrites are influenced by its sample composition, the method involved in synthesis, surface and morphology, size, etc. For most applications, lower density, higher surface areas, and small-sized material are preferred; thus, the technique for synthesis is adopted accordingly.

Researchers in different fields like chemistry, metallurgy, physics, and engineering focus on developing ferrite materials with improved synthesis techniques according to the needs of rapidly growing new technologies, especially developing electronic components with dimensions suitable for the applications [6].

1.1.1 History of ferrites

Compounds of Iron (III) oxides are mostly referred to as ferrites, which are ceramic materials having magnetic properties. The first known ferrite material was a naturally occurring mineral, lodestone [7,8]. Magnetite (Fe_3O_4) or lodestone was recognised from the sixth century BC. The use of lodestone in compass-like devices used for navigation dates back to the fourth century BC [9].

William Gilbert scientifically explained the properties of lodestones in one of his published books in 1600 [10]. This was the first ever modern scientific detail given by anybody. Hundreds of years later, the work on electromagnetic theory and crystal structures was learned by various people. In 1819, it was discerned that the current in the wire would deflect the magnetic compass [11]. In 1909, Hilpert successfully synthesised spinel ferrites and studied their magnetic properties with a change in composition [12,13]. The first ever synthesis was carried out in 1930 when Yogoro Kato and Takeshi Takei at the Tokyo Institute

of Technology realized that iron oxide and various other divalent ions can produce ferrites, which are very useful in electrical applications. By 1935, they set up their company named TDK Corporation, and by 1937, they massively started the production of ferrite cores for wireless communication devices. Snoek, in 1935, developed high-resistance ferrite material with a low loss factor and high permeability [14]. Later in 1947, J. Snoek published a book named 'New Development in Ferrimagnetism' [15]. As the years progressed, a new concept of magnetism was proposed by Neel in the year 1948, which explained the magnetic properties of a non-magnetic ion-based ferrite, i.e., zinc ferrite. He explained ferrimagnetism; he suggested a two-sublattice model in which the spins interact, producing interesting magnetic properties. This paved the way to the development of microwave devices [16].

In the years between 1940 and 1950, the advancement in ferrite synthesis and production increased. Snoek and Verwey synthesized materials that could produce high resistivity and low relaxation losses, which could be utilized to generate ferrite cores for different applications. They successfully produced hexaferrite ($BaFe_{12}O_{19}$) using cost-effective materials and techniques, and materials with high coercivity values. Years later, strontium hexaferrite was developed, which had enhanced and improved properties. The ferrites are since used worldwide in various applications like antennas, recording devices, ferrite cores, EMI suppressors, transistors, etc. In modern times, these materials have entered into medicine and quantum computing, as sensors, supercapacitors, and antimicrobial agents. Due to their economical and straightforward method of synthesis, stability, and tremendous properties that they showcase, they are exploited ever since.

The research in this field further continued, with development of garnets, hexagonal and ortho ferrites paving their way in, in the years 1950 to 1956 as reported by Went et al. [17], Bertaut et al [18] and, Frostier et al. [19,20,21], respectively. The stacking of ions in tetrahedral A site and octahedral B sites was first given by Verwey et al. [22], while Anderson reported the antiferromagnetic superexchange interactions in ferrite [23]. The uniaxial anisotropy in cobalt ferrite was first noted by Iida and his co-workers [24,25]. Copper-zinc ferrite was first utilised for its antenna core applications in Japan, and in the following years, modified Ni-substituted Cu-Zn ferrites were also developed [26].

The golden era of ferrites began from 1935 to 1970, when many technological advancements in ferrites were developed concerning the synthesis and materials properties. Further, in the

1990s, the improvement in magnetic properties with changing dopant composition and synthesis techniques was studied. Various mixed ferrites were learned during this time to explore their applications. Suyal et al [27] investigated the high-frequency power applications of Mn-Zn ferrites, Ba-Ni hexaferrites were synthesised by Shin and others [28] for their applications as microwave absorbers. Many reports are available on Ni-Zn ferrites, with different approaches [29,30]. Ni-Co-Zn ferrites were also inspected for their microwave absorber capacity [31]. Ferrites as inductors [32-34], magnetic heads [35,36], optical recorders [37,38], and anticorrosive paint [39] were a few other applications under study. In recent times, the need of ferrites in the biomedical field has been profound and increasing because of their properties [40-42]. Catalysis and wastewater treatment are a few more applications of ferrite material owing to their excellent optical and ferri-magnetic properties [43,44].

1.1.2 Crystal structure of ferrites

Ferrites can further be classified depending on their crystal structure type, namely:

i) Spinels
ii) Hexagonal
iii) Perovskites
iv) Garnets

A simple spinel ferrite can be identified by its universal formula of AB_2O_4, where 'A' is a divalent metal (Zn, Ni, Mn, Ca, Co, Mg, etc) ion, while 'B' is the trivalent Fe atom. This ferrite type is derived from a mineral analogous to ferrite, i.e., spinel $MgAl_2O_4$.The spinel crystal structure comprises of a unit cell of 32 closed-packed oxygen atoms. Between the oxygen atoms in the unit cell, two different sites are available, namely the tetrahedral or the A site, and the octahedral or B site. The smallest unit comprises of 32 octahedral sites and 64 tetrahedral sites. Out of the 64 sites, only eight are filled in tetrahedral sites, and only 16 are filled in octahedral sites. Therefore, eight cations are present in the tetrahedral site, and 16 cations are present in the octahedral site. In total, in the unit cell, there are 56 atoms, of which 32 are anions and 24 are cations in an eight-formula unit [45]. The ferrite spinel material possesses the Oh7 Fd3m space group and the 227-space group number. The oxygen anion is not present precisely at the FCC lattice, but the oxygen ion parameter 'u' determines its exact position. The readjustment to accommodate the cations in sites with different radius ratios conferred the parameter u. When u=3/8, the packing is done exactly within the lattice.

The occupation of metal ions on the respective lattice sites depends on several factors, such as

i. The electrostatic energy caused by attraction and repulsion between anions and cations.
ii. The polarisation energy of anions.
iii. Electronic configuration and CFSE.
iv. The energy of ordering ions on the sublattice, thus acquiring electrostatic energy
v. Magnetic ordering energy.

The occupation of a specific metal site relies on the stabilisation energy of that site. The degenerate d orbital electrons are lifted under the application of electrostatic anions, resulting in splitting, which is called the crystal field stabilisation energy. The CFSE values were calculated by Maclure [46] and Dunitz and Orgel [47]. These values obtained in the reports indicate the site preferences for cations in the spinel ferrite structure. Furthermore, site preferences including transition and non-transition metals were deduced by calculating site preference energies by Miller [48], his extended CFSE calculation incorporated Madelung constant and short-range energy terms such as Coulomb and valence terms. These predictions were in agreement with experimentally determined data.

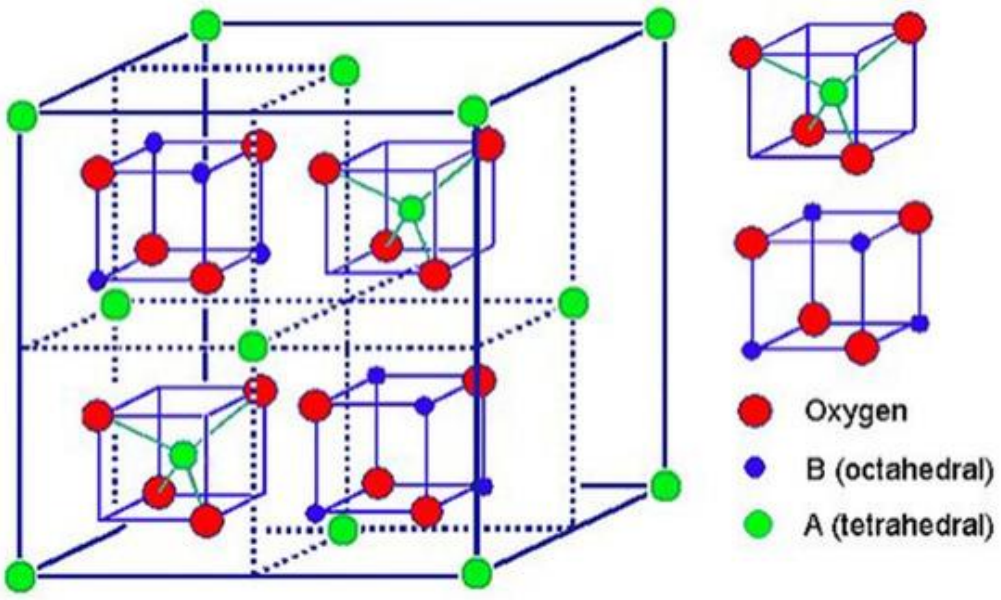


Fig. 1.1: Spinel structure of ferrite unit cell

Furthermore, these spinel ferrites are classified based on preferences of the divalent and trivalent metal ions at tetrahedral and octahedral sites. The spinels can be classified into

three types, namely normal spinels, inverse spinels, and random spinels, depending on the occupancy of the metal ions in tetrahedral or octahedral sites as suggested by Barth and Ponjak [49,50].

In the case of normal spinel, the divalent metal ion is present in the tetrahedral site while the trivalent metal ion is in the octahedral site. Examples of such ferrites are $ZnFe_2O_4$ and $CdFe_2O_4$. Though Zn^{2+} is larger, it prefers a tetrahedral position instead of a larger octahedral site because its electronic configuration prefers tetrahedral bonding to the oxygen atom. The other type of spinel is the inverse spinel in which half the trivalent ions are present in the octahedral site while the remaining half are present at the tetrahedral site. Here, the divalent ion occupies the octahedral site. $NiFe_2O_4$ is an example of an inverse spinel-type structure. Eight units of $NiFe_2O_4$ are present in the unit cell. Half the Fe^{3+} ions occupy the tetrahedral site while the other half are filled in the octahedral site along with the eight Ni^{2+} ions. The Fe^{3+} and Ni^{2+} ions are arranged antiparallel to the eight Fe^{3+} ions in the tetrahedral site. Due to the antiparallel arrangement of Fe^{3+} in tetrahedral and octahedral sites, the magnetic moment cancels out, but the moments on Ni give rise to the magnetisation. The third class of compounds is called random spinels, where the 2+ and 3+ ions are equally distributed between tetrahedral and octahedral sites.

Hexaferrites have a general formula of $MFe_{12}O_{19}$; their crystal structure is similar to that of the mineral magneto plumbite. Two of the known hexaferrites are $BaFe_{12}O_{19}$ and $SrFe_{12}O_{19}$.

Perovskite material has a general formula of ABO_3. The first ever perovskite discovered was calcium titanium oxide ($CaTiO_3$)

Garnets form an essential class of ferrimagnetic compounds exhibiting interesting electromagnetic and thermal properties. They have a general formula of $A_3B_5O_{12}$. One of the most common examples is ytterium iron garnets.

1.1.3 Classification of spinel ferrites depending on their magnetic properties.

a. Soft ferrites: These ferrites hold high magnetic permeability and low coercivity. Once magnetised, they can easily be demagnetised, which makes them suitable for high-frequency applications, such as in transformers, as electronic components in devices, and inductors. Most common examples of soft ferrite are manganese zinc ferrite and nickel zinc ferrite. Soft ferrites also

show high magnetic shielding capacity and find use as EMI suppressors in many devices.

b. Hard ferrites: These materials are tough to demagnetize once magnetized. They have high coercivity values and low permeability. They are used in making permanent magnets. The most common examples of hard ferrite are strontium ferrite and barium ferrite. These ferrites are primarily used in motors, speakers, and magnetic separators.

1.1.4 Magnetic properties of ferrites

Ferrites are magnetic owing to the presence of Fe in the samples. Magnetism is a consequence of the spin and orbital movement of electrons. When magnetic material is placed in an applied magnetic field, the spins align in a particular fashion, giving rise to various types of magnetism. The material thus can be classified into diamagnetic, paramagnetic, ferro/ferrimagnetic, and antiferromagnetic based on the alignment of the spins. The diamagnetic and paramagnetic materials are weakly magnetic compared to ferrimagnetic, ferromagnetic, and antiferromagnetic samples [51,52].

I. Diamagnetic material: The materials in which the electronic shells are filled, i.e., they are paired, thus cancelling out the magnetic moment, giving rise to magnetism referred to as diamagnetism. This type of magnetism is lacking form and is non-persistent. The material is weak or does not repel the externally applied force. And the lines of force do not pass through the material. They possess small negative susceptibility independent of temperature. Their permeability is less than one.

II. Paramagnetic material: The samples that possess unpaired electrons show paramagnetism. These materials have small positive susceptibility. They possess permeability greater than one. This type of compound is attracted to the applied field—the magnetic lines of force pass through material. The spins align according to an applied magnetic field, but if removed, they disorient immediately.

III. Ferrimagnetic material: The materials possessing ferrimagnetism are those whose spins are antiparallel with uneven magnitude. Thus, producing a permanent magnetic moment. There is net magnetisation due to the unequal opposite arrangement of spins.

IV. Antiferromagnetic material: These are materials similar to ferrimagnetism. They also possess opposite spins but with equal magnitude. This results in the cancellation

of the magnetic moments, producing zero magnetisation. They show low susceptibility and high permeability. When antiferromagnets are subjected to temperature, the susceptibility increases up to Neel's temperature, above which a decrease is encountered, leading to the paramagnetic character of the sample rising with temperature.

In ferrites, the metal ions are present in the octahedral B-site or the tetrahedral A-site, as Neel's model suggests. Metal and oxygen ions can interact through super-exchange interaction in three ways: A-A, B-B, and A-B. In the case of A-A interaction, two ions from the A-site interact with each other, and the same is the case for B-B interaction. In A-A and B-B interactions, the ions are at the same site. While in the A-B interaction, the A and B ions are from two different sites. The spins are aligned antiparallelly and possess negative energy. The sublattices have small magnetization due to their unequal magnetization [53-55]. The extent of energy between the metal and oxygen depends on i) the angle between the metal and oxygen, and ii) the distance between the M-O. The energy is highest in A-B interactions, followed by B-B, and lowest in A-A interactions [56].

1.1.5 Magnetic Hysteresis

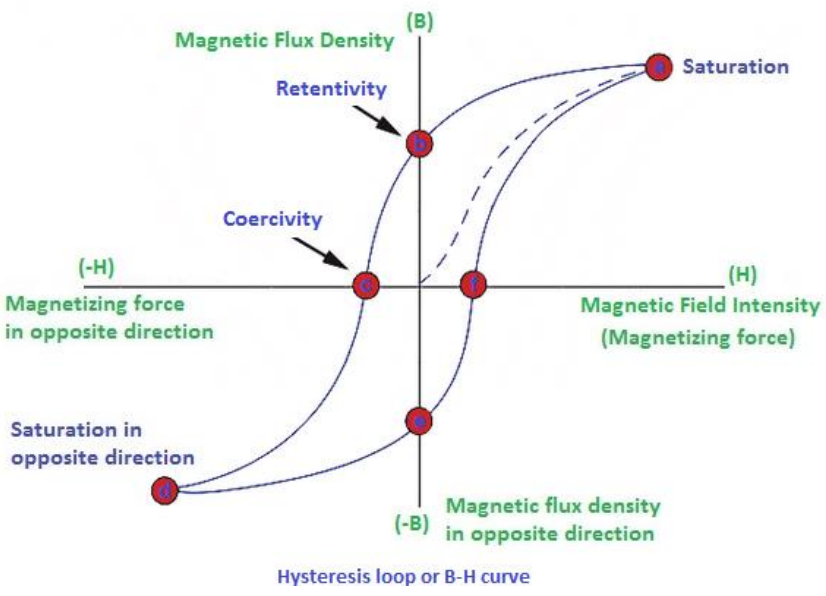


Fig. 1.2: Hysteresis curve

Figure 1.2 represents the hysteresis curve of magnetic ferrite material. Upon exposure to the external magnetic field, the material exhibits a hysteresis loop in its magnetisation response. After the magnetisation is removed, the material retains a remanent magnetisation

characteristic of ferromagnetic behaviour. An opposite magnetic field removes or reduces the magnetization to zero. Saturation magnetisation (M_s) represents the maximum saturation attained by the material, i.e., with an increase in applied field, there is no further change in M_s, which is called saturation magnetisation. Coercivity (H_c) is the ferromagnetic material's ability to remain magnetised and withstand an external magnetic field. Even after removing the magnetic field, the magnetization that is retained by the material is termed as remanent magnetization (M_r).

1.1.6 Electrical and Dielectric Properties

Transition metal ferrites are found to be extensively used in microwave frequency applications because of their lower electrical conductivity. These compounds are semiconducting, and their resistivity is between 10^{-2} and 10^{11} ohm.cm [57]. The conductivity results from the hopping of electrons between the metal present in two different oxidation states. Generally, conductivity arises in Fe in 2+ and 3+ valence states due to the movement of the holes or electrons in the lattice. These form the basis for semiconducting behaviour in Ni and Co ferrite as reported successfully by Jonker and Elwell et al. [58, 59]. The electronic exchange between cations and electrons or holes causes polarization of the region around them. The carrier is trapped in the lattice, and hopping to neighbouring metal ions is determined via thermal activation. The hopping of electrons is proportional to $e^{A/kT}$, where 'A' is activation energy, 'k' is Boltzmann's constant, and 'T' is absolute temperature. Various factors are responsible for resistivity, such as porosity in the samples, grain size, sintering temperatures, inhomogeneity of the samples, etc. [60]. Ferrites possess a high dielectric constant, which varies as the frequency is changed from Hz to the MHz region. The system acquires an electric dipole moment when such material is placed in an alternating magnetic field. Thus, the dipole moment for each unit volume is referred to as polarization. The dispersion in dielectric properties has been given by Koop's [61].

1.2 Literature Review

1.2.1 Literature review on Methods of preparation

1.2.1.1 Literature Review on Combustion Method

Combustion technique depends on the principle of propellant chemistry. The technique is self-propagating or self-sustaining, i.e., it requires no external heat or energy [62]. This exothermic reaction produces large gases, porous material, and nano-sized particles. The heat generated in the process is sufficient for the continuity of chemical change to occur. This is an oxidation-reduction reaction and involves the oxidiser: fuel ratio. It is calculated by assessing the metal, carbon, and hydrogen as reducing in nature, having valences of 2+/3+, 4+, and 1+, respectively. Nitrogen is supposed to have zero valence, and oxygen to have a 2- valence. Thus, the morphology of material changes depending upon the heat and gases released during the process [63-65], resulting in varying solid-state properties of the compounds.

Selvan et al [66] produced Cu ferrite using urea as fuel for combustion. The tetragonal structure was revealed from XRD. The resistivity studies showed a decreasing trend with an increase in heat, thus confirming the semiconducting nature of the samples. Nickel zinc ferrite was fabricated by Hwang et al. [67] via the combustion method using different fuels: carbohydrazide, glycine, alanine, urea, and citric acid to study its effect on various properties. Using carbohydrazide as fuel resulted in the largest particle size, whereas the smallest particle size was achieved when urea was used as the fuel. M_s values were reported for the samples, out of which the sample prepared using glycine results in maximum magnetisation. Balaji et al [68] synthesised Sn-doped Ni ferrite using urea as the fuel. XRD confirmed a single phase with no impurities and a crystalline nature of the samples. DC conductivities recorded at increasing temperatures showed a continuous increase. Depending on its structural and electrical properties, the synthesized material was a good candidate for an anode material. Bahadur et al [69] produced ferrite with different metal: fuel ratios of 1:1, 1:2, 1:3 via the auto-combustion technique using citric acid as the fuel. The sample synthesised with a ratio of 1:2 was found to be single-phase, pure crystalline. VSM studies revealed the saturation magnetisation of 55 emu/g and coercivity of 5000 Oe. The zinc ferrite was prepared using polyethylene glycol as fuel to facilitate the reaction. The samples were obtained in pure and cubic spinel structures. XRD confirmed the nano size with 45 nm as the crystallite size as reported by Swamy et al. [70]. In another report,

Salunkhe et al. [71] studied various metal nitrate to fuel combinations. As the ratio increased, the particle size was seen to increase as well. The saturation magnetisation reported for fuel-deficient was 33 emu/g, fuel-appropriate was 45 emu/g, and the high fuel content sample showed saturation magnetisation of 59 emu/g. Manganese-substituted copper ferrite was synthesised by varying the fuel content (50, 75, and 100%) by Kumar et al. [72]. With the rise in fuel content, the particle size increased, whereas the saturation magnetisation decreased. The dielectric properties were studied with respect to frequency, and a decline in dielectric constant was observed as frequency increased. Kooti et al. [73] developed pure nickel ferrite using glycine as the fuel. Three different metal fuel combinations were chosen for the study, and it was observed that the sample containing the highest fuel concentration contained slight impurities. The particle size grew with the escalation in fuel content. SEM revealed spongy agglomerate morphology. M_s and H_c values shrinked with an addition in fuel content. Hajarpour et al. [74] synthesised Mn ferrite with increasing Zn content using glycine as the fuel. The combustion temperature elevated with zinc content. The size of the crystals was found to be 34-49nm, and the samples were monophasic in nature. The lattice constant was calculated using Vegard's law and was found to increase with increase in zinc content. SEM revealed a large porous morphology of the particles. Similarly, in another report, S. Hajarpour et al. [75], systematically examined the influence of varying glycine-to-metal ratios on structural and magnetic behaviour of synthesised Mn-Zn ferrite. The magnetic properties were also investigated of the samples, wherein coercivity was found to increase and remained constant with higher fuel ratios. Mn-doped cobalt ferrite (0.0 to 0.4) was developed by Salunkhe et al. [76] using glycine as the fuel. XRD patterns indicated the formation of a pure phase. The magnetic measurements were carried out using a VSM instrument, which determined that saturation magnetisation increased with Mn content up to sample x=0.3, followed by a decrease for x=0.4. $Mn_{0.6}Zn_{0.4}Fe_2O_4$ was synthesised using glycine, citric acid, and citric acid-EDTA mixture as fuels, producing three samples. XRD pattern revealed a single phase and cubic structure of the samples. The citric acid-EDTA mix fuel sample had the particles with smallest size and spongy morphology, indicating the presence of large pores in the samples as reported by Szczygiel et al. [77]. Manikandan et al. [78] synthesised Mg ferrite doped with manganese using the microwave-assisted combustion method, using urea as the fuel. The effect of Mn content on size and lattice parameter was studied and it was observed that, as Mn content increased, crystallite size decreased while lattice parameter increased. The bad gap of this material was also determined and it was observed that as the Mn content decreased, the band gap increased

from 2.0 eV to 2.32 eV. The photocatalytic property was greatly enhanced with the addition of TiO_2. Sample $Mn_{0.5}Mg_{0.5}Fe_2O_4$-TiO_2 showed the best results for photocatalytic decomposition of 4-chlorophenol. Cobalt ferrite was synthesised by Prabhakaran et al. [79] using DL alanine as the fuel. The ferrite samples were annealed at 500 °C and 800 °C to investigate the effect of heat treatment on parameters such as crystallite size, phase formation, purity, and Curie temperature. When the sample was calcined at 500 °C, no impurity peaks were obtained in the XRD pattern, thus confirming single-phase cubic spinel structure formation, while at 800 °C, the single phase was not observed. The T_c at 800 °C was also found to be lower than that of the as-prepared ferrite. Cobalt ferrite was synthesised by Babu et al. [80] using glycine-analine amino acid mixture as the fuel. Various fuel ratios were considered for the study, keeping the ratios fuel-deficient. All the samples were pure and crystalline, and the crystallite size ranged from 39-43 nm. Variation in saturation magnetisation was observed based on hysteresis curve data with values 4 to 49 emu/g. $NiCrFe_2O_4$ and $CoCrFe_2O_4$ were synthesised by taking glycine as the fuel. The samples were prepared in stoichiometric metal nitrate and fuel, fuel-deficient, and fuel-efficient combinations. The sample with a fuel deficiency caused the formation of an impurity phase, while the 1:1 and fuel-efficient ratios were formed in pure phase. 1:1 ratio had the lowest Ms value, and anisotropy and blocking temperature were affected by metal nitrate to fuel conditions [81].

Gawas et al. [82] synthesised Mg-doped Ni-Zn ferrite $Mg_xNi_{0.6-x}Zn_{0.4}Fe_2O_4$ (x=0.0 to 0.6). A novel fuel malic acid dihydrazide was prepared using diethyl malate and hydrazine hydrate. The fuel was thoroughly characterised by IR and NMR spectroscopy. A series of samples with varying metal nitrate to fuel ratios were synthesised, among which the optimal ratio was identified, characterised, and used to prepare the final compounds. The chosen ratio was 1:0.7, for which further studies were carried out. XRD patterns revealed a single-phase pure material with a cubic spinel structure. The magnetic parameters declined as the Mg content increased. Coutinho et al [83] synthesised Ni-doped Cd-Co ferrite using hexamine as the fuel. The fuel-deficient ratio was chosen for the study. XRD and IR confirmed phase purity and formation of spinel ferrite. Ms value were found to rise and fall after a specific composition, which is explained by the Yafet-Kittel model. With the rise in Nickel content, the blocking temperature was reduced, as obtained from ZFC/FC curves. Curie temperature also increased with Ni content, and the dielectric constant decreased with frequency and became constant. $Ni_{0.5}Co_{0.5}Fe_2O_4$ was synthesised by Sedhgi et al [84] using different fuels such as urea, citric acid, and glycine, and studied their effect on various

properties. Among all the fuels, samples prepared using urea showed an impurity phase, thus eliminating urea as a fuel for the synthesis of samples. The fuel also affected the size of the materials. Magnetic properties and coercivity were also determined, from which Ms and Mr were determined. Ni-Zn ferrite was synthesised with Al as a dopant using malic acid as fuel. The cation distribution was confirmed via Rietveld refinement and Mossbauer spectroscopy. SEM images confirmed spherical nano-sized particles. The particle size distribution was determined by histogram analysis, revealing a relatively uniform size range. Additionally, magnetic measurement indicated that the Curie temperature decreased progressively with increasing Aluminium content, suggesting weakening of magnetic interactions due to Al substitution. Similarly, the magnetic parameters like saturation magnetisation, coercivity, and remanence decreased with increase in Al content [85].

1.2.1.2 Literature review on Precursor -combustion method

Metal-hydrazinated carboxylate compounds are known to be thermoactivated. This intermediate is a single source precursor; therefore, it has proven to yield compounds of highly pure phases, stoichiometric, in nano size, and at considerably low temperatures. $(N_2H_5)Ni_xZn_{1-x}Fe_2(N_2H_3COO)_9.3H_2O$ precursor was decomposed to obtain Ni-Zn (x=0.2 to 0.8) ferrite material as reported by Ravindranathan et al. [86]. TG-DTA studies revealed a low decomposition temperature of 120- 220 °C. The samples were reported to have a nano-crystallite size of 10-14nm, and the surface area determined from nitrogen isotherms was found to be 42-104m^2/g.

Kanade et al [87] synthesised Mn-Zn ferrite from a precursor combustion technique, having the formula Mn-Zn-$Fe(C_2O_4)_3.4N_2H_4$. The sample decomposed at 500 °C in two steps: dehydrazination and decarboxylation. XRD revealed a pure phase in the system with no impurity peaks. Magnetic characterisation was carried out via VSM, which showed Ms of 35 emu/g and coercivity of 128Oe. Mossbauer studies revealed Fe in the respective oxidation state, and the material was said to possess a superparamagnetic nature. Angermann et al. [88] synthesised pure-phase Mn-Zn ferrite by calcining the $Mn_{0.229}Zn_{0.078}Fe_{0.694}(CO_3)$ at 500 °C. The TG curve revealed the decomposition temperature to be 300 °C. VSM studies revealed the saturation magnetisation to be 66emu/g.

Naseri et al. [89] synthesised manganese pyrrolidone precursor, which was decomposed to obtain the desired pure ferrite. The calcination was done at various temperatures, and their effect on multiple properties was studied. An increase in calcination temperature was accompanied by increase in particle size. Gupta et al. [90] formulated Rubidium ferri-

carboxylate precursor. They used different carboxylate sources like formic, propionic, acetic, and butyric acids. Leng et al. [91] developed $Ni_{0.25}Zn_{0.75}Fe_2O_4$ from a metal salt and polyvinyl pyrrolidone precursor. The precursor underwent calcination at a range of temperatures to study the effect of thermal treatment on the properties. The crystallite size increased from 7-25 nm while the saturation magnetisation increased from 11-126 emu/g with the rise in calcination temperature. Co-Zn ferrite was synthesised via the precursor method by Gonsalves et al. [92-94]. The TG-DTA method showed the decomposition of the precursor in two steps. The ferrite material was formed after decomposition of the precursor via dehydrazination and decarboxylation process. The author also reported several other reports on a similar preparation method in which they synthesized Co-Ni ferrites [95,96]. U.B. Gawas et al. [97] synthesised Mn-doped Ni-Zn ferrite having the general formula $Ni_{0.5-x}Mn_xZn_{0.5}(C_4H_2O_4)_3.6N_2H_4$ with varying composition from x=0.0-0.5. They thoroughly evaluated the precursor, which gave them an idea about bonding in the precursor. The hydrazine was present as a bidentate linkage, while the fumarate dianion showed a monodentate linkage, as revealed by IR spectroscopy. The purity of the developed ferrite was confirmed via XRD. The author also published reports on similar work and the same synthesis route [98-103]. $Ni_{0.4}Co_{0.2}Zn_{0.4}Fe_2O_4$ composition was prepared by Gawas et al. [104] via a similar method. The precursor was made up of hydrazine-fumarate, which helps catalyze the desired product's decomposition. Various instrumental techniques confirmed the formation of pure ferrite material in the nano-range. Resistivity studies revealed semiconducting behaviour of the samples, while dielectric studies, when conducted at RT at variable frequencies, showed a decline in dielectric constant with an increase in frequency.

Gawas et al synthesised $Co_xNi_{0.6-x}Zn_{0.4}Fe_2O_4$ ferrite (x=0.1 and x=0.4) by decomposing the synthesised precursor. The sample had a crystallite size well within the 26-30 nm nano-range as revealed by XRD data. Particle size characterisation was carried out using TEM, and the crystallinity was confirmed by SAED [105].

Coutinho et al. [106] synthesised $Ni_{0.5}Co_{0.5}Fe_2O_4$ via precursor combustion method. The precursor included metal salts, hydrazine, and succinic acid, which form the fuel and ligands in the compound. XRD revealed nano-pure phased ferrite while SEM confirmed spherical nano ferrite. Solid state properties, such as magnetic and dielectric properties, were also investigated.

1.2.2 Literature review on Ni-Co-Zn and Ni-Mn Zn ferrites

1.2.2.1 Literature Review of Ni-Co-Zn Ferrites

F. Schnettler et al. [107] studied the permeabilities of several Ni-Zn-Co ferrites, analysing their behaviour across different frequencies. The study revealed that initial permeability and relaxation frequency were closely linked to specific compositional and structural factors. M. Mizushima [108] prepared cobalt-substituted nickel-zinc ferrite by the ceramic method. The imaginary part of permeability was linearly related to the fundamental part of magnetic permeability; both increased when exposed to a demagnetized field. Also, both were found to decrease when annealed at high temperatures. J. Kulikowski et al. [109] prepared cobalt-substituted nickel-zinc ferrite and studied the effect of cobalt content on the magnetostriction of Ni-Zn ferrites.

H. T. Hahn [110] synthesized $Co_xNi_{0.5-x}Zn_{0.5}Fe_2O_4$ (x=0.033 to 0.50) ferrites and researched the impact of cobalt substitution for nickel in the high-loss, high-frequency area. Their main emphasis was on increased losses. There was a slight decrease in density with a larger reduction in relaxation time and equilibrium susceptibility for samples having composition x=0.04 to 0.50. At lower frequencies, samples having composition x=0.03 to 0.04 showed increased magnetic loss. B. Parvatheeswara et al. [111] prepared $Ni_{0.35}Zn_{0.65-x}Co_xFe_2O_4$ ferrites by the ceramic method. The phase obtained was pure, and the samples were crystalline, as revealed by the PXRD technique. The magnetic measurements, permeability, and loss measurements were also carried out. There was an increase in magnetic moment and relative loss factor, while permeability was reduced, with the doping of cobalt ions. X. Shen et al. [112] prepared Ni-Zn-Co ferrite granular films of 1.5 μm in thickness and were prepared on glass substrates by the spray plating method at 900 °C. The fabricated thin films were analysed by electron microscopy, and the hysteresis loops were measured via a vibrating sample magnetometer. The film exhibited large saturation magnetization while the coercivity value was small. The permeability of the thin film at reduced frequency was about 89, and the resonance frequency reached a maximum of 61.7 at as high as 2.1 GHz. The losses were higher than 15 over a broad frequency range from 1 to 3.5 GHz.

J. Xie et al. [113] had investigated the synthesized material for its efficiency as a microwave absorbing material. The ferrites were obtained using the ceramic method. PXRD verified the material in the nano-range, and the peak width and intensity confirmed the crystallinity of the material. The XPS techniques verified the elements in the compounds. Cumulating the

entire data concludes that the ferrite can be used as an EM absorber material. $Ni_{0.25}Co_{0.25}Zn_{0.5}Fe_2O_4$ ferrite was synthesized by O. Suwalka et al. [114] via the co-precipitation approach. The magnetization studies revealed that the magnetic parameter decreases while coercivity rises till the particle size of the sample reaches 23nm, but then tends to fall with annealing temperature. The Mössbauer studies revealed that with increasing annealing temperatures, there is a difference between the hyperfine magnetic fields at the B sites. M. Kim et al. [115] investigated the effect of doping of cobalt, sintering temperature, and absorber thickness on the electromagnetic wave absorption properties in a thin sheet of $(Ni_{0.4}Co_xZn_{0.6-x}O)_{1.02}(Fe_2O_3)_{0.98}$ ferrite produced by co-precipitation method, giving a pure phase to the compound as verified by PXRD. The particle sizes of all the samples ranged from 32 to 49 nm and were calculated using the Debye-Scherrer formula. When the thickness of sheet-type microwave Ni-Co-Zn ferrite absorbers was 2 mm, they were most reflective. Consequently, it was proposed that it could serve as a ferrite-rubber composite microwave absorber when sintered at 1250 ^{0}C. The initial permeability of the NiCoZn ferrite powder sintered at 1250 °C was less than other temperatures. A. K. Subramani et al. [116] conducted a study on Ni-Co-Zn ferrite via the spin-spray plating technique at a relatively low temperature of 900 °C. A series of these films was produced to investigate their structural and magnetic characteristics. Scanning electron microscopy revealed a columnar microstructure aligned perpendicular to the substrate surface. The films exhibited a saturation magnetisation value ranging from 325-520emu/cc and coercivity between 5 and 20 Oe. At optimised composition, the film achieved an initial permeability of approximately 190 and a resonance frequency of 300MHz. Due to their higher permeability, these films are promising candidates for use in trimming conductor layers to enhance inductance. Additionally, those with high resonance frequencies are well suited for application in high-frequency electromagnetic noise suppression.

Z. W. Li et al. [117] investigated $Ni_{0.97-x}Zn_xCo_{0.03}Fe_2O_4$ spinel ferrites with compositions x=0.5 and 0.65. To synthesise the ferrite, a stoichiometric mixture of NiO, ZnO, Co_3O_4, and Fe_2O_3 was prepared and calcined at 1080 °C for four hours. The calcined materials were then crushed, ball milled, pressed into shape, and sintered at temperatures ranging from 1200–1300 °C for 4 h. The resulting spinel ferrites exhibited excellent EM attenuation properties characterised by low reflectivity and a broad absorption bandwidth within the very high frequency and ultrahigh frequency ranges. The permittivity had a direct relation with the sintering temperature.

J. S. Ghodake et al. [118] worked on Co-substituted Ni–Zn ferrites formulated by the co-precipitation method using oxalate precursor. With the addition of Co, the lattice parameter, magnetocrystalline anisotropy constant ($K1$), and magnetostriction constant (λs) showed an increase, and the grain size decreased; hence, the value of permeability (μi) decreased, whereas saturation magnetization (M_s), and magnetic moment (n_B) remained constant throughout across all the samples. S. B. Waje et al. [119] studied the physical and magnetic properties of cobalt nickel zinc ferrite synthesised from mechanically alloyed nanoparticles with particle sizes ranging between 10-50 nm. The initial permeability (μ') and permittivity were evaluated as functions of frequency and sintering temperature. The results showed that permeability increased with rising sintering temperature, while permittivity increased with the larger grain sizes. K. C. Mouli et al. [120] investigated nickel-substituted cobalt zinc ferrite, prepared using the co-precipitation method. The X-ray diffraction analysis confirmed the formation of a single-phase face-centered cubic (fcc) spinel structure. As the nickel concentration increased, the lattice parameter decreased. The saturation magnetization decreased sharply with the substitution of small amounts of Ni for Co; however, beyond x = 0.20, no significant variation in magnetization was observed. M. M. Mallapur [121] investigated cobalt-substituted nickel-zinc ferrites (x 0.0 and 0.3) synthesised via the precursor method. The XRD technique was employed to estimate the crystallite size, which ranged between 10-20 nm. Similarly, TEM images further confirmed the particle sizes of approximately 10 nm. An increase in cobalt content led to a corresponding enhancement of magnetization. M. S. Khandekar et al. [122] synthesised $Ni_{0.35-x}Co_xZn_{0.65}Fe_2O_4$ (x=0.00 - 0.10) ferrites using the co-precipitation oxalate precursor method. The XRD pattern confirmed the formation of a single-phase structure. The gradual reduction in both lattice parameter and x-ray density was observed with an increasing cobalt content. A decline in initial permeability was also reported, attributed to a reduction in grain size, lowered saturation magnetisation, and increased magnetocrystalline anisotropy. S. Waje et al. [123] fabricated $Co_{0.2}Ni_{0.3}Zn_{0.5}Fe_2O_4$ ferrite via mechanical alloying followed by sintering. As the sintering temperature increased, porosity decreased, while both density and shrinkage in the material increased. The sample sintered at 1200 °C exhibited the highest saturation magnetisation of 83emu/g. The coercivity and remanence values were found to diminish with rising temperatures.

M.A. Amer et al. [124] utilised the ceramic technique to prepare $Zn_{0.35}Ni_{0.65-x}Co_xFe_2O_4$. The studies of these samples were carried out using room temperature Mössbauer, X-ray, and infrared spectroscopy. The phase obtained was found to have no impurities. The Mössbauer

analysis showed a paramagnetic phase for x=0 and a six-line magnetic pattern and a central paramagnetic phase for x=0.1. K. Raju et al. [125] prepared $NiFe_2O_4$, $Ni_{0.50}Zn_{0.50}Fe_2O_4$, and $Ni_{0.50}Zn_{0.25}Co_{0.25}Fe_2O_4$, ferrites by wet chemical citrate sol–gel process. The main aim was to investigate the doping impact with different cation and their effect on magnetic properties. The XRD uncovered a single phase, while the SEM confirmed the particle size of 100nm. The stoichiometric studies were done by energy-dispersive spectroscopy. The doping of nickel in cobalt zinc ferrite enhanced the magnetic properties as revealed by VSM. M. C. Varma et al. [126] investigated the cobalt substitution and change in framework and magnetic response of $Ni_{0.65-x}Zn_{0.35}Co_xFe_2O_4$ ferrites. The XRD revealed the formation of a structurally consistent cubic spinel phase. The X-ray diffraction analysis, FT-IR spectroscopy, theoretical calculations, lattice constant calculations, and measurements of saturation magnetization suggested that Co^{2+} ions occupy both [A] and [B] sites. Based on these findings, a cation distribution model for $Ni_{0.65-x}Zn_{0.35}Co_xFe_2O_4$ was proposed. This model provided further insights into changes in magnetic anisotropy, thereby aiding the understanding of variation in saturation magnetisation, coercivity, and initial permeability in relation to the shift in critical frequency. The composition $Ni_{0.2}Co_{0.2}Zn_{0.6}Fe_2O_4$ was employed in the design of resonator antennas (FRA) and analysed in cylindrical, triangular, and cuboid shapes by K. Mohita et al. [127]. The antenna performance was simulated using high-frequency structure simulation (HFSS) software, and a good, strong correlation was found between the experimental measurements and simulation outcomes. Among the different shapes, the cuboid-shaped FRA exhibited the highest bandwidth of 990 MHz, whereas the cylindrical-shaped FRA achieved a maximum gain of 3.34 dB.

P. Liu et al. [128] developed novel composites of $Ni_{0.4}Zn_{0.4}Co_{0.2}FeO_4$ ferrite particles anchored onto reduced graphene oxide sheets using a straightforward, efficient, and controllable three-step synthesis process. The structural, morphological, and compositional characteristics of the composite were thoroughly analyzed using techniques such as Fourier Transform Infra-red spectroscopy, X-ray diffraction, elemental analysis, thermogravimetric analysis, Field-emission scanning electron spectroscopy, and transmission electron microscopy. The characterization confirmed that the modified ferrite nanoparticles were evenly distributed and firmly attached to the r-GO nanosheets. Microwave absorption performance was assessed at room temperature over a frequency range of 2- 18 GHz. The composite demonstrated a minimum reflection loss of -51.8 dB. at 15.1GHz with a material thickness of 2.1mm. owing to its outstanding microwave absorption performance, this

innovative composite shows great potential as a lightweight material for electromagnetic wave attenuation.

A. Hassan et al. [129] adopted the co-precipitation method to fabricate single-phase cobalt and nickel-substituted zinc ferrites. The lattice constant was found to decrease as the addition of Ni and Co concentration increased, as they are replaced by zinc, having a higher ionic radius (0.82Å). The magnetization studies showed an uplift initially followed by a decrease. The remanence and coercivity were observed to be inconsistent. There was a change in the dielectric constant and an uplift in DC-resistivity. R. Kumar et al. [130] synthesized $Ni_{0.6-x}Zn_{0.4}Co_xFe_2O_4$ (x= 0.0, 0.03, 0.09, 0.27) nanoparticles using a sol-gel method and annealed at 700 °C to select a material for future electromagnetic interference (EMI) shielding application. The instrumental methods used for characterization were XRD, FESEM, XPS, and VSM. The variations in values of saturation magnetization were observed. They concluded that $Ni_{0.6-x}Zn_{0.4}Co_xFe_2O_4$ with x = 0.27 possesses the best saturation magnetization and therefore can be useful in EMI shielding material.

S. G. Gawas et al. [105] prepared $Ni_{0.4}Co_{0.2}Zn_{0.4}Fe_2O_4$ using a hydrazine-mixed Ni-Co-Zn-Fe fumarate precursor. The decomposition behaviour was studied by thermal technique, TG, alongside DTA. Chemical analysis, along with TG-DTA, infrared IR, and mass loss studies, were employed to determine the composition of the precursor. X-ray diffraction of the decomposed material confirmed the formation of monophasic nickel-cobalt-zinc ferrite; the IR spectrum displayed two characteristic bands in the regions 340–420 and 550–660 cm^{-1}. TEM revealed that the average grain size was in the range of 15–20 nm. Additionally, the DC resistivity measurement and dielectric properties were also measured as a function of frequency. S.G. Gawas et al. [104] also synthesized $Co_xNi_{0.6-x}Zn_{0.4}Fe_2O_4$; (x=0.0 to 0.4) from precursors, with the formula $Co_xNi_{0.6-x}Zn_{0.4}Fe_2(C_4H_2O_4).6N_2H_4$ (x=0.0 to 0.4). The TG–DTG–DTA profile revealed a multistage decomposition pathway, culminating in the formation of ferrite phases at approximately 410 °C. The synthesised ferrite materials were subjected to X-ray diffraction analysis to assess their crystallographic structure and phase purity. XRD patterns confirmed the successful formation of single-phase spinel compounds, without any detectable secondary phases. Complementary FTIR was employed to validate the decomposition of organic compounds further. The presence of two distinct absorption bands in the region characteristic of metal oxygen vibrations provided strong evidence for the complete elimination of organic moieties from the precursor matrices, confirming the integrity of the ferrite structure.

TEM analysis was conducted to examine the morphology and particle size of the ferrite. The TEM images demonstrated well-defined particle shapes and sizes within the nanometer scale, supporting the successful formation of nanocrystalline ferrite materials. Furthermore, AC magnetic susceptibility measurements revealed that particles exhibited single-domain particle behaviour along with pronounced superparamagnetic characteristics indicating their potential suitability for high-frequency magnetic applications or biomedical use, such as magnetic hyperthermia and targeted drug delivery.

J. S. Ghodake et al. [131] developed material suitable for microwave-absorbing rubber composite, highlighting their potential applications in radar and stealth technologies. They systematically investigated the initial permeability and magnetic loss factor as a function of both as a function of material composition and applied frequency. The study revealed that both the real and imaginary components of the initial permeability lowered while the loss factor elevated with the increasing cobalt content. Furthermore, the imaginary part of the initial permeability was observed to decline sharply with a rise in frequency across all the compositions, indicating frequency-dependent magnetic response. The imaginary part of the initial permeability of all samples was found to be decreasing rapidly with increasing frequency. In addition, the saturation magnetization was significantly higher than pure Ni–Zn ferrite. The coercivity and retentivity of cobalt-substituted Ni–Zn ferrites improved with excess cobalt. In a related study, H. Huili et al. [132] synthesized Co-substituted Ni–Zn ferrites with the formula $Co_{0.2}Ni_{0.3}Zn_{0.5}Fe_2O_4$ using the polyol synthesis method. Their work focused on understanding how stoichiometric variation and grain morphology influence the magnetic behaviour of the resulting ferrite materials. To characterize the samples, they employed variety of techniques, including X-ray diffraction (XRD), Fourier transform infrared spectroscopy (FTIR), energy-dispersive X-ray spectroscopy (EDX), transmission electron microscopy (TEM), and vibrating sample magnetometry (VSM). R. Kumar et al. [133] synthesized ($Ni_{0.6-x}Zn_{0.4}Co_xFe_2O_4$) (x = 0, 0.0165, 0.033, 0.264, and 0.528) ferrites. The saturation magnetization showed a reverse trend in their samples, i.e., Ms decreased with increasing Co contents, as analysed by vibrating sample magnetometer measurements. The X-ray diffraction measurements revealed that the samples have a single-phase spinel cubic structure, except for (x=0.0165), where there was a partial hematite phase, as indicated by an impurity peak. The ferrite showed soft magnetic behaviour, i.e., low magnetization and retentivity, and hence could be used in recording devices.

H. Nikmanesh et al. [134] investigated $Ni_{1-x}Zn_xFe_{2-x}Co_xO_4$ (x=0.0 to 0.5) ferrites prepared by the PVA-assisted sol-gel approach. The XRD showed a crystalline structure and the

formation of pure, single-phase spinel ferrites. Morphological features like size and shape were illustrated from images captured by FESEM studies. The IR spectroscopy showed two prominent peaks in the frequency range 400-600cm^{-1}. The vibrating sample magnetometry showed a gradual increase in the magnetisation with doping concentration, 0.4, and then decreased with further concentration. Also, the impact of these substitutions on vacancy distribution was identified via positron annihilation lifetime spectroscopy.

A.V. Knyazev et al. [135] used a solid-state reaction synthesis process to prepare $Ni_{0.5}Zn_{0.5}Fe_2O_4$ and $Ni_{0.5}Zn_{0.3}Co_{0.2}Fe_2O_4$, and periodically ground the samples during the calcination at 1073 K. The coercivity and Curie temperatures were seen to increase as the cobalt concentration increased. The ferrite particles were crystalline and had a particle size from 130–630nm for $Ni_{0.5}Zn_{0.5}Fe_2O_4$ and 140–350 nm for $Ni_{0.5}Zn_{0.3}Co_{0.2}Fe_2O_4$ ferrites. The saturation magnetization values recorded at room temperature were higher for $Ni_{0.5}Zn_{0.5}Fe_2O_4$ than for $Ni_{0.5}Zn_{0.3}Co_{0.2}Fe_2O_4$ ferrites.

B. J. Rani et al. [136] studied two compounds of ferrite, i.e., pure and zinc-incorporated cobalt nickel mixed ferrite ($Zn_xCo_{0.005-x}Ni_{0.005}Fe_2O_4$, where x =0.0, 0.002, 0.004) nanoparticles via the co-precipitation method. The addition of zinc ions and their influence on the material's physical properties, as evidenced by XRD, Raman, PL, and FTIR studies, have been studied. The increase in concentration of zinc ions from 0.002 to 0.004 resulted in a reduced specific capacitance. The Raman spectra showed typical phonon vibration modes T_{2g} (1), T_{2g} (2), and E_g of the cubic ferrite system. B. B. V. S. Vara Prasad et al. [137] have worked on nickel-substituted cobalt-zinc nanoferrites synthesized via citrate gel formation followed by the combustion method. The XRD studies confirmed the single phase with a spinel structure. The lattice parameter showed a downward trend. The concept of Williamson-Hall was used to calculate crystallite size. The DTA analysis recorded ferritization temperatures. The TEM measurements confirmed an average particle size of 35 nm. The far IR displayed two prominent absorption bands. The SEM micrograph showed mixed grains with spherical as well as near-spherical grains. The EDAX measurements confirmed the stoichiometry ratio of the samples. The saturation magnetization, remanence, and coercivity were determined using M-H loops recorded at room temperature.

Y. Lei et al. [138] synthesized Co-doped Zn Ni ferrite/polyaniline composites via an interfacial polymerization approach. The researcher optimised the key important parameters, including polymerization temperature and duration, to enhance the functional properties of the material. The composite fabricated under optimal conditions of 20 °C for 12 h, exhibited exceptional microwave attenuation performance, achieving a peak reflection loss of -54.3

dB. Furthermore, the material presented a broad effective bandwidth (RL=-10 dB), making it a strong candidate for advanced electromagnetic wave absorption and shielding applications. The $Ni_{0.3}Zn_{0.4}Co_{0.3}Fe_2O_4$ (N3Z4C3) was prepared by the co-precipitation method, which was embedded within the multi-walled carbon nanotubes matrix to improve the microwave absorption as reported by M. Dalal et al. [139]. The Rietveld method was employed to determine the distributions of cations between A and B-sites of the spinel structure. The high magnetization was achieved, indicating strong magnetic performance. The microwave absorption performance of the composite was evaluated through reflection losses measurement, a notable RL maximum of 22 dB was recorded at 15.24 GHz, indicating excellent microwave absorption efficiency. Additionally, the AC induction heating potential of NZCF nanoparticles was assessed to explore their suitability for magnetic hyperthermia applications.

S. Hcini et al. [140] have studied the microstructural, magnetic, and electrical properties of $Zn_{0.4}Ni_{0.3}Co_{0.3}Fe_2O_4$ (ZNCFO) and $Zn_{0.4}Cu_{0.3}Co_{0.3}Fe_2O_4$ (ZCCFO) ferrites prepared using the gel method. The lattice parameter, mean grain size, and X-ray density are higher for ZCCFO than ZNCFO. The magnetic parameters were found to decrease with the substitution of Ni by Cu. The Maxwell–Wagner's model and Koop's theory were used to study the behaviours of permittivity and loss tangent. A. Lassoued et al. [141] investigated the impact of variation in composition of $Ni_xCo_{(0.5-x)}Zn_{0.5}Fe_2O_4$ with x = (0.1, 0.2, 0.3, 0.4) on the structural, optical, magnetic, and photo-catalytic activity. The thermal decomposition was investigated by TGA/DTA. The XRD results indicated that each sample possessed a pure cubic spinel phase. The TEM and SEM analyses showed cubic morphology. FT-IR spectra displayed two distinct stretching frequency bands. The Raman spectroscopy determined ferrites and their phonon modes. The UV–Visible studies were used to calculate the optical band gap energies. The samples showed high saturation magnetization. The enhanced photo-catalytic activity was obtained for the samples having higher nickel content. J. Mattei et al. [142] worked on electromagnetic properties of composition $Ni_{0.5}Zn_{0.3}Co_{0.2}Fe_yO_{4-d}$, where y was iron deficient and iron excess, and was prepared by chemical co-precipitation. The iron excess sample showed lower total losses (magnetic and dielectric) than the iron-deficient sample for TA = 900 ° centigrade. At frequencies above 700 MHz, the total loss values (IE and ID samples) are prohibitive for antenna downsizing, whatever the firing temperature value (8000 °C and 900 ^{0}C). Whereas at frequencies below 700 MHz, $Ni_{0.5}Zn_{0.3}Co_{0.2}Fe_yO_{4+d}$ may lead to better antenna performances than $Ni_{0.5}Zn_{0.3}Co_{0.2}Fe_yO_{4-d}$.

$Ni_{0.6-x}Zn_{0.4}Co\,Fe_2O_4$ (x = 0.00, 0.033, 0.066, 0.132, 0.264, and 0.528) was synthesized using a novel low-temperature technique. The samples x=0.033, 0.066, and 0.528 yielded single-phase nano-ferrite with a size well below 100nm. SEM revealed spherical morphology with agglomeration due to magnetic interactions. XPS data confirmed the elements in the ferrite in their respective oxidation states. The sample with higher cobalt content exhibited saturation magnetization of 37 emu/g. These ferrites were evaluated for their antibacterial activity against two pathogens, E. coli and Bacillus subtilis, and demonstrated good efficacy against both [143].

The metal chloride precipitate was refluxed to obtain $Ni_{0.3}Zn_{0.7-x}Co_xFe_2O_4$ (x=0.00, 0.05, 0.15, 0.25, 0.35) nano-ferrites. The XRD studies were employed to study the structural and morphological aspects of the compounds. With an addition of cobalt, the lattice constant was seen to diminish. The crystallite size was found to be in between 9 and 10 nm. Magnetic parameters such as magnetization, coercivity, remanent magnetization, and anisotropy constant were also determined. The oxidation state of Fe as 3+ was verified by Mossbauer spectroscopy in samples except for x=0.0 and 0.15, where there was the tendency of coexistence of Fe^{3+} /Fe^{2+}. Cation distribution showed Zn^{2+} in the B site except for x=0.35. As Co content increased, samples showed the transition from an unordered paramagnetic state to an ordered magnetic state, which also showed a decrease in sensing behaviour. Sample x=0.0 showed the highest sensing property towards propanol gas. Among all three gases (propanol, ethanol, and methanol), all samples were selective towards propanol [144].

$Co_{0.3}Zn_{0.7-x}Ni_xFe_2O_4$, (x=0.0 to 0.7), was obtained through solid-state route. Samples showed a monophase behaviour with cubic structure and the Fd3m space group. As Ni concentration progressively elevated the lattice parameter contracted from 8.434 to 8.348 Å. Influence of the interpretation of magnetic behavior and cation distribution was studied using Mossbauer spectroscopy at two different temperatures. Curie temperature was found to increase from 647K to 849K with addition in Ni content in the samples. Magnetic characters were studied using a Vibrating sample magnetometer, revealing that the saturation magnetization initially increased with Ni substitution before decreasing at higher concentration. Coercivity and remnant magnetization also rose with the addition of Ni content. Sample x=0.4 showed the highest saturation magnetization at RT, while sample x=0.3 showed the highest magnetization at 100K [145].

Co-doped Ni-Zn ferrite was synthesized via the sol-gel method, followed by the auto-catalytic combustion method. PXRD was used to determine the phase purity and cation

distribution. The X-ray patterns were refined using the FullProf Suite Rietveld refinement software. The crystallite size obtained was well within the nanoscale region [146].

1.2.2.2 Literature Review of Ni-Mn-Zn Ferrites

The X-ray diffraction, infrared, and magnetization studies of the $Zn_{0.3}Ni_{0.7+x}Mn_xFe_{2-2x}O_4$ ferrite system prepared using the ceramic method was reported by B. V. Bhise et al. [147] with no impurity. The rise in lattice parameter was slow up to x = 0.2 and then declined to a persistent value. The magnetic moment first decreases for x = 0.05 and then increases at x = 0.1, with a continuous decrease thereafter for any value of x.

The $Mn_xNi_{0.5-x}Zn_{0.5}Fe_2O_4$ (x = 0.05, 0.1, 0.2, 0.3, 0.4) ferrites were produced by citrate precursor approach as reported by A.K. Singh et al. [148]. A decrease in resistivity with Mn addition was observed, except for sample $Mn_{0.3}Ni_{0.2}Zn_{0.5}Fe_2O_4$, where it shows a rise. The frequency variations of the relative loss factor (rlf) dielectric variables have been studied by them. The $Ni_xMn_{0.4-x}Zn_{0.6}Fe_2O_4$, with x=0.1–0.4, was synthesized using citrate precursor method. Magnetic properties along with relaxation intensity, loss factors, electrical parameters, and the B–H curves have been studied by A. K. Singh et al. [149]. They found that with doped nickel, the properties changed accordingly. B–H curves were rectangular in shape and had low coercivity.

A. Verma and others [150] selected zinc-doped Ni-Mn ferrite for their study, selecting the citrate precursor strategy for synthesis. Some common solid-state properties were discussed for samples sintered at different temperatures and with changing zinc composition. The structural properties, such as size and density, were studied using XRD data. The saturation magnetisation was maximum for the sample sintered at 1200 °C, and T_c dropped with zinc content. The permeability, however, was higher, and AC-resistivity lowered with sintering and increase in zinc content. For Mn–Zn ferrites, dielectric constant was lowered. A. R. Bueno et al. [151] have synthesized Mn-substituted Ni-Zn ferrites and studied their microstructural and magnetic properties. The method used for synthesis is the nitrate–citrate precursor method. All the ferrite samples showed low-coercive forces (*H*c), which is characteristic of soft magnetic materials. The results indicated that Mn substitution increases induction magnetization (*B*m) and remanent magnetization (*B*r). Substitution of Mn led to a rise in the lattice constant. The maximum density was obtained on addition of Mn.

A. A. Sattar et al. [152] have worked on Mn-substituted nickel zinc ferrite by the standard ceramic method. The theoretical lattice values were found to be larger than the experimental. Thermoelectric power (TEP) against temperature and Mn concentration for $Ni_{0.6-t}Mn_t$

$Zn_{0.4}Fe_2O_4$, (t=0.0 to 0.5), was studied. They found that the resistivity increases as the Mn concentration increases. The thermoelectric power measurements showed n-type conduction for all samples.

C. Venkataraju et al. [153] have worked on $Mn_{(0.5-x)}Ni_xZn_{0.5}Fe_2O_4$ (x=0.0,0.1,0.2,0.3) synthesized by co-precipitation route. XRD pattern determined the cation occupation in the A and B sites. The deviation in the normal cation distribution was revealed by X-ray intensity calculations. The determined M_s values were lower as the Ni was substituted, except for x=0.3, where it showed an increasing trend. The T_c was reduced with a rise in nickel concentration, except for x=0.3, where it showed a rise. The coercivity values were very low and were found to be inversely proportional to the grain size.

U. B. Gawas et al. [98] synthesized $Ni_{0.5}Mn_{0.1}Zn_{0.4}Fe_2O_4$ by the precursor method using metal carboxylato-hydrazinates as a precursor. This precursor was characterized by different techniques like XRD, IR, SEM-EDS, and chemical analysis. A sophisticated TG-DSC facility was utilised for the study of the decomposition behaviour of the samples. The XRD corroborated the formation of pure $Ni_{0.5}Mn_{0.1}Zn_{0.4}Fe_2O_4$. D. R. Mane and others [154] prepared a series of $Ni_{0.7-x}Mn_xZn_{0.3}Fe_2O_4$(where x=0.0–0.7 in steps of x=0.1), which was synthesized by a sol–gel followed by combustion synthesis. Purity of the samples was concluded from XRD plots, where seven authentic peaks of spinels were observed. The Ni ions were verified to be located at the octahedral (B-site) and Zn ions at the A-site, whereas Mn and Fe ions were present at both A- and B-sites. The magnetization reached the maximum for x=0.2, and then a fall in magnetization was observed.

S. Y. Tong et al. [155] investigated the outcome of Ni concentration in mixed Mn ferrites on electromagnetic absorption properties. The plot of resistivity vs temperature gave the activation energy of hopping carriers. The prepared ferrite showed soft magnetic behaviour as the Hc value was low, while the Ms values were high. With increasing Ni substitution for Mn in ferrites, the ferrite–resin composite has a wider bandwidth and a higher potential to be designed as a microwave absorber in the GHz range with a thinner thickness.

The Ni-substituted Mn-Zn nano-ferrites were synthesized via co-precipitation methodology by C. Venkatraju et al. [156]. The PXRD plots shows no impure phase, while the FTIR data support the spinel structure formation. The line width decreased with Ni content. The experimental values of magnetic moment evaluated from EPR spectra were lower than the theoretical value, confirming the existence of spin canting in the B site, which results in a noncollinear magnetic structure.

S. Ramesh et al. [157] have studied the microstructural and magnetic behaviour of mixed Ni–Zn–Co and Ni–Zn–Mn ferrites produced by the sol-gel approach. The incorporation of Co/Mn in Ni–Zn ferrites has revealed a notable reduction in permeability. The tan δ/μi decreased with the rise in frequency. The $Ni_xZn_{0.9-x}Mn_{0.1}Fe_2O_4$, x=0.3 to 0.7, were fabricated via a ceramic processing method by F. Genc et al. [58]. The magnetization values increased as the nickel concentration hiked up to x = 0.6, with the highest value of 78 emu/g. The well-defined grain boundaries were shown by $Ni_{0.6}Zn_{0.3}Mn_{0.1}Fe_2O_4$ and $Ni_{0.4}Zn_{0.5}Mn_{0.1}Fe_2O_4$. The $Ni_{0.6}Zn_{0.3}Mn_{0.1}Fe_2O_4$ has minimum RL values of above −20 dB at 1.8 GHz. It was deduced that the material can be exploited in microwave absorbing devices.

F. Genc et al. [159] have worked on Mn-doped $Ni_xZn_{0.9-x}Fe_2O_4$ particles produced by the solid-state ceramic method. The AC conductivity studies revealed a temperature-dependent behaviour at smaller frequencies and temperature-independent behaviour at high frequencies, which could stem from ionic conductivity because of activated frequency ranges. A. Elahi et al. [160] synthesized polypyrrole $Zn_{0.5}Ni_{0.45}Mn_{0.05}Fe_2O_4$ nanocomposites ferrite by the sol-gel and polymerization method. Characterisation was conducted to reveal the purity, size, and shape of the compounds. The crystallite size was quite low in the nano range, as expected with spherical morphology.

S. Ramesh et al. [161] have worked on $Ni_{0.4}Zn_{0.6-x}Mn_xFe_2O_4$, a ferrite series where x varies from 0.00 to 0.25 in steps of 0.05. A sol-gel approach was employed in the process. The X-ray diffractometry, electron microscopy, thermogravimetry, and Faraday's magnetometer were employed for the study. The saturation magnetization and coercivity values of Ni–Zn–Mn ferrite showed impressive results for Mn substitutions, x = 0.10 and 0.15 concentrations, and could be used as core materials for high-frequency applications.

The $Ni_{0.6-x}Mn_xZn_{0.4}Fe_2O_4$ (x = 0.0–0.6) ferrite samples were synthesized by the combustion technique using hexamine as the fuel by U. B. Gawas et al. [162]. The monophase was confirmed by X-ray technique, and the calculated lattice constant showed a direct relation to the addition of manganese. The FTIR spectra supported the XRD data and confirmed two peaks of ferrite. The DC resistivity values were in the range of 10^6 to 10^7 *ohms* cm, observed at room temperature. The resistivity vs inverse temperature plots showed a lowering in resistivity with Mn substitution at elevated temperatures. The T_c lessened with Mn concentration. K. Jalaiah et al. [163] explored Ni-substituted manganese zinc ferrite processed by the sol-gel method. The structural parameters, lattice constant and crystallite size, were computed from XRD data. The morphological studies were conducted using a

SEM/EDS technique. The ESR and VSM instruments surveyed the magnetic parameters. The results of dielectric studies were comparable to many other reported data.

T. Kuru and co-authors [164] selected the study of $Mn_{0.2}Ni_{0.3}Zn_{0.5}Fe_2O_4$ ferrite synthesised via the co-precipitation method. The assessed dielectric parameters showed a rise with increase in temperature. The uplift of frequency and temperature also accelerated DC conductivity. The activation energy for low and high temperature regions was also calculated. The semiconductor character of the $Mn_{0.2}Ni_{0.3}Zn_{0.5}Fe_2O_4$ ferrite material is confirmed by using Nyquist curves. The material was sensitive as a humidity sensor in the 20 Hz to 1 kHz frequency range. F. A. Ahmed and his co-authors [165] investigated nickel-substituted Mn-Zn spinel ferrite formed by the sol-gel method. The PXRD pattern substantiated the purity of the material under study and corroborated the cubic spinel structure of ferrite nanoparticles. The calculated size and lattice parameter were observed to decrease with the addition of nickel. The magnetization reached a maximum for the sample for x=0.1 and then dropped with the nickel substitution. The linewidth and g-value fell with the addition of nickel content till x=0.2 and then increased.

The zinc ion substitution on Mn-Ni ferrite, dried and calcined at 100 °C and 600 °C, of chemical formula $Zn_xMn_{0.5-x}Ni_{0.5}Fe_2O_4$, x=0.0 to 0.4, was studied by M. Ismail et al. [166]. The consequence of the substitution of zinc on structural and solid-state parameters was measured. The Zn ions substitution and calcination process increased the average grain diameter, reformed the shape, and improved the magnetization of dried and calcined $Zn_xMn_{0.5-x}Ni_{0.5}Fe_2O_4$ nano-ferrites. PXRD and TEM/SAED extracted the size and the morphology of dried and calcined nano-ferrites, respectively. VSM examined magnetic properties such as saturation magnetization, coercivity, and remanence parameters.

P.P.G.Dessai et al. [167] investigated $Ni_{0.7-x}Mn_xZn_{0.3}Fe_2O_4$ (x = 0.1–0.6) ferrite series prepared by precursor combustion method using nickel–manganese–zinc–iron fumarate–hydrazine as a precursor. These precursors were studied using TG–DTA, IR, CHN analysis, isothermal mass loss, and total mass loss studies. The precursors' experimental hydrazine content and C, H, N, Ni, Mn, Zn, and Fe matched the theoretical values. The XRD patterns and the IR spectra of the ferrites obtained by burning these precursors confirmed the single-phase cubic nature of these ferrites. The resistivity studies indicated a lowering in resistivity as the Mn^{2+} content of the ferrites rose. The Curie temperature also showed the same trend.

1.2.3. Literature review on Applications of Ferrites

1.2.3.1 Literature Review of Gas Sensing

Nowadays, the use of gas-sensitive, higher-performance materials for detecting hazardous gases is increasing. One of the classes of compounds used in such studies is semiconducting ferrite materials, which have tremendous scope in the area.[168]

The gas-sensing properties of zinc ferrite were measured for various gases. The samples were prepared via the molten salt route [169]. Samples showed outstanding selectivity and sensitivity toward 200 ppm of H_2S when measured at 250 °C. Similarly, Ni was developed via the co-precipitation technique [170]. The response was measured by exposing the sensing elements to various gases, namely O_2, LPG, ammonia, and Cl_2, in a closed chamber at RT. The thick film showed a superior response to the pellet sensor. Cl_2 and ammonia displayed 96% and 68% response, respectively, at RT. The Mn-substituted spinel ferrite ($MnZnFe_2O_4$, $MnCuFe_2O_4$, $MnNiFe_2O_4$, and $MnCoFe_2O_4$ was synthesised by the evaporation method. They studied their gas sensing application on reducing gases like LPG (E. R. Kumar et al) [171]. The synthesized Mn–Zn ferrite nanoparticles presented a higher response than the other samples.

Liu et al. [172] synthesized $MgFe_2O_4$. The gas sensing studies were carried out on various gases like ethanol, H_2S, CH_4, and LPG. The test was conducted at different temperatures, wherein a temperature of 335 °C showed a response for almost all the gases except H_2S, which showed a response at 160 °C. Darshane et al. [173] synthesized impurity-free spinel $ZnFe_2O_4$. XRD and TEM revealed the particle size on the nanoscale. Ethanol, NO_x, SO_x, LPG, and H_2S gases were studied in detail. At a 200ppm concentration, the sensor showed high selective sensitivity for H_2S at 250 °C.

Kim et al. [174] outlined the preparation of Mn-substituted Co ferrite having a nanowire structure as efficient gas sensors. The samples performed well as humidity sensors at 200 °C, while at RT, the results declined. The ferrite produced a linear response with a fast recovery within 6 s as the humidity content increased.

Kapse et al. [175] prepared Ni-Zn ferrite to investigate the response % for various reducing gases (H_2S, LPG, ethanol gas, and NH_3). Various factors were responsible, such as temperature, composition, and test gas species, correspondingly giving the response. Kadu et al. [176] synthesized $Zn_{0.6}Mn_{0.4}Fe_2O_4$, Pd-doped $Zn_{0.6}Mn_{0.4}Fe_2O_4$ nanomaterials to study their gas sensing applications. The crystallite size was revealed by XRD and TEM in the range of 30-35 nm. The reducing gases selected for sensing were LPG, CH_4, CO, and

ethanol. The ethanol gas illustrated the best response at 200 ppm and 300°C. 1.5 wt.% Pd-doped $Zn_{0.6}Mn_{0.4}Fe_2O_4$ was tested, with higher sensitivity and selectivity toward ethanol in the 300 to 230 °C temperature range. $MgFe_2O_4$ was developed by Patil et al. [177]. The ferrite was studied for sensing acetone, ethanol, ammonia, LPG, at different temperatures. The studies were reproducible and showed reproducibility after six months as well. Sutka et al. [178] used the sol-gel auto-combustion method to prepare zinc-doped Ni ferrite. Structural, microstructural properties revealed high porosity in samples ranging from 62-66%. The sample was indicative of a p-type semiconductor. The sample response was higher for lower zinc content compounds; with an increase in zinc content, the response declined. $Ni_{0.5-x}Mn_xZn_{0.5}Fe_2O_4$(x = 0.0-0.5) ferrite was synthesized by Gawas et al. [179]. They have studied the gas sensing property of 'as-synthesized' ferrite for H_2S, and a great response and selectivity were observed from 100 °C to 450 °C. The sample x = 0.2 had the highest response percentage at around 350 °C for H_2S gas at 200 ppm concentration. NH_3, CO_2 Cl_2, LPG, and ethanol showed lower response even at the higher concentration of 1000 ppm. $Mn_{0.3}Ni_{0.3}Zn_{0.4}Fe_2O_4$ was found to show the highest response towards NH_3 at RT and proved as a good candidate as a sensor.

Kumar et al. [180] synthesized Mn-doped MFe_2O_4 (M- Zn, Co, Cu, Ni). Their structural, solid-state properties, dielectric, and applications like gas sensing were investigated. The particle size was determined by XRD, which tallied very well with the TEM data. EDX verified cations and anion content in the ferrite. The Mn-Zn ferrite showed good results for LPG, while Cu-Mn ferrites showed the lowest response-recovery time compared to other ferrites.

Kannan et al. [181] synthesized $ZnFe_2O_4$ and checked the detection of alcohols named methanol, ethanol, and propanol. The propane gas was highly detected, followed by ethanol and methanol. The samples could detect a minimum concentration of 100ppm upto limit of 1000 ppm. $Mg_{0.5}Zn_{0.5}Fe_2O_4$ sensor was developed by Karmakar et al. [182]. They analysed the ability of sensor to detect ethanol and acetone. Acetone and ethanol were successfully sensed at 350 °C. Ethanol was also sensed with a good response at 375 °C.

Bagade et al. [183] developed single-phase $Co_{1-x}Mn_xFe_2O_4$ (where x =0.0 to 0.5) thin films via spray pyrolysis. The solid-state properties were thoroughly investigated, such as DC resistivity, which unveiled the semiconducting property of ferrites. At the same time, dielectric studies exhibited a reduction in dielectric constant with hike in frequency. Gas sensing was studied with LPG, SO_2, NH_3, NO_2, and H_2S test gases. The Sample $Co_{0.7}Mn_{0.3}Fe_2O_4$ film showed the highest gas response of 1.62 towards NO_2 compared to

other compositions and other test gases. Zhang et al [184] synthesized nanorods and nanoparticles of Ni ferrite. The examination of gas sensor properties towards NH_3 and methane was carried out. The nanorods showed better and higher results than nanoparticles towards NH_3 than towards methane.

Ghosh et al [185] synthesized Ni ferrite. They used ball milling at various times, producing samples with decreased size with prolonged milling time, thus changing their properties. The sensors were subjected to gases to study their gas-sensing properties. Therefore, samples with decreased size showed excellent H_2S and H_2 gas results at 150 and 100ºC, respectively. Thus, size plays an important role here. Wu et al. [186] synthesized $ZnFe_2O_4$ with a normal spinel and an inverse spinel structure. The inverse spinel showed a better response to H_2S gas versus the normal spinel $ZnFe_2O_4$. The operating temperature was 260°C, and within 8s, a response was obtained and recovered to the initial stage in 20s. Thus, the distribution of metal cations majorly affects gas sensing properties. Kumar et al. [187] synthesized Mn-doped Cu ferrites via the evaporation method using egg whites and metal nitrates. The annealing was done at 600 °C and 900 °C. XRD, TEM, and EDX, and their magnetism was estimated at room temperature by VSM. Mn-Cu ferrite showed an increment in percentage of response with a rise in temperature. After a specific high temperature, the sensor response reduced. The 1000 ppm of gas gave the highest response to LPG compared to other test gases, resulting in the highest percentage. A temperature of 275 °C proved to be the optimum temperature for good results.

Yadav et al. [188] synthesized a lanthanum ferrite sensor for LPG sensing. The ferrite showed

response towards LPG up to 5000-ppm concentration within 50 to 100 s and a longer reversing time of 350 to 400 s. Yuan et al. [189] synthesized Co ferrite via the sol-gel method. They sintered the ferrite at 600 and 1400 °C. They also developed Co ferrite by sintering it at 1400 °C with an electrolyte. The three samples were measured for sensor performance, out of which the highest sensitivity was towards LPG for the co-sintered sample, with a quick recovery of 8-10 seconds. It was noted that sintering temperature played a significant role, as the response escalated with sintered sample temperatures. Rao et al. [190] developed Ni ferrite and Cu-doped nickel ferrite and studied the material for its applications towards reducing gases. At temperatures of 325- 375 °C, ethanol gas showed high selectivity. It was also seen that as the Cu content increased, the sensitivity increased to 1% Cu, after which the response % decreased with a rise in Cu. Li et al. [191] produced Mn-ferrite nanospheres that showed great results against NO_2 gas. The maximum response

was attained at 200 °C at 250ppb concentration with 150 sec to respond and 180 sec to recover. P. Durga Prasad et al. [192] synthesized cobalt ferrite ($CoFe_2O_4$) fibers by electrospinning. The $CoFe_2O_4$ fibers showed good reproducibility and a maximum response of 0.42 at a 900-ppm concentration of ammonia. The ferrite fibers also exhibited the ability to sense a very low concentration of ammonia (even at 25 ppm) at room temperature.

Zou et al. [193] developed $Ni_xCo_{1-x}Fe_2O_4$ (x = 0.0, 0.33, 0.5, 0.67) ferrites, which showed sensing ability towards toluene vapors. The compositions, $Ni_{0.33}Co_{0.67}Fe_2O_4$, responded with the outstanding results at 300 °C. The samples were studied at variable ppm levels of toluene concentrations (10-500 ppm).

S. Gawas et al. [194] synthesized $Co_{0.3}Ni_{0.3}Zn_{0.4}Fe_2O_4$ using the combustion technique. The synthesized product was treated as a sensor material and tested against NO_2, Cl_2, H_2S, NH_3, and C_2H_5OH. After recording the results of all test gases at varying temperatures, at 200°C yielded the best results. Furthermore, the study revealed that NO_2 gas produced the highest response, and further tests conducted using varying amounts of gas in ppm clearly showed an elevation in response with a rise in the test gas.

$Co_{0.87}Ni_{0.13}Fe_2O_4$ and $CoFe_2O_4$ were synthesized by Sankaran [195] from metallurgical waste. Various techniques were adopted to check for phase purity, morphology, and magnetic studies. The results indicated an appropriate material for sensing. The results of the sensors on LPG gas were remarkable. It gave a good response, quick recovery, reproducibility, and high stability for LPG gas. These sensors were studied at different temperatures; when measurements were done at 250 °C, the results were optimum, while at 400 °C, sample $Co_{0.87}Ni_{0.13}Fe_2O_4$ showed a high sensitivity of 97%, and sample $CoFe_2O_4$'s response was 86%. The investigation of zinc ferrite as a humidity sensor was reported by Nikita et al. [196]. The ferrites were annealed at various temperatures of 300 °C, 500 °C, and 700 °C. The X-ray diffraction techniques revealed the crystallite sizes as 5.55 nm, 6.62 nm, and 32.9 nm, respectively. The study was conducted in a 15-90% humidity range and discovered that the increasing annealing temperature was responsible for better results. The ferrite sample annealed at 700 °C showed the highest humidity sensitivity. Madake et al. [197] adopted the spray pyrolysis technique to prepare $Cu_{0.1}Ni_{0.3}Zn_{0.6}Fe_2O_4$ thin films. XRD pattern confirmed the monophasic cubic spinel nano material ferrite, while the porosity in the samples was estimated using the SEM micrographs. The samples showed the highest response towards SO_2 at 120 °C. 5-50 ppm concentration was purged each time, giving a linear increase in gas response and showing good sensitivity. The response to the recovery rate was quick. P.P. Gauns Dessai et al. [198] conducted a study to test Mn-doped Ni-Zn

ferrite fabricated films towards chlorine, NH_3, LPG, and NO_2 gases at various temperatures - 30, 50, 100, and 150°C. The study revealed that the gas sensor was highly sensitive and selective towards Cl_2 gas compared to the other gases tested. Furthermore, the sample x=0.3 showed the highest response percentage at 100°C. Further investigation was done with varying amounts of test gas (20 ppm – 300 ppm), and the outcome was replicable with quick response and recovery rates.

T. Ravikumar et al. [199] produced thin films of zinc ferrite via spray pyrolysis at variable substrate temperatures of 225–300 °C. The morphology was determined to be nanorods with laminated cubes and rectangular grains with laminated sheets. They synthesized a thin film to detect NH_3 gas at RT. The substrate temperature significantly impacts the proposed sensor's performance. Among the temperatures studied, 225 °C showed a good sensing response of S = 1.91 towards 25 ppm of NH_3. The films have a large surface-to-volume ratio and surface roughness due to the nanorod structure. For stability and reproducibility checking, the sensor response was repeated after 90 days, which indicates that the samples validated as NH_3 gas-sensitive sensor. Xua et al. [200] synthesised Copper ferrite ($CuFe_2O_4$) with polyoxometalate (POMs) electron acceptor, $CuFe_2O_4$/POMs composite nanofibers. A convenient and straightforward electrospinning technique synthesized the $CuFe_2O_4$/POMs composite. These nanofibers were prepared with different amounts of phosphor-tungstic acid. The POMs' effect on the gas-sensor performance of ferrite was investigated. The response toward (5ppm) NO_2 gas was 2.63 with quick response and recovery, which is relatively higher than the pure $CuFe_2O_4$ sensor. The samples also exhibited a very low concentration of 12.86 ppb. The sensing performance is due to $CuFe_2O_4$-PW12 n-n heterojunctions, which can help reduce carrier recombination and separate electron-hole pairs.

A. Sharma et al. [201] have synthesized Ni-doped Mn-Zn ferrite by the combustion method, with the gas sensing response for various gases like LPG, CO, and acetone. Interestingly, the highest response was for LPG gas compared to the others. The response was enhanced with the increase in Ni content in the synthesized series. The analysis was also conducted at different operating temperatures and times. B. Deya et al. [202] synthesized Copper-substituted nickel ferrite via the hydrothermal method. XRD and IR confirmed phase purity with no impurity and a nanosized particle below 50nm. SEM and TEM confirmed non-uniform cuboidal-shaped nano-sized particles. X-ray photoelectron spectroscopy (XPS) revealed the oxidation of elements, Cu^{2+}, Fe^{3+}, and Ni^{2+}. Mössbauer spectra confirmed the

3+ valence state of iron. Magnetic properties were also manifested using VSM. Supercapacitance studies were conducted via cyclic voltammetry, disclosing a capacitance of 1417 F/g for sample x=0.5. Gas sensing performance of LPG gas at RT showed a highly selective response (1300 s for 250 ppm) compared to other tested gases. B. Deya et al. [203] adopted the hydrothermal method for synthesizing Zn-substituted nickel ferrite nanoparticles. X-ray diffraction analysis evaluated a spinel ferrite to be cubic structure, and the crystallite size was found to be in the range of 41-31nm, which reduced with rise in dopant concentration. Morphological study authenticated the cubic shape of the material. Raman spectra also confirmed pure ferrite material. The elements Zn^{2+}, Ni^{2+}, and Fe^{3+} in Zn-doped $NiFe_2O_4$ were in their exact oxidation states as revealed by XPS measurements. Mossbauer spectra determined that the iron in its respective oxidation state. The coercivity increased with increasing Zn content. The pseudo-single-domain nature of the samples was evaluated via the Day plot. They studied two applications for their samples, supercapacitance and gas sensing. Electrochemical study showed pseudocapacitive behavior with the highest Csp value of 598 F/g. The sensors were studied against the LPG test gas. They performed well with faster response and quick recovery times of 13 and 31 s when exposed to a very low concentration of 10 ppm. Mehere et al. [204] synthesized Nickel-doped cobalt ferrite ($Ni_{0.3}Co_{0.7}Fe_2O_4$) via the sol-gel auto-combustion technique. X-ray analysis validated a single cubic spinel phase with excellent crystallinity. The particle size obtained from Scherrer's equation was around 14.3 nm, well within the nanoscale region. The material's porosity was 28.01%, as revealed by XRD, which matched the porosity determined from SEM, which was 30.01%. SEM and TEM studies revealed the spherical shape of the compound and confirmed all the elements present. The band gap was calculated to be 1.74 eV based on UV–Vis spectroscopy. H_2S gas gave a response of 74%.

V. Jhadhav et al [205] synthesized the Sm^{3+}doped $ZnFe_2O_4$, Sm^{3+}-$ZnFe_{2-x}O_4$ (x =0.000, 0.100, 0.150) to study its gas sensing property towards H_2S gas. The sol–gel auto-combustion approach was utilized to synthesize the material, yielding pure-phase nanoparticles. The material's structural, morphological, optical, thermal, and magnetic properties were characterized via XRD, SEM, EDS, UV–Visible, FT-IR, TEM, TG-DTA, and VSM techniques. The sample possessed a crystallite size of 12-25 nm. The morphology of the sample was spherical and was revealed by TEM. The band gap was estimated to be between 3.3066 eV and 2.4031 eV. The gas sensor's selectivity, sensitivity, and stability were evaluated by purging the sensor with H_2S gas. The analysis was performed from room

temperature (RT) to 400°C; the response declined with an increase in temperature. When Samarium was doped into zinc ferrite, the response decreases as it peaks at five ppm, seven ppm, and 10ppm at RT. It was concluded that doping samarium improved the sensor performance.

1.2.3.2 Literature Review of Electrochemical properties

The energy demand is ever-increasing with the increase in population. The conversion of energy and storage is growing globally. Supercapacitor is the best option for such increasing demands. Since nanomaterials, especially ferrites, have exceptional properties, these compounds have been explored in energy storage. Supercapacitors possess high energy and power density, greater storage capacity, fast charging [205,206] [207-209]. Power density and energy density should be high for good supercapacitance, which is governed by operating voltage and specific capacitance [210]. Nanomaterials with porous structures have been proven to act as better supercapacitors. Metal oxides with two or more transition elements are reported to be excellent materials compared to single metal oxides because of their high-power density, good storage, fast charging/ discharging, and long life [211-213]. Ferrites are one class of oxides explored in this field because of their non-toxic nature, easy availability, easy synthesis, and excellent electrochemical behavior [214-218].

Zinc-doped nickel ferrite was synthesized by S. Costa et al. [219] using the precursor combustion method. The ferrite material was thoroughly characterized, and its solid-state properties were studied. The author has also studied supercapacitance performance in the 0.0-0.5 V potential range at varying scan rates (2, 5, 10, 20,50, 100, 200 mV). All the CV curves recorded featured pseudocapacitive behavior. The oxidative and reductive peaks indicated a reversible redox reaction. The sample with x=0.3 showed the highest specific capacitance value of 67.1 F/g at the slowest scan rate of 2mV/s.

The $CoFe_2O_4$ nanorods and nano rings were fabricated by Deng et al. [220] via solvothermal methodology. They utilized a three-electrode system for the measurements. The specific capacitance obtained was 195F/g and 99F/g at 10mV/s for nano rings and nanorods, respectively. The results show a higher value for nano rings owing to nano rings' more significant surface area than nanorods. This indicates the role of morphology, i.e., size and surface area, on the properties. Wang et al. [221] studied the supercapacitance property of $MnFe_2O_4$ colloidal nanocrystal clusters with different 2M electrolytic solutions, KOH, NaOH, LiOH, and Na_2SO_4. The electrochemical performances of each solution were 97.1, 93.9, 74.2, and 47.4 F/g, respectively, at 0.1 A/g current density. When samples were

measured at increasing scan rates, the capacitance decreased. M. K. Zate et al. [222] produce thin films of $Ni_xMn_{1-x}Fe_2O_4$ (x = 0.2, 0.4, 0.6, 0.8) whose supercapacitor properties were studied. The CV measurements were conducted in a potential window of -1.2 to -0.2V at varying scan rates of 5, 10, 20, 30, 50, and 100mV/s in a 1M KOH solution. High capacity was measured for sample x=0.8, 185 F/g at the scan rate of 5mV/s. Furthermore, a galvanic charge-discharge study obtained 147F/g capacity with an energy density of 19.5Wh/kg and 75.5% coulombic efficiency. Liao et al. [223] studied the performance of $ZnFe_2O_4$ produced by the sol-gel technique. The author adopted a different approach, wherein the three-electrode system was utilized, and the reference electrode was a Li foil; Li wire was used as the counter electrode, and 1M $LiPF_6$ as the electrolyte in a 1:1 ratio of ethylene carbonate and diethyl carbonate. The sintering was done at various temperatures and annealed at 600 °C, producing the best results. It showed excellent stability and capacity.

Nilmoung *et al.* [224] developed a composite of carbon nanofiber and manganese ferrite via electro-spinning following the carbonization process at variable temperatures. When the lowest scan rate was selected at 700 °C carbonization temperature, the specific capacitance obtained was 375 F/g, while GCD studies conducted at 5A/g at the same temperature showed 291.9 F/g capacitance. It was also noted that as the decomposing temperature increased, there was increased Mn content on the tetrahedral A-site. Fu *et al.* [225] produced Ni ferrite nanocomposites with graphene ($NiFe_2O_4$/graphene) using a hydrothermal synthesis. The study was performed in 6M KOH electrolyte; the specific capacitance at 0.1A/g was found to be 481.3F/g, while at 10A/g, it was 298.2F/g. Overall cycling stability was 10000 cycles with very little loss. The hydrothermally obtained Ni ferrite was reported by Kumar et al. [226]. A three-electrode system with a 2M electrolyte was used. The electrode material was deposited on the Ni foam, which worked as the electrode. The sample showed superior capacitance of 1040 F/g at 1 A/g and retention up to 70 % after 500 cycles at 2 A/g. B. Jhansi Rani et al. [227] analyzed $MgFe_2O_4$ synthesized by the sol-gel technique, annealed at various temperatures (300, 500, 700, and 900°C), and studied their electrochemical properties. Five scan rates were selected (5, 10, 15, 20, 25mV/s). The CV curves indicated pseudocapacitive behavior. As the scan rate decreased, the specific capacitance value increased. The performance of $MgFe_2O_4$ at 5mV/s, annealed at 500°C, was found to be 119.50 mV/s, the highest compared to the samples annealed at other temperatures. Kennaz et al. [228] developed pure $CoFe_2O_4$ by two techniques, namely the co-precipitation and hydrothermal methods. The samples synthesized by the hydrothermal method proved to be

better supercapacitors with a specific capacitance of 315F/g, while that obtained from the co-precipitation method was 249F/g; each particular capacitance was obtained at a five-mV scan rate. R. Gandhi et al. [229] synthesized $Cd_xNi_{1-x}Fe_2O_4$ (x = 0.3, 0.5, and 0.7) via co-precipitation method. They annealed at variable temperatures,600 °C, 700 °C, and 800 °C for three hr. Sample x=0.3 showed the best results in 2M KOH electrolyte solutions compared to other samples. The specific capacitance of 338 F/g was obtained at a 2 mV/s. Sathiyamurthy et al. [230] synthesized $ZnFe_2O_4$ for the study of supercapacitance. The as-prepared and sintered ferrites were studied and compared. 212 F/g at 10mV /s scan rate supercapacitance for the sintered sample was measured. In contrast, the same sample as prepared showed a capacitance of 101 F/g, indicative of temperature as the factor that played an essential role in determining good capacitance. Huang et al. [231] adopted the citric acid-assisted sol-gel auto-combustion process to synthesize cobalt ferrites. Further study was conducted using a three-electrode system and 6M KOH solution and yielded the C_{sp} of 443.89F/g at a 1A/g. After 6000 cycles, the sample showed a loss of 20%. Pure ($NiFe_2O_4$) and doped ($NiFe_2O_4/SiO_2$) were synthesized and fabricated using the sol-gel auto-combustion method by Baig et al. [232]. The electrochemical performance was conducted at variable scan rates of 5-100mV/s. The curves showed prominent oxidation and reduction peaks, which symbolise pseudocapacitive property. When the two samples were compared, the pure Ni ferrite showed a capacitance of 525 F/g. In contrast, the SiO-doped ferrite exhibited very high supercapacitance of 925 F/g with a good retention of 95.5% even after 5000 cycles.

1.2.3.3 Literature Review of Ferrites as an Anti-microbial Agent

Ferrites as anti-microbial agents have gathered the researcher's interest as they contain the potential to be antimicrobial in nature. The drugs available in the market have shown resistance towards the bacteria, thus posing a challenge and urging the need for an alternative. The nano-ferrites are simple compounds that are easy to prepare and economical; their magnetic nature provides easy access to recover them. Furthermore, these ferrite nanoparticles in low concentrations are biocompatible [233,234]. This section lists reports on antimicrobial studies using various spinel ferrites as antibacterial and antifungal agents. Multiple techniques have been employed to synthesize these ferrites, leading to changes in morphological, physical, and chemical properties, thus producing good results. Apart from the synthesis followed, the dopants also play a significant role against the pathogens.

Sharma et al. [235] synthesized $CoFe_2O_4$ by the sol-gel technique. They performed several studies on the ferrite material. Their main aim was antibacterial properties against pathogens such as B. subtilis, S. aureus, E. coli, and *P. aeruginosa*. The material showed the best antimicrobial activity toward E. coli with a 15mm inhibition zone, while the least activity was toward S. aureus. The cell rupture leading to antibacterial activity was due to the creation of reactive oxygen species. C. H. Vinuthna [236] developed a Zn-doped Co ferrite, where zinc increased from 0.0 to 1. The citrate precursor method was adopted to synthesize the compound, whose anti-bacterial properties were investigated. Specific gram-positive bacterial efficacy was shown by samples x=1 and x=0.4 as compared to other samples.

M. Maksoudnet et al. [237] employed the Sol-gel method to produce $M_xCo_{1-x}Fe_2O_4$ (M= Zn, Cu, Mn, x=0.0, 0.25, 0.5, and 0.75). They studied the photocatalytic and antibacterial properties of the ferrite. Sample $Zn_{0.75}Co_{0.25}Fe_2O_4$ showed the highest antibacterial properties against S. aureus, E. coli, and A. viridans among all the prepared samples. M. Naik et al. [238] synthesized $ZnFe_2O_4$ using a microwave-assisted method using Limonia acidissima juice. This green method produced particles of 25-30 nm. The antibacterial properties of the material against various pathogens were investigated. The ferrite material inhibited *S. aureus, E. coli, P. desmolyticum, and K. aerogenes* to a reasonable extent. R. Sharma et al. [239] also developed nano $ZnFe_2O_4$ via the citrate sol-gel method. The sample size and morphology of the particles were discussed as well. Zinc ferrite, studied for its antimicrobial applications, revealed that 62.5 μm/mL inhibited the growth of C. albicans.

N. Sanpo et al. [240] studied the antibacterial activity of $Co_{1-x}Zn_xFe_2O_4$ (0.0,0.3,0.5,0.7, and 1.0) synthesized via citrate sol-gel method. When the samples were characterized, they showed changes in microstructural properties with increased zinc content. Samples show excellent results for E. coli and S. aureus. Similarly, Co_{1-x} $M_xFe_2O_4$ where M is Cu, Mn, Zn, Ni, x=0.5 was synthesized and Cu-substituted ferrite showed excellent results towards the E. coli pathogen [241].

K. Venkatesan [242] adopted a solution combustion synthesis route, to synthesize cobalt ferrite. XRD revealed phase purity to be monophasic, and the particles with size of 16nm was determined. They studied the antibacterial effect of the samples against pathogens causing diseases. Actions were recorded when a 50mg/mL dosage concentration was used to study bacterial inhibition, and a 3mm zone of inhibition was found against E. coli bacteria. $CoFe_2O_4$ synthesis was done using the co-precipitation method by R. Zalneravicius [243]; they obtained ferrites ranging from 15nm, 5nm to 1.65nm, from which they correlated size with antimicrobial properties. Structural and morphological parameters of the material were

confirmed by XRD, AFM, and TEM techniques. Four yeast cultures were studied: S. cerevisiae, C. parapsilosis, C. krusei, and C. albicans. From the results, it was obtained that size played a significant role. The smaller samples from 1.6- 5.5 nm showed better activity owing to a larger area of the sample surface.

P. Suppuraj et al. [244] developed pure Zn ferrites using a simple co-precipitation method. They aimed to study catalytic and antibacterial properties. The samples did show good photocatalytic action. The pathogens selected for study were the gram-positive Lactobacillus and Bacillus cereus and the gram-negative E. coli, Aeromonas hydrophila, and Vibrio harveyi. A. H. Ashour [245] synthesized $Zn_xCo_{1-x}Fe_2O_4$, $Cu_xCo_{1-x}Fe_2O_4$, $Mn_xCo_{1-x}Fe_2O_4$, each with four compositions (0.0, 0.25, 0.5, 0.75). They employed the sol-gel technique for the preparation of these compounds. The radiation caused a lowering of particle size, thus improving the antibacterial properties. Compared to all the samples, Zn-substituted cobalt ferrite showed the best results.

M. Naik et al. [246] synthesized $NiAl_xFe_{2-x}O_4$ (0.0-0.7) via the sol-gel auto-combustion technique. The samples' structural and optical properties were thoroughly characterized. They studied the photocatalytic and antibacterial applications. The growth of gram-negative bacteria was compared with the standard antibiotic chloramphenicol. The samples showed promising results. S. Mandal et al. [247] used the co-precipitation methodology to prepare the zinc ferrite samples. They studied the antimicrobial effect of the sample. The bacterial inhibitions were studied via the well-diffusion method. Streptomycin, a standard antibiotic, was used to compare the data and proved satisfactory. E.S. Anooj et al. [248] also synthesized $ZnFe_2O_4$; the hydrothermal method was utilised for synthesis. The E. coli pathogen was studied and compared with the potency of commercially available drugs, and the results were similar. Many such reports on antibacterial studies on various metal ferrites are available [249-256]. Ferrites as catalysts and photocatalysts are also explored. C. Chiang et al. [257] have studied the decomposition or methanation of CO_2 with flowing H_2 over oxygen-deficient $ZnFe_2O_4$ and $MnFe_2O_4$ nano-catalysts at 300- 400 °C and 1 atmosphere. $ZnFe_2O_4$/$MnFe_2O_4$ nano-catalysts were prepared using a hydrothermal method. X. Feng et al. [258] synthesized $CoFe_2O_4$ nanoparticles, and dye degradation capabilities from water were investigated using cobalt ferrite by oxidation of Methylene Blue (MB) dye in water with H_2O_2 as the oxidizing agent. The material had a size in the range of 2–6 nm. The oxidation of MB by $CoFe_2O_4$ was excellent. A few researchers have studied the magnetic silica-supported spinel ferrite catalyst for Rhodamine B oxidation [259]. The catalysts performed excellently at a neutral pH.

1.3 Aim and Objective

The literature review demonstrates that ferrite materials have made remarkable strides in present and future technology. Presently, ferrite material is ubiquitous and dominates a significant industry with extensive applications. Ferrites are multifunctional, in electrical components such as transformer cores, isolators, and circulators. It is also used in electronic devices, storage devices, and permanent magnets. In addition, they are extensively valuable for medicine and are effective in drug delivery, as biosensors, and magnetic hyperthermia agents. Recently, ferrite has also been a significant topic of discussion among researchers in supercapacitors and energy storage. Recently, Ferrites have been researched extensively as sensors and antimicrobial agents. Ease of tuning these materials into the desired shape, size, and morphology gives them a significant advantage. Many reports on synthesis techniques are present in the literature, and these methods are simple and cost-friendly. Simple ferrites can be easily substituted or doped, and various such materials can be obtained with varying properties. Ni-Zn ferrite is known to show high resistivity and low losses. Mn-Zn ferrites possess high permeability, magnetic induction, and low power losses. Similarly, Co is known to have high anisotropy. Due to such properties, two series were synthesized, i.e., the Zn-doped Ni-Mn series and the Zn-doped Ni-Co series, to study the effect of non-magnetic dopants. With the series and its composition selected, our next step was to decide on the synthesis method. Literature gives reports on many techniques, namely hydrothermal, precursor combustion method, combustion technique, ceramic method, co-precipitation method, sol-gel technique, etc. The precursor combustion technique and combustion method were chosen for the present study. Doping zinc into the system alters the properties of ferrites. This is due to cation distribution in the tetrahedral and octahedral sites by incorporation of the dopant. Apart from the dopant, various other factors are responsible for the properties of ferrite, like the morphology of the particles, which is dependent on the method of preparation. Therefore, the first series, $Ni_{0.6-x}Co_{0.4}Zn_xFe_2O_4$ (x=0.0,0.1,0.2,0.3,0.4,0.5,0.6) was synthesised via the precursor-combustion method. The precursor combustion method involves the formation of a precursor, which is stoichiometric in nature, making it a good technique. This technique works at a lower temperature and is environmentally friendly. The synthesised precursor was ignited to give auto-ignited ferrite. The precursor as well as the ferrite was characterized, TG-DTA, IR spectroscopy, elemental analysis, and thermal studies characterized the former, while XRD, TEM, SEM, Raman analysis, BET, and XPS characterized the latter. Further,

their detailed solid-state study was conducted, which revealed their electrical, dielectric, and magnetic behaviour.

The second method for synthesis chosen was the combustion method. This methodology is simple, and the products have broad applicability. This technique involves several exothermic reactions between the fuel and an oxidizer. This method involves a fast-heating rate and less reaction time. The fuel used in the combustion process in the current study is hexamine. Large amounts of gases are released while inhibiting particles' agglomeration, leading to fine powder and high-purity nanomaterials. This great technique yields particles of different sizes and shapes and can be tuned according to the requirements. Various parameters, such as dopant method selection, play a crucial role in the formation of pure-phase compounds, as well as the role of fuel. $Ni_{0.6-x}Mn_{0.4}Zn_xFe_2O_4$ (x=0.0, 0.1, 0.2, 0.3, 0.4, 0.5, 0.6) was synthesised via this method using hexamine as the fuel. The hexamine and metal nitrate ratio was optimized to select the appropriate ratio. The suitable ratio was selected, which gave a pure phase, small size, good electrical, magnetic, and dielectric properties.

Another objective of our research work is to check the suitability of the synthesised as-prepared ferrites for various applications. Spinel ferrite is found to be multifunctional in nature, and recent advances in the field of sensors and supercapacitors are promising. Apart from this, their potential as an antibacterial agent is also investigated; therefore, we analysed the synthesised as-prepared materials to evaluate their potential in such fields. The gas sensing studies were conducted to test the sensor performance against Cl_2, NH_3, LPG, and NOx gases by fabricating the ferrite into thick films. The studies were done in different temperature conditions to optimize the suitable temperature condition of the ferrite to perform at its best. The electrochemical performance of the samples was evaluated in the aqueous medium using a three-electrode system in a cyclic voltammetry instrument. The antibacterial activity was tested at different dosages of the ferrite samples against S. aureus bacteria.

The thesis is divided into five chapters, which discuss the above-mentioned work. Each chapter is briefly described below.

Chapter 1: This chapter includes the introduction to ferrites, literature review on ferrites studied in the current work, different methods of preparation, and various applications it

possesses. Also, the aim and objectives of the research and the plan for the present research work are written.

Chapter 2: This chapter gives a detailed procedure adopted to synthesise the two series under investigation and multiple characterisation techniques used for the study.

Chapter 3: This chapter gives a detailed study on characterization of zinc-doped nickel cobalt fumarato-hydrazinate precursor, $Ni_{0.6-x}Co_{0.4}Zn_xFe_2(C_4H_2O_4)_3.6N_2H_4$ (x=0.0,0.1,0.2,0.3,0.4,0.5,0.6) and characterization of $Ni_{0.6-x}Co_{0.4}Zn_xFe_2O_4$ (x=0.0,0.1,0.2,0.3,0.4,0.5,0.6) via the precursor-combustion method for as-prepared and sintered ferrites. It provided the applicative study of the as-prepared samples.

Chapter 4: This chapter deals with the optimisation of the metal nitrate fuel ratio, followed by the characterisation of $Ni_{0.6-x}Mn_{0.4}Zn_xFe_2O_4$ (x=0.0, 0.1, 0.2, 0.3, 0.4, 0.5, 0.6) synthesised via the combustion method using hexamine as the fuel and its application.

Chapter 5: This chapter gives a summary of the entire research work and the conclusion of the thesis work.

References

1. L. Satyanarayana, K. M. Reddy, S. V. Manorma, Sens. Actuators B, 89 (2003)62.
2. K. Sreekumar, T. Mathew, B. M. Devassy, R. Rajagopal, R. Vetrivel, B. S. Rzo, Appl. Catalysis A, 205 (2001)11.
3. T. Mathew, S.Shylesh, S.N. Reddy, C.P Sebastian, S.K. Date, B.S. Rao, S.D. Kulkarni, Catalysis Lett., 93 (2004)155.
4. K. Mukherjee, S. B. Majumdar, Nanotechnology, 21(2010) 255504.
5. N. N. Gedam, P. R. Padole, S. K. Rithe, G. N. Chaudhari, J. Sol-Gel Sci. Tech., 50 (2009) 296.
6. M. Sugimoto, J. Am. Ceram. Soc., 82 (1999) 269.
7. R. Srivastava, B. C. Yadav, Int. J. Green Nanotechnol., 4 (2012) 141.
8. V. Melfos, B. Helly, P. Voudouris, Archaeol. Anthropol. Sci., 3 (2011) 165.
9. A.A. Mills, Ann. Sci., 61 (2004) 273.
10. S. Malin, D. Barraclough, Eos Trans. Am. Geophys. Union, 81 (2000) 233.
11. S. Stringari, R.R. Wilson, Rend. Fis. Acc. Lincei., 11 (2000) 115.
12. S. Hilpert, Ber. Deutsch. Chem. Ges., 42 (1909) 2248.
13. S. Hilpert, A. Wille, Z. Phys. Chem., B18, (1932) 291.
14. L. Snoek, Phys., 3 (1936) 463.
15. J. L. Snoek, New Development in Ferromagnetic Materials, Elsevier, New York (1947).
16. L. Neel, Ann. Phys. Paris, 3 (1948) 137.
17. J. L. Went, G.W. Ratenau, E. W. Gorter, G. W. V. Oosterhout, Philips Tech. Rev., 13 (1951)194.
18. F. J. Bertaut, F. Forrat, Compt. Rend., 242 (1956) 382.
19. H. Forestier G. Guiot-Guillain, Compt. Rend., 230 (1950) 1844.
20. H. Forestier, G. Guiot-Guillain, Compt. Rend., 235 (1952) 48.
21. C. L. Hogan, Bell Syst. Tech. J., 31 (1952) 1.
22. E. J. W. Verway, E. L. Heilmann, J. Chem. Phys., 15 (1947) 174.
23. P. W. Anderson, Phys. Rev., 79 (1950) 350.
24. S. Iida, H. Sekizawa, Y. Aiyama, J. Phys. Soc. Jpn., 10 (1955) 907.
25. S. Iida, H. Sekizawa, Y. Aiyama, J. Phys. Soc. Jpn., 13 (1958) 58.
26. T. Nakamura, Y. Okano, J. Phys. IV France, 7 (1997) 91.

27. N. C. Suyal, A. R. Das, Trans. Indian Ceram. Soc., 51 (1992) 57.
28. J. Y. Shin, J. H. Oh, IEEE Trans. Magn.,29 (1993) 3437.
29. S.-S. Kim; D.-H. Han; S.-B. Cho, IEEE Trans. Magn., 30 (1994) 4554.
30. H. Ueno, T. Yasuyoshi, S. Yoshikado, J. Magn. Soc. Jpn., 22 (1998) 369.
31. S. B. Cho, D. H. Kang, J. H. Oh, J. Mater. Sci., 31 (1996) 4719.
32. J.-Y. Hsu, H.-C. Lin, H.-D. Shen, C.-J. Chen, IEEE Trans. Magn., 33 (1997) 3325.
33. T. Nomura, M. Takaya, Hybrids, 3 (1987) 15.
34. V. S. R. Raju, IEEE Trans. Magn., 51 (2015) 1.
35. C. J. M. Rooijmans (Ed.), Magnetic Spinel Single Crystals by Bridgman Technique, Springer-Verlag, Berlin, Heidelbergand New York, (1978).
36. M. Sugimoto, Jpn. J. Appl. Phys., 5 (1966) 557.
37. C. Tsang, M.-M. Chen, T. Yogi, K. Ju, IEEE Trans. Magn., MAG-26, (1990) 1689.
38. M.M. Dovek, D.J. Seagle, T.J. Beau lieu, E.R. Christensen, R.E. Fontana Jr., IEEE Trans. Magn., MAG-28, (1992) 2301.
39. I. Sekine, T. Kal, Ind. Eng. Chem. Prod. Res. Dev., 25 (1986) 7.
40. A. Meidanchi, H. Ansari, J. Clust. Sci., 32 (2021) 657.
41. W. H. De Jong, P. J. Borm, Int. J. Nanomed., 3 (2008) 133.
42. Y.-T. Chen, A.G. Kolhatkar, O. Zenasni, S. Xu, T.R. Lee, Sens., 17 (2017) 2300.
43. B. I. Kharisov, H. V. R. Dias, O. V. Kharissova, Arab. J. Chem., 12 (2019) 1234.
44. V. Hencl, P. Mucha, A. Orlikova, D. Leskova, Water Res., 29 (1995) 383.
45. V. Blanco-Gutierrez, E. Climent-Pascual, M. J. Torralvo-Fernandez, R. Saez-Puche, M.T. Fernandez-Diaz, J. Solid State Chem., 184 (2011) 1608.
46. D. S. Maclure, J. Phys. Chem. Solids, 3 (1957) 311.
47. J. D. Dunitz and L. E. Orgel. J Phys Chem. Solids, 3 (1957) 20.
48. A Miller, J. Appl. Phys., 30 (1959) 245.
49. T. F. W. Barth, E. Ponjak, Z. fur Krist.-Cryst. Mater., 82 (1932) 325.
50. P. N. Anantharamaiah, P. A. Joy, Phys. Chem. Chem. Phys., 18 (2016) 10516.
51. A. R. West, Solid-State Chemistry and its Applications, Wiley and Sons, (1984).
52. B. M. Moskowitz, Hitchhiker's Guide to Magnetism, (2002).
53. R. Topkaya, A. Baykal, A. Demir, J. Nanopart. Res., 15 (2013) 1359.
54. G. Kumar, J. Shah, R.K. Kotnala, V.P. Singh, Sarveena, G. Garg, S.E. Shirsath, K.M. Batoo, M. Singh, Mater. Res. Bull., 66 (2015) 216.
55. J. S. Smart, Am. J. Phys., 23 (1955) 356.

56. S. Noor, M. A. Hakim, S. S. Sikder, S. M. Hoque, K. H. Maria, P. Nordbad, J. Phys. Chem. Solids, 73 (2012) 227.
57. L. G. Van Uitert, Proc LR.E.,44 (1956) 1294.
58. G. H. Jonker, J, Phys, Chem. Solids, 9 (1959) 165.
59. D Elwell, B.A. Griffiths, R., Parker, Brit. J. Appl. Phys., 17 (1966) 249.
60. W.D. Kingeri, Ceramic Fabrication Processes, M.L.T. Technical Press, John Wiley, New York, 1958.
61. C. G. Koops, Phys. Rev., 83 (1951) 121.
62. K. C. Patil, M.S. Hegde, T. Rattan, S.T. Aruna, Chemistry of Nanocrystalline Oxide Materials, World Scientific, (2008).
63. A.S. Mukasyan, A.S. Rogachev, S. T. Aruna, Adv. Powder Tech., 26 (2015) 954.
64. F. Deganello, A. K. Tyagi, Prog. Cryst. Growth Charact. Mater., 64 (2018) 23.
65. K. V. Manukyan, A. Cross, S. Roslyakov, S. Rouvimov, A.S. Rogachev, E.E. Wolf, A. S. Mukasyan, J. Phys. Chem. C, 117 (2013) 24417.
66. R. K. Selvan, C. O. Augustin, L. J. Berchmans, R. Saraswathi, Mater. Res. Bull., 38 (2003) 41.
67. C. Hwang, T. Wu, J. Wan, J. Tsai, Mater. Sci. Eng. B, 111 (2004) 49.
68. S. Balaji, R. K. Selvan, L. J. Berchmans, S. Angappan, K. Subramanian, C.O. Augustin,
    Mater. Sci. Eng. B, 119 (2005) 119.
69. D. Bahadur, S. Rajakumar, A. Kumar, J. Chem. Sci., 118 (2006) 15.
70. P. M. P. Swamy, S. Basavaraja, A. Lagashetty, N. V. Srinivas Rao, R. Nijagunappa, A. Venkataraman, Bull. Mater. Sci., 34 (2011) 1325.
71. A. B. Salunkhe, V. M. Khot, M. R. Phadatare, S.H. Pawar, J. Alloys Compd., 514 (2012) 91.
72. E. R. Kumar, R. Jayaprakash, J. Chandrasekaran, Superlattices Microstruct., 64 (2013) 343.
73. M. Kooti, A. N. Sedeh, Mater. Sci. Technol., 29 (2013) 34.
74. S. Hajarpour, A. H. Raouf, K. Gheisari, J. Magn. Magn. Mater., 329 (2013) 165.
75. S. Hajarpour, A. H. Raouf, K. Gheisari, J. Magn. Magn. Mater., 363 (2014) 21.
76. A. B. Salunkhe, V. M. Khot, M.R. Phadatare, N.D. Thorat, R.S. Joshi, H.M. Yadav, S.H. Pawar, J. Magn. Magn. Mater., 352 (2014) 91.
77. Szczygieł, K. Winiarska, J. Therm. Anal. Calorim., 115 (2014) 471.
78. Manikandan, M. Durka, K. Seevakan, S.A. Antony, J. Supercond. Nov. Magn., 28 (2015) 1405
79. T. Prabhakaran, J. Hemalatha, Ceram. Int., 42 (2016) 14113.

80. D. R. Babu, K. Venkatesan, J. Cryst. Growth, 468 (2017) 179.
81. A. K. Sijo, J. Magn. Magn. Mater., 441 (2017) 672.
82. S. G. Gawas, S. S. Meena, P. Bhatt, V. M. S. Verenkar, Mater. Chem. Front., 2 (2018) 300.
83. D. M. Coutinho, V. M. S. Verenkar, J. Alloys Compd., 782 (2019) 392.
84. Sedghi, E.A. Salehkooh, M. Chadorbafzade, Mater. Sci.-Poland, 38 (2020) 341.
85. P. P. G. Dessai, S. S. Meena, V. M.S. Verenkar, J. Alloys Compd., 842 (2020) 155855.
86. P. Ravindranathan, K.C. Patil, J. Mater. Sci., 22 (1987).
87. K.G. Kanade, D.P. Amalnerkar, H.S. Potdar, B.B. Kale, Mater. Chem. Phys., 117 (2009) 187.
88. A. Angermann, E. Hartmann, J. Töpfer, J. Magn. Magn. Mater., 322 (2010) 3455.
89. M. G. Naseri, E. B. Saion, H. A. Ahangar, M. Hashim, A.H. Shaari, J. Magn. Magn. Mater.,323 (2011) 1745.
90. M. Gupta, B. S. Randhawa, J. Anal. Appl. Pyrol., 95 (2012) 25.
91. P. L. Leng, M. G. Naseri, E. Saion, A. H. Shaari, M. A. Kamaruddin**,** Adv. Nanoparticles, (2013) 378.
92. L. R. Gonsalves, S. C. Mojumdar, V. M. S. Verenkar, J. Therm. Anal. Calorim., 104 (2011) 869.
93. L. R. Gonsalves, V. M. S. Verenkar, S. C. Mojumdar, J. Therm. Anal. Calorim., 96 (2009) 53.
94. L. R. Gonsalves, V. M. S. Verenkar, J. Therm. Anal. Calorim., 108 (2012) 871.
95. L. R. Gonsalves, S. C. Mojumdar, V. M. S. Verenkar, J. Therm. Anal. Calorim., 100 (2010) 789.
96. L. R. Gonsalves, S. C. Mojumdar, V. M. S. Verenkar, J. Therm. Anal. Calorim., 108 (2012) 859.
97. U. B. Gawas, V. M. S. Verenkar, Thermochem. Acta, 556 (2013) 41.
98. U. B. Gawas, S. C. Mojumdar, V. M. S. Verenkar, J. Therm. Anal. Calorim., 96 (2009) 49.
99. U. B. Gawas, S. C. Mojumdar, V. M. S. Verenkar, J. Therm. Anal. Calorim., 100 (2010) 867.
100. U. B. Gawas, V. M. S. Verenkar, S. C. Mojumdar, J. Therm. Anal. Calorim., 104 (2011) 879.
101. U. B. Gawas, V. M. S. Verenkar, S. C. Mojumdar, J. Therm. Anal. Calorim., 108 (2012) 865.
102. U. B. Gawas, V. M. S. Verenkar, J. Therm. Anal. Calorim., 115 (2014) 375.
103. U. B. Gawas, V. M. S. Verenkar, S. S. Meena, P. Bhatt, J. Supercond. Nov. Magn., 30 (2017) 3241.
104. S. G. Gawas, V. M. S. Verenkar, Thermochem. Acta, 605 (2015) 16.

105. S. G. Gawas, V. M. S. Verenkar, S. C. Mojumdar, J. Therm. Anal. Calorim., 119 (2015) 825.
106. D. M. Coutinho, V. M. S. Verenkar, J. Therm. Anal. Calorim., 128 (2017) 807.
107. F. J. Schnettler and F. R. Monforte, J. Appl. Phy., 29 (1958) 3.
108. M. Mizushima, Jpn. J. Appl. Phy., 3 (1964) 2.
109. J. Kulikowski, A Bienkowski, J. Magn. Magn. Mater., 26 (1982) 297.
110. H. T. Hahn, J. Appl. Phys., 699 (1991) 15.
111. B. Parvartheeswara Rao, O. F. Caltun, J. Optoelect. Adv. Mater., 8 (2006) 995.
112. X. Shen, R. Gong, Z. Feng, Y. Nie J. Am. Ceram. Soc., 90 (2007) 2196.
113. J. Xiea, M. Hana, L. Chena, R. Kuanga, L. Deng, J. Magn. Magn. Mater., 314 (2007) 37.
114. O. Suwalka, R. K. Sharma, V. Sebastian, N. Lakshmi, K. Venugopalan, J. Magn. Magn. Mater., 313 (2007) 198.
115. M. S. Kim and J. G. Koh, J. Korean Phys. Soc., 53 (2008) 737741.
116. A. K. Subramani, N. Matsushita, W.M. Abe, M. Yoshimura, J. Mater. Sci., 43 (2008) 2372.
117. Z. W. Li, L. B. Kong, and Z. H. Yang, J. Appl. Phy., 105 (2009) 113912.
118. J. S. Ghodake, R. C. Kambale, S. D. Kulkarni, S. R. Sawant and S. S. Suryavanshi, Smart Mater. Struct., 18 (2009) 125009.
119. S. Waje, M. Hashim, W. Daud, W. Yusoff, Z. Abbas, Aust. J. Basic Appl. Sci., 3 (2009) 1991.
120. K. C. Mouli, T. Joseph, and K. Ramam, J. Nanosci. Nanotechnol., 9 (2009) 5596.
121. M. M. Mallapur, B. K. Chougule, Mater. Lett., 64 (2010) 231.
122. M.S. Khandekar, J. Y. Patil, S. S. Pawar, A. V. Rajgure, S. S. Suryavanshi, AIP Conf. Proc., 1349 (2011) 1205.
123. S. B. Waje, M. Hashim, I. Ismail, J. Magn. Magn. Mater., 323 (2011) 1433.
124. M. A. Amer, A. Tawfik, A. G. Mostafa, A. F. El-Shora, S. M. Zak, J. Magn. Magn. Mater., 323 (2011) 1445.
125. K. Raju, D.H. Yoon, J. Supercond. Nov. Magn., 27 (2014) 1285.
126. M. Chaitanya Varma, G.S.V.R.K. Choudary, A. M. Kumar, K. H. Rao, Phys. Res. Int., 579745 (2014) 9.
127. K. Mohita, V. Guptaa, N. Guptaa, S. K. Routb, Ceram. Int., 40 (2014) 1575.
128. P. Liu, Z. Yao, J. Zhou, RSC Adv., 5(2015) 93739.

129. A. Hassan, M. Khan, M. Shahid, M. Asghar, I. Shakir, S. Naseem, S. Riaz, M. Warsi, J. Magn. Magn. Mater., 393(2015)56.
130. R. Kumar, H. Kumar, M. Kumar, R. Raj Singh, P. B. Barman, J. Supercond. Nov. Magn., 28 (2015) 3557.
131. J. S. Ghodake, R. C. Kambale, T. J. Shinde, P. K. Maskar, S. S. Suryavanshi, J. Magn. Magn. Mater., 401 (2016) 938.
132. H. Huili, B. Grindi, G. Viau, L. Ben Tahar, Ceram. Int., 42 (2016) 1759.
133. R. Kumar, H. Kumar, R. R. Singh, P. B. Barman, J. Sol-Gel Sci. Technol.,78 (2016) 566.
134. H. Nikmanesh, P. Kameli, S. M. Asgarian, S. Karimi, M. Moradi, Z. Kargar, J. Ventura, B. Bordalo, H. Salamatia, RSC Adv., 7 (2017) 22320.
135. A.V. Knyazev, I. Zakharchuk, E. Lähderanta, K.V. Baidakov, S. S. Knyazeva, I. V. Ladenkov, J. Magn. Magn. Mater., 435 (2017) 9.
136. B. J. Rani, R. Mageswari, G. Ravi, V. Ganesh, R. Yuvakkumar, J. Mater. Sci. Mater. Electron., 28 (2017) 16450.
137. B. B. V. S. Vara Prasad, K. V. Ramesh, A. Srinivas, J. Supercond. Nov. Magn., 31 (2018) 3223.
138. Y. Lei, Z. Yao, H. Lin, J. Zhou, A. Ali Haidry, P. Liuab, RSC Adv., 8 (2018) 29344.
139. M. Dalal, A. Das, D. Das, R. S. Ningthoujam, P. Kumar Chakrabarti, J. Magn. Magn. Mater., 460 (2018) 12.
140. S. Hcini, A. Omri, M. Boudardm, M. L. Bouazizi, A. Dhahri, K. Touileb. J. Mater. Sci. Mater. Electron., 29 (2018) 6879.
141. A. Lassoued, M. S. Lassoued, B. Dkhil, S. Ammar, A. Gadril, J. Mater. Sci. Mater. Electron., 29 (2018) 7333.
142. J. Mattei, D. Souriou, A. Chevalier, J. Magn. Magn. Mater., 447 (2018) 9.
143. R. Kumar, R. Jasrotia, Himanshi, J. Ahmed, A.V. Nidhi, Saad M. Alshehri, Louis W.Y. Liu, S. A. Patil, R. Aggarwal, S. K. Godara, P.B. Barman, R. R. Singh, A. Kandwal, Inorg. Chem. Commun., 157 (2023) 111355.
144. S. Dlamini, S. Nkosi, T. Moyo, A. Nhlapo, Mater.Sci. Eng. B, 294 (2023) 116554.
145. D.A. Vinnik, D.P. Sherstyuk, V.E. Zhivulin, S.A. Gudkova, D.A. Pankratov, N.S. Perov, Yu. A. Alekhina, E.D. Shipkova, S.V. Trukhanov, K.A. Astapovich, T.I. Zubar, A.V. Trukhanov, J. Magn. Magn. Mater., 605 (2024) 172344.
146. H.V.Shrikanth, S. Ramesh, K. Ch Varada Rajulu, B. Dhanalakshmi, D. J. Rao, B. P. Rao, J. Indian Chem. Soc., 101 (2024) 101312.

147. B. V. Bhise, M. B. Dongare, S. A. Patil, S. R. Sawant, J. Mater. Sci. Lett.,10 (1991) 922.
148. A. K. Singh, A. Verma, O.P. Thakur, C. Prakash, T.C. Goel, R. G. Mendiratta, Mater. Lett., 57 (2003) 1040.
149. A. K. Singh, A. K. Singh, T.C. Goel, R.G. Mendiratta, J. Magn. Magn. Mater., 281 (2004) 276.
150. A. Verma, R. Chatterjee, J. Magn. Magn. Mater., 306 (2006) 313.
151. A. R. Buenoa, M. L. Gregori, M.C.S. Nobrega, Mater. Chem. Phy., 105 (2007) 229.
152. A. A. Sattar, H. M. El-Sayed, K. M. El-Shokrofy, M. M. El-Tabey, J. Mater. Sci., 42 (2007) 149.
153. C. Venkataraju, G. Sathishkumar, K. Sivakumar, J. Magn. Magn. Mater., 322 (2010) 230.
154. D. R. Mane, D. D. Birajdar, S. E. Shirsath, R. A. Telugu, Ram. H. Kadam, Phys. Status Solidi A, 207 (2010) 2355.
155. S. Tong, J. Wua, M. Tung, W. Kob, Y. Huang, Y. Wang, J. Alloys Compd., 525 (2012) 143.
156. C. Venkataraju, R. Paulsingh, J. Nanosci., 81538 (2014) 5.
157. S. Ramesh, B. C. Sekhar, P. S.V. S. Rao, B. P. Rao, Ceram. Int., 40 (2014) 8729.
158. F. Genc, B. Unal, A. Baykal, H. Sozeri, J. Supercond. Nov. Magn., 28 (2015) 1055.
159. F. Genc¸ E. Turhan, H. Kavas, U. Topal, A. Baykal, H. Sozeri, J. Supercond. Nov. Magn., 28 (2015) 1047.
160. A. Elahi, N. A. Niaz, M. S. Awan, A. Shakoor, K. Mahmood, Y. Khan, Polym. Sci., Ser. B, 57 (2015) 738.
161. S. Ramesh, B. Dhanalakshmi, B. C. Sekhar, P. S. V. Subba Rao, B. P. Rao Appl. Phys. A,122 (2016) 984.
162. U. B. Gawas, M. M. Kothawale, R. Pednekar, S. S. Meena, N. K. Prasad, S. K. Alla, J. Supercond. Nov Magn., 30 (2017) 1287.
163. K. Jalaiaha, K. Vijaya Babu J. Magn. Magn. Mater., 423 (2017) 275.
164. T. Ş. Kuru, M. Kuru, S. Bağcı, J. Mater. Sci. Mater. Electron., 29 (2018) 17160.
165. F. A. Ahmed, L. N. Singh, J. Mater. Sci. Sur. Eng., 6 (2018) 825.
166. M. Ismail, Mater. Res. Express, 5 (2018) 095004.
167. P. P. Gauns Dessai, V. M. S. Verenkar, J. Therm. Anal. Calorim., 142 (2020) 1399.
168. N. Rezlescu, C. Doroftei, E. Rezlescu, P.D. Popa, Phys. Stat. Sol., 203 (2006) 306.

169. S. L. Darshane, R. G. Deshmukh, S. S. Suryavanshi, I. S. Mullaw, J. Am. Chem. Soc., 91 (2008) 2724.
170. R. B. Kamble, V. L. Mathe, Sens. Actuators B, 131 (2008) 205.
171. R. Kumar, P. S. Prasad Reddy, G. S. Devi, S. Sathiyaraj, J. Magn. Magn. Mater., 398 (2016) 281.
172. Y. Liu, Z. Liu, Y. Yang, H. Yang, G. Shen, R. Yu, Sens. Actuators B, 107 (2005) 600.
173. S.L. Darshane, R.G. Deshmukh, S.S. Suryavanshi, I.S. Mulla, J. Am. Ceram. Soc., 91 (2008) 2724.
174. C.H. Kim, Y. Myung, Y. J. Cho, H. S. Kim, S. Park, J. Park, J. Kim, B. Kim, J. Phys. Chem. C, 113 (2009)7085.
175. V.D. Kapse, S.A. Ghosh, F. C. Raghuwanshi, S.D. Kapse, U.S. Khandekar, Talanta, 78 (2009)19.
176. A.V. Kadu, S.V. Jagtap, G.N. Chaudhari, Curr. Appl. Phys., 9 (2009) 1246.
177. J.Y. Patil, M.S. Khandekar, I.S. Mulla, S.S. Suryavanshi, Curr. Appl. Phys., 12 (2012) 319.
178. A. Sutka, G. Mezinskis, A. Lusis, M. Stingaciu, Sens. Actuators B, 171–172 (2012) 354.
179. U.B. Gawas, PhD Thesis (2013).
180. E. R. Kumar, R. Jayaprakash, G.S. Devi, P.S.P. Reddy, Sens. Actuators B, 191 (2014) 186.
181. P. K. Kannan, R. Saraswathi, Talanta, 129 (2014) 545.
182. M. Karmakar, P. Das, M. Pal, B. Mondal, S. B. Majumder, K. Mukherjee, J. Mater. Sci., 49 (2014) 5766.
183. A. A. Bagade, K.Y. Rajpure, Ceram. Int., 41 (2015) 7394.
184. L. Zhang, W. Jiao, Sens. Actuators B, 216 (2015) 293.
185. Ghosh, A. Mukherjee, M. Fu, S. Chattopadhyay, P. Mitra, Phys. E, 74 (2015) 570.
186. J. Wu, D. Gao, T. Sun, J. Bi, Y. Zhao, Z. Ning, G. Fan, Z. Xie, Sens. Actuators B, 235 (2016) 258.
187. E. R. Kumar, P. S. P. Reddy, G. S. Devi, S. Sathiyaraj, J. Magn. Magn. Mater., 398 (2016) 281.
188. A. K. Yadav, R. K. Singh, P. Singh, Sens. Actuators B, 229 (2016) 25.
189. Y. Yuan, B. Wang, C. Wang, Xi. Li, J. Huang, H. Zhang, F. Xia, J. Xiao, Sens. Actuators B, 239 (2017) 462.
190. P. Rao, R. V. Godbole, S. Bhagwat, Mater. Chem. Phys., 171 (2016) 260.

191. Y. Li, L. Cheng, X. Zhang, X. Guo, Solid State Ion., 336 (2019) 102.
192. P.D. Prasad, J. Hemalatha, J. Magn. Magn. Mater., 484 (2019) 225.
193. Y. Zou, H. Wang, R. Yang, X. Lai, J. Wan, G. Lin, D. Liu, Sens. Actuators B, 280 (2019) 227.
194. S. G. Gawas, V. M. S. Verenkar, Mater. Sci. Eng. B, 265 (2021) 114948.
195. K. J. Sankaran, S. Suman, A. Sahaw, U. Balaji, R. Sakthivel, J. Magn. Magn. Mater., 537 (2021) 168231.
196. Nitika, A. Rana, V. Kumar, Appl. Phys. A, 127 (2021) 609.
197. S. B. Madake, J. B. Thorat, K. Y. Rajpure, Sens. Actuators A, 331 (2021) 112919.
198. P. P. G. Dessai, A. K. Singh, V. M. S. Verenkar, Mater. Res. Bull., 149 (2022) 111699.
199. T. Ravikumar, L. Thirumalaisamy, S. Madanagurusamy, K. Sivaperuman, J. Alloys and Compd., 959 (2023) 170568.
200. J. Xua, T. Wang, M. Weib, Y. Yanga, D. Lia, H. Yua, X. Dong, J. Industrial Eng. Chem., 136 (2024) 615.
201. A. Sharma, N. Aggarwal, N. Kumar, P. Patial, S. Kumar, S. Jindal, Phys. B**:** Condens**.** Matter, 668 (2023) 415237.
202. B. Dey, M. Bououdina, G. Abdelfadeel, P. Dhamodharan, S. Asath Bahadur, M. Venkateshwarlu, C. Manoharan J. Alloy Compd., 970 (2024) 172711.
203. B. Dey, C. M. M. Venkateshwarlu, C. Singh Pawar, Suresh Sagadevand, Ceram. Int., 50 (2024) 12121.
204. A. C. Mehere, V. R. Jadhav, S. M. Kasabe, S. Mansing Rathod, Results Surf. Interfaces, 18 (2025) 100461.
205. V. R. Jadhav, R. Baburao Bhise, M. Daryav Dhiware, U. N. Shelke, Inorg. Chem. Commun., 174 (2025) 113892.
206. P. Sharma, Shipra, Int. J. Res. Eng. Appl. Sci., 9 (2019) 2349.
207. P. Simon, Y. Gogotsi, Nat. Mater., 7 (2008) 845.
208. S.-C. Lin, Y.-T. Lu, Y.-A. Chien, J.-A. Wang, T.-H. You, Y.-S. Wang, C.-W. Lin, C. C.M. Ma, C.-C. Hu, J. Power Sources, 362 (2017)258.
209. Z. Yang, J. Zhang, M.C. Kintner-Meyer, X. Lu, D. Choi, J.P. Lemmon, J. Liu, Chem. Rev.,111 (2011) 3577.
210. B. Mendoza-Sánchez, Y. Gogotsi, Adv. Mater., 28 (2016) 6104.
211. M. R. Lukatskaya, B. Dunn, Y. Gogotsi, Nat. Commun., 7 (2016) 12647.
212. M. S. Javed, Z. Jiang, Q. Yang, X. Wang, X. Han, C. Zhang, X. Gu, C. Hu, Electrochim. Acta, 295 (2019) 558.

213. Z. Xing, Z. Ju, J. Yang, H. Xu, Y. Qian, Nano Res., 5 (2012) 477.
214. X. Cui, R. Lv, R.U.R. Sagar, C. Liu, Z. Zhang, Electrochim. Acta, 169 (2015) 342.
215. D. A. Andersson, C. R. Stanek, Phys. Chem. Chem. Phys., 15 (2013) 15550.
216. J. Jiang, Y. Li, J. Liu, X. Huang, C. Yuan, X.W.D. Lou, Adv. Mater., 24 (2012) 5166.
217. M. M. Vadiyar, S. S. Kolekar, N. G. Deshpande, J.-Y. Chang, A. A. Kashale, A.V. Ghule, Ionics, 5 (2016) 1.
218. M. Zhu, X. Zhang, Y. Zhou, C. Zhuo, J. Huang, S. Li, RSC Adv., 5 (2015) 39270.
219. S. Costa, V.M.S. Verenkar, J. Mater Sci: Mater Electron., 33 (2022) 25717.
220. D. H. Deng, H. Pang, J. M. Du, J. W. Deng, S.J. Li, J. Chen, J. S. Zhang, Cryst. Res. Technol.,47 (2012) 1032.
221. R. Wang, Q. Li, L. Cheng, H. Li, B. Wang, X.S. Zhao, P. Guo, Colloids Surf. A: Physicochem. Eng. Asp., 457 (2014) 94.
222. M. K. Zate, S. M. F. Shaikh, V. V. Jadhav, K. K. Tehare, S. S. Kolekar, R. S. Mane, M.Naushad, B. N. Pawar, K. N. Hui, J. Anal. Appl. Pyrol., 116 (2015) 177.
223. L. Liao, T. Fang, G. Yin, D. Zhang, B. Li, Int. J. Electrochem. Sci., 12 (2017) 10211.
224. S. Nilmoung, P. Kidkhunthod, S. Maensiri, Mater. Chem. Phys., 220 (2018) 190.
225. M. Fu, W. Chen, X. Zhu, Q. Liu, J. Power Sources, 396 (2018) 41.
226. N. Kumar, A. Kumar, S. Chandrasekaran, T.Y. Tseng, J. Clean Energy Technol., 6 (2018) 51.
227. B.J. Rani, M. Durga, G. Ravi, P. Krishnaveni, V. Ganesh, S. Ravichandran, R. Yuvakkumar, Appl. Phys. A, 124 (2018) 319.
228. H. Kennaz, A. Harat, O. Guellati, D.Y. Momodu, F. Barzegar, J.K. Dangbegnon, N. Manyala, M. Guerioune, J. Solid State Electrochem., 22 (2018) 835.
229. C. Rajeevgandhi, P. Sivagurunathan, Int. J. Adv. Sci. Technol., 28 (2019) 431.
230. K. Sathiyamurthy, C. Rajeevgandhi, S. Bharanidharan, P. Sugumar, S. Subashchandrabose, Chem. Data Collect., 28 (2020) 100477.
231. T. Huang, Z. Qiu, Z. Hu, X. Lu, J. Energy Storage, 35 (2021) 102286.
232. M. M. Baig, E. Pervaiz, M. Azad, Z. Jahan, M.B.K. Niazi, S. M. Baig, Ceram. Int., 47 (2021) 12557.
233. R. Salomoni, P. L'eo, A. Montemor, B. Rinaldi, M. Rodrigues, Nanotechnol. Sci. Appl., 10 (2017) 115.
234. S.J. Salih¸Heliyon 10 (2024) e31428.
235. R. Sharma, S. Raut, V. V. Jadhav, A. S. Kadam, R. S. Mane, Mater. Lett. 237 (2019) 165.

236. C.H. Vinuthna, K.C.B. Naidu, C.C. Sekhar, R. Dachepalli, J. Appl. Ceram. Technol., 16 (2019) 1944.
237. M. Maksoud, G.S. El-Sayyad, A.H. Ashour, A.I. El-Batal, M.S. Abd-Elmonem, H.A.M. Hendawy, E. K. A. Khalek, S. Labib, E. Abdeltwab, M.M. El-Okr, Mater. Sci. Eng. C, 92 (2018)644.
238. M. M. Naik, H. Naik, G. Nagaraju, M. Vinuth, K. Vinu, S. K. Rashmi, J. Mater. Sci. Mater. Electron., 29 (2018) 20395.
239. R.P. Sharma, S.D. Raut, R.M. Mulani, A.S. Kadam, R.S. Mane, Int. Nano Lett., 9 (2019) 141.
240. N. Sanpo, J. Wang, C.C. Berndt, Adv Mater. Res., 436 (2012) 535.
241. N. Sanpo, C.C. Berndt, C. Wen, J. Wang, Acta Biomater., 9 (2013) 5830.
242. K. Venkatesan, D.R. Babu, M.P.K. Bai, R. Supriya, R. Vidya, S. Madeswaran, P Anandan, M. Arivanandhan, Y. Hayakawa, Int. J. Nanomedicine, 10 (2015) 189.
243. R. Žalnėravičius, A. Paškevičius, M. Kurtinaitiene, A. Jagminas, J. Nanoparticles Res., 18 (2016) 300.
244. P. Suppuraj, G. Thirunarayanan, M. Swaminathan, I. Muthuvel, Mater. Sci. Appl. Chem., 34 (2017) 5.
245. A.H. Ashour, A. El-Batal, M.I.A. A. Maksoud, G. S. El-Sayyad, S. Labib, E. Abdeltwab, M. M. El-Okr, Particuology, 40 (2018) 141.
246. M. M. Naik, H. S. Bhojya Naik, G. Nagaraju, M. Vinuth, H.R. Naika, K. Vinu, Microchem. J, 146 (2019) 1227.
247. S. Mandal, S. Natrajan, A. Tamilselvi, S. Mayadevi, J. Environ. Chem Eng., 4 (2016) 2706.
248. E. S. Anooj, S.J. Sreelekshmi, S.T. Gopukumar, P.K. Praseetha, Int. J. Pharm. Sci. Rev. Res., 46 (1) (2017) 22
249. A. Nigam, S. J. Pawar, Ceram. Int., 46 (2020) 4058.
250. M. K. Satheeshkumar, E.R. Kumar, C. Srinivas, N. Suriyanarayanan, M. Deepty. C.L. Prajapat, T. V. C. Rao, D.L. Sastry, J. Magn. Magn. Mater., 469 (2019) 691.
251. S. B. Patil, H. Naik, G. Nagaraju, R. Viswanath, S.K. Rashmi, M.V. Kumar, Mater. Chem. Phys., 212 (2018) 351.
252. S. V. Bhosale, P. S. Ekambe, S. V. Bhoraskar, V. L. Mathe, Appl. Surf. Sci., 441 (2018) 733.
253. C.C. Naik, S. K. Gaonkar, I. Furtado, A.V. Salker, J. Mater. Sci. Mater. Electron., 29 (2018) 14746.

254. A. S. Hathout, A. Aljawish, B.A. Sabry, A.A. El-Nekeety, M.H. Roby, N.M.Deraz, S.E. Aly, M. Wahhab, J. Appl. Pharm. Sci., 7 (2017) 11.

255. D. Gingasu, I. Mindru, L. Patron, A. Ianculescu, E. Vasile, G. Marinescu, S. Preda, L. Diamandescu, O. Oprea, M. Popa, C. Saviuc, M.C. Chifiriuc, J. Inorg. Organomet. Polym. Mater., 28 (2018) 1932.

256. S. Iqbal, M. Fakhar-e-Alam, M. Atif, N. Amin, K.S. Alimgeer, A. Ali, Aqrab-ul-1, S. Ahmad, A. Hanif, W A. Farooq, Results Phys., 15 (2019) 102529.

257. C. Chiang, K. Lin, P. Hsu, Y. Lin, Int. J. Hydrogen Energy, 42 (2017) 22123.

258. X. Feng, G. Y. Mao, F. X. Bu, X. L. Cheng, D. M. Jiang, J. S. Jiang, J. Magn. Magn. Mater., 343 (2013) 126.

259. N. M. Mahmoodi, Mater. Res. Bull., 48 (2013) 4255.

Chapter 2

Experimental Protocols and Characterisation Techniques

2.1 Introduction

The properties of nanomaterials are influenced by their method of synthesis is no more a secret. Various techniques are available in the literature for synthesizing nanomaterials; these methods substantially impact the materials' morphology, particle size, and surface area. Thus, it exhibits superior physical and chemical properties and adds to the excellence of the applications [1]. The nanomaterials synthesis method is divided into two main categories: bottom-up and top-down [2]. Top-down is a destructive technique in which the bulk material is broken down or decomposed into smaller particles, ultimately leading to a nanomaterial. Mechanical ball milling [3-9], laser ablation, and sputtering are examples of this method. The bottom-up technique is the constructive technique in which the atoms/ions combine to form clusters and nanomaterials. These methods includes sol-gel [10-20], co-precipitation [21-31], precursor combustion [32-45], combustion [45-49], hydrothermal [49-53], and sonochemical [54-58].

In the present work, we have synthesized two series, namely nickel cobalt ferrites doped with zinc, $Ni_{0.6-x}Co_{0.4}Zn_xFe_2O_4$ (x=0.0,0.1,0.2,0.3,0.4,0.5,0.6) synthesized by precursor-combustion method and nickel manganese ferrites doped with zinc $Ni_{0.6-x}Mn_{0.4}Zn_xFe_2O_4$ (x=0.0,0.1,0.2,0.3,0.4,0.5,0.6) prepared by combustion method using hexamine as the fuel. in both the series zinc has been doped to understand the effect of doping Zn^{2+} ions in the systems. The detailed protocol for forming the series under study is given in the following sections.

2.2. Experimental Procedure

2.2.1 Synthesis using precursor combustion method

Mixed metal hexahydrazine fumarate complex having the general formula $Ni_{0.6-x}Co_{0.4}Zn_xFe_2(C_2H_4O_2)_3.6N_2H_4$ (x=0.0, 0.1, 0.2, 0.3, 0.4, 0.5, 0.6) was synthesised using this method [59], which on decomposition gave product $Ni_{0.6-x}Co_{0.4}Zn_xFe_2O_4$ (x=0.0, 0.1, 0.2, 0.3, 0.4, 0.5, 0.6) ferrites.

2.2.1.1 Synthesis of hexahydrazine fumarate complex

The first step is the preparation of hexahydrazine fumarate complex, is stirring of appropriate amount of sodium fumarate (99% SRL) in water in three-necked flasks along with optimised amount of hydrazine hydrate in an N_2 atmosphere, for two hours. In the

second step hydrated metal chloride salts, i.e., nickel chloride, zinc chloride, and cobalt chloride, were weighed appropriately and dissolved together in water along with freshly prepared ferrous choride solution. The ferrous chloride solution was separately prepared by adding HCl solution to the weighed solid iron powder under a carbon dioxide atmosphere. The solution of all metal chloride salt was added to the above-mentioned ligand mix solution of hexahydrazine fumarate and hydrazine hydrate to form a precursor of hydrazinated mixed metal fumarate. The obtained precipitate was filtered and washed with ethanol and dried with diethyl ether under a vacuum. This precursor was then characterised immeditely using different analytical techniques.

The reaction for formation of hydrazinated mixed metal fumarate is given below.

$$(0.6\text{-}x)\ NiCl_{2\,(aq)} + 0.4\ CoCl_{2\,(aq)} + x\ ZnCl_{2(aq)} + 2\ FeCl_{2\,(aq)} + 3\ Na_2(C_2H_4O_2)_{(aq)} + 6\ N_2H_4.H_2O_{(aq)} \downarrow Ni_{0.6\text{-}x}Co_{0.4}Zn_xFe_2(C_2H_4O_2)_3.6N_2H_{4(s)} + 6NaCl_{\,(aq)} + 6H_2O_{\,(l)} \quad (2.1)$$

2.2.1.2 Formation of oxide

The formed precursor was taken into a clay dish and lit with a matchstick. The precursor caught fire and burned autocatalytically covering the entire precursor to form a blackish-brown powder. This obtained powder was further calcined at 500^0C for five hours, to remove any unburnt organic content. The obtained compound was called as-burnt ferrite and was utilized for further studies.

$$Ni_{0.6x}Co_{0.4}Zn_xFe_2(C_2H_4O_2)_3.6N_2H_4(s) + 14O_2(g) \downarrow Ni_{0.6\text{-}x}Co_{0.4}Zn_xFe_2O_4 + 6CO_2(g) + 6N_2(g) + 18H_2O(g) \quad (2.22)$$

2.2.2 Synthesis using combustion technique

A combustion technique was adopted to synthesize the Zn-doped Ni-Mn ferrite having the general formula $Ni_{0.6\text{-}x}Mn_{0.4}Zn_xFe_2O_4$ (x=0.0,0.1,0.2,0.3,0.4,0.5,0.6). The redox combustion reaction between metal nitrates as oxidiser and hexamine as fuel was exploited to prepare ferrites. This fuel is a tetradentate ligand that binds the metal ions strongly and is combustible in nature, which helps in the autocatalytic decomposition of the material [60].

The metal nitrates, i.e., nickel nitrate hexahydrate (99% Thomas Baker), zinc nitrate hexahydrate (97% Thomas Baker), manganese nitrate tetrahydrate (99% SRL), and ferric nitrate nonahydrate (99% Thomas Baker), were taken into a beaker and melted on a hot plate. Once the melt was cooled, the fuel, hexamine (Thomas Baker 99%), was added to it and stirred to make it homogeneous. The fuel and metal nitrate mix were kept on a hot plate for further heating until a sticky mass was formed, which soon autocatalytically ignited and decomposed into foamy powder. This foamy powder was ground for an hour to generate fine powder and calcined at 500 °C for five hours in a muffle furnace. The calcined compound was ground for two hours, and the resultant powder was called 'as-prepared' ferrite.

$$(0.6\text{-}x)Ni(NO_3)_2.6H_2O + 0.4Mn(NO_3)_2.4H_2O + xZn(NO_3)_2.6H_2O + 2Fe(NO_3)_3.9H_2O + \xrightarrow{C_6H_{12}N_4} Ni_{0.6-x}Mn_{0.4}Zn_xFe_2O_4 + 6CO_2 + 6H_2O + 4N_2 + 5O_2 \quad (2.3)$$

2.3 Annealing Process

2.3.1 Pellet formation

The 'as prepared' ferrites were converted into pellets to study their properties. The 'as-prepared' $Ni_{0.6-x}Co_{0.4}Zn_xFe_2O_4$ (x=0.0,0.1,0.2,0.3,0.4,0.5,0.6) synthesized by the precursor combustion method was subjected at a pressure of 5 tonnes for 5 min using a conventional die and hydraulic press. In comparison, the $Ni_{0.6-x}Mn_{0.4}Zn_xFe_2O_4$ (x=0.0,0.1,0.2,0.3,0.4,0.5,0.6) synthesized by the combustion technique was pelletized using a pressure of 3 tonnes for 3 min. The pellets had a diameter of 1cm while the thickness was 2-3mm.

2.3.2 Pre-sintering process

Pre-sintering is an important step that is conducted before the primary sintering process. Pre-sintering results in shrinkage, which helps minimize distortion, such as cracks and improper crystal growth during final sintering. It makes the sample dense. This process was carried out using as-prepared pellets, pre-sintered at 800 °C for five hours in a muffle furnace. The obtained pre-sintered pellets were ground into fine powder with consistency for two hours.

2.3.3 Sintering process

Sintering is the solid-state diffusion process between particles, making them come together, thus compacting the material. This heating process is done at a temperature below their melting point. At sintering temperatures, material densification occurs, thus reducing the pores in the samples and increasing the particle size.

The pre-sintered powder was pelletized into a cylindrical shaped pellet using 5 tonnes pressure for 5 min on a hydraulic press using a die. The pellets had 2-3 mm thicknesses and a radius of 5 mm. The toroids were also prepared from the pre-sintered powder using a toroidal die on a hydraulic press. A few drops of binding agent, (1% PVA solution) was utilized to hold the powder in toroidal form. These toroids were prepared by applying a pressure of 6 tonnes for 4 min. The thickness of the toroids was 3-5 mm, with the outer diameter being 20mm, while the inner diameter was 10mm. The Zn-doped Ni-Co series pellets and toroids were sintered at 1000 °C for 10 h, while the Zn-doped Ni-Mn ferrite series Pellets and toroids were sintered at 1100 °C for 10 h, after doing the temperature and time optimization.

2.4 Characterisation techniques

2.4.1. Chemical Analysis

The precursor hexahydrazine nickel cobalt zinc ferrous fumarate complex was analysed using various techniques to determine the stoichiometry. The Elementar Vario Micro Cube CHNS analyzer was used to determine the C, H, and N content of precursors. The hydrazine content in the samples was determined by the titrimetric method under Andrews' conditions [61].

The chemical analysis helps determine the stoichiometry of the sample and is an essential tool in determining whether the sample composition is as the formula or not. For chemical analysis study, the Inductively Coupled Plasma- Atomic Emission Spectroscopy (ICP-AES) technique was used of make Spectro analytical instruments GmbH, Germany. The Acros simultaneous spectrometer was used to study all the 'as-prepared' ferrites. Here, the Ar plasma generates high temperatures, which excite the electrons. This excited electron emits energy at a given wavelength at the ground state level. Each element emits energy at a specific wavelength, which is characteristic of its atomic character. The intensity of

emitted radiation is directly proportional to the concentration of the sample; hence, one can find quantitative and qualitative data from this study.

2.4.2 Thermal studies

TG-DTA techniques help determine the change in mass loss and physical and chemical variations with temperature or time. The results are expressed as a thermogram of mass loss versus temperature or time. The TG curve can be represented as DTG, i.e., derivative of TG, which further helps determine the minor changes or resolves broad peaks indicating mass loss at each step. In DTA, the temperature difference between the reference and the sample crucible is detected as a function of temperature. Thermal techniques are a significant step in both combustion and precursor combustion methods in determining the final decomposition temperature of the samples. The precursor combustion technique also helps determine the formula of the final product. The total mass loss study was done by heating a known amount of precursor sample in the furnace at 500°C for five hours, while the isothermal mass loss study was performed by heating the sample at a known set temperature and noting the weight change. The hydrazine estimation was done at various set temperatures. TG-DTG-DTA study: The thermogravimetric research was performed to determine the decomposition temperature. The TG curve gives stepwise decomposition of the precursor with an increase in temperature, and the DTA gives the corresponding peak to the mass loss in the form of a peak. The peaks obtained are either endothermic or exothermic. This analysis was conducted on the NETZSCH STA 409 PC (Luxx) analyzer in a zero-air atmosphere. The analysis was run from RT-850°C at a heating rate of 10°C per minute and gas flow of 60 m/min.

2.4.3 X-ray Diffraction Study

Powder X-ray diffraction, or PXRD, is the most crucial technique while studying solid-state chemistry. This technique provides valuable information about phase purity, the sample's nature. When a beam of X-rays hits the sample, there is interaction between the X-ray photons and electrons present in the atoms, thus scattering occurs. The X-rays will be diffracted when the x-ray is incident on periodically arranged atoms. The peaks obtained as a result are directly related to atomic distance.

In our study, the 'as prepared' and 'sintered' ferrites were subjected to X-ray analysis using the Rigaku Smart Lab instrument with a Cu target and wavelength of 1.541Å, with a Ni absorber filter. The scan was performed from 20- 80° at a step size of 0.02°.

Several cell parameters, like lattice constant, measured density, X-ray density, porosity, and crystallite size, were estimated from the obtained data. The lattice parameter was calculated using the following equation:

$$\alpha = d\sqrt{h^2 + k^2 + l^2} \qquad (2.4)$$

Where 'α' is the lattice parameter, d ' *is the lattice spacing obtained from Bragg's equation,* and '*h, k, l'* are Miller indices of the plane.

The X-ray density and measured density are calculated using the formulas given below.

$$d_x = \frac{8M}{NV} \qquad (2.5)$$

' dx 'is the X-ray density, 8 is the number of formula units in a unit cell, 'M' is the molecular weight of the formula unit, 'N' is Avogadro's number, and '*V'* is the volume of the unit cell.

$$d_m = \frac{m}{\pi r^2 h} \qquad (2.6)$$

' dm 'is the measured density, m ' is the mass, 'r' is the radius, and 'h' is the height of the pellet.

Porosity is one of the essential properties of ferrite and can also be determined by X-ray data using the equation as follows:

$$P = 1 - \frac{d_m}{d_x} \qquad (2.7)$$

The sample's average crystallite size was determined using the Scherrer formula.

$$\tau = \frac{0.9\lambda}{\beta cos\theta} \qquad (2.8)$$

Where 'τ' is the crystallite size, 'λ' is the X-ray wavelength, 'β' is the full width at half maxima, and 'θ' is the Bragg angle.

2.4.4. Infrared spectroscopy studies

IR spectroscopy is also known as vibrational spectroscopy due to the vibrational transitions in the molecules. This non-destructive technique involves the absorption of IR radiation by the sample, which changes the dipole moment; thus, such molecules can be referred to as IR active. Therefore, absorption of IR radiation vibrates the molecule, bringing about a change such as a change in bond lengths or stretching vibrations, or a change in bond angle or bending vibrations. These stretching vibrations can happen in two ways, i.e., in phase stretching or symmetric stretching vibration, or out of phase or asymmetric stretching vibrations. It is the most common technique employed due to its use in determining various functional groups present in the samples. In the case of spinel, the bands are observed in the region of 400-600 cm^{-1}. The low-lying band at ~400 cm-1 is due to metal oxygen bonding at the octahedral site or ($M-O_{oct}$) stretching, while the higher frequency band is due to ($M-O_{tet}$) stretching vibration, i.e., metal oxygen stretching at the tetrahedral site. In the present study, IR spectra were taken in the full range from 350-4000cm^{-1} for precursor, a;s-prepared;, and ;sintered; samples. The analysis was done using a Shimadzu FTIR Prestige-21 spectrophotometer. The sample was dispersed in KBr and ground before analysis.

2.4.5 Raman Spectroscopy Technique

Raman spectroscopy is an excellent technique for unveiling the vibrational structure of the material. The molecular vibrations induce the inelastic scattering of photons from matter, which is called the Raman effect. When a laser beam of light is incident on the sample, some photons are absorbed while others are scattered. When the photons are re-emitted, the wavelength of the emitted light will be either shorter or longer than the incident light. Information about symmetry and phase can be obtained from the Raman data. Correlation between structural, chemical, and vibrational properties and the functional behaviour can be done using Raman spectroscopy. In our present study, the analysis of all the 'as-prepared' and 'sintered' ferrite samples has been done using the Horiba Jobin Yvon, Laser Raman Microscope model: Lab Ram HR. The 'as-prepared' analysis was done in the laser source of 532 nm, whereas for sintered it was at 633nm.

2.4.6 X-ray photoelectron spectroscopy

The XPS technique quantifies the elemental composition and chemical and electronic state of the element. When high-energy x-rays hit the sample surface, the core-shell electron is ejected. The kinetic energy of the ejected electron is studied, which is characteristic of the orbital. The X-ray beam irradiates the sample to obtain XPS spectra. The analysis is performed under high vacuum. The full scan spectra are recorded so that all the elements in the materials can be recorded. The PHI 5000 Versa Prob II, FEI Inc. model instrument was used to analyzed all the' as-prepared' ferrite samples in the present study. The data obtained deduced the oxidation states present in the samples. Deconvolution of the spectra was performed by XPSPEAK41 software. The binding energy of the C1 core, 284.4 eV, was taken as a reference.

2.4.7 Microstructural studies

2.4.7.1 Scanning Electron Microscopy & Transmission Electron Microscopy

Microstructural studies were done using SEM and TEM techniques to determine the surface topology, size of the particles, shape, and pores in the sample. SEM generally works on the principle that when the beam of electrons is focused on the sample surface, the electrons are reflected or ionized within the sample. The secondary electrons or back-scattered electrons are detected, producing an image. In the case of TEM analysis, a monochromatic beam of electrons is allowed to pass through the sample surface, which leads to scattering to give images on a photographic film or detected with a camera. The selected area electron diffraction results from elastic scattering, while the inelastic scattering gives the photos. TEM studies were done using the JEOL instrument of model no. JEM 2100F with an accelerating potential of 200kV. The 'as-prepared' ferrite samples were investigated by TEM, whose TEM images and SAED patterns were obtained after the analysis. Image J software extracted more information from TEM data, such as interplanar distance and average particle size. The sample size of less than 50 nm can be determined by TEM analysis. The SEM technique was employed for samples greater than 50nm, i.e., 'as-prepared' and 'sintered' ferrite samples. SEM images helped define its shape and size, while EDS, recorded alongside SEM, gave spectra of elements present in the sample and

their percentages. SEM was recorded using the Carl Zeiss SEM model, EVO18 microscope.

2.4.8. BET Surface area study

Physical adsorption or physisorption is the most common type of adsorption. Based on the famous Brunauer, Emmett, and Teller theory, one can find out the molecules required to cover the adsorbent surface with a monolayer of adsorbed molecules, Nm; the surface area can further be calculated by multiplying the cross-sectional area of the adsorbate by Nm. The BET surface area and N_2 isotherm of all the 'as-prepared' ferrite samples were estimated using a Quantachrome Autosorb iQ-MP-C instrument. At first, the sample was degassed. Before starting with the sorption process, the solid is freed from any contaminants by degassing in a glass cell with heating at 250 °C for two hours. Then the N_2 sorption study was continued at 77 K. This technique helps understand the size and shape of pores, chemically active sites, and surface area of the solid samples.

2.4.9 Resistivity

Electrical resistivity is an intrinsic property. It is an essential property of ferrite materials that measures the resistance to the current flow. Resistivity studies for all the 'as-prepared' and 'sintered' ferrites were conducted using a two-probe DC resistivity setup in the temperature range from 60°C to 500°C. A pellets whose dimensions were known was used for the study. The pellets used for the study had a 1cm diameter and a 2-3mm thickness. The setup was maintained at 2V, and its current was recorded. The resistance was calculated using the following equation.

$$R = \frac{V}{I} \qquad (2.9)$$

Where '*R'* is the resistance of the sample, '*V'* is the voltage maintained at 2 V, and '*I'* is the current recorded. Further, the resistivity ρ was calculated using the equation given below.

$$\rho = \frac{Rl}{A} \qquad (2.10)$$

'ρ' is the resistivity, '*R'* is the resistance, '*l'* is the thickness of the pellet, and '*A'* is the area of the cross-section.

2.4.10 AC Susceptibility

AC Susceptibility is a technique used to investigate the spin dynamics and change in phase of the magnetic materials. Also, Curie temperature and domain structure can be evaluated in the study and are obtained from the plots of normalized a.c. Susceptibility versus temperature. At the Curie temperature, when the sample changes from ferrimagnetic to paramagnetic, there is a fall in susceptibility, which is seen in the plots. The susceptibility studies were conducted on finely ground ferrite samples from 300K to 850K on an instrument provided by ADEC Embedded Technology and Solution Pvt. Ltd, Corlim-Goa.
The plots determine the type and nature of the samples, whether they are single domain, multidomain, or superparamagnetic. For single domain type of samples, there is an increase in susceptibility with an increase in temperature until a certain point, after which there is a continuous fall. In the multi-domain type, the susceptibility is constant with a sharp fall at the Curie temperature, whereas for superparamagnetic material, the susceptibility decreases with an increase in temperature. Particles with a size from 10 – 50nm are grouped under single-domain nature, and particles with dimensions greater than 100 nm can be categorized as multi-domain. In contrast, sizes less than 10nm can be classified as superparamagnetic particles.

2.4.11 Vibrating Sample Magnetometer

VSM is a crucial tool for understanding the magnetic properties of the samples. It gives you an insight into the structure of solid materials. In this technique, samples whose magnetic property is to be determined are first placed in a constant magnetic field. The magnetic field magnetizes the sample and then allows it to vibrate in a sinusoidal manner, which generates an electrical signal in the pickup coil. These signals are proportional to the magnetic moment of the sample. In the present study, all the ‘as-prepared’ and ‘sintered’ ferrite samples were analysed using a Quantum Design, cryogen-free Versa Lab vibrating sample magnetometer instrument. The magnetic moment vs magnetic field was studied at RT and 60K from -3 to +3Tesla to determine various magnetic parameters like saturation magnetisation, remanent magnetisation, and coercivity. ZFC-FC studies were conducted in the 60-350K temperature range at different magnetic fields like 250, 500, 1000, and 2000 Oe.
In the field study, the first step is the zero-field-cooled process (ZFC). In this process, the sample is first cooled from 300K to 60K without application of a magnetic field, and then

measurement was done at a constant field during the heating process from 60K to 350 K. in case of field cooled (FC) study the sample was again cooled from RT to 60K but this time with application of field and then while heating the measurements were conducted from 60K to 350K. The blocking temperature was determined for the samples from the data plotted using Origin 8 software.

2.4.12 Dielectric study

Dielectric is the material in which an electric field is induced with minimum energy loss. Dielectric materials are electrical insulators that get polarised on the application of a field. The study of dielectric materials deals with energy storage and dissipation in materials. The capacitance and D factor measurement was conducted on a Wayne Kerr 6500P LCQR meter in the frequency range of 20Hz to 1MHz at RT. The measurements were also conducted from RT to 500°C at every 10°C at different selected frequencies. The measurements were done on disk-shaped pellets with a diameter of 1cm and a 2 mm thickness. The data obtained gave the capacitance of the sample and the dielectric loss value. The capacitance values were converted into dielectric constant values using the following formula.

$$\varepsilon' = \frac{Cd}{\varepsilon_{\circ} A} \tag{2.11}$$

Where ε' is the dielectric constant, C is the capacitance (in Farads), d is the thickness of the pellet (m), A is the pellet's cross-section area (m^2), and permittivity of free space, $\varepsilon_{\circ} = 8.854 \times 10^{-12}$ F/m. The dielectric constant and dielectric loss vs frequency at RT and dielectric constant and dielectric loss vs temperature at constant frequency have been plotted using Origin software for all the' as-prepared' and 'sintered' ferrite samples.

2.4.13 Permeability study

The following equation defines the initial permeability:

$$\mu i = \lim_{H \to 0} \frac{B}{H} \tag{2.12}$$

'μi' is initial permeability, 'H' is the applied field, and 'B' is magnetic induction.

The initial permeability analysis of the 'sintered' ferrites using their toroids were done. These measurements helped determine the homogeneity of the samples. The 'sintered'

toroids were wound with 30 SWG enameled Cu wire, and their inductance was measured using the Wayne Kerr 6500P LCQR meter. The study was conducted at frequencies ranging from 20 Hz to 10 MHz and at a constant frequency from RT-500 ^{O}C. The results demonstrated that the toroids possess a certain level of initial permeability and that their inductance was measured with respect to variation in the frequency and temperature. This study provides valuable insights into the properties of the toroids and how they can be effectively utilized in different applications. From the evaluation of the inductance, the initial permeability was determined using the following relation.

$$L = 0.0046N^2 h log\frac{d1}{d2} \qquad (2.13)$$

Where 'L' is the inductance observed in(μH), 'N' is the number of turns of copper wire, 'h' is the height of the core in (inches), and 'd_1' and 'd_2' are the outer and inner diameters of the toroid.

2.5 Gas sensing studies

In recent years, the studies on gas sensors have increased as demand for detecting hazardous environmental gases has increased. The research in this field has grown faster in recent times due to the need for in-situ gas sensors that are selective and sensitive to target gases. The first-ever gas sensor indicator was made commercially available by Oliver W. Johnson in the year 1927. In 1938, Wagner and Hauffe found that atoms and molecules, when interacting with semiconducting surfaces, lead to changes in surface properties such as conductivity and potentials. Semiconducting materials that reversibly bind oxygen on their surface can be good sensor materials.

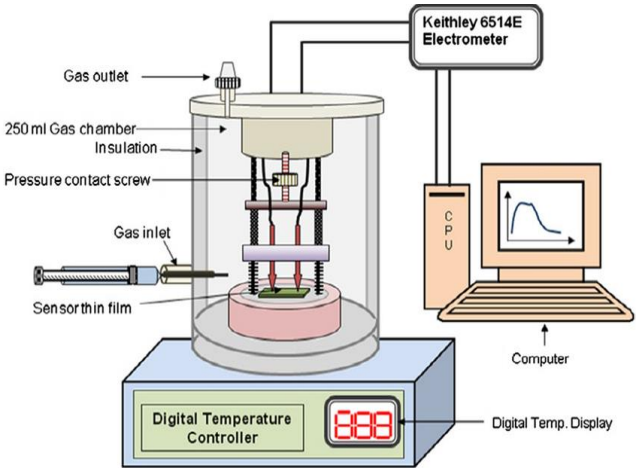


Fig. 2.1 Gas sensing setup used for sensing measurement

2.5.1 Fabrication of thick films

Ferrite materials can be fabricated in three ways: pellets, thick, or thin films. We used the thick film method to prepare the sensor material as it is a low-cost and easy technique. Either screen printing, casting, spraying, or coating results in thick film deposition. We utilised the screen-printing method to produce rectangular-shaped thick films.

Our study involved the preparation of thick films of 'as-prepared' ferrites which were analysed for its sensing properties. We used a screen-printing method to prepare ferrites from a mixture of ferrite powder and ethyl cellulose, which acted as a binder, and using butyl carbitol as solvent having a ratio of 70:30 of ferrite and ethyl cellulose. The mixture was then screen printed onto a glass substrate using a mesh screen of nylon with a density of 200 mesh. After drying the thick films at 60 °C for 1 hour, we baked them in a tubular furnace at 400 °C for 30 minutes to remove any organic moieties. The final product was a glass-based thick film with dimensions of 9x4 mm, to which silver paste was applied on the edges to make electrical contacts

2.5.2. Test system and gas sensing measurements

A static gas sensing technique was used to examine the gas sensing performance of our 'as prepared' ferrite samples. The setup used is showcased in Fig. 2.1. The gas sensing setup is a 250 mL airtight stainless-steel container with an electrical feed at the base plate. The base's heater helps set the desired operating temperature during analysis. The thermocouple inside the system senses the operating temperature, which controls the temperature. The voltage applied was 2V. The gas is passed into the sample chamber through an inlet by a syringe (5- 50 mL). Any change in the resistance after injection of test gas is recorded on the Keithley 6514 electrometer. Once the data is acquired, the chamber is flushed with inert gas, i.e., nitrogen.

An extensive study on the detection of hazardous gases such as Cl_2, NH_3, LPG, and NOx was conducted in our present study. We utilized both oxidizing and reducing gases for the analysis and tested them at various temperatures, such as RT, 50, 100, and 150°C. Each gas was optimized to select a temperature that would allow for the analysis of all the samples. We also examined the gas sensing using different ppm of gases, ranging from 20 to 200. We aimed to detect these gases at very low ppm to protect human health and the environment from increasing hazardous pollutants around us.

The test gases were synthesised in the laboratory, and the procedure is explained below. NO_x gas was produced using Cu powder, treated with concentrated HNO_3 in a tightly closed setup, and using $CaCl_2$ as the trap. NH_3 gas was generated in a tightly sealed container by mixing Calcium hydroxide and ammonium chloride in the appropriate amount. CaO was used as a trap to remove any moisture present. LPG tested for sensing was taken directly from a commercially available LPG cylinder, while Cl_2 was generated by dissolving $KMnO_4$ in concentrated HCl using a $CaCl_2$ moisture trap. The % gas response is measured using the value of resistance in the following equation

$$\%\text{Response} = \frac{Ra-Rg}{Ra} \text{ X } 100 \text{ for (n type gas sensor)} \quad (2.14)$$

$$\%\text{Response} = \frac{Rg-Ra}{Rg} \text{ X } 100 \text{ for (p-type gas sensor)} \quad (2.15)$$

Ra is the resistance of the thick film sample in air, and Rg is the resistance of the thick film sample in the test gas.

2.6 Electrochemical studies

Ferrites have exceptional potential as a material for supercapacitors. With their superior energy storage capacity and fast charge and discharge capabilities, they are undoubtedly the best candidate for energy storage. The advancements made in this field in recent years are remarkable. Therefore, in the present study, we have studied the electrochemical properties of 'as-prepared' ferrites using cyclic voltammetry.

2.6.1 Fabrication of electrodes

The 'as-prepared' ferrite samples of both series were used to prepare the working electrode. Carbon black was chosen as the conducting material, while poly (vinylidene fluoride) functioned as the binder alongside the ferrite material. After mixing the three solids in a motor and pestle with N-methyl pyrrolidone solvent, a paste was cast onto a 1x1 cm cleansed, dried, and weighed Ni foam. The resulting electrode was then dried for an hour at 60 °C before being subjected to 15 hours of drying at 100 °C. The ratio of Carbon black, binder, and ferrite used, which was 75:15:15, was determined through an extensive optimization process. The electrode was then subjected to a pressure of 10MPa for 30 seconds using a hydraulic press. The electrode was weighed and used as it was for analysis.

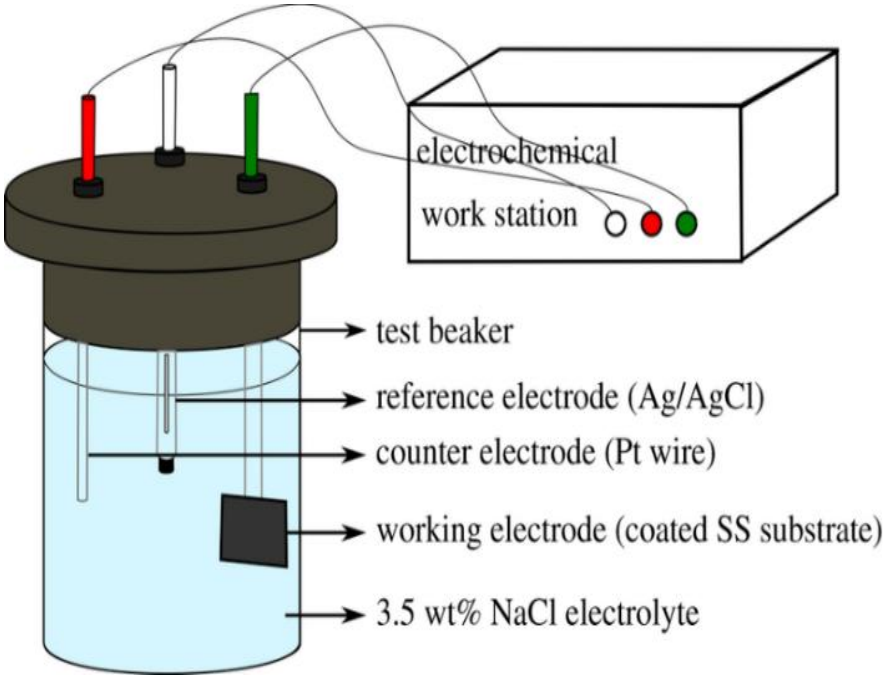


Fig. 2.2: Schematic representation of electrochemical performance using Cyclic voltammetry

2.6.2 Electrochemical measurements

The capacitance of the material was studied using electrochemical measurements through cyclic voltammetry. A three-electrode system was used, including a working electrode fabricated on a Ni foam with the sample material and dipped in 3M KOH solution. The reference electrode was Ag/AgCl, and the counter electrode was Pt. The CV measurements were taken at different scan rates ranging from 3 to 80 mV/s in the potential window of 00.5 V. To calculate the specific capacitance, the following formula was used.

$$C = \frac{S}{2\ m\ k\ \Delta v} \tag{2.16}$$

Where S is the surface area, m is the mass of the active material in grams, k is the scan rate in volts, and Δv is the potential difference in volts. The GCD and EIS studies were conducted at a current density of 1A/g using the same electrodes.

2.7 Antibacterial studies

Antibacterial studies were performed on the 'as-prepared' ferrite samples of all the series. The ferrite samples were tested against a gram-positive pathogen, *Staphylococcus aureus*, at two different concentrations, i.e.,500 µg/mL and 1000 µg/mL. An 18-hr-old culture of *Staphylococcus aureus* was inoculated in nutrient broth medium to which two different

concentrations (500 µg/mL and 1000 µg/mL) of ferrite were prepared in saline. Nutrient broth medium containing no added ferrite powder was kept as a control. The flasks were incubated at 37℃, 110 rpm for 18 h. After incubation, the growth of Staphylococcus aureus was checked by examining the optical density at 600 nm. Serial dilution of the culture broth was carried out using 0.85% saline, and the required dilutions were spread plated on nutrient agar plates. Viable count was thus determined, and the percentage survival of the bacteria in the presence of nanoparticles was calculated using the formula:

$$\text{Survival (\%)} \frac{\text{Number of colonies forming units in presence of nanoferrite}}{\text{Number of colonies forming units in absence of nanoferrite}} \times 100 \qquad (2.17)$$

References:

1. M. K. Zate, S. D. Raut, S. D. Shirsat, S. Sangale, A.S. Kadam, Spinel Ferrite Nanostructures for Energy Storage Devices, Ferrite nanostructures, R. Mane, V. Jadhav (ed.), Elsevier, 2020.
2. B. Mekuye, B. Abera, Nano Select, 4 (2023) 463.
3. C. A. P. Gómez, C. A. B. Meneses, A. Matute, Mater. Sci. Eng. B, 48 (2018) 236.
4. S. Zahi, A.R. Daud, M. Hashim, Mater. Chem. Phys., 106 (2007) 452.
5. M. A. Ahmed, N. Okasha, S. I. El-Dek, Nanotech., 19 (2008) 065603.
6. Z. Zhang, G. Yao, X. Zhang, J. Ma, H. Lin, Ceram. Int., 41 (2015) 4523.
7. E. Manova, B. Kunev, D. Paneva, I. Mitov, L. Petrov, C. Estournès, C. D'Orléan, J.L. Rehspringer, M. Kurmoo, Chem. Mater., 16 (2004) 5689.
8. Z. G. Zhang, Y. H. Liu, G. C. Yao, G. Y. Zu, Y. Hao, Int. J. Appl. Ceram. Technol., 10 (2013) 142.
9. A. Hajalilou, M. Hashim, H.M. Kamari, J. Mater. Sci. Mater. Electron., 26 (2014) 1709.
10. S. Zahi, M. Hashim, A.R. Daud, J. Magn. Magn. Mater., 308 (2009) 177.
11. M. Stefanescu, M. Stoia, C. Caizer, O. Stefanescu, Mater. Chem. Phys., 113 (2009) 342.
12. M. Atif, M. Nadeem, R. Grössinger, R.S. Turtelli, J. Alloys Compd., 509 (2011) 5720.
13. L. S. Cividanes, T. M. B. Campos, L. A. Rodrigues, D. D. Brunelli, G. P. Thim, J. Sol. Gel. Sci. Technol., 55 (2010) 111.
14. M. Srivastava, S. Chaubey, A.K. Ojha, Mater. Chem. Phys., 118 (2009) 174.
15. I. C. Masthoff, M. Kraken, D. Mauch, D. Menzel, J. A. Munevar, E. B. Saitovitch, F. J. Litterst, G. Garnweitner, J. Mater. Sci., 49 (2014) 4705.
16. D. R. Mane, D.D. Birajdar, S. Patil, S.E. Shirsath, R.H. Kadam, J Sol. Gel. Sci. Technol., 58 (2011) 70.
17. S. Ramesh, B.C. Sekhar, P.S.V.S. Rao, B.P. Rao, Ceram. Int., 40 (2014) 8729.
18. S.M. Reda, Mater. Sci. Semicond. Process, 13 (2010) 417.
19. T. Meron, Y. Rosenberg, Y. Lereah, G. Markovich, J. Magn. Magn. Mater., 292 (2005) 11.
20. L. Avazpour, M.A.Z. Khajeh, M.R. Toroghinejad, H. Shokrollahi, J. Alloys Compd., 637 (2015) 497.

21. R. Rahimi, A. Maleki, S. Maleki, A. Morsali, M.J. Rahimi, Solid State Sci., 28(2014) 9.
22. S. Amiri, H. Shokrollahi, J. Magn. Magn. Mater., 345 (2013) 18.
23. H. Li, L. Qin, Y. Feng, L. Hu, C. Zhou, J. Magn. Magn. Mater., 384 (2015) 213.
24. Y. Xing, Y. Jin, J. Si, M.L. Peng, X. Wang, C. Chen, Y. Cui, J. Magn. Magn. Mater., 380 (2015) 150.
25. J.A. Lopez, F. González, F.A. Bonilla, G. Zambrano, M.E. Gómez, Rev. Lat. Met. Mat., 30 (2010) 60.
26. Z. Karimi, Y. Mohammadifar, H. Shokrollahi, S. K. Asl, G. Yousefi, L. Karimi, J. Magn. Magn. Mater., 361 (2014) 150.
27. C. F. Zhang, X. C. Zhong, H.Y. Yu, Z.W. Liu, D. C. Zeng, Phys. B Condens. Matter, 404 (2009) 2327.
28. D. Makovec, A. Kodre, I. Arčon, M. Drofenik, J. Nanopart. Res., 11(5) (2008)1145.
29. T. Jahanbin, M. Hashim, K. Amin Mantori, J. Magn. Magn. Mater., 322 (2010) 2684.
30. I. Sharifi, H. Shokrollahi, M.M. Doroodmand, R. Safi, J. Magn. Magn. Mater.,324 (10) (2012) 1854.
31. C. G. Reddy, S. V. Manorama, V. J. Rao, Sens. Actuator B Chem., 55 (1999) 90.
32. L. R. Gonsalves, V. M. S. Verenkar, S.C. Mojumdar, J. Therm. Anal. Calorim.,96(1) (2009) 53-57.
33. L. R. Gonsalves, S. C. Mojumdar, V. M. S. Verenkar, J. Therm. Anal. Calorim., 100 (2010) 789.
34. L. R. Gonsalves, S. C. Mojumdar, V. M. S. Verenkar, J. Therm. Anal. Calorim., 104 (2011) 869.
35. L. R. Gonsalves, S. C. Mojumdar, V. M. S. Verenkar, J. Therm. Anal. Calorim., 10 (2012) 859.
36. L. R. Gonsalves, V. M. S. Verenkar, J. Therm. Anal. Calorim., 108 (2012) 877.
37. U. B. Gawas, V. M. S.Verenkar, Thermochim. Acta, 556 (2013) 41.
38. U. B. Gawas, S. C. Mojumdar, V.M.S. Verenkar, J. Therm. Anal. Calorim., 96(1) (2009) 49.
39. U. B. Gawas, S. C. Mojumdar, V.M.S. Verenkar, J. Therm. Anal. Calorim., 100 (2010) 867.

40. U. B. Gawas, V. M. S.Verenkar, S.C. Mojumdar, J. Therm. Anal. Calorim., 104 (2011) 879.
41. U. B. Gawas, V. M. S. Verenkar, S.C. Mojumdar, J. Therm. Anal. Calorim., 108 (2012) 865.
42. U. B. Gawas, V. M. S. Verenkar, J. Therm. Anal. Calorim., 115 (2014) 375.
43. U. B. Gawas, V. M. S.Verenkar, S.S. Meena, P. Bhatt, J. Supercond. Nov. Magn., 30 (2017) 3241.
44. S. G. Gawas, V. M. S. Verenkar, Thermochem. Acta, 605 (2015) 16.
45. P. P. Gauns Dessai, V. M. S. Verenkar, J. Mater. Sci. Mater. Electron., 29 (2018) 6924.
46. P. Arunkumar, R. Aadhavan, S. Bhanuchandar, K.S. Babu, Mater. Res. Express, 1(2014) 035011.
47. A. Gaffoor, D. Ravinder, Int. J. Eng. Res. Appl., 4 (2014) 60.
48. C. C. Hwang, J.S. Tsai, T.H. Huang, Mater. Chem. Phys., 93 (2005) 330.
49. A. Costa, V. J. Silva, C.C. Xin, D.A. Vieira, D.R. Corneja, R. Kiminami, J. Alloys Compd., 495 (2010) 503.
50. A. F. Junior, T. Alves, E.C. De, O. Lima, L. Da, S. Nunes, V. Zapf, Appl. Phys. A, 94 (2009) 131.
51. S. Pauline, A.P. Amaliya, Arch. Appl. Sci. Res., 3 (2011) 213.
52. T. Taniguchi, K. Nakagawa, T. Watanabe, N. Matsushita, M. Yoshimura, J. Phys. Chem. C, 113 (2009) 839.
53. H. Parmar, R. Desai, R.V. Upadhyay, Appl. Phys. A, 104 (2011) 229.
54. X. Liu, J. Liu, S. Zhang, Z. Nan, Q. Shi, J. Phys. Chem. C, 120 (2016) 1328.
55. B. Baruwati, R. K. Rana, S.V. Manorama, J. Appl. Phys., 101 (2007) 014302.
56. A. Pradhan, R. C. Jones, D. Caruntu, C. J. O'Connor, M.A. Tarr, Ultrason. Sonochem., 15 (2008) 891.
57. S. Zhang, Y. Zhang, Y. Wang, S. Liu, Y. Deng, Phys. Chem. Chem. Phys., 14 (2012) 5132.
58. W. Lv, B. Liu, Z. Luo, X. Ren, P. Zhang, J. Alloys Compd., 465 (2008) 261.
59. S.Y. Sawant, K.R. Kannan and V.M.S. Verenkar, C.G.S. Pillai, K.L. Ramakumar, P.V. Ravindran, V. Venugopal, edited, Proc. 13th National Symposium on Thermal Analysis, B.A.R.C. Mumbai, Indian Thermal Analysis Society, (2002) 154.
60. A. S. Prakesh, A. M. A. Khadar, K.C. Patil, M.S. Hedge, J. Mater. Sci. Process., 10 (2002) 135.

61. J. Mendham, R.C. Denney, J.D. Barnes, M. Thomas, B. Sivashankar, (1989) Vogel's textbook of quantitative chemical analysis (5th edition), New York: John Wiley & Sons.

Chapter 3

A comparative study of 'as prepared' and 'sintered' $Ni_{0.6-x}Co_{0.4}Zn_xFe_2O_4$(x=0.0-0.6) ferrites and their applications

3.1 Introduction

Ferrites are an important class of materials and have proven to be precious because of their broad utility. Due to their phenomenal physical and chemical properties, they possess applications from supercapacitors to photocatalysts, biomedical applications, sensors, etc. The properties of these ferrites change according to the conditions provided. One of the main factors is the method of synthesis, which helps in tuning the morphology and microstructure of the materials. Several methods are available in the literature, from solid-state to wet chemical methods. The properties of materials are highly influenced by the method of preparation of the compounds. Apart from this, the dopant added and sintering temperature also plays an essential role in controlling the properties of the samples. The addition of a dopant either improves or alters specific characteristics, such as its magnetism. The material can change from soft to hard magnets with increased dopant concentration. Th magnetic property also changes with change in size, the dopant added and sintering temperatures. Size plays a significant role and can be controlled through the synthesis route adopted in preparing the compounds [1]. Various preparation methods are available in the literature, such as combustion, hydrothermal, co-precipitation, microemulsion, etc. [2-4]. The present study uses the precursor combustion method to prepare ferrites. This technique involves the mixture of metal solution added to carboxylate solution, in the present study fumarate is used along with hydrazine to form the metal fumarate hydrazine complex as the precursor. The precursor technique employed successfully lead to the formation of crystalline ferrite after calcining at a lower temperature of 450- 500 °C [5]. This precursor included a hydrazine carboxylate metal complex. Hydrazine compounds are endothermic and used as rocket fuels. Hydrazine is used as fuel in the combustion technique by proper complexation with an appropriate metal ion. The metal and hydrazine can be complexed with oxalates and fumarates, reducing their explosivity. These compounds possess a minimum kindling point, and once ignited, autocatalytic decomposition occurs. During ignition, large amounts of gases are released (NH_3, H_2O, CO_2), which lowers the heat generated and prevents the ferrites from sintering [6]. This is an excellent technique to obtain nano-sized materials with outstanding electrical, dielectric, and magnetic properties due to their morphological and structural properties, making them excellent catalysts and sensors in various applications.

The parent compound in the present study is Ni-Co ferrite, and a non-magnetic Zn ion is doped, which replaces Ni ions. The Ni-Co ferrite material is stable due to its chemical and thermal properties. Apart from this, high resistivity is also seen in these samples [7]. Magnetic properties are essential in various applications like ferrofluids, recording devices, microwave devices, etc. Cobalt ferrite shows magnetic anisotropy and moderate magnetization, whereas coercivity is high. Ni-Co together shows high resistance towards dielectric behavior, low coercivity, and moderate magnetization [8]. The dopant affects various parameters. The effect of doping non-magnetic zinc with larger ionic radii is studied in this chapter. Zinc, being larger, changes structural properties, such as magnetism, electrical, and dielectric properties.

Therefore, in the ongoing study, we have focused on preparing $Ni_{0.6-x}Co_{0.4}Zn_xFe_2O_4$ (x=0.0,0.1,0.2,0.3,0.4,0.5,0.6) via the precursor-combustion method. The precursor $Ni_{0.6-x}Co_{0.4}Zn_xFe_2(C_4H_2O_4)_3.6N_2H_4$ (x=0.0,0.1,0.2,0.3,0.4,0.5,0.6) obtained was thoroughly investigated to confirm its stoichiometry, which, when ignited, gave the as-prepared ferrite in a stoichiometric ratio.

3.2 Synthesis of Zn-doped Ni-Co ferrites $Ni_{0.6-x}Co_{0.4}Zn_xFe_2O_4$(x=0.0-0.6) by precursor combustion method

The synthesis of $Ni_{0.6-x}Co_{0.4}Zn_xFe_2O_4$ (x=0.0,0.1,0.2,0.3,0.4,0.5,0.6) was done via the precursor-combustion method. The synthesis route for the precursor and ferrite is discussed in Chapter 2 in Section 2.1. The Characterization of these ferrites is conducted using various analytical techniques. The solid-state properties of as-prepared and sintered ferrite is compared and discussed further in this chapter, along with the application of the materials.

3.3 Characterisation of $Ni_{0.6-x}Co_{0.4}Zn_xFe_2(C_4H_2O_4)_3.6N_2H_4$ (x=0.0-0.6) precursors

The synthesized $Ni_{0.6-x}Co_{0.4}Zn_xFe_2(C_4H_2O_4)_3.6N_2H_4$ (x=0.0,0.1,0.2,0.3,0.4,0.5,0.6) precursor was thoroughly characterized to verify the stoichiometric ratio. The hydrazine content was determined by titrimetric determination to reveal the coordination of hydrazine in the precursor. The C, H, N content was obtained from the C, H, N, S analyzer. At the same time, IR and thermoanalysis were carried out to study the decomposition of the compound, which added support to the perfect stoichiometry of the compound.

3.3.1. CHNS Analysis

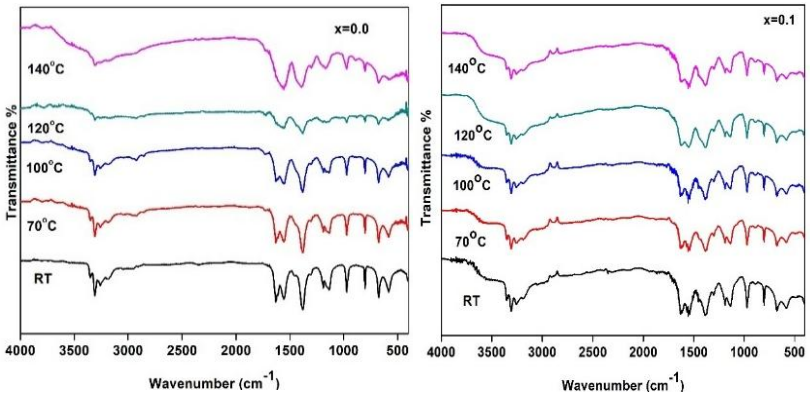
The C, H, N content in the $Ni_{0.6-x}Co_{0.4}Zn_xFe_2(C_4H_2O_4)_3.6N_2H_4$ (x=0.0,0.1,0.2,0.3,0.4,0.5,0.6) precursors was determined using a C, H, N, S analyzer. The analysis of the freshly synthesized precursor was carried out within an hour on this analyzer. It was observed that the obtained experimental data matched very well with the calculated theoretical values, as depicted in Table 3.1. With the help of CHN data, it was possible to fix the formula of the precursor's C, H, and N content. It is clear through Table 3.1 that theoretical percentages and experimentally obtained data agreed well, thus proving its perfect stoichiometry.

Table 3.1: The theoretical and experimental percentages of C, H, N, in $Ni_{0.6-x}Co_{0.4}Zn_xFe_2(C_4H_2O_4)_3.6N_2H_4$ (x=0.0,0.1,0.2,0.3,0.4,0.5,0.6)precursors

Elements		**Composition**						
		0.0	**0.1**	**0.2**	**0.3**	**0.4**	**0.5**	**0.6**
C (%)	**Theoretical**	20.4	20.40	20.40	20.40	20.34	20.33	20.30
	Experimental	19.9	20.00	19.61	19.14	19.12	19.54	19.22
H (%)	**Theoretical**	4.25	4.25	4.25	4.25	4.24	4.23	4.23
	Experimental	4.59	4.08	3.89	4.32	4.43	4.39	4.47
N (%)	**Theoretical**	23.8	23.83	23.80	23.80	23.70	23.70	23.69
	Experimental	22.7	22.44	22.3	23.08	22.93	22.41	22.44

3.3.2 Infrared spectroscopy

The zinc-doped nickel cobalt precursor formation in a stoichiometric manner was also confirmed with the help of IR spectroscopy. The IR spectra of all $Ni_{0.6-x}Co_{0.4}Zn_xFe_2(C_4H_2O_4)_3.6N_2H_4$ (x=0.0,0.1,0.2,0.3,0.4,0.5,0.6) precursors isothermally heated from RT to 140°C and 180°C to as burnt ferrites are depicted in Fig. 3.1 and Fig. 3.2, respectively. The data tabulated in Table 3.2 represents the peak positions of various groups observed in the IR spectrum. The spectra were recorded by running a full scan from 4000-350cm^{-1}. The peaks obtained in the study are due to two major organic groups present in the precursor, namely the carboxylate group and the hydrazine moiety. The spectra revealed three major peaks due to the presence of hydrazine group [9]. The N-H stretching frequency was observed between 3190-3355 cm^{-1}. The NH_2 deformation region was observed from 1559- 1571 cm^{-1}. The third band was found to be at 972-985 cm^{-1} owing to N-N stretching [10]. Due to NH_2 wagging, NH_2 rocking, and N-N bending, more bands are also observed [11], whose values are tabulated in Table 3.2. The data revealed that hydrazine acts as a bidentate bridging ligand in the precursor [12]. The carboxylate group showed two major bands, first due to asymmetric stretching vibration at ~1629 cm^{-1}, and the other due to symmetric stretching vibration observed at around 1385-1397 cm^{-1}. The frequency difference between asymmetric and symmetric vibration was 243 to 231 cm^{-1}. This significant separation points to the monodentate linkage of the dianion carboxylate group [13]. This confirms the coordination of the hydrazine group as a bridged bidentate ligand and the fumarate group as a bidentate ligand linked to the metal via both carboxylate groups.



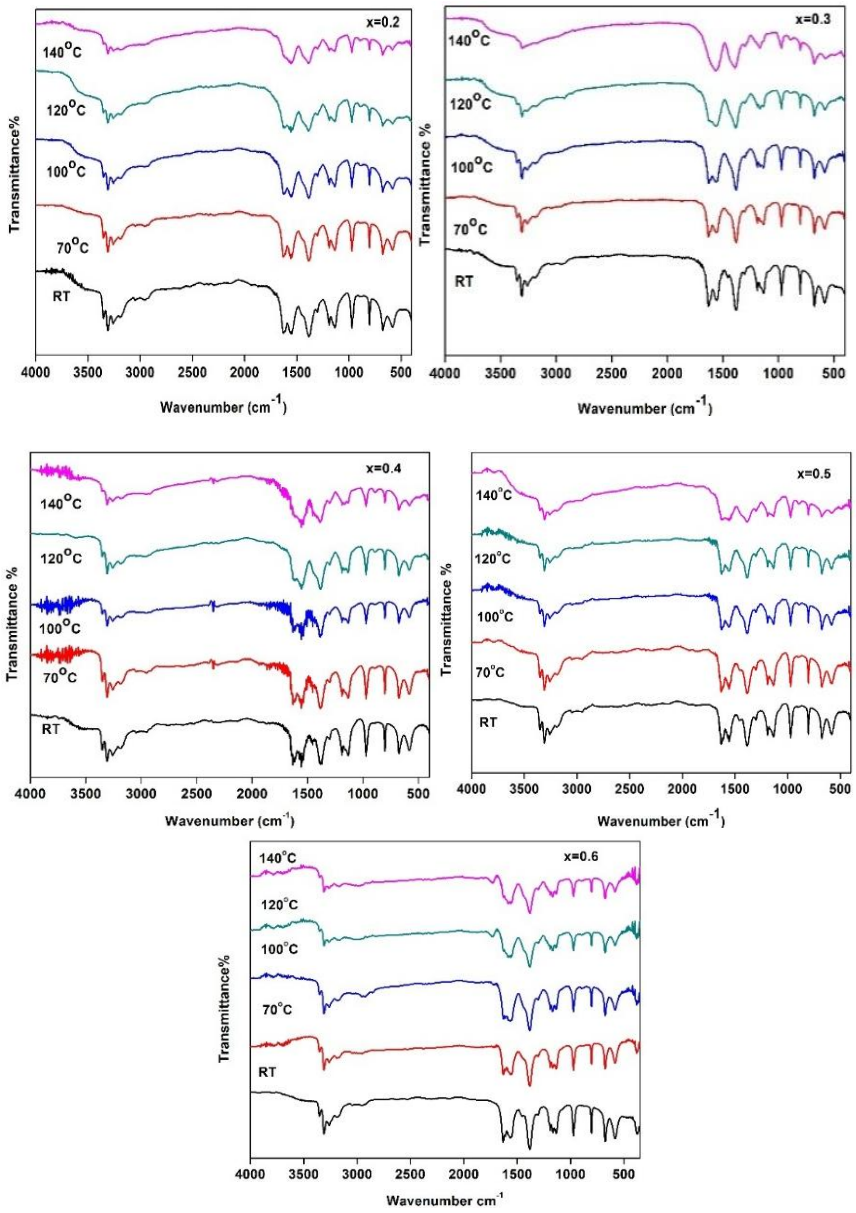


Fig.3.1: IR spectra of $Ni_{0.6-x}Co_{0.4}Zn_xFe_2(C_4H_2O_4)_3.6N_2H_4$ (x=0.0,0.1,0.2,0.3,0.4,0.5,0.6) precursors isothermally heated from RT-140^oC

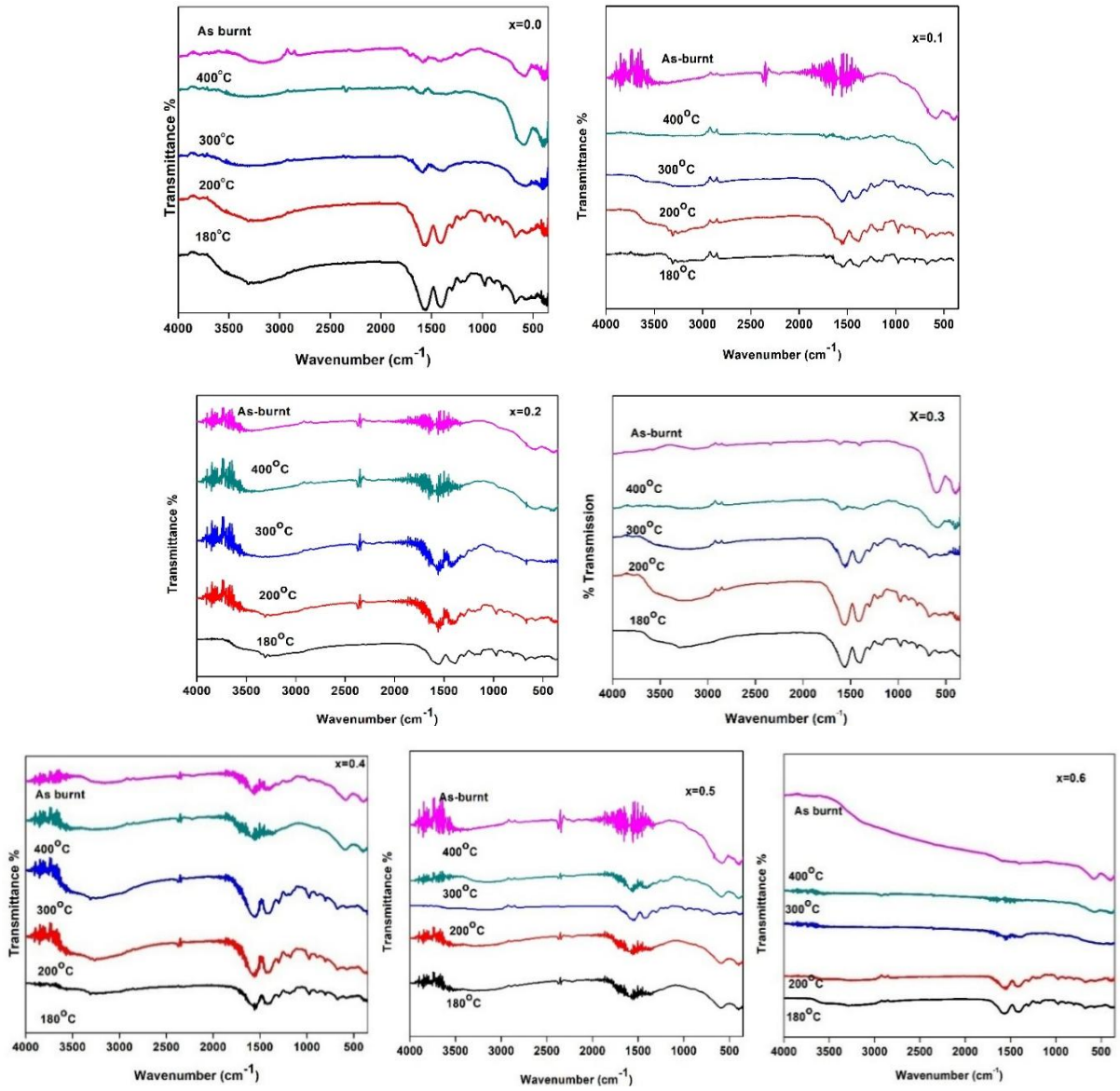


Fig. 3.2: IR spectra of $Ni_{0.6-x}Co_{0.4}Zn_xFe_2(C_4H_2O_4)_3.6N_2H_4$ (x=0.0,0.1,0.2,0.3,0.4,0.5,0.6) precursors isothermally heated from 180°C-As-burnt

Table 3.2: IR peak position of various organic moieties for all the $Ni_{0.6-x}Co_{0.4}Zn_xFe_2(C_4H_2O_4)_3.6N_2H_4$ (x=0.0,0.1,0.2,0.3,0.4,0.5,0.6) precursors

	Wavenumber (cm^{-1})						
x	0.0	0.1	0.2	0.3	0.4	0.5	0.6
N-H stretching	3368-3194	3360-3196	3368-3194	3375-3181	3360-3181	3356-3194	3360-3181
COO^-asy stretching	1646	1629	1646	1629	1644	1646	1644
NH_2 deformation	1559	1569	1571	1569	1569	1571	1571
COO^- stretching	1385	1390	1397	1390	1390	1397	1390
C-C sym	1197	1211	1197	1211	1197	1197	1172
NH_2 wagging	1122	1152	1147	1152	1147	1147	1135
N-N sym stretching	972	972	985	972	972	985	972
N-N bending	789	808	798	823	811	798	811
NH_2 rocking	673,598	674,584	673,586	674,584	673,586	673,586	673,586

3.3.3 TG/DTA analysis

TG-DTA studies were carried out of $Ni_{0.6-x}Co_{0.4}Zn_xFe_2(C_4H_2O_4)_3.6N_2H_4$ (x=0.0,0.1,0.2,0.3,0.4,0.5,0.6) precursor samples from RT to 800 ^oC in an oxygen atmosphere, and the thermograms of the same are depicted in Fig. 3.3 (a-g). 100 mL of the carrier gas was purged per minute during the heating process at a 10 ^oC ramping rate with a 10 mg sample. The TG curve showed two main mass losses with corresponding two DTA exothermic peaks. The

initial weight reduction was caused due to de-hydrazination, i.e., the depletion of six hydrazine molecules, while the second was due to the loss of carboxylate group or total decarboxylation. When the precursor is ignited, hydrazine is released, which reacts with the oxygen molecules, evolving heat energy of -625 kJ/mol. The energy released during hydrazine decomposition helps in the exothermic decarboxylation process.

$$N_2H_4 + O_2 \rightarrow N_2 + H_2O \qquad \Delta H = -625\ kJ/mol$$

Table 3.3 indicates the percentage of mass loss obtained from TG, and the corresponding peaks obtained in DTG and DTA.

The TG-DTA -DTG thermogram of x=0.0 is shown in Fig. 3.3 a. A mass loss of 5.36% obtained corresponds to a mass loss of approximately one hydrazine molecule with a DTG peak at 98°C and exothermic peak of DTA at 96°C. This step is followed by dehydrazination process of remaining hydrazine molecules which takes place from 100-230°C with a mass loss of 24.24% with corresponding DTG and DTA peaks at 152°C and 166°C, respectively. From temperature range 230°C- 410°C, an exothermic DTA peak at 304 °C and DTG peak at 311°C is seen with corresponding mass loss of 36.57% indicating total decarboxylation in the compound leading to formation of oxide with residual content of 33.83% which closely matches with the theoretical residual content 33.31%.

Fig. 3.3 b showcases the TG-DTG-DTA plot of sample x=0.1. A mass loss of 4.01% is calculated from the thermogram, which is estimated to be due to the loss of 1 molecule of hydrazine between RT and 100 °C. Further, total de-hydrazination is estimated to happen in between 100-230°C temperature range with a mass loss of 24.85%. The DTG plot shows a peak corresponding to the mass loss at 164°C and DTA shows a peak at 164°C. The three carboxylate groups attached to the precursors are lost beyond the temperature of 230°C with a mass loss of 36.74%, accompanied by a DTG peak at 297°C and an exothermic peak of DTA at 330°C.

Table 3.3: The TG/DTA/DTG data of $Ni_{0.6-x}Co_{0.4}Zn_xFe_2(C_4H_2O_4)_3.6N_2H_4$ (x=0.0,0.1,0.2,0.3,0.4,0.5,0.6) precursors

x	Temperature Range/°C	TG Mass loss %	DTG peak/°C	DTA peak/°C (Exo)	Remarks
0.0	RT-100	5.36	98.7	96.5	Beginning of dehydrazination
	100 - 230	24.24	152	166	Total dehydrazination
	230-410	36.57	311	304	Total Decarboxylation
0.1	RT-100	4.01			Beginning of dehydrazination
	100-230	24.85	164	164	Total dehydrazination
	230-410	36.74	297	330	Total Decarboxylation
0.2	RT-100	6.39	-	-	Beginning of dehydrazination
	100-230	25.58	148	156	Total dehydrazination
	230-410	35.46	321	321	Total Decarboxylation
0.3	RT-100	6.34	-	-	Beginning of dehydrazination
	100-230	23.67	150	161	Total dehydrazination
	230-410	36.4	289,304	310	Total Decarboxylation
0.4	RT-100	3.15	-	-	Beginning of dehydrazination
	100-230	25.45	175	184	Total dehydrazination
	230-410	37.55	318	323	Total Decarboxylation
0.5	RT-100	3.43	-	-	Beginning of dehydrazination
	100-230	24.86	161	163	Total dehydrazination
	230-410	36.97	296	331	Total Decarboxylation
0.6	RT-100	5.69	98	94	Beginning of dehydrazination
	100-230	24.92	166	171	Total dehydrazination
	230-410	34.46	317	315	Total Decarboxylation

The thermogram of x=0.2 is depicted in Fig. 3.3c. From the TG-DTG-DTA data evaluated, a mass loss of 6.39% from RT-100°C was seen, and the loss of hydrazine molecules is expected to occur. Approximately two hydrazine molecules are depleted at this step. Further in the temperature range, 100-230°C, 25.58% mass loss is observed, indicating total dehydrazination. A DTG peak accompanies this loss at 148°C and an exothermic DTA peak is observed at 156°C. The next step is the decarboxylation, which initiates soon after dehydrazination from 230-410°C with a mass loss of 35.46% and simultaneously a DTG peak at 321°C and an exothermic DTA peak at 321°C is observed. A total mass loss of 66.43% is obtained, leaving behind 32.57% residual content.

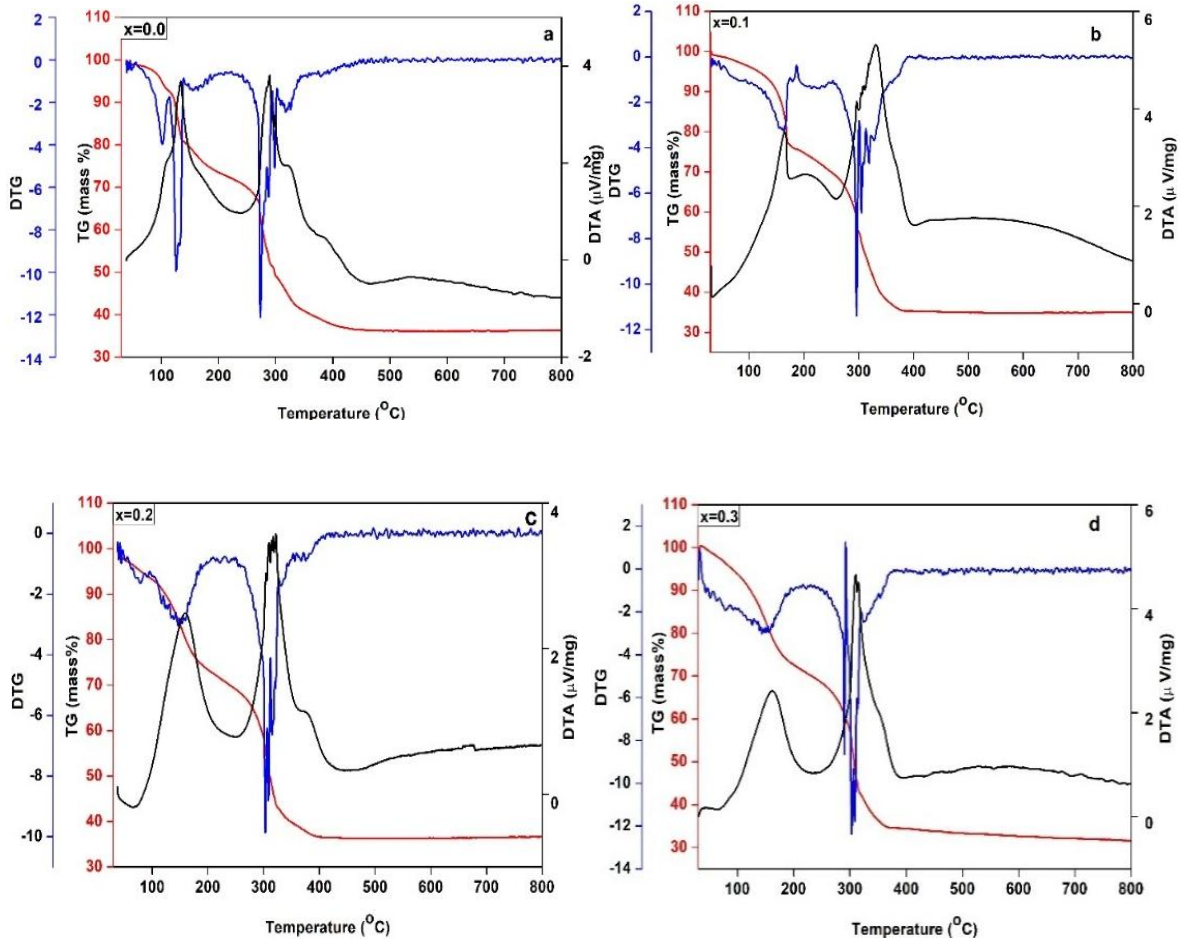
In the case of sample x=0.3 showcased in Fig. 3.3d, the mass loss of 6.34% indicates the loss of approximately two molecules of hydrazine from RT-100°C. From a 100-230 °C temperature range, a loss of 23.67% is obtained, corresponding to the loss of all remaining hydrazine molecules. The DTG peak accompanies this mass loss at 150°C, and the exothermic peak of DTA at 161°C confirms the same. Followed by dehydrazination decarboxylation begins (230-410°C), which is shown by a mass loss of 36.4% alongside a DTG peak at 289 and 304°C, which corresponds to the loss of carboxylate groups in the process and an exothermic thermal peak at around 310°C is observed in the DTA. The total mass loss that occurred in the two-step decomposition process of the precursor is 66.41%, with a residual content of 33.59%.

The TG-DTG-DTA thermogram of sample x=0.4 is showcased in Fig. 3.3e. The starting weight loss is shown from RT-100°C. The mass is about 3.15%, equivalent to approximately the loss of one hydrazine molecule. The loss of hydrazine molecules continues from 100-230°C with a mass loss of 25.45%, corresponding to a loss of all remaining hydrazine molecules. A DTG peak complements the TG mass loss at 175°C and a DTA peak at 184°C. Further, the decarboxylation process starts and continues till 410°C. The mass loss obtained is 37.55%, accompanied by a DTG peak at 318°C and a DTA peak at 323°C. The total mass loss after the dehydrazination and decarboxylation process comes to 66.15%, which evenly matches the calculated data.

Fig. 3.3f illustrates the TG-DTA-DTG plot of the sample with composition x=0.5 in which from RT- 100°C a mass loss of 3.43%, closely equal to little less than one hydrazine molecule is obtained. This is followed by a DTA peak at 163°C with exothermic nature and DTG peak at 161°C with a mass loss of 24.86%. A total mass loss of 28% is seen from RT-230°C, which

indicates the total loss of all six hydrazine molecules and the start of decarboxylation. In the final step, 36.97% mass loss is obtained with a DTG peak at 296°C and a DTA peak at 331°C due to the decarboxylation of the fumarate group.

The thermogram of the x=0.6 sample is depicted in Fig. 3.3g, from which it is observed that an initial mass loss of 5.69% occurs from RT to 100°C. This mass loss results from a loss of approximately one hydrazine molecule, shown by a DTG peak at 98°C and an exothermic DTA peak at 94°C. The next step from 100°C -230°C corresponds to the total dehydrazination of hydrazine molecules with a peak shown in DTG plot at 166°C and in DTA plot at 171°C with a mass loss of 24.92% is observed in the TG curve. The final step is the decarboxylation of the carboxylate group, which starts at 230°C with a DTG peak at 317°C and a DTA peak at around 315°C with a mass loss of 34.46%. All the mass losses and observed DTA and DTG peaks correspond to the theoretical mass loss of the compound.



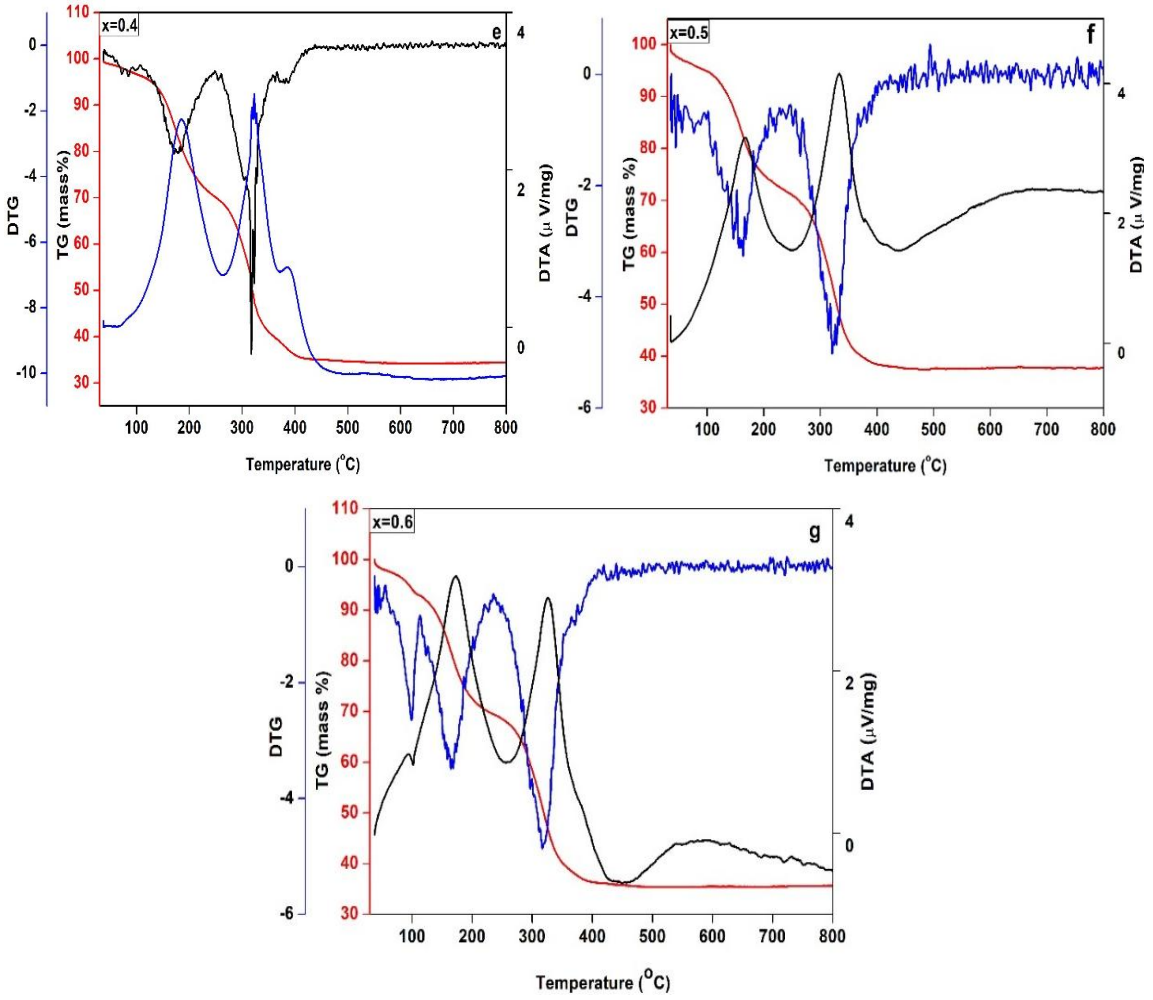


Fig. 3.3: TG-DTA-DTG curves of $Ni_{0.6-x}Co_{0.4}Zn_xFe_2(C_4H_2O_4)_3.6N_2H_4$ (x=(0.0=a, 0.1=b, 0.2=c, 0.3=d, 0.4=e, 0.5=f, 0.6=g) precursors

3.3.4 Isothermal mass loss study/ Total mass loss study

The isothermal mass loss study was conducted at set temperatures from RT to 500 °C for all the $Ni_{0.6-x}Co_{0.4}Zn_xFe_2(C_4H_2O_4)_3.6N_2H_4$ (x=0.0,0.1,0.2,0.3,0.4,0.5,0.6) precursors. The data obtained for the said analysis is given in Table 3.4. The data shows that there is loss of different organic moieties at varied temperature. From RT to 180 °C, a mass loss of around ~27% is obtained owing to the de-hydrazination of the sample, this data is backed by hydrazine estimation conducted alongside isothermal studies. The loss of the carboxylate group initiates at around 180°C and continued till 450°C with a loss of ~39%. After the decomposition of the precursor, the residual content obtained was ~ 33%, and the mass loss was around ~66%. Thus,

Table 3.4: Isothermal mass loss and simultaneous hydrazine study of $Ni_{0.6-x}Co_{0.4}Zn_xFe_2(C_4H_2O_4)_3.6N_2H_4$ (x=0.0,0.1,0.2,0.3,0.4,0.5,0.6) precursors

x	0.0	0.1	0.2	0.3	0.4	0.5	0.6
RT-70	2.9/ 24.9	4/ 27.0	3.5/ 26.1	1.4/ 26.7/	7.3/ 26.7	0.4/ 25.7	4.5/ 27.0
70-100	3.79/ 19.9	1.7/ 23.2	4.1/ 21.6	0.3/ 21.4	2.2/ 23.3	1.95/ 24.4	2.1/ 25.3
100-120	7.44/ 17.4	4.5/ 17.3	1.8/ 17.5	5.4/ -	5.9/ 19.0	0.59/ 23.0	4.8/ 20.0
120-140	3.6/ 7	3.4/ 15.0	5.5/ 14.3	6.4	7.3/ 12.2	9.5/ 14.6	4.9/ 13
140-180	3.6/ -	3.7/ 13.2	4.93/ 8.6	5.5	4.7 -	1.5/ 7.0	5.1 -
180-200	0.97	3.8/ -	4.5/ -	0.6	3.2	2	2.6
200-220	2	3.1	1.6	0.6	1.5	5	2.4
220-240	0.5	2.1	3.2	1.6	4.5	0.8	0.7
240-300	8	7.3	8.8	8.1	28	8.8	24
300-350	25.36	28	22.6	24.2	2.4	22.8	2.3
350-400	2.5	3.3	3.64	4.5	1	4.14	2.43
400-450	2	0.93	2.47	6	0	4.27	10.17
>500	1.7	0	0	3	0	3.67	0
	65.09%	66.03%	66.50%	66.60%	67.60%	65.09%	66.17%

confirming the stoichiometry of the synthesized precursors. It is observed from Table 3.4 that the theoretically determined mass loss is very well aligned with the experimental results.

3.3.5 Hydrazine estimation and Total mass loss study

Table 3.5 represents the hydrazine content in the precursors at room temperature obtained via the titration method and total mass loss study data of all the $Ni_{0.6-x}Co_{0.4}Zn_xFe_2(C_4H_2O_4)_3.6N_2H_4$ (x=0.0,0.1,0.2,0.3,0.4,0.5,0.6) precursors at 500°C.

Table 3.5: Hydrazine estimation and total mass loss study of $Ni_{0.6-x}Co_{0.4}Zn_xFe_2(C_4H_2O_4)_3.6N_2H_4$ (x=0.0,0.1,0.2,0.3,0.4,0.5,0.6) precursors

Sample	Hydrazine content (%) Theoretical	Hydrazine content (%) Experimental	Total mass loss (%) Theoretical	Total mass loss (%) Experimental
x=0.0	27.27	27.60	66.69	66.02
x=0.1	27.25	27.18	66.68	67.00
x=0.2	27.21	26.40	66.61	67.50
x=0.3	27.18	27.20	66.00	66.35
x=0.4	27.16	27.93	66.64	66.20
x=0.5	27.12	26.45	66.43	66.79
x=0.6	27.12	27.17	66.35	66.21

3.4 Characterisation of 'as prepared' and 'sintered' $Ni_{0.6-x}Co_{0.4}Zn_xFe_2O_4$(x=0.0-0.6)

The precursor $Ni_{0.6-x}Co_{0.4}Zn_xFe_2(C_4H_2O_4)_3.6N_2H_4$ (x=0.0,0.1,0.2,0.3,0.4,0.5,0.6) was decomposed by igniting it to obtain 'as-prepared' $Ni_{0.6-x}Co_{0.4}Zn_xFe_2O_4$(x=0.0-0.6) ferrite. The ferrites were thoroughly characterised to confirm the purity of the samples. Various instrumental techniques were utilized for their characterization, like XRD, IR spectroscopy, SEM, and TEM.

3.4.1 Phase purity and elemental analysis

3.4.1.1 Powder X-ray Diffraction

Powder X-ray diffraction studies evaluated the phase purity and identified parameters like crystallite size, crystallinity, etc. The XRD patterns of Zn-doped Ni-Co ferrite $Ni_{0.6-x}Co_{0.4}Zn_xFe_2O_4$ (x=0.0, 0.1, 0.2, 0.3, 0.4, 0.5, 0.6) ferrites were recorded, and the same are depicted in Fig. 3.4a. The diffractogram indicates seven peaks corresponding to spinel ferrites; the peaks are assigned with the (hkl) values, (220), (311), (222), (400), (422), (511), (440). Amongst this (311) peak has the highest intensity [14]. The observed peaks are typical of spinel. Thus, the monophasic nature of the samples from x=0.0-0.5 is confirmed. A trace of α-Fe_2O_3 was observed for sample with composition x=0.6. Various parameters were calculated from the PXRD patterns, and the data pertaining to the same are tabulated in Table 3.6. It is observed from this table that the lattice constant increased with the rise in zinc content; this trend is explained by Vegard's law [15]. This linear increase with the upsurge in zinc content is due to the replacement of smaller ions like Ni^{2+} and Fe^{3+} ions having ionic radii of 0.64Å and 0.69Å by a larger ion, Zn^{2+} (0.84Å) [16]. The results of the lattice constant obtained are comparable to the reported data [17]. A shift in the 2theta value at the (311) lattice plane was observed as the zinc concentration increased as illustrated in Fig. 3.4b. This is due to strong interactions between zinc, nickel, cobalt, and iron. As the zinc concentration rises, due to lattice expansion, the lattice constant values increases, and the interplanar distance 'd' rises. According to Bragg's equation, the interplanar distance 'd' is inversely proportional to the diffraction angle, and hence, we see a shift in the (311) plane peak to a lower value [18]. The crystallite size calculated from the PXRD data ranges from 36 to 56 nm. It is observed that the crystallite size decreases with zinc

doping. This can be explained by the fact that the grain growth mechanism is restricted due to decreased nucleation of particles, which reduces grain growth [19]. X-ray density is also found to decrease, and the unit cell volume is found to increase with a rise in content from x=0.0-0.6. The values of X-ray density, bulk density, and porosity are given in Table 3.6. Bulk density and porosity do not show any particular trend. Ferrite sample with composition x=0.5 shows the lowest crystallite size with a porosity of 46% and low bulk density. The tetrahedral and octahedral hopping lengths have also been calculated and found to increase with an increase in zinc concentration.

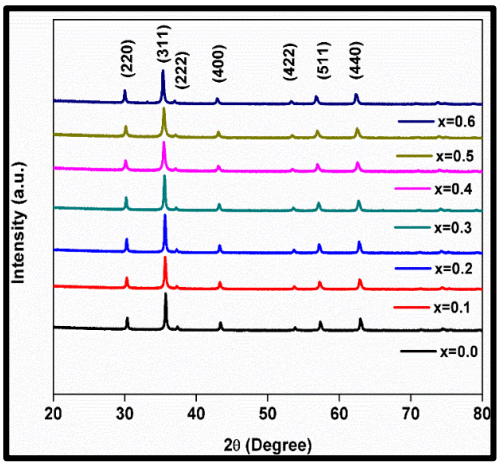


Fig. 3.4 a: X-ray diffraction patterns of 'as-prepared $Ni_{0.6-x}Co_{0.4}Zn_xFe_2O_4$ (x=0.0, 0.1, 0.2, 0.3, 0.4, 0.5, 0.6) ferrites

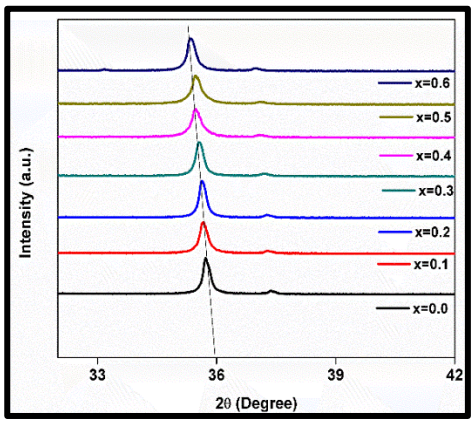


Fig. 3.4 b: Plot of Intensity versus 2theta for (311) plane of 'as prepared' $Ni_{0.6-x}Co_{0.4}Zn_xFe_2O_4$ (x=0.0, 0.1, 0.2, 0.3, 0.4, 0.5, 0.6) ferrites

The sintered ferrites were prepared by heating the 'as prepared' ferrites at 1000 °C, and the diffractogram of all the samples is reported in Fig. 3.5. The diffractogram was recorded from 20- 80 ° range, and the peaks obtained were indexed to all the diffraction peaks of spinel ferrites. No extra peak was obtained; thus, we confirmed the pure phase of sintered ferrite. The sintered ferrite showed highly crystalline nature with narrow FWHM and higher intensity peaks, indicating higher crystallite size and crystallinity than the 'as prepared' ferrite. The crystallite size obtained for 'sintered' samples was in the range of 100-150nm. These samples showed higher density and lower porosity due to sintering. The calculated lattice parameter and the different data obtained from the XRD pattern of the 'as prepared' samples are tabulated in Table 3.6. The lattice constant is found to increase with increase in zinc content in the samples, as larger zinc ions expand the lattice, the unit cell volume is also found to increase. The lattice constant of 'sintered' ferrites is found to be greater than the 'as-prepared' ferrites. The shift in diffraction peaks is also observed in the sintered samples, as the lattice constant increases. The interplanar spacing of the planes is also found to increase. According to Bragg's law, the d-spacing has an inverse relation with theta, or the angle of incidence. Hence, the peaks shift towards the lower theta value with increased zinc content. The density in the samples is also found to increase with increase in zinc content.

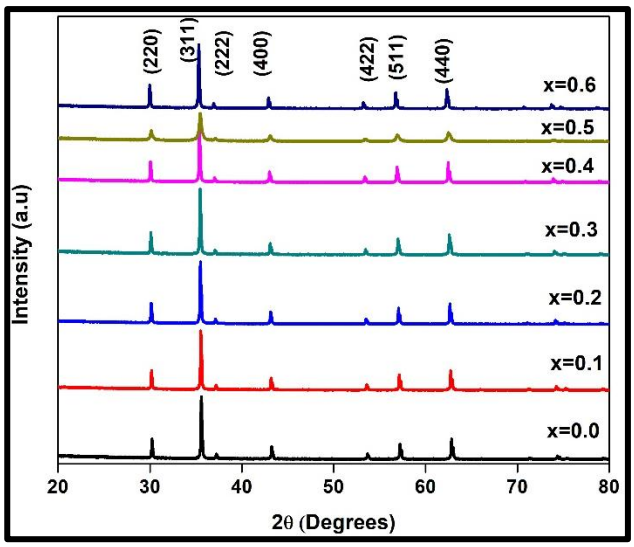


Fig. 3.5 The X-ray diffraction patterns of sintered $Ni_{0.6-x}Co_{0.4}Zn_xFe_2O_4$ (x=0.0, 0.1, 0.2, 0.3, 0.4, 0.5, 0.6) ferrites

Table 3.6: Lattice constant (a), Unit cell (V), crystallite size (D), X-ray density (dx), bulk density (dm), and porosity % (P) of 'as prepared' and 'sintered' $Ni_{0.6-x}Co_{0.4}Zn_xFe_2O_4$ (x=0.0, 0.1, 0.2, 0.3, 0.4, 0.5, 0.6) ferrites

x	a (Å)		V (Å)		D (nm)		dx (g/cm^3)		Dm (g/cm^3)		P (%)	
0.0	8.333	8.360	578	584	34	107	5.381	5.331	3.13	3.15	39	41
0.1	8.349	8.371	581	586	48	146	5.370	5.391	2.85	3.21	47	40
0.2	8.357	8.381	583	588	51	134	5.373	5.326	3.04	3.12	43	41
0.3	8.369	8.388	586	590	41	112	5.361	5.320	3.25	3.36	39	36
0.4	8.392	8.402	591	593	38	121	5.330	5.350	3.68	3.72	31	30
0.5	8.392	8.414	591	595	36	139	5.345	5.308	2.86	3.33	46	37
0.6	8.418	8.421	596	597	33	114	5.311	5.307	3.34	3.44	37	35

3.4.1.2 Elemental analysis

Chemical analysis is a crucial characterization technique to confirm the presence of elements in their stoichiometric amounts. The primary step in characterizing any compound is to prove its stoichiometry first and then utilise other characterization techniques. Chemical analysis was carried out using the ICP-AES instrument. Table 3.7 shows the theoretically and experimentally obtained percentages of Nickel, Cobalt, Zinc and Iron ions present in 'as prepared' $Ni_{0.6-}$

$_xCo_{0.4}Zn_xFe_2O_4$ (x=0.0, 0.1, 0.2, 0.3, 0.4, 0.5, 0.6) ferrites. These percentages confirm the stoichiometry of all the compounds.

Table 3.7: Theoretical and experimental percentages of Ni^{2+}, Co^{2+}, Zn^{2+}, and Fe^{3+} present in 'as prepared' $Ni_{0.6-x}Co_{0.4}Zn_xFe_2O_4$ (x=0.0-0.1, 0.2, 0.3, 0.4, 0.5, 0.6) ferrites

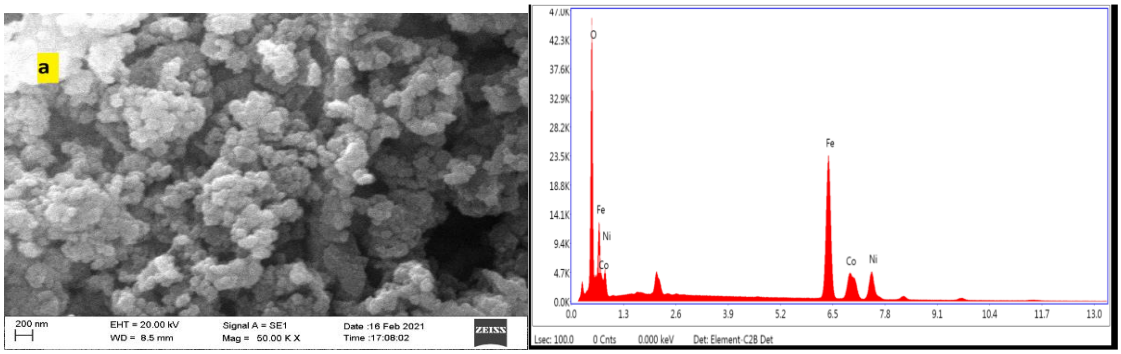
Composition	**Ni^{2+} (%)**		**Co^{2+} (%)**		**Zn^{2+} (%)**		**Fe^{3+} (%)**	
	Theoretical	Experimental	Theoretical	Experimental	Theoretical	Experimental	Theoretical	Experimental
0.0	15.0	14.2	10.1	9.2	-	-	47.6	46.3
0.1	12.5	13.8	10.2	10.9	2.78	2.5	47.5	48.0
0.2	10.0	10.2	9.99	10.5	5.54	5.0	47.3	47.2
0.3	7.5	7.8	9.96	9.8	8.29	7.4	47.2	47.2
0.4	5.0	4.9	9.94	9.5	11.0	10.8	47.1	47.8
0.5	2.5	2.4	9.91	9.1	13.7	13.0	46.9	47.0
0.6	-		9.88	10	16.4	15.6	46.8	46.8

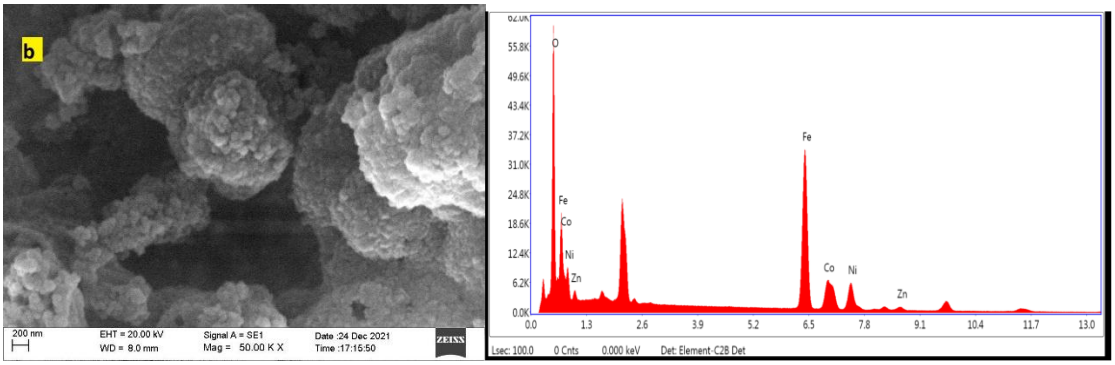
3.4.2 Morphological studies

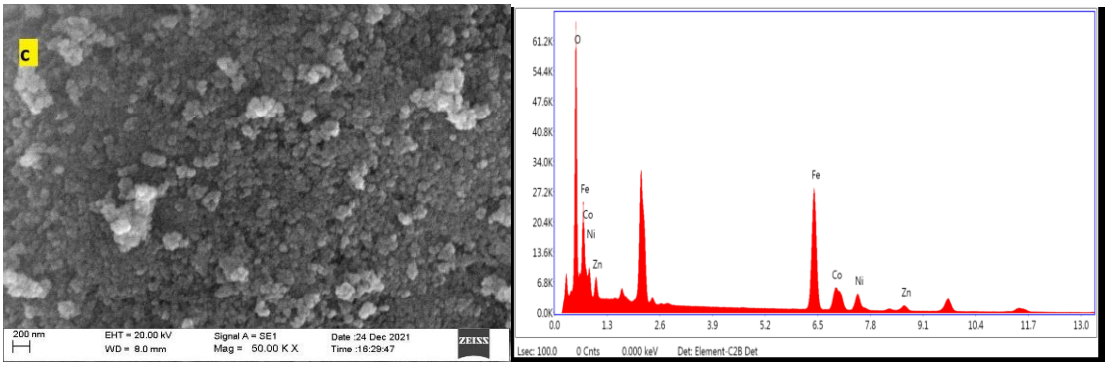
3.4.2.1 Scanning Electron Microscopy

The morphology of the 'as-prepared' and 'sintered' $Ni_{0.6-x}Co_{0.4}Zn_xFe_2O_4$ (x=0.0, 0.1, 0.2, 0.3, 0.4, 0.5,0.6) ferrites was recorded using SEM. The images obtained for the same are depicted in Fig. 3.6 (a-g) and Fig. 3.7 (a-g), respectively. The SEM images represents the wide distribution of particles, with agglomerations, due to magnetic interactions between the nanoparticles [20-22]. When the SEM analysis was performed on 'sintered' samples, it is observed that the particle size increases compared to the 'as prepared' samples. The EDX study

was also carried out for both 'as prepared' and 'sintered' samples along with their SEM study. The EDX study helps in determining the elemental composition in any compound. Fig. 3.6 shows the EDX spectra of 'as prepared' ferrite samples. From these spectra, it can be confirmed that all the constituent elements are present in the 'as prepared' ferrite samples.







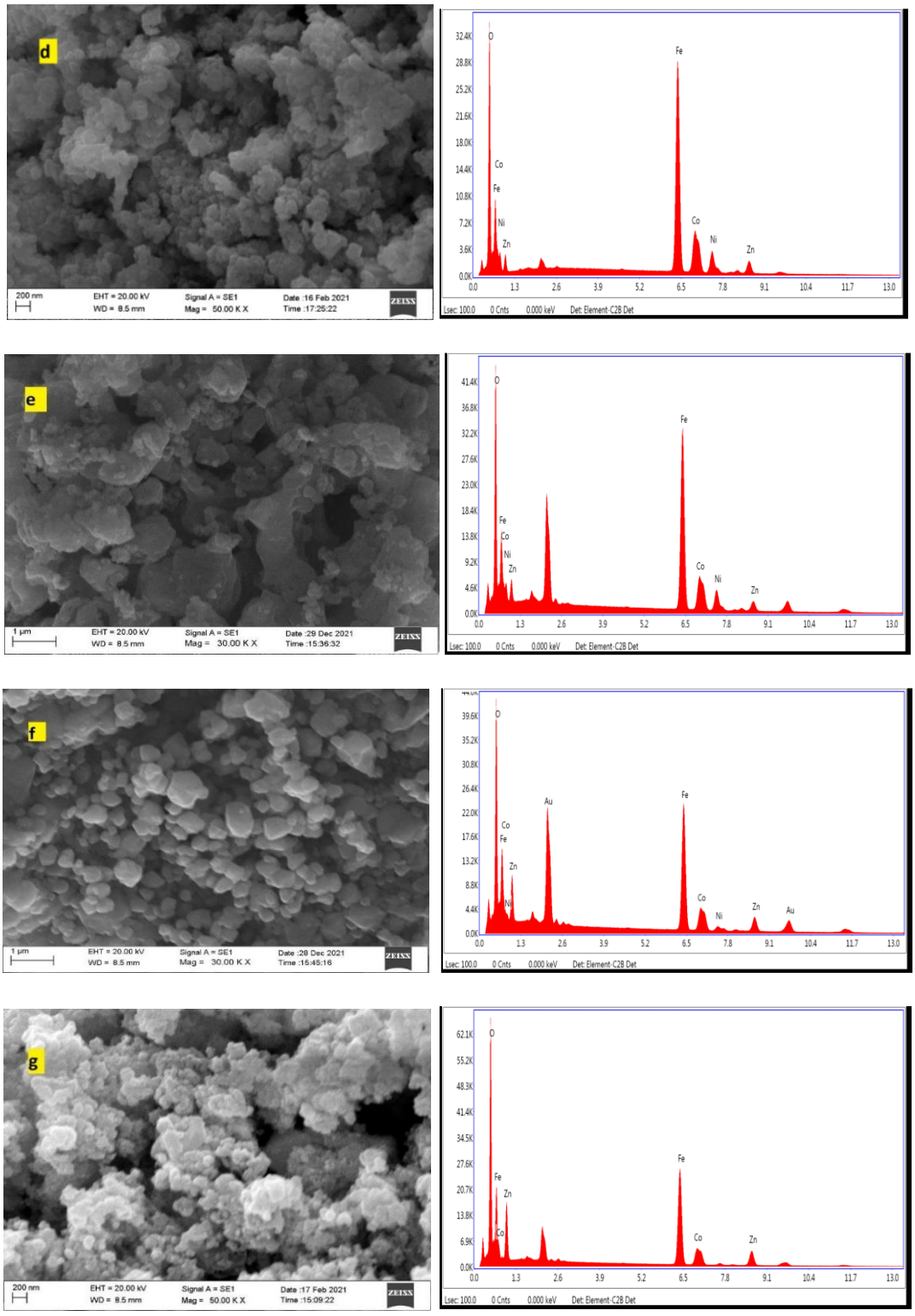


Fig. 3.6 (a-g): SEM images along with EDX patterns of 'as prepared' $Ni_{0.6-x}Co_{0.4}Zn_xFe_2O_4$ (x=0.0, 0.1, 0.2, 0.3, 0.4, 0.5,0.6) ferrite

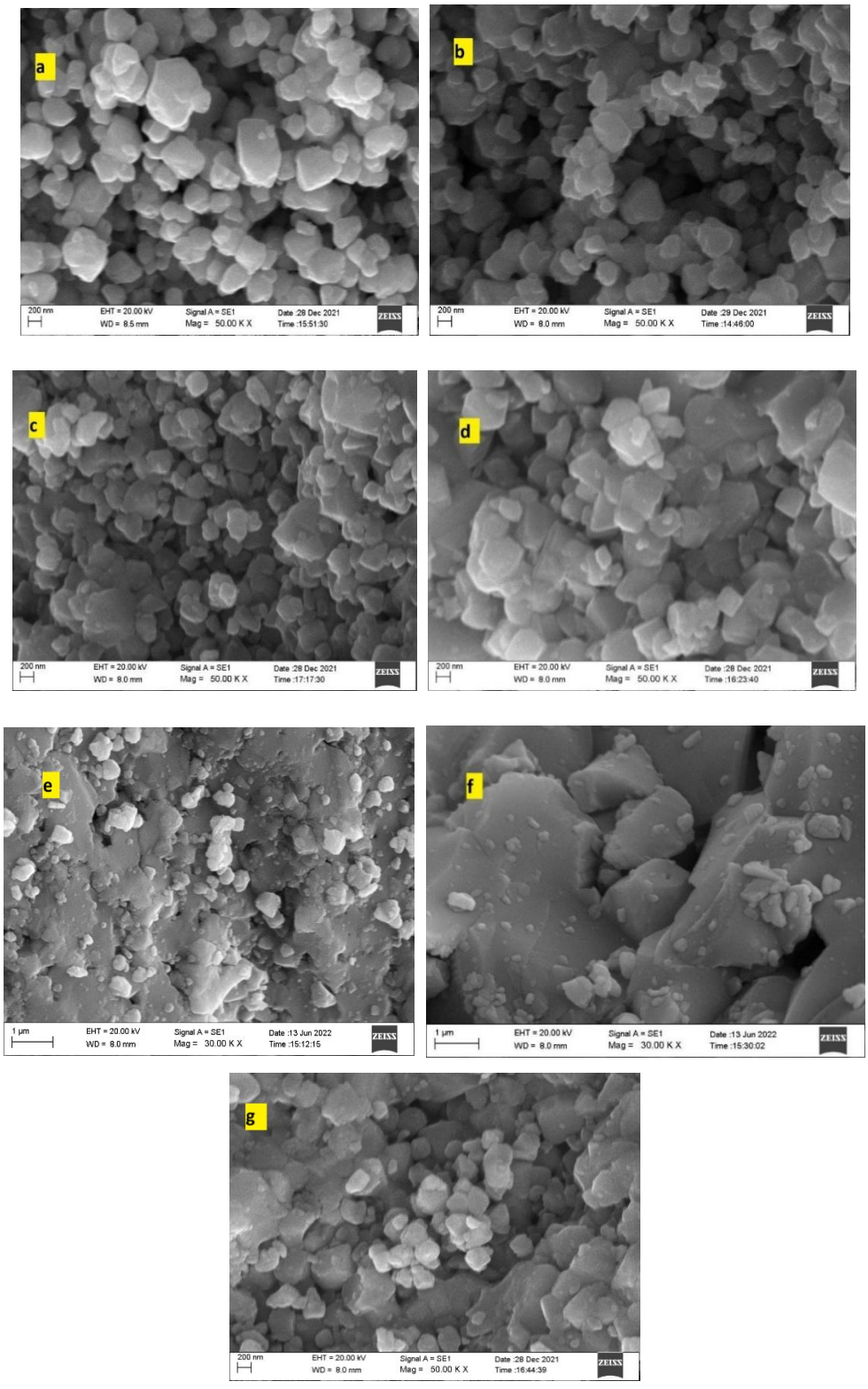
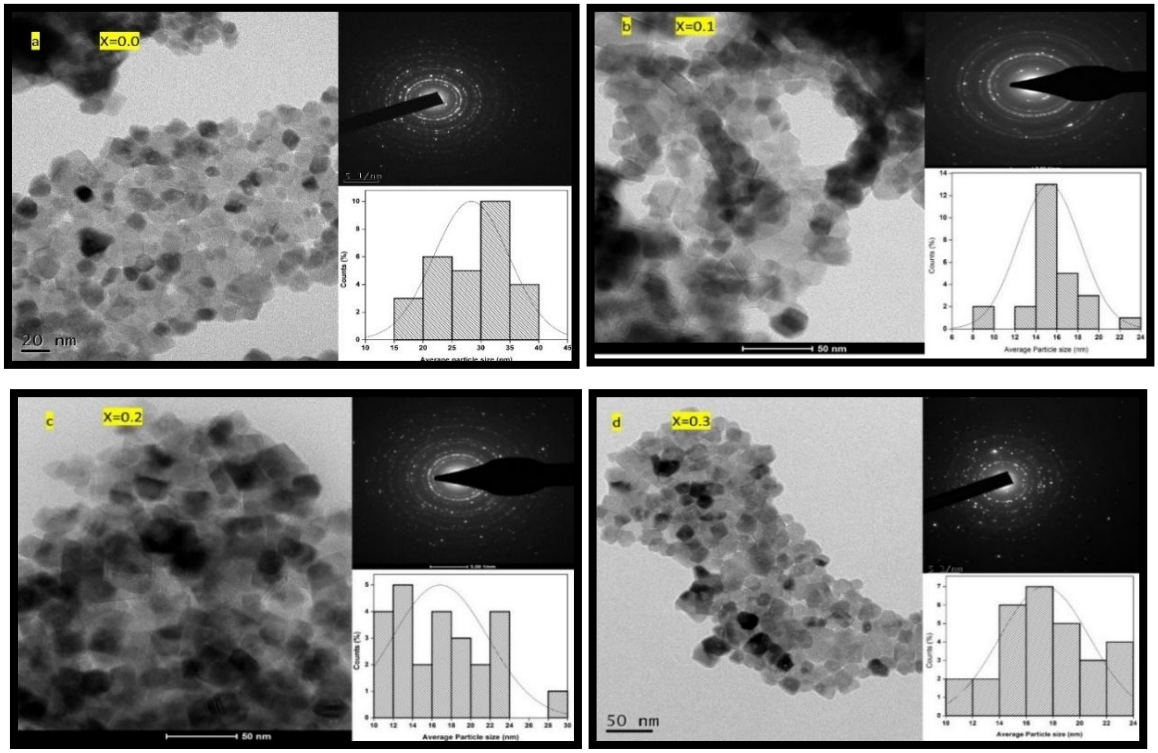


Fig. 3.7 (a-g) SEM images of 'sintered' $Ni_{0.6-x}Co_{0.4}Zn_xFe_2O_4$ (x=0.0, 0.1, 0.2, 0.3, 0.4, 0.5,0.6) ferrites

3.4.2.2 Transmission Electron Microscopy

Transmission electron microscopy studies were carried out to study the morphology and particle size of the 'as prepared' ferrite samples. Fig 3.8 (a-g) illustrates each composition's TEM image, SAED patterns, and histogram plot. TEM images revealed a cuboidal-shaped crystal clubbed together in a particle due to the magnetostatic coupling of the samples and the weak Van der Waals force between the particles[23-25]. Along with the TEM images, single electron diffraction patterns were also recorded, showing a concentric ring with bright spots related to the diffraction patterns of the spinel materials. The bright ring also suggests polycrystalline materials pertaining to different planes in the crystal. The area and length were determined using ImageJ software to obtain the histogram plots. The average particle size obtained from the histogram for each compound ranges from 15-40nm. Sample x=0.0 showed the largest average particle size, supporting the XRD data, wherein the same sample had shown the highest crystallite size.



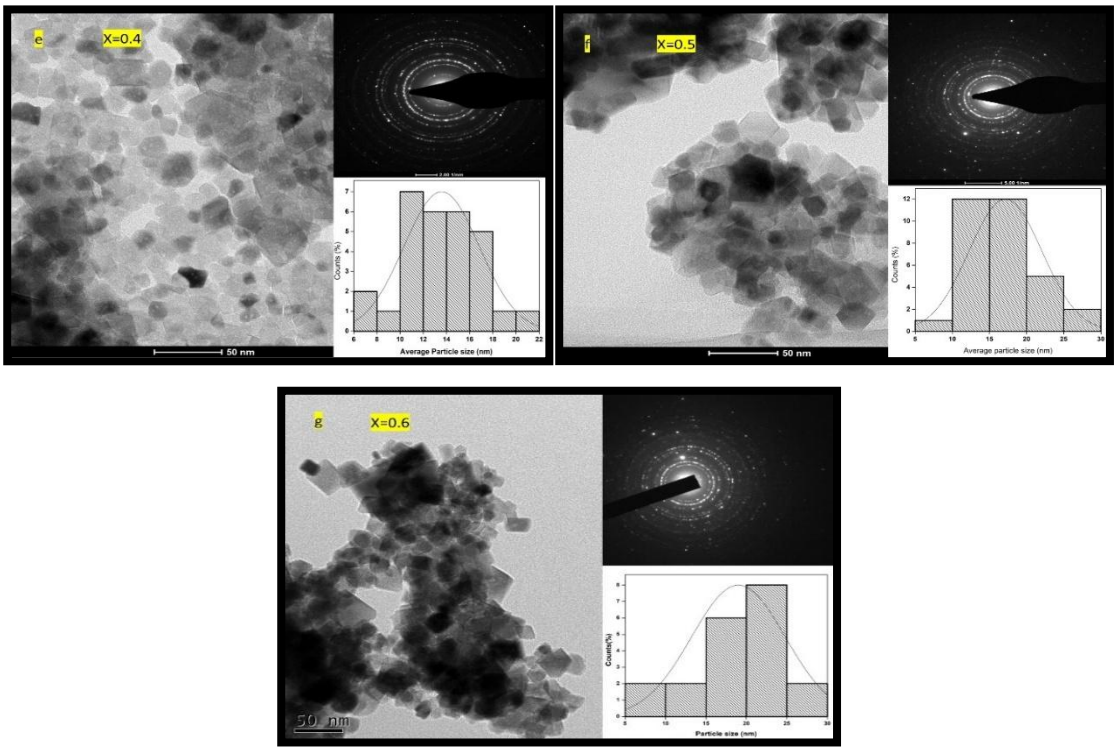


Fig. 3.8 (a-g): TEM images alongside SAED patterns and histogram of 'as prepared' $Ni_{0.6-x}Co_{0.4}Zn_xFe_2O_4$ (x=0.0, 0.1, 0.2, 0.3, 0.4, 0.5,0.6) ferrites

3.4.3 Surface Area Studies (BET Analysis)

Determination of surface area plays a crucial role in the characterization of the surface of a material. This is achieved by adsorbing an inert gas like nitrogen on the molecules surface, including the pores and other surface irregularities. The BET analysis of $Ni_{0.6-x}Co_{0.4}Zn_xFe_2O_4$ (x=0.0-0.6) ferrites was carried out for all the 'as prepared' ferrite samples, and the plots of the same are shown in Fig. 3.9. The surface area obtained from these plots for the ferrite samples with zinc addition (x=0.0 to 0.6) in the composition $Ni_{0.6-x}Co_{0.4}Zn_xFe_2O_4$ is 14, 18, 15, 18, 19, 39, and 25m^2/g, respectively. The volume adsorbed vs. relative pressure (p/po) graph depicts multipoint data of the volume of nitrogen adsorbed on the adsorbent, which is preceded by multilayer adsorption followed by capillary condensation. The isotherm in Fig. 3.9 is seen to have type IV isotherm patterns, which are particular to mesoporous materials. Pores are categorized into three types: micropores of less than 2nm, mesopores ranging from 2 to 50nm, and macropores of 50nm and more [26]. The hysteresis loop of H3 type is observed with plate-like particle aggregates, resulting in slit-like pores [27]. At a relative pressure of 0.8, capillary

condensation begins, while at lower pressure, only monolayer formation is observed [28]. It can be noted that $Ni_{0.6}Co_{0.4}Fe_2O_4$ possesses the lowest surface area of 14 m^2/g with the largest crystallite size of 56 nm among all the other ferrites. While the sample with composition x=0.5 shows the highest surface area of 39 m^2/g and possesses the smallest crystallite size of 36nm in the entire series of compounds, confirming that surface area and particle size have an inverse relationship. A larger surface area results in more active sites available for adsorption, thus making the catalyst or sensors more efficient. We could get better results as compared to some reported data [29].

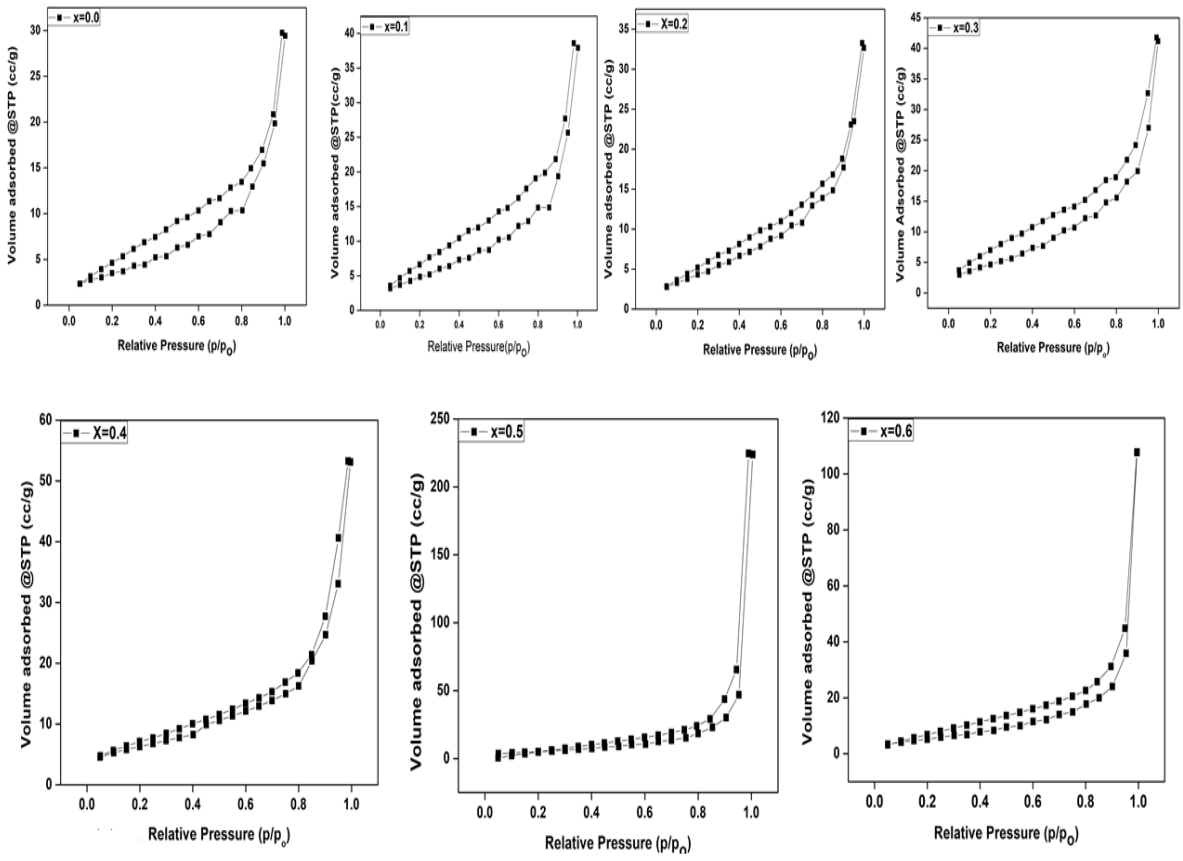


Fig. 3.9: BET surface area curves for 'as prepared' $Ni_{0.6-x}Co_{0.4}Zn_xFe_2O_4$ (x=0.0, 0.1, 0.2, 0.3, 0.4, 0.5,0.6) ferrites

3.4.4 Raman studies

The Raman spectra of 'as prepared $Ni_{0.6-x}Co_{0.4}Zn_xFe_2O_4$(x=0.0-0.6) ferrites is shown in Fig. 3.10 and of 'sintered' ferrite is shown in Fig. 3.11. The assigned peaks for 'as prepared' and 'sintered' ferrites are tabulated in Tables 3.8 and 3.9, respectively. They indicate spinel ferrite formation and display Raman active modes, including E_g, $2T_{2g}$, and A_{1g} at RT. One of the peaks observed at~695cm^{-1}, denoted by A_{1g} (1), corresponds to a tetrahedral mode resulting from the symmetric stretch of oxygen atoms along the M-O bond. A shoulder peak at around 630 cm^{-1}, denoted by A_{1g} (2), is observed, which can be attributed to the mixed nature of spinel ferrites. The intensity of the A_{1g} peak increases with zinc content, whereas the intensity of the shoulder peak rises with an increase in zinc content. It can be noted that Co is present in the octahedral site and also Fe, which can magnetically interact with Co, leading to an increase in distance between Fe and O atom; thus, the bonding energy between them decreases, thereby shifting the Raman frequency [30]. It is also known from the literature that as the lattice parameter increases, the Raman modes change to a lower value. A low-intensity Eg mode is also observed at 320 cm^{-1}, which is due to the symmetric bending of the M-O bond; due to bending in the bonds, the intensity lowers. Slight shifting in the peaks is obtained with an increase in zinc content. The T_{2g} (2) mode is observed at 472-478cm^{-1} because of the asymmetric stretching of the metal-oxygen bond at the octahedral site. At the same time, a low-intensity peak T_{2g} (3) occurring due to asymmetric bending vibration, is obtained at around 545-562cm^{-1} [31, 32]. In the spinel ferrite samples, the vibrational modes observed above 600cm^{-1} are due to the vibrational motion of oxygen at the tetrahedral site [33]. At the same time, those obtained at a lower frequency are attributed to vibration at the octahedral site. A sharp peak at 240cm^{-1} indicates the presence of Fe_2O_3 in the sample, which is absent in our case, thus confirming the formation of a single monophasic spinel ferrite.

The 'sintered' $Ni_{0.6-x}Co_{0.4}Zn_xFe_2O_4$(x=0.0-0.6) ferrites were also analyzed by Raman spectroscopy (Fig. 3.11), from which the three first-order Raman active modes were observed (E_g+T_{2g}+A_{1g}). The higher frequency peak above 600cm^{-1} is assigned as A_{1g} due to the symmetric stretching of metal-oxygen at the tetrahedral site, and the peaks are obtained in the spectral range of 634-694cm^{-1}. Apart from the main A_{1g} peak from 682-694cm^{-1}, which results from Fe-O stretching vibration [34], a shoulder peak in the range of 634-646cm^{-1} is also

observed in the resolved Raman image. This shoulder peak results from the Zn-O symmetric stretch at the tetrahedral site, as reported in the literature [33]. This confirms the presence of Zn and Fe in the tetrahedral sites. The lower frequency peak is E_g and T_{2g}. The broad E_g peak is associated with symmetric bending obtained in the 307-335 cm^{-1} range. The T_{2g} (3) mode corresponds to asymmetric bending vibration, whereas the T_{2g} (2) corresponds to asymmetric stretching vibration, observed at spectral ranges of 566-574cm^{-1} and 470-479cm^{-1}, respectively. The translational motion of the tetrahedron unit is designated by T_{2g} (1), which occurs at around 200cm^{-1} and is observed only for two of our samples, which are x=0.4 and 0.6. A more proper trend was seen in the 'sintered' samples versus the 'as prepared ones. It was observed that the intensity of peaks diminished as the zinc content in the samples increased; the Raman shift values also shifted to a lower value with the intensity. This trend in lowering the Raman shift value and decrease in intensity with an increase in dopant concentration can be very well explained by the trend with the lattice parameter. In our case, the lattice constant increases with an increase in zinc content, as it is reported that unit cell parameters have an inverse relation with the vibrational frequency [30].

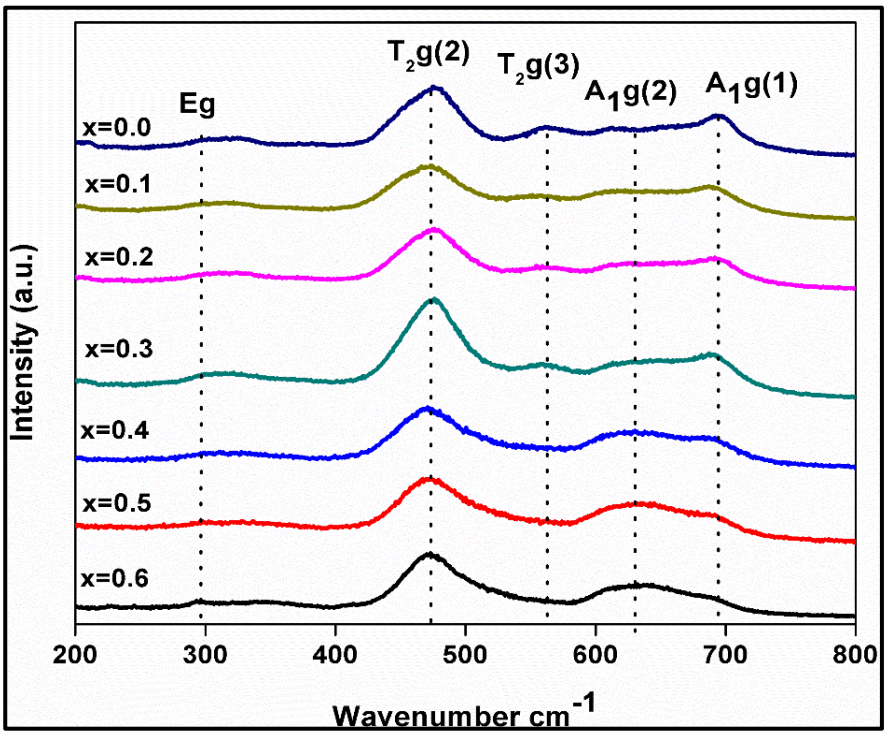


Fig. 3.10 The Raman spectra of 'as prepared' $Ni_{0.6-x}Co_{0.4}Zn_xFe_2O_4$ (x=0.0, 0.1, 0.2, 0.3, 0.4, 0.5,0.6) ferrites

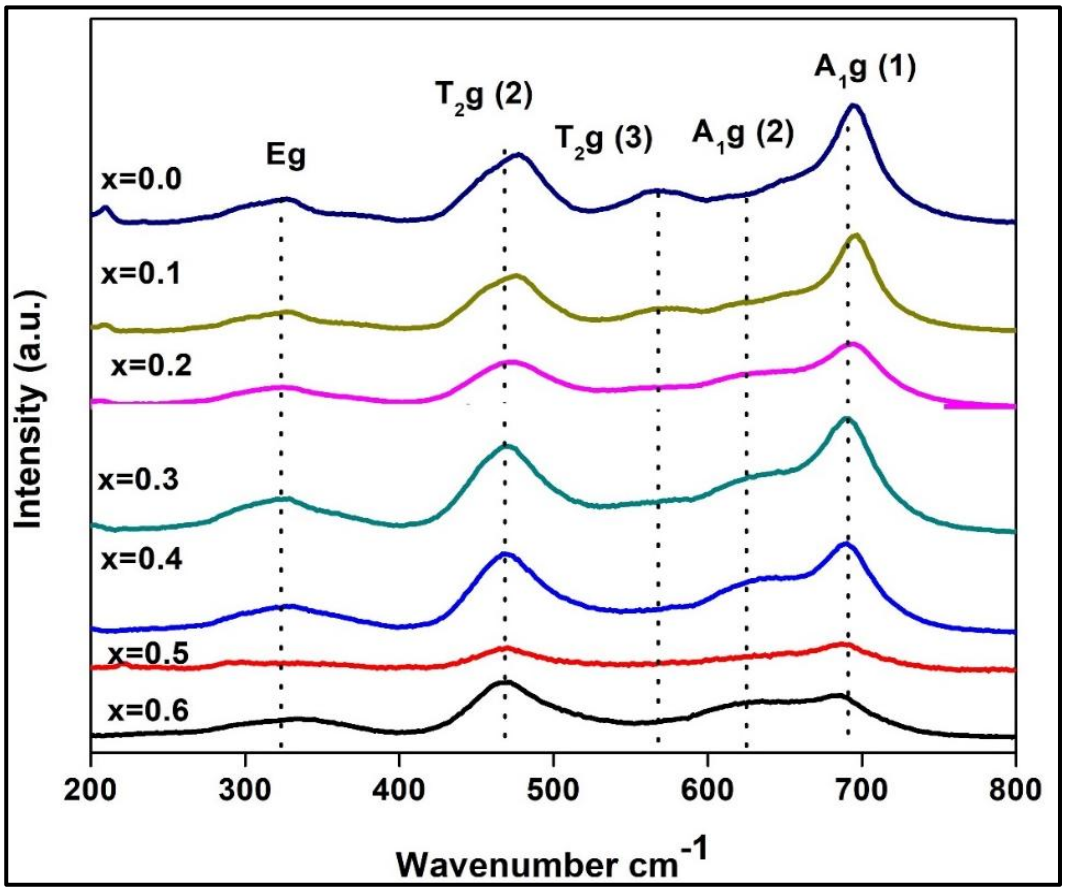


Fig. 3.11 The Raman spectra of 'sintered' $Ni_{0.6-x}Co_{0.4}Zn_xFe_2O_4$ (x=0.0, 0.1, 0.2, 0.3, 0.4, 0.5,0.6) ferrites

Table 3.8: The values of the Raman active modes of 'as prepared' $Ni_{0.6-x}Co_{0.4}Zn_xFe_2O_4$ (x=0.0, 0.1, 0.2, 0.3, 0.4, 0.5,0.6) ferrites.

X	**0.0**	**0.1**	**0.2**	**0.3**	**0.4**	**0.5**	**0.6**
Eg	316	316	316	313	316	316	295
T_{2g}(2)	478	474	476	476	472	472	473
T_{2g}(3)	562	554	562	560	-	-	-
A_{1g}(2)	614	615	621	636	632	636	642
A_{1g}(1)	693	685	691	689	687	689	684

Table 3.9: The values of Raman active modes of 'sintered' $Ni_{0.6-x}Co_{0.4}Zn_xFe_2O_4$ (x=0.0, 0.1, 0.2, 0.3, 0.4, 0.5,0.6) ferrites

x	0.0	0.1	0.2	0.3	0.4	0.5	0.6
Eg	329	327	324	326	329	307	335
$T_{2g}(2)$	479	480	472	473	467	472	472
$T_{2g}(3)$	568	574	566	586	573	-	-
$A_{1g}(2)$	-	646	625	634	640	634	634
$A_{1g}(1)$	694	694	691	691	691	687	682

3.4.5 X-Ray Photoelectron Spectroscopic studies (XPS analysis)

X-ray photoelectron spectroscopy was employed to determine the oxidation states of the elements in the ferrite samples and further investigate their cation distribution. C 1s peak set to 284 eV was used to normalize any peak shift occurring due to the apparent charging of the samples. A full scan survey of XPS of all the 'as prepared' $Ni_{0.6-x}Co_{0.4}Zn_xFe_2O_4$ (x=0.0, 0.1, 0.2, 0.3, 0.4, 0.5, 0.6) ferrites is showcased in Fig. 3.12, and the deconvoluted spectra of each element after Tougaard background subtraction is also plotted as depicted from Fig. 3.13 to Fig. 3.17.

The chemical state of Fe was determined by XPS, whose deconvoluted spectra is reported in Fig. 3.13, and its binding energies are tabulated in Table 3.10. In the case of Fe, two prominent peaks are observed in the binding energy range of 700-740 eV. The two peaks correspond to Fe $2p_{3/2}$ and Fe $2p_{1/2}$, also accompanied by satellite peaks. The Fe $2p_{3/2}$ peak has a degeneracy of four states, while Fe $2p_{1/2}$ has a degeneracy of two states in spin-orbit coupling, which makes the $2p_{3/2}$ peak greater than $2p_{1/2}$ [35]. The prominent peak $2p_{3/2}$ is obtained at around ~710 eV with a satellite peak of ~718 eV, 8eV above the prominent peak, corresponding to Fe in a 3+ oxidation state. If the satellite peak is obtained ~6eV higher than the main $2p_{3/2}$ peak, it corresponds to Fe in a 2+ oxidation state. Thus, we can say that in our ferrite material, Fe is in

its respective oxidation state of 3+ [35,36]. The $2p_{3/2}$ peak further splits into two, one obtained at ~710eV, representing the Fe^{3+} in the octahedral site, and the other at ~713eV, corresponding to Fe^{3+} in the tetrahedral site. The $2p_{1/2}$ peak also splits and is obtained at a binding energy of ~724eV, which is due to Fe^{3+} at the octahedral site, and another peak is obtained at ~ 726eV, corresponding to Fe^{3+} in the tetrahedral site. The satellite peak obtained for $2p_{1/2}$ is ~732eV. The XPS peak positioning for Fe has been investigated by different researchers and has been reported in the literature [37,38].

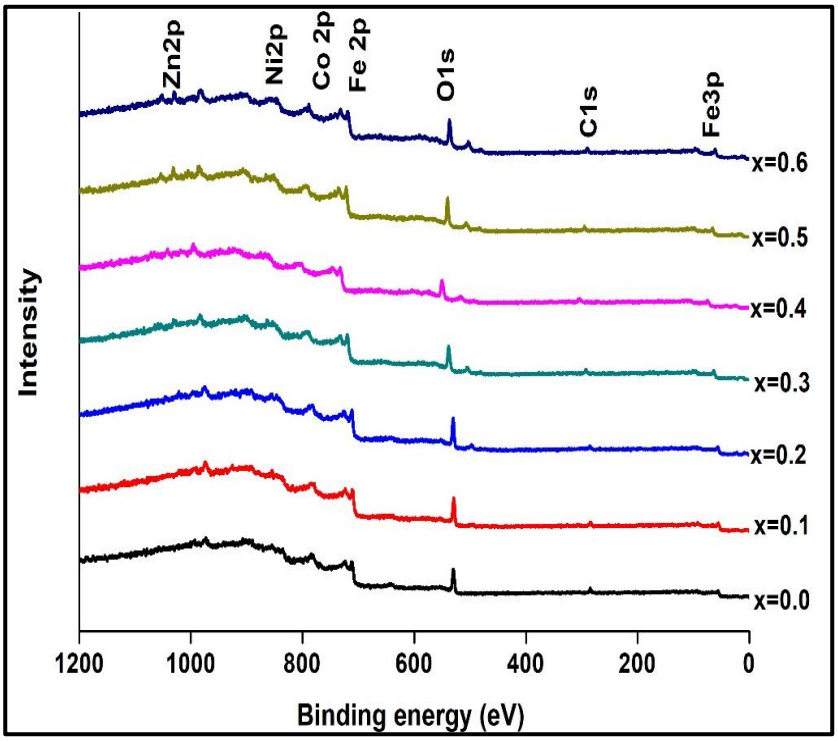


Fig 3.12: The full scan spectrum of 'as prepared' $Ni_{0.6-x}Co_{0.4}Zn_xFe_2O_4$ (x=0.0, 0.1, 0.2, 0.3, 0.4, 0.5, 0.6) ferrites

The core-shell spectra of Zn^{2+} of all the 'as prepared' $Ni_{0.6-x}Co_{0.4}Zn_xFe_2O_4$ (x=0.0, 0.1, 0.2, 0.3, 0.4, 0.5, 0.6) ferrites are represented in Fig. 3.14, and the values obtained for Zn $2p_{3/2}$ and $2p_{1/2}$ are tabulated in Table 3.11. The XPS spectra of Zn showed two distinct peaks,$2p_{3/2}$ at ~1021 eV and another 2p1/2 at ~1044eV, which confirms zinc in its divalent state [39]. The literature shows that the $2p_{3/2}$ is broad and resolved into two peaks, the first peak at ~1021eV, while the immediate split peak is at ~1023eV. This broadness in the peak is due to three different types of Zn^{2+} present: i) zinc present in the tetrahedral site as spinel ferrite, ii) due to ZnO formation, and iii) due to the presence of zinc in the octahedral site [40,41]. No such splitting is observed

in the spectra reported in Fig. 3.14, confirming the presence of Zinc 2+ in only the tetrahedral sites with spinel structure.

Table 3.10: Binding energies of $Fe^{3+}2p_{3/2}$ and $2p_{1/2}$ along with their satellite peaks obtained from the XPS study of 'as prepared' $Ni_{0.6-x}Co_{0.4}Zn_xFe_2O_4$ (x= 0.0- 0.6) ferrites

x	Binding energy (eV)					
	Fe^{3+} $2p_{3/2}$ (Octahedral)	Fe^{3+} $2p_{3/2}$ (Tetrahedral)	Sat. peak Fe^{3+} $2p_{3/2}$	Fe^{3+} $2p_{1/2}$ (Octahedral)	Fe^{3+} $2p_{1/2}$ (Tetrahedral)	Sat. peak Fe^{3+} $2p_{1/2}$
0.0	710.9	713.5	718.4	724.1	727.3	734.3
0.1	710.4	712.7	718.3	724.0	727.2	733.5
0.2	710.5	712.9	718.2	723.9	726.9	733.6
0.3	710.6	712.8	718.5	724.1	726.8	733.8
0.4	710.7	713	718.5	724.1	727	733.4
0.5	710.6	712.9	718.4	724.1	727.1	733.6
0.6	710.7	713.0	718.4	724.2	726.7	733.5

Table 3.11: Binding energies of $Zn^{2+}2p_{3/2}$, $2p_{1/2}$, and O1s along with their satellite peaks obtained from the XPS study of 'as prepared' $Ni_{0.6-x}Co_{0.4}Zn_xFe_2O_4$ (x= 0.0- 0.6) ferrites

x	Binding energy (eV)			
	Zn^{2+} $2p_{3/2}$	Zn^{2+} $2p_{1/2}$	O 1s	O1s
0.0	-	-	529.8	531
0.1	1020.9	1044.3	529.8	532
0.2	1020.9	1044.5	529.9	532.7
0.3	1021.0	1044.2	529.8	-
0.4	1020.9	1044.1	529	530.4
0.5	10211.0	1044.0	529.2	530.2
0.6	1021.2	1044.3	529.6	531

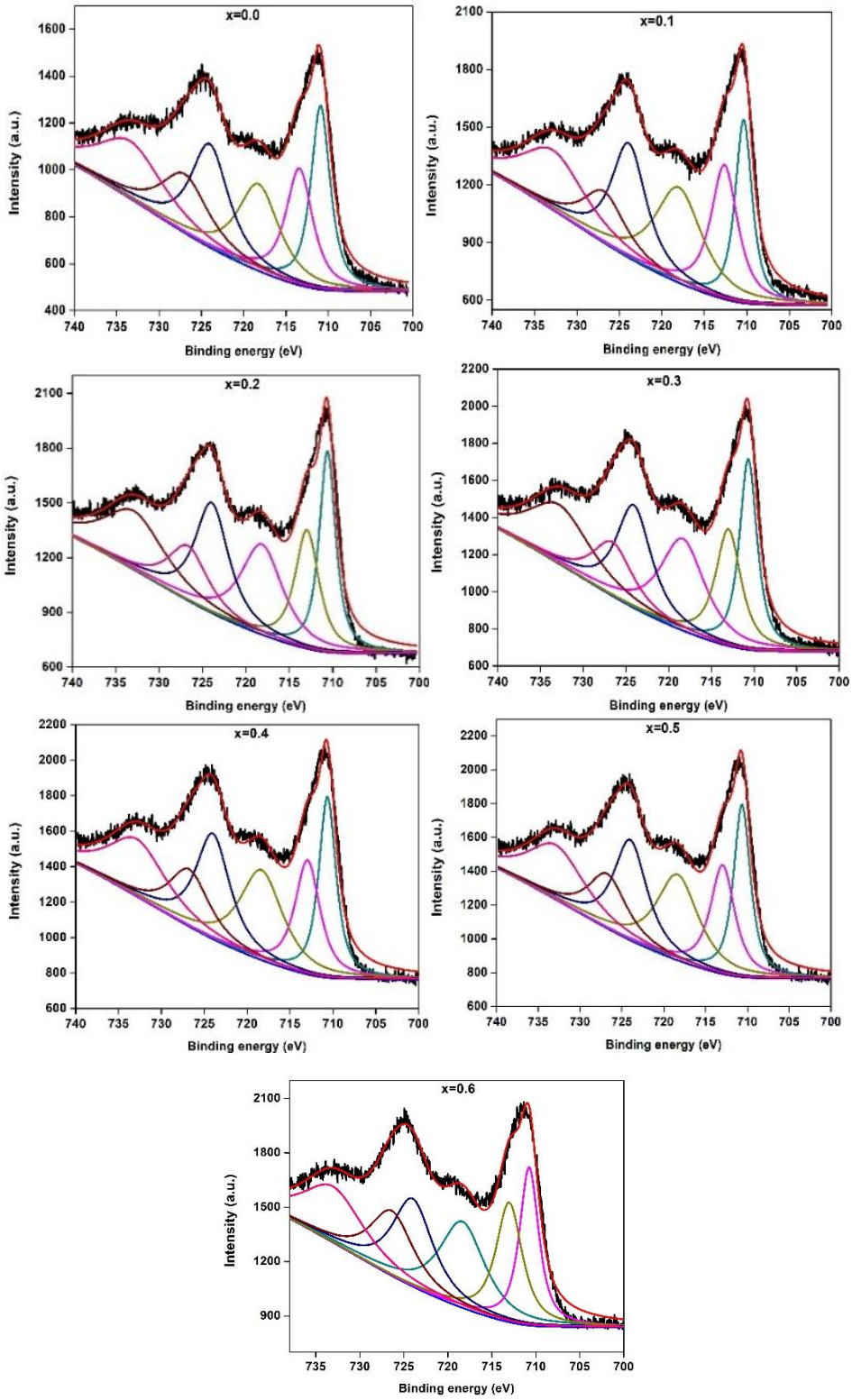


Fig. 3.13: The deconvoluted XPS data of Fe 2p for all the 'as prepared' $Ni_{0.6-x}Co_{0.4}Zn_xFe_2O_4$ (x=0.0, 0.1, 0.2, 0.3, 0.4, 0.5, 0.6) ferrites

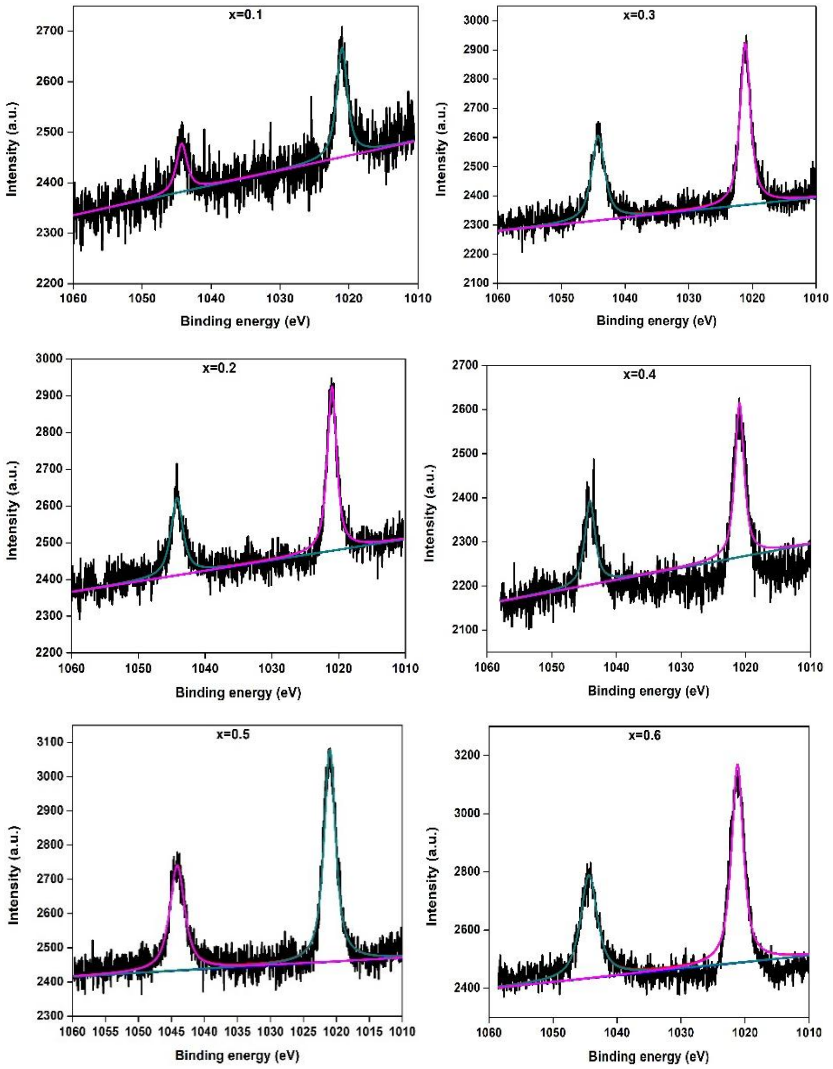


Fig. 3.14: The deconvoluted XPS data of Zn 2p for all the 'as prepared' $Ni_{0.6-x}Co_{0.4}Zn_xFe_2O_4$ (x=0.0, 0.1, 0.2, 0.3, 0.4, 0.5, 0.6) ferrites

Oxygen 1s spectra of all the 'as prepared' $Ni_{0.6-x}Co_{0.4}Zn_xFe_2O_4$ (x=0.0, 0.1, 0.2, 0.3, 0.4, 0.5, 0.6) ferrites are illustrated in Fig. 3.15 and the values are depicted in Table 3.11. The deconvoluted spectra of O1s peaks show two peaks at ~529eV and another at ~530-532eV. The peak at ~529 eV corresponds to metal oxygen linkage or lattice oxygen, whereas the peak at ~532 eV results in oxygen vacancies or oxygen-deficient regions arising from chemisorbed water on the surface [42,43].

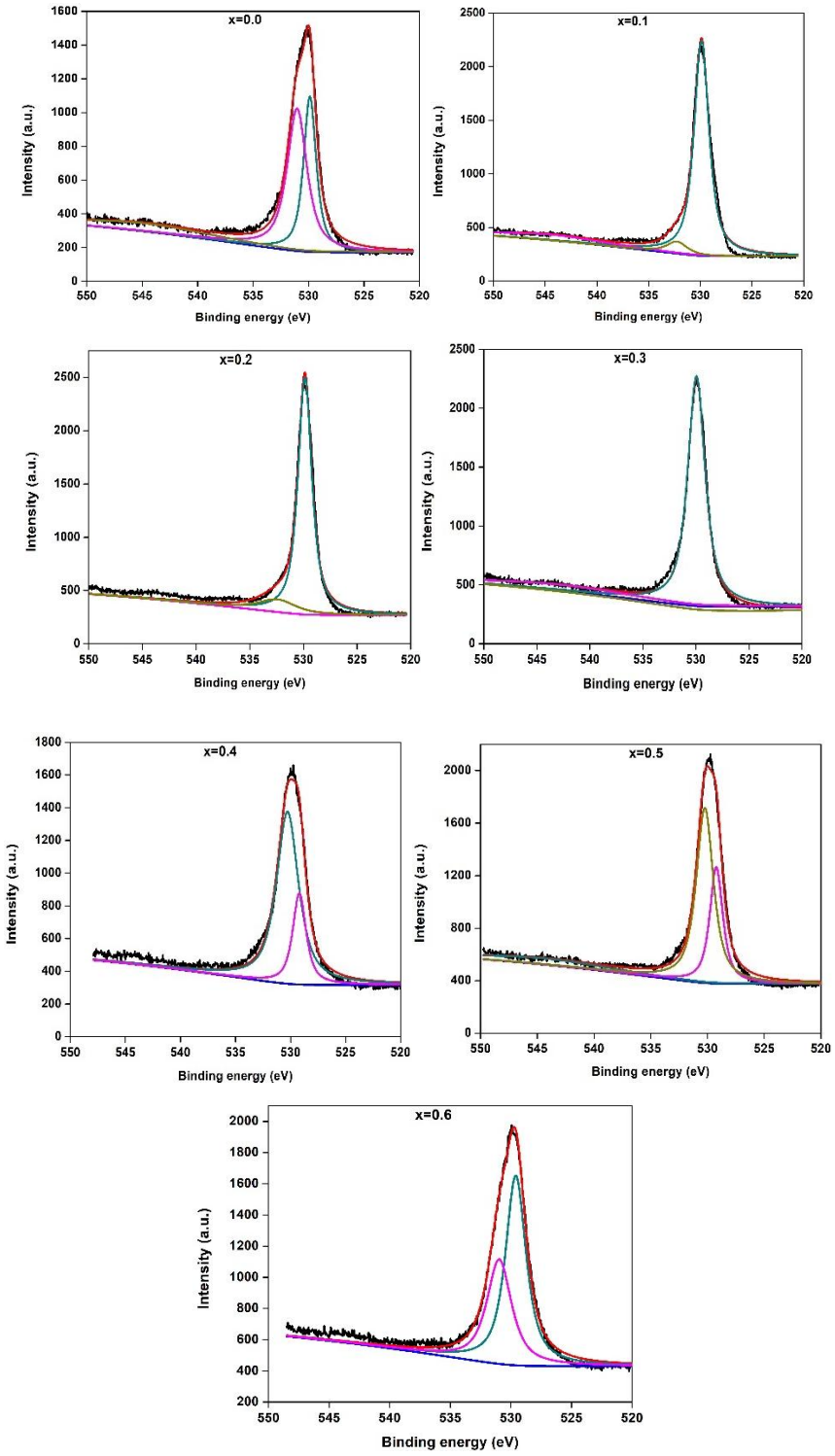


Fig. 3.15: The deconvoluted XPS data of O 1s for all the 'as prepared' $Ni_{0.6-x}Co_{0.4}Zn_xFe_2O_4$ (x=0.0, 0.1, 0.2, 0.3, 0.4, 0.5, 0.6) ferrites

The fitted 2p Ni core level spectra for all the 'as prepared' $Ni_{0.6-x}Co_{0.4}Zn_xFe_2O_4$ (x=0.0, 0.1, 0.2, 0.3, 0.4, 0.5, 0.6) ferrites are showcased in Fig. 3.16 and the values are depicted in Table 3.12. The deconvoluted spectrum is seen to have two doublets along with shakeup satellite peaks. The main peak of Ni $2p_{3/2}$ is obtained at ~855eV, while the other Ni $2p_{1/2}$ peak is obtained at around ~872eV. The main peak also split up, distributing cations in tetrahedral and octahedral sites. The main peak of Ni $2p_{3/2}$ is obtained at ~855eV. This value corresponds to Ni in the octahedral site [44]. The presence of a satellite peak is of great importance in probing the chemical state of the metal due to the appearance of a peak at very close binding energies for different oxidation states of Ni. The satellite peak for Ni $2p_{3/2}$ appears around 861eV. The composition is pure spinel and no NiO is confirmed by the absence of a shoulder peak at 1.2eV above the main Ni $2p_{3/2}$ peak [45,46].

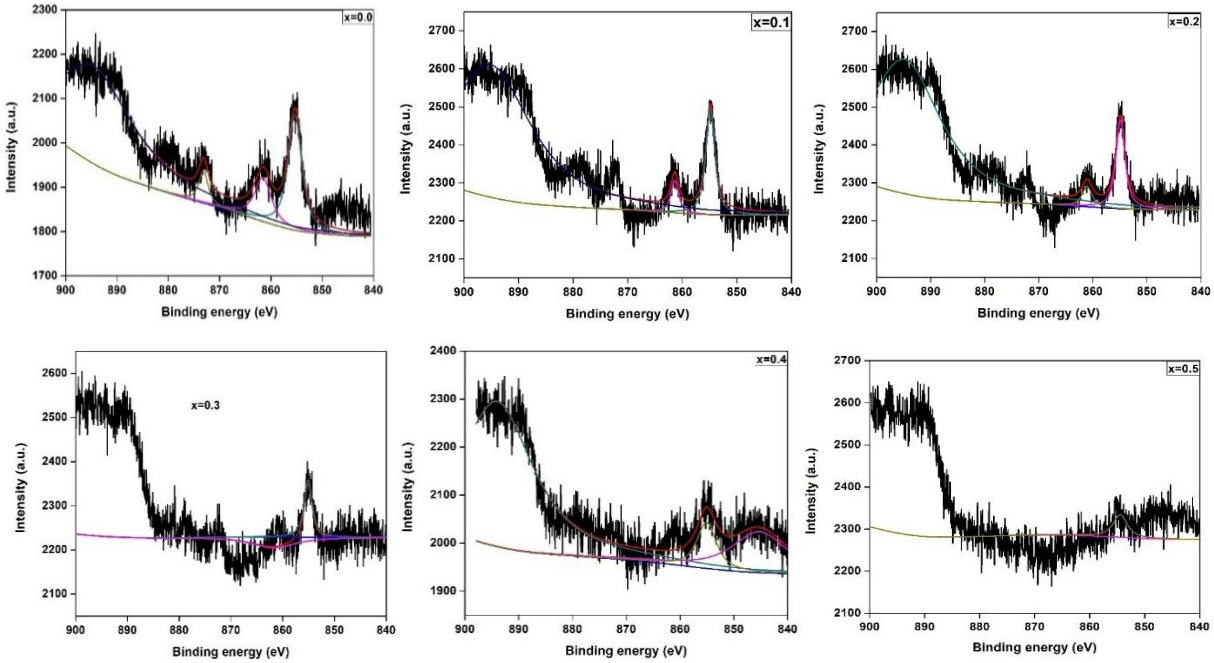
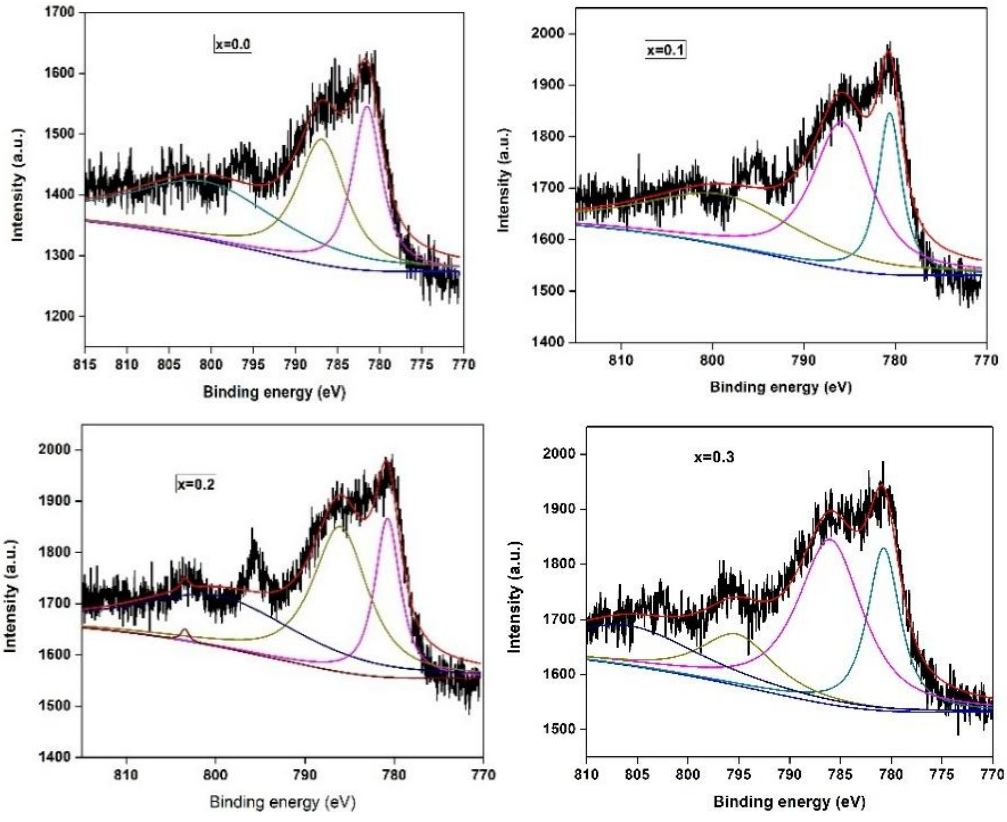


Fig. 3.16: The deconvoluted XPS data of Ni for all the 'as prepared' $Ni_{0.6-x}Co_{0.4}Zn_xFe_2O_4$ (x=0.0, 0.1, 0.2, 0.3, 0.4, 0.5, 0.6) ferrites

Table 3.12: Binding energies of $Ni^{2+}2p_{3/2}$ along with their satellite peaks obtained from the XPS study of 'as prepared'$Ni_{0.6-x}Co_{0.4}Zn_xFe_2O_4$ (x= 0.0- 0.6) ferrites

x	Binding energy (eV)	
	Ni^{2+} $2p_{3/2}$	Sat. peak Ni^{2+} $2p_{3/2}$
0.0	855.3	861.5
0.1	854.8	861.3
0.2	854.8	861.0
0.3	855.1	-
0.4	855.0	-
0.5	854	-



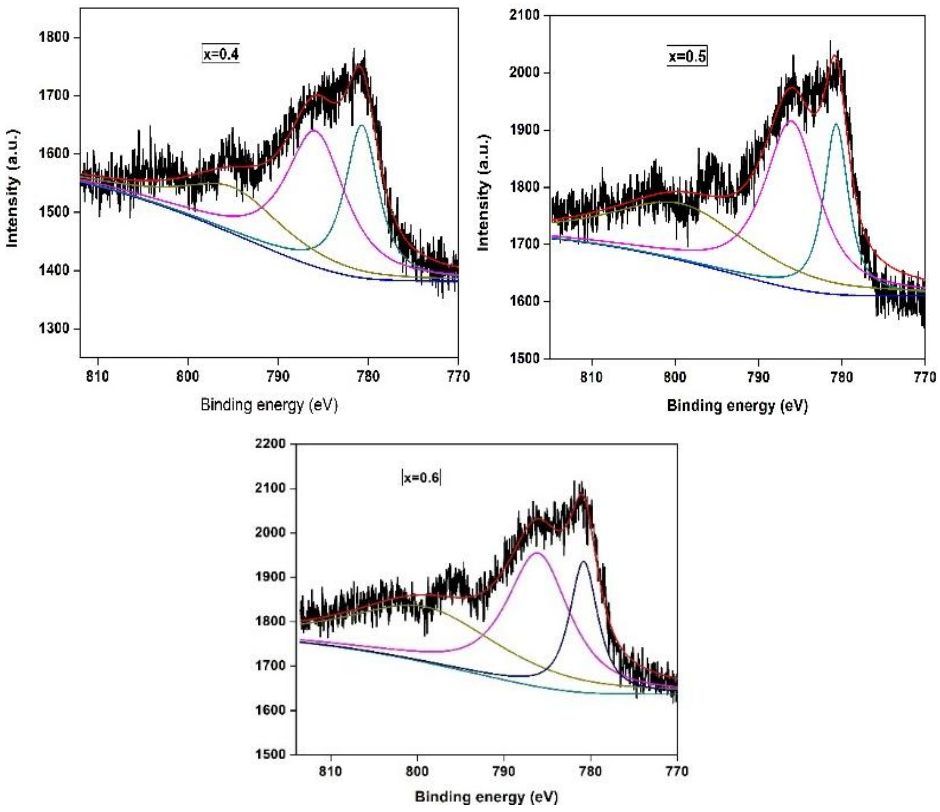


Fig. 3.17: The deconvoluted XPS data of Co for all the 'as prepared' $Ni_{0.6-x}Co_{0.4}Zn_xFe_2O_4$ (x=0.0, 0.1, 0.2, 0.3, 0.4, 0.5, 0.6) ferrites.

The core-shell deconvoluted spectra of Co 2p of all the composition of $Ni_{0.6-x}Co_{0.4}Zn_xFe_2O_4$ (x=0.0, 0.1, 0.2, 0.3, 0.4, 0.5, 0.6) ferrites are represented in Fig. 3.17 and the binding energies are given in Table 3.13. The main peaks, Co2p 3/2 and Co 2p1/2, are observed at ~780eV and ~795eV, along with the shakeup satellite peaks at ~786 and ~800eV. The satellite peaks are observed at around 5-6eV higher than the main peak. The satellite peaks are a major source for confirming the 2+ oxidation state of Co [47,48,49]. The Co $2p_{3/2}$ usually splits into two peaks with a value of ~780eV associated with cobalt in the octahedral site and the other at ~782eV for cobalt in the tetrahedral site. No such splitting occurs in the present study, confirming cobalt's presence in only the octahedral site [47].

Table 3.13: Binding energies of $Co^{2+}2p_{3/2}$ and $2p_{1/2}$ along with their satellite peaks obtained from the XPS study of 'as prepared' $Ni_{0.6-x}Co_{0.4}Zn_xFe_2O_4$ (x= 0.0- 0.6) ferrites.

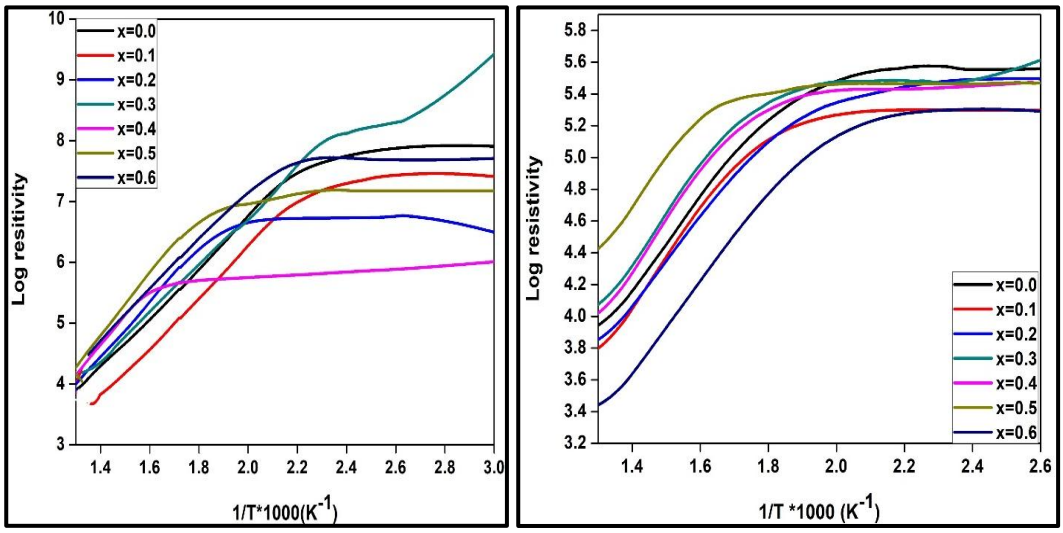
x	**Binding energy (eV)**			
	Co^{2+} $2p_{3/2}$	Sat. peak Co^{2+} $2p_{3/2}$	Co^{2+} $2p_{1/2}$	Sat. peak Co^{2+} $2p_{1/2}$
0.0	781.5	786.8	-	801.3
0.1	780.5	785.8	-	800.6
0.2	780.6	786.0	-	803.4
0.3	780.7	786.0	795.5	805.8
0.4	780.7	786.0	796.3	-
0.5	780.5	785.9	-	800.4
0.6	780.6	786.1	-	799.6

3.5 Solid State Studies

The 'as prepared' and 'sintered' $Ni_{0.6-x}Co_{0.4}Zn_xFe_2O_4$ (x=0.0-0.6) ferrites powder and pellets were studied using various techniques and the results of the same are discussed in the section below.

3.5.1 DC Electrical Resistivity

The DC resistivity studies of 'as prepared' and 'sintered' $Ni_{0.6-x}Co_{0.4}Zn_xFe_2O_4$ (x=0.0-0.6) ferrites was carried out from RT- 500^oC during the heating and cooling process. The plot of log resistivity vs 1/T* 1000 is illustrated in Fig. 3.18 for 'as prepared' ferrite and Fig. 3.19 for 'sintered' ferrite. The comparison between the 'as prepared' and 'sintered' ferrite was made based on the various factors that affect the properties: grain size, porosity, grain boundary and stoichiometry. The synthesis method also changes the material's properties or resistivity. Also, with a temperature change, the resistivity changes. Spinel ferrite usually shows three regions in the plot from RT to 773K. The first zone is from RT-400K, and the break in the linear curve is observed due to impurities and voids in the samples. The second zone is observed from 400K to the Curie temperature; the break usually occurs at the T_c in this region. This zone is attributed to the ferrimagnetic region. Meanwhile, the third region above Tc is paramagnetic. The resistivity of the 'as prepared' ferrite decreases with an increase in temperature, confirming the semiconducting behaviour of the samples in the heating and cooling curve. For samples with composition x=0.1 and 0.2, a slight increase in resistivity is seen. Various factors can explain this behaviour. One reason can be the presence of moisture in the sample, which increases resistivity. On further heating, as the moisture evaporates, the resistivity starts decreasing. [50]. The charge carriers are scattered due to the setting up of phonon vibration, which blocks the mean free path of these charge carriers [51], leading to an increment in resistivity at lower temperatures.

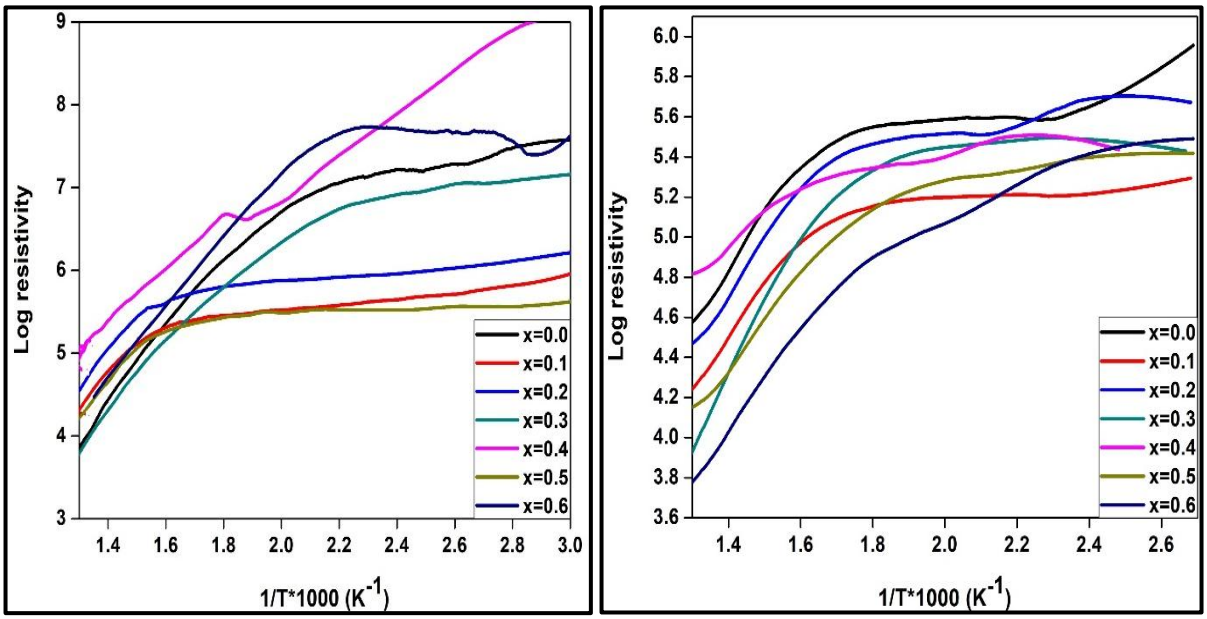


a **b**

Fig. 3.18 a: Plots of log resistivity vs. 1/T*1000 during heating cycle for 'as prepared' $Ni_{0.6-x}Co_{0.4}Zn_xFe_2O_4$ ferrites (x=0.0-0.6), and **Fig. 3.18 b:** Plots of log resistivity vs. 1/T*1000 during cooling cycle for 'as prepared' $Ni_{0.6-x}Co_{0.4}Zn_xFe_2O_4$ ferrites (x=0.0-0.6)

The 'sintered' ferrite shows a decreasing trend in resistivity with no break in the slope with an increase in temperature. This points to the semiconducting trend of ferrites except for the sample with composition x = 0.4, which shows a break in the linear plot at a temperature range of 570-600 K. This might be because, as it is known that Ni and Co are present in the octahedral site while zinc is in the tetrahedral site, whereas Fe is found in both the A and the B sites. Cation distribution leads to shifting of ions, which is likely the case, but does not alter composition but can change the electrical properties. As the temperature approaches 500K, Fe^{3+} ions migrate from the tetrahedral site to the octahedral site. Here, the hopping of electrons between Fe^{3+} and Fe^{2+} is increased; therefore, the resistivity is decreased. The transfer of Fe^{3+} ions continue until the temperature is 700K, after which saturation is reached, leading to no further migrations of Fe^{3+}ion to the octahedral site [52]. This results in the anomaly in the resistivity plot. The cooling curve recorded shows a similar pattern of semiconducting behaviour. It also shows a similar trend with an increase in zinc content. The resistivity decreases with an increase in zinc except for the sample with composition x=0.5, which is out of trend. It is known from the literature that Zn ions prefers to occupy the tetrahedral site. In contrast, Ni occupies the octahedral B site, and Fe is present in both the tetrahedral and octahedral sites. With increased Zn content, the Fe

ions are shifted to the octahedral site. Thus, the probability of electron hopping between ions of the same elements having different oxidation states is increased, as explained by Verwey's conduction mechanism [53]. Therefore, cobalt zinc ferrite has lower resistivity, while nickel cobalt has the highest. The resistivity values obtained for 'sintered' ferrites are found to be lower than those for 'as prepared' ferrites. The rise in sintering temperature affects the electrical properties. This can be due to factors like cation distribution, grain size increment, or formation of Fe^{2+} ions in the system. Upon sintering, the Zn^{2+} ions evaporate, giving rise to cation vacancies, and unsaturated oxygen ions bind to Fe^{3+}, which creates Fe^{2+} ions in the system. Thus, the electron hopping between Fe^{2+} and Fe^{3+} in the presence of Fe^{2+} ions leads to oriented polarisation in the lattice, causing a decline in resistivity for 'sintered' samples [54]. It is observed that 'sintered' ferrites show lower resistivity than 'as prepared' ferrites because the smaller the particle size, the higher the resistivity; hence, it follows the pattern. Small-sized particles have larger grain boundaries. These grain boundaries restrict current flow; thus, conduction decreases and resistance increases; therefore, smaller-sized 'as prepared' samples have higher resistivity than 'sintered' samples [55, 56, 57]. 'Sintered' samples have higher density, which means lower porosity. In comparison, 'as-prepared' ferrites have higher porosity and lower density; higher porosity means a higher number of vacancies and more scattering centers and pores for charge carriers, which leads to higher resistivity of 'as prepared' ferrites [58]. The 'as prepared' sample with composition x=0.5, shows the highest resistivity, as visible from the plot, and shows the smallest crystallite size, i.e., 36nm, as calculated from Scherrer's formula, which matches the explanation provided in the literature.



a **b**

Fig. 3.19a: Plots of log resistivity vs. 1/T*1000 during heating for 'sintered' $Ni_{0.6-x}Co_{0.4}Zn_xFe_2O_4$ (x=0.0-0.6) ferrites and **Fig. 3.19b:** Plots of log resistivity vs. 1/T*1000 during cooling for 'sintered' $Ni_{0.6-x}Co_{0.4}Zn_xFe_2O_4$ (x=0.0-0.6) ferrites

3.5.2 Magnetisation study (Vibrating sample magnetometer)

The DC magnetization study of all the 'as-prepared' and 'sintered' $Ni_{0.6-x}Co_{0.4}Zn_xFe_2O_4$ ferrites with x value ranging from 0.0-0.6 was carried out on a vibrating sample magnetometer at 300 K and 60 K at a magnetic field of -30000 Oe to 30000 Oe. Fig. 3.20 & 3.21 depict the hysteresis loop of 'as prepared' ferrite at RT and 60K, respectively, whereas Fig. 3.22 & 3.23 represent the hysteresis loop of 'sintered' ferrite at RT and 60K. The data evaluated from this hysteresis loop is depicted in Table 3.14. The plots depict a sigmoidal curve confirming the soft ferrimagnetic nature of the samples. A comparative study of the 'as prepared' and 'sintered' ferrites has been carried out. The RT studies of the M-H hysteresis loop showed a particular trend in Ms, Mr, and Hc parameters, which were found from the data obtained by VSM. In the $Ni_{0.6-x}Co_{0.4}Zn_xFe_2O_4$, where x = 0.0 to 0.6, the Ms values increased from 56 emu/g to 76 emu/g for x = 0.3 and then decreased to 55 emu/g for x=0.6. This variation in trend due to increased Zn dopant has been explained further and is related to cation distribution in A and B sites. The values for Ms were very well matched with the reported data [59]. Saturation magnetization

showed an increase in Ms value from x=0.0 to x=0.3, after which a decreasing trend was obtained till x=0.6. This behaviour of increase followed by decrease can be very well explained by two models, depending upon the type of arrangement of Zn ion in the B site, i.e., by a collinear or a non-collinear arrangement. The increase in Ms values is explained by Neel's two sub-lattice models or collinear arrangement. In contrast, the decrease is described by the three sublattice models, the Yafet-Kittel model, or the non-collinear arrangement. Spinels with inverse structure have the divalent metal ion in the octahedral site, while the trivalent ion is equally distributed in both the tetrahedral and the octahedral sites. Therefore, Ni and Co will occupy the octahedral site while Fe^{3+} will be shared between both sites. The reports of such distribution are indicated in the literature [60]. The net magnetization is given by the difference between the magnetic moment of the B site and that of the A site. As the dopant is introduced in the ferrite, the Zn ion occupies the tetrahedral site [61]. The replacement of the Ni^{2+} ion by Zn^{2+} pushes the trivalent Fe3+ ion from the tetrahedral site to the octahedral site; this, in turn, changes the magnetization value of the system. Fe^{3+} has a magnetic moment of 5BM, while that of Zn^{2+} is 0 BM. As the Zn content increases, Fe with a higher magnetic moment moves to the B site, thus increasing the B site's magnetic moment while decreasing the A site's magnetic moment. Therefore, with increased Zn content, magnetization increases according to Neel's collinear model due to increased superexchange interactions between ions of A and B sites. However, it is observed from Table 3.14 that after x=0.3, the Ms value shows a continuous decrease. With the increase in the content of Zn^{2+}, Neel's two-sublattice model does not hold well; instead, the Yafet-Kittel model of non-linear arrangement explains the decreasing behaviour. Above x=0.3, the zinc content increases to such an extent that the A- B super-exchange interaction decreases due to a decrease in the magnetic moment of the A site, and instead, the intra-sub lattice, i.e., the interaction between the B-B lattice dominates. This strengthened B-B interaction leads to spin canting, which decreases magnetization. In the case of 'sintered' samples, the same trend was seen, i.e., the Ms value initially increases with an increase in zinc content, and further decrease is observed, which is explained by the two-sub lattice model and three-sub lattice model, respectively. The Ms values obtained for 'sintered' samples were found to be slightly higher than those of 'as prepared' ferrite samples, at RT. The lower values of 'as prepared' ferries can be attributed to spin canting which is because of antiferromagnetic exchange interactions.

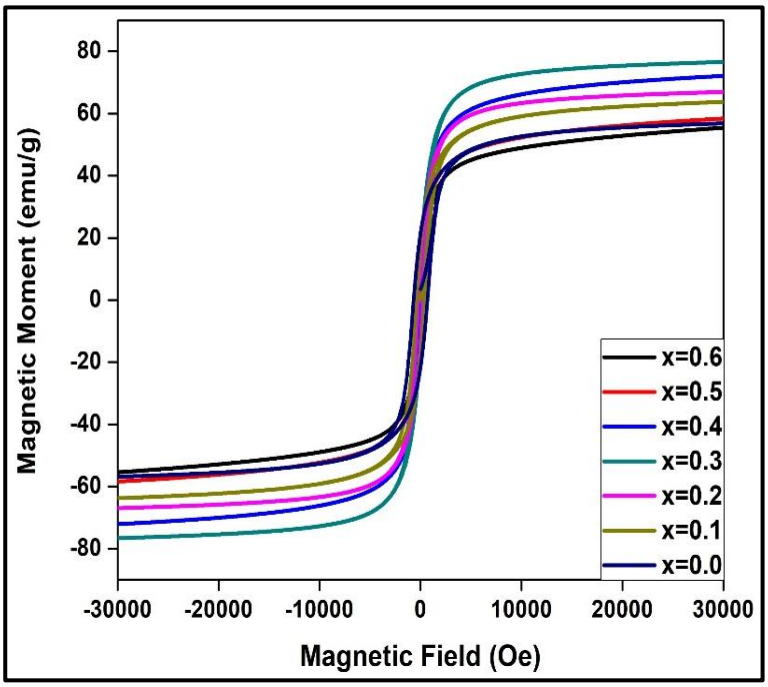


Fig. 3.20 The plot of magnetic moment v/s magnetic field of 'as prepared' $Ni_{0.6-x}Co_{0.4}Zn_xFe_2O_4$ (x=0.0, 0.1, 0.2, 0.3, 0.4, 0.5,0.6) ferrites measured at RT

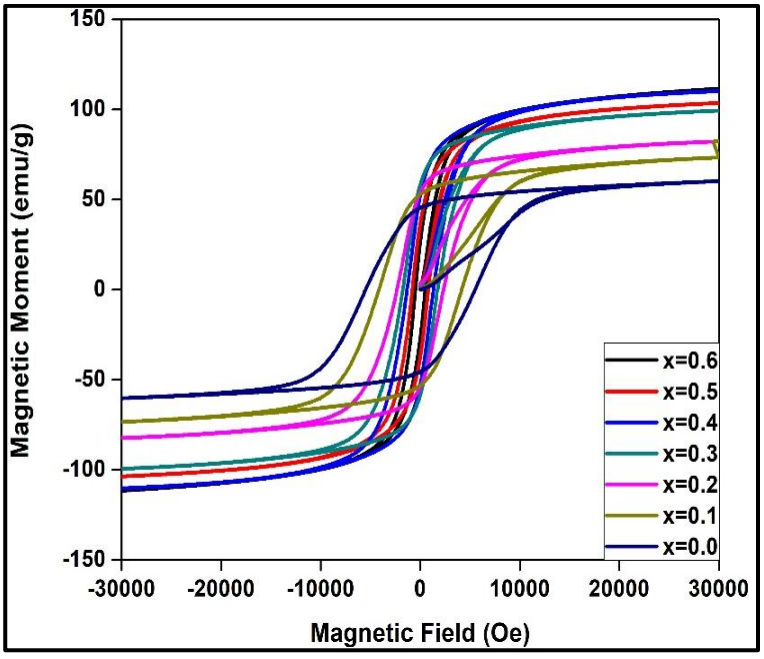


Fig. 3.21: The plot of magnetic moment v/s magnetic field of 'as prepared' $Ni_{0.6-x}Co_{0.4}Zn_xFe_2O_4$ (x=0.0, 0.1, 0.2, 0.3, 0.4, 0.5,0.6) ferrites measured at 60K

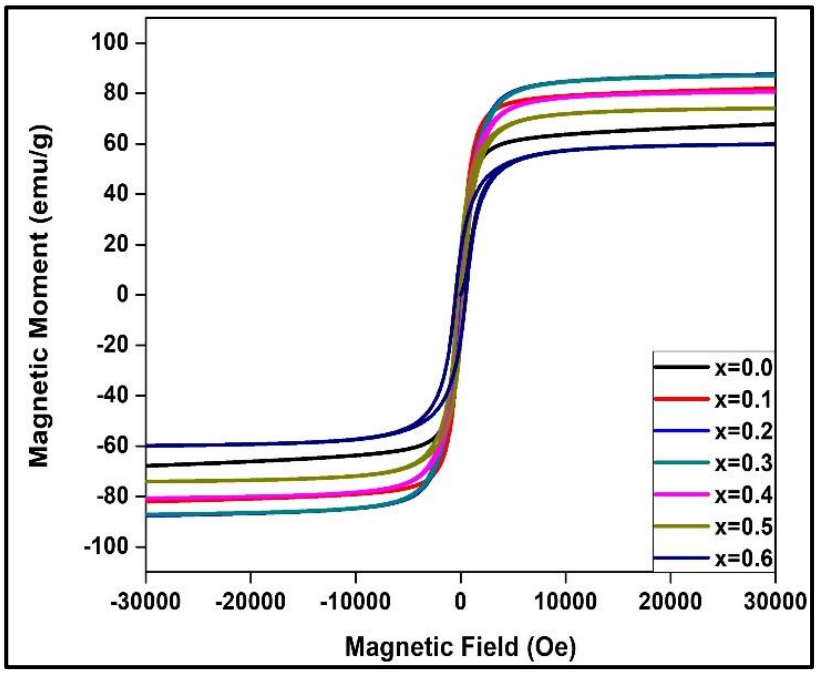


Fig. 3.22. The plot of magnetic moment v/s magnetic field of 'sintered' $Ni_{0.6-x}Co_{0.4}Zn_xFe_2O_4$ (x=0.0, 0.1, 0.2, 0.3, 0.4, 0.5,0.6) ferrites measured at RT

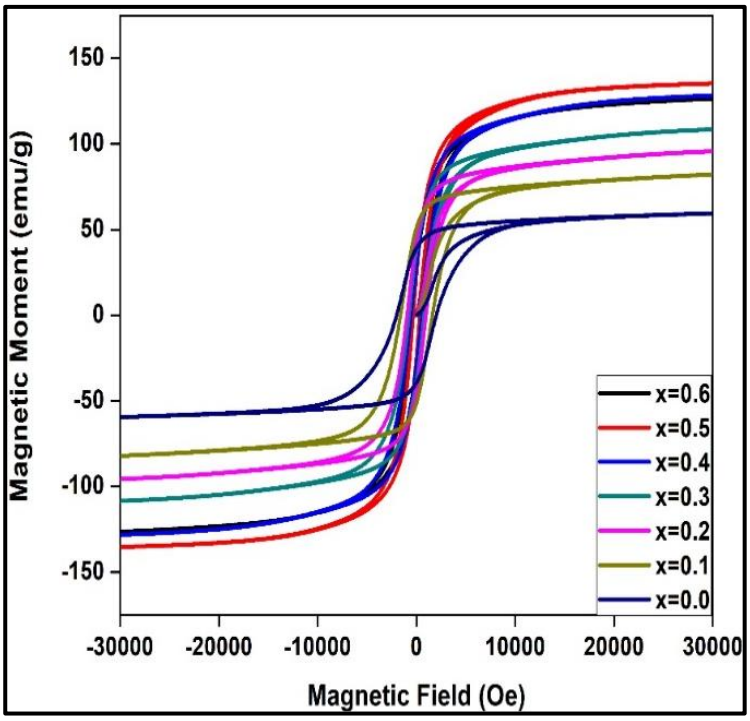


Fig. 3.23 The plot of magnetic moment v/s magnetic field of 'sintered' $Ni_{0.6-x}Co_{0.4}Zn_xFe_2O_4$ (x=0.0, 0.1, 0.2, 0.3, 0.4, 0.5,0.6) ferrites measured at 60K

Fig.3.22 & 3.23 depict the MH studies carried out at RT and 60K for 'sintered' ferrite samples. As expected, the M_s values obtained for the 'as prepared' and 'sintered' ferrite performed at 60 K were higher than those of RT because at lower temperatures, there are fewer thermal fluctuations on magnetic ions. M_r values and H_c values decreased with an increase in zinc content in the samples.

The M-T studies or the temperature-dependent studies were carried out in the temperature range of 60K to 350K at a constant field of 250, 500, and 1000Oe for both the 'as prepared ' and 'sintered' $Ni_{0.6-x}Co_{0.4}Zn_xFe_2O_4$ (x=0.0, 0.1, 0.2, 0.3, 0.4, 0.5, 0.6) ferrites. The zero-field cooled magnetisation (ZFC) and field cooled magnetisation (FC) studies for all the ferrites were carried out and the plots of the same are represented in Fig: 3.24 and Fig: 3.25. In the case of ZFC analysis, the sample was first cooled to 60 K. Here, the field applied is zero; when the sample attains 60K, the field is applied, and heating is initiated from 60K to 350 K. The FC studies were measured during the heating cycle. The material was first cooled to 60K in the presence of a field, and the applied field measurements were done during the heating process. Fig. 3.24 represents the plot of magnetization versus temperature for 'as-prepared' $Ni_{0.6-x}Co_{0.4}Zn_xFe_2O_4$ (x=0.0, 0.1, 0.2, 0.3, 0.4, 0.5, 0.6) ferrites whereas Fig. 3.25 represents the magnetization versus temperature curve for 'sintered' $Ni_{0.6-x}Co_{0.4}Zn_xFe_2O_4$ (x=0.0, 0.1, 0.2, 0.3, 0.4, 0.5, 0.6) ferrites at a constant field of 250, 500 and1000Oe. As mentioned above, the plots show two curves. The lower curve represents the ZFC, while the upper represents the FC. In the case of the ZFC curve for 'as prepared' ferrite, it was observed that initially, the magnetization increases to attain a maximum value and shows a broad maximum. This broad maximum results from wide particle distribution within the samples and dipole-dipole interactions [62-64]. Further, as the temperature increases, a decrease in the curve is seen; this maximum that is attained is referred to as blocking temperature (T_B) [Table 3.11]; the blocking temperature is the temperature where the thermal energy overcomes the anisotropy in the domain which aligns the magnetic spins in the direction of the applied field and hence a high magnetization is obtained at that temperature. At temperature below T_b, we see that the value of magnetization is low i.e., is near 60 K; this can be explained by the fact that during the cooling process, when no magnetic field is applied, the magnetic moments in the domain align along the easy axis which is expected but magnetic anisotropic energy curtain the alignment along the easy axis hence explains the lower values at 60K [62]. Above T_B, we see that the magnetization decreases monotonically with an increase in

temperature, but only for a few samples. In the case of the FC curve, the curve shows a continuous decrease as expected for single-domain nanoparticles [62,63,64]. At low temperatures, the FC curve shows the highest magnetization, indicating long-range magnetic ordered particles with high anisotropy [65,66]. It is observed that the magnetisation curve decreases rapidly with temperature for samples containing higher zinc content, which can be attributed to weak interactions between particles due to surface layer disorder [67]. Another factor determined from the ZFC-FC curve is the irreversible temperature (Tirr), which is defined as the temperature at which the ZFC and FC curves meet. But in our studies, we noticed that not all the ZFC and Fc curves meet at 350K This can be due to a fraction of molecules that are still magnetically blocked. The large size and magnetic interaction between these larger particles lead to such behaviour. Blocking temperature was seen to decrease with an increase in the applied field. T_B value was found to be lowest at 1000 Oe, while at 250 Oe, the ferrite sample showed the highest T_B value. T_B also varied with dopant content. It can be seen from Table 3.14 that, as the zinc content increased, the value of T_B also increased. Except for the sample with the highest zinc content (x=0.6), where T_B decreased or showed the lowest value as compared to all the other ferrite samples. The large gap between the ZFC and FC curves for lower zinc content samples can be explained by the large anisotropy, due to which high energy is required for the spins to flip and align according to the applied field [67].

The magnetisation studies as a function of temperature for 'sintered' ferrite samples were also measured in variable fields, 1000, 500, and 250Oe, with an increasing temperature from 60K to 350 K. The FC and ZFC curves showed a similar trend to 'as prepared' ferrites. The blocking temperature for most of the samples was not gained as it lay beyond 350K, and the irreversible temperature could not be determined. The ample space between the ZFC and FC curves indicates a large particle size distribution in the ferrite samples.

Table: 3.14: M_s, H_c, M_r, and T_B obtained from the MH and MT plots of 'as prepared' and 'sintered' $Ni_{0.6-x}Co_{0.4}Zn_xFe_2O_4$ (x=0.0, 0.1, 0.2, 0.3, 0.4, 0.5, 0.6) ferrites at RT, 60 K and a constant field of 250, 500 and 1000Oe

	X		**0.0**	**0.1**	**0.2**	**0.3**	**0.4**	**0.5**	**0.6**
Ms (emu/g)	RT	'As prepared'	56	63	66	76	71	58	55
		'sintered'	59	73	80	87	87	81	67
	60K	'As prepared'	60	73	82	99	110	103	111
		'sintered'	59	81	95	107	127	135	126
Hc (Oe)	RT	'As prepared'	687	397	236	205	100	54	35
		'sintered'	502	299	234	192	123	42	51
	60K	'As prepared'	5506	4164	2322	1753	1318	800	492
		'sintered'	1993	1607	943	756	536	329	469
Mr (emu/g)	RT	'As prepared'	21	34	13	14	7	4	2
		'sintered'	17	15	14	11	6	3	4
	60K	'As prepared'	27	36	52	58	54	52	45
		'sintered'	28	24	29	37	43	50	39
T_B (Oe)	250	'As prepared'	-	300	345	350	-	-	245
		'sintered'	-	-	-	-	-	-	-
	500	'As prepared'	-	243	304	348	349	348	211
		'sintered'	-	-	-	-	-	321	261
	1000	'As prepared'	348	193	239	324	329	346	160
		'sintered'	-	-	-	-	332	282	171

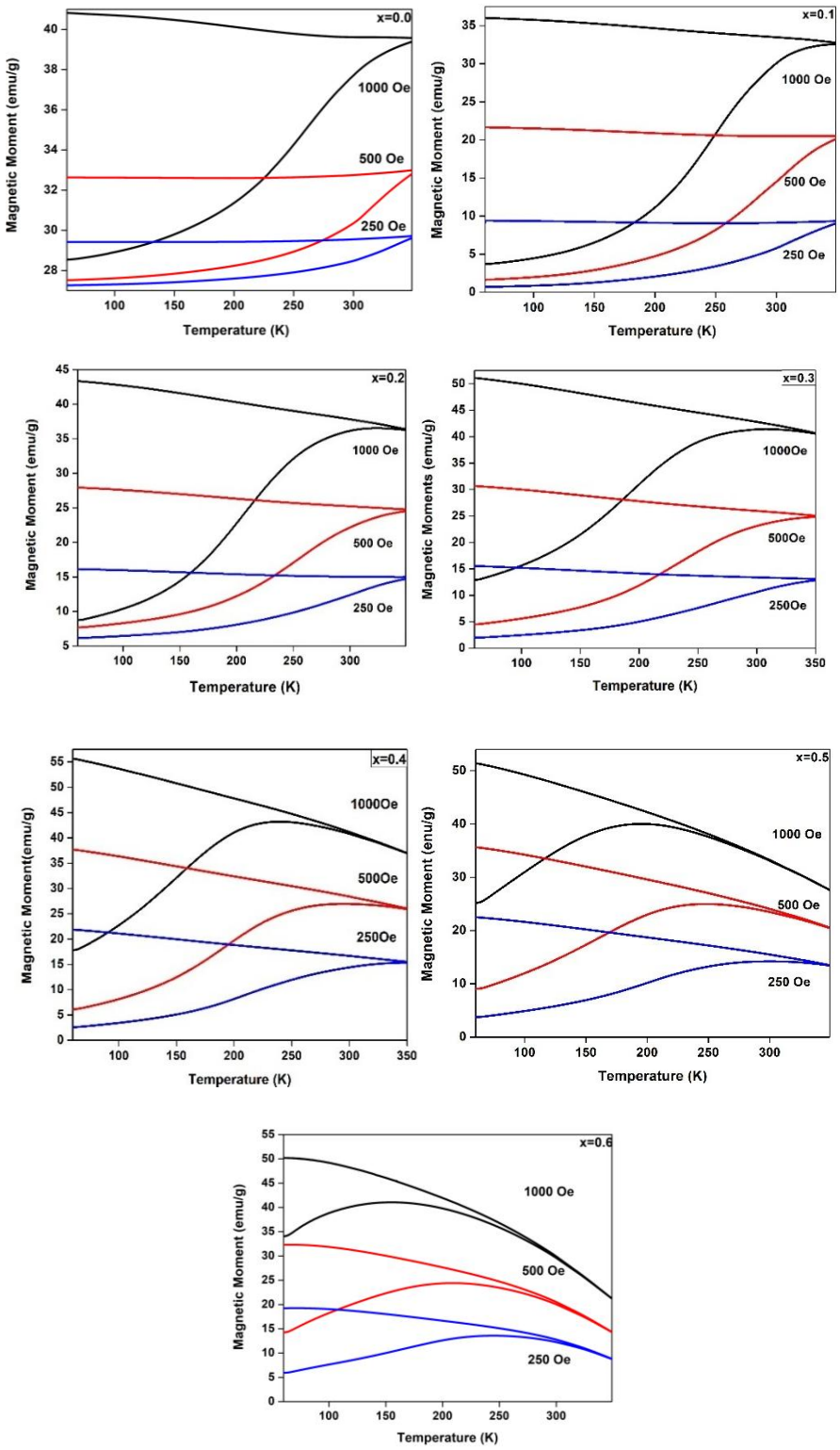


Fig. 3.24 MT plots (FC and ZFC curves) of 'as prepared' $Ni_{0.6-x}Co_{0.4}Zn_xFe_2O_4$ (x=0.0, 0.1, 0.2, 0.3, 0.4, 0.5, 0.6) ferrites at 1000,500 &250 Oe.

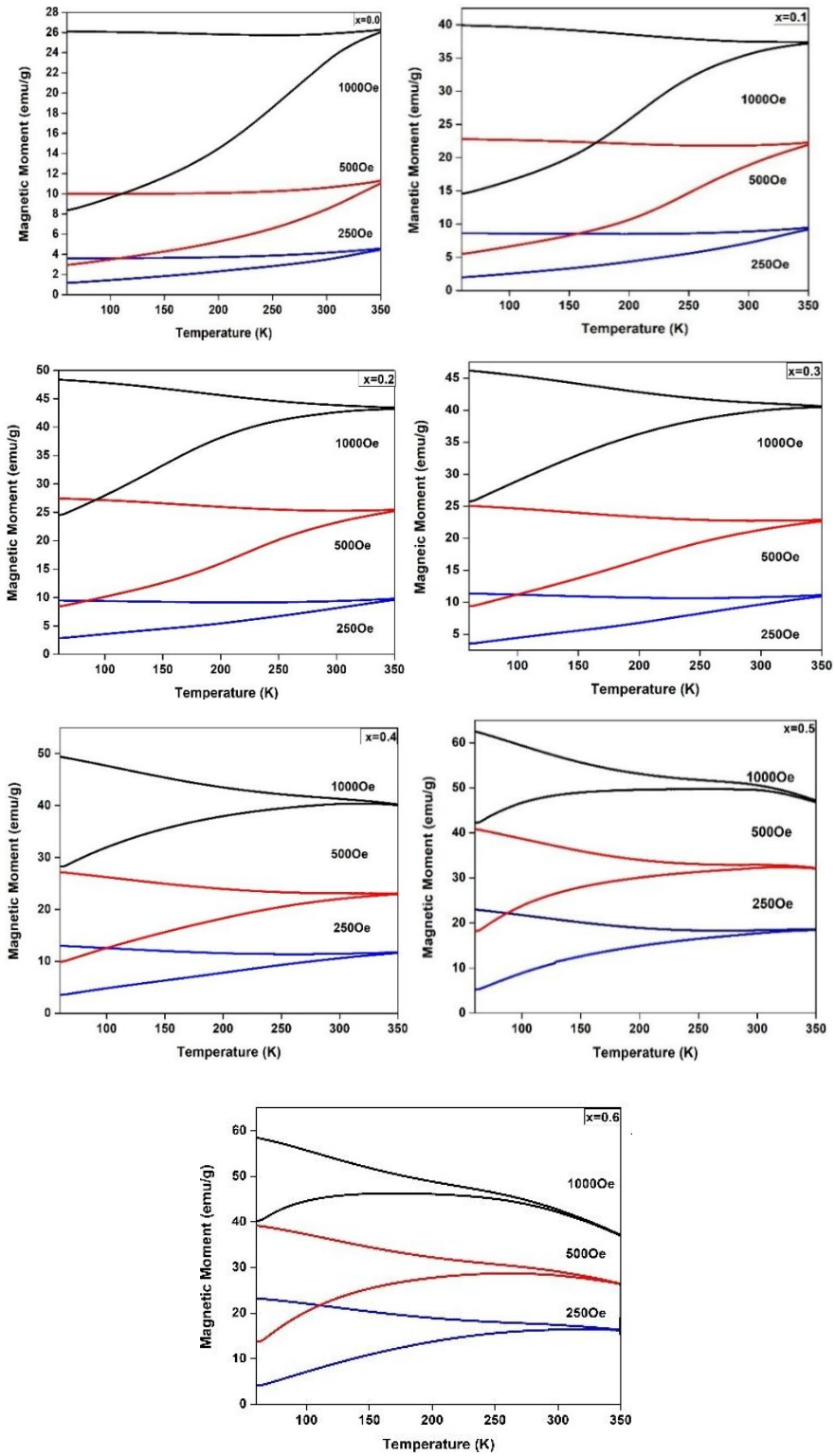


Fig. 3.25: MT plots (FC and ZFC curves) of 'sintered' $Ni_{0.6-x}Co_{0.4}Zn_xFe_2O_4$ (x=0.0, 0.1, 0.2, 0.3, 0.4, 0.5, 0.6) ferrites at 1000,500 &250 Oe.

3.5.3 AC Susceptibility

The AC susceptibility measurements of the 'as prepared' as well as the 'sintered' $Ni_{0.6-x}Co_{0.4}Zn_xFe_2O_4$ (x=0.0, 0.1, 0.2, 0.3, 0.4, 0.5, 0.6) ferrites have been carried out from room temperature to 850 K. Curie temperature and domain structure are evaluated from the obtained data. Fig. 3.26 represents the susceptibility plots of 'as-prepared' ferrites, while Table 3.15 summarises the Tc values. From the AC susceptibility curves, it can be seen that, as the temperature rises, susceptibility increases linearly with the formation of a peak or the Hopkinson peak at elevated temperatures. Further, as the Tc is approached, there is a steady decrease in the susceptibility, confirming a pure phase formation as only a single Curie temperature is obtained [68-70]. Like in XRD, AC susceptibility is another technique to confirm phase purity. The plot indicates a peak-like formation in the samples, especially in the case of the samples with the composition x=0.0 and x=0.1. Such peak behaviour suggests the presence of single-domain characteristics of particles [68,69]. The peak seen in the case of ferrite sample with composition x=0.0 is quite pronounced and is not visible as zinc concentration increases, finally leading to a superparamagnetic curve for sample x=0.6. Thus, it is inferred that, addition of zinc into the ferrite system leads to superparamagnetic particles [71]. The presence of Hopkinson's peak with an increase in thermal energy and the increase at the peak is an engaging process of thermo-magnetic randomization and magnetic alignment due to boundary wall domain expansion [72]. After the susceptibility reaches its highest, the alignment in the magnetic ordering is broken, leading to a fall in the susceptibility, giving the Curie temperature. This is where the ferrimagnetic materials behave like a paramagnetic one, called the Curie temperature [73]. It is seen that as the zinc content increases, the size of the material also decreases in the 'as prepared' and 'sintered' state, with some variation [75]. As the size from bulk to nanomaterials changes, the particle's nature also changes from multi-domain to a single domain and superparamagnetic, which also alters the Tc [74]. The Ni-rich samples show peaking behavior, which reduces with zinc content, thus indicating the superparamagnetic nature of samples with higher zinc content [71]. In the case of the 'as prepared' ferrites showcased in Fig. 3.26, it is clear that the Tc decreases with the increase in dopant concentration, which is a non-magnetic zinc. Several factors affect the decrease in the trend, like the occupation of the metal cations in the octahedral and tetrahedral sites, which in turn depends on the synthesis route, size of the particles, etc. [76].

It has been reported that Curie temperatures depend on the occupation and interaction of all the metal ions in the lattices [77]. Several interactions can occur, like A-A, B-B, and A-B interactions. The interaction seen with higher intensity is the A-B interaction as given by Neel's two-sublattice model. The magnetic superexchange interactions between A-B ions of Fe^{3+}-O-Fe^{3+} can explain the decline in Tc with increased zinc content. It is known that all the zinc ions occupy the tetrahedral site, while Fe^{3+} can be present at the tetrahedral (A site) and octahedral (B site) sites. Introducing Zn^{2+} ions into the system forces the Fe^{3+} into the B site, thus increasing the zinc content in the A site, decreasing the Fe^{3+} content in the A site, and increasing it in the B site. The larger zinc ions will increase the distance between the A and B sites, as indicated by the increased lattice constant values from XRD, reducing the A-B interactions. Hence, less energy will be required to destroy the alignment of spins, so the Curie temperature is lowered with doping with Zn^{2+} ions. [78]. Table 3.15 shows the Curie temperature for 'as prepared' and 'sintered' ferrites. It was noticed that Tc decreases with zinc content for both series. This is attributed to the size of the particles. As the size decreases, the Curie temperature declines. However, in the case of 'sintered' ferrites, the sizes vary, and the Curie temperature continuously declines. The 'as prepared' ferrites and the 'sintered' ferrites showed a similar trend with zinc content.

Fig. 3.27 illustrates the plots of ac susceptibility studies of 'sintered' ferrite samples. It can be noted that the 'sintered' ferrite shows a lower Curie temperature than the 'as prepared' ferrite. As mentioned above, this trend can be correlated to the lattice constant. The lattice constant of 'sintered' ferrite is higher than that of 'as prepared' ferrite. A higher lattice constant means more distance between the A and B sites, reducing their interaction and requiring lower energy to break the magnetic alignment. Thus, the lowering of Tc is accountable. The samples with composition x=0.4, 0.5, and 0.6 show a slow increase in susceptibility with temperature and further falls to zero at Tc with a tailing effect; therefore, we can conclude the presence of some superparamagnetic single domain fraction of particles [79]. Meanwhile, the samples with composition x=0.0 to 0.3 show a peak with significant susceptibility, from which we can conclude the fraction of multidomain particles within homogeneous particles [80].

Table 3.15: T_c of 'as prepared' and 'sintered' $Ni_{0.6-x}Co_{0.4}Zn_xFe_2O_4$(x=0.0, 0.1, 0.2, 0.3, 0.4,0.5, 0.6) ferrites

x	Tc (K) As-Prepared	Tc (K) Sintered
0.0	825	812
0.1	781	762
0.2	724	718
0.3	707	684
0.4	585	581
0.5	489	513
0.6	482	452

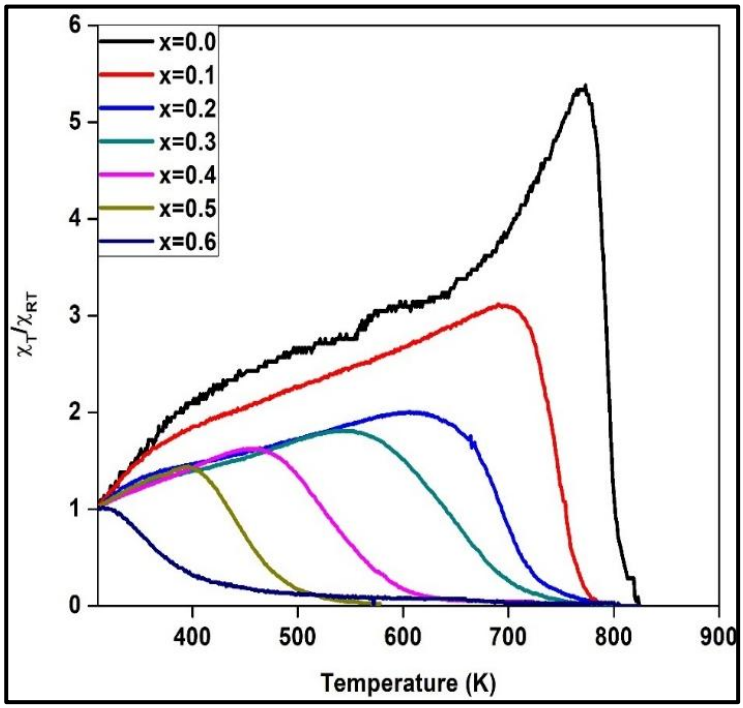


Fig. 3.26 AC susceptibility plots of 'as prepared' $Ni_{0.6-x}Co_{0.4}Zn_xFe_2O_4$ (x=0.0-0.6) ferrite

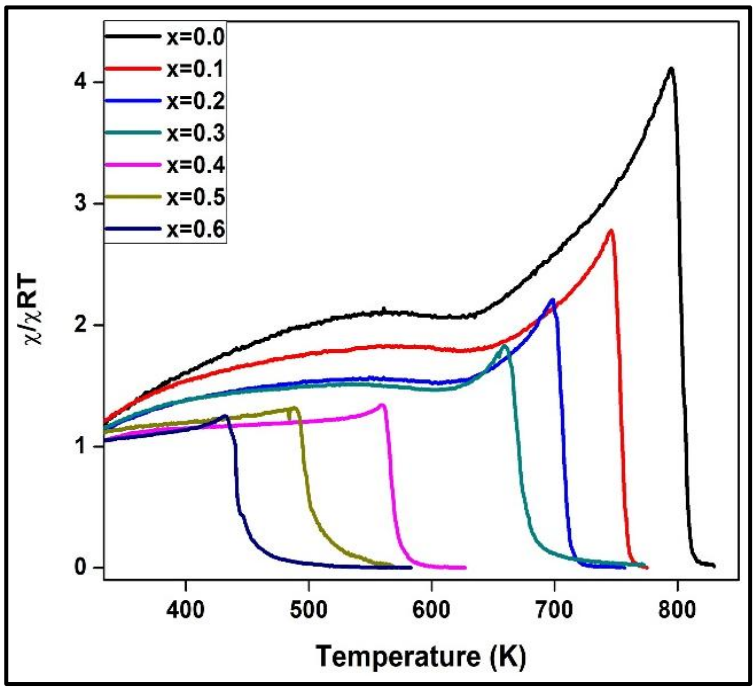


Fig. 3.27 AC susceptibility plots of 'sintered' $Ni_{0.6-x}Co_{0.4}Zn_xFe_2O_4$ (x=0.0-0.6) ferrites

3.5.4 Dielectric study

The dielectric properties in the ferrites are governed by various factors that affect the performance of the samples. Cation distribution, stoichiometry of the samples, sample density, sample size, method of synthesis, and temperatures at which samples were treated are some of the few factors affecting the properties. The dielectric study of all the 'as-prepared' and 'sintered' $Ni_{0.6-x}Co_{0.4}Zn_xFe_2O_4$ (x=0.0-0.6) ferrite samples was carried out.

Ferrites synthesized were studied concerning frequency at a variable temperature and a fixed frequency. The plots of dielectric constant versus log frequency and dielectric loss versus log frequency are represented in Fig.3.28a and b, respectively, for 'as prepared' ferrite, and Fig. 3.31 and Fig. 3.32 represent the 'sintered' ferrite samples, respectively. The plots for the temperature-dependent study are plotted as dielectric constant versus temperature and dielectric loss versus temperature at fixed frequencies of 1 kHz and 1MHz. The plots are illustrated in Fig. 3.29(a-c) & Fig. 3.30(c-d) for 'as prepared ferrite and Fig. 3.33 (a-d) for 'sintered' ferrite.

3.5.4.1 Dielectric constant versus frequency

In The frequency variation plots, the dielectric constant was observed to decrease continuously with an increase in frequency; this is the typical trend of ferrite materials. At lower frequencies, the dielectric constant was high, and as the frequency increases, the dielectric constant starts to decrease and further becomes independent of frequency. The initial drop is rapid, followed by a gradual decrease, and further beyond 10 kHz, the dielectric constant becomes independent of frequency. After analyzing the dielectric constant, it is observed that sample with composition x=0.1 shows an unbelievably significant value as compared to other samples. The conduction mechanism in ferrites is explained by two models: Koop's phenomenological theory and Maxwell-Wagner's principle [81-83]. According to Koop's theory, the higher value of the dielectric constant at lower frequencies is due to grain boundaries with high resistance. Maxwell- Wagner's theory explains grain boundary polarisation due to material defects. Therefore, these two theories were utilized to describe the trend observed in the samples.

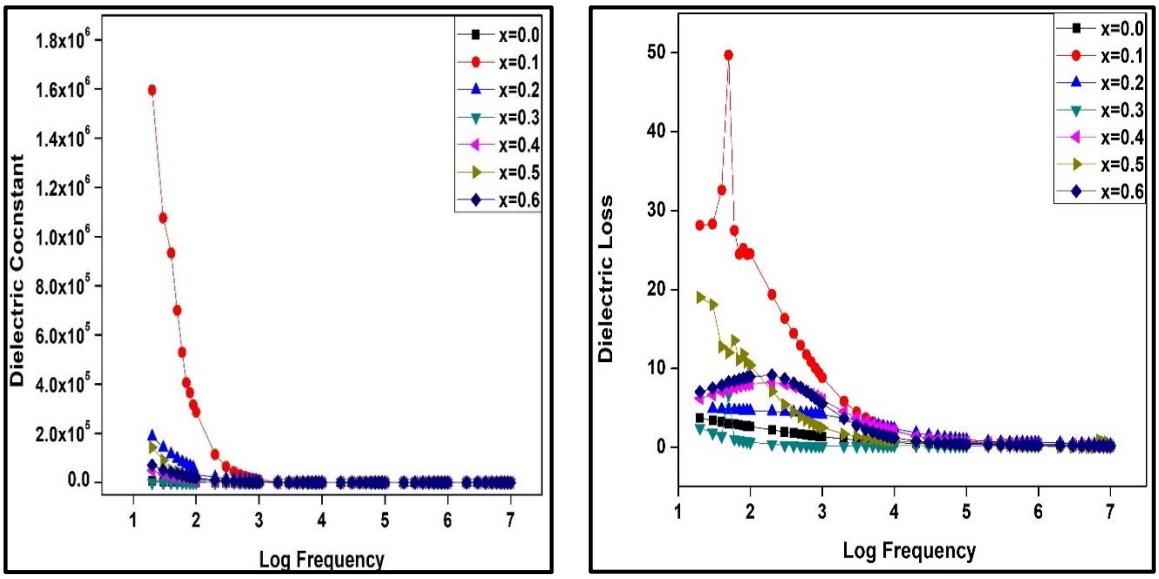
During the synthesis process or sintering of the sample, defects in the samples occur, which results in polarisation; therefore, we observe that at lower frequencies, the dielectric constant is dominated by ionic and interfacial polarisations, whereas in the higher frequency region, the dielectric constant is impacted by electronic and dipolar polarisation [84]. According to Koop's theory, ferrites contain highly conducting grains compared to poorly performing or insulating grain boundaries. When the external fields are applied, the charge carriers hop towards the grain boundary, and accumulation occurs due to the grain boundary's weakly conducting nature. This results in high interfacial polarization, resulting in a high value of dielectric constant at lower frequency in the samples. At high-frequency regions, the interfacial charges cannot match up with the fast-oscillating external field. Due to such lag, the dielectric constant decreases, or in other words, when the external field overpowers the hopping frequency of electrons, there is a reversal in the motion of electrons; hence, the polarisation decreases, and so does the dielectric constant [85]. The conduction mechanism in ferrites can result from the hopping of electrons or the movement of holes. The conduction mechanism and dielectric properties have a close relationship. The exchange of electrons between ions of the same elements having different oxidation states results in the displacement of charges and causes polarization. The dielectric constant depends on the number of Fe^{2+} and Fe^{3+} ions present in the samples; the sample x=0.1

shows an exceptionally high dielectric constant, which can be attributed to a smaller grain size. Smaller grain sizes result in more grains and larger grain boundaries. These grain boundaries result in scattering, accounting for a high dielectric constant. A larger surface area of material leads to larger surface polarization, which certainly tallies with the surface area obtained for sample x=0.1 from BET data. The surface area obtained for x=0.1 is $128 m^2/g$, which is relatively high compared to the other samples in the series [86]. The lowest dielectric constant was observed for the sample with x=0.3.

The dielectric loss vs log frequency plots for 'as prepared' ferrite samples is illustrated in Fig. 3.28 b. It showcases a high dielectric loss at a lower frequency for all the samples. This enormous loss significantly drops as the frequency rises. This phenomenon agrees with Koop's phenomenological principle [87]. Various factors can affect the dielectric loss, such as magnetostriction anisotropy, microstructure alteration, imperfection in the lattice, and stoichiometric Fe^{2+} content. Due to the lower applied frequency, the electron hopping frequency between the ions Fe^{2+} and Fe^{3+} is more significant at low frequencies. This makes it easier for the dipoles to align parallel to the direction of the field, which enhances the loss factor. A sharp drop is observed at higher frequencies due to a lag in polarisation, and interfacial polarisation leads to the adoption of a resistive layer. A slight hump in the plot is observed in the case of the ferrite sample with compositions x=0.2, 0.4, and 0.6. These resonance peaks are typical to spinel ferrites. The peak observed is referred to as the Debye relaxation peak. The relaxation occurs when the hopping of electrons between the Fe^{2+} and Fe^{3+} becomes equal to the applied frequency field, and the phenomenon is known as ferrimagnetic resonance [88].

3.5.4.2 Dielectric properties versus temperature

Fig. 3.29 (a,b) and Fig 3.30 (a, b) represents the temperature-dependent dielectric constant plots of 'as prepared' ferrite for fixed frequencies, 1 kHz and 1 MHz, respectively. Two regions are observed in the plots due to low and high temperatures. It can be observed that the dielectric constant is almost independent of temperature at low temperatures. The temperature is very low and insufficient to activate the charge carriers. After which, a rapid increase in the dielectric constant is observed. The variation in dielectric constant can be explained by the formation of Fe^{2+} ions, which are formed due to unsaturated oxygen and cation vacancies.

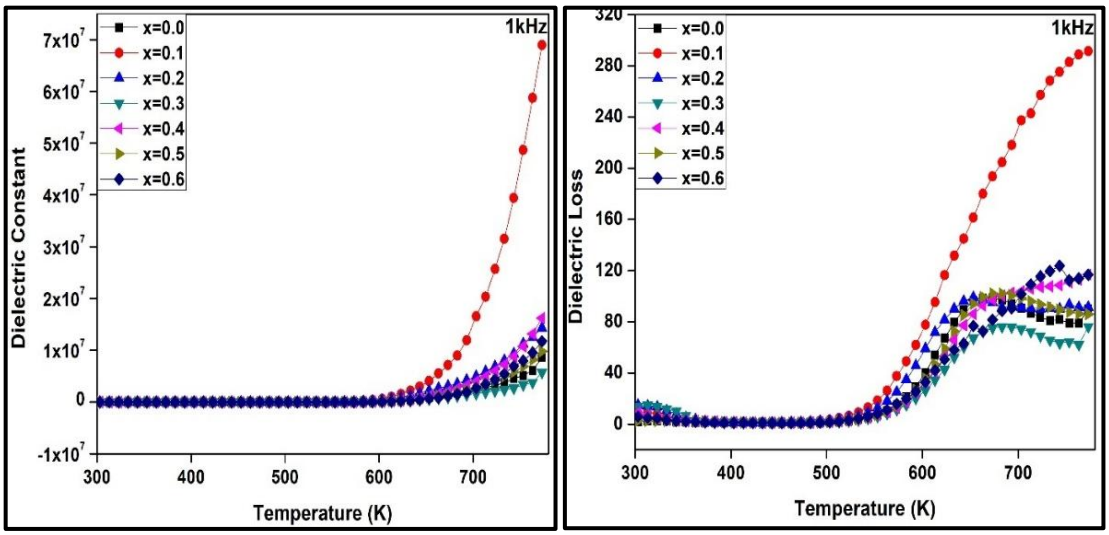


a **b**

Fig. 3.28 a: The plot of Dielectric Constant vs. Log Frequency at RT for 'as prepared' $Ni_{0.6-x}Co_{0.4}Zn_xFe_2O_4$ (x=0.0-0.6) ferrites and **Fig. 3.28b:** The plot of Dielectric Loss vs. Log Frequency at RT for 'as prepared' $Ni_{0.6-x}Co_{0.4}Zn_xFe_2O_4$ (x=0.0-0.6) ferrites

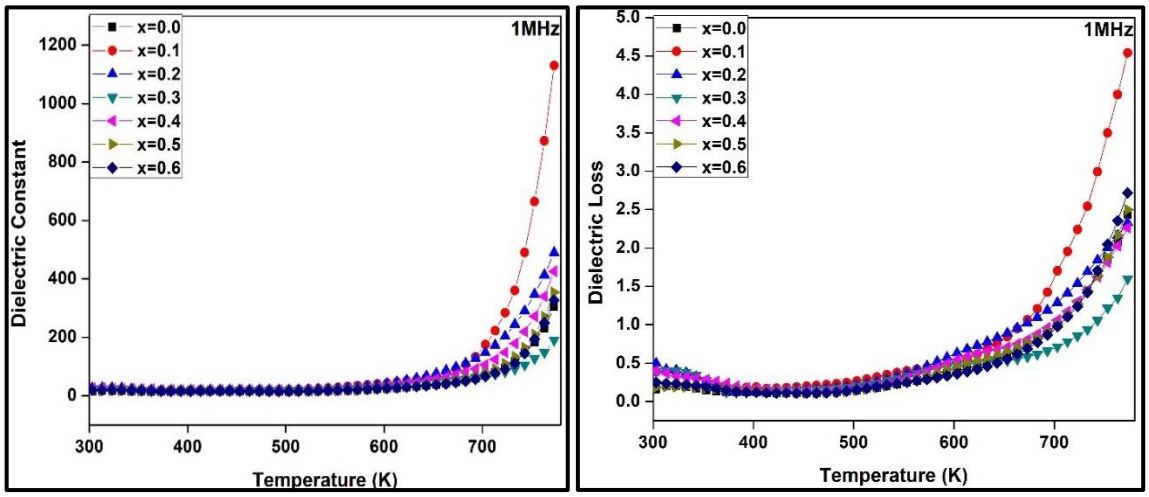
The presence of Fe in two different valence states causes the hopping of electrons between the Fe ions. The Fe in the 2+ state acts like p-type carriers, which releases electrons, while Fe in the 3+ valence state helps neutralize electrons, being the n-type carrier. Thus, this gives rise to orientational polarisation and the trend [89]. Iron (Fe^{3+}/Fe^{2+}), Cobalt (Co^{3+}/Co^{2+}), and Nickel (Ni^{3+}/Ni^{2+}) ions in the octahedral site increases the dielectric constant and loss significantly. The polarization in such materials is similar to the conduction process wherein the hopping of electrons between holes and electrons gives rise to dielectric polarisation in ferrites [90,91]. Comparing the two frequencies, it is observed that the 1MHz frequency gives a lower dielectric constant than the 1kHz frequency. All four types of polarisations, interfacial, dipolar, ionic, and electronic, contribute towards the dielectric constant at low frequency. The onset of the dielectric constant shifts to a higher temperature in the case of a 1 MHz frequency plot. This rapid increase for the lower 1 kHz frequency is mainly due to interfacial and dipolar polarisation. The lower values of the dielectric constant are due to the contribution of ionic and electronic polarization [92].

The dielectric loss concerning temperature at 1 kHz and 1 MHz frequencies shows a similar pattern to that of the dielectric constant. The dielectric loss can be explained as a lag polarisation caused when the field is applied. It can be seen from Fig.3.29 b and 3.30 b that dielectric losses are lower for the high frequency of 1MHz for all the ferrite materials. It can be seen that the dielectric loss is minimum or independent up to 500K, after which an increase in loss is observed with a hump or peak-like behaviour in the case of a 1kHz frequency plot. Similar behaviour is observed for samples at higher frequencies. This is due to thermal energy at higher temperatures boosting the charge carriers, which results in better hopping of electrons, increasing the polarisation, and thus increasing the losses. The sudden increase in loss with an increase in temperature is attributed to conduction losses [89]. The dielectric loss behaviour can be compared with resistivity as both have an inverse relationship, which means the sample possessing the highest resistivity will maintain the lowest dielectric loss, which again very well matches in the present study, ferrite sample with the composition x=0.3 shows the highest resistivity with the lowest dielectric loss. Thus, high resistivity and low dielectric loss materials can be used in power applications at high frequencies.



a **b**

Fig. 3.29 a: The plot of Dielectric Constant vs. Temperature for 'as prepared' $Ni_{0.6-x}Co_{0.4}Zn_xFe_2O_4$ (x=0.0-0.6) ferrites at 1 kHz, and **Fig. 3.29 b:** The plot of Dielectric Loss vs Temperature for 'as prepared' $Ni_{0.6-x}Co_{0.4}Zn_xFe_2O_4$ (x=0.0-0.6) ferrites at 1 kHz



a **b**

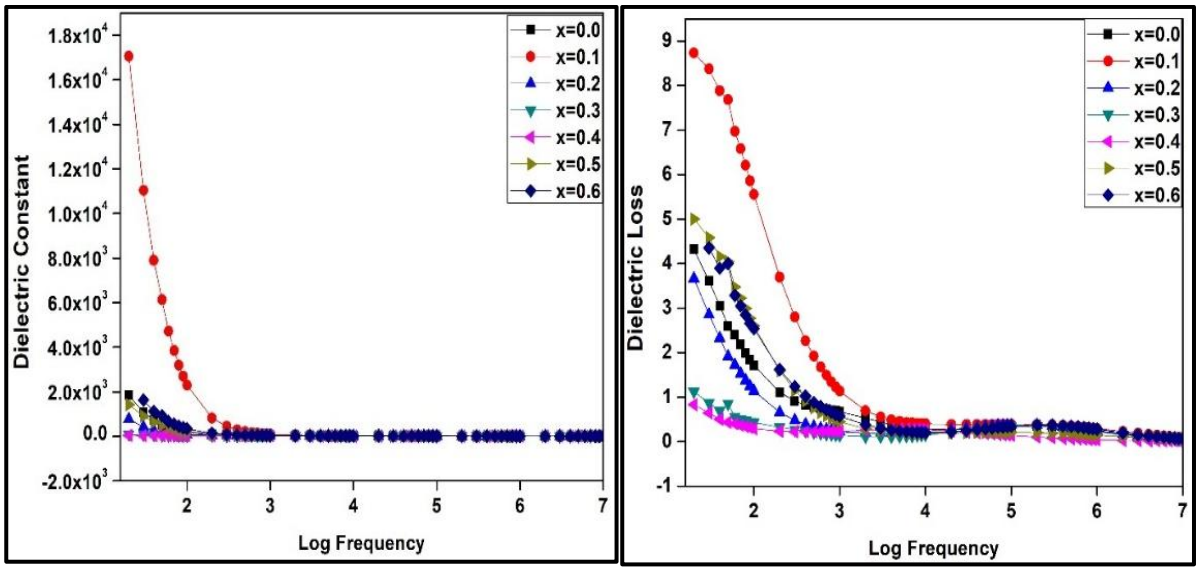
Fig. 3.30a: The plot of Dielectric Constant vs. Temperature for 'as prepared' $Ni_{0.6-x}Co_{0.4}Zn_xFe_2O_4$ (x=0.0-0.6) ferrites at 1MHz, and **Fig. 3.30 b:** The plot of Dielectric Loss vs. Temperature for 'as prepared' $Ni_{0.6-x}Co_{0.4}Zn_xFe_2O_4$ (x=0.0-0.6) ferrites at 1MHz

3.5.4.3 Dielectric properties of 'sintered' ferrites

The dielectric constant represents the energy stored during the imaginary part of the dielectric constant, which represents the energy loss. It is known from the literature that the dielectric properties or polarisation are highly influenced by the method of preparation, homogeneity, cation distribution, grain size, density, porosity, and also the sintering temperature [93]. A comparative study between 'as prepared' and 'sintered' dielectric properties is discussed to understand how sintering influences the properties. Figs. 3.31 and 3.32 illustrate the frequency dependence of the dielectric constant and dielectric loss in the samples. It is observed that the trend seen in the figure is similar to that of the 'as prepared' ferrite, i.e., with an increase in frequency, the dielectric constant decreases and is saturated, which is a normal trend expected for ferrites. This trend arises from interfacial polarisation in the Maxwell-Wagner model and agrees with Koop's phenomenological principle [94, 95, 96]. The dielectric constant of 'sintered' ferrite is found to be lower than that of 'as prepared' ferrite due to better crystal formation and increased sintering density.

Dielectric loss is a delay in polarisation or when polarisation lags or does not match the applied external field, caused by impurities or homogeneous materials. Therefore, it is noted that ferrite

samples sintered at 1000 °C show a very low dielectric loss as compared to the 'as prepared' samples calcined at 500 °C, as sintered samples are structurally perfect and homogenous. The decrease in dielectric loss with an increase in frequency follows the Maxwell-Wagner interfacial model [97]. Low dielectric losses mean high resistivity; the ferrite sample with composition x =0.4 possesses the lowest dielectric loss and shows the highest resistivity, which can be observed from Fig. 3.18 and 3.19.



a **b**

Fig. 3.31 a: The plot of Dielectric Constant vs. Log Frequency of 'sintered' $Ni_{0.6-x}Co_{0.4}Zn_xFe_2O_4$ (x=0.0-0.6) ferrites

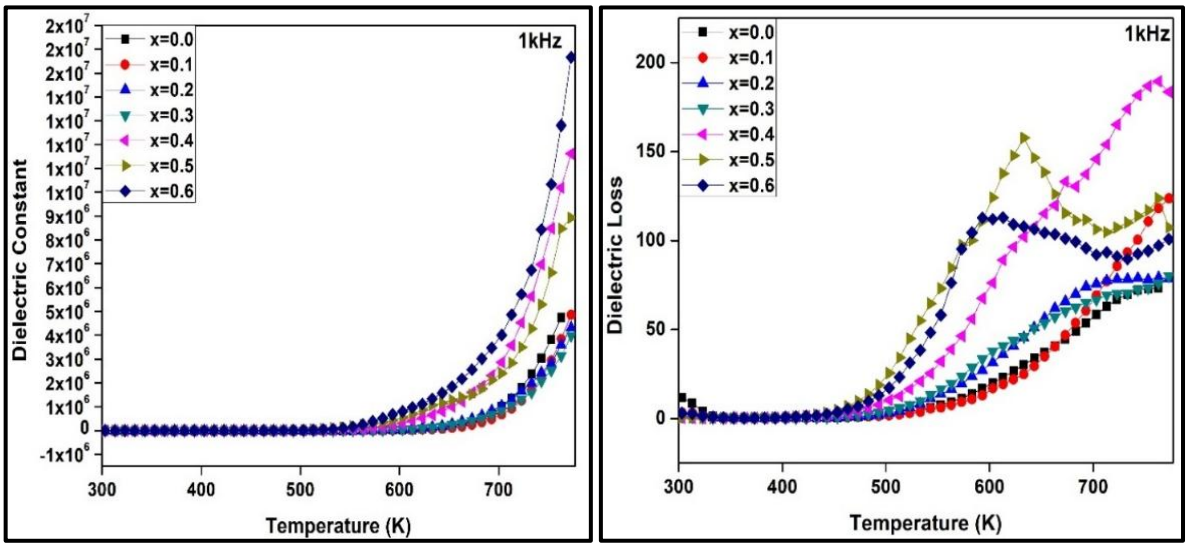
Fig. 3.32 b: The plot of Dielectric Loss vs. Log Frequency of 'sintered' $Ni_{0.6-x}Co_{0.4}Zn_xFe_2O_4$ (x=0.0-0.6) ferrites

3.5.4.4 Dielectric properties concerning temperature of 'sintered' ferrites

The dielectric constant and dielectric loss studies of 'sintered' $Ni_{0.6-x}Co_{0.4}Zn_xFe_2O_4$ (x=0.0-0.6) ferrites conducted at frequencies of 1 kHz and 1 MHz at increasing temperatures are illustrated in Fig. 3.33 (a-b) and 3.34 (a-b), respectively. This trend follows a similar trend observed in 'as prepared' ferrites. The dielectric constant at lower temperatures is independent of temperature and almost remains the same until a specific temperature, after which an increase in the dielectric value is seen. This trend is the same for both frequencies. The sample shows lower

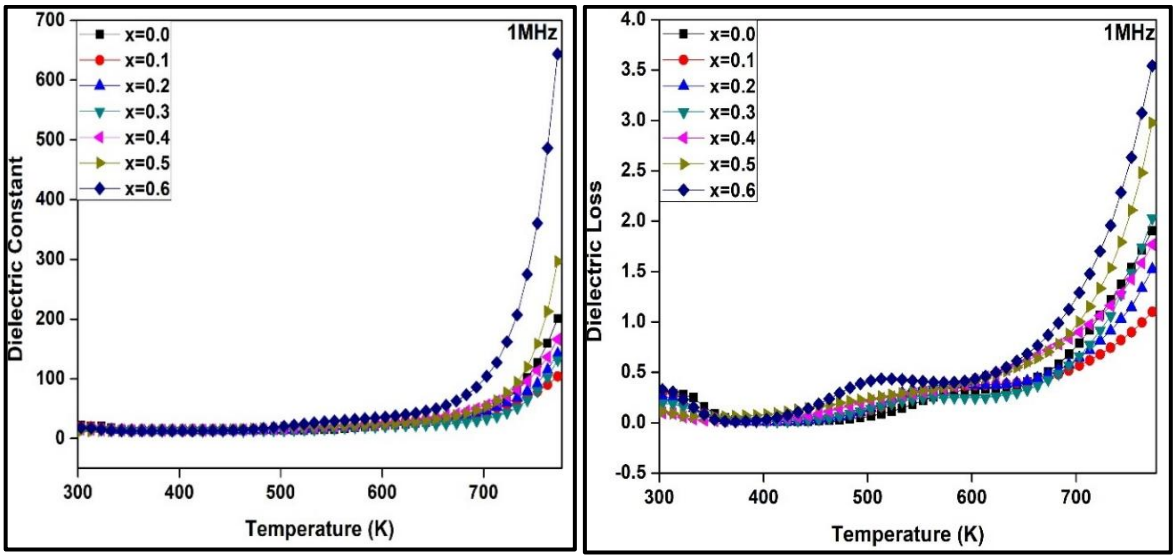
dielectric constant at 1MHz frequency than at 1kHz frequency. Dielectric constant mainly contributes to 4 types of polarisations, out of which dipolar and interfacial polarisation play a significant role at lower frequencies and are dependent on temperature. The dipolar polarisation decreases with temperature while interfacial polarisation increases; hence, interfacial polarisation dominates, increasing the dielectric constant. In the case of higher frequency, ionic and electronic polarisation are associated; therefore, a rapid increase in dielectric constant is observed at lower frequencies and a slow increase at higher frequencies [98, 99]. The onset of the dielectric constant decreases with a decrease in zinc content. Cobalt zinc ferrite shows the highest dielectric constant at both frequencies. Dielectric constant and resistivity shows opposite trends. Cobalt zinc, which has the highest dielectric constant, should show the lowest resistivity, which follows the trend in the present study. The cooling curves of resistivity illustrate the same. This implies that the conduction mechanism governs dielectric behaviour. Lower resistivity suggests ease of flow of charge carriers, which results in space charge polarization, thus increasing the dielectric constant. In comparison, higher resistivity obstructs the piling up of space charge carriers, resulting in lower dielectric constant values. Higher zinc content shows a higher dielectric constant; sample x=0.6, where zinc is in a higher ratio, shows a higher value. During sintering at higher temperatures, the chances of zinc evaporation are high. Due to the loss, the tendency to form Fe^{2+} ions increases. The increase in zinc content, which prudentially occupies the tetrahedral site, pushes the Fe present in the tetrahedral site to the octahedral site, with more ions of Fe^{3+} and Fe^{2+} in the octahedral site. The hopping of electrons between ions increases, thus increasing the dielectric constant.

The dielectric constant and dielectric loss at 1 kHz and 1 MHz were lower than those of the 'as prepared' samples. This points out the formation of structurally perfect crystals through sintering.



a **b**

Fig. 3.33a: The plot of Dielectric Constant vs. Temperature for 'sintered' $Ni_{0.6-x}Co_{0.4}Zn_xFe_2O_4$ (x=0.0-0.6) ferrites at 1 kHz and **Fig. 3.33b:** The plot of Dielectric Loss vs Temperature for 'sintered' $Ni_{0.6-x}Co_{0.4}Zn_xFe_2O_4$ (x=0.0-0.6) ferrites at 1 kHz



a **b**

Fig. 3.34 a: The plot of Dielectric Constant vs. Temperature for 'sintered' $Ni_{0.6-x}Co_{0.4}Zn_xFe_2O_4$ (x=0.0-0.6) ferrites at 1MHz and **Fig. 3.34 b:** Dielectric Loss vs Temperature for 'sintered' $Ni_{0.6-x}Co_{0.4}Zn_xFe_2O_4$ (x=0.0-0.6) ferrites at 1MHz

3.5.5 Initial Permeability Study

The initial permeability and Tan δ studies for all the 'sintered' $Ni_{0.6-x}Co_{0.4}Zn_xFe_2O_4$ (x=0.0, 0.1, 0.2, 0.3, 0.4, 0.5, 0.6) ferrites have been performed at RT at variable frequencies, whose schematics are portrayed in Fig. 3.35 a& band initial permeability vs. temperature plots for all the samples is illustrated in Fig. 3.36a. Initial permeability strongly depends on domain wall motion and spin. These two factors play a significant role at specific frequencies, i.e., the domain wall motion is substantial at lower frequencies. In comparison, at higher frequencies, the spin rotation is more dominant [84,100,101,102]. The figure shows that all the samples exhibit an identical pattern where the permeability slightly increases at a lower frequency and remains constant for the entire frequency range except for sample x=0.6, where an increase is seen at a higher frequency. It is observed that there is an initial increase in permeability at a lower frequency up to a particular frequency; this phenomenon is observed when there is a weak magnetic field present, which leads to the unpinning of the domain wall. As the frequency increases, the permeability of the samples become independent. This region is called the zone of utility [103].

Initial permeability is influenced by microstructural parameters like stoichiometry, composition, impurity concentration, crystallite size, saturation magnetization, and anisotropy values, which determine the initial permeability of the samples. It is seen that with an increase in Zn content in the samples, the permeability increases except for sample x=0.5, which shows a lower value than x=0.4. This can be attributed to increased bulk density and reduced grain size. Also, reduced magnetocrystalline anisotropy constant may be caused by reduced stress and a decreased crystal anisotropy [84]. With the increase in Zn content, permeability is seen to increase, and so is the crystallite size and saturation magnetization, and anisotropy is found to decrease. All these factors very well explain the trend in permeability of the samples [104]. A sample with high zinc content has no constraint on domain wall motion compared to other samples in the series and, therefore, can be considered for higher-frequency applications. The loss tangent vs. log frequency is depicted in Fig. 3.35b, which results from the difference in domain wall motion and applied magnetic field. It is observed from the plot that at lower frequencies, the loss is high, and as the frequency increases, it lowers and becomes constant. There is no proper trend obtained with an increase in zinc content.

We have also attempted to study temperature-dependent plots of initial permeability vs temperature (K) carried out from RT to 550 °C. Table 3.16 represents the T_c obtained from temperature studies of initial permeability compared with T_c obtained from AC susceptibility studies of the 'sintered' samples. The plots indicate an increase in permeability with an increase in temperature, showing a peak and then a sudden drop at T_c, as seen in AC susceptibility studies. This technique also provides the T_c values comparable to those obtained from AC susceptibility. Sharp fall at T_c also includes information on the presence of a multi-domain type domain structure. Sharp fall at T_c also complements the XRD data, which tells about the single-phase formation of the ferrite samples. It is seen that the T_c value decreases as the Zn content in the samples increases. As the zinc concentration increases, zinc ions prefer the tetrahedral (A) site, which pushes the Fe ions to move to the B site, replacing Ni ions. The lattice parameter also increases, leading to an increased distance between the A and B sites, meaning that the energy required to break the magnetic interactions is low. Thus, the T_c values decrease as Zn concentration increases. Fig. 3.36 b represents a Tan δ vs. Temperature plot of the 'sintered' $Ni_{0.6-x}Co_{0.4}Zn_xFe_2O_4$ (x=0.0-0.6) ferrites. As the temperature is increased, the loss is seen to remain constant at the beginning with an abrupt rise, and again shows a steady increase. The initial plateau seen with an increase in temperature reduces with an increase in zinc content. For the sample with composition x = 0.0, the plateau is seen almost for entire temperature while x = 0.6 sample shows highest losses. The sudden rise in the temperature is at same temperature as the fall in initial permeability plot.

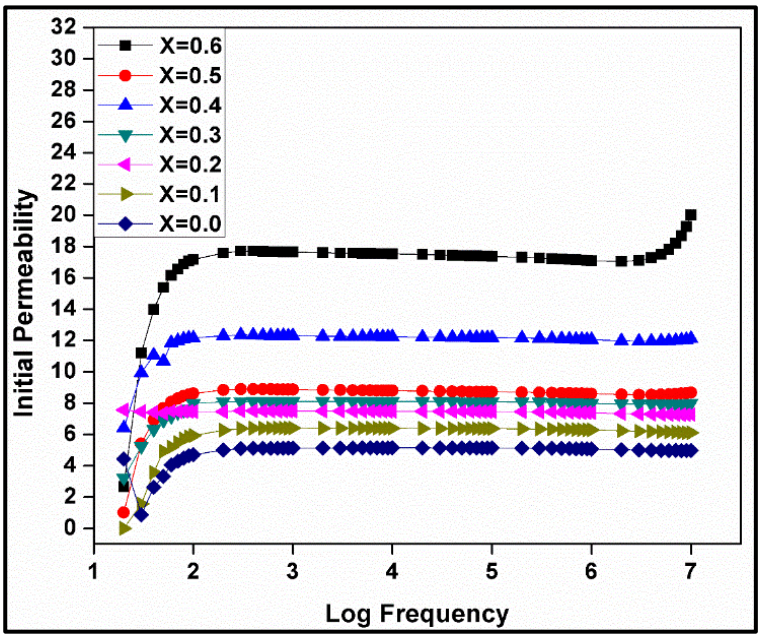


Fig. 3.35a: The plot of Initial permeability vs Log Frequency of 'sintered' $Ni_{0.6-x}Co_{0.4}Zn_xFe_2O_4$ (x=0.0, 0.1, 0.2, 0.3, 0.4, 0.5, 0.6) ferrites

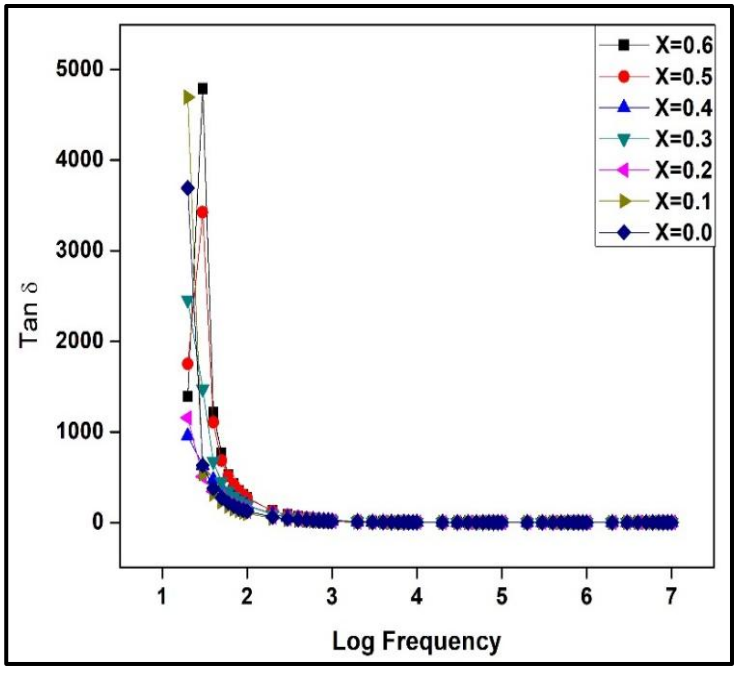


Fig. 3.35 b: The plot of Tan δ vs Log Frequency of 'sintered' $Ni_{0.6-x}Co_{0.4}Zn_xFe_2O_4$ (x=0.0, 0.1, 0.2, 0.3, 0.4, 0.5, 0.6) ferrites

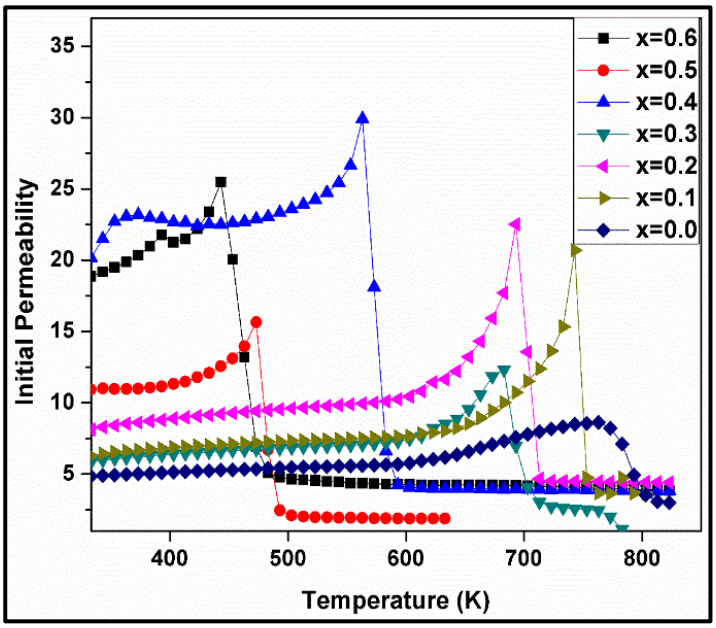


Fig. 3.36a: The plot of Initial Permeability vs Temperature of 'sintered' $Ni_{0.6-x}Co_{0.4}Zn_xFe_2O_4$ (x=0.0, 0.1, 0.2, 0.3, 0.4, 0.5, 0.6) ferrites

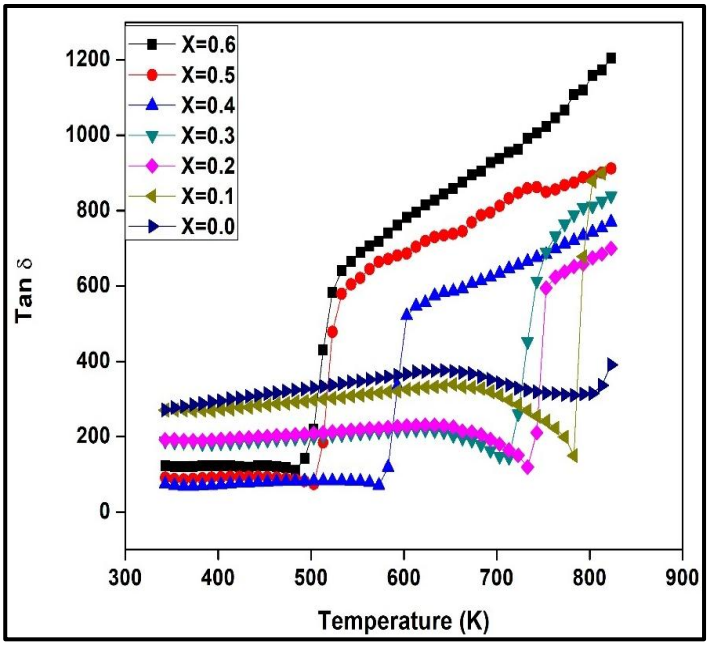


Fig. 3.36b: The plot of Tan δ vs Temperature of 'sintered' $Ni_{0.6-x}Co_{0.4}Zn_xFe_2O_4$ (x=0.0, 0.1, 0.2, 0.3, 0.4, 0.5, 0.6) ferrites

Table 3.16: The Curie Temperature (T_c) of 'sintered' $Ni_{0.6-x}Co_{0.4}Zn_xFe_2O_4$ (x=0.0, 0.1, 0.2, 0.3, 0.4, 0.5, 0.6) ferrites evaluated from AC susceptibility and Initial permeability studies

Composition (x)	**0.0**	**0.1**	**0.2**	**0.3**	**0.4**	**0.5**	**0.6**
Tc (K) AC Susceptibility	812	762	718	684	581	513	452
Tc (K) Initial Permeability	817	760	730	715	594	494	480

3.6 Applications of Ferrites

3.6.1 Gas Sensing applications of 'as prepared' $Ni_{0.6-x}Co_{0.4}Zn_xFe_2O_4$ (x=0.0, 0.1, 0.2, 0.3, 0.4, 0.5, 0.6) ferrites

In this section, the gas sensing studies of 'as prepared' Ni0.6-xCo0.4ZnxFe2O4 (x=0.0, 0.1, 0.2, 0.3, 0.4, 0.5, 0.6) ferrites have been discussed. The 'as prepared' ferrites were utilized to prepare a thick film resistor for the application. The gas sensing set-up unit is discussed in detail in Chapter 2. Under this application, we have studied the response of gases at variable temperatures to select the best-suited temperature for studies such as the percentage response of gases towards different compositions, the response at variable concentrations of test gases, the reproducibility studies, etc. Two types of gases were chosen for the application study: oxidizing and reducing gases (Cl_2, NO_X, NH_3, LPG). Optimization was conducted at RT, 50, 100, 150, and 200°C.

Nowadays, gas sensors have been an essential topic of talk in the town due to their ability to detect gases at minimum ppm levels and stop unwanted disasters. Metal oxide semiconductor sensors have been proven to work at RT and higher temperatures, producing reproducibility, sensitivity, and quick response and recovery [105]. The sensor's activity depends on material properties like surface area, which directly depends on the size of the ferrite, which can be tuned accordingly by the synthesis method used for the synthesis of the materials. Doping the materials with other ions also leads to more significant activity of the compounds [106-108]. The smaller the size, the greater the sensor response size. Particles are poor conductors due to fewer charge carriers, which are activated as they come in contact with the test gases and show greater conductance [109].

3.6.2 Selection of optimum temperature for gas sensing studies

Temperature-dependent sensor response of 'as prepared' $Ni_{0.6-x}Co_{0.4}Zn_xFe_2O_4$ (x=0.0, 0.1, 0.2, 0.3, 0.4, 0.5, 0.6) ferrites is represented in Fig. 3.17. The optimum temperature for each gas was selected by testing the gases at different temperatures. The optimum temperature for NO_X sensing was selected by subjecting the mid-sample x=0.3 to various temperatures. Sensing was performed at five different temperatures, ranging from room temperature to 200°C, with a difference of 50°C between each. Tests were conducted by taking 100 ppm of test gas each

time. Results showed that the best response was observed at room temperature, with a response of 51%. The response percentage decreased as the temperature increased [110], but the recovery time was found to decrease.

The response to recovery time was prolonged at 50°C, with a response of 18%. At 100°C, the response was 10%, while the sample showed very low response at 150 °C and 200°C. Hence, further studies concerning composition were conducted at 100°C. The Cl_2 gas is an obnoxious, known gas among a few naturally occurring toxic gases. Its detection is a concern, so we have also chosen it for our present study. 100 ppm of this gas was taken to detect its response percentage at variable temperatures using the x=0.3 sensor. At RT, a response of 20% was detected, and the response subsequently dropped at 50 °C and 100°C to 5 % and 4%, respectively; at 150 °C and 200°C, the obtained response was relatively low. The recovery at RT was quite faster; recovery time is the time required by the sensor to get its initial state [111]. Since the recovery was quick at RT, the remaining compositions were analysed at RT. Our sensors also detected some other gases, such as NH3 and LPG.

The ferrite sensor showed a response of 31% for NH_3 gas at RT, but the recovery was extended or slow. The response was reduced to 10% at 50°C, and the recovery was delayed, while at 100°C, a quick recovery was seen with a low response of 8 %. The response was negligible at 150 and 200°C; therefore, the temperature selected for sensing the NH_3 gas was 100°C. The commercially used LPG gas was used to study the sensing property of the sensors, and the ferrite sample with composition x=0.3 was used to optimise the temperature. At RT, a very low response of 5% was seen to be observed with an increase in temperature, i.e., at 50°C, the response was 30%, while the highest response obtained was at 100°C which was 67% with quick recovery with further increase in temperature, i.e., at 150°C the response dropped to 18% and finally at 200°C, the response was negligible. Therefore, the gas sensing studies of LPG were conducted at 100°C. Fig. 3.38 represents the excellent sensor's response towards NO_x, NH_3, and Cl_2 at RT, but with prolonged recovery rates.

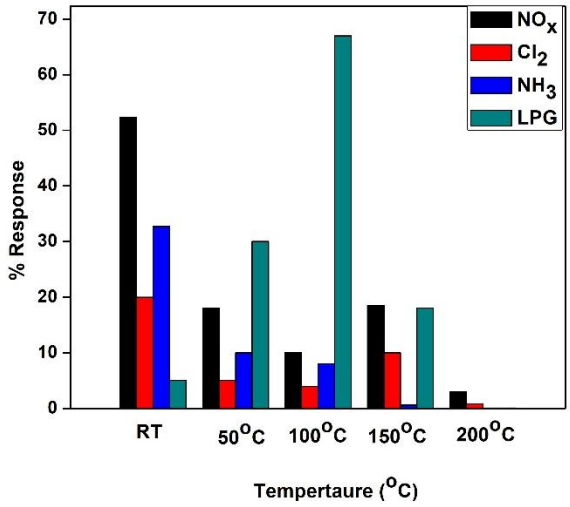


Fig. 3.37: Temperature dependent sensor response of 'as prepared' $Ni_{0.6-x}Co_{0.4}Zn_xFe_2O_4$ (x=0.0, 0.1, 0.2, 0.3, 0.4, 0.5, 0.6) ferrites

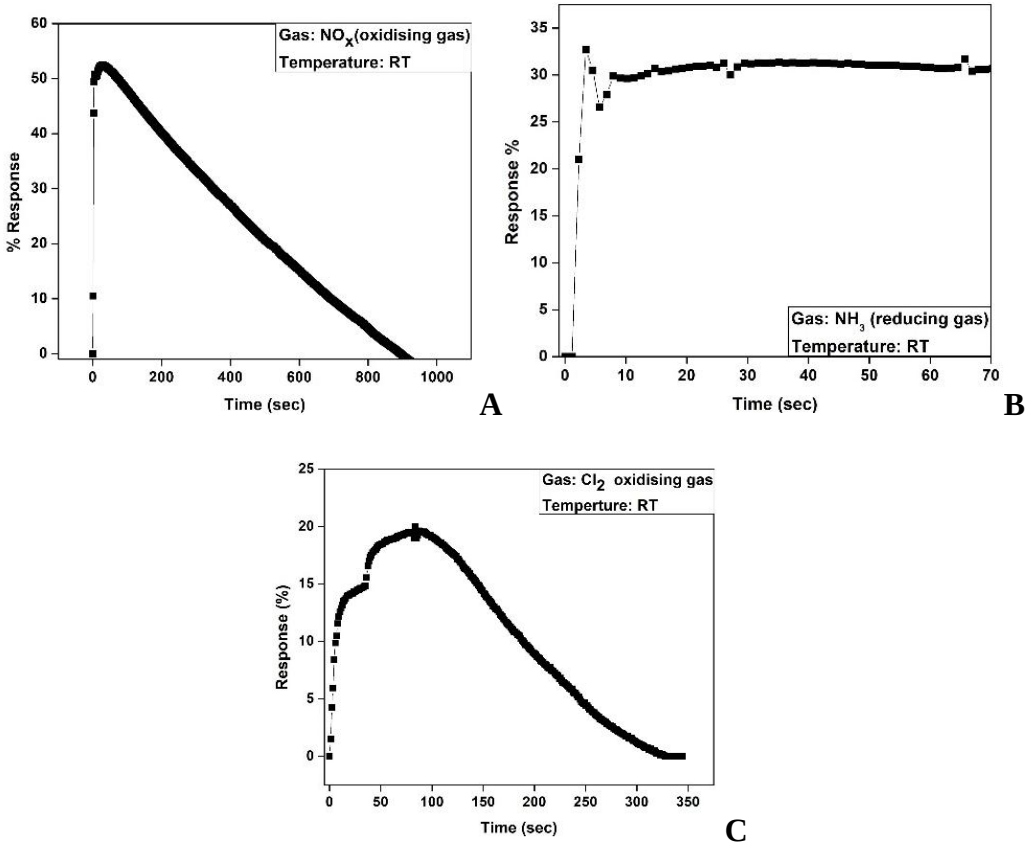


Fig. 3.38: The plot of % response vs time of $Ni_{0.6-x}Co_{0.4}Zn_xFe_2O_4$ (x= 0.3) ferritefor A:NO_x, B:NH_3, and C:Cl_2 at RT.

3.6.3 % Response at variable x concentration

All the compositions sensed the NOx gas using 100 ppm of test gas at 100°C and is represented using a bar graph in Fig. 3.39. It was observed that with an increase in zinc content, the sensor response decreased from x=0.0 to x=0.6, and further, a decrease in response was observed. Though the response percentage was not so profound. The ferrite sample with composition x=0.0 was found to have the highest % response out of all the samples. To further study the variation in concentration of test gas in ppm, Test samples at various ppm levels (20, 50, 75, 100, 150, 200) were injected to study their effect, which resulted in an increase in the % response with the rise in concentration. A reproducibility study for x=0.4 was conducted to check the efficiency of the sensor. The sample showed excellent reliability after three continuous purges.

For the Cl_2 response, room temperature was selected as it gave a quick and higher response for the x=0.3 sample. Fig. 3.40 A represents the % responses for variable compositions, and it is observed from Fig. 3.40 B that sample x=0.5 showcased a good percentage of detection of Cl_2 gas at RT. The percentage response obtained for the same was 63%, while the rest of the composition showed a response below 50%. Further studies on a variation in gas concentration were performed, where it was observed that, unlike the previous case in NO_X, here, as the ppm of gas concentration increased, the response % decreased. This results from saturation of the sensor with an increase in gas content.

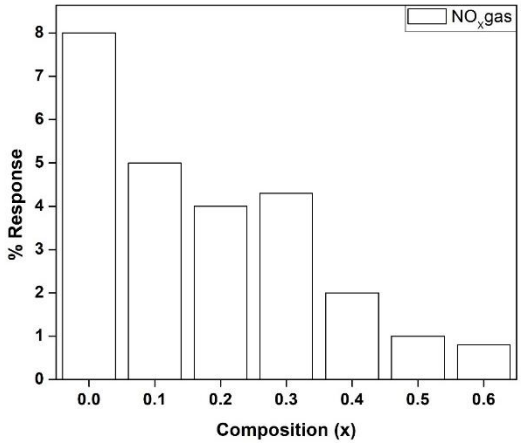
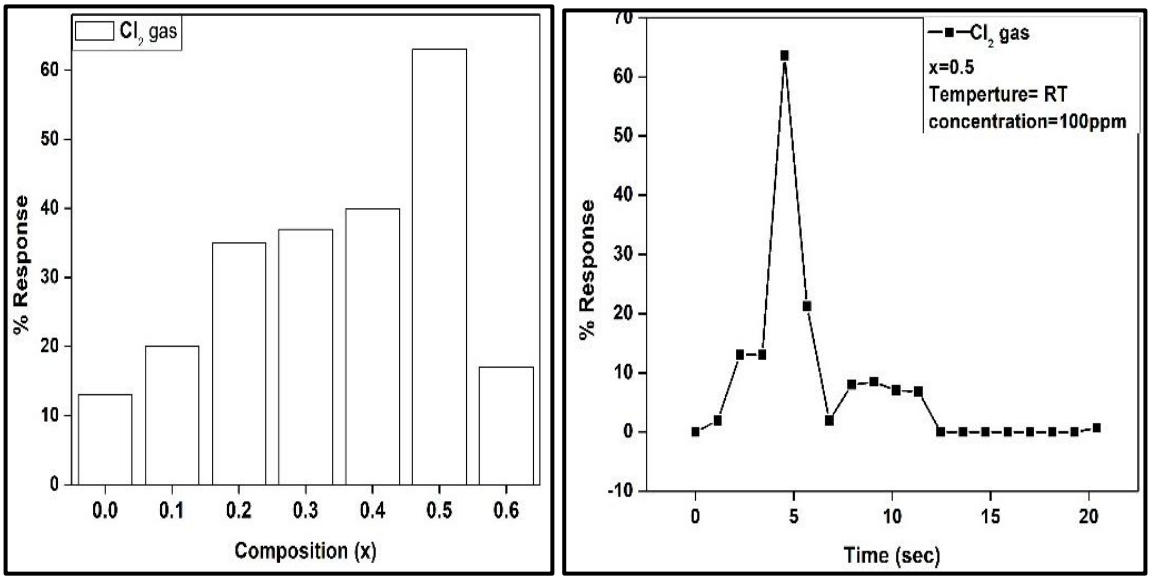


Fig. 3.39: The plot of % Response vs. composition of $Ni_{0.6-x}Co_{0.4}Zn_xFe_2O_4$ (x=0.0, 0.1, 0.2, 0.3, 0.4, 0.5, 0.6) ferrites towards NO_x gas



A **B**

Fig. 3.40 A: The plot of % Response vs. Compositions of 'as prepared' $Ni_{0.6-x}Co_{0.4}Zn_xFe_2O_4$ (x=0.0, 0.1, 0.2, 0.3, 0.4, 0.5, 0.6) ferrites for Cl_2 gas. **B**: The plot of % Response vs. Time of 'as prepared'' $Ni_{0.6-x}Co_{0.4}Zn_xFe_2O_4$ (x = 0.5) ferrites for Cl_2 gas at RT

LPG and NH_3 gases were selected as the test gases for the reducing gas studies. A temperature optimisation study for LPG suggests that 100°C gave the best % response for 100 ppm test gas. At RT temperature, the %response was 5%, and as the temperature increased to 50°C, it showed 30% response; as the temperature went beyond 100°C, the response was found to decrease, i.e., 18% at 150°C, and at 200°C, it was 10%. The selected temperature for the study was 100°C, using which the % response for all the samples in the series was conducted and is depicted in Fig. 3.41 (A-E). As the zinc content in the sample increased, the % response also increased upto x=0.3 and then decreased with higher zinc content. This arises due to the particle sizes of the samples. Various ppm of the test gases were purged into the sample, from which we understood that with an increase in the gas volume, the % response increased, but with further increase, saturation was established, due to which the % response was reduced. Reproducibility studies were also studied for sample with composition x=0.6, and we could get the reproducibility maximum times.

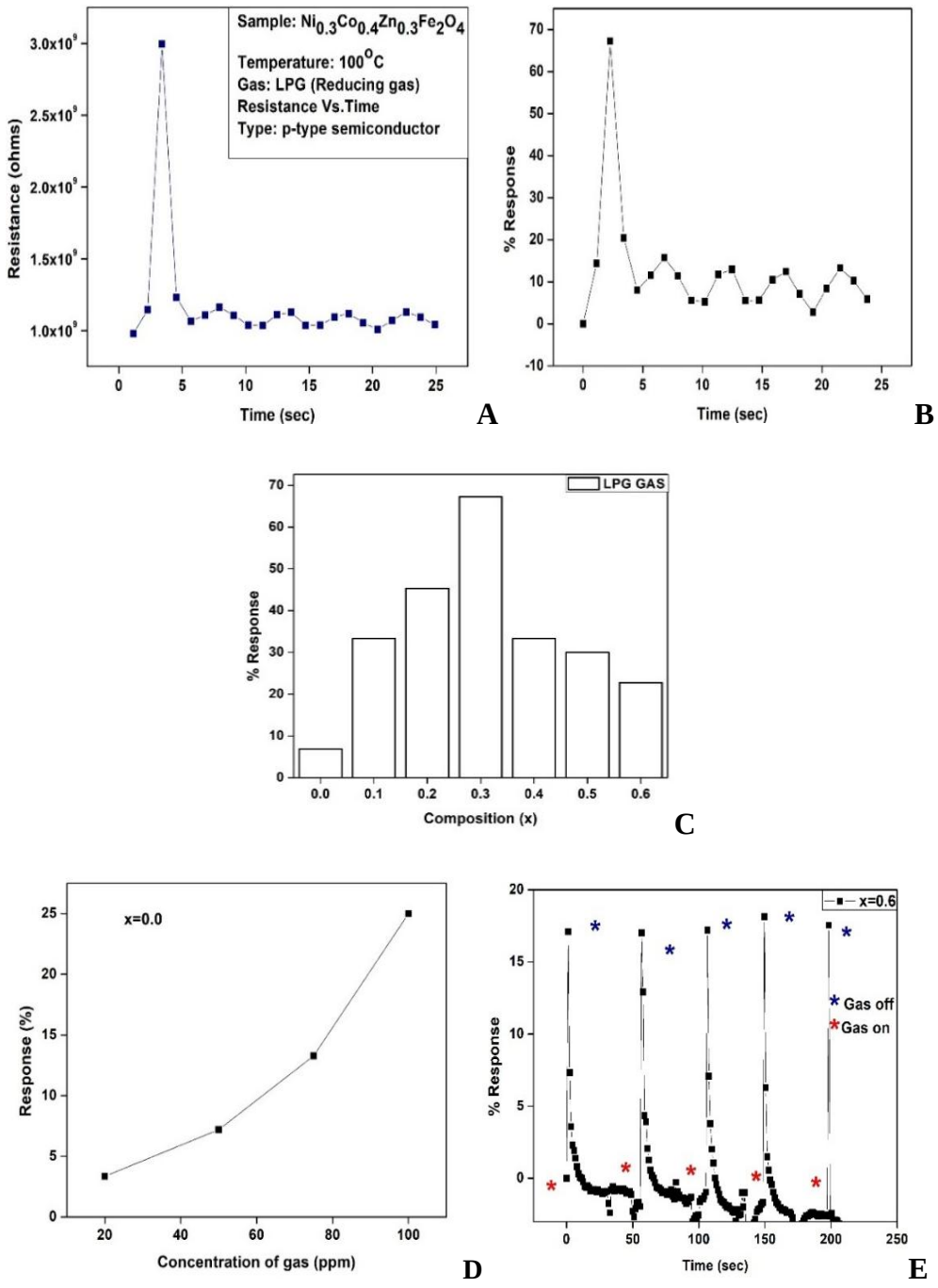


Fig. 3.41: A: The plot of resistance vs. Time for sample x=0.3, **B:** Plot of % Response vs. Time for sample x=0.3, **C:** % Response vs. Composition for LPG, **D:** % Response vs. Increasing concentration in gas, x=0.0, **E:** Plot of % Response vs. Time to test the reproducibility studies of sample x=0.6.

Fig. 3.42 showcases % response vs. composition (x) for NH_3 gas at 100°C using 100 ppm of test gas; during the optimization study of temperature, it was noted that the highest % response was obtained for RT, but the recovery rate was longer; with further increase in temperature, the response decreased at 50 °C and also had a more prolonged recovery rate while at the higher temperatures, the recovery was quick therefore 100 °C was chosen as the temperature to study the samples. Unlike LPG, the reducing gases couldn't be sensed more than 50% by the 'as prepared' ferrite sample.

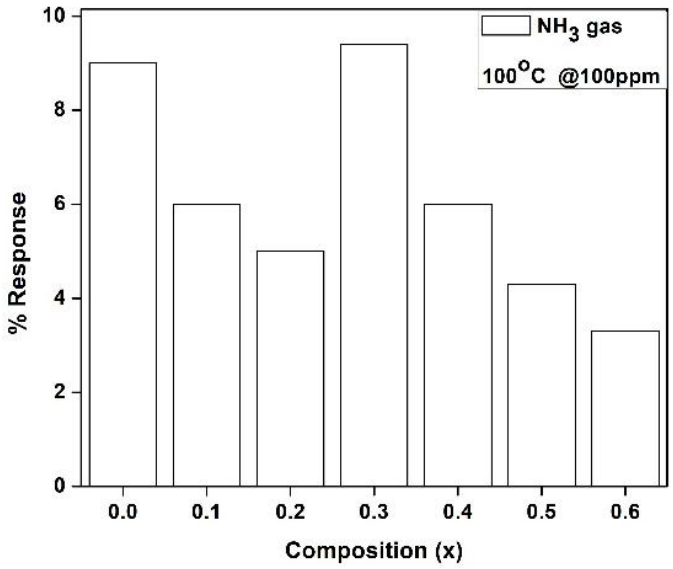


Fig. 3.42: The plot of % response vs. composition (x) of 'as prepared' $Ni_{0.6-x}Co_{0.4}Zn_xFe_2O_4$ (x=0.0, 0.1, 0.2, 0.3, 0.4, 0.5, 0.6) ferrites for NH_3 gas at 100 °C using 100 ppm of test gas.

3.6.4 Gas Sensing Mechanism

Metal oxide gas sensors are temperature-dependent and can be categorized into two categories: the first category involves the sensors showing surface conductance and working in the low to moderate temperature range. In contrast, the second category of materials is the one that follows the bulk effect and work above 700 °C [112]. Sensing is a surface adsorption-desorption phenomenon [113]. The interplay of gas molecules in contact with the sensor causes changes in the materials, thereby increasing or decreasing the resistance [114]. The variation in resistance or sensitivity of sensing is greatly affected by the grain size, surface area, oxygen adsorption, and lattice defects. Apart from this, the type of semiconductor (n-type or p-type), composition, type of gas (oxidizing or reducing), and gas concentration are also responsible for the response

[115-116]. Oxygen adsorption on the surface of the material and its interaction with the gas molecules lead to changes in the resistance, which is an essential step in the process of gas sensing [117].

When the sensor material is exposed to air, the oxygen molecules get adsorbed on its surface, forming ionized oxygen molecules. The chemisorbed oxygen molecules are formed by trapping electrons from the conduction band of the ferrite material which is represented as follows:

$$O_{2\,(gas)} \rightarrow O_{2\,(ads)} \qquad (1)$$

$$O_{2\,(ads)} + e^- \rightarrow O_{2\,(ads)}^- \qquad (\sim 25\text{-}150^oC) \qquad (2)$$

$$O_{2\,(ads)}^- + e^- \rightarrow 2O_{(ads)}^- \qquad (> 150\text{-}300\ ^oC) \qquad (3)$$

$$O_{(ads))}^- + e^- \rightarrow O_{(ads)}^{2-} \qquad (> 300^oc) \qquad (4)$$

The chemisorbed oxygen (Eq. 2-4) will behave like surface receptors, and increases surface resistivity.

3.6.5 Working Principle of Metal Oxide Sensors

The semiconductor sensors are quite sensitive to various gases in the air. The alteration in conductivity or resistance when adsorbed on the surface is essentially because of two main factors:electron trapping and band bending. When sensor material is exposed to air, O_2 is adsorbed on the surface and electrons from the conduction band are trapped at the sensor's surface, forming ions. The negative charge is thus trapped in the O_2 species, which causes upward bending where the depleted layer is smaller than the size of the grains.

Consequently, when exposed to reducing gases, the electrons in the O_2 species are freed and the bent band is reversed, increasing the conductivity or decreasing resistivity [118].

$$R + Os^- \rightarrow RO + e^-$$

When the gas sensor is exposed to reducing gas, it gets oxidized by O^-, and the electron captured by the oxygen species is released back to the bulk material. The O^- species reduces along with the thickness of space charge layer. This in turn reduces the Schottky barrier, making electrons to conduct through the grains. When exposed to reducing gases the barrier becomes smaller easing the conduction of electrons. Similarly, when oxidizing gases are sensed the Schottky

barrier increases making the ionic charges higher than oxygen reducing its resistivity. When material are p-type semiconductors, when exposed to reducing gases, the resistance increases and for oxidizing gases, it decreases while for n-type it is vice-versa.

3.7 Electrochemical Application

3.7.1 Electrochemical studies of $Ni_{0.6-x}Co_{0.4}Zn_xFe_2O_4$ (x=0.0, 0.1, 0.2, 0.3, 0.4, 0.5,0.6) ferrites

The study of electrochemical properties of ferrite for their application in supercapacitors has been broadly examined for the increasing demand for electronic and electric storage devices. Ferrite materials have high power density, longer life, and durability, rendering them appropriate for applications [119-121]. Key factors such as size, surface area, composition, calcination temperature, and preparation method are essential in deciding on a good supercapacitor [122]. Supercapacitors may be grouped into two types based on the charge storage mechanism: 1. Electric double-layer supercapacitor (EDLC), and 2. Pseudocapacitors. In EDLC, the capacitance results from charge separation at the interface between the electrode and electrolyte. In contrast, in the case of pseudocapacitors, the faradaic reaction occurring at the interface leads to pseudocapacitance. The materials used for the capacitance study include carbon black, conducting polymer, and active metal oxide [123,124].

Cyclic voltammetry study helped obtain information on sample oxidation and reduction. The energy storage capability of 'as prepared' samples x=0-0.6 was determined by subjecting the samples to cyclic voltammetry analysis, which was done using a three-electrode system in the potential range of 0- 0.5V in 3M KOH electrolyte. Further details are provided in Chapter 2. The CV plots of the calcined $Ni_{0.6-x}Co_{0.4}Zn_xFe_2O_4$ (x=0.0, 0.1, 0.2, 0.3, 0.4, 0.5,0.6) ferrites are illustrated in Fig. 3.44, and the corresponding specific capacitance values are summarized in Table 3.17. The Variation in specific capacitance is also studied at variable scan rates (3, 5, 10, 20, 30, 50, and 80 mV). Apart from the electrode material, charge storage properties depend on the hydrated ionic radius, conductivity, and electrolyte ion mobility. The electrolyte ionic radius is an essential factor in the ion transfer process. [125] K^+ ions possess suitable ionic radii,

mobility, and conductivity. Also, OH^- has small ionic radii and helps the ion transfer process; thus, KOH was selected as the electrolyte solution.

The plots show a well-developed cyclic voltammogram; the oxidation and reduction peaks appeared in all the samples, indicating stable and reversible redox reactions, hence confirming the pseudocapacitive behavior of the samples [126]. These findings imply that the ferrite samples show a Faradaic-type mechanism [127]. The following response can express the reversible redox reaction occurring in the electrochemical process [128]:

$$MFe_2O_4 + H_2O + OH^- \leftrightarrow MOOH + 2FeOOH + e^-$$

$$MO + OH \leftrightarrow MOOH + e^-$$

Fig. 3.43 represents the plot of specific capacitance versus scan rate of 'as prepared' $Ni_{0.6-x}Co_{0.4}Zn_xFe_2O_4$ (x=0.0, 0.1, 0.2, 0.3, 0.4, 0.5,0.6) ferrites and Fig. 3.44 depicts voltamograms of 'as prepared' $Ni_{0.6-x}Co_{0.4}Zn_xFe_2O_4$ (x=0.0, 0.1, 0.2, 0.3, 0.4, 0.5,0.6) ferrites. the specific capacitance calculated from the plots are tabulated in Table 3.13.

It is seen from Fig. 3.44 that as the scan rate increases, the surface area also increases. From the plotted voltammogram, one can note that as the scan rate increases, the peaks shift; the oxidation peak shift towards the anodic potential, while the reduction peak shifts towards the cathodic potential. The electrochemical polarisation may be responsible for the change in peak position observed at different scan rates [129]. Lower scan rates showed higher capacitance values, and similar observations were made in many ferrites [130-131]. Under the condition of reduced scan rate, the OH^- ions are effectively utilized at the inner and outer surface due to sufficient time available to access the surface area of the electrode. While during higher scan rates, the time available to the electrolyte to diffuse and access the active centers present at the electrode interface is less, here only the outer active sites participate in the Faradaic redox reaction. In contrast, the inner active sites are inaccessible [132]. More considerable ohmic resistance at a high scan rate could also add up to a lower capacitance value at a higher scan rate [133].

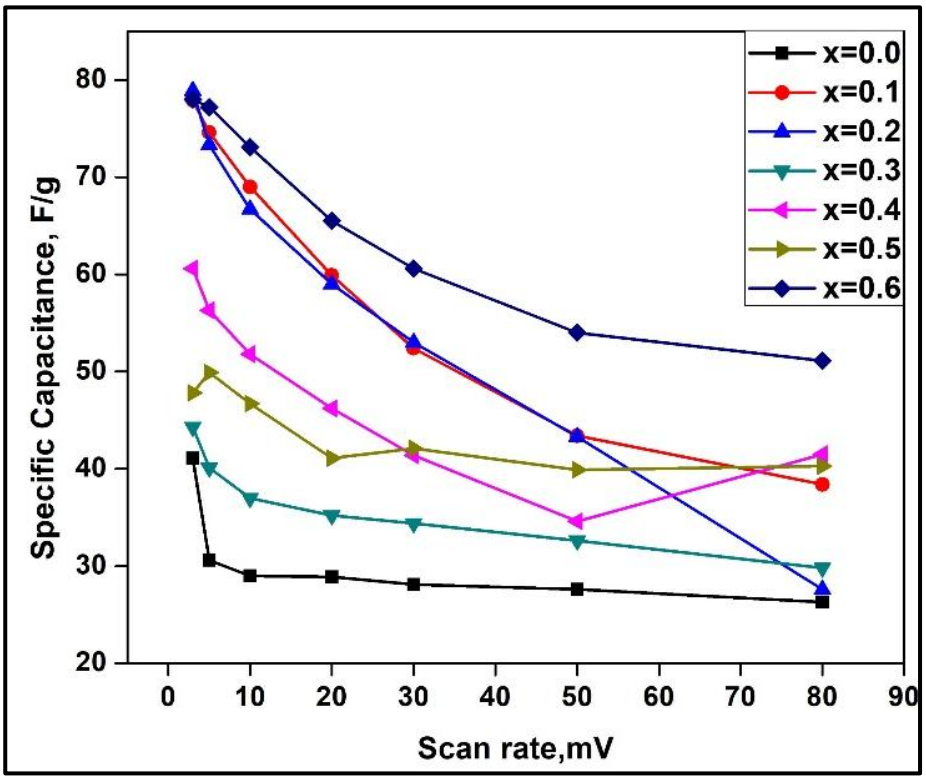


Fig. 3.43: The plot of specific capacitance versus scan rate of 'as prepared' $Ni_{0.6-x}Co_{0.4}Zn_xFe_2O_4$ (x=0.0, 0.1, 0.2, 0.3, 0.4, 0.5,0.6) ferrites

Fig. 3.44b displays the galvanic charge/ discharge plots of 'as prepared' $Ni_{0.6-x}Co_{0.4}Zn_xFe_2O_4$ (x=0.0, 0.1, 0.2, 0.3, 0.4, 0.5, 0.6) ferrites at a current density of 1A g^{-1} and The Nyquist plot of $Ni_{0.6-x}Co_{0.4}Zn_xFe_2O_4$ (x=0.0, 0.1, 0.2, 0.3, 0.4, 0.5, 0.6) was obtained from electrochemical impedance spectroscopic studies (EIS). Fig. 3.44c shows the plot, and all the samples show a similar pattern. the data on capacitance obtained from galvanic charge-discharge analysis are displayed in Table 3.17 along with the solution resistance value from the Nyquist plot. The solution resistance may be due to the intrinsic resistance of the active matter, ionic resistance of the solution, interfacial resistance, or contact resistance, and is quite low in our case, indicating good potential of the material in supercapacitor activity.

Table 3.17: Specific capacitance of 'as prepared' $Ni_{0.6-x}Co_{0.4}Zn_xFe_2O_4$ (x=0.0, 0.1, 0.2, 0.3, 0.4, 0.5, 0.6) ferrites at variable scan rate and current density of 1A/g, and R_s

Scan rate (mV/s)	**Csp (F/g)**						
	0.0	0.1	0.2	0.3	0.4	0.5	0.6
3	41.1	77.9	78.9	44.3	60.6	47.8	78.0
5	30.6	74.6	73.3	40.1	56.3	49.9	77.2
10	29.0	69.0	66.7	37.0	51.8	46.7	73.1
20	28.9	59.9	59.0	35.2	46.2	41.1	65.5
30	28.1	52.4	53.0	34.4	41.4	42.1	60.6
50	27.6	43.4	43.3	32.6	34.6	39.9	54.0
80	26.3	38.4	27.6	29.8	41.5	40.3	51.1
Specific capacitance@ Current density: 1A/g	61	42	20	22	38	20	23
R_s	1.00538	0.69664	0.929	0.87695	0.8096	0.73279	0.85726

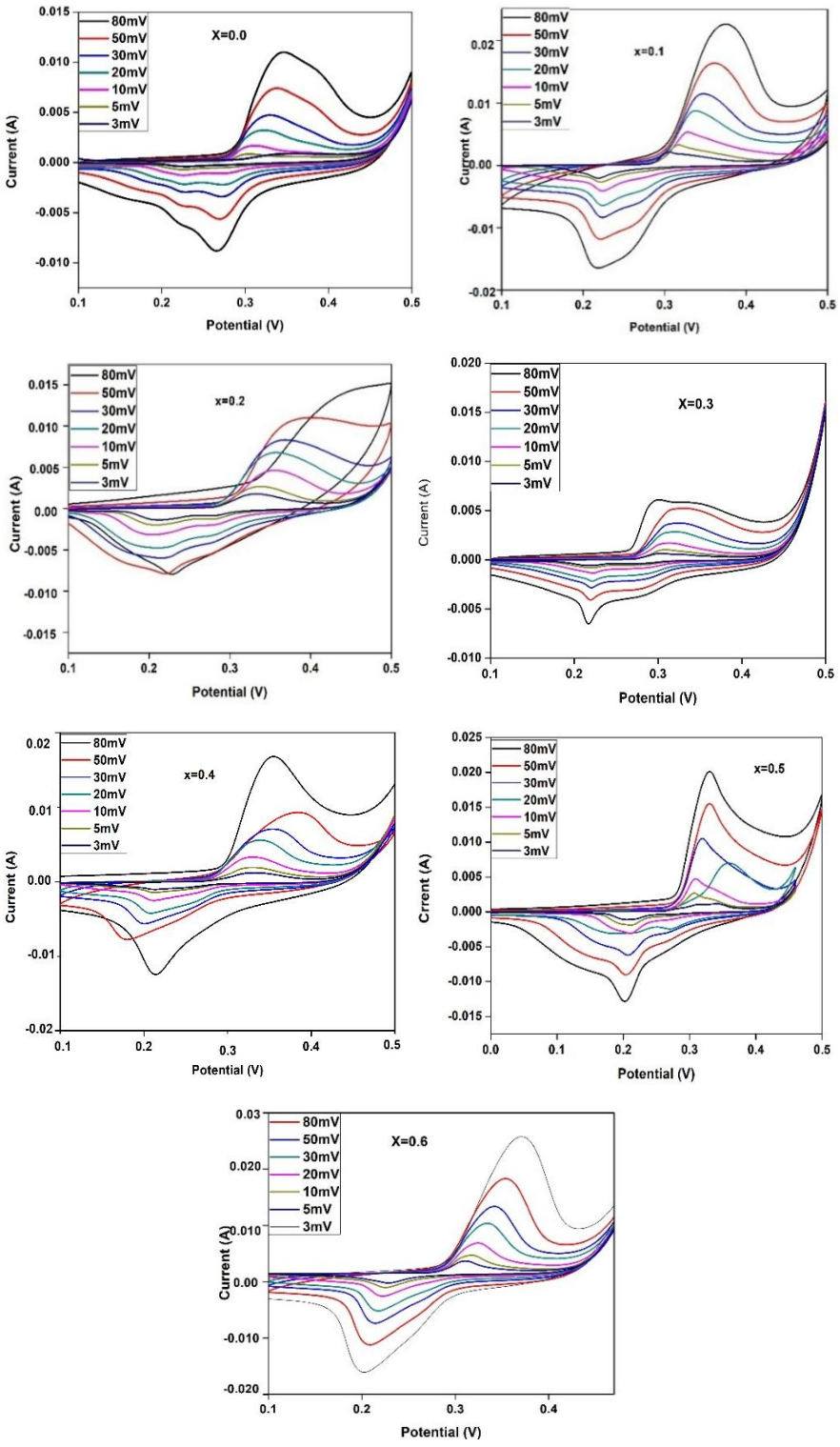


Fig. 3.44a: CV Plots of 'as prepared' $Ni_{0.6-x}Co_{0.4}Zn_xFe_2O_4$ (x=0.0, 0.1, 0.2, 0.3, 0.4, 0.5,0.6) ferrites

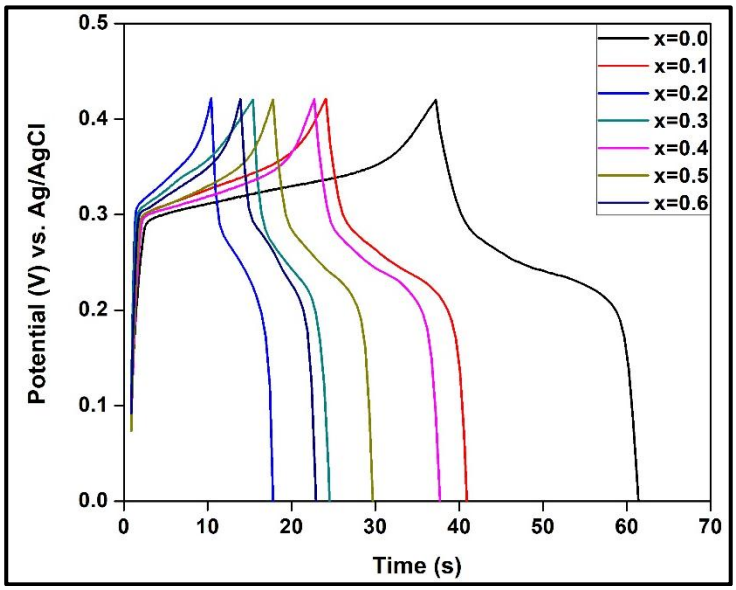


Fig. 3.44 b: The galvanic charge/discharge plots of 'as prepared' $Ni_{0.6-x}Co_{0.4}Zn_xFe_2O_4$ (x=0.0, 0.1, 0.2, 0.3, 0.4, 0.5, 0.6) ferrites

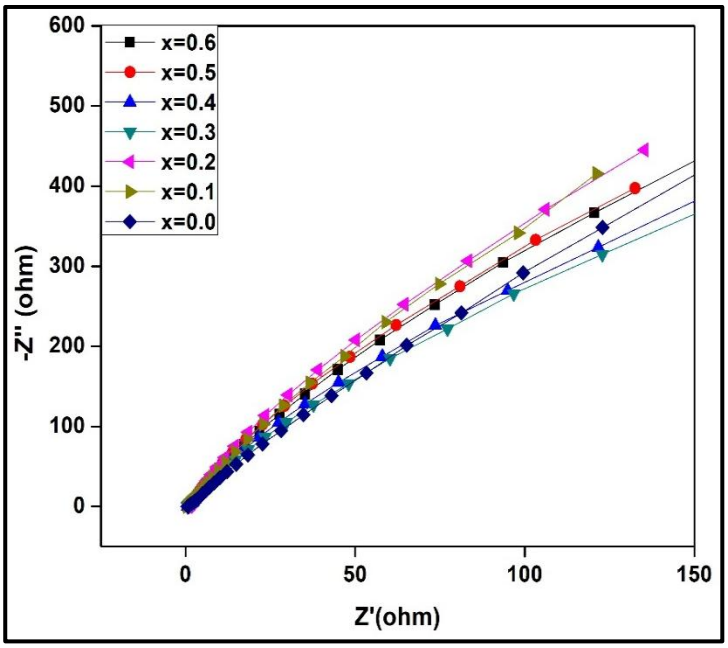


Fig. 3.44 c: The Nyquist plot of 'as prepared' $Ni_{0.6-x}Co_{0.4}Zn_xFe_2O_4$ (x=0.0, 0.1, 0.2, 0.3, 0.4, 0.5, 0.6) ferrites

3.8 Antibacterial Application

Owing to the escalating resistance of pathogens to available drugs, the role of antibacterial agents has become increasingly vital. The antibacterial study of all the $Ni_{0.6-x}Co_{0.4}Zn_xFe_2O_4$ (x=0.0, 0.1, 0.2, 0.3, 0.4, 0.5,0.6) ferrites was done to study the potential of the sample as a potent antibacterial agent. *Staphylococcus aureus,* a gram-positive bacterium, was used to investigate the sample's antibacterial activity. A comprehensive description of the procedure is provided in Chapter 2. Fig. 3.45 represents a graph showing the effect of two different concentrations of Ni0.6-xCo0.4ZnxFe2O4 (x=0.0, 0.1, 0.2, 0.3, 0.4, 0.5,0.6) ferrites on the percentage survival of *Staphylococcus aureus*. Fig. 3.46 and 3.47 show the 500 and 1000 µg/mL survival percentages for all the 'as prepared' samples with the best dosage loading for better antibacterial activity by varying the dosage mass to the solvent. The samples show promising results for the ferrites against this human pathogen. The survival percentages of the samples were assessed about the control, which is considered 100%. At 500 µg/mL, sample x=0.0 showed the best results, with a survival percentage of 10%, followed by x=0.4 with a 30% survival rate. Significant findings were obtained when studies were conducted at 1000 µg/mL. Sample x=0.4 showed excellent results with no bacterium survival at all, and sample x=0.0 showed a 3% survival percentage. Antibacterial results of the compounds were in the order: x=0.0>0.4>0.6>0.3>0.1>0.2>0.5 for 500µg/mL, whereas for 1000µg/mL the order was x=0.4>0.0>0.6>0.3>0.2>0.1>0.5. From the data, it is noted that as the ferrite dosage increases, the antibacterial activity increases; therefore, 1000µg/mL gave impressive results for the samples under the study against the gram-positive pathogen. S. aureus is known to cause wound infection, causing complications [134]. The gram-positive bacteria contain a thick layer of peptidoglycan, which is 20-80nm [135], with no outer membrane like in gram-negative bacteria, which protects it from toxins, chemicals, antibiotics, and degrading enzymes, and therefore are resistant and cause the spread of diseases. The ferrite nanoparticle produces pits and gaps, causing the fragmentation of the bacteria's cell membrane [136]. Various reports give hypotheses on the antibacterial activity of the material on pathogens: i) generation of reactive oxygen species, ii) release of all metal ions into the bacteria alters the protein structure by forming bonds with the sulfhydryl groups, and iii) binding of nanomaterial on the bacterial surface, in turn, destroying the bacterial cell [137,138]. The positively charged metal cations get attracted to the negatively charged surface of the bacteria, thus accumulating at the surface

and entering the cells by producing pores in the wall or the membrane and leaking out the intracellular content of the bacteria, resulting in the breaking of the cell membrane [139]. Lima et al. [140] showed that size plays a significant role in influencing the cytotoxicity and calcination temperature. The smaller the calcination temperature, the smaller the size, and the greater the cytotoxicity. In the present study, sample with composition x=0.4 showed the best results, with the smallest size compared to all the samples.

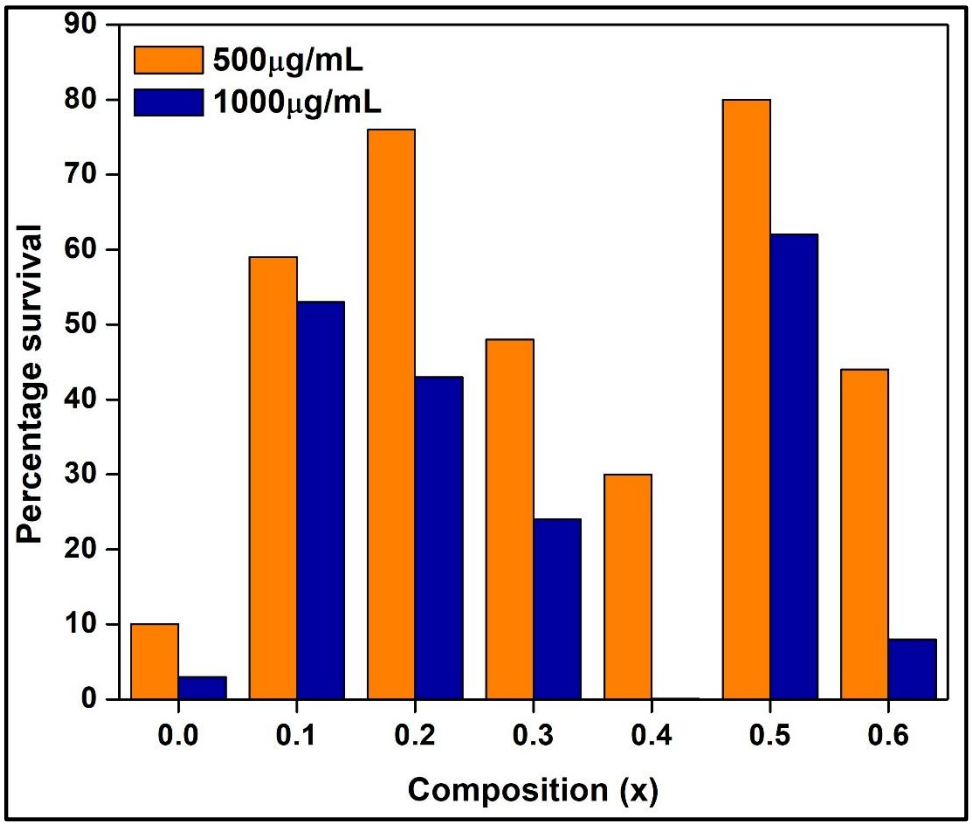


Fig. 3.45: Graph showing the effect of two different concentrations of $Ni_{0.6-x}Co_{0.4}Zn_xFe_2O_4$ (x=0.0, 0.1, 0.2, 0.3, 0.4, 0.5,0.6) ferrites on percentage survival of *Staphylococcus aureus.*

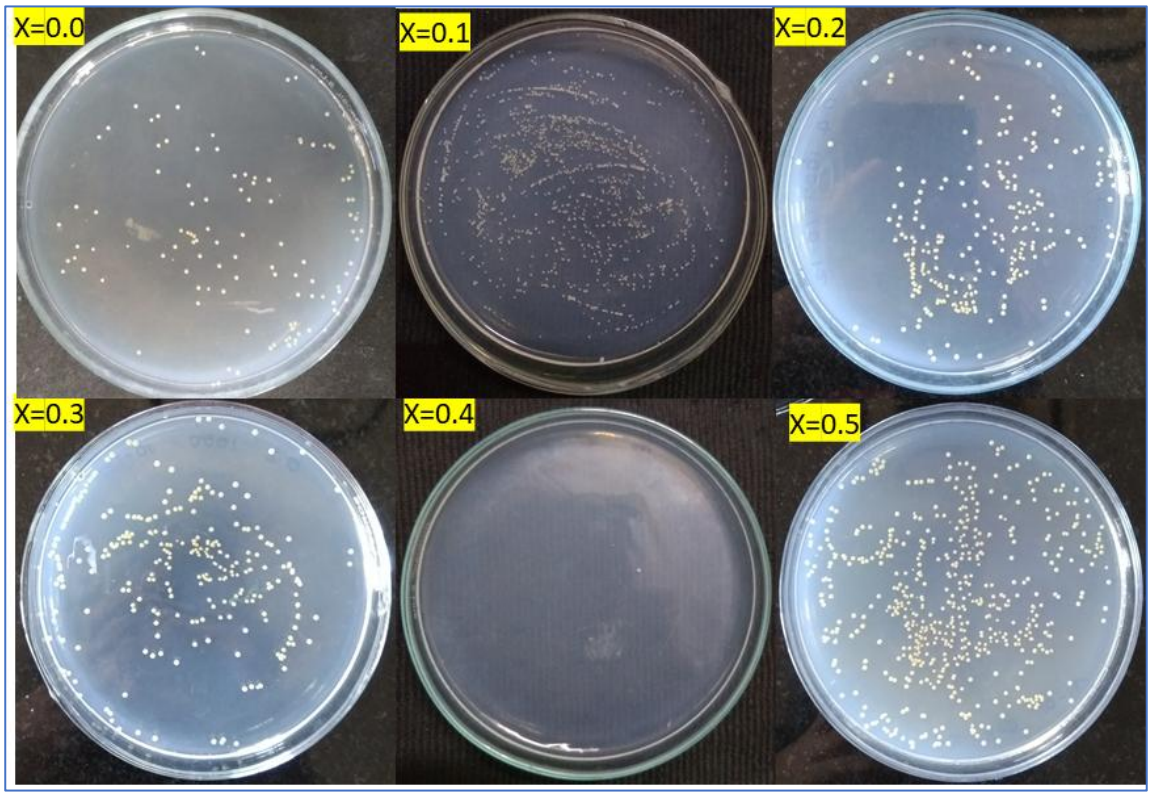


Fig. 3.46: Antibacterial activity of $Ni_{0.6-x}Co_{0.4}Zn_xFe_2O_4$ (x=0.0, 0.1, 0.2, 0.3, 0.4, 0.5,0.6) ferrites and control at (Conc: 1000 µg/mL) on percentage survival of *Staphylococcus aureus.*

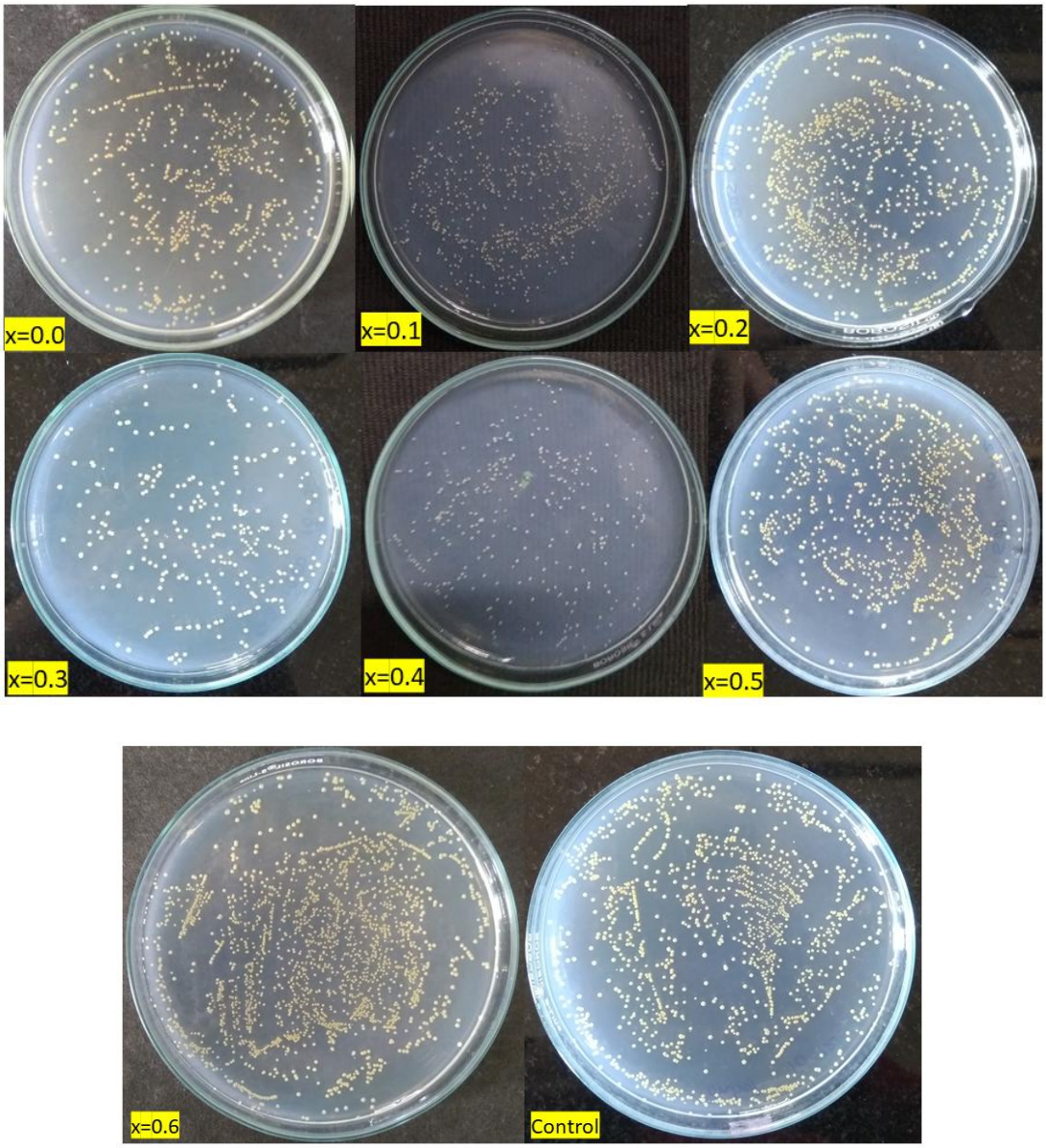


Fig. 3.47: Antibacterial activity of $Ni_{0.6-x}Co_{0.4}Zn_xFe_2O_4$ (x=0.0, 0.1, 0.2, 0.3, 0.4, 0.5,0.6) ferrites and control (Conc: 500 µg/mL) on percentage survival of *Staphylococcus aureus.*

3.9 Summary

The precursor-combustion methodology was used to synthesize $Ni_{0.6-x}Co_{0.4}Zn_xFe_2O_4$ (x =0.0, 0.1, 0.2, 0.3, 0.4, 0.5, 0.6) ferrites. The precursor $Ni_{0.6-x}Co_{0.4}Zn_xFe_2(C_4H_2O_4)_3.6N_2H_4$ (x=0.0,0.1,0.2,0.3,0.4,0.5,0.6) obtained was hexahydrazine fumarate ligand bound to metal ions. The synthesized yellow-coloured precursor complex was characterized to determine its stoichiometric proportions. The C, H, N analysis, hydrazine estimation, TG-DTG-DTA, IR, total mass loss, and isothermal mass loss were done, and the precursor was found to have exact stoichiometry. Soon, the precursor was ignited to obtain the as-burnt product, which was calcinated at 500 °C for five hours. The 'as-prepared' ferrite was pre-sintered at 800 °C for five hours before sintering it with a final temperature of 1000 °C for 10h, which was selected by optimizing multiple times the time of sintering and temperature of sintering combinations. The 'as-prepared' and 'sintered' ferrites were then characterized by multiple techniques for phase purity and morphology, and their solid-state properties were also studied. The X-ray diffraction studies revealed a single phase in the 'as prepared' and 'sintered' ferrite samples. The lattice constant, crystallite size, and porosities were determined using the XRD data. The sharp, intense peaks were seen in the case of 'sintered' ferrites, while the peaks were broad and shorter in case of 'as-prepared' ferrites. The SEM morphological studies showed agglomerated images due to magnetic interactions in 'as prepared' and 'sintered' ferrites. The EDS studies carried out alongside SEM showed the elements present in the samples in the proper proportions. The TEM images showed the shape of the particles, which were cubic in nature. The SAED patterns showed a bright concentric circle, indicating the crystalline nature of samples. The BET technique was employed to determine the surface area, which showed the highest surface area of 39 m^2/g for sample x = 0.5. The Raman analysis showed the five Raman active modes. The A_{1g} (1) peak diminished as the zinc content increased and became visible in the 'sintered' ferrite samples. The XPS spectra showed a full scan spectrum wherein all the elements were present per the composition. The deconvoluted spectra confirmed the exact valence state of the metal ions.

A comparative study of 'as prepared' and 'sintered' ferrites was done based on their solid-state properties. The electrical resistivity, magnetic properties (using VSM and AC susceptibility), RT and high-temperature dielectric studies, and initial permeability were studied. The resistivity

studies confirmed the semiconducting behaviour of the samples as the resistivity decreased with an elevation in temperature; as the zinc content increased, the resistivity showed a decrease. Dielectric studies carried out at RT showed a usual trend for dielectric constant and dielectric loss and higher temperature studies in both 'as prepared' and 'sintered' samples. The dielectric and resistivity studies show an inverse trend, which can be seen clearly for sample x = 0.1. The initial permeability studies of 'sintered' toroids showed promising results, and the T_C was estimated for the samples, which were in relatively good accordance with results obtained from AC susceptibility. The magnetic study conducted using the VSM instrument deduced many parameters. The magnetization vs. magnetic field performance was found out via hysteresis loop; it was revealed that the sample material had a soft ferrimagnetic nature in 'as prepared' and sintered ferrites. The magnetization increased with zinc content, followed by a decrease. Similar results were obtained for studies at 60K but with a broader hysteresis loop the FC and ZFC performance of 'as prepared' and 'sintered' samples at 250, 500, and 1000Oe. The blocking temperature for the same was also recorded. It was observed that T_B lowered with a rise in the field under study. The AC susceptibility technique estimated the Curie temperature for both 'as prepared' and 'sintered' ferrite. The 'as prepared' ferrite had a higher Tc than the sintered ferrite.

The various applications of the 'as prepared' ferrite were performed to see its performance in different fields. The 'as prepared' $Ni_{0.6-x}Co_{0.4}Zn_xFe_2O_4$ (x=0.0, 0.1, 0.2, 0.3, 0.4, 0.5,0.6) ferrites was subjected to gas sensing applications. Two oxidizing and two reducing gases were used as the test gas to study all the samples. The optimization to select the appropriate temperature was conducted singly for each gas. The variable temperatures selected for optimization were RT, 50, 100,150, and 200 °C. The temperature chosen for the study of NOx was 100 °C, although at RT the response% was relatively high, but recovery was slow. The NOx gas gave a low response %. The temperature to study Cl_2 was room temperature. The sample x=0.5 showed the best results with a response% of 63%. 100 °C was chosen as the temperature for the study of all the samples for LPG gas, and sample x=0.3 showed excellent results with 67% response. A reproducibility study of the sample was also conducted to ensure its reproducibility. With the increase in concentration, the response % also increased. NH_3 gas was studied at 100°C, the response% was low and below 50%. The electrochemical performance of the samples to study their capacitance properties was studied using cyclic voltammetry using a three-electrode

system. The sample was drop-cast on Ni foam, which worked as the working electrode. The electrolyte used was a 3M KOH solution. The study was carried out at variable scan rates. It was observed that as the scan rate decreased, the specific capacitance increased. Sample x=0.2 showed the best results with 78.9 F/g specific capacitance at a three-mV scan rate.

To test the material for its potential as an anti-bacterial agent, the gram-positive pathogen *S. aureus* was selected. Two different concentrations of dosages (500µg/mL and 1000µg/mL) were studied. 1000µg/mL showed better results than 500µg/mL, with sample x=0.4 and x=0.0 showing promising results.

References

1. Y. Wang, L. Li, Y. Zhang, X. Chen, S. Fang, G. Li, J. Phys. Chem. C, 121 (2017) 19467.
2. J. Ding, P.G. McCormick, R. Streey, Solid State Comm., 95 (1995) 31.
3. M. Mozaffari, J. Amighian, E. Darsheshdar, J. Magn. Magn. Mater., 350 (2014) 19.
4. V. Sepelak, I. Bergmann, A. Feldhoff, P. Heitjans, F. Krmeich, D. Menzil, F. J. Litterst, S. J. Campbell, K. D. Becker, J. Phys. Chem. C, 111 (2007) 5026.
5. K. C. Patil, D. Gajapathy, V.R. Vernekar, Mat. Res. Bull., 17 (1982) 29.
6. P. P. Sarangi, B. D. Naik, N. N. Ghosh, J. Am. Ceram. Soc., 91 (2008) 4145.
7. N. B. Velhal, N.D. Patil, A. R. Shelke, N. G. Deshpande, V. R. Puri, AIP Advances, 5 (2015) 097166.
8. A. Lassoued, J. F. Li, Solid State Sci., 104 (2020) 106199.
9. T. Premkumar, S. Govindarajan, Thermochim. Acta, 386 (2002) 35.
10. B. N. Sivasankar, S. Govindarajan, Synth. React. Inorg. Met.Org. Chem., 24 (1994) 1573.
11. L. Sacconi, A. Sabatini, J. Inor. Nucl. Chem., 25 (1963) 1389.
12. U. B. Gawas, V.M.S. Verenkar, Thermochim. Acta., 556 (2013) 41.
13. L.R. Gonsalves. V.M.S. Verenkar Therm. Anal. Calorim., 96(2009) 53.
14. M. Shakir, Z. Nasir, M. S. Khan, Lutfullah, M. F. Alam. H. Younus, S. I. Al-Resayes, Inter. J. Bio. Macromol., 72 (2015) 1196.
15. T. J. Shinde, A.B. Gadkari, P.N. Vasambekar, Mater. Chem. Phys., 111 (2008) 87.
16. S. B. Khan, S. Irfan, S-L. Lee, Nanomaterials, 9 (2019) 1024.
17. D. A. Vinnik, D. P. Sherstyuk, V. E. Zhivulin, S. A. Gudkova, D. A. Pankratov, N. S. Perov, Y. A. Alekhina, E. D. Shipkova, S.V. Trukhanov, K.A. Astapovich, T. I. Zubar, A.V. Trukhanov, J. Magn. Magn. Mater., 605 (2024) 172344.
18. X. Zhao, A. Sun, W. Zhang, L. Yu, Z. Zuo, N. Suo, X. Pan, Y. Han, J. Mater. Sci.: Mater. Electron., 31 (2020) 526.
19. P. Monisha, P. Priyadharshini, S. S. Gomathi, M. Mahendran, K. Pushpanathan, Appl. Phys. A, 125 (2019) 736.
20. P. Kashid, S.N. Mathad, Mahadev R. Shedam, A. Somya, A. Ansari, M. Hashem, M. M. Alsarani, O. Alageel, Ain Shams Eng. J., 15 (2024) 102549.

21. S. Das, C. Manoharan, M. Venkateshwarlu, P. Dhamodharan, J. Mater. Sci. Mater. Electron., 30 (2019) 19880.
22. M. Dabla, M. Sharma, B. K. Kuanr, J. Magn. Magn. Mater., 614 (2025) 172746.
23. T. L. Thokoane, T.A. Nhlapo, V. N. Adoons, L. Kotsedi, T.P. Mokoena, T.S. Mahule, T. C. Mokhena, T. Moyo, J. Mol. Struct., 1315 (2024) 138906.
24. T. A. Wania, G. Suresha, R. Masrourb, K. M. Batooc, A. Rasool, Mater. Chem. Phys., 307 (2023)128169.
25. F. Naaz, P. Lahiri, V. K. Mishra, H. K. Dubey, P. K.Tripathi, E. Shakerzadeh, Inorg. Chem. Commun., 162 (2024) 112185.
26. P. Schneider, Appl. Catal A: Gen., 129 (1995) 157.
27. S. Yurdakal, C. Garlisi, L. Özcan, M. Bellardita, G. Palmisano, (2019) (Photo)catalyst Characterization Techniques, Heterogenous catalysis, Joseph P. Hayton.
28. N. Dhanda, S. Kumari, R. Kumar, D. Kumar, A. A. Sun, P. Thakur, A. Thakur, Inorg. Chem. Commun., 151 (2023) 110569.
29. R. Kumar, R. Jasrotia, Himanshi, J. Ahmed, A. Nidhi, S. M. Alshehri, L. W.Y. Liue, S. A. Patil, R. Aggarwal, S. Kumar Godara, P. B. Barman, R. Singh, A. Kandwal, Inorg. Chem. Commun., 157 (2023) 111355.
30. K. Mohita, V. R. Gupta, N. Gupta, S. K. Rout, Ceram. Int., 40 (2014)1575.
31. A. Lassoued, J.F. Li, Solid State Sci., 104 (2020)106199.
32. N. Monni, V. Mameli, S. A. Sahadevan1, S. Gai, C. Cannas, M. L. Mercuri, J. Nanosci. Nanotechnol., 19 (2019) 5043.
33. Z. Wanga, D. Schiferla, Y. Zhaoa, H. St. C. O'Neill, J. Phys. Chem. Solids, 64 (2003) 2517.
34. M. Khan, J. Duan, Y. Chen, H. Yao, S. Lyu, H. Shou, K. Heng, Q. Xu, J. Alloys Compd., 701 (2017) 147.
35. T. Yamashita, P. Hayes, Appl. Surf. Sci., 254 (2008) 2441.
36. P. C. J. Graat, Marcel A. J. Somers, Appl. Surf. Sci., 100/101 (1996) 36.
37. S. J. Roosendaal, B. van Asselen, J. W. Elsenaar, A.M. Vredenberg, F. H. P. M. Habraken, Surf. Sci., 442 (1999) 329.
38. P. Mills, J. L. Sullivan, J. Phys. D: Appl. Phys., 16 (1983) 723.

39. R. Ling, X. Yang, Y. Li, L. Huan, Y. Cai1, A. Wang, X. Tan, G. Sun, J Mater Sci: Mater. Electron., 35 (2024) 543.
40. J. G. Monsalve, C. Ostos, E. Ramos, J. G. Ramírez, O. Arnache, Curr. Appl. Phys., 22 (2021) 77.
41. S. Bera, A. A. M. Prince, S. Velmurugan, P. S. Raghavan, R. Gopalan, G. Panneerselvam, S. V. Narasimhan, J. Mater. Sci., 36 (2001) 5379.
42. E. Paparazzo, Surf. Interface. Anal., 12, (1988) 115.
43. S. P. Sahare, A. V. Wankhade, S. P. Zodape, Appl. Phys. A, 129 (2023) 43.
44. Hua M., Xu, L., Cui, F. Cui, J. Lian, Y. Huang, J. Bao, J. Qiu, Y. Xu, H. Xu, Y. Zhao, H. Li, J. Mater. Sci., 53 (2018) 7621.
45. Panwar, S. Tiwari, K. Bapna, N. L. Heda, R. J. Choudhary, D. M. Phase, B. L. Ahuja, J. Magn. Magn. Mater., 142 (2017) 25.
46. V. K. Mittal, S. Bera, R. Nithya, M. P. Srinivasan, S. Velmurugan, S. V. Narasimhan, J. Nucl. Mater., 335 (2004) 302.
47. M. Hua, L. Xu, F. Cui, J. Lian, Y. Huang, J. Bao, J. Qiu, Y. Xu, H. Xu, Y. Zhao, Huaming Li, J. Mater. Sci., 53 (2018) 762.
48. R. Singh Yadav, I. Kuritka, J. Vilcakova, J. Havlica, J. Masilko, L. Kalina, J. Tkacz, J. Svec, Vojtech Enev, M. Hajduchova, Adv. Nat. Sci: Nanosci. Nanotechnol., 8 (2017) 045002.
49. S. R. Naik and A. V. Salker, J. Mater. Chem., 22 (2012) 2740.
50. N. Rezelescu, E. Rezelescu, C. Doroftei, P.D. Popa, J. Phys. Conf. Ser., 15 (2005) 296.
51. K. Y. Salkar, R. B. Tangsali, R. S. Gad, A. Gangwar, N. K. Prasad, J. Mater. Sci.: Mater. Electron., 30 (2019) 18374.
52. V. L. Mathe, R.B. Kamble, Mater. Res. Bull., 43 (2008) 2160.
53. J. W. Verwey and J.M. De Boer, Rec. Trav. Chim. Phys. Bas., 55 (1936) 53.
54. A. Verma, T.C. Goel, R.G. Mendiratta, R.G. Gupta, J. Magn. Magn. Mater., 192 (1999) 271.
55. A. K. Singh, A. Verma, O. P. Thakur, C. Prakash, T. C. Goel, R. G. Mendiratta, Jpn. J. Appl. Phys., 41 (2002) 5142.
56. Z.Ž. Lazarević, Č. Jovalekić, D.L. Sekulić, A. Milutinović, S. Baloš, M. Slankamenac, N. Ž. Romčević, Mater. Res. Bull., 48 (2013) 4368.

57. A. S. Ramesh, B. Dhanalakshmi, B. Chandra Sekhar, P.S.V. Subba Rao, B. Parvatheeswara Rao, Ceram. Int., 42 (2016) 9591.
58. A. Hajalilou, H.M. Kamari, K. Shameli, J. Alloys Compd., 708 (2017) 813.
59. K. Raju, G. Venkataiah, D.H. Yoon, Ceram. Int., 40 (2014) 9337.
60. A.V. Knyazeva, I. Zakharchukb, E. Lähderantab, K.V. Baidakova, S.S. Knyazevaa, I.V. Ladenkov, J. Magn. Magn. Mater., 435 (2017) 9.
61. V. S. Sharon, V. K. Haripriya, Swapna S. Nair, E. Veena Gopalan, Aneesh George, K. A. Malini, Sol-Gel Sci. Technol., 114 (2025) 169.
62. S. G. Gawas, S. S. Meena, S. M. Yusuf, V. M.S. Verenkar, New J. Chem., 40 (2016) 9275.
63. S. G. Gawas, S. S. Meena, P. Bhat, V. M.S. Verenkar, Mater. Chem. Front., 2 (2018) 300.
64. P. P Gauns Dessai, V. M.S. Verenkar, J. Mater. Sci. Mater. Electron., 29 (2018) 6924.
65. D. Peddis, N. Yaocoub, M. Ferretti, A. Martinelli, G. Piccaluga, A. Musinu, C. Cannas, G. Navarra, J.M. Greneche, D. Fiorani, J. Phys. Conden. Matter, 23 (2011) 426004.
66. D. Peddis, F. Orru, A. Ardu, C. Cannas, A. Musihu, G. Piccaluga, Chem Mater., 24 (2012) 1062.
67. R. Topkaya. O. Akman, S. Kazan, B. Aktas, Z. Durmus, A. Baykal, J. Nanopart. Res., 14 (2012)1156.
68. C. C. Naik, A.V. Salker, J. Mater. Sci.: Mater. Electron., 29 (2018) 5380.
69. S. U. Bhasker, G.S.V.R.K. Choudary, M.V.R. Reddy, J. Magn. Magn. Mater., 454 (2019) 349.
70. L. M. Thorat, J.Y. Patil, D.Y. Nadargi, U.R. Ghodake, R.C. Kambale, S.S. Suryavanshi, J. Sol-Gel Sci. Technol., 86 (2018) 731.
71. M.C. Sable, B.K. Labde, N.R. Shamkumar, Bull. Mater. Sci., 28 (2005) 35.
72. M. U. Sawal, V.M.S. Verenkar, J. Mater. Sci. Mater. Electrons., 32 (2021) 21350.
73. P. Yaseneva, M. Bowker, G. Hutchings, Phys. Chem. Chem. Phys., 13 (2011) 18609.
74. B. D. Cullity, C. D. Graham. Introduction to Magnetic Materials (New Jersey: Wiley) 2nd ed, Ch 11, 360 (2009).
75. M. Aliahmad, M. Noori, Indian J. Phys., 87 (2013) 431.
76. M.A. Gabal, Y.M.A. Angari, F.A. Al-Agel, J. Magn. Magn. Mater., 391 (2015) 108.

77. P. P Gauns, V.M.S. Verenkar, J. Mater. Sci. Mater. Electrons., 29 (2018) 6924.
78. T.J. Shinde, A.B. Gadkari, P.N. Vasambekar, J. Magn. Magn. Mater., 333 (2013) 152.
79. B. P. Ladgaonkar, P.N. Vaambekar, A. S. Vaigankar, J. Magn. Magn. Mater., 210 (2000) 289.
80. P. Yasenva, M. Bowker, G. Hutchings, Phys. Chem. Chem. Phys., 13 (2011)18609.
81. J.C. Maxwell, Electricity and Magnetism, Oxford University Press, New York, 1973
82. C.G. Koops, Phys. Rev., 83 (1951) 121.
83. K.W. Wagner, Am. Phys., 40 (1973) 317.
84. A. Anwar, U. S. Akther, K. H. Maria, M. K. Alam, A. Kumar, M. N. I. Khan, J. Mater. Sci: Mater. Electron., 35 (2024) 19.
85. V. Murthy, J. Sobhanadri, Phys. Stat. Sol. A, 36 (1976) 133.
86. R. Nongjai, Shakeel Khan, K. Asokan, Hilal Ahmed, I. Khan, J. Appl. Phy., 112 (2012) 084321.
87. M. A. Iqbal, M .U. Islam, I. Ali, M. Azhar khan, I. Sadiq, Ihsan Ali, J. Alloys Compd., 586 (2014) 404.
88. M. N. Ashiq, M. J. Iqbal, I. H. Gul, J. Magn. Magn. Mater., 323 (2011) 259.
89. S. Minz, S. C. Sahoo, S. K. Rout, B. Behera, J. Mater. Sci.: Mater. Electron., 34 (2023) 649.
90. M. Aliuzzaman, M. M. Haque, M. J. Ferdous, S. M. Hoque, M. A. Hakim, World J. Condens. Matter Phys., 4 (2014) 13.
91. P.V. Reddy, T. S. Rao, S. M. D. Rao, J. Less Common. Met., 79 (1981) 191.
92. J. Parashar, V.K. Saxena, Jyoti, D. Bhatnagar, K.B. Sharma, J. Magn. Magn. Mater., 394 (2015) 105.
93. M. C. Dimri, A. Verma, Subhash C. Kashyap, D.C. Dube, O.P. Thakur, C. Prakash, Mater. Sci. Eng. B, 133 (2006) 42.
94. M. George, S. S Nair, K. A. Malini, P. A. Joy, M. R. Anantharaman, J. Phys. D: Appl. Phys. 40 (2007) 1593.
95. E. Gopalan, K. A. Malini, S. Saravanan, D. S. Kumar, Y. Yoshida, M. R. Anantharaman, J. Phys. D Appl. Phys., 41 (2008) 185005.
96. K. Sultan, M. Ikram, K. Asokan, Vacuum 99 (2014) 251.
97. N. M. Burange, R. K. Pinjari, B. A. Aldar, J. Electr. Electron. Eng., 9 (2014) 10.

98. Y. Yafet, C. Kittel, Phys. Rev., 87 (1952) 290.
99. L. L. Hench, J. K. West, Principles of Electronic Ceramics, John Wiley, New York, (1990) 205.
100. A. Globus, P. Duplex, J. Appl. Phys., 39 (1968) 727.
101. J. S. Ghodake, T. J. Shinde, R. P. Patil, S. B. Patil, S. S. Suryavanshi, J. Magn. Magn. Mater., 378 (2015) 436.
102. V. A. Pandit, N. N. Kapse, V. K. Kashte, N. D. Chaudhari, J. Magn. Magn. Mater., 601(2024) 172184.
103. Y. Liu, Z. Yi, J. Li, T. Qui, F. Min, M. Zhang, J. Am. Ceram. Soc., 98 (2013) 151.
104. J. S. Ghodake, R. C. Kamble, T. J. Shinde, P. K. Maskar, S. S. Suryavanshi, J. Magn. Magn. Mater., 401 (2016) 938.
105. N. Rezlescu, C. Doroftei, E. Rezlescu, P. D. Popa, Phys. Stat. Sol. (a), 203 (2006) 306.
106. C. Xu, J. Tamaki, N. Miura, N. Yamazoe, Sens. Actuators B, 3 (1991) 147.
107. Y. Shimizu M. Egashira, MRS Bull., 24 (1999) 18.
108. C. Xu, T. Jun, N. Miura, N. Yamazoe, Chem. Lett., 3 (1990) 441.
109. A. K. Yadav, R.K. Singh, P. Singh, Sens. Actuators B, 229 (2016) 25.
110. G. Zhang, C. Li, F. Cheng, J. Chen, Sens. Actuators B: Chem., 120 (2007) 403.
111. Y. Kumar, A. Sharma, P.M. Shirage, RSC Adv., 7 (2017) 55778.
112. N. Goel, K. Kunal, A. Kushwaha, M. Kumar, Eng. Rep., 5 (2023)12604.
113. J. Xu, Q. Pan, Y. Shun, Z. Tian, Sens. Actuators B, 66 (2000) 277.
114. A. B. Bodade, H.G. Wankhade, G.N. Chaudhari, D.C. Kothari, Talanta, 89 (2012) 183.
115. Y. Cao, H. Qin, X. Niu, D. Jia, Ceram. Int., 42 (2016) 10697.
116. F. Tudorache, E. Rezlescu, P.D. Popa, N. Rezlescu, J. Optoelectron. Adv. Mater., 10 (2008) 1889.
117. A.V. Kadu, S.V. Jagtap, G.N. Chaudhari, Curr. Appl. Phys., 9 (2009) 1246.
118. R. Shedam, P. Kashid, S. Mathad, R. Deshmukh, M. Shedam, A. Gadkari, Phys. Chem. Soli State, 23 (2022) 626.
119. S. Sharifi, A. Yazdani, K. Rahimi, Sci. Rep.,10 (2020) 10916.
120. X. Zhang, P. Yu, H. Zhang, D. Zhang, X. Sun, Y. Ma, Electrochim. Acta, 89 (2013) 523.

121. A. Sonam, R. Kumar, P. K. Sahoo, C. Mahender, B. Kumar, N. Arya, M. Singh, S. Parida, R.O. Dusane, Chem. Select, 4 (2019) 9952.
122. P. Kharat, P. B., Somvanshi, S. B., Dawi, E. A. Dawi, A. Moprai, N. Bansod, J. Mater. Sci.: Mater. Electron., 35 (2024) 606.
123. E. Mitchell, R. K. Gupta, K. Mensah-Darkwa, D. Kumar, K. Ramasamy, B. K. Gupta, New J. Chem., 38 (2014) 4344.
124. A. Rai, A. L. Sharma, A.K. Thakur, Solid State Ion., 262 (2014) 230.
125. V. Vignesha, K. Subramanib, M. Sathish, R. Navamathavan, Colloids Surf., 538 (2018) 668.
126. N. Matinise, K. Kaviyarasu, N. Mongwaketsi, S. Khamlich, L. Kotsedi, N. Mayedwa, Appl. Surf. Sci., 446 (2018) 66.
127. A. Pendashteh, J. Palma, M. Anderson, R. Marcilla, J. Mater. Chem. A, 3 (2015) 16849.
128. M. B. Askari, P. Salarizadeh, Int. J. Hydrog. Energy, 45 (2020) 27482.
129. N. Kumar, A. Kumar, S. Chandrasekaran, T.Y. Tseng, J. Clean Energy Technol., 6 (2018) 51.
130. D. K. Pawar, J. S. Shaikh, B. S. Pawar, S. M. Pawar, P. S. Patil, S. S. Kolekar, J. Porous Mater.,19 (2012) 649.
131. D. K. Pawar, S. M. Pawar, P. S. Patil, S. S. Kolekar, J. Alloys Compd., 509 (2011) 3587.
132. K. Sathiyamurthy, C. Rajeevgandhi, S. Bharanidharan, P. Sugumar, S. Subashchandrabose, Chem. Data Collect., 28 (2020) 100477.
133. L. Liao, T. Fang, G. Yin, D. Zhang, B. Li, Int. J. Electrochem. Sci., 12 (2017) 10211.
134. M. N. Kiani, M. S. Butt, I. H. Gul, M. S. M. Irfan, A. H. Baluch, M. A. Akram, M. A. Raza, ACS Omega, 8 (2023) 3755.
135. H. Yun, J. D. Kim, H. C. Choi, C. W. Lee, Bull. Korean Chem. Soc., 34 (2013) 3261.
136. K. Ishaq, A. Ambali Saka, A. O. Kamardeen, A. Ahmed, M. I. Alhassan, H. Abdullahi, Eng. Sci. Technol. Int. J., 20 (2017) 563.
137. A. Mahmood, S. B. Syed, Z. Hasan, M. Islam, R. Hossain, S. Rahman, Results Surf. Interfaces, 17 (2024) 100303.
138. A. S. Shafaay, R. Ramadan, J. Supercond. Nov. Magn., 36 (2023) 1465.

139. A. Raghunath, E. Perumal, Int. J. Antimicrob. Agents, 49 (2017) 137.
140. D. R. Lima, N. Jiang, X. Liu, J. Wang, V. A. S. Vulcani, A. Martins, Douglas, S. Machado, R. Landers, P. H. C. Camargo, Al. Pancotti, ACS Appl. Mater. Interfaces, (2017) 1.

Chapter 4

A comparative study of 'as prepared' and 'sintered' $Ni_{0.6-x}Mn_{0.4}Zn_xFe_2O_4$ (x= 0.0, 0.1, 0.2, 0.3, 0.4, 0.5, 0.6) ferrites and their applications

4.1 Introduction

The properties of ferrites highly depend on the nature of the synthesis techniques, and their structure and sizes can be modified accordingly. The combustion method is a technique that involves a self-sustained exothermic redox reaction between the fuel and the oxidizer. Upon heating, the fuel-oxidizer mixture undergoes rapid combustion, generating sufficient heat to decompose the precursor, yielding ferrite nanoparticles. According to the literature, various fuels such as glycine, urea, tartaric acid, and so on have been utilized for synthesizing many ferrite nanoparticles. Amongst them, hexamine, a nitrogen-rich compound, stands out as an effective fuel, producing porous ferrite nanomaterials.

Mn-Zn-Ni ferrite is extensively used due to its ability to incorporate the beneficial magnetic properties of manganese, zinc, and nickel, resulting in materials with excellent performance. Mn-Zn ferrites in particular have been employed in high-frequency applications owing to their high magnetic permeability and low core losses. The addition of nickel enhances electrical resistivity, magnetic properties, and thermal stability, thereby reducing eddy current losses and improving the overall performance. Therefore, this makes these compounds are suitable for various EMI suppressors, power electronics materials, and microwave absorbers.

4.2 Optimization study of $Ni_{0.3}Mn_{0.4}Zn_{0.3}Fe_2O_4$ ferrites

The detailed procedure of optimization is discussed in Chapter 2. The optimization was carried out using the mid-composition $Ni_{0.3}Mn_{0.4}Zn_{0.3}Fe_2O_4$ ferrite, where ten different oxidizer: fuel ratios were optimized to select the best oxidizer: fuel ratio. The metal nitrates serve as oxidizers, whereas hexamine was selected as the fuel for further study. Table 4.1 represents the various ratios selected to study the $Ni_{0.3}Mn_{0.4}Zn_{0.3}Fe_2O_4$ ferrite.

The combustion synthesis technique is a high-temperature procedure that may lead to the formation of impurity phases. Therefore, the main objective of the optimization is to obtain pure ferrite compounds with fine particle sizes and no impurity. Optimization studies help select the appropriate oxidizer: fuel ratio based on various characterization techniques.

Table 4.1: Metal nitrate: fuel ratio, Lattice constants, Average crystallite size, Saturation magnetization, Coercivity, Remanence, and Curie temperature.

Sample No.	**Metal: Fuel ratio**	**Lattice constant (Å)**	**Average crystallite size (nm)**	**Saturation magnetization (M_s)emu/g**	**Coercivity (H_c)**	**Remanence (M_r)**	**Curie Temperature (K)**
1	(1:0.25)	8.395	4	13.06	3.92	0.049	647
2	(1:0.375)	8.398	4	22.40	8.050	0.350	613
3	(1:0.50)	8.398	12	24.47	13.99	0.600	677
4	(1:0.625)	8.401	10	25.24	47.50	0.278	755
5	(1:0.75)	8.402	22	53.02	35.44	3.482	822
6	(1:0.875)	8.395	29	58.10	43.65	2.565	839
7	(1:1)	8.399	32	61.46	40.37	2.776	818
8	(1:1.125)	8.397	33	57.72	45.06	3.650	805
9	(1:1.25)	8.396	31	69.71	42.75	3.790	780
10	(1:1.375)	8.401	26	59.02	62.40	3.750	797

The selected ratio for further synthesis was (1:0625) based on the characterization analysis performed. The initial step was to investigate its phase purity, which was done using powder X-ray diffraction, from which it was observed that the ratio (1:0.625) showed monophasic with characteristic spinel peaks. In contrast, the fuel-deficient ratio showed a more amorphous nature in the powder XRD peaks, while fuel-efficient peaks had a slight impurity phase. The crystallite size was found to be around 10 nm, which is quite suitable for various applications. Table 4.1 shows a discontinuity in the lattice constant with an increase in fuel, but it does not increase with increasing crystallite size. Infrared spectroscopy revealed the two major spinel ferrite peaks

in the 400-600 cm^{-1} range. Magnetic studies were performed to determine the magnetic parameters, which further helped to decide the metal: fuel ratio. The saturation magnetization obtained for all the samples was between 13-69 emu/g. The crystallite size and M_s showed a close relationship between them. The highest M_s value of 69 emu/g was obtained for the sample (1:1.25) ratio. Higher fuel content showed higher M_s values. $Ni_{0.3}Mn_{0.4}Zn_{0.3}Fe_2O_4$, synthesized by the citrate method by [1], showed a M_s value of 53 emu/g. In our present study, by varying the fuel content, we can obtain variable sizes and M_s values; thus, optimization helps in deciding the size and various parameters for synthesizing the ferrite series. Curie temperature was determined from AC susceptibility studies. The sample showed a single-domain nature with Tc at 755 K for the selected ratio. Dielectric constant and dielectric loss studies showed a moderate result for the ratio (1:0.625). Resistivity studies were performed at 498 K for the ratio ~~(~~1:0.625~~),~~ which confirmed the semiconducting nature of the ferrite. Though higher fuel ratios also observed high resistivity, but had greater particle size and slight impurities in samples, hence the oxidizer: fuel ratio of 1:0.625 was chosen for synthesizing the ferrite series.

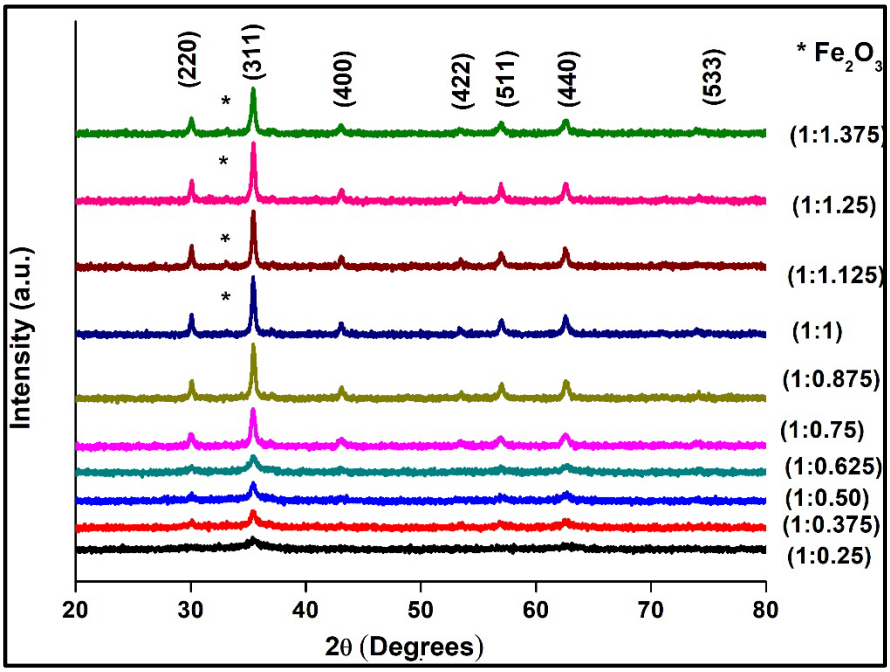


Fig. 4.1: The powder XRD patterns of $Ni_{0.3}Mn_{0.4}Zn_{0.3}Fe_2O_4$ at different metal nitrate: fuel ratios

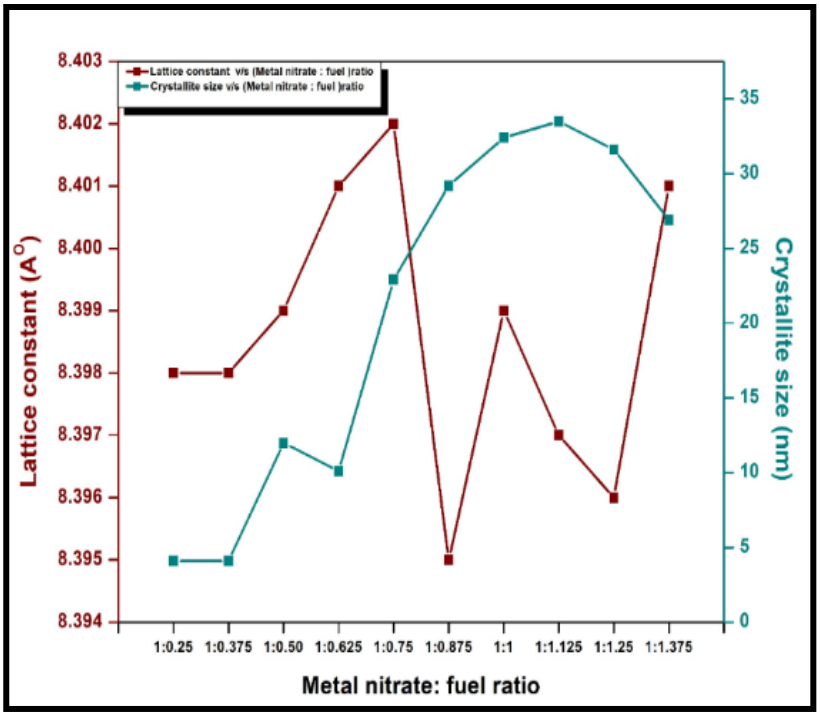


Fig. 4.2: Plot of lattice constant and crystallite size as a function of metal nitrate: fuel ratio.

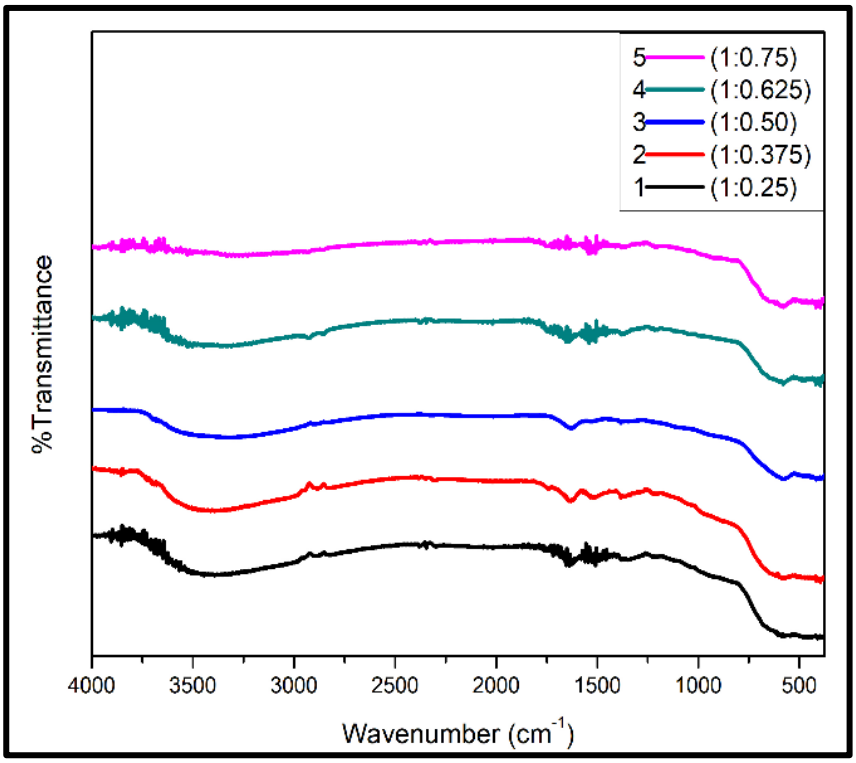


Fig. 4.3a: IR spectra of $Ni_{0.3}Mn_{0.4}Zn_{0.3}Fe_2O_4$ ferrite with different metal nitrate: fuel ratios (1-5).

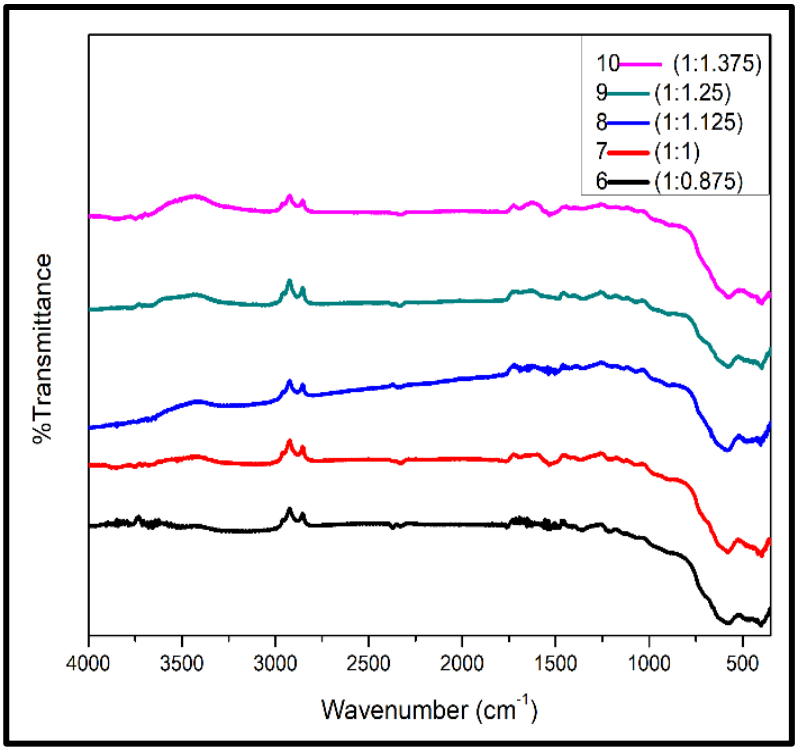


Fig. 4.3b: IR spectra of $Ni_{0.3}Mn_{0.4}Zn_{0.3}Fe_2O_4$ ferrite with different metal nitrate: fuel ratios (6-10)

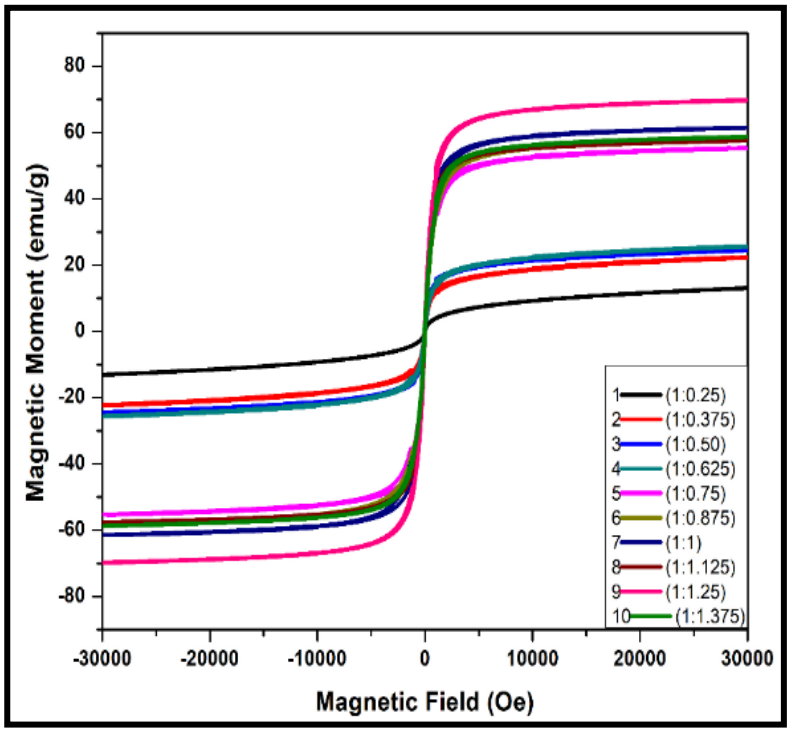


Fig. 4.4: The plot of magnetic moment versus magnetic field of $Ni_{0.3}Mn_{0.4}Zn_{0.3}Fe_2O_4$ ferrite with different metal: fuel ratios.

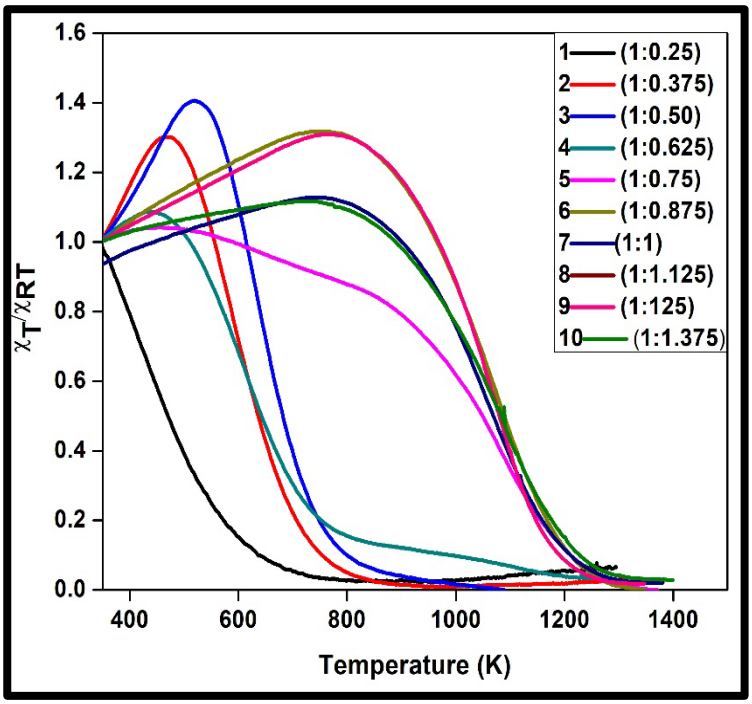


Fig. 4.5: The plot of normalized AC susceptibility as a function of temperature of $Ni_{0.3}Mn_{0.4}Zn_{0.3}Fe_2O_4$ ferrite with different metal: fuel ratios.

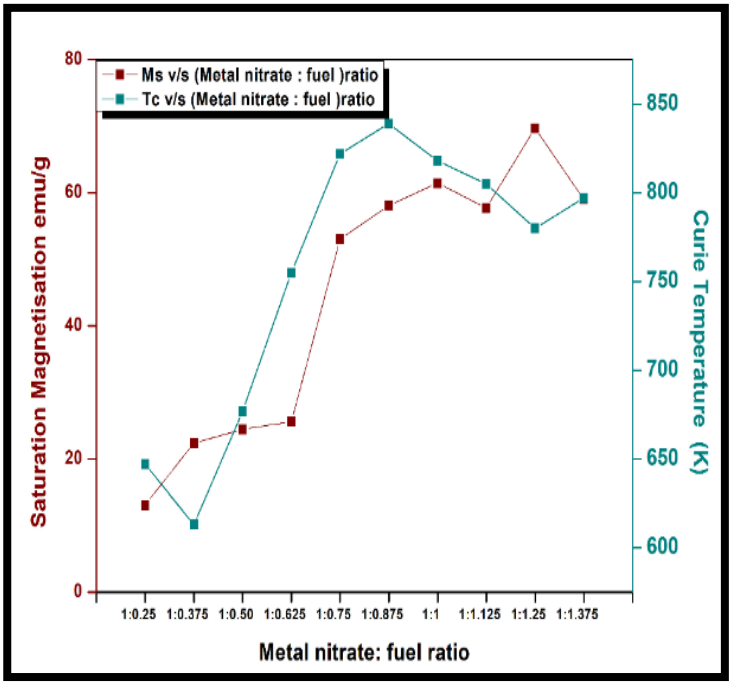


Fig. 4.6: The plot of saturation magnetization and Curie temperature as a function of temperature of $Ni_{0.3}Mn_{0.4}Zn_{0.3}Fe_2O_4$ ferrite with different metal: fuel ratios.

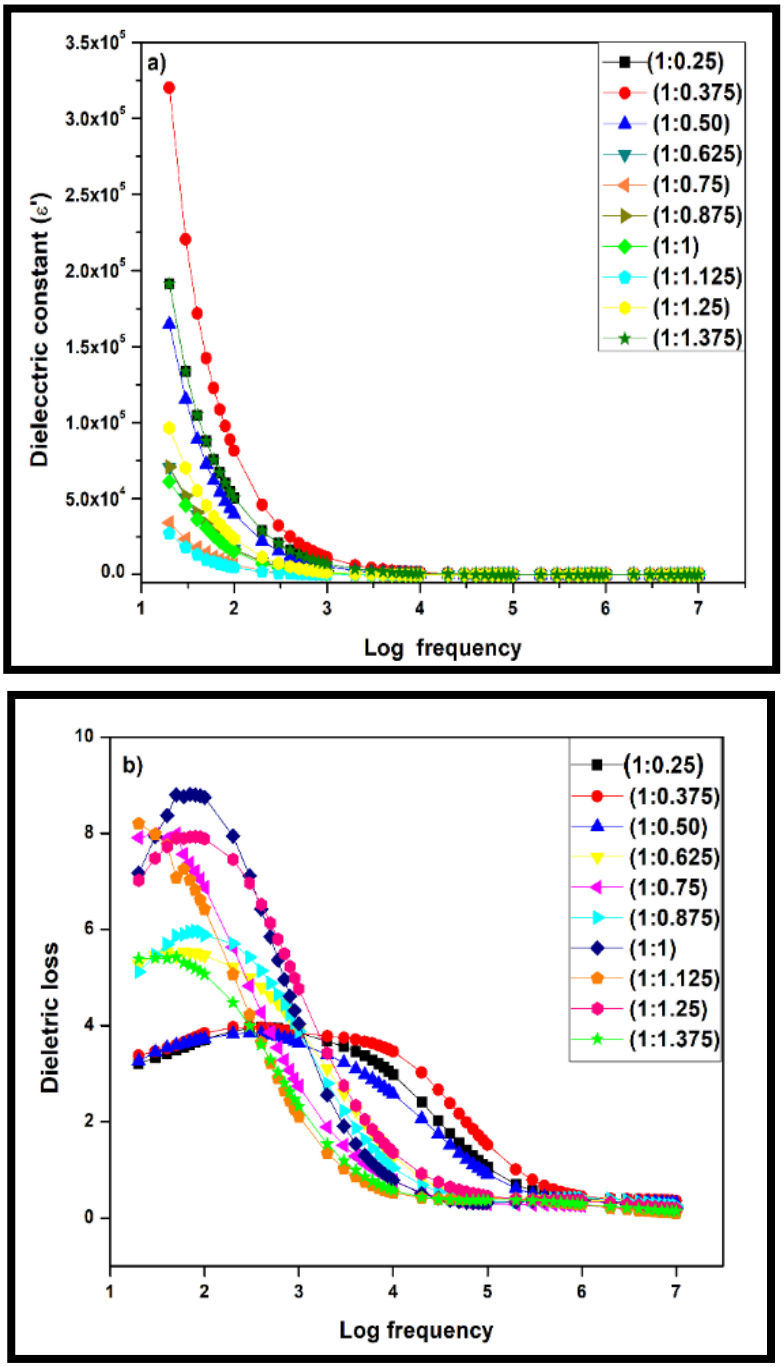


Fig. 4.7: a: plot of dielectric constant versus log frequency and, b: dielectric loss versus log frequency for $Ni_{0.3}Mn_{0.4}Zn_{0.3}Fe_2O_4$ ferrite samples with different metal: fuel ratios.

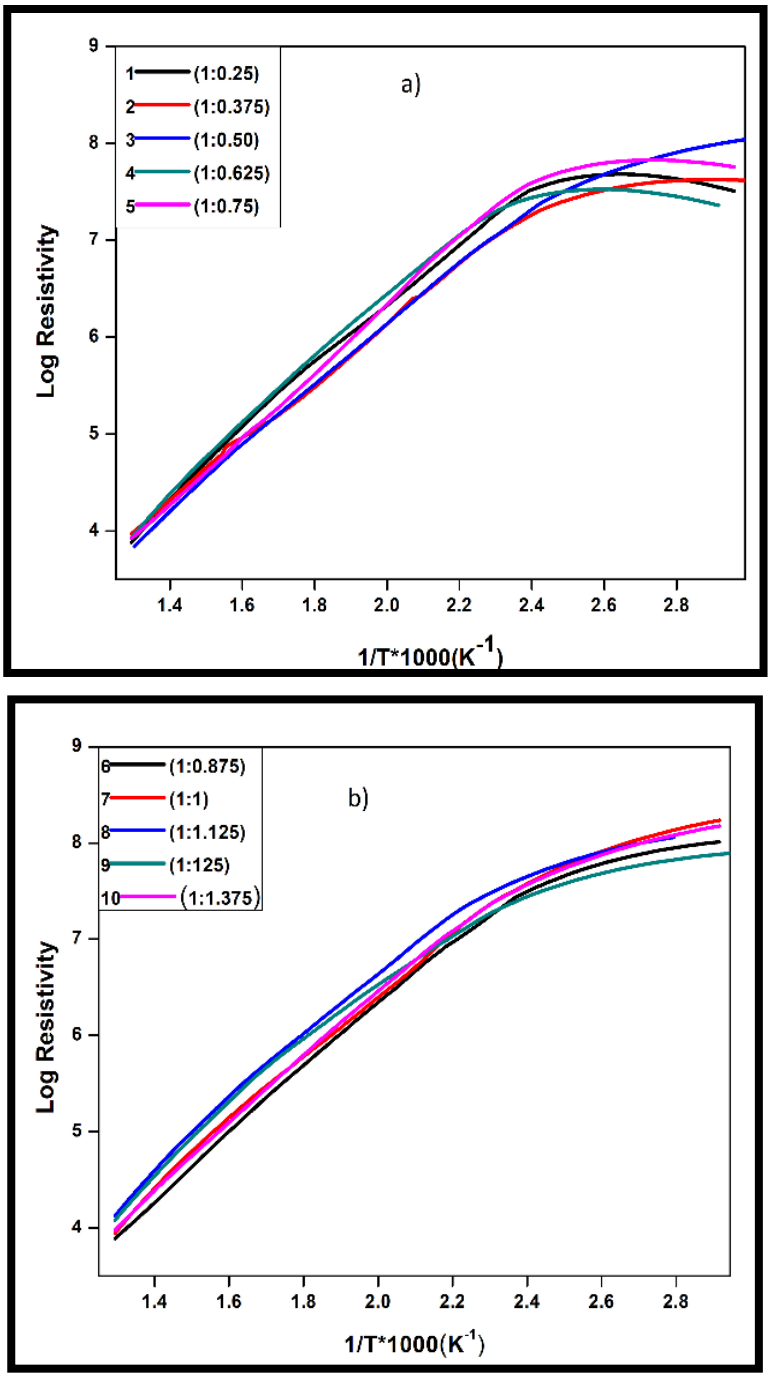


Fig. 4.8: The plot of log resistivity v/s 1/T * 1000 of $Ni_{0.3}Mn_{0.4}Zn_{0.3}Fe_2O_4$ ferrite from (a) 1-5 samples and b: 6-10 samples with different metal nitrate: fuel ratio.

4.3 Synthesis of $Ni_{0.6-x}Mn_{0.4}Zn_xFe_2O_4$ (x= 0.0, 0.1, 0.2, 0.3, 0.4, 0.5, 0.6) ferrites via combustion method using hexamine as the fuel

The detailed procedure for the synthesis of $Ni_{0.6-x}Mn_{0.4}Zn_xFe_2O_4$ (x=0.0, 0.1, 0.2, 0.3, 0.4, 0.5, 0.6) ferrites via the combustion method using hexamine as the fuel is given in Chapter 2. The details of the optimization study using various techniques to select suitable metal nitrate, such as fuel ratio, are mentioned in section 4.2. Multiple methods have been used to characterize the 'as prepared' and 'sintered' ferrites, and the effect of zinc substitution is studied in this chapter.

4.4 Characterization of 'as prepared' and 'sintered' $Ni_{0.6-x}Mn_{0.4}Zn_xFe_2O_4$ (x= 0.0, 0.1, 0.2, 0.3, 0.4, 0.5, 0.6) ferrites

4.4.1 Powder X-ray Diffraction Studies

The powder X-ray diffraction analysis of zinc-doped Ni-Mn ferrite, viz. $Ni_{0.6-x}Mn_{0.4}Zn_xFe_2O_4$ (x=0.0, 0.1, 0.2, 0.3, 0.4, 0.5, 0.6) ferrites was performed to determine the phase purity of the samples. Fig. 4.9 depicts the powder XRD patterns of all the 'as prepared' ferrite samples. The calculated parameters, such as lattice constant, X-ray density, porosity, and crystallite size, are calculated from the data tabulated in Table 4.2. The powder XRD patterns in Fig. 4.9 show a peak with broad FWHM having small intensities, indicating smaller crystallite sizes. Six well-defined peaks have been observed with (h k l) values (2 2 0), (3 1 1), (4 0 0), (4 2 2), (5 1 1), and (4 4 0). Lattice constants calculated from the data were found to increase linearly as the zinc content in the samples increases, and are according to Vegard's law. According to this law, at a constant temperature, the lattice constant of a crystal has a linear relationship with the concentration. In this case, zinc ions having ionic radii of 0.84Å are getting replaced by smaller ionic radii of Ni^{2+} and Fe^{3+} ions having ionic radii of 0.64 Å and 0.67 Å, respectively[5,6]. Due to doping, the more significant ions in the system, the lattice parameters increase [7]. The crystallite size was found in the nano range of 8-13 nm.

The X-ray diffractogram shown in Fig. 4.11 was utilized to determine the optimum final sintering time, temperature, and duration. It was observed from the figure that the powder XRD patterns for the sample sintered at 1100 °C for 10 h were the only ones showing a cubic spinel phase structure, while the other three samples were seen to have the formation of a partial

secondary phase. Consequently, 1100 °C for 10 h was chosen as the final sintering temperature for the further preparation of the compound.

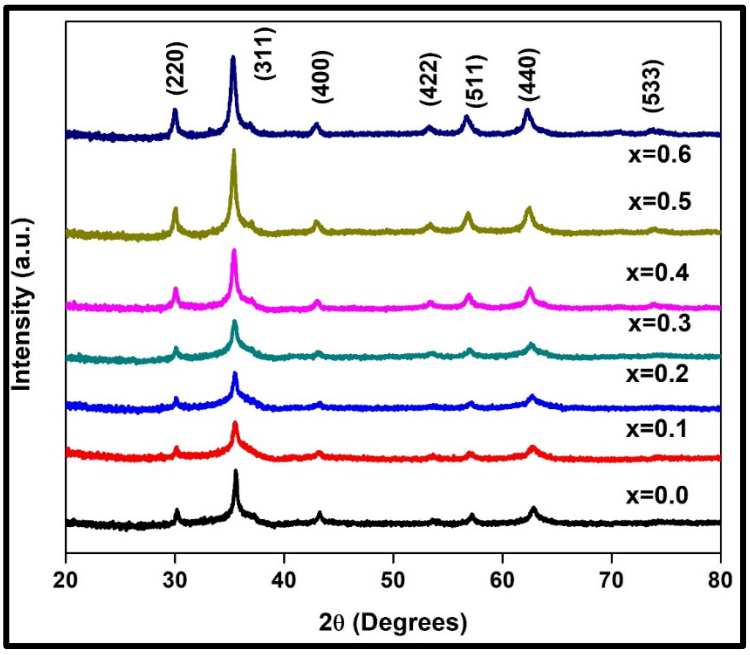


Fig. 4.9: The powder XRD patterns of 'as prepared' $Ni_{0.6-x}Mn_{0.4}Zn_xFe_2O_4$ (x=0.0, 0.1, 0.2, 0.3, 0.4, 0.5, 0.6) ferrites

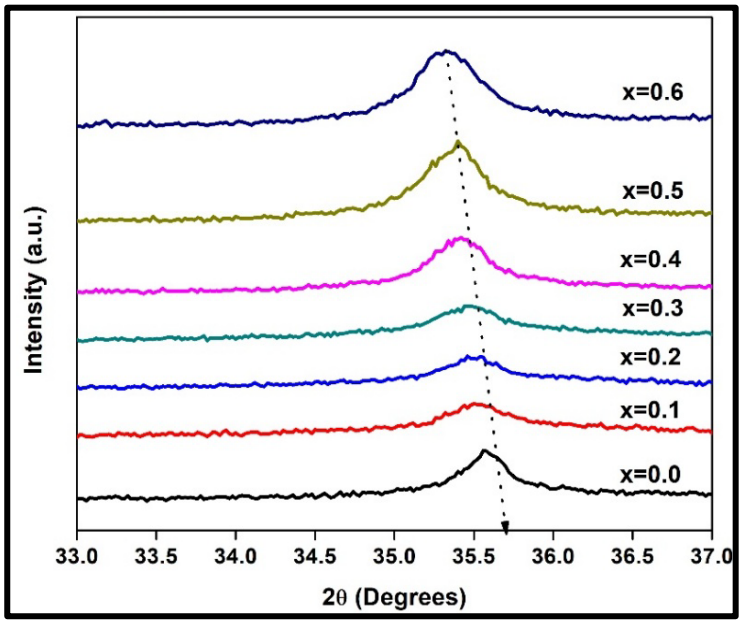


Fig. 4.10: The 311 peaks of 'as prepared' $Ni_{0.6-x}Mn_{0.4}Zn_xFe_2O_4$ (x=0.0, 0.1, 0.2, 0.3, 0.4, 0.5, 0.6) ferrites

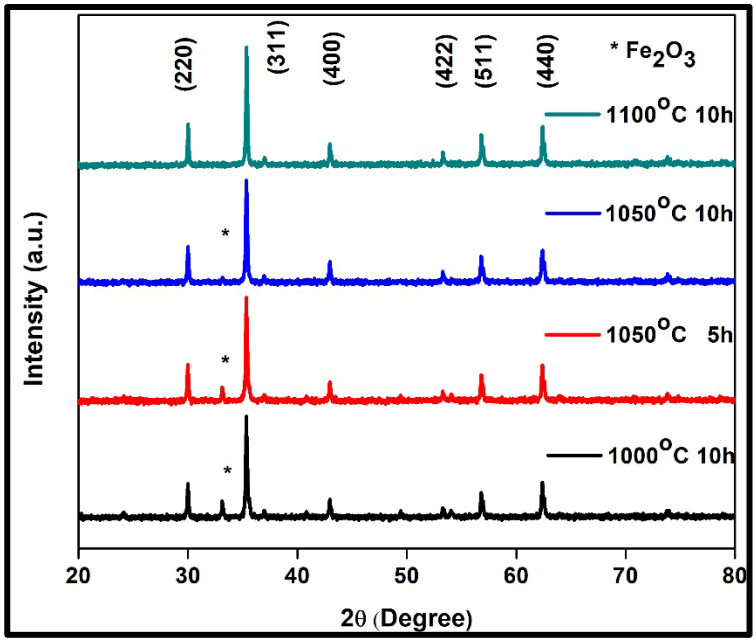


Fig. 4.11: Powder X-ray diffraction pattern of $Ni_{0.3}Mn_{0.4}Zn_{0.3}Fe_2O_4$ ferrite at different sintering temperatures: 1000 °C for 10 h, 1050 °C for 5 h, 1050 °C for 10 h, and 1100 °C for 10 h.

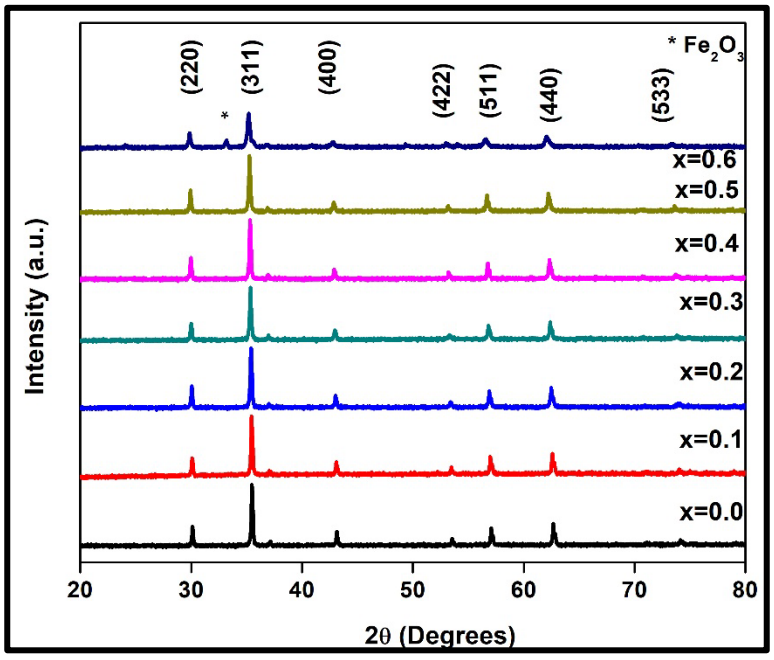


Fig. 4.12: The powder XRD patterns of 'sintered' $Ni_{0.6-x}Mn_{0.4}Zn_xFe_2O_4$ (x=0.0, 0.1, 0.2, 0.3, 0.4, 0.5, 0.6) ferrites

Table 4.2: Lattice constant (a), Unit cell (V), the crystallite size (D), x-ray density (dx), bulk density (dm), and porosity % (P) of 'as prepared' and 'sintered' $Ni_{0.6-x}Mn_{0.4}Zn_xFe_2O_4$ (x=0.0, 0.1, 0.2, 0.3, 0.4, 0.5, 0.6) ferrites

x	a (Å)		V (Å)		D (nm)		dx (g/cm^3)		Dm (g/cm^3)		P (%)	
0.0	8.353	8.387	583	589	15	59	5.341	5.399	2.393	3.465	55.1	35.8
0.1	8.367	8.395	585	590	10	60	5.295	5.242	2.149	3.472	59.4	33.7
0.2	8.370	8.407	586	594	8	54	5.305	5.235	2.126	3.475	59.9	33.6
0.3	8.380	8.420	588	597	11	56	5.301	5.226	2.174	3.432	58.9	35.2
0.4	8.403	8.428	593	599	13	59	5.098	5.576	2.205	3.478	56.7	33.3
0.5	8.414	8.441	595	601	13	54	5.267	5.217	2.347	3.471	55.4	33.4
0.6	8.423	8.458	597	605	12	33	5.265	5.185	2.450	3.519	53.4	32.1

In case of sintered ferrite, sharp peaks were obtained compared to 'as prepared' ferrite, as seen from Fig. 4.12; FWHM was narrow, leading to a higher crystallite size of the ferrite samples. The porosity was lower than that of the 'as prepared' ferrite analogues due to their increased density. Sintering of the ferrites leads to merging of the grains, thus increasing the crystallite size and density while lowering the porosity. The lattice constant increased with zinc content and shows a similar trend to that of the 'as prepared' ferrites. The lattice constant values were higher in the case of 'sintered' ferrites, which is also attributed to a larger crystallite size. With a rise in temperature, the cation distribution is stable, leading to an increase in lattice constants. The zinc and manganese ions are highly stable and prefer to occupy a tetrahedral site. Their radius is higher than the radius of a tetrahedral site. In the 'as prepared' ferrites, as the size of

the nanoparticles is very small, disorder is created, leading to a lowering of electrostatic energy, which results in Zn^{2+} and Mn^{2+} ions occupying the octahedral site and pushing the Fe^{3+} into the tetrahedral site. Therefore, the contraction in the A site will be more than the expansion of the octahedral B site.

4.4.2 Chemical Analysis

Chemical analysis is a fundamental characterization technique to confirm the presence of elements in their stoichiometric ratios. The primary step in characterizing any sample is to prove its stoichiometry and carry forward with further characterization. In our research work, chemical analysis was carried out using the ICP-AES instrument. Table 4.3 presents the theoretical and experimentally obtained percentages of 'as prepared' $Ni_{0.6-x}Mn_{0.4}Zn_xFe_2O_4$ (x=0.0, 0.1, 0.2, 0.3, 0.4, 0.5, 0.6) ferrites. The close agreement between these percentages confirms the stoichiometric accuracy of the synthesized compounds.

Table 4.3: Theoretical and experimental percentages of 'as prepared' $Ni_{0.6-x}Mn_{0.4}Zn_xFe_2O_4$ (x= 0.0, 0.1, 0.2, 0.3, 0.4, 0.5, 0.6) ferrites

Composition	**Ni^{2+} (%)**		**Mn^{2+} (%)**		**Zn^{2+} (%)**		**Fe^{3+} (%)**	
	Theoretical	Experimental	Theoretical	Experimental	Theoretical	Experimental	Theoretical	Experimental
0.0	15.12	14.50	9.40	9.30	-	-	47.90	47.17
0.1	12.50	12.20	9.40	10.0	2.80	1.58	47.82	47.30
0.2	10.02	10.30	9.37	9.40	5.58	4.70	47.68	47.70
0.3	7.49	6.80	9.34	9.87	8.41	7.42	47.50	46.74
0.4	4.98	5.05	9.32	9.54	11.10	11.3	47.40	48.00
0.5	2.48	1.92	9.29	9.50	13.80	14.20	47.20	48.10
0.6	-	-	9.27	10.00	16.50	17.10	47.10	47.17

4.4.3 Infrared spectroscopy

The infrared spectroscopy (IR) study was conducted of all the 'as prepared' and 'sintered' $Ni_{0.6-x}Mn_{0.4}Zn_xFe_2O_4$ (x=0.0, 0.1, 0.2, 0.3, 0.4, 0. 5, 0.6) ferrites. Fig. 4.13 represents the IR spectra of 'as prepared' ferrites, while Fig. 4.14 represents the IR spectra of the 'sintered' ferrites. The infrared spectrum for spinel ferrites with point group Fd*3m* usually shows four bands belonging to T_{1u} symmetry. The IR spectral data has been tabulated in Table 4.4.

Figure 4.13 shows two prominent absorption bands in the frequency absorption range of ~ 400-600 cm^{-1}. These bands are characteristic of spinel ferrites and confirm the phase purity of the ferrite samples. The absorption band at a higher frequency, represented as ν_1, roughly obtained at ~ 600 cm^{-1}, is due to the stretching of the metal-oxygen bond, where the metal is present at a tetrahedral site. The second band, ν_2, is caused by the metal-oxygen stretching vibration at the octahedral site. The absorption bands were observed in the range of ~ 412-579cm^{-1} in the 'as prepared' spectra. While in the case of 'sintered' samples, the IR frequency absorption band was in the range of ~ 412- 598 cm^{-1}. It is observed that with an increase in zinc concentration, the ν_1 shows a slight shift towards lower frequency values.

The sintered ferrite ν_1 band shows a decrease in values with an increase in zinc content or as nickel content is decreased. From the literature, it is known that nickel ions prefer to occupy an octahedral site [8], while zinc prefers a tetrahedral site because of its ability to form sp^3 covalent hybrid orbitals [9]. As the zinc content increases, the nickel content simultaneously decreases, making Fe^{3+} ions move into an octahedral site, which are present in the tetrahedral site initially, making space for the incoming Zn^{2+} ions. The increase in zinc content in the A-site increases the radius of the site; hence, there is a decrease in IR frequency. In the case of the ν_2 band, there was no significant decrease in the values, but a lowering trend was seen. During sintering, there are chances of volatilization of Zn^{2+} ions, leading to the formation of Fe^{2+} ions in the system. The occurrence of Fe^{2+} ions leads to deformation in the lattice, which is attributed to the Jahn-Teller effect. Therefore, in the case of sintered IR spectra, there is the presence of shoulder peaks indicating an excess of Fe^{2+} ions.

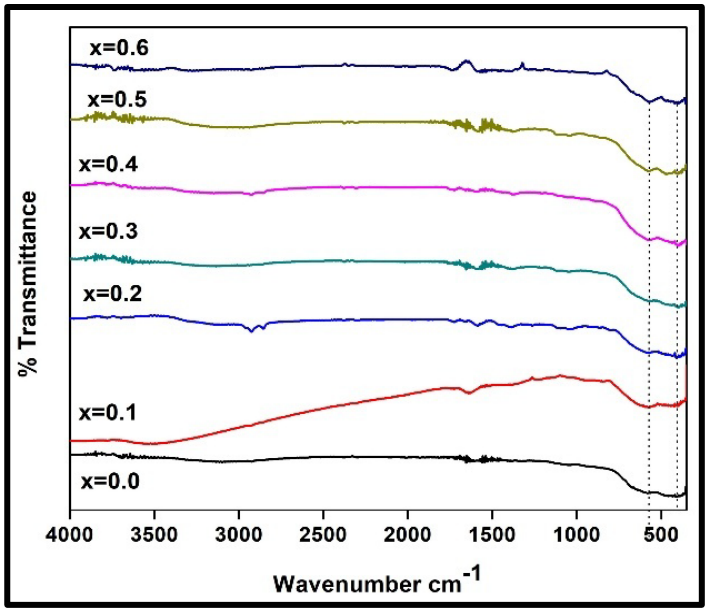


Fig. 4.13: IR spectra of 'as prepared' $Ni_{0.6-x}Mn_{0.4}Zn_xFe_2O_4$ (x=0.0, 0.1, 0.2, 0.3, 0.4, 0.5,0.6) ferrites

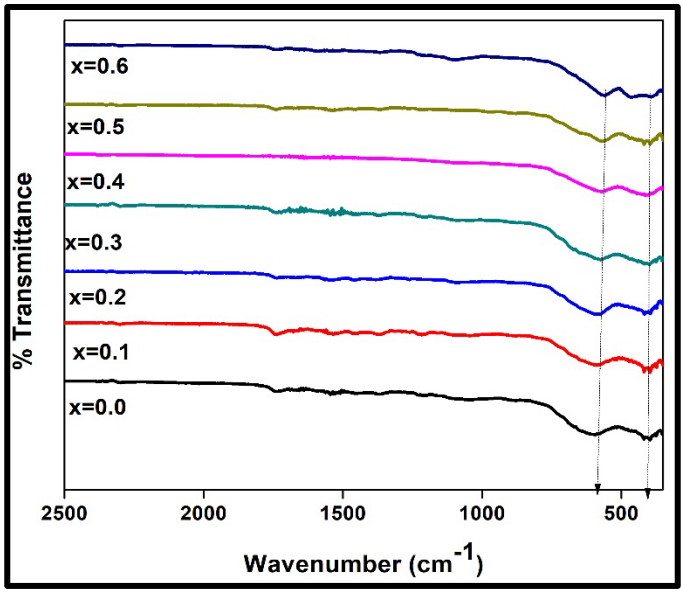


Fig. 4.14: IR spectra of 'sintered' $Ni_{0.6-x}Mn_{0.4}Zn_xFe_2O_4$ (x=0.0, 0.1, 0.2, 0.3, 0.4, 0.5, 0.6) ferrites

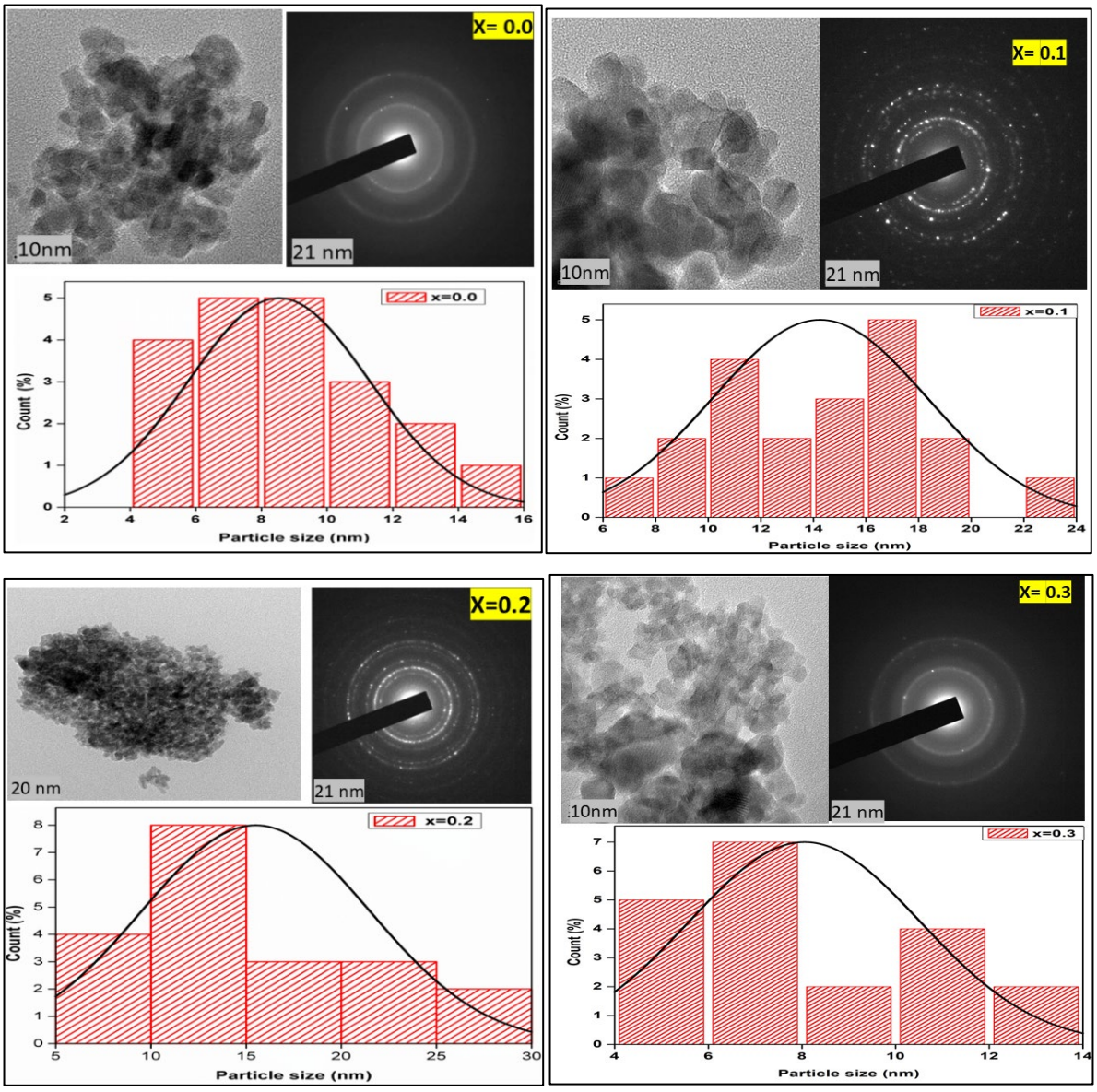
Table 4.4: IR data of 'as prepared' and 'sintered' $Ni_{0.6-x}Mn_{0.4}Zn_xFe_2O_4$ (x= 0.0, 0.1, 0.2, 0.3, 0.4, 0.5,0.6) ferrites

x	υ_1	υ_2	υ_1	υ_2
	'as prepared'		'sintered'	
0.0	579	415	598	430
0.1	575	423	596	415
0.2	579	412	581	413
0.3	563	398	579	415
0.4	579	397	573	415
0.5	579	464	568	412
0.6	579	415	562	412

4.4.4 Morphological Studies

4.4.4.1 High Resolution Transmission Electron Microscopy (HR-TEM)

The HR-TEM analysis of 'as prepared' $Ni_{0.6-x}Mn_{0.4}Zn_xFe_2O_4$ (x= 0.0, 0.1, 0.2, 0.3, 0.4, 0.5, 0.6) ferrites is depicted in Fig. 4.15 (x= 0.0- 0.6) along with their SAED patterns and histogram. The HR-TEM images showed agglomerated particles due to the particle's very fine, highly magnetic nature [10-12]. The particles exhibited irregular shapes and were difficult to distinguish as the size of the particles was relatively small, as indicated by the histogram. The histogram depicts the average particle size as 4-15 nm and can be correlated to the size obtained from powder XRD data. The Selected Area Electron Diffraction (SAED) patterns showed discontinuous concentric rings or bright spots, confirming the semi-crystalline nature of the samples. The particle size was evaluated from the histogram, and the size was comparable to powder XRD data. The nature of the material was semi-crystalline, as illustrated by the SAED pattern.


X= 0.0
10nm
21 nm
x=0.0
Count (%)
Particle size (nm)
X= 0.1
10nm
21 nm
x=0.1
Count (%)
Particle size (nm)
X=0.2
20 nm
21 nm
x=0.2
Count (%)
Particle size (nm)
X= 0.3
10nm
21 nm
x=0.3
Count (%)
Particle size (nm)

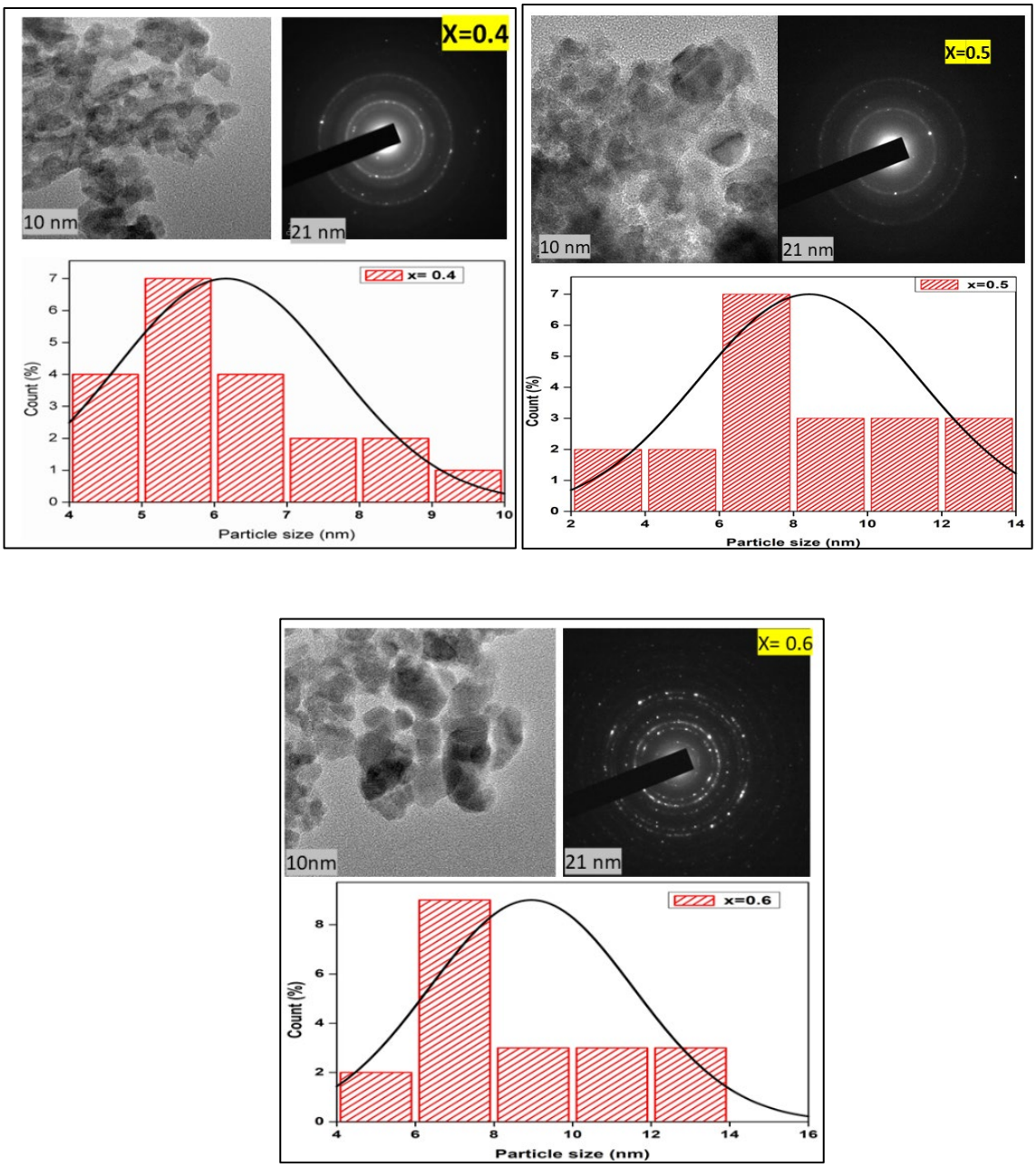


Fig. 4.15 HRTEM images, SAED pattern and histogram of 'as prepared' $Ni_{0.6-x}Mn_{0.4}Zn_xFe_2O_4$ (x=0.0, 0.1, 0.2, 0.3, 0.4, 0.5,0.6) ferrites

4.4.4.2 Scanning Electron Microscopy (SEM)

Surface morphology is a critical aspect of surface characterization. The SEM-EDX analysis revealed significant information regarding the same as presented in Fig. 4.16. SEM images revealed spherical to cuboidal morphology accompanied by noticeable agglomeration, which is attributed to the strong magnetic nature of the samples. As the zinc content increased, the agglomeration was minimized; therefore, the samples with high nickel content appeared bigger as compared to those with higher zinc content [13-15]. EDX analysis helps determine and confirm the presence of all the constituent elements in the ferrite samples in exact proportions. No impurity peaks were observed, indicating the purity of the synthesized materials. The peak that was obtained at 2.0- 2.5 eV is of Au, which was used as a coating material before analysis. Thus, apart from a peak of gold, no other material peaks were observed other than the elements present in the ferrite system. Additionally, the EDX images show that as the nickel content decreases, the intensity of the peak decreases, while for zinc, the peak intensity increases.

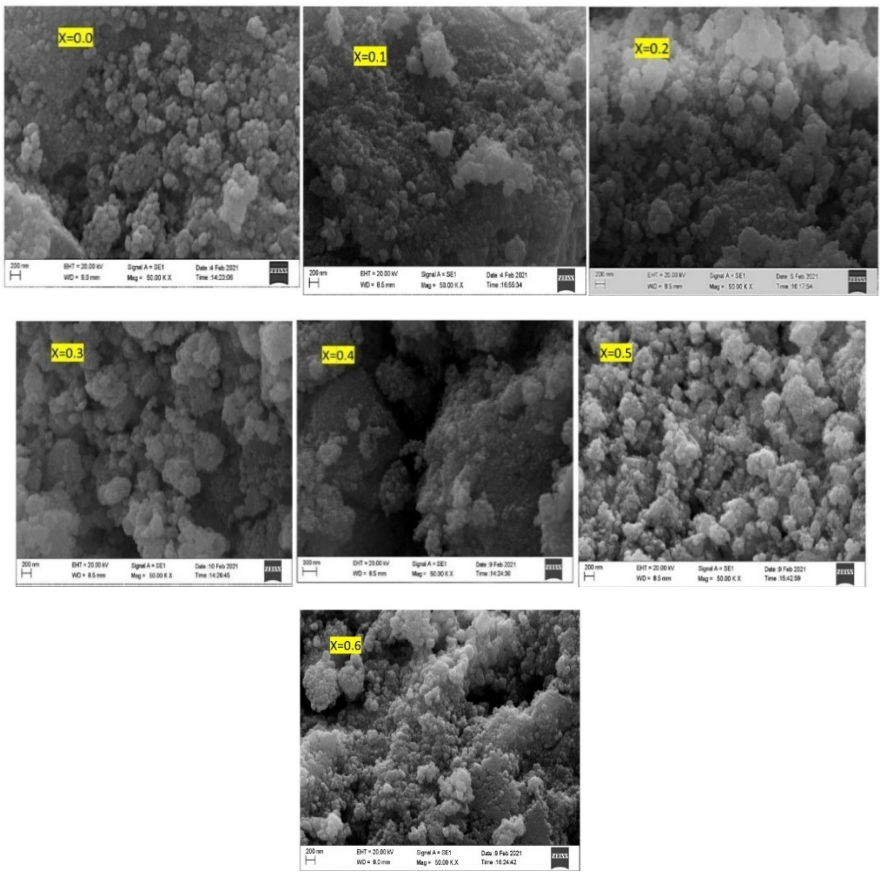


Fig. 4.16 a: SEM images of $Ni_{0.6-x}Mn_{0.4}Zn_xFe_2O_4$ (x=0.0, 0.1, 0.2, 0.3, 0.4, 0.5,0.6) ferrites

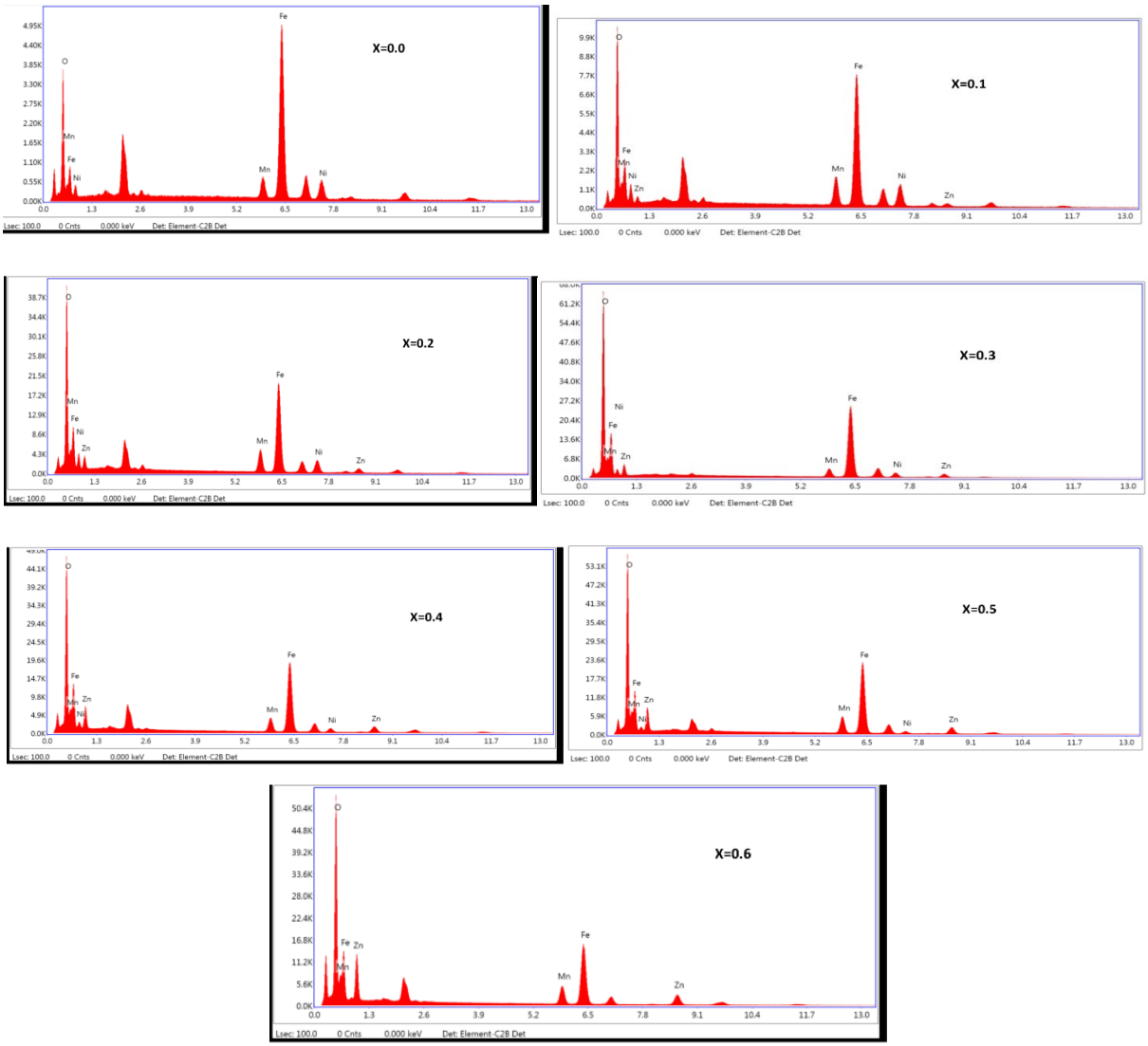


Fig. 4.16 b: EDX images of $Ni_{0.6-x}Mn_{0.4}Zn_xFe_2O_4$ (x=0.0, 0.1, 0.2, 0.3, 0.4, 0.5,0.6) ferrites

4.4.5 Surface area studies (BET Analysis)

The BET surface area studies were performed using the multipoint BET measurement system for all the 'as prepared' $Ni_{0.6-x}Mn_{0.4}Zn_xFe_2O_4$ (x=0.0-0.6) ferrites. Fig. 4.17 showcases the N_2 adsorption-desorption isotherm plotted for all the 'as prepared' samples ranging from x= 0.0-0.6. The surface areas of the samples x=0.0 to x=0.6 were 80, 128, 99, 72, 65, 58, 56 m^2/g, respectively. Considering the IUPAC nomenclature, the isotherms in Fig. 4.17 can be classified under Type IV isotherms with H3 hysteresis loop [16,17], indicating mesoporous structures having slit-like pores.

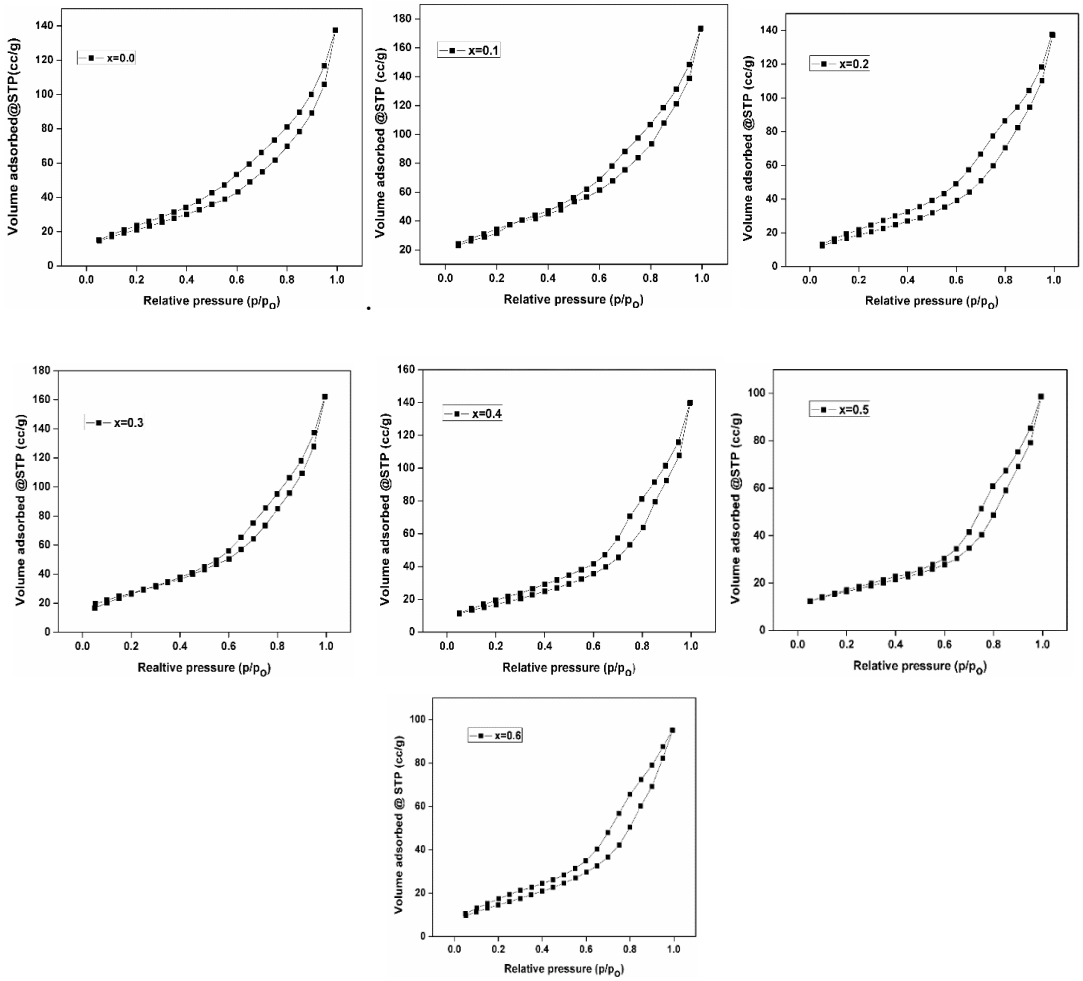


Fig. 4.17: The N_2 isotherm of 'as prepared'$Ni_{0.6-x}Mn_{0.4}Zn_xFe_2O_4$ (x=0.0, 0.1, 0.2, 0.3, 0.4, 0.5,0.6) ferrites

The Type IV isotherm results from adsorption on mesoporous solids that proceed via multilayer adsorption, and the H3 type hysteresis suggests the presence of aggregates (assemblages) of platelike particles forming slit-like pores. The initial increase in surface area observed from x= 0.0 to x= 0.1 suggested enhanced N_2 adsorption at lower zinc content. However, there was a continuous decrease in surface area with further increase in Zn ion concentration. The highest surface area obtained was 128.640 m^2/g for the ferrite sample x= 0.1, whereas the lowest surface area value was 56.671 m^2/g calculated for the compound having the highest Zn content, i.e., x=0.6. The surface area and crystallite size have an inverse relationship, which can also be seen from the obtained results. As the zinc content increases, the crystallite size increases, and the surface area declines, as confirmed by the crystallite size obtained from powder XRD pattern and the surface area obtained from BET surface area analysis.

4.4.6 Raman Spectroscopy

One of the essential tools for characterization of the samples is the Raman spectroscopy technique, which is sensitive to minute structural disorder while being non-destructive in nature. As a surface technique, it provides insights into the structural properties of the compounds by determining vibrational modes in the molecules; hence, it is also known as vibrational spectroscopy. The Raman analysis was conducted at room temperature (RT), and the results of the 'as prepared' and 'sintered' $Ni_{0.6-x}Mn_{0.4}Zn_xFe_2O_4$ (x=0.0, 0.1, 0.2, 0.3, 0.4, 0.5,0.6) ferrites have been depicted in Fig. 4.18 and Fig. 4.19 respectively, and the obtained Raman shift values for 'as prepared' ferrites are tabulated in Table 4.5.

The Raman analysis reveals three active Raman modes mainly ($A_{1g}+E_g+T_{2g}$). 'A' refers to one-dimensional representation, 'E' a two-dimensional representation, and 'T' for three-dimensional representation, and the subscript 'g' represents the symmetry concerning the inversion center. It is known in spinel ferrites that the bands observed in the spectral region above 600 cm^{-1} are said to arise from vibrations at the tetrahedral (A) site, while the bands in the lower region than 600 cm^{-1} are from the octahedral (B) site [18]. The band observed at high frequency corresponds to A_{1g}, mainly due to the symmetric stretching of oxygen atoms at the tetrahedral site.

The lower frequency band below 600 cm^{-1} is Eg, due to symmetric bending between M-O bonds, and T_{2g}, due to asymmetric stretching and asymmetric bending vibration between M-O bonds. [19]. In the present study, the E_g mode was observed in the 273-310 cm^{-1} range, the T_{2g} mode was obtained at 455-612 cm^{-1}, and the A_{1g} in the spectral range of 667-673 cm^{-1}. The Raman spectra also reveal that the A_{1g} (1) peak intensity decreases as the zinc content increases, while the peak intensity of the A_{1g} (2) peak shows a corresponding increase.

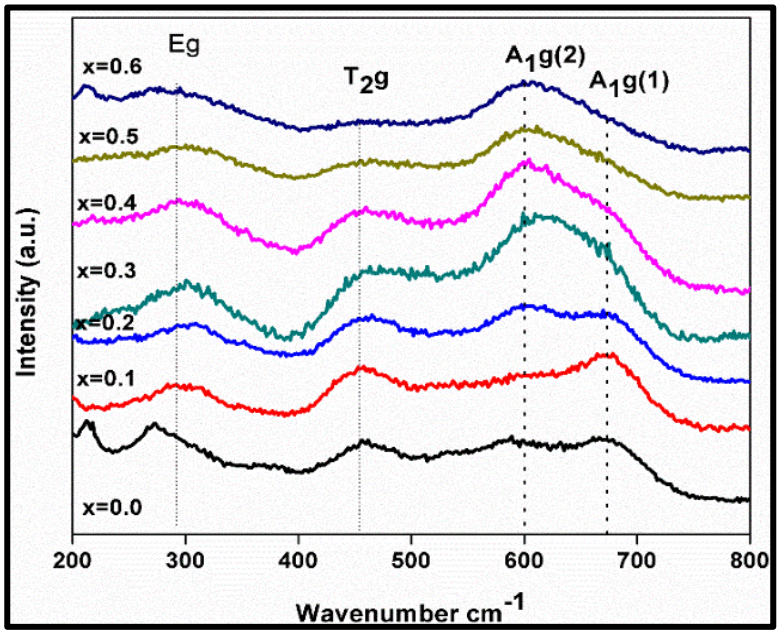


Fig. 4.18: Raman spectra of 'as prepared' $Ni_{0.6-x}Mn_{0.4}Zn_xFe_2O_4$ (x=0.0, 0.1, 0.2, 0.3, 0.4, 0.5,0.6) ferrites

The Raman analysis performed at RT of 'sintered' $Ni_{0.6-x}Mn_{0.4}Zn_xFe_2O_4$ (x=0.0, 0.1, 0.2, 0.3, 0.4, 0.5,0.6) ferrites is depicted in Fig. 4.19, and the corresponding values of the peaks are tabulated in Table 4.6. The A_{1g} modes appeared at frequency values beyond 600 cm^{-1} within the spectral range 605-681 cm^{-1}. These prominent peaks indicate the formation of single-phase (monophasic) samples. A noticeable shoulder peak around 600 cm^{-1} was observed, and as the zinc content is increased, the peak representing Fe-O stretching, i.e., A_{1g}(1) stretching, slowly diminishes. The force constant greatly causes a red shift or a blue shift. In the case of A_{1g} (1) peak, the Raman shift value is highest for a sample containing no Zn^{2+} ions, which can be explained by the fact that Fe^{3+} is equally distributed in octahedral and tetrahedral sites since there is no zinc. Therefore, the small size of Fe^{3+} ions and O^{2-} ions will have a high bond strength

among them, thus resulting in a high force constant in the tetrahedral site. Hence, with progressive zinc substitution, Fe^{3+} ions are slowly displaced towards the octahedral sites, which leads to a reduction in the force constant and hence a corresponding shift to lower Raman frequencies.

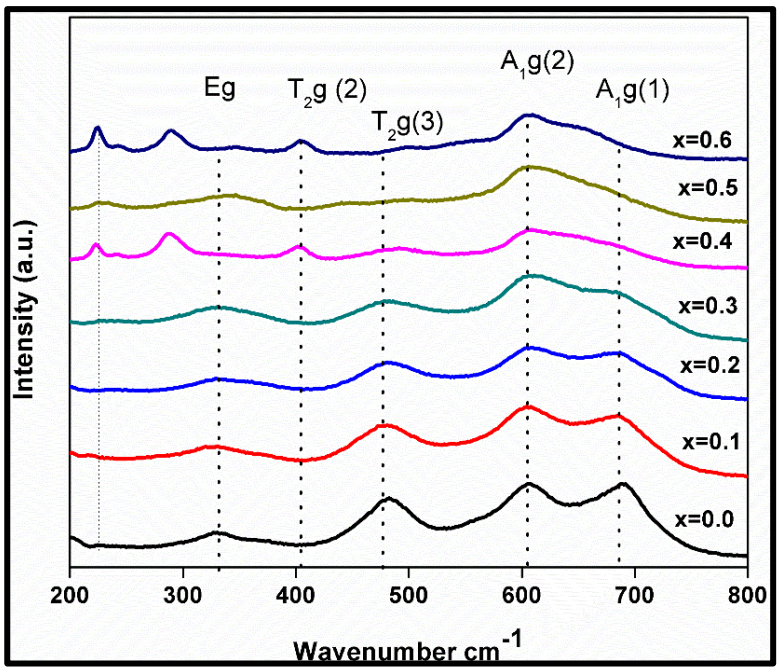


Fig. 4.19: Raman spectra of 'sintered' $Ni_{0.6-x}Mn_{0.4}Zn_xFe_2O_4$ (x=0.0, 0.1, 0.2, 0.3, 0.4, 0.5,0.6) ferrites

Table 4.5:-Raman active modes of 'as prepared' $Ni_{0.6-x}Mn_{0.4}Zn_xFe_2O_4$ (x=0.0, 0.1, 0.2, 0.3, 0.4, 0.5,0.6) ferrites

X	**0.0**	**0.1**	**0.2**	**0.3**	**0.4**	**0.5**	**0.6**
Eg	273	295	310	309	295	309	274
T_{2g}	459	455	463	465	460	460	460
$A_{1g}(2)$	588	591	599	-	-	-	-
$A_{1g}(1)$	667	673	668	-	-	-	-

Table 4.6: Raman active modes of 'sintered' $Ni_{0.6-x}Mn_{0.4}Zn_xFe_2O_4$ (x=0.0, 0.1, 0.2, 0.3, 0.4, 0.5,0.6) ferrites

X	0.0	0.1	0.2	0.3	0.4	0.5	0.6
Eg	344	324	330	332	288	288	290
T_{2g}	498	480	481	481	493	495	500
A_{1g} (2)	605	607	607	609	605	607	607
A_{1g} (1)	687	688	681	-	-	-	-

4.4.7 X-Ray Photoelectron Spectroscopy

XPS is a sophisticated surface-sensitive technique used to determine the presence of all the elements in the system in their respective chemical state within a material. In this study, XPS was utilized to analyze the 'as prepared' $Ni_{0.6-x}Mn_{0.4}Zn_xFe_2O_4$ (x=0.0, 0.1, 0.2, 0.3, 0.4, 0.5,0.6) ferrites. The full scan XPS spectrum of the elements is presented in Fig. 4.20, which shows the presence of Ni, Mn, Zn, Fe, and O in all the ferrites without any additional peaks, thereby indicating the formation of a pure phase. A minor peak is seen for carbon (C) in the spectrum, which must have come from deposited carbon during sample preparation for XPS analysis. XPS works on the principle that the binding energy of the core electron ejected is characteristic of the specific element.

The photoelectron peaks of Ni 2p, Mn 2p, Zn 2p, Fe 2p, and O 1s, along with their satellite peak, confirmed the Ni, Mn, and Zn to be in their respective 2+ oxidation state, while Fe was in the 3+ oxidation state. The full scan spectra 'as prepared' $Ni_{0.6-x}Mn_{0.4}Zn_xFe_2O_4$ (x=0.0, 0.1, 0.2, 0.3, 0.4, 0.5, 0.6) ferrites has been shown in Fig. 4.20. The resolved (deconvoluted) spectra of individual elements are depicted in Fig. 4.21-Fig. 4.25 for all the $Ni_{0.6-x}Mn_{0.4}Zn_xFe_2O_4$ (x= 0.0, 0.1, 0.2, 0.3, 0.4, 0.5,0.6) ferrites and corresponding peak values are tabulated in Table 4.7-4.10.

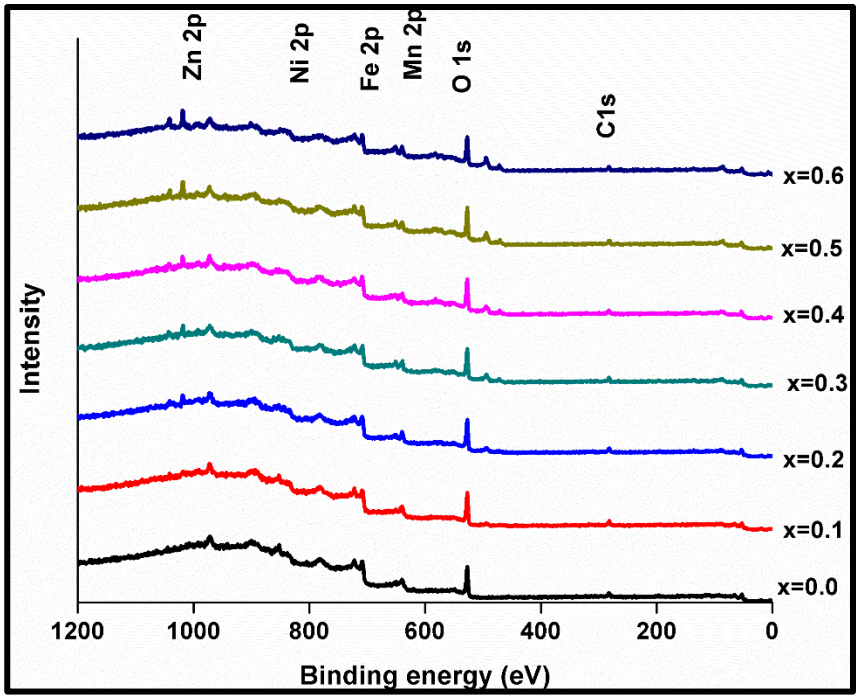


Fig. 4.20: Full scan spectra of 'as prepared' $Ni_{0.6-x}Mn_{0.4}Zn_xFe_2O_4$ (x=0.0, 0.1, 0.2, 0.3, 0.4, 0.5, 0.6) ferrites

The XPS spectra of Mn $^{2+}$ in $Ni_{0.6-x}Zn_xMn_{0.4}Fe_2O_4$ (x= 0.0, 0.1, 0.2, 0.3, 0.4, 0.5, 0.6) ferrites are depicted in Fig. 4.21 and their corresponding binding energies are tabulated in Table 4.7. The core level emission peaks are observed at ~642 eV, which corresponds to Mn^{2+} $2p_{3/2}$, and the second peak is observed at ~ 653 eV, which is due to Mn^{2+} $2p_{1/2}$. The presence of a satellite peak confirms the valence state of Mn to be 2+ [20,21]. Literature reports show the satellite peak ~ 4.5 eV higher than the central peak. We observed the satellite peak ~ 2.3- 4 eV higher than the main Mn^{2+} $2p_{3/2}$ peak. With an increase in zinc, the difference between the two peaks decreased.

The deconvoluted spectra of Zn^{2+} for all the $Ni_{0.6-x}Mn_{0.4}Zn_xFe_2O_4$ (x=0.0, 0.1, 0.2, 0.3, 0.4, 0.5, 0.6) are represented in Fig. 4.22, whose corresponding values of binding energy are tabulated in Table 4.8. The fitted Zn^{2+} spectra show two distinct peaks corresponding to Zn $2p_{3/2}$ at ~1021eV and Zn $2p_{1/2}$ at ~1044eV. The difference in the two peaks representing the spin-orbit splitting energy is ~ 23eV in all the recorded samples and agrees with the reported data [22]. The presence of two signals in the spectra confirms the 2+ oxidation state of Zn in the samples [23, 24].

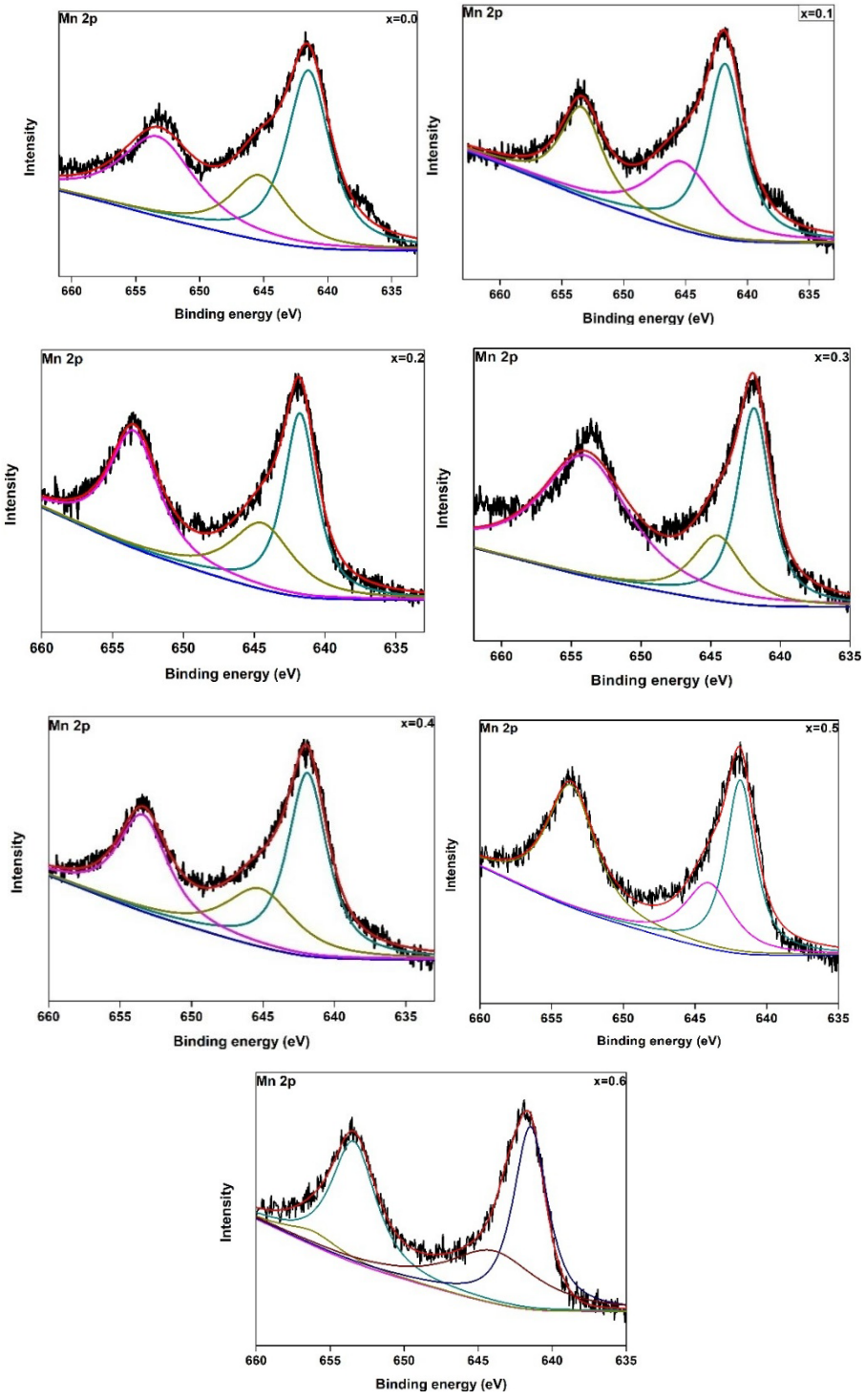


Fig. 4.21: The deconvoluted XPS spectra of Mn for all the 'as prepared' $Ni_{0.6-x}Mn_{0.4}Zn_xFe_2O_4$ (x=0.0, 0.1, 0.2, 0.3, 0.4, 0.5, 0.6) ferrites

Table 4.7: Binding energies of $Mn^{2+}2p_{3/2}$ and $2p_{1/2}$ along with their satellite peaks.

x	Binding energy (eV)		
	Mn^{2+} $2p_{3/2}$	Mn^{2+} $2p_{3/2}$ (Sat. peak)	Mn^{2+} $2p_{1/2}$
0.0	641.5	645.0	653.0
0.1	641.8	645.3	653.4
0.2	641.7	644.6	653.5
0.3	641.8	644.5	654.0
0.4	641.9	645.3	653.4
0.5	641.8	644.1	653.7
0.6	641.8	644.3	653.4

The resolved spectra of O1s for $Ni_{0.6-x}Mn_{0.4}Zn_xFe_2O_4$ (x=0.0, 0.1, 0.2, 0.3, 0.4, 0.5, 0.6) are depicted in Fig. 4.23 with data in Table 4.8. It is revealed that the O1s peak is split into two peaks, one at ~529eV, while the other at 531eV. The ferrite samples x= 0.3 and x= 0.5 also show a further splitting of the 531 peak. The peak at ~529eV is of oxygen in the lattice, while the shoulder peak is due to surface adsorbed oxygen or defects in the ferrite oxide.

Table 4.8: Binding energies of Zn^{2+} $2p_{3/2}$, $2p_{1/2}$, and O1s

x	Binding energy (eV)			
	Zn^{2+} $2p_{3/2}$	Zn^{2+} $2p_{1/2}$	O 1s	O1s
0.0	-	-	529.5	531.0
0.1	1021.2	1044.4	529.7	531.1
0.2	1021.0	1044.2	529.5	531.1
0.3	1021.2	1044.2	529.8	531.1
0.4	1021.4	1044.3	529.6	531.1
0.5	1021.1	1044.4	529.4	531.4
0.6	1021.0	1044.1	529.4	531.1

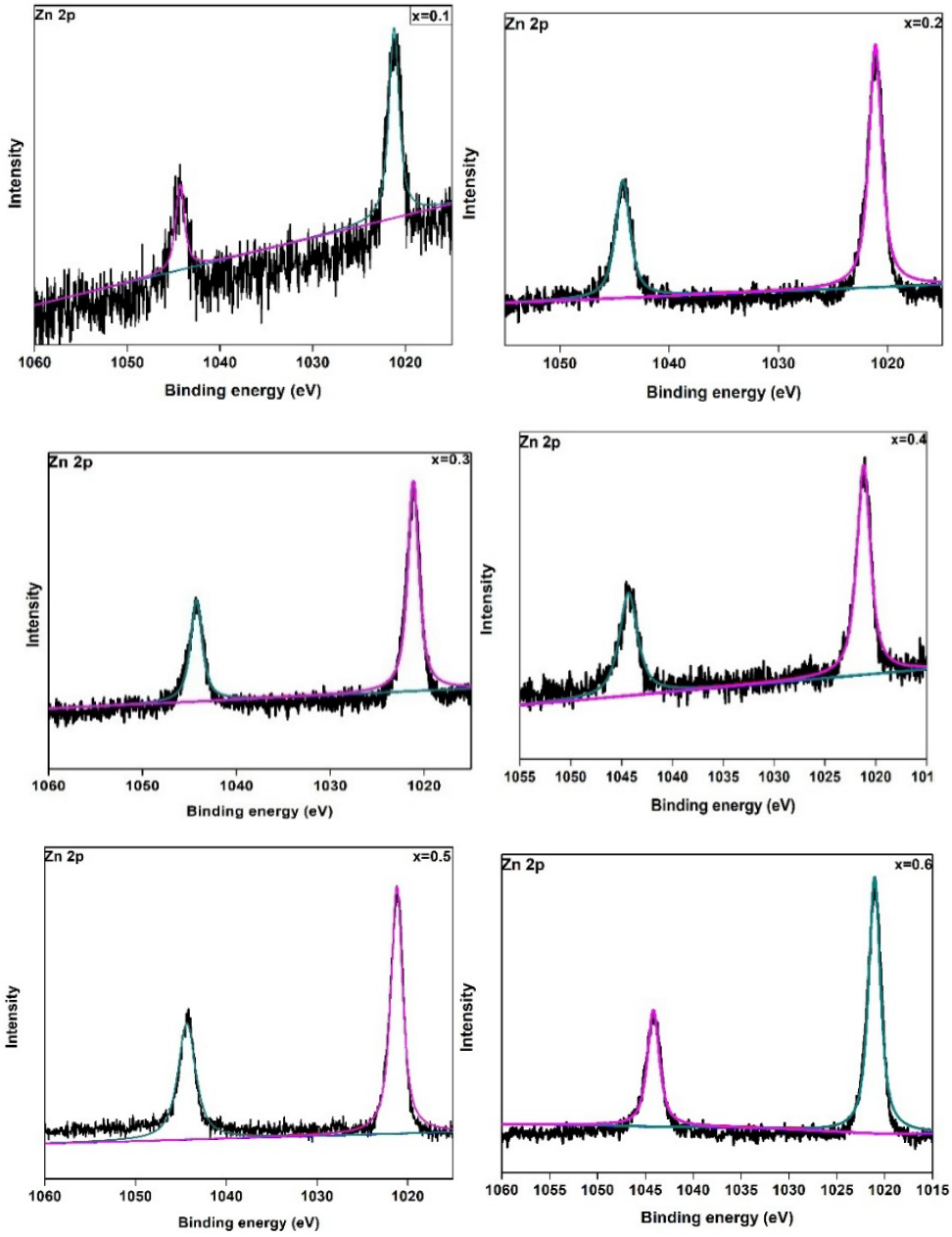


Fig. 4.22: The deconvoluted XPS spectra of Zn 2p for all the 'as-prepared' $Ni_{0.6-x}Mn_{0.4}Zn_xFe_2O_4$ (x=0.0, 0.1, 0.2, 0.3, 0.4, 0.5, 0.6) ferrites

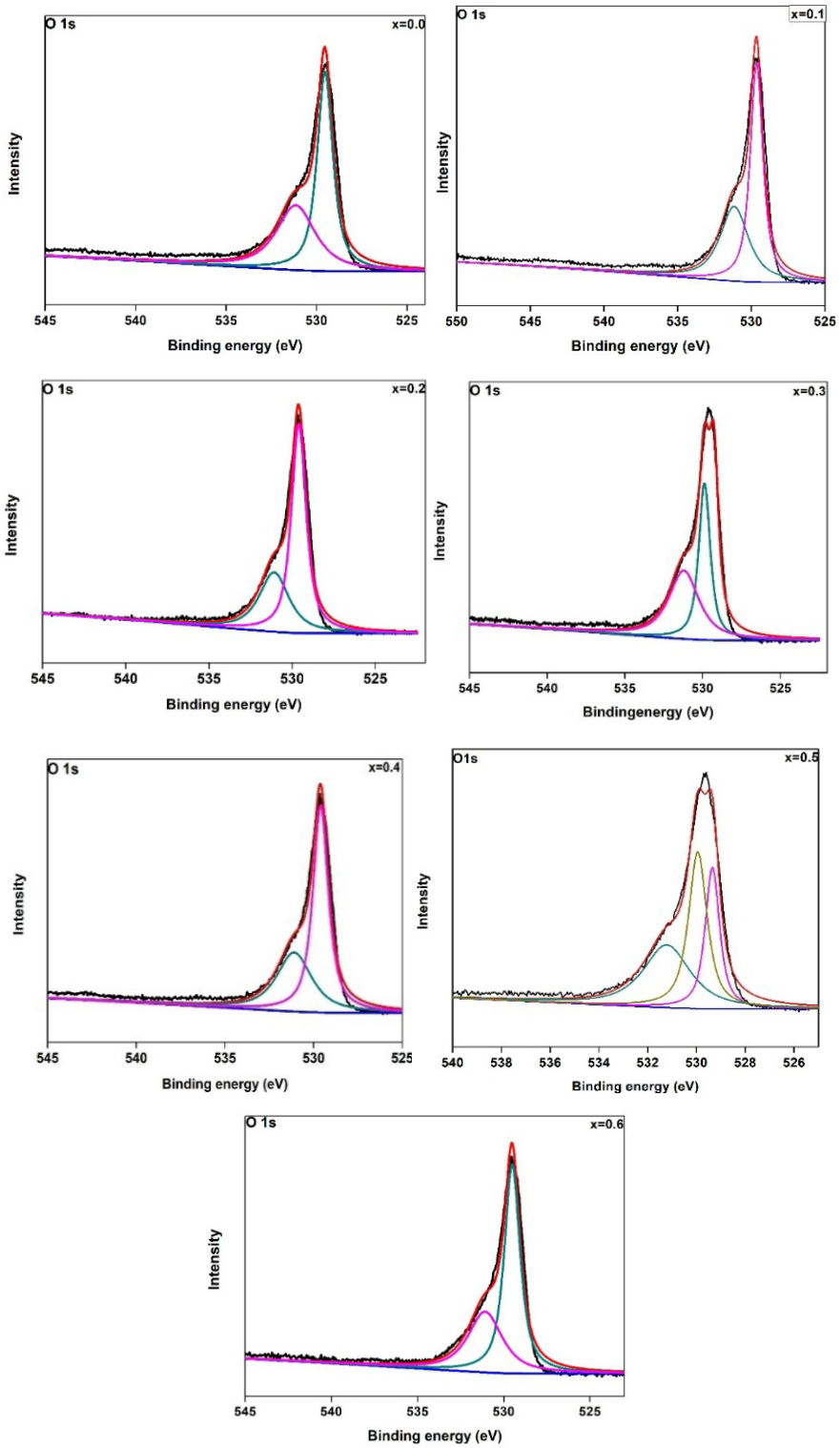


Fig. 4.23: The deconvoluted XPS spectra of O 1s for all the 'as prepared' $Ni_{0.6-x}Mn_{0.4}Zn_xFe_2O_4$ (x=0.0, 0.1, 0.2, 0.3, 0.4, 0.5, 0.6) ferrites

Table 4.9: Binding energies of $Ni^{2+}2p_{3/2}$ and Ni^{2+} $2p_{1/2}$ along with their satellite peak

x	Binding energy (eV)			
	Ni^{2+} $2p_{3/2}$	Sat. peak Ni^{2+} $2p_{3/2}$	Ni^{2+} $2p_{1/2}$	Sat. peak Ni^{2+} $2p_{1/2}$
0.0	855.0	861.1	872.6	879.4
0.1	855.2	861.4	872.8	-
0.2	854.7	861.1	-	879
0.3	854.7	860.7	-	-
0.4	854.8	861.1	872.6	879.4
0.5	854.7	-	-	-
0.6	-	-	-	-

The fitted spectra of Ni^{2+} for all the 'as prepared' $Ni_{0.6-x}Mn_{0.4}Zn_xFe_2O_4$ (x=0.0, 0.1, 0.2, 0.3, 0.4, 0.5, 0.6) ferrites are illustrated in Fig. 4.24, and binding energies of the deconvoluted peaks are given in Table 4.9. The two spin-orbit peak was observed at ~855 eV and ~872eV corresponding to Ni $2p_{3/2}$ and Ni $2p_{1/2}$ respectively alongside the prominent peaks corresponding satellite peaks were also observed at ~861eV and ~879eV these shake up like peaks helps determine the valence state if Ni in the samples and confirms it to be in 2+ state [25,26]. The Ni $2p_{3/2}$ peak appears at 855eV, but in a few samples it is observed at ~854 eV. Although the value is a little lower than expected, it is still present in the spinel structure, which is confirmed by the peak shape; the peak Ni $2p_{3/2}$ does not show any shoulder peak. And the possibility of having NiO is also ruled out as its value comes much lower [27].

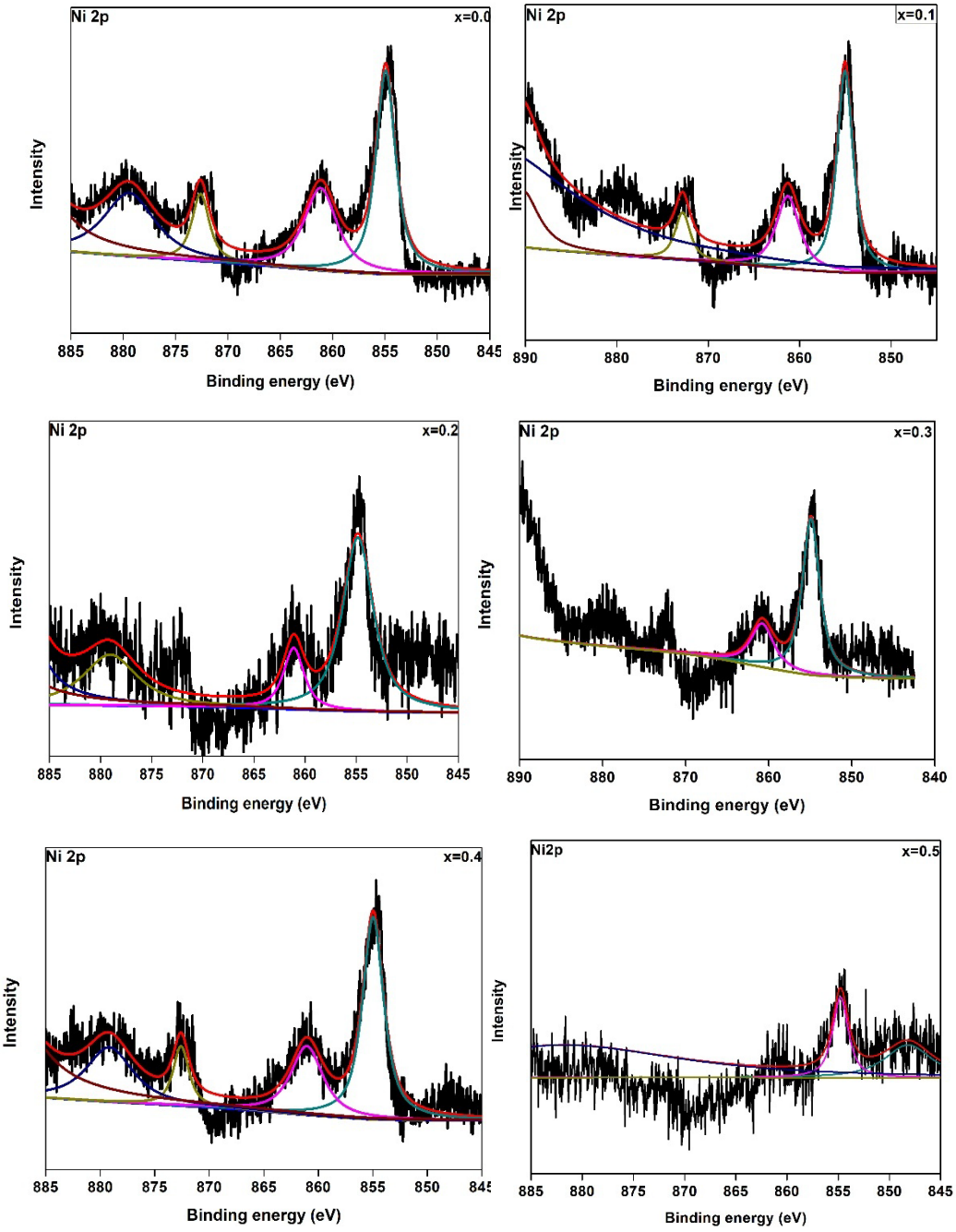


Fig. 4.24: The deconvoluted XPS spectra of Ni 2p for all the 'asprepared' $Ni_{0.6-x}Mn_{0.4}Zn_xFe_2O_4$ (x=0.0, 0.1, 0.2, 0.3, 0.4, 0.5, 0.6) ferrites

The XPS analysis of Fe 2p for all the $Ni_{0.6-x}Mn_{0.4}Zn_xFe_2O_4$ (x=0.0, 0.1, 0.2, 0.3, 0.4, 0.5, 0.6) ferrites is evaluated from the deconvoluted spectrum represented in Fig. 4.25. Tougaard's background subtraction for the Fe 2p was considered. The Fe 2p exhibited two prominent peaks, including Fe $2p_{3/2}$ and Fe $2p_{1/2}$ ~13eV apart due to spin-orbit coupling [28]. The first peak was further resolved into a multi-component peak. The peak appeared at ~710 eV, corresponding to Fe at the octahedral site, while the peak at ~713 eV corresponds to Fe at the tetrahedral site. The peak obtained alongside this main peak is the shake-up-like satellite peak at ~718 eV. This peak, 8 eV higher than the main peak, confirms Fe in a 3+ valence state. The $2p_{1/2}$ peak appears at ~724 eV due to Fe present in the cathedral site, while the split peak appears at ~726 eV, which is due to Fe in the tetrahedral site. The satellite peak at ~732 eV is also present alongside the main peak [29-31]. No peaks were obtained at binding energies of 708 eV and 709 eV, ruling out the occurrence of Fe in the 2+ oxidation state.

Table 4.10: Binding energies of $Fe^{3+}2p_{3/2}$ and $2p_{1/2}$ along with their satellite peaks

x	**Binding energy (eV)**					
	Fe^{3+} $2p_{3/2}$ (Octahedral)	Fe^{3+} $2p_{3/2}$ (Tetrahedral)	Sat. peak Fe^{3+} $2p_{3/2}$	Fe^{3+} $2p_{1/2}$ (Octahedral)	Fe^{3+} $2p_{1/2}$ (Tetrahedral)	Sat.. peak Fe^{3+} $2p_{1/2}$
0.0	709.9	712.0	718.4	724.4	727.0	732.8
0.1	710.3	712.5	718.0	724.0	727.0	732.9
0.2	710.2	712.1	718.1	724.5	724.5	732.5
0.3	709.9	712.8	718.5	724.2	724.3	733.2
0.4	710.0	713.6	718.2	724.5	727	732.9
0.5	710.5	712.6	718.3	724.2	726.8	733.5
0.6	710.4	712.4	718.1	725.2	725.2	732.9

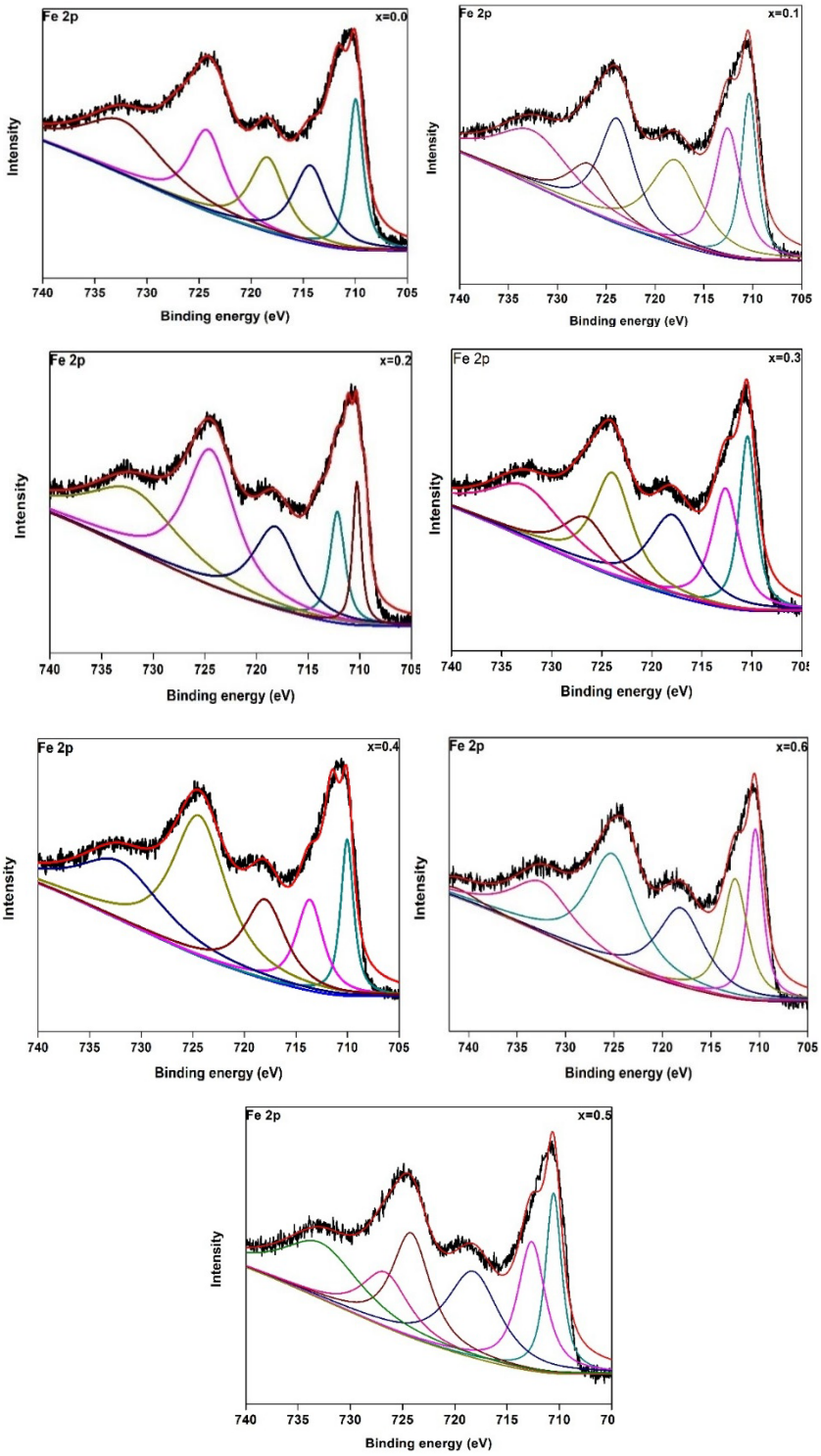


Fig. 4.25: The deconvoluted XPS spectra of Fe 2p for all the 'as prepared' $Ni_{0.6-x}Mn_{0.4}Zn_xFe_2O_4$ (x=0.0, 0.1, 0.2, 0.3, 0.4, 0.5, 0.6) ferrites

4.5 Solid-state properties of 'as prepared' and 'sintered' $Ni_{0.6-x}Mn_{0.4}Zn_xFe_2O_4$ (x= 0.0, 0.1, 0.2, 0.3, 0.4, 0.5, 0.6) ferrites.

4.5.1 DC Electrical Resistivity

4.5.1.1 DC Electrical Resistivity of 'as prepared' and 'sintered' $Ni_{0.6-x}Mn_{0.4}Zn_xFe_2O_4$ (x= 0.0, 0.1, 0.2, 0.3, 0.4, 0.5, 0.6) ferrites.

The DC resistivity studies for 'as prepared' and 'sintered' $Ni_{0.6-x}Mn_{0.4}Zn_xFe_2O_4$ (x=0.0, 0.1, 0.2, 0.3, 0.4, 0.5, 0.6) ferrites were conducted in the range of RT-500 °C during heating as well as cooling, and the plots are illustrated in Fig. 4 .26a and Fig. 4.26 b. The plots of log resistivity vs. 1/T*1000 (K^{-1}) showcase the electrical resistivity behavior concerning temperature, which depicts the semiconducting nature of the samples. It was observed that the resistivity decreases with increasing temperature following Arrhenius-type behavior. Due to the rise in temperature, the collision between ions increases; thus, the conductance and resistance decrease. The measured resistivity values obtained are of the order 10^3–10^5ohm cm. The resistivity of a sample is influenced by several factors such as synthesis technique, composition, size, shape, distribution of ions, etc., all of which can change material's behaviour [32,33,34].

The Verwey model [35] explains the electrical conductivity of ferrites, according to which the electron hopping is involved between the same metal having different valence states. The structure of spinels is such that the anion, i.e., oxygen, forms a closed pack lattice, while the metal occupies the tetrahedral [A] site and octahedral sites [B]. The metals present in tetrahedral and octahedral sites are secluded from each other. The distance between the cations in the A site is larger than the B-B distances. Thus, electron hopping is favorable between metal ions of mixed valence at the B-sites, allowing electrical conductivity.

Hence, the hopping between Fe^{2+} and Fe^{3+} occurs in the octahedral B site and is responsible for conduction [36, 37]. Apart from electron jump, conductivity is also influenced by particle size, grains, and grain boundaries, the dopant metal, and its concentration [38, 39]. Fig. 4.26a depicts the plot of log resistivity vs. 1/T for 'as prepared' ferrites showing a continuous drop in resistivity with increased temperature. This indicates the semiconductor behavior of the samples. The sample x=0.6 shows a slightly different approach; resistivity at the beginning is

lower, and with an increase in temperature, it increases slightly, reaches a maximum, and then starts decreasing. Such a trend can be due to the presence of pores in the loosely agglomerated sample, which leads to trapped moisture [40, 41]. The continuous increase in temperature leads to evaporation of the moisture, after which a decline is noticed. At RT, the resistivity was found to be lower due to protonic conductivity because of the moisture in the samples, as reported by others [42, 43]. This kind of observation has been reported in the literature for Fe_2O_3 material having high moisture [44]. Furthermore, an increase in temperature results in a linear resistivity plot exhibiting a negative temperature coefficient of resistance behavior [45]. The effect of Zn concentration on the DC resistivity of the 'as prepared' ferrites did not show a consistent trend. Thus, one can conclude that in 'as prepared' ferrites, the particle size, porosity, and entrapped moisture predominantly influence the resistivity rather than Zn content alone.

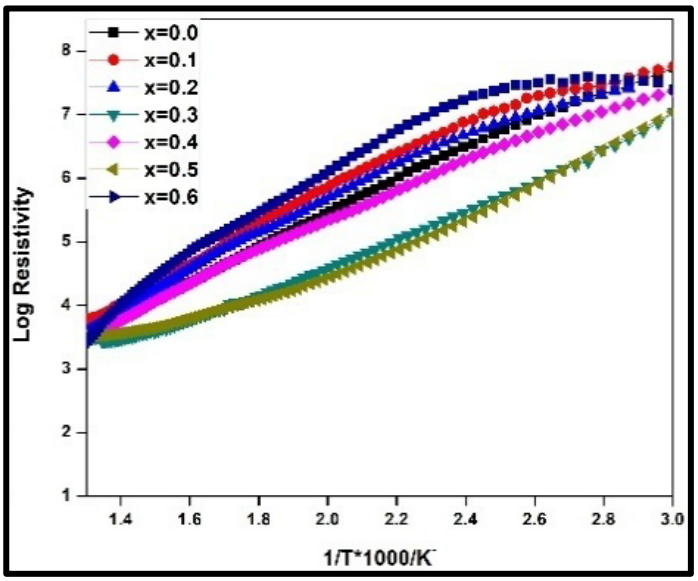


Fig 4.26a: Plots of log resistivity vs. 1/T during heating and cooling for 'as prepared' $Ni_{0.6-x}Mn_{0.4}Zn_xFe_2O_4$ (x= 0.0, 0.1, 0.2, 0.3, 0.4, 0.5, 0.6) ferrites

In the case of 'sintered' ferrites, a semiconducting trend is observed similar to that of the prepared, as shown in 4.26 b (sintered) for heating and cooling analysis. Verwey's hopping mechanism can explain the resistivity in ferrites. According to this mechanism, an electron hop occurs between the same elements having variable oxidation states. The electron jumps from the A site to the B site, or the electron hops between the B sites. The probability of B-B interaction is much higher due to the shorter distance between the elements at the B-site.

According to the literature, Ni^{2+} ions prefer the octahedral site, while Fe^{3+} ions are present in both tetrahedral (A) and octahedral (B) sites. Mn^{2+} ions are usually found in the tetrahedral site, but can also be at the octahedral site, while Zn^{2+} strongly prefers the tetrahedral location. As zinc is doped into the system, it occupies the tetrahedral site, which ultimately pushes the Fe^{3+} ions into the octahedral site. As more and more Fe^{3+} is shifted to the B site, the hopping of electrons becomes more accessible and probable. Thus, conductivity increases, reducing the resistivity [46, 47]. In the case of the 'as prepared' ferrites of the cooling curve at approximately 546K, it is observed that the value of resistivity decreased from x= 0.0 to x= 0.1 and further increased for sample x= 0.2, after which a continuous decrease was obtained till x=0.6. Mn-Zn ferrite has the lowest resistivity in the series, consistent with previously reported trends in the literature [48].

In the case of the sintered heating curve at RT, the resistivity value is higher than that of the 'as prepared' ferrites. Generally, the observed trend in sintered ferrite is that the resistivity value for sintered ferrite is lower than that of 'as prepared' ferrites, i.e., the particle sizes are smaller, and the resistivity is higher. Other than grain size, other factors contribute to the higher value of sintered samples. As the sintering process is done at high temperatures, the amorphous, semi-amorphous compound changes to a highly crystalline compound, which leads to improved structures and fewer imperfections. However, when the cooling curves of sintered ferrite were compared with 'as prepared' ferrite samples, it was observed that 'sintered' samples showed lower resistivity values, which corresponded with the grain size trend.

The compositional variation of resistivity with zinc substitution indicates a decreasing trend in the case of sintered ferrite. This observation is explained based on the distribution of cations in the octahedral and tetrahedral sites. The iron in ferrite samples is present as Fe^{3+}, while Mn is 2+. During the sintering of the sample, due to the volatile nature of Zn^{2+} ions, there is the possibility of introducing Mn^{3+} ions, creating an imbalance of charge in the system. To maintain such a charge imbalance, Fe^{3+} ions are converted to Fe^{2+}, resulting in increased conductivity due to increased hopping of electrons between Mn^{2+} and Mn^{3+} and Fe^{2+} and Fe^{3+}. During sintering, the grains come together to form one whole mass, which reduces the total surface energy of the system. Thus, sintering affects the grain size, and therefore, it increases. And the resistivity is often lower [46, 47]. But in our case, the sintered ferrite shows a higher resistivity

value than the 'as prepared'. This trend suggests that the lower resistivity values at RT for 'sintered' ferrites are due to a factor other than grain size. Thus, sintering leads to structural improvement and fewer imperfections. Therefore, one can suggest that improved structure is responsible for increased resistivity [48]. However, as the temperature increases, the usual trend for both 'as prepared' and 'sintered' samples is observed. At higher heating temperatures, the 'sintered' ferrites show lower resistivity values than the 'as prepared' ferrites, which is attributed to enhanced microstructure and reduced grain boundary resistance.

This means that grain size is responsible at higher temperatures, i.e., the 'as prepared' ferrites have a smaller grain size; therefore, the grain boundaries will be more significant. These grain boundaries are insulating in nature and hence act as scattering centers, increasing the resistance towards the flow of electrons [49].

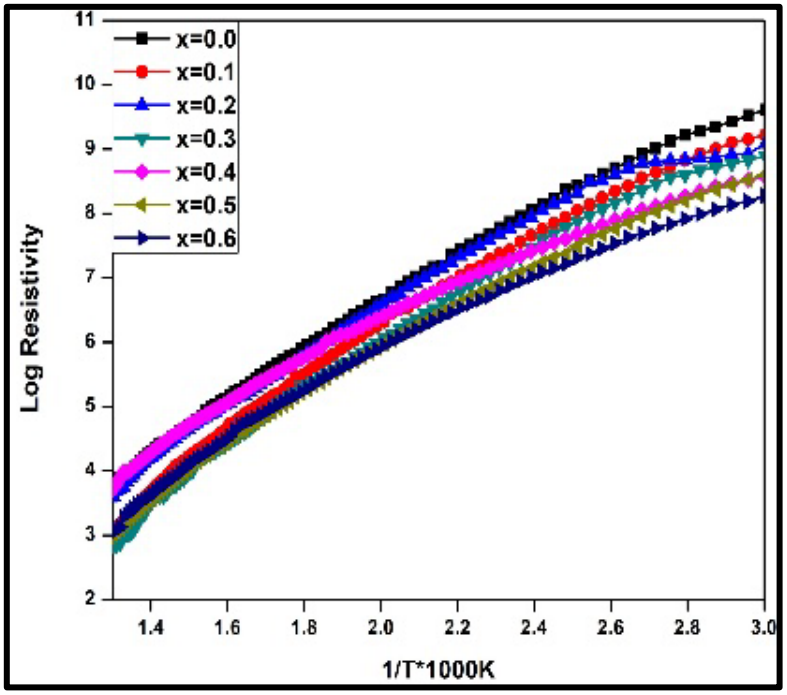


Fig 4.26b: Plots of log resistivity vs. 1/T during heating and cooling for 'sintered' $Ni_{0.6-x}Mn_{0.4}Zn_xFe_2O_4$ (x= 0.0, 0.1, 0.2, 0.3, 0.4, 0.5, 0.6) ferrites

4.5.2 AC Susceptibility studies

The AC susceptibility measurements of the 'as prepared' as well as the 'sintered' $Ni_{0.6-x}Mn_{0.4}Zn_xFe_2O_4$ (x=0.0, 0.1, 0.2, 0.3, 0.4, 0.5, 0.6) ferrites have been carried out from room temperature to 850 K. Temperature-dependent AC susceptibility measurements were performed to obtain information on their domain structure and Curie temperature. The plots of ac susceptibility v/s temperature for 'as prepared' and 'sintered' ferrites in Kelvin are depicted in Fig. 4.27a and Fig. 4.27b, respectively. It is observed from figures that the material shows a domain structure with a steady increase in susceptibility with an increase in temperature, whereas, in the case of sintered samples, a multi-domain type of particles is observed with negligible single domain particles, which might be due to increased grain sizes and improved magnetic interactions resulting from the sintering process.

In both 'as prepared' and 'sintered' ferrite samples, it is seen that with an increase in thermal energy, the spin gets randomized more quickly until a point after which the sample completely loses its magnetization and becomes demagnetized. This point is called Curie temperature; it is at which the orderly arrangement of magnetic moments of the magnetic domain is destroyed, the magnetic domain collapses, and the average magnetic moment becomes zero. At the Curie temperature, there is a gradual fall in susceptibility values in the case of 'as prepared' samples, whereas a sharp fall is observed for sintered samples [50].

The Curie temperature was determined from AC susceptibility measurements, and the values are summarized in Table 4.11. The values of Tc greatly depend on the metal ions present and the occupation of those ions at different sites; this, in turn, relies on the synthesis technique utilized, the temperature at which calcination occurred, and the size of the particles [51]. It can be observed from the Fig.4.27a and Fig. 4.27b that both 'as prepared' and 'sintered' ferrites samples show a similar trend, i.e., with an increase in zinc content, the Tc values decrease up to x= 0.5, and for a sample containing x= 0.6, which Manganese zinc ferrite the Tc again increased, except for as-prepared x=0.3 sample which shows a sudden increase disrupting the trend.

The Curie temperature values obtained for the 'as prepared' ferrites are higher than those obtained for their 'sintered' analogues. This trend can be correlated to the lattice parameter, and it is known that it has an inverse relation to the Curie temperature.

The doping of zinc ions having higher ionic radii increases the lattice parameter in the series and the interatomic distance between the magnetic ions on the A and B lattice, decreasing the super-exchange interactions, thus decreasing T_c. Besides, the decrease in Curie temperature with zinc substitution is clearly seen in the 'sintered' samples persistent with the expected behavior depending on their structural and magnetic interactions.

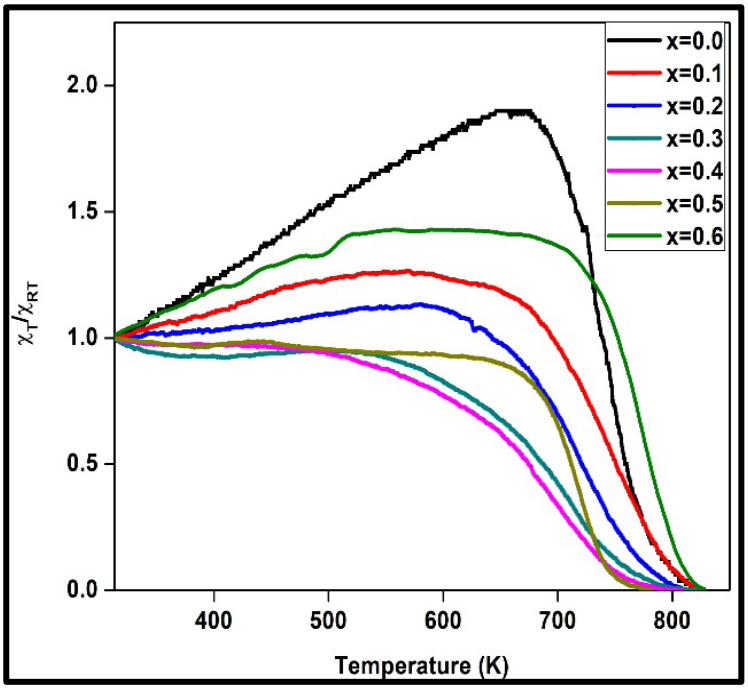


Fig.4.27 a: AC susceptibility plots of 'as prepared' $Ni_{0.6-x}Mn_{0.4}Zn_xFe_2O_4$ (x=0.0-0.6) ferrites

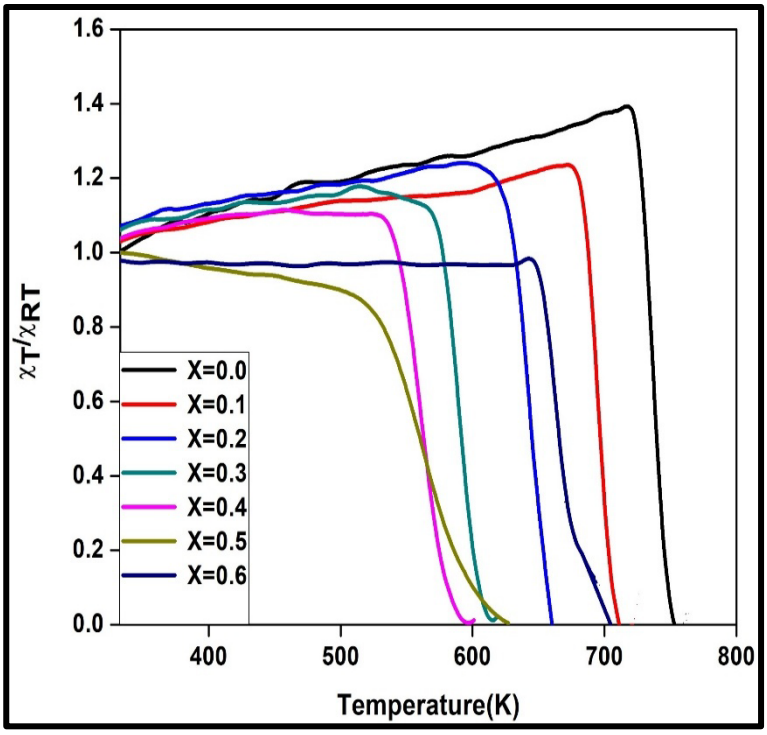


Fig. 4.27 b: AC susceptibility plots of 'sintered' $Ni_{0.6-x}Mn_{0.4}Zn_xFe_2O_4$ (x=0.0-0.6) ferrites

Table 4.11: 'T_c' of 'as prepared' and 'sintered' $Ni_{0.6-x}Mn_{0.4}Zn_xFe_2O_4$ (x=0.0-0.6)ferrites

x	Tc (K) 'As-Prepared'	T_c (K) 'Sintered'
0.0	860	755
0.1	826	702
0.2	810	650
0.3	820	618
0.4	802	598
0.5	789	624
0.6	822	729

4.5.3 Magnetisation studies (Vibrating Sample Magnetometer)

The DC magnetisation study was carried out via VSM to study the magnetic properties of 'as prepared' and 'sintered' $Ni_{0.6-x}Mn_{0.4}Zn_xFe_2O_4$ (x=0.0, 0.1, 0.2, 0.3, 0.4, 0.5, 0.6) ferrites was conducted at 60 K and room temperature (RT) in the field from -30,0000 to 30,000 Oe. Similarly, magnetic properties as a function of temperature were also employed from 60 K to 350K at a constant magnetic field. The chosen magnetic fields for the study were 250 Oe, 500 Oe, and 1000 Oe. The hysteresis loop for the synthesized 'as prepared' $Ni_{0.6-x}Mn_{0.4}Zn_xFe_2O_4$ ferrites at 300 K and at 60 K is shown in Fig. 4.28a and Fig. 4.28b, respectively, while Fig. 4.29a and Fig. 4.29b represent the sigmoidal curves for sintered ferrite at 300K and 60K. This technique was helpful in obtaining various parameters such as the saturation magnetization, coercivity, and remanent magnetization of the ferrites. All the parameter values are tabulated in Table 4.12.

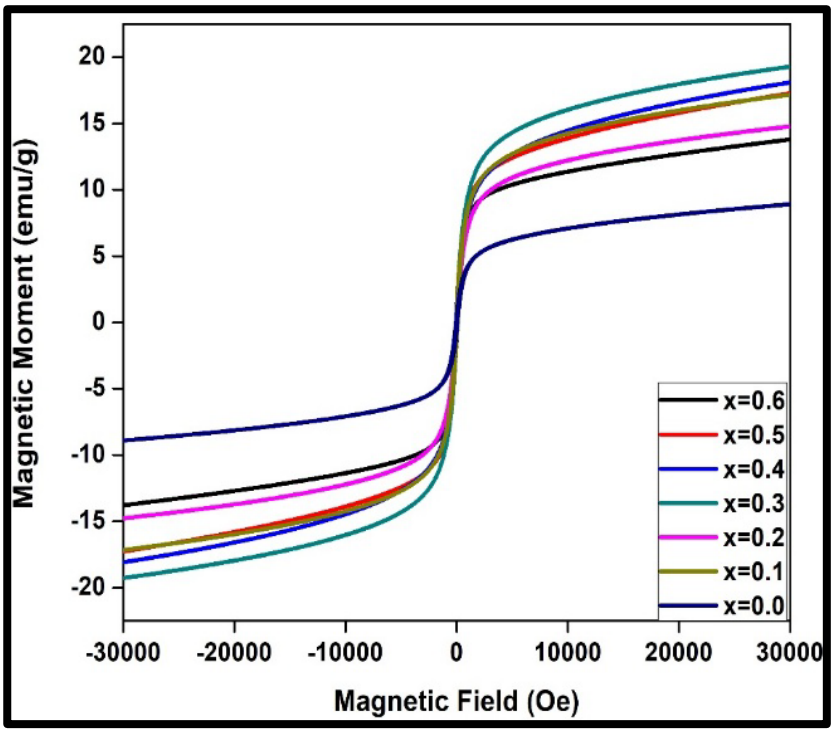


Fig. 4.28 a: The plot of magnetization versus magnetic field of 'as prepared' $Ni_{0.6-x}Mn_{0.4}Zn_xFe_2O_4$ (x=0.0, 0.1, 0.2, 0.3, 0.4, 0.5, 0.6) ferrites at 300 K

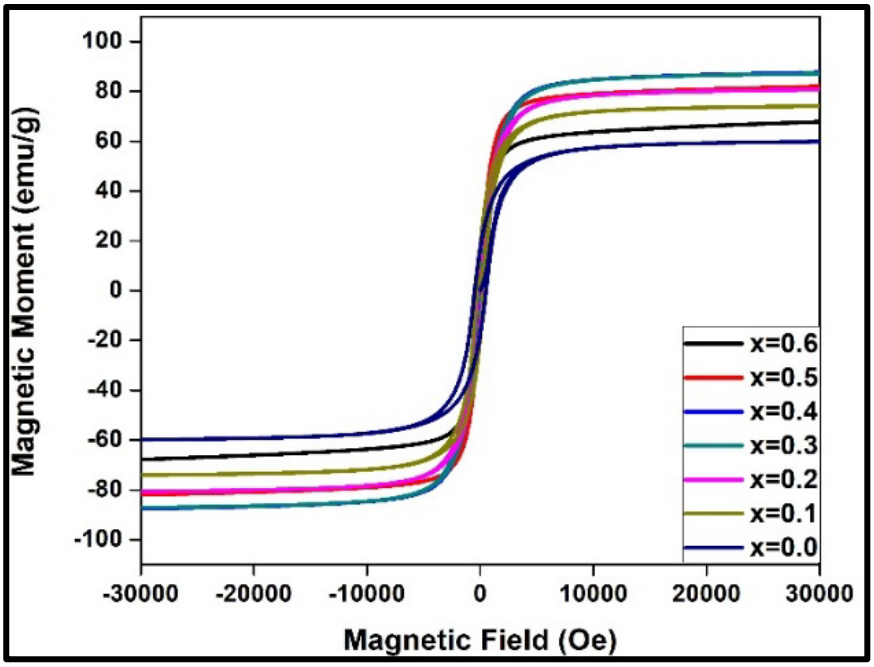


Fig. 4.28 b: The plot of magnetization versus magnetic field of 'as prepared' $Ni_{0.6-x}Mn_{0.4}Zn_xFe_2O_4$ (x=0.0, 0.1, 0.2, 0.3, 0.4, 0.5, 0.6) ferrites at 60 K

The hysteresis loops show narrow sigmoidal curves indicating soft ferrimagnetic materials. Fig. 4.28 a for the 'as prepared' ferrites measured at 300 K shows that saturation magnetisation has yet to reach the maximum applied field of 30,000Oe. The magnetic field required to attain magnetisation depends on the nanoparticle size. The sample calcined at 500 °C and measured at RT exhibited relatively lower saturation magnetization values ranging from 9-19 emu/g and lower coercivity values, thus validating the soft magnetic nature and nanoscale particle effects.

A decrease in the crystallite size normally leads to a smaller saturation magnetization attributed to the surface effects. As per the core-shell model, the nanosized particles lead to the canting of spins or non-collinearity of magnetic moments at the surface, hence reducing the overall magnetization [52]. As reported by many authors, the presence of Fe^{2+} ions in the octahedral site in the samples also reduces the saturation magnetisation [53].

However, in the present study, the presence of Fe^{2+} ions is ruled out, as confirmed by XPS analysis, which indicates it exists in a 3+ oxidation state. In the case of 'as prepared' samples in the MH study at RT, the saturation magnetisation increases with zinc up to the sample with composition x= 0.3, except x=0.2, where there is a drop in Ms. After x= 0.3, with further

increase in Zn^{2+} ions substitution, there is a continuous decrease in saturation magnetisation. In comparison to the 'sintered' $Ni_{0.6-x}Mn_{0.4}Zn_xFe_2O_4$ (x=0.0, 0.1, 0.2, 0.3, 0.4, 0.5, 0.6) ferrites studied at RT, a similar trend was observed, i.e., the saturation magnetization increased up to a sample composition of x= 0.2, and further a decrease was obtained till x= 0.6.

Fig.4.28 b and Fig. 4.29 b show the magnetisation curves versus magnetic field for $Ni_{0.6-x}Mn_{0.4}Zn_xFe_2O_4$ (x=0.0, 0.1, 0.2, 0.3, 0.4, 0.5, 0.6) ferrites studied at 60K. The 'as prepared' ferrite studied at 60 K showed higher magnetisation values compared to RT studies. It is observed that with an increase in Zn^{2+} concentration, the M_s value increased up to sample x= 0.5 and further decreased. Sintered $Ni_{0.6-x}Mn_{0.4}Zn_xFe_2O_4$ (x=0.0, 0.1, 0.2, 0.3, 0.4, 0.5, 0.6) ferrite samples analyzed at 60 K. The M_s increased to sample x= 0.4, and a decreasing trend was observed with an increase in Zn^{2+} concentration; the M_s values observed in this case were also higher than those of 'sintered' samples studied at RT.

The increase in saturation magnetization with an increase in zinc content up to a certain zinc composition, this characteristic feature of magnetization can be explained by Neel's two-sublattices collinear model, according to which magnetization is given as $M_s = M_B - M_A$. This trend depends on the amount of zinc doped in the sample and the fraction of zinc ions present at the site or cation distribution. The exchange interaction between ions in the octahedral and tetrahedral sites also plays a major role. The magnetic moments are antiferromagnetically coupled between the ions in the tetrahedral site and the octahedral site via the oxygen atom. The zinc prefers the tetrahedral A site while the Ni^{2+} ions prefer to occupy the octahedral sites. The manganese and iron ions do not have specific site preferences and can occupy both tetrahedral and octahedral sites within the spinel structure. However, manganese ions tend to occupy the octahedral sites mainly at higher concentrations or depending on the synthesis route.

In the present study, the Ni^{2+} ions occupy the octahedral site as the Zn^{2+} ions are introduced; they occupy the tetrahedral site as expected, which pushes the Fe^{3+} in the tetrahedral site to move to the octahedral B-site, making space for Zn^{2+} ions, thus leading to magnetic dilution due to non-magnetic zinc ions. The shifting of Fe^{3+} ions into the octahedral site increases the magnetic moment in the B site while the magnetic moment of the A site decreases. Therefore, we see the increasing trend of saturation magnetisation with an increase in zinc content in the samples. As the concentration of Zn^{2+} ions is increased in the A-site, it causes the B lattice to

split into B_1 and B_2, causing spin canting, i.e., the spins are no longer ferromagnetically coupled but instead bend at an angle to each other; this phenomenon is explained by the Yafet-Kittel model [53-55].

Coercivity (H_c) was measured from the sigmoidal curve of 'as prepared' and 'sintered' $Ni_{0.6-x}Mn_{0.4}Zn_xFe_2O_4$ (x=0.0, 0.1, 0.2, 0.3, 0.4, 0.5, 0.6) ferrites for samples studied at RT and 60K. The obtained results are tabulated in Table 4.12. H_c depends on several factors such as anisotropy constant, average grain size, and domain wall energy [56]. Zinc ferrite has comparably lower coercivity than nickel ferrite. The observed decrease in coercivity with increased zinc content in the samples up to x= 0.5 can be due to increased grain size of the particles as zinc content increases. Grain size and coercivity have an inverse relationship; larger grains assist easier domain wall motion, thus reducing coercive fields. Hence, the coercivity of the 'as prepared' ferrites was higher than their 'sintered' analogues for both 300 K and the 60K study. This behavior can be due to the presence of pores in the 'as-prepared' ferrite samples. The presence of pores causes demagnetisation of the field and curtails the free movement of domain walls.

Thus, the applied magnetic field is reduced. Lower porosity in samples leads to lower coercivity, as a higher field will be required to push the domain wall. [56-58,] The smaller the size, the higher the coercivity; hence, for 'sintered' samples, the size increases on sintering. Thus, the coercivity becomes smaller than that of the 'as prepared' ferrites. The sintered samples have a higher size and, therefore, lower porosity; the number of domain walls present is more; therefore, the phase lag between the applied field and domain rotation increases. As a consequence of this, the magnetisation or the demagnetisation process requires more energy; therefore, 'sintered' samples have lower coercivity [59-61].

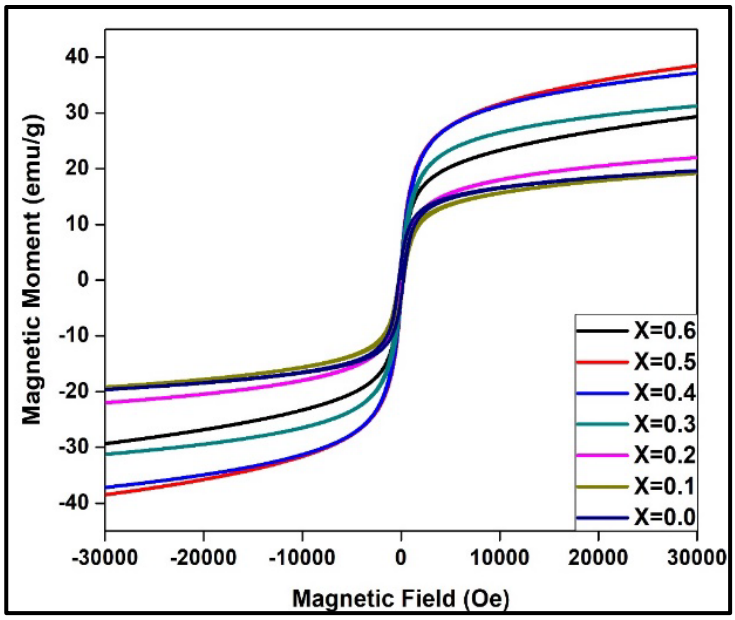


Fig. 4.29a: The plot of magnetization versus magnetic field of 'sintered' $Ni_{0.6-x}Mn_{0.4}Zn_xFe_2O_4$ (x=0.0, 0.1, 0.2, 0.3, 0.4, 0.5, 0.6) ferrites at 300 K

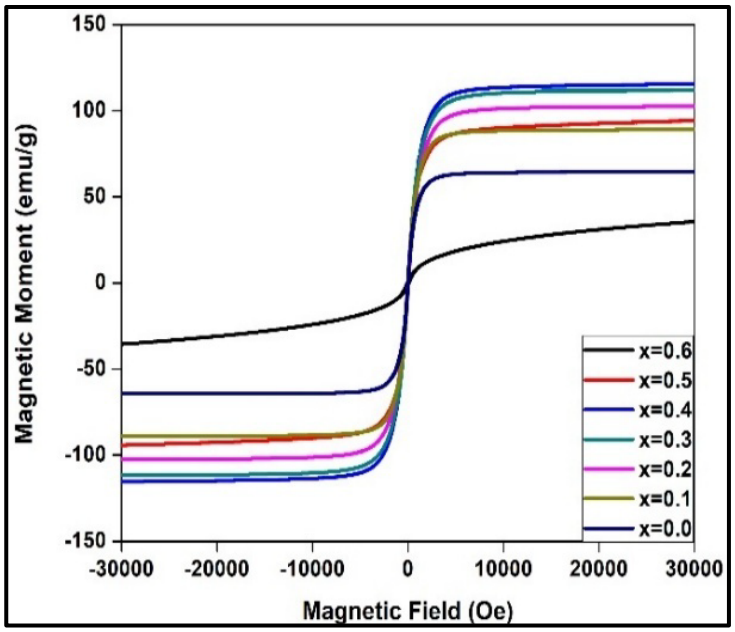


Fig.4.29b: The plot of magnetization versus magnetic field of 'sintered' $Ni_{0.6-x}Mn_{0.4}Zn_xFe_2O_4$ (x=0.0, 0.1, 0.2, 0.3, 0.4, 0.5, 0.6) ferrites at 60 K

The zero-field cooled (ZFC) and field cooled (FC) studies were performed from 60 K to 350 K temperature range for all the 'as prepared' as well as 'sintered' ferrite at different fields, i.e., 250, 500, and 1000 Oe. Fig.4.30 (x= 0.0-0.6) is depicted for 'as prepared' ferrite, while Fig. 4.31 (x=0.0-0.6) is for the 'sintered' ferrites at variable fields. The M-T curves show a change in magnetism as the zinc content is increased. It is observed that with an increase in zinc content, the magnetism changes from ferrimagnetic to superparamagnetic in nature. During ZFC measurements, the nanoparticles were initially cooled to 60 K. Here, no magnetic field was applied. The measurements were done during the heating process in the applied magnetic field. While in the case of FC, the cooling was done up to 60K in the applied field, the measurements were done in the presence of the applied field during heating, i.e., from 60K to 350K.

The FC curves for all the samples showed a continuous drop. The decline in magnetization was seen for all the magnetic fields. It is observed that at 60K, the magnetization is the highest. The high magnetization is achieved due to the following reason. In the FC study, the samples are cooled to 60 K in the presence of a magnetic field. The magnetic moment present in each particle tends to align in the direction of the magnetic field, resulting in high magnetization. At 60 K, the magnetic moments are frozen, and an anisotropic energy barrier alters the flipping of these moments. During the warming cycle, the temperature increases, thus randomizing the spins and disturbing the aligned spins; therefore, the magnetization decreases along with magnetic anisotropy [62-64]. The ZFC curve shows a different trend compared to the FC curve. Here, as the temperature increases, the magnetic spins get charged due to thermal agitation and align along the magnetic field. Therefore, one sees an increase in the curve. The maxima reached in the ZFC curve and is called as the blocking temperature (T_B). T_B is the temperature at which the energy barrier due to magnetic anisotropy is overcome by thermal energy. This is the temperature above which the ferrimagnetic substances start behaving in a superparamagnetic manner. Below the blocking temperature, the material is in a ferrimagnetic state. Where the magnetic moments are aligned in the easy axis of direction and the magnetic anisotropy energy barriers are high, not allowing the change in the easy axis of magnetization. As the temperature increases, the magnetic spins get aligned in the direction of the field, and thus the magnetic moment increases. Beyond T_B, the material exists as superparamagnetic as the energy barrier is overcome by the thermal energy [65-67]. Table 4.12 tabulates the values of blocking temperature. From which it is observed that in all the 'as prepared' samples, with an increase in

zinc concentration, the T_B decreases; moreover, as the applied field increases, the T_B values decrease and are attributed to decreases in the magnetocrystalline anisotropy constant. The 'as prepared' sample had widely distributed particles, which were confirmed from the broad maxima attained at T_B [68]. MT studies can also be used to determine the irreversible temperature (T_{irr}). T_{irr} is the temperature at which the ZFC and FC curves meet. It was observed that the ZFC and FC curves did not meet at 350K and remained separated. This was due to larger particles present in the samples and can also be seen from uneven-sized particle distribution and agglomerated particles as seen from SEM and TEM images [69]. As reported, with an increase in non-magnetic zinc content, the T_{irr} decreased. This can be explained by the fact that as anisotropy decreased, the ability to flip the spin and align them to the applied field reduced with zinc content. [68-70]. The MT studies were also conducted for all the 'sintered' $Ni_{0.6-x}Mn_{0.4}Zn_xFe_2O_4$ (x=0.0, 0.1, 0.2, 0.3, 0.4, 0.5, 0.6) ferrites. The ZFC and FC curves were obtained in the temperature range of 350 -60 K, just like the 'as prepared' ferrite, at three different fields. The plots of the same are represented in Fig. 4.30 (x= 0.0- 0.6) while the magnetization parameters are tabulated in Table 4.12. From the figures, it is observed that as the zinc content increases, the ferrimagnetic behavior changes from superparamagnetic to paramagnetic in nature. Also, with the increase in the field, the splitting between ZFC and FC is reduced.

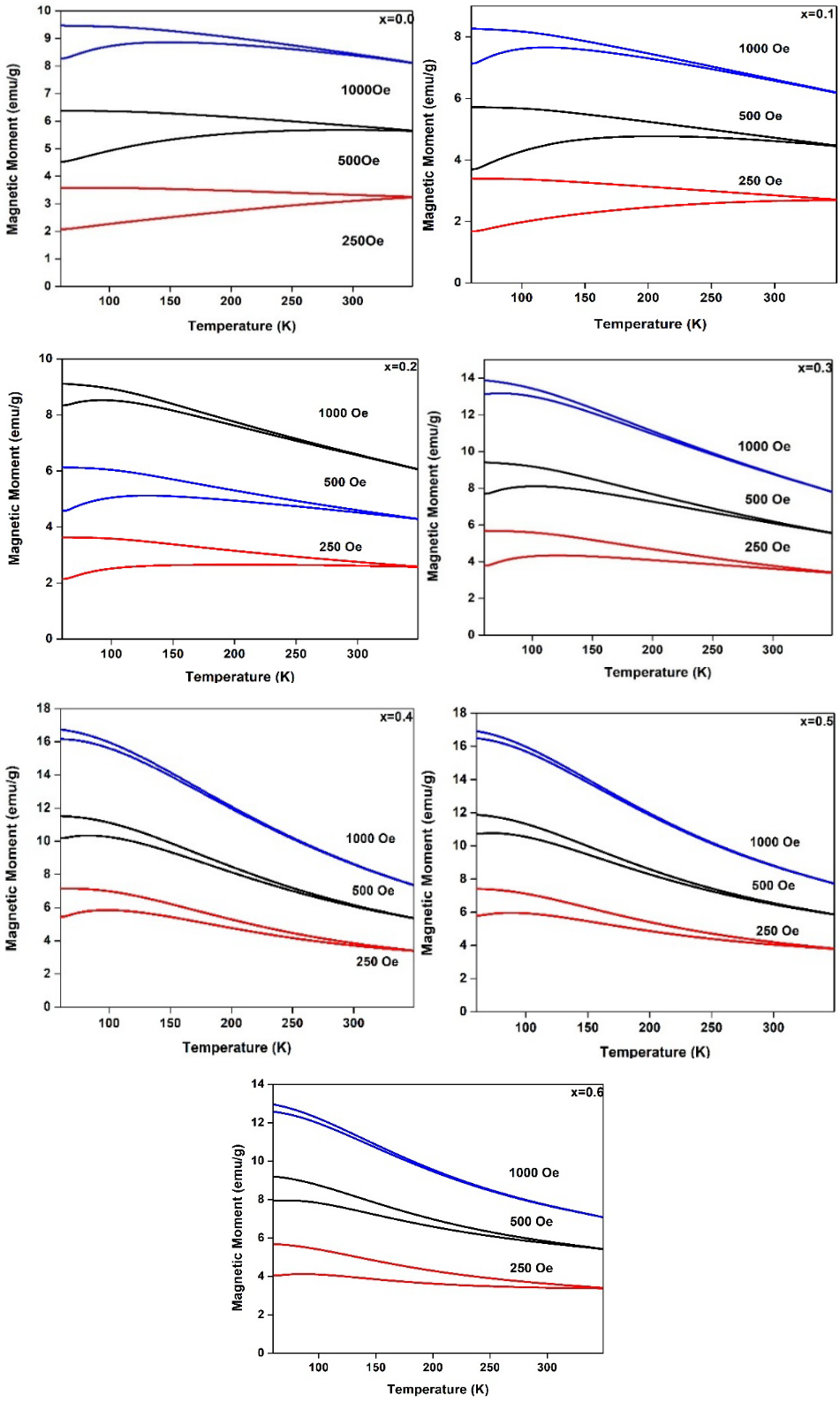


Fig. 4.30: Zero field cooled and field cooled curves of 'as prepared' $Ni_{0.6-x}Mn_{0.4}Zn_xFe_2O_4$ (x=0.0, 0.1, 0.2, 0.3, 0.4, 0.5, 0.6) ferrites at the fields of 1000,500 and 250 Oe

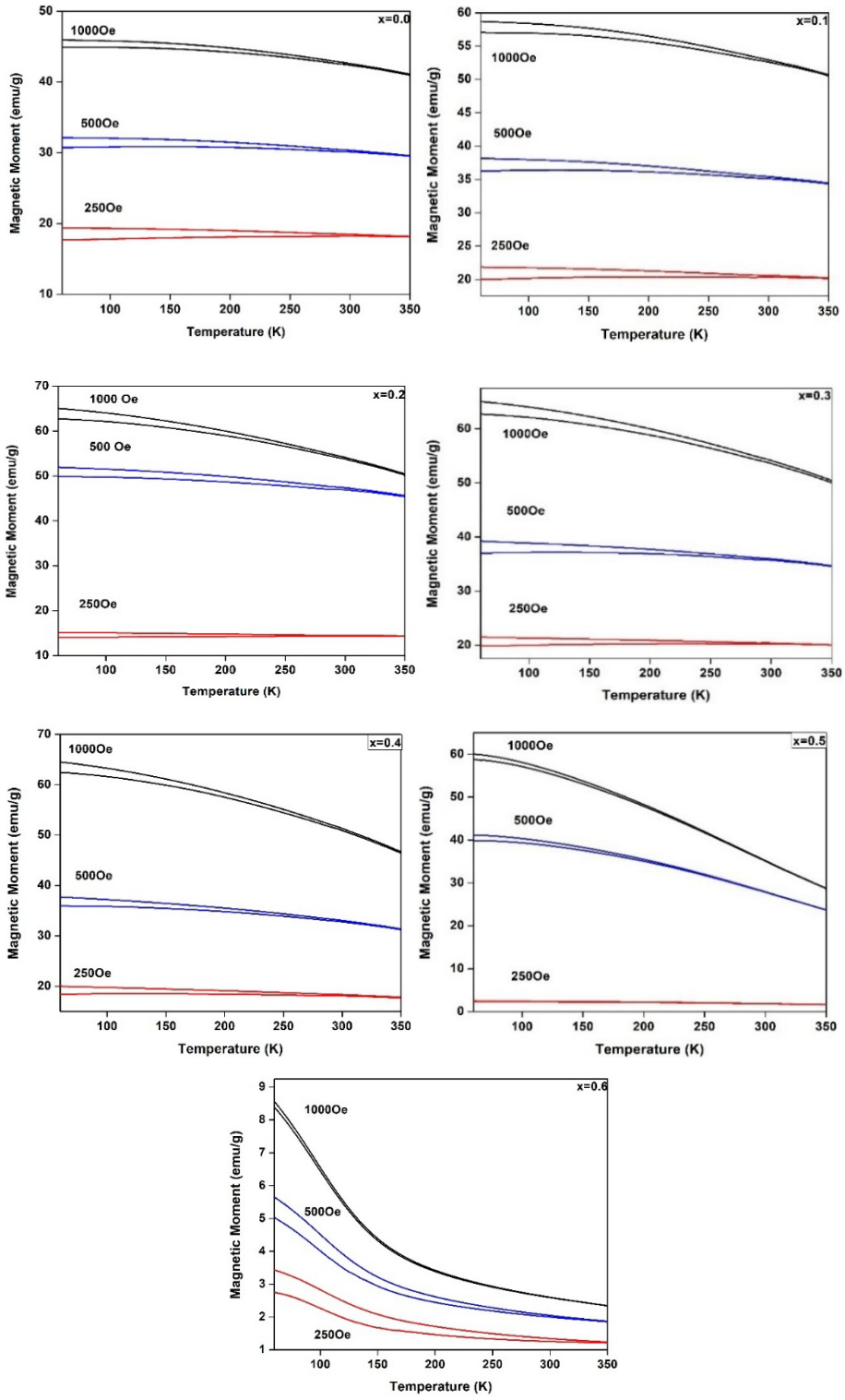


Fig. 4.31: Zero field cooled and field cooled curves of 'sintered' $Ni_{0.6-x}Mn_{0.4}Zn_xFe_2O_4$ (x=0.0-0.6) ferrites at the fields of 1000,500 and 250 Oe

Table 4.12: M_s, H_c, M_r, and T_B of 'as prepared' and 'sintered' $Ni_{0.6-x}Mn_{0.4}Zn_xFe_2O_4$ (x=0.0, 0.1, 0.2, 0.3, 0.4, 0.5, 0.6) ferrites at 300 K, 60K, 250, 500, 1000Oe

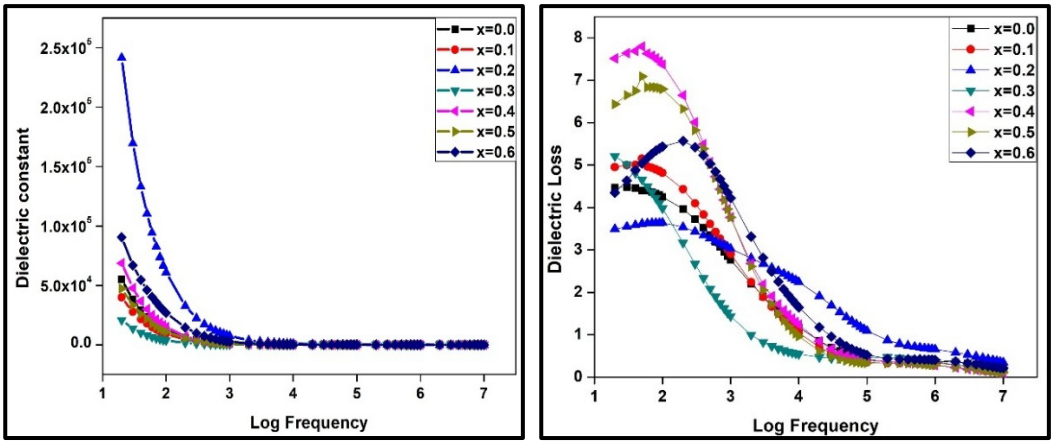
x			**0.0**	**0.1**	**0.2**	**0.3**	**0.4**	**0.5**	**0.6**
M_s (emu/g)	RT	'As prepared'	9	17	15	19	18	17	13
		'sintered'	60	68	82	72	70	42	6.7
	60K	'As prepared'	20	19	22	31	37	39	29
		'sintered'	64	88	103	111	116	94	35
H_c (Oe)	RT	'As prepared'	69	58	47	29	33	36	80
		'sintered'	35	19	17	11	6	7	104
	60K	'As prepared'	232	249	183	141	89	83	131
		'sintered'	40	34	34	20	12	13	90
M_r (emu/g)	RT	'As prepared'	0.6	1.1	0.7	0.8	0.5	0.7	1.3
		'sintered'	1.8	1.1	1.35	0.8	0.5	0.3	0.7
	60K	'As prepared'	3.3	2.8	2.3	3	2.4	2.4	3
		'sintered'	3.5	3.3	2.4	1.8	1.1	1.5	1.2
T_B (Oe)	250	'As prepared'	-	311	271	120	96	90	87
		'sintered'	297	199	-	219	120	-	-
	500	'As prepared'	290	233	128	101	82	73	64
		'sintered'	-	137	-	120	-	-	-
	1000	'As prepared'	150	110	94	73	62	-	-
		'sintered'	-	-	-	-	-	-	-

4.5.4 Dielectric study

4.5.4.1 Dielectric study with respect to frequency of 'as prepared' and 'sintered' $Ni_{0.6-x}Mn_{0.4}Zn_xFe_2O_4$ (x= 0.0, 0.1, 0.2, 0.3, 0.4, 0.5, 0.6) ferrites

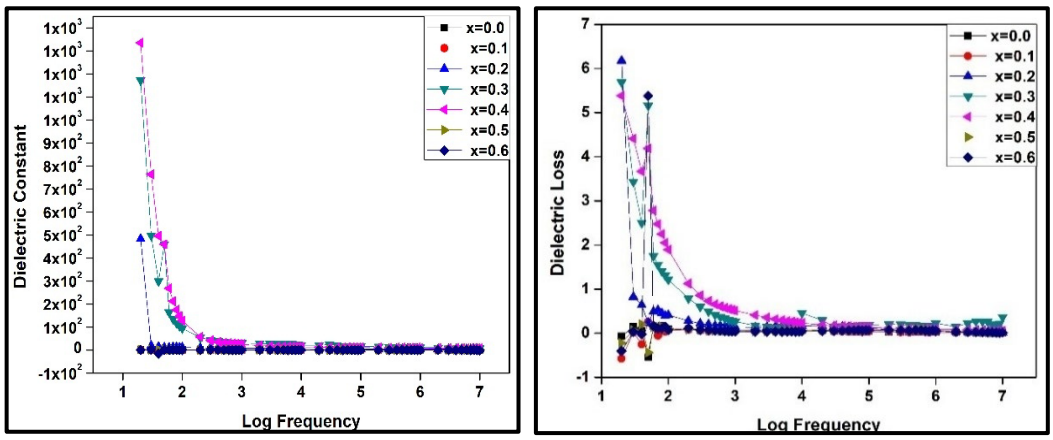
$Ni_{0.6-x}Mn_{0.4}Zn_xFe_2O_4$ (x=0.0, 0.1, 0.2, 0.3, 0.4, 0.5, 0.6) ferrites were analyzed for their dielectric properties. The dielectric constant and dielectric loss as a function of frequency were evaluated for both 'as prepared' and 'sintered' ferrites, which are represented in Fig. 4.32(a, b) and Fig. 4.33 (a, b), respectively. From the observation, it is seen that the dielectric constant decreases with an increase in frequency. The decrease was swift and sharp at lower frequencies, and as the frequency increased, the dielectric constant lowered and became constant, independent of frequency. This is a typical trend of spinel ferrite. Maxwell Wagner's two-layer model explains the trend based on space charge polarization. According to Maxwell and Wagner's model, the ferrites contain conducting grains and are well separated from other grains through a grain boundary, which is resistive or insulating in nature. These charges build up at the grain boundary in the applied field, leading to space charge polarization. Thus, a high dielectric constant is observed. This charge accumulation occurs when space charge carrier moves through the resistive boundary; therefore, it takes a while for them to arrange in parallel alignment to the applied field. If the frequency of reversal increases during this process, then the space charges won't be able to accumulate; instead, there will be a reversal in their movement due to lag in the field, thus the dielectric constant decreases as frequency increases [73,74]. The dielectric loss is a structural property and depends on the composition, its stoichiometry, and sintering temperatures [75]. The dielectric loss studies, when conducted on as-prepared and sintered samples, revealed a similar behaviour, i.e., with an increase in frequency, the dielectric loss decreases with little initial increase in the beginning. This initial increase leads to peak formation, which is usually observed when the hopping frequency of electrons is equal to the applied field [76]. The peak is only observed in the case of 'as prepared' ferrite. Like the dielectric constant, the dielectric loss is observed to be higher at lower frequencies; this trend is explained by Koop's model. As seen in the case of the dielectric constant, the charges move through insulating grain boundaries, the energy required for the hopping of electrons is also high, and thus, the energy losses also increase [77].

With an increase in zinc content, there was no proper trend observed. But the sample x=0.2 showed the highest dielectric constant with the lowest dielectric loss. Whereas, x=0.4 showed the highest dielectric constant in the case of sintered ferrite. It is observed that the dielectric constant and dielectric loss for sintered ferrite were lower than those of 'as prepared' ferrite.



a **b**

Fig 4.32 a: Dielectric constant vs. Log frequency of 'as prepared' $Ni_{0.6-x}Mn_{0.4}Zn_xFe_2O_4$ (x=0.0-0.6) ferrites and **Fig 4.32 b:** Dielectric loss vs. Log frequency of 'as prepared' $Ni_{0.6-x}Mn_{0.4}Zn_xFe_2O_4$ (x=0.0-0.6) ferrites



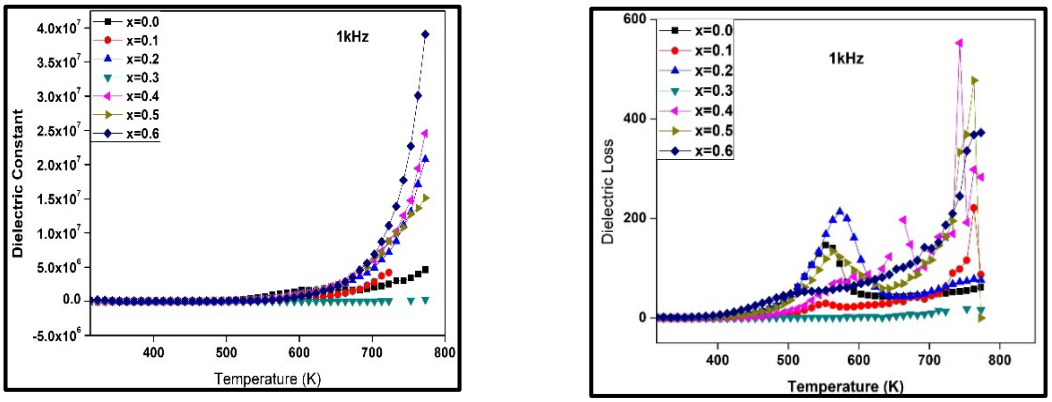
a **b**

Fig 4.33 a: Dielectric constant vs. Log frequency of 'sintered' $Ni_{0.6-x}Mn_{0.4}Zn_xFe_2O_4$ (x=0.0-0.6) ferrites and **Fig 4.33 b:** Dielectric loss vs. Log frequency of 'sintered' $Ni_{0.6-x}Mn_{0.4}Zn_xFe_2O_4$ (x=0.0-0.6) ferrites

4.5.4.2 Dielectric study with respect to temperature of 'as prepared' and 'sintered' $Ni_{0.6-x}Mn_{0.4}Zn_xFe_2O_4$ (x= 0.0, 0.1, 0.2, 0.3, 0.4, 0.5, 0.6) ferrites

The dielectric studies were performed with respect to temperature for both 'as prepared' and 'sintered' $Ni_{0.6-x}Mn_{0.4}Zn_xFe_2O_4$ (x=0.0, 0.1, 0.2, 0.3, 0.4, 0.5, 0.6) ferrites at constant frequencies of 1kHz and 1MHz. The plot of dielectric constant and dielectric loss at 1kHz and 1MHz frequencies is represented in Fig.4.34 (a, b) and Fig.4.34 (c,d)for as-prepared ferrite. While for sintered ferrite, Fig.4.35 (a,b) represents a constant frequency of 1kHz, and Fig. 4.35 (c,d) is for a 1MHz frequency.

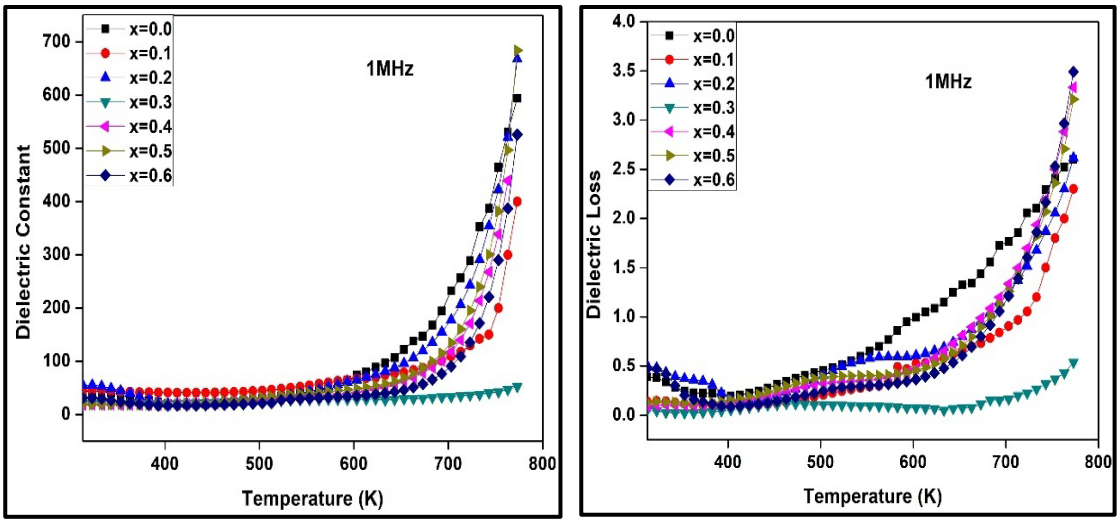
The plots show that at lower temperatures, the dielectric constant remains unchanged and is almost constant. With a further increase in temperature, the dielectric constant increases and reaches a maximum. It is seen that the onset of increase decreases with an increase in zinc content in the case of 1kHz frequency. In the case of dielectric loss, a similar trend was seen, i.e., with an increase in temperature, the loss increases. But in this case, a hump was seen in almost all the samples for 1kHz frequency, while in the case of 1MHz frequency, slight humps were observed. The dielectric constant was seen to increase with zinc content in the case of 1kHz frequency with x=0.3, showing anomalous behaviour and being out of trend. But in the case of 1MHz, the trend seems to have reversed and is improper.



a **b**

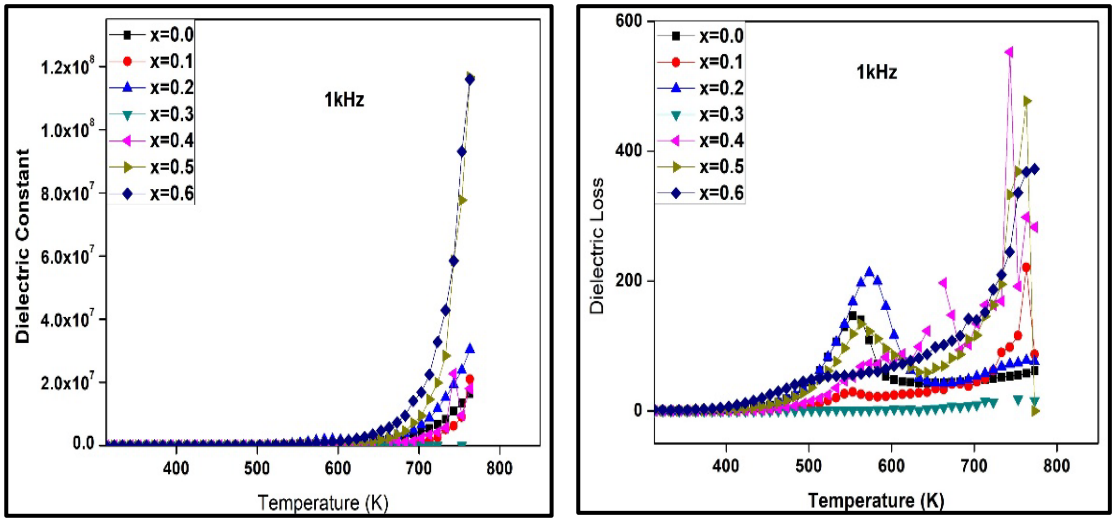
Fig. 4.34 a: Dielectric constant vs. Temperature at 1kHz for 'as prepared' $Ni_{0.6-x}Mn_{0.4}Zn_xFe_2O_4$ (x=0.0-0.6) ferrites

and **Fig. 4.34 b:** Dielectric loss vs. Temperature at 1kHz for 'as prepared' $Ni_{0.6-x}Mn_{0.4}Zn_xFe_2O_4$ (x=0.0-0.6) ferrites



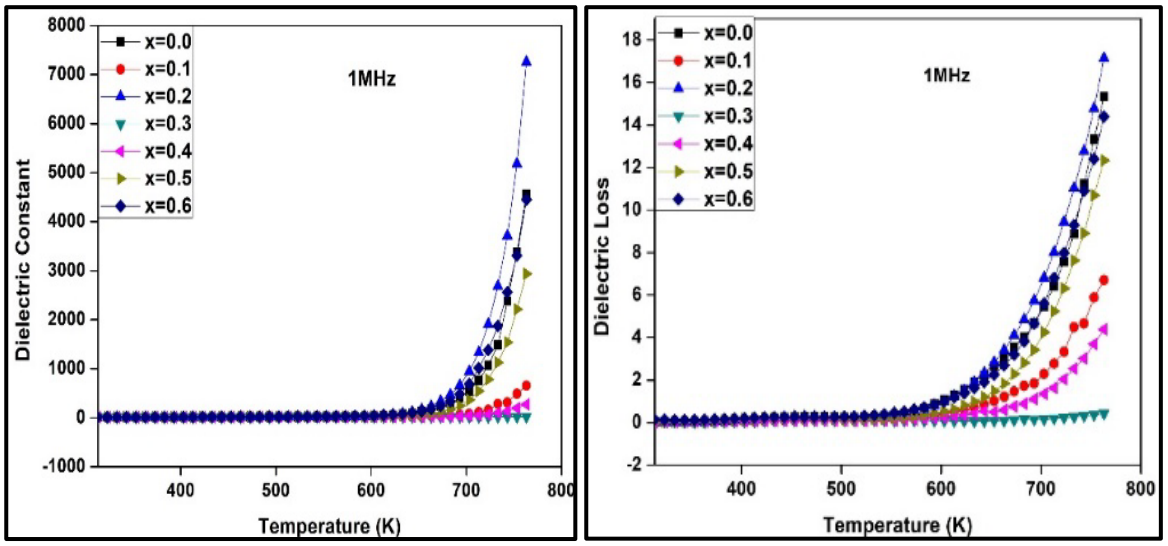
c **d**

Fig. 4.34c: Dielectric constant vs. Temperature at 1MHz for 'as prepared' $Ni_{0.6-x}Mn_{0.4}Zn_xFe_2O_4$ (x=0.0-0.6) ferrites and **Fig. 4.34d:** Dielectric loss vs. Temperature at 1MHz for 'as prepared' $Ni_{0.6-x}Mn_{0.4}Zn_xFe_2O_4$ (x=0.0-0.6) ferrites



a **b**

Fig. 4.35 a: Dielectric constant vs. temperature at 1kHz for 'sintered' ferrite $Ni_{0.6-x}Mn_{0.4}Zn_xFe_2O_4$ (x=0.0-0.6) ferrites and **Fig. 4.35 b**: Dielectric loss vs. temperature at 1kHz for 'sintered' ferrite $Ni_{0.6-x}Mn_{0.4}Zn_xFe_2O_4$ (x=0.0-0.6) ferrites



c **d**

Fig. 4.35 c: Dielectric constant vs. Temperature at 1MHz 'sintered' $Ni_{0.6-x}Mn_{0.4}Zn_xFe_2O_4$ (x=0.0-0.6) ferrites and **Fig. 4.35 d:** dielectric loss vs Temperature at 1MHz 'sintered' $Ni_{0.6-x}Mn_{0.4}Zn_xFe_2O_4$ (x=0.0-0.6) ferrites

4.5.5 Initial permeability

4.5.5.1 Variation of initial permeability and permeability loss vs. frequency for sintered $Ni_{0.6-x}Mn_{0.4}Zn_xFe_2O_4$ (x=0.0, 0.1, 0.2, 0.3, 0.4, 0.5, 0.6) ferrites

The initial permeability of all 'sintered' $Ni_{0.6-x}Mn_{0.4}Zn_xFe_2O_4$ (x=0.0, 0.1, 0.2, 0.3, 0.4, 0.5, 0.6) ferrites has been measured at RT in the frequency range of 20 Hz- 10MHz and is represented in Fig. 4.36 a, b. Also, temperature-based studies were performed from RT to 550 °C, whose plots are plotted in Fig. 4.37a, b. The variation of permeability at various frequencies is referred to as permeability dispersion. It was found that the initial permeability of the samples was affected by their grain size and porosity [78,79]. The ferrite material has grains separated by grain boundaries. The grain boundaries are a barrier to domain wall motion. Samples with larger grain sizes have thinner grain boundaries or fewer grain boundaries, subsequently having higher initial permeability. Two magnetization processes, domain wall motion and spin resonance, are responsible for the initial permeability of ferrites. It can be represented by the following equation $\mu_i = 1 + \chi_w + \chi_{spin}$, where μi, χw, and χspin are initial permeability, domain wall

susceptibility, and rotational susceptibility, respectively [80-83]. The domain wall motion participates at a lower frequency and is responsible for the initial permeability in that region. While spin rotation contributes to the higher frequency region, which results in higher permeability [84-86].

Fig. 4.36 represents the plots of initial permeability vs log frequency. From the plot, a rise in permeability is observed at lower frequencies up to a specific frequency (300Hz). This rise is attributed to displacement in domain walls, and with further increase in frequency, it is independent until, finally, at a much higher frequency, there is again a rise observed in permeability due to resonance at a higher frequency. This resonance frequency is the frequency at which the sample can be used in the devices. The region where the permeability is constant is the region utilized in the devices. 1 MHz is attributed to the spin resonance in the internal anisotropy field. The composition variation of the samples shows an increasing trend in permeability up to x=0.4 and further decreases. This trend is in perfect alignment with saturation magnetization values. This explanation is supported by the following relation, $\mu_i \frac{Ms^2.D}{\sqrt{K_i}}$ where Ms is saturation magnetization, D is the crystallite size, Ki is anisotropic constant [87]. According to the relation, the initial permeability increased with zinc, and the anisotropic constant decreased. The increase in permeability with zinc content up to x=0.4 shows the relation between permeability saturation magnetization and size and anisotropy constant, and that permeability depends on all the factors. Sample x=0.4 exhibited the highest initial permeability and can be accounted for lower small size and less saturation magnetization. For sample x=0.0, the initial permeability is the lowest and is constant throughout, independent of frequency. For samples x=0.1-0.5, the samples show constant permeability. Samples x=0.4, 0.3, and x=0.2 show a slight decreasing trend with an increased frequency. This is attributed to the difference in the applied field and displacement of the domain wall [88]. These samples exhibited a further increase in frequency to 10MHz and increased permeability. With the increase in zinc content, the onset of resonance decreased, as clearly observed from x=0.0 to x=0.4.

Tanδ or loss tangent vs. log frequency is depicted in Fig.4.36b. From the plots, it is clear that at lower frequencies, the loss tangent is higher, while with an increase in frequency, it drops and almost becomes constant. The loss tangent is a result of the lag in domain wall motion and

the applied magnetic field. The imperfections in the crystal lattice are the major cause of the lag [88].

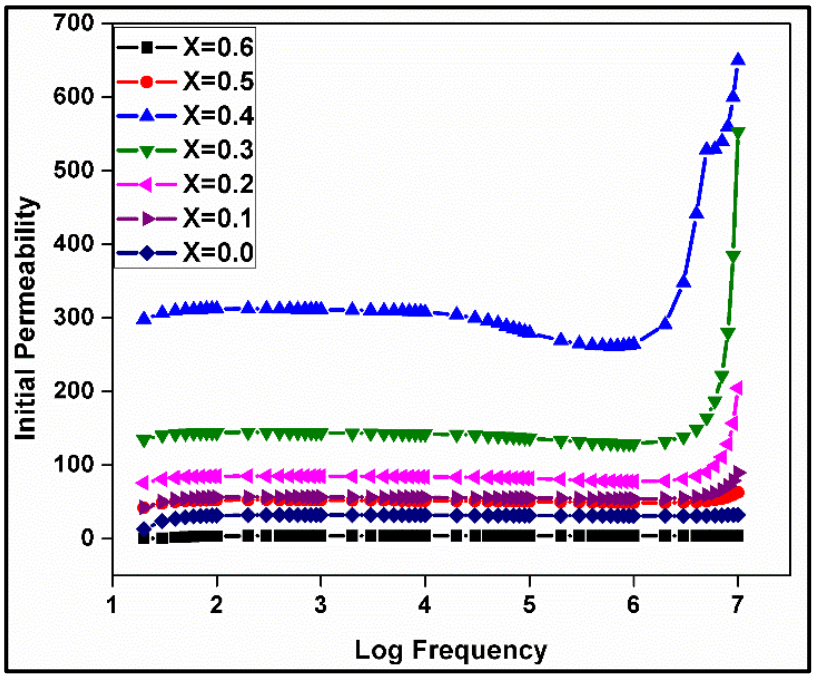


Fig. 4.36 a: Initial permeability vs Log frequency of 'sintered' $Ni_{0.6-x}Mn_{0.4}Zn_xFe_2O_4$ (x= 0.0, 0.1, 0.2, 0.3, 0.4, 0.5, 0.6) ferrites

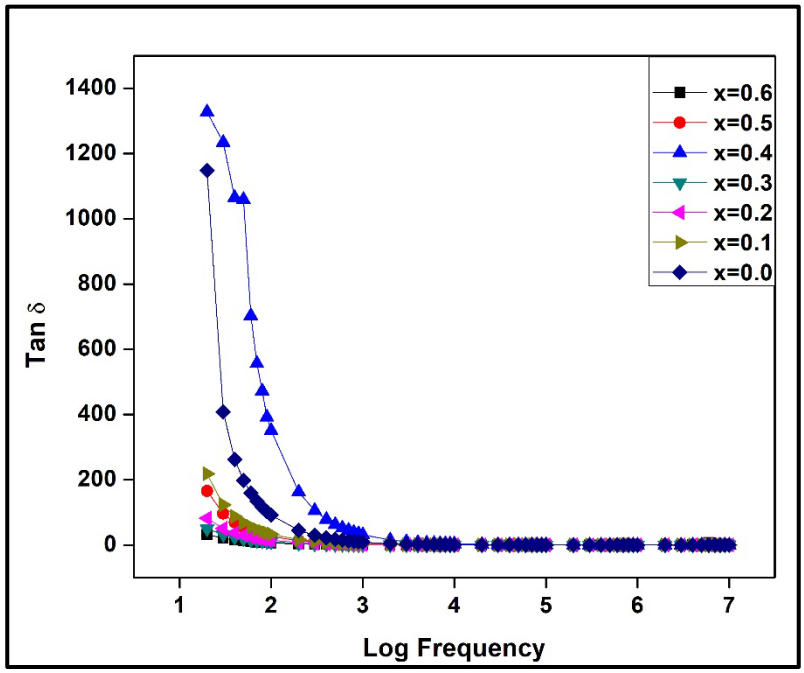


Fig. 4.36 b: Tan δ vs Log frequency of sintered $Ni_{0.6-x}Mn_{0.4}Zn_xFe_2O_4$ (x=0.0, 0.1, 0.2, 0.3, 0.4, 0.5, 0.6) ferrites

4.5.5.2 Variation of initial permeability and permeability loss with temperature for 'sintered' $Ni_{0.6-x}Mn_{0.4}Zn_xFe_2O_4$ (x=0.0, 0.1, 0.2, 0.3, 0.4, 0.5, 0.6) ferrites

The temperature-dependent initial permeability studies were done for all the 'sintered' $Ni_{0.6-x}Mn_{0.4}Zn_xFe_2O_4$ (x=0.0, 0.1, 0.2, 0.3, 0.4, 0.5, 0.6) ferrites. The plot of initial permeability vs. temperature is depicted in Fig. 4.37a, while Fig. 4.37b shows the Tanδ vs. temperature plot.

For a temperature study, with an increase in temperature, permeability increases. A peak is observed just before a sharp fall in permeability at Tc. This is when ferrimagnetic materials lose their property and become paramagnetic. As the alignment of spins is destroyed at a very high temperature, the sample spins cannot maintain their order. The temperature-dependent study allows us to determine the domain structure from the plot and the Curie temperature. The plots designate the single-domain type of structure, and the T_c decreases with increased zinc content. This trend is similar to those obtained in AC susceptibility studies. The increase in permeability is more tremendous with lower zinc content samples, and the sharp fall at T_c indicated the presence of monophase in the ferrites and homogeneity in samples, which is supported by XRD data as well [87,89]. The samples show the presence of a peak or Hopkinson's peak in almost all the samples except x=0.5 and x=0.6. Such peaks indicate a lowering of magneto-crystalline anisotropy with temperature [90,91]. Hopkinson's peaks are also a significant indication of single-domain particle nature [92]. The values of Curie temperature were evaluated by drawing a tangent of the decreasing curve and extrapolating it towards the temperature axis, giving us the T_c. The trend adopted by the T_c from the initial permeability plot very well matched the trend of AC susceptibility. The T_c was seen to decrease from x=0.0 to x=0.4 and further increase as the zinc content increased. The values evaluated are tabulated in the Table. 4.13 The T_c values are seen to decrease as the Zinc content increases due to the fact that zinc prefers to go in the tetrahedral site, while Fe from the tetrahedral site gets pushed towards the octahedral site; thus, the interaction between the tetrahedral and octahedral sites increases, also seen in the lattice parameter values. Leading to a drop in T_c. Mn Zn ferrite had the lowest saturation magnetization and crystallite size, resulting in the lowest initial permeability according to the Globus model [93]. Coercivity was inversely proportional to initial permeability, indicating that higher

coercivity values resulted in lower permeability values. Anisotropy also played a significant role in permeability measurements.

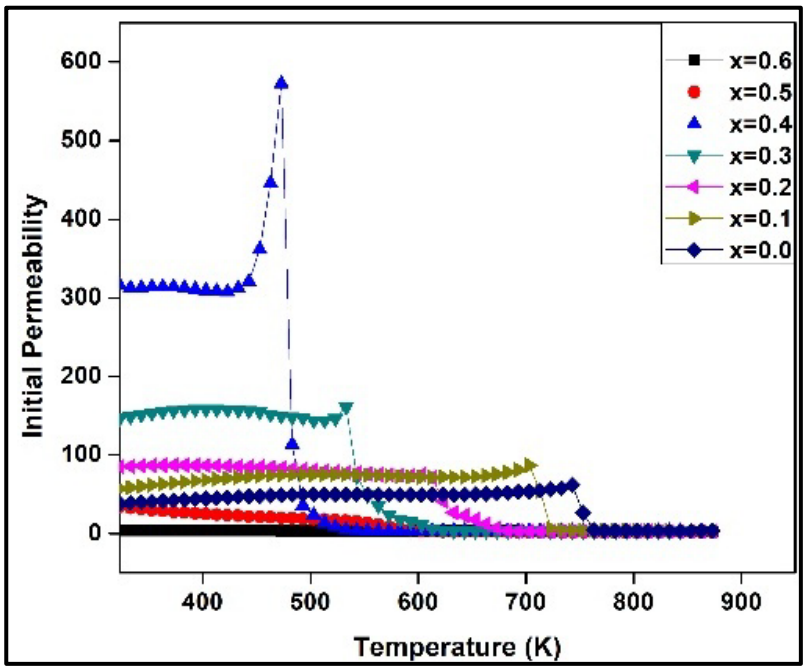


Fig. 4.37 a: Initial permeability vs Temperature of 'sintered' $Ni_{0.6-x}Mn_{0.4}Zn_xFe_2O_4$ (x=0.0, 0.1, 0.2, 0.3, 0.4, 0.5, 0.6) ferrites.

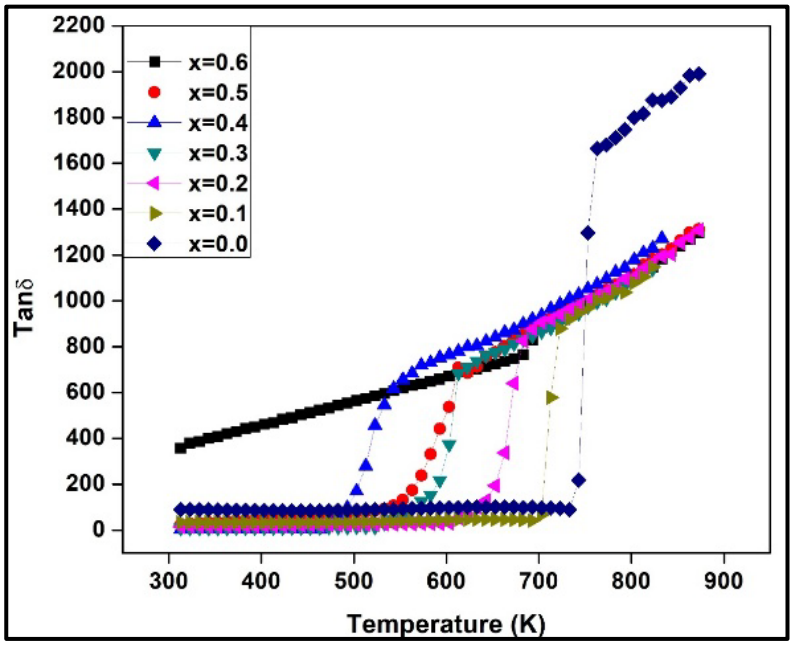


Fig. 4.37 b: Tan δ vs Temperature of 'sintered' $Ni_{0.6-x}Mn_{0.4}Zn_xFe_2O_4$ (x=0.0, 0.1, 0.2, 0.3, 0.4, 0.5, 0.6) ferrites.

The temperature-dependent loss tangent in Fig.4.37b shows that with an increase in temperature, the loss tangent remains almost constant after a point. There is an increase in the loss for each sample at a specific temperature. It is seen that this point, where there is a sharp increase in a loss at a particular temperature, is similar to the temperature that shows a fall in initial permeability just before Curie's temperature. The third part of the plot shows a gradual increase in loss with a further temperature rise; this indicates a change in slope, and the point at which the linear increase starts is similar to the Curie temperature that is obtained and is caused by the damping effect of domain walls [94,95]. It was also observed that the loss decreased with increased zinc content in samples.

Table 4.13: The Curie temperature (T_c) of 'sintered' $Ni_{0.6-x}Mn_{0.4}Zn_xFe_2O_4$ (x=0.0, 0.1, 0.2, 0.3, 0.4, 0.5, 0.6) ferrites evaluated from AC susceptibility and Initial permeability studies and Anisotropy constant.

Composition	**0.0**	**0.1**	**0.2**	**0.3**	**0.4**	**0.5**	**0.6**
AC Susceptibility	755	702	650	618	598	624	729
Initial Permeability	789	747	667	606	523	582	729
$Ki*10^3$	2.1	1.3	1.4	0.8	0.4	0.2	0.7

4.6 Gas Sensing Application

4.6.1 Gas Sensing application of 'as prepared' $Ni_{0.6-x}Mn_{0.4}Zn_xFe_2O_4$ (x=0.0, 0.1, 0.2, 0.3, 0.4, 0.5, 0.6) ferrites

Gas sensors are increasingly in demand due to their ability to detect dangerous gases. Numerous gases are polluting and can be toxic and harmful to human life. Therefore, detecting them and monitoring the levels of gases in the environment is very essential. The semiconductor gas sensors are highly sensitive, selective, and stable, making them necessary and valuable [96]. A suitable sensor can both act as a receptor and a transducer. The first step in this study is sensing the desired gas in the system by adsorption or surface chemical reaction. After the gas is identified, the sensor translates this interaction into a measurable signal, which can be detected as a change in electrical properties like resistance or capacitance.

Industries are a significant source of polluting gases such as NO_x, NH_3, H_2S, Cl_2, and CO_2; monitoring these gases is necessary [97]. The current study attempts to determine the ability of the synthesized 'as prepared' $Ni_{0.6-x}Mn_{0.4}Zn_xFe_2O_4$ (x= 0.0, 0.1, 0.2, 0.3, 0.4, 0.5,0.6) ferrites as a gas sensor material. The study is done using two oxidizing gases and two reducing gases: Cl_2, NO_x, NH_3, and LPG. These gases have been studied at different temperatures to select the most promising ones: RT, 50ºC, 100ºC, 150ºC, and 200ºC. Furthermore, the selected temperature was chosen to study in depth for concentration and reproducibility, which has been discussed further. The detailed setup procedure, thick film preparation, and sensing have been discussed in chapter 2.

4.6.2 Selection of optimum temperature for gas sensing studies:

The optimum temperature selection was done by subjecting each gas at different temperatures using the $Ni_{0.3}Zn_{0.3}Mn_{0.4}Fe_2O_4$ ferrite sample using 100 ppm of gas, and the plot of which is depicted in Fig. 4.38. NO_x was first studied, and it was observed that at RT, the response was small, about 8%, and as the temperature increased from 50 to 100 °C, the response also increased from around 15% for 50 °C to 20% for 100 °C. Beyond 100 ºC, the response dropped to below 5%. Therefore, the temperature of 100 ºC was chosen to be studied for this series from x=0.0 to x=0.6. In the case of chlorine gas, the RT response was below 15%, while for 50 °C, the response was relatively high, but the recovery was a bit slower; the response was close to 60%. At 100

°C, the response again lowered to around 20%, while the response started reducing further for higher temperatures. NH_3 sensing was performed similarly to the other two and gave good results, showing a good response. At RT and 50 °C, the response was 50% and 52%, but the recovery rate was slow, while as the temperature increased to 100 °C, the response reduced to 40%, and with a further increase in temperature, more decrease was observed. Therefore, 100 °C was selected as the temperature for further study. LPG gas, which is commercially available, was directly used to study the gas-sensing properties of the material. The results were profoundly good as the sensor detected the gas at RT with a good response and quick recovery. At RT, the highest response of ~40% was observed with quick recovery; with an increase in temperature, the response started decreasing; for 50 °C, it was~ 30%, and for 100 °C, it was ~25%. At 150 °C, the response obtained was~5%, while at 200 °C, it was very low, i.e., below 5%. Therefore, further detailed studies were done at RT.

4.6.3 % Response at variable x concentration

NO_x gas was purged over all the 'as prepared' samples $Ni_{0.6-x}Mn_{0.4}Zn_xFe_2O_4$ (x=0.0, 0.1, 0.2, 0.3, 0.4, 0.5,0.6) ferrites at 100 °C. It was observed that sample x= 0.3 showed the highest response and quick recovery of 20.6%, whereas all the other samples showed poor results below 20%. Since the sample x=0.3 showed the highest response, we studied the sample with respect to variable gas concentration levels. It was found that with an increase in gas (in ppm), 20, 50, 75, 200, 150, the response also increased.

Chlorine gas was sensed at 50 ºC for all the as-prepared compositions. The highest response was obtained for x=0.3 of 61.5%, followed by x=0.6 with 60% response. X=0.0 showed 54% response, x=0.1 with 25%, x=0.2 with 20% gas response, x=0.4 and x=0.5 showed 38 % and 22% respectively. All these responses were for 100 ppm of gas. When different concentrations of gases were purged separately, each time onto the sample surface. The response was seen to increase respectively. Also, reproducibility was obtained up to 4 times. 100 °C temperature was selected for NH_3 gas sensing, and the results were excellent. 31% of the gas response was obtained for sample x=0.0. 28.8% for sample x=0.1, sample x=0.2 showed 35% of response. 48% of the response was obtained for x=0.3, and so it is seen that as the zinc content is increasing, the response is also increasing up to x=0.3. For example, for x= 0.4, the response

reduced to 25% while x= 0.5 showed a response of 38% and finally, x= 0.6, the response percentage was 14.9%. sample x= 0.3 was further studies w.r.t to different ppm of test gas (20, 50, 75, 100,150) it was noted that as the concentration level increased the response increased except for 150ppm concentration where there was slight decrease and can be assumed due to saturation effect and the responses is as follows respectively: 9.2 %, 21%, 38.9%, 48.7% and 43%. When LPG gas was studied for composition, the following results were obtained for sample x=0.0. A quick response of 76% was obtained, while x=0.1 showed 70% results. sample x=0.2 75%, x=0.3 gave 66.5% response, x=0.4 showed 48% of results, 58% response for x=0.5 while x=0.6 showed 22%. Overall, all the as-prepared samples at RT showed the best LPG sensing outcome. Reproducibility was checked for the samples x=0.4 and x=0.6, and the sensor was found to be reproducible. When sample x= 0.0 was subjected to different ppm levels of gas, it was noted that as the amount of gas increased, the response % also increased.

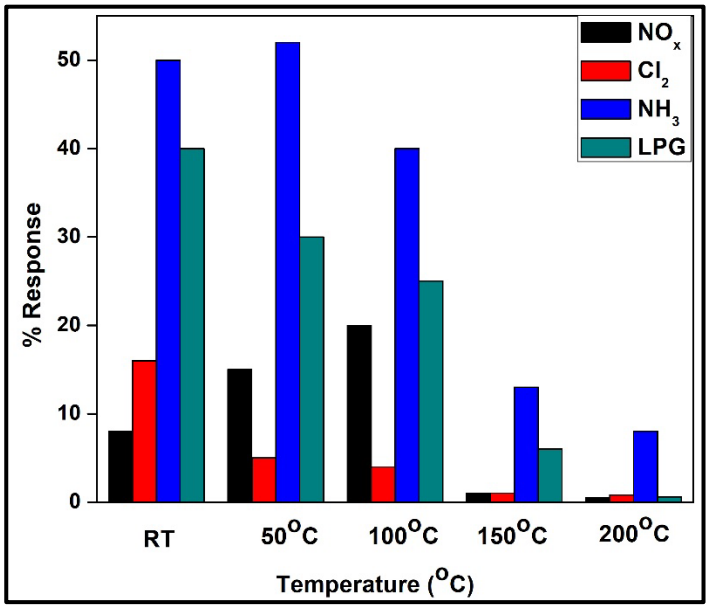
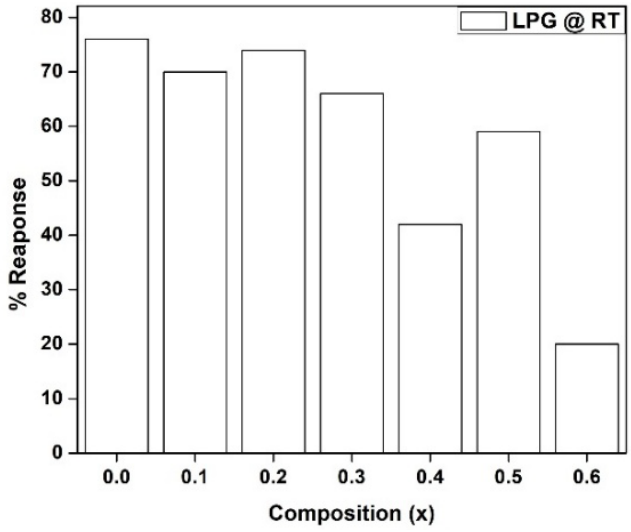
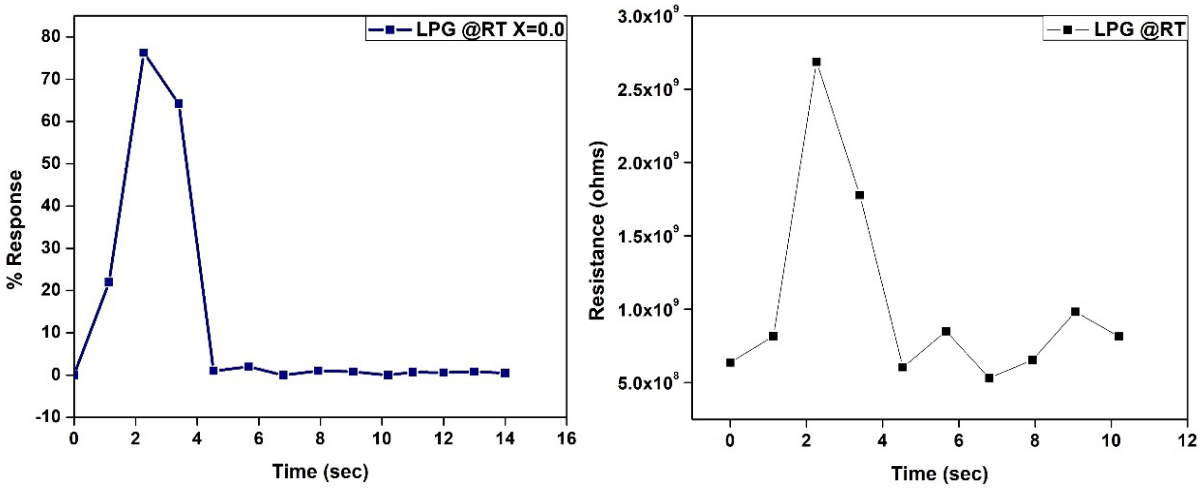


Fig. 4.38: Gas sensing study of 'as prepared' $Ni_{0.3}Mn_{0.4}Zn_{0.3}Fe_2O_4$ ferrite at variable temperatures against oxidizing and reducing gases

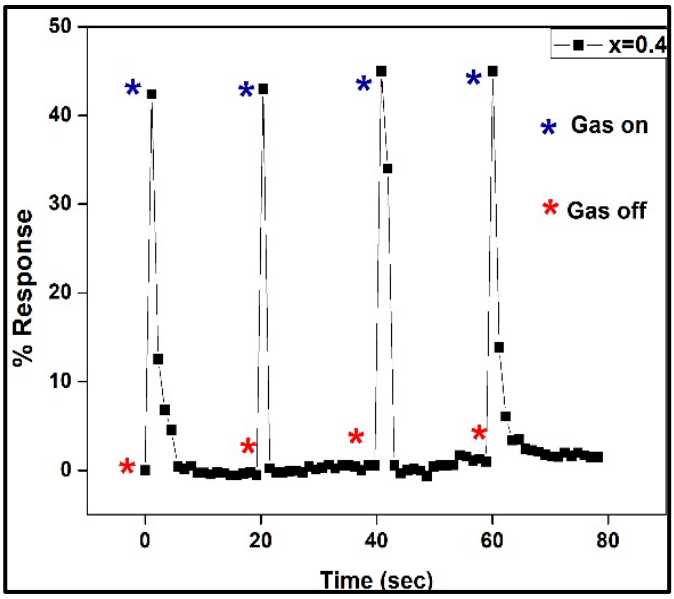


A

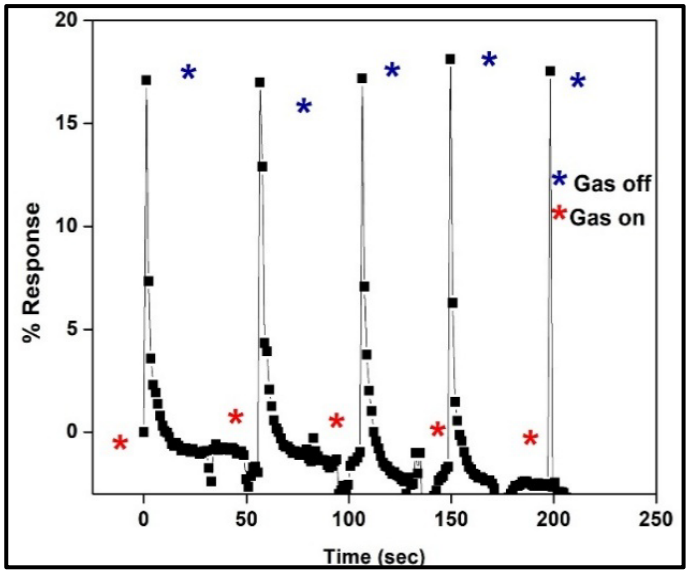


B C

Fig. 4.39 A: % Response vs. composition of 'as prepared' $Ni_{0.6-x}Mn_{0.4}Zn_xFe_2O_4$ (x=0.0-0.6) ferrite at RT for LPG gas, B: % Response vs. Time for sample x=0.0 at RT for LPG gas, C: Plot of resistance vs. Time for sample x=0.0 at RT for LPG gas



a



b

Fig. 4.40 a: The reproducibility plot of sample x=0.4, b:The reproducibility plot of sample x=0.6

Various parameters play an important role in determining the criteria for a suitable sensor. Pore structures are mainly of three kinds: open, closed, and internal pores [97]. This pore can further be classified as micropores with a pore size of 2 nm, mesopores with a 2-200 nm pore size, and macropores with a 200 nm diameter. Pore influences the sensing properties like sensitivity [98]. In our study, BET determined the pore structure in our ferrites to be mesoporous in nature, thus showing improved sensitivity towards LPG gas at RT. Open pores show faster gas adsorption

on the surface, resulting in quicker reaction and more rapid response. Reports available in the literature showed excellent results when samples had an open-pore nanostructure with high porosity and an increased number of pores [99,100]. Crystallite sizes, particle sizes, or grain sizes are also valuable in selecting excellent material as a sensor. The sample size of less than 100nm proves a good candidate for the same. The smaller the size, the higher the strength and hardness, and the better is the material [101]. The effect of grain size was investigated by [102] for different ferrite materials, and it was concluded that small grain sizes had a larger surface area. In comparison, larger grains had a smaller surface area. Therefore, samples with larger surfaces and smaller sizes were efficient gas sensors. In our study, all the 'as prepared' samples had sizes smaller than 100 nm, confirming their nano nature and small crystallite size, which was found from powder XRD data, SEM, and TEM studies. Another criterion that influences gas sensing is dopant concentration. Satyanarayan et al. [103] studied the effect of Pd, Co, and Mn-doped nickel ferrite. They observed improved sensitivity, selectivity, good response, and lower operating temperature. Other reports on Pd-substituted ferrites also show similar results [104,105]. The manganese-substituted Ni-Co ferrite showed excellent sensitivity when studied under variable temperature ranges [106]. In the current study, we discussed the reducing gas at RT, from which it is observed that doping zinc reduced the % response when 100ppm of gas was purged with samples with increasing zinc concentration. The presence of acidic and basic sites is also responsible for good sensor response, and hence, the CO_2-TPD and NH_3-TPD studies were carried out. The CO_2-TPD and NH_3-TPD profiles are presented in Fig. 4.40c and 4.40d, which clearly show that these ferrites possess weak and strong basic sites as well as weak and strong acidic sites. In both cases, the intensity of acidic and basic sites decreases from x=0.0 to x=0.3 and then increases for x=0.6. It is also observed that the intensity of strong acidic and basic sites is higher at high temperatures. The total acidity of the materials corresponding to NH_3-TPD profiles of the materials x=0.0,0.3,0.6 are 0.261, 0.202, and 0.212 mmol, respectively, and the total basicity of the materials corresponding to CO_2-TPD profiles of the materials x=0.0,0.3,0.6 are 0.160, 0.112, and 0.130 mmol, respectively.

Operating temperature is also an essential factor that gives maximum response, and it depends on the type of gas, ferrite composition, catalyst, or additives added [107]. In the case of LPG gas, the ferrites under study showed excellent results at RT. Meanwhile, for other gases, higher temperatures were preferable. As the temperature increases, samples show an increasingly

incredible response. This response of gas depends on the interaction of the gas sample. The gas molecules cannot interact with surface-adsorbed oxygen at low temperatures due to a lack of thermal energy. Therefore, the sensitivity is lowered. When the thermal energy is increased, there is enough energy to overcome the surface reaction's activation energy barrier and oxygen formation at higher temperatures [108]. With further increments in temperature, the exothermic adsorption of gas becomes harder and reduces sensitivity. Therefore, initially, we optimized each gas to find the optimum temperature at which it would provide the highest %response; hence, optimizing is the key to better results. [109, 110] In the case of LPG gas, the recovery was fast at RT, but for other gases at RT, the recovery time was longer; recovery time is required for the response to fall back to the original value once the test gas is removed [111,112]. Hence, higher temperatures were selected for gases other than LPG.

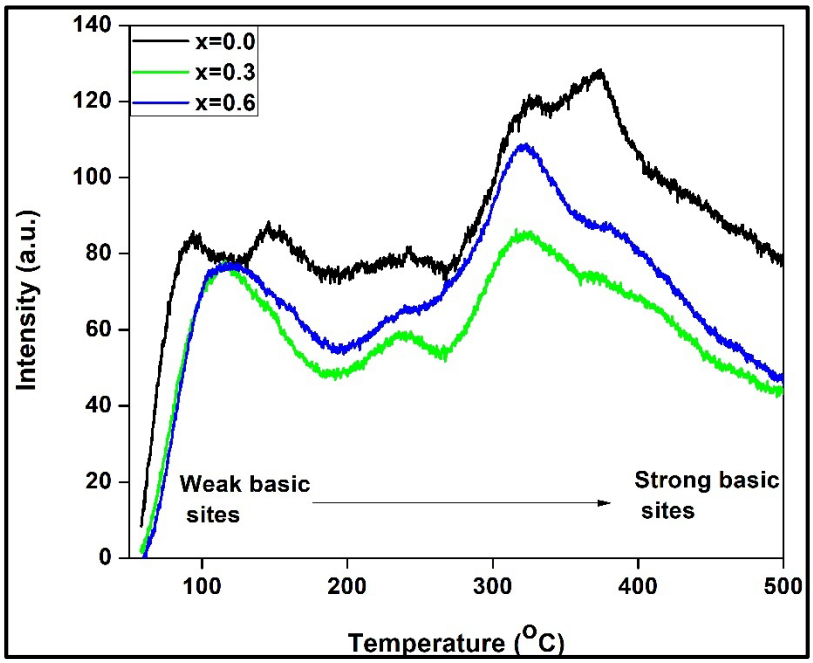


Fig.4.40c: CO_2-TPD profile of $Ni_{0.6-x}Mn_{0.4}Zn_xFe_2O_4$ (x=0.0, 0.3,0.6) ferrites

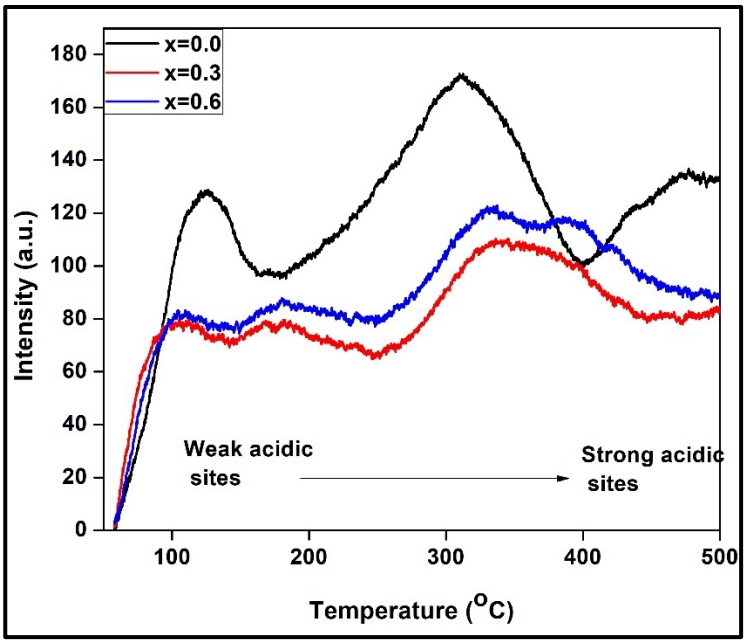


Fig.4.40 d: NH_3-TPD profile of $Ni_{0.6-x}Mn_{0.4}Zn_xFe_2O_4$ (x=0.0, 0.3,0.6) ferrites

4.6.4 The gas sensing mechanism for reducing gases

Resistance changes are observed when reducing gases interact with the test gas. When oxygen is adsorbed from the air onto the sensor's surface, it extracts the electron from the bulk, which ionizes it to O^- and O^{2-}. O is predominantly present at temperatures of 100-500 °C. When reducing gases come in contact with the sensor material, the trapped electron is released back to the conduction band, increasing its conductivity and resistance. The change in resistance is proportional to the gas present [113]. The changes in capacitance or resistance are due to chemisorbed oxygen species like OH^-, O^-, and O^{2-}[114, 115]. The semiconductor gas sensor adopts the following mechanism when oxygen is adsorbed and ionized from the air. [116,117].

$$O_{2gas} \Leftrightarrow O_{2ad},$$

$$O_{2ad} + e- \Leftrightarrow 2O^-_{ad}$$

$$O^-_{ad} - + e- \Leftrightarrow O_{ad}{}^{2-}.$$

The reducing gas is adsorbed on the sensor material as [101,102]

$$R \Leftrightarrow Rad$$

The adsorbed gas and oxygen species then interact by following the equation.

$$R_{ad} + O_{ad}^{-} \Leftrightarrow RO_{ad} + e^{-},$$

$$R_{ad} + O_{ad}^{2-} \Leftrightarrow RO_{ad} + 2e^{-}$$

Lastly, desorption of products results as per [118].

$$RO_{ad} \Leftrightarrow RO gas$$

The sensitivity, response time, and recovery depend on the type of gas and the material under study. The sensitivity of a gas is higher when the amount of gas adsorbed is greater, and its reaction with adsorbed oxygen species is easy [117]. This may vary with different gases due to differences in interaction with adsorbed species. The more adsorbed oxygen species on the surface provide better reaction and response [119].

The mechanism for sensors depends on the alteration of charge carriers (electrons) upon contact with the gas. The kinetics of the process is given in the above equations. In our study, LPG showed an excellent response at room temperature. At room temperature, it is common than other oxyanions. Therefore, the samples act like a p-type semiconductor, where charges accumulate or a hole accumulation layer is formed near the surface, creating an oxyanion, while for an n-type semiconductor material, a depletion layer of charges is observed near the surface. Due to the surface adsorbed oxyanion, a change in resistance is detected. When LPG is used as the test gas, electrons are released once the gas and the sample surface interact. Thus, changing the resistance, an increase is observed for p-type material while a decrease is observed for n-type material. The reaction, undergoing the release of electrons when in contact with LPG gas, can be written as

$$C_nH_{2n+2} + O^{2-} \longrightarrow C_nH_{2n}O + H_2O + e^{-}$$

This released charge combines with the holes since more acceptor ions are generated at the p-type semiconductor, thus reducing the width of the hole accumulation layer and increasing the sample's resistance. Inversely, for an n-type semiconductor, the electrons fill the electron depletion layer, decreasing the resistance.

4.7 Electrochemical performance

4.7.1Electrochemical performance of $Ni_{0.6-x}Mn_{0.4}Zn_xFe_2O_4$ (x=0.0, 0.1, 0.2, 0.3, 0.4, 0.5, 0.6) ferrites

The electrochemical performance of all the 'as prepared' $Ni_{0.6-x}Mn_{0.4}Zn_xFe_2O_4$ (x=0.0, 0.1, 0.2, 0.3, 0.4, 0.5, 0.6) ferrites was carried out on a cyclic voltammetry instrument. The curve of all the samples carried at different scan rates is depicted in Fig. 4.41b, and the corresponding specific capacitances are tabulated in Table 4.14. The analysis was carried out using a three-electrode system in the potential window of 0-0.5 V in a 3M KOH electrolytic solution. The selected scan rates were between 3 and 80 mV. The curves indicated a cathodic and anodic peak in the selected potential window. The voltamogram points out the pseudocapacitive nature of the material [120]. It is also observed that as the scan rate decreases, the area under the curve is also reduced. This indicates that the current density directly relates to the scan rate. Furthermore, the peak shift is also observed, i.e., the anodic peak shifts towards the right side while the cathodic peak shifts towards the left side, increasing the scan rate from 3-80mV.

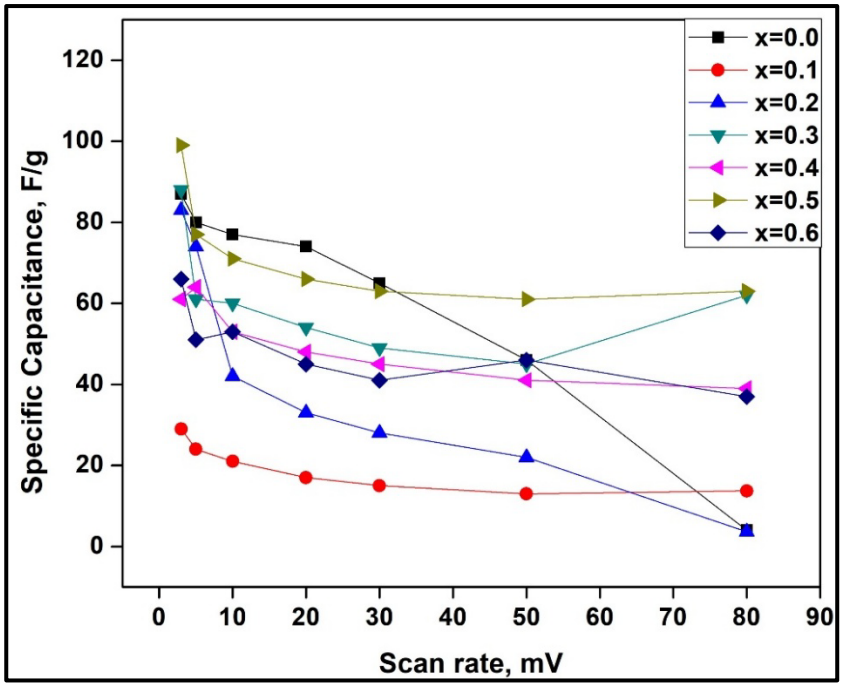


Fig. 4.41: Plot of specific capacitance versus scan rate of 'as prepared' $Ni_{0.6-x}Mn_{0.4}Zn_xFe_2O_4$ (x=0.0, 0.1, 0.2, 0.3, 0.4, 0.5,0.6) ferrites

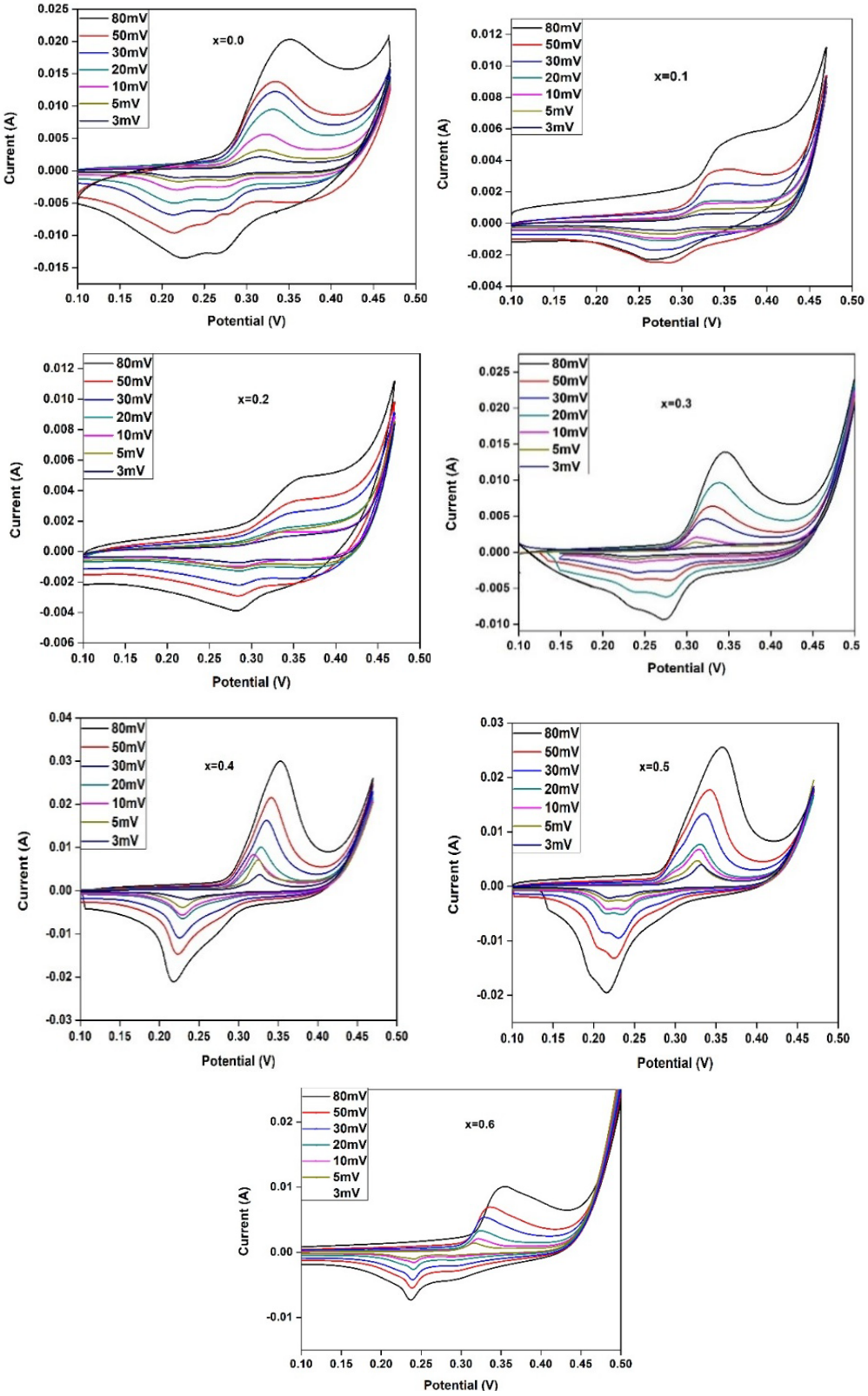


Fig. 4.42a: CV Plots of 'as prepared' $Ni_{0.6-x}Mn_{0.4}Zn_xFe_2O_4$ (x=0.0, 0.1, 0.2, 0.3, 0.4, 0.5, 0.6) ferrites.

Table 4.14: Specific capacitance of 'as prepared' $Ni_{0.6-x}Mn_{0.4}Zn_xFe_2O_4$ (x=0.0, 0.1, 0.2, 0.3, 0.4, 0.5, 0.6) ferrites at variable scan rate.

Scan rate (mV/s)	**Csp (F/g)**						
	0.0	0.1	0.2	0.3	0.4	0.5	0.6
3	87	29	83	88	61	99	66
5	80	24	74	61	64	77	51
10	77	21	42	60	53	71	53
20	74	17	33	54	48	66	45
30	65	15	28	49	45	63	41
50	46	13	22	45	41	61	46
80	4.0	13.7	3.6	62	39	63	37

The specific capacitance (C_{sp}) was calculated from the area of the voltamogram for all the 'as prepared' ferrite material using the formula discussed in chapter 2. The data is tabulated in Table 4.13, sample x= 0.5 showed the highest Csp value of 99 F/g at 3 mV scan rate, followed by sample x= 0.3 with specific capacitance of 88 F/g. There was no proper trend concerning zinc concentration doping. It is also observed that the particular capacitance decreases with an increase in scan rate. The high scan rate is faster; therefore, the electrolyte ions do not diffuse into the inner pores and structure. Only outer sites participate in the Faradaic redox reaction; hence, the diffusion is difficult, leading to a lowering of C_{sp}. The active site on the inner surface cannot undergo the redox reaction due to the faster speed at a high scan rate, thus reducing the capacitance [121-122]. At high scan rates, significant Ohmic resistance results in such observations [122]. Whereas at a lower scan rate, the speed is slower; therefore, electrolyte diffusion over the entire electrode takes place, and hence, the inner and outer active sites get more time for the interaction with the electrolyte [123- 126]

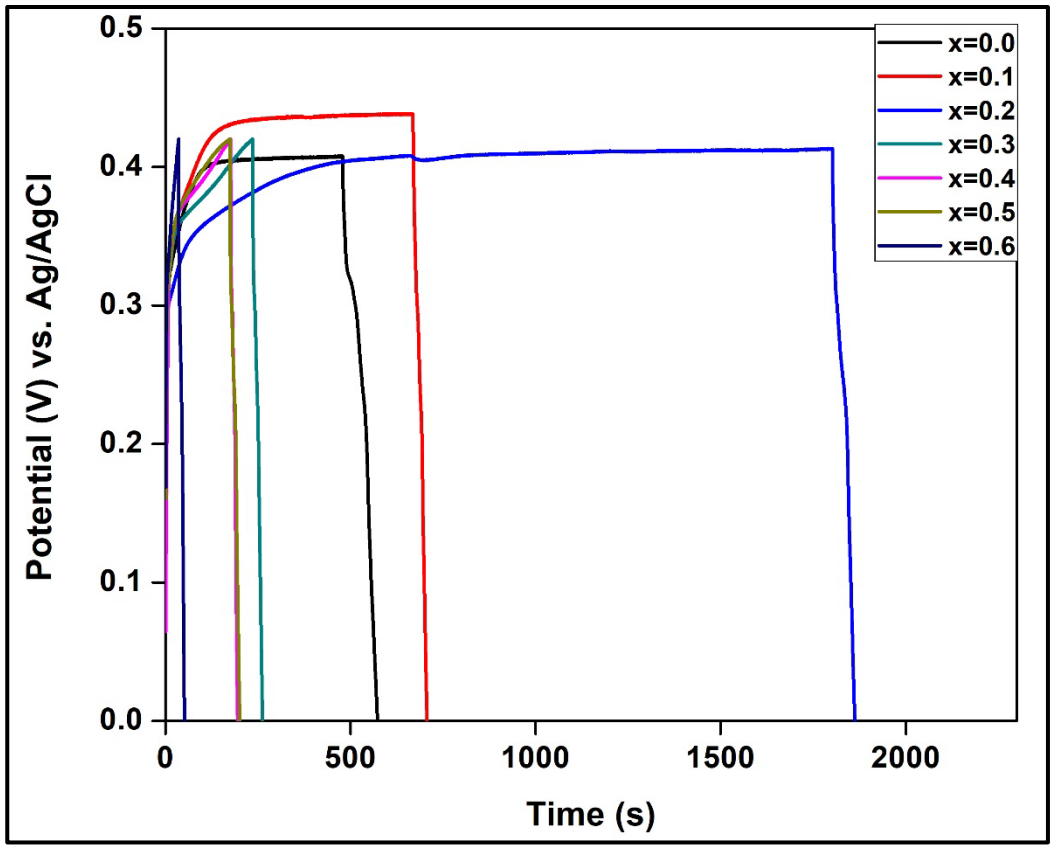


Fig. 4.42b: Galvanic charge/ discharge plots of 'as prepared' $Ni_{0.6-x}Mn_{0.4}Zn_xFe_2O_4$ (x=0.0, 0.1, 0.2, 0.3, 0.4, 0.5, 0.6) ferrites at a current density of 1A g^{-1}

Specific capacitance can be evaluated using another technique apart from CV, galvanic charge/discharge at a particular current density. This can be used to compare the specific capacitance from the data obtained via cyclic voltammetry, in case the curves in CV were not perfectly rectangular. The sample under study acts as a pseudo-capacitor; therefore, GCD is a better technique [127,128]. Fig. 4.42 c displays the galvanic charge/ discharge plots of as-prepared $Ni_{0.6-x}Mn_{0.4}Zn_xFe_2O_4$ (x=0.0, 0.1, 0.2, 0.3, 0.4, 0.5, 0.6) ferrites at a current density of 1A g^{-1}

The non-linearity in curves is obtained for all the samples, indicating Faradaic-type behaviour. This is attributed to the adsorption of ions and quasi-reversible redox reaction at the electrolyte electrode interface [129-134].

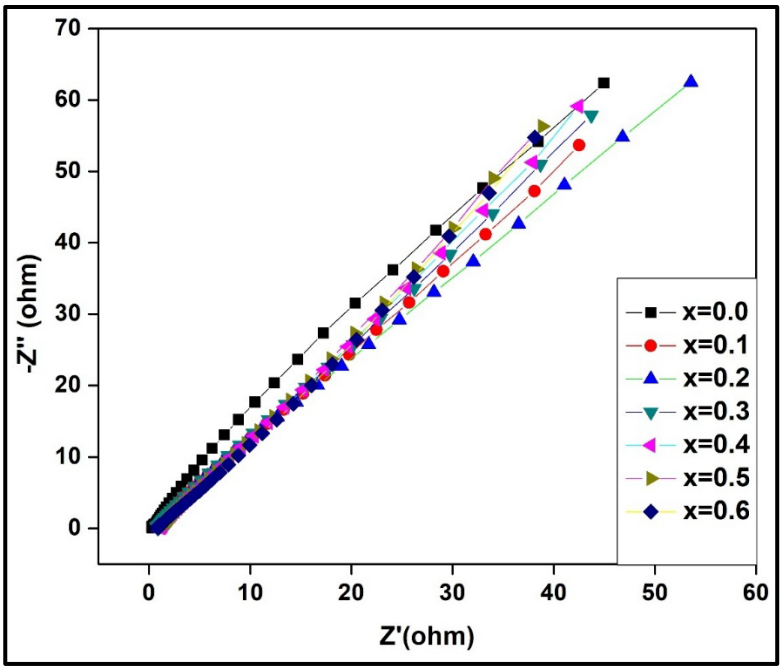


Fig. 4.42 c: The Nyquist plot of 'as prepared' $Ni_{0.6-x}Mn_{0.4}Zn_xFe_2O_4$ (x=0.0, 0.1, 0.2, 0.3, 0.4, 0.5, 0.6) ferrites

The Nyquist plot of 'as prepared' $Ni_{0.6-x}Mn_{0.4}Zn_xFe_2O_4$ (x=0.0, 0.1, 0.2, 0.3, 0.4, 0.5, 0.6) ferrites was obtained from electrochemical impedance spectroscopic studies (EIS). Figure 4.42 c shows the plot, and all the samples show a similar pattern. The electrode/ electrolyte interface in the supercapacitors is determined from the data. The internal resistance and charge transfer reaction are indicated in EIS [135,136]. The figure clearly shows that the plot shows a straight line in the lower frequency range. But at higher frequencies, the plots usually show a semicircle. The higher frequency zone is related to the charge transfer resistance. As the diameter of the circle increases, the charge transfer resistance increases. The electrode/electrolyte redox reaction is related to the lower frequency straight line and indicates that the response is regulated via a mass transfer process. The intercept on the x-axis or Z' corresponds to the solution resistance represented by (R_s). The solution resistance may be due to the intrinsic resistance of the active matter, ionic resistance of the solution, interfacial resistance, or contact resistance [137-140]. The Warburg behaviour is also displayed by the electrolyte diffusion resistance material that varies with frequency [137, 141,142]. All the samples show low Rs values in the range of 0.51-1.37Ω. Thus, a lower value of Rs implies that the electrode material is more active

in KOH electrolytic solution, has high potential in supercapacitor application, and possesses good charge transfer and better Faradaic reaction [137, 143-144].

Table 4.15: Specific capacitance via galvanic charge/ discharge study of 'as prepared' $Ni_{0.6-x}Mn_{0.4}Zn_xFe_2O_4$ (x=0.0, 0.1, 0.2, 0.3, 0.4, 0.5, 0.6) ferrites at current density of 1A g^{-1}

Composition (x) ⟶ / **Current density (A/g)** ↓		**0.0**	**0.1**	**0.2**	**0.3**	**0.4**	**0.5**	**0.6**
Specific Capacitance (F/g)	**1 A/g**	26	50	147	67	46	27	39

4.8 Antibacterial studies

The antibacterial studies of 'as prepared' $Ni_{0.6-x}Mn_{0.4}Zn_xFe_2O_4$ (x=0.0, 0.1, 0.2, 0.3, 0.4, 0.5, 0.6) ferrites against *S. aureus* pathogen were conducted to study the effect of the synthesized material at different zinc concentrations. The protocol followed for the study is discussed in Chapter 2. The doses of 500µg/mL and 1000µg/mL were selected to study the effect of concentration on the pathogen. Figure 4.43 shows the percentage survival versus composition plot, which is self-explanatory and shows the antibacterial activity by varying the doses. The study shows promising results against the ferrites. The results obtained for the samples were compared with the control, which was considered 100% and are represented in Figs. 4.44 and 4.45 for 500 and 1000 µg/mL dosages. At 500µg/mL, sample x=0.5 showed the best results with a minimum survival percentage of 44%, followed by x=0.2 with a survival percentage of 51%. Regarding the 1000µg/mL dose, the results were excellent for specific samples and relatively better than those at 500µg/mL. The sample x=0.5 showed the best results with a survival percentage close to 0%, while the sample x=0.1 showed the best results with a survival percentage of 32%. The antibacterial results of the compounds were in the order: x=0.5>0.1>0.2>0.6>0.3>0.0>0.4 for 500µg/mL g/mL, whereas for 1000µg/mL, the order was x=0.5>0.1>0.2>0.6>0.3>0.0>0.4. From the data, it is revealed that the higher the concentration of the dose, the better the antibacterial activity of the compounds. The antibacterial activity of gram-positive *Staphylococcus aureus* results from ferrite material's ability to produce gaps and pits in the bacterium's membrane, causing it to disrupt and fragment, as reported in the literature [145,146]. The gram-positive *S. aureus* bacteria comprise a thick peptidoglycan layer, a polymer made of sugars and amino acids, which is approximately 20-80 nm in the outer cell wall and does not possess an outer membrane. The gram-positive bacterium's peptidoglycan layer may also include teichoic and lipoteichoic acids and complex polysaccharides, which act as chelating agents and are sometimes used for adhering purposes. Thus, this peptidoglycan layer protects the bacteria from the effects of toxins, chemicals, etc. The high antibacterial activity of sample x=0.5 results from the sound dispersion of the nanoparticles in a solvent medium. The metals in the nanomaterial attack the cell membrane, altering the membrane's permeability, consequently leading to leakage of sugars and proteins and inactivation of respiratory chain dehydrogenases. The formation of free radical species and reactive oxygen also leads to irregular fragmentation of pathogens, leading to antibacterial activity. Another

report suggests that a change in the material's structural properties promotes the release of zinc ions and produces ROS, thus inhibiting the pathogen [147]. Zinc ions are said to bind to the membrane of the pathogen, therefore dispersing and destroying the bacterial cell membrane, resulting in a change in osmotic pressure, thus leaking the internal fluids of the cells [148]. The $Ni_{0.6-x}Mn_{0.4}Zn_xFe_2O_4$ (x=0.0, 0.1, 0.2, 0.3, 0.4, 0.5, 0.6) nanoferrites obtained in the present study showed excellent antimicrobial inhibition properties, thus making it a good source of disinfectant in the contaminated water system.

Various reports suggest that many parameters, like surface structure, porosity, grain size, oxygen vacancy, and degradation rate, may destroy bacterial organelles, thus inhibiting their growth. As reported by many authors, the most critical aspect is forming reactive oxygen species as free radicals when irradiated with visible or UV light. These ROS penetrate the pathogen cell, leading to cell mortality by interacting with the bacterial cell [149-151]. The formation of radical species can be explained by the following mechanism [152]:

$$MFe_2O_4 + hv \rightarrow e^- + h^+ \quad (1)$$

$$e^- + O_2 \rightarrow O_2^{*-} \quad (2)$$

$$e^- + O_2^{*-} + 2H^+ \rightarrow H_2O_2 \quad (3)$$

$$2e^- + HO_2^{*-} + H^+ \rightarrow OH^* + OH^- \quad (4)$$

According to the first step, the result is formation of an electron-hole pair. In contrast, in the last step, an active hydroxyl radical is formed, which results in the peroxidation of lipids and damages the cell. Amorphous samples favor the formation of hydroxyl radicals. As seen from XRD, the size of our 'as-prepared' ferrites is relatively small and shows more amorphous nature than crystalline nature. This also depends on the method of synthesis, which is the combustion method and the annealing temperature.

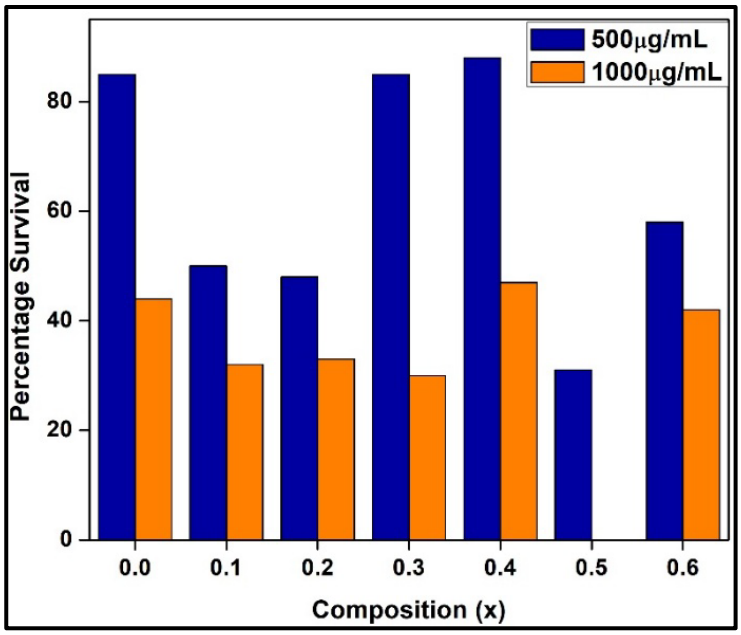
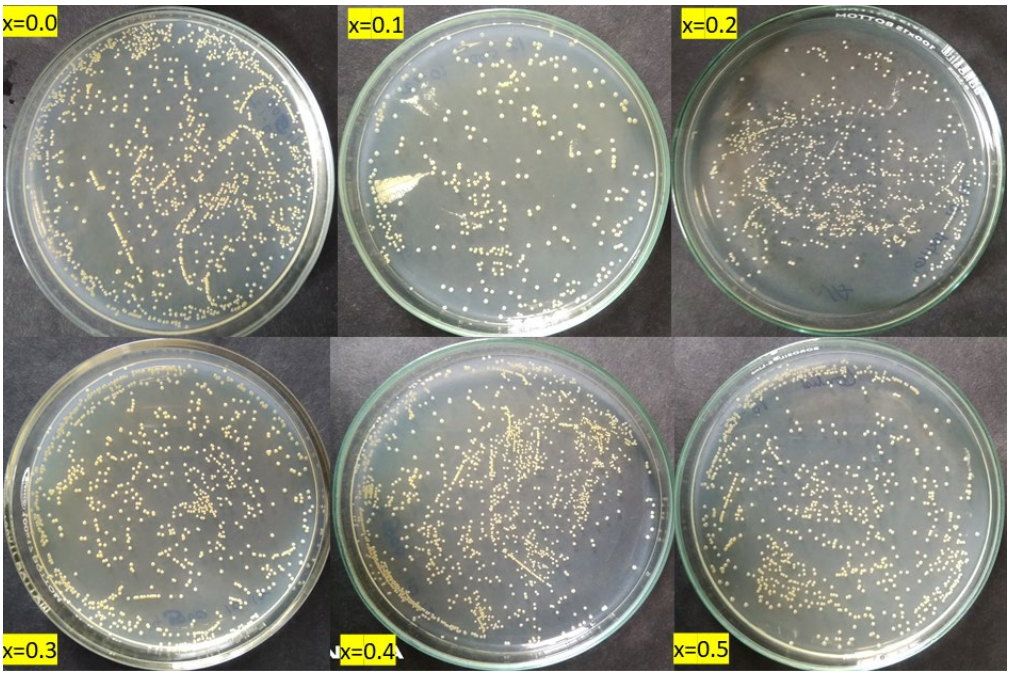


Fig. 4.43: Graph showing the effect of two different concentrations of $Ni_{0.6-x}Mn_{0.4}Zn_xFe_2O_4$ (x=0.0, 0.1, 0.2, 0.3, 0.4, 0.5,0.6) ferrites on percentage survival of *Staphylococcus aureus.*



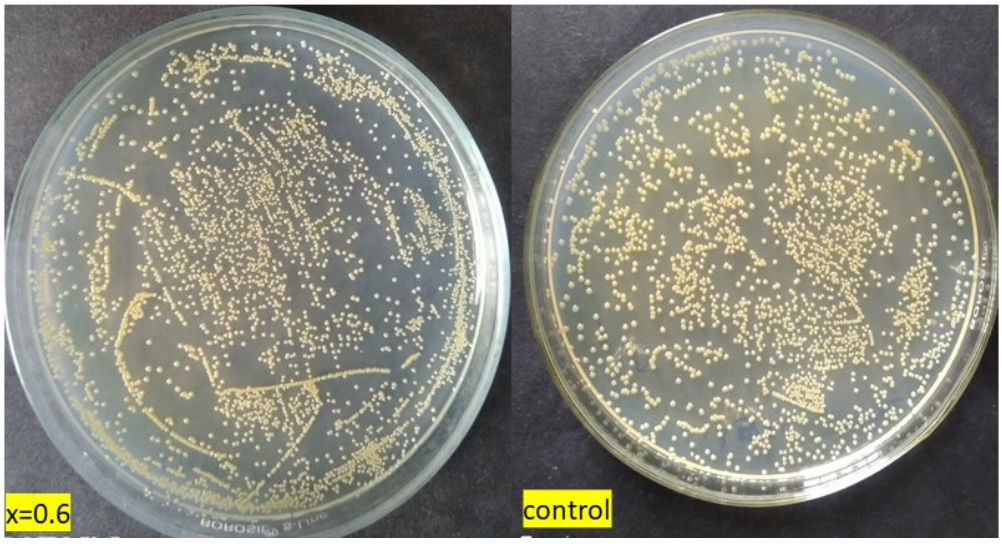
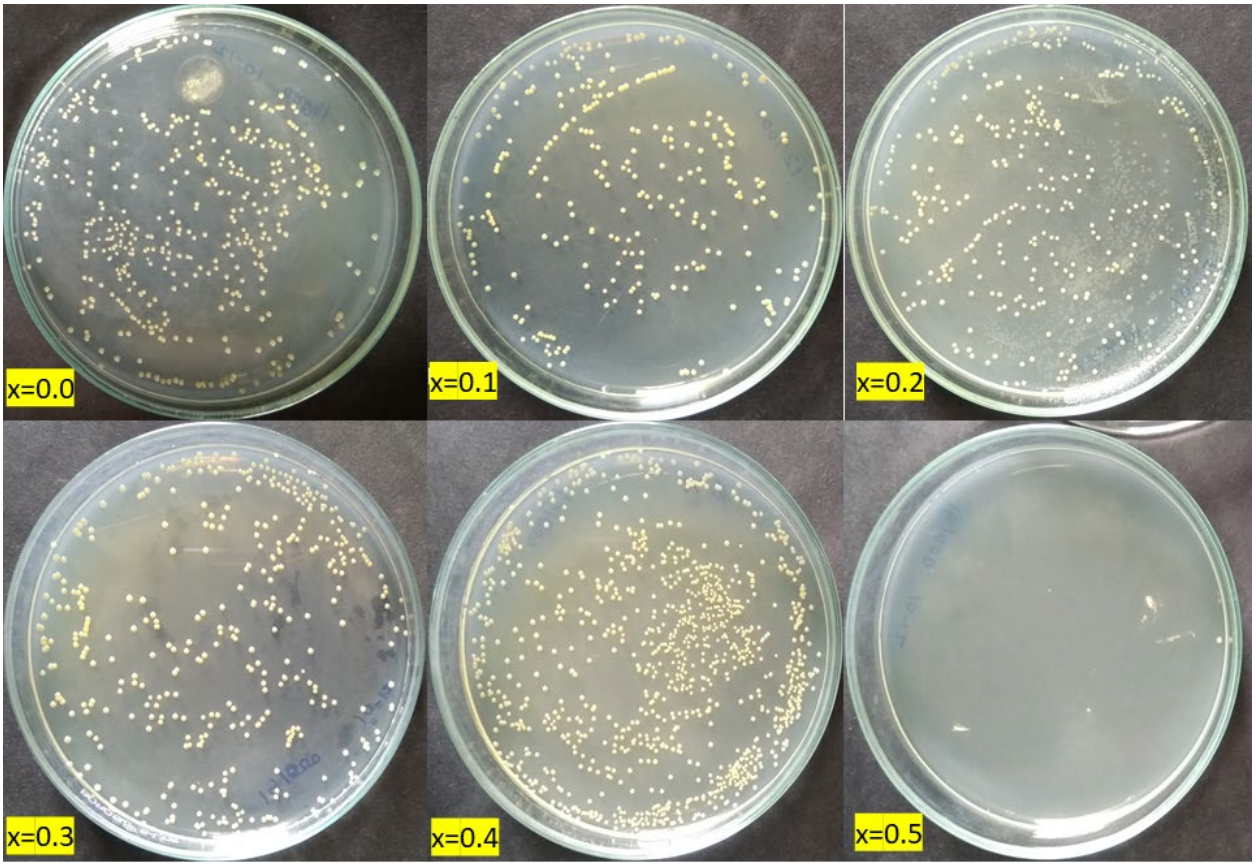


Fig. 4.44: Antibacterial activity of $Ni_{0.6-x}Mn_{0.4}Zn_xFe_2O_4$ (x=0.0, 0.1, 0.2, 0.3, 0.4, 0.5,0.6) ferrites and control at (Conc: 500 µg/mL) on percentage survival of *Staphylococcus aureus*



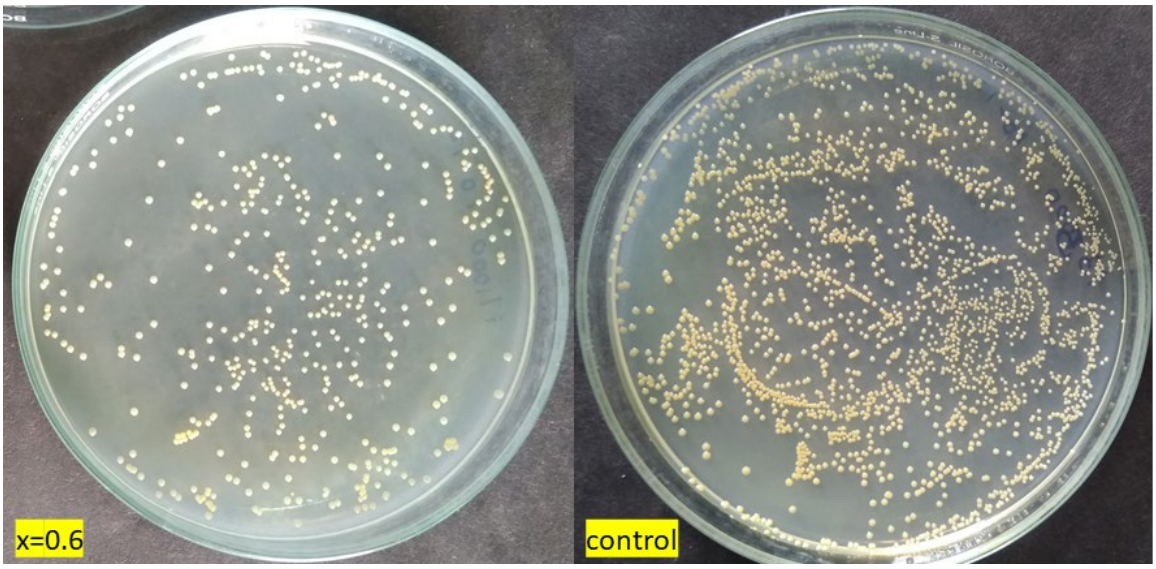


Fig. 4.45: Antibacterial activity of $Ni_{0.6-x}Mn_{0.4}Zn_xFe_2O_4$ (x=0.0, 0.1, 0.2, 0.3, 0.4, 0.5,0.6) ferrites and control at (Conc: 1000 µg/mL) on percentage survival of *Staphylococcus aureus*

4.9 Summary

The $Ni_{0.6-x}Mn_{0.4}Zn_xFe_2O_4$ (x=0.0, 0.1, 0.2, 0.3, 0.4, 0.5, 0.6) ferrites was synthesized via the combustion method using hexamine fuel for the combustion process. The ratio (1:0.625) was selected when optimized via various techniques. The X-ray diffraction patterns of 'as-prepared' and 'sintered' ferrites showed small and broad peaks, while a sharp, intense peak appeared in the latter. The crystallite size was 8-13nm for a's-prepared' ferrites, and that of 'sintered' ferrites is 33-60 nm. The lattice constant followed Vegard's law in both cases. The chemical content was estimated via ICP-AES, and Ni, Zn, Fe, and Mn were present in stoichiometric amounts, with the theoretical result. The infrared spectra of 'as-prepared' and 'sintered' ferrites illustrate two peaks in 400-600cm^{-1} range. The higher band is the ν_1, while the lower is the ν_2. The ν_1 lessens with the addition of zinc. With more Zn, Fe ions move from tetrahedral to octahedral, enlarging the tetrahedral site and reducing vibrational frequency. For the ν_2 band, the change is minimal, but a slight downward trend is observed. The SEM images showed agglomeration with a spherical shape. The sample x=0.1 showed the highest surface area, 128m^2/g, with minimum crystallite size.

Raman studies supported the XRD data by revealing the authentic peaks of spinel ferrites. The A_{1g} peaks in Raman shifted and diminished with zinc addition. The XPS spectra of each element were resolved, from which the prominent peaks and satellite peaks were observed at appropriate positions, thus confirming the valence state of the elements.

DC resistivity showed semiconducting behaviour of ferrites; in the 'sintered' ferrites, the trend decreased with the addition of zinc. The 'sintered' ferrites had higher resistivity than the 'as-prepared' material at RT. The magnetic saturation was lower for the 'as-prepared' than the' sintered' ferrites at RT and 60K studies. The coercivity was higher for 'as-prepared' ferrites at RT and 60K, while the remanence was lower. The blocking temperature is reduced with zinc and with an increase in the field. When the critical temperature was determined, the Tc of the 'sintered' ferrite was found to be lower due to the larger size. The addition of zinc also reduced the Tc from x=0.0 to x=0.5 and suddenly increased it to x=0.6. The dielectric constant and dielectric loss for 'as-prepared' and 'sintered' ferrites at RT and varying temperatures were comparable to literature reports. The Initial permeability at RT slightly increased initially and remained constant, with a drastic increase at high frequency. The Tc was also obtained from the initial permeability studies conducted at varying temperature ranges.

For gas sensing studies, temperature optimization was conducted for each test gas using sample x=0.3. When LPG was studied, it gave the best response at the lowest temperature, with a response as high as 75%. The cyclic voltammetry studies revealed that with a lesser scan rate, the specific capacitance was enhanced with sample x=0.5, giving the best results. The specific capacitance determination via GCD studies showed similar supercapacitance behaviour. The Gram-positive *S. aureus* pathogen was used to study the antibacterial properties of the ferrites, wherein sample x=0.5 showed the best activity against both dosages.

References

1. M. R. Syue, F.-J. Wei, C.-S. Chou, C.-M. Fu, Thin Solid Films, 519 (2011) 8303.
2. L. D. Jadhav, S.P. Patil, A.P. Jamale, A.U. Chavan, Mater. Sci. Forum, 757 (2013) 85.
3. V. D. Sudheesh, N. Thomas, N. Roona, H. Choudhary, B. Sahoo, N. Lakshmi, V. Sebastian, J. Alloys Compd., 742 (2018) 577.
4. V.D. Sudheesh, N. Thomas, N. Roona, P.K. Baghya, V. Sebastian, Ceram. Int., 43(17) (2017) 15002.
5. M. Arshad, M. Asghar, M. Junaid, M.F. Warsi, M. Naveed Rasheed, M. Hashim, M. A. Al-Maghrabi, M.A. Khan, J. Magn. Magn. Mater., 474 (2019) 98.
6. G. Nandhini, M.K. Shobana, Mater. Today Commun., 39 (2024) 109046.
7. F. Bibi, A. Ahmed, Y. Ajaj, A. Abd Al-Sattar Dawood, M. Usman, A. Alodhay, S. Mohammad, Z. Ahmad, A. Kalsoom, Polyhedron, 250 (2024) 116826.
8. A. Sattar, H. M. El-Sayed, K.M. El-Shokrofy, M. M. El- Tabey, J. Appl. Sci., 5 (2005) 162.
9. Tejera-Centeno, C. Rico, R. Gallego, S., J. Mater. Sci., 58 (2023) 5658.
10. A. Dar, M., Shah, J., Siddiqui, W.A. Appl Nanosci., 4 (2014) 675.
11. T. L. Thokoane, T.A. Nhlapo, V. N. Adoons, L. Kotsedi, T. P. Mokoena, T. S. Mahule, T. C. Mokhena, T. Moyo, J. Mol. Struct., 1315 (2024) 138906.
12. T. A. Wania, G. Suresha, R. Masrourb, K. M. Batooc, A. Rasool, Mater. Chem. Phys., 307 (2023) 128169.
13. A. Mahmood, A.Maqsood, Mater. Sci. Eng. B, 296 (2023) 116615.
14. D. Andhare, S. R. Patade, J. S. Kounsalye, K. M. Jadhav, Phys. B: Condens. Matter, 583 (2020) 412051.
15. E. A. Alghamdi, Refka Sai, Results in Phys., 59 (2024) 107549.
16. M. Thommes, K. Kaneko, A.V. Neimark, J. P. Olivier, F. Rodriguez-Reinoso, J. Rouquerol, K.S.W. Sing, Pure Appl. Chem., 87 (2015) 1051.
17. M. Ben Yahia, Y. Ben Torkia, S. Knani, M. A. Hachicha, M. Khalfaoui, A. Ben Lamine, Ads. Sci. Technol., 31(2013) 341.
18. L. George, Viji C, M. Maheen, E.M. Mohammed, Mater. Res. Express, 7 (2020) 015014.
19. X. Zhou, J. Wang, L. Zhou, D. Yao, Appl. Phys. A, 128 (2022) 306.

20. S. Liu, L. Wang, K. Chou, Magn. Magn. Mater., 449 (2017) 49.
21. R. Grissa, H. Martinez, S. Cotte, J. Galipaud, B. Pecquenard, F. Le Cras, Appl. Surf. Sci., 411 (2017) 449.
22. L. Phor, S. Chahal, V. Kumar, J. Adv. Ceram., *9(*2020) 576.
23. N. Guijarro, P. Bornoz, M. Prevost, X. Yu, X. Zhu, M. Johnson, X. Jeanbourquin, F. Le Formal, and K. Sivula, Sustain. Energy Fuels, 2 (2018) 103.
24. R. Dom, A. Sadananda Chary, R. Subasri, N. Y. Hebalkar, P. H. Borse, Int. J. Energy Res., 39 (2015)1378.
25. M. Hua, L. Xu, F. Cui, J. Lian, Y. Huang, J. Bao, J. Qiu, Y. Xu, H. Xu, Y. Zhao, H. Li, J. Mater. Sci., 53(2018) 7621.
26. G. Liu, X. Gao, K. Wang, D. He, Ji. Li, Int. J. hydrogen energy, 41 (2016) 1797.
27. K. Mittal, S. Bera, R. Nithya, M.P. Srinivasan, S. Velmurugan, S.V. Narasimhan, J. Nucl. Mater., 335 (2004) 302.
28. M. Fantauzzi, F. Secci, M. S. Angotzi, C. Passiu, C. Cannas, A. Rossi, RSC Adv., 2019, 9, 19171.
29. B. Jeevanantham, Y. Song, H. Choe, M.K. Shobana, Mater. Letters, 12 (2021) 100105.
30. R. Singh Yadav, I. Kuritka, J. Vilcakova, J. Havlica, J. Masilko, L. Kalina, J. Tkacz, J. Svec,V. Enev, M. Hajdúchová, Adv. Nat. Sci.: Nanosci. Nanotechnol., 8 (2017) 045002.
31. C. Tian, S. Fu, L. A. Lucia, Cellulose, 22 (2015) 2571.
32. I. H. Gul, W. Ahmed, A. Maqsood, J. Magn. Magn. Mater., 320 (2008) 270.
33. R.V. Mangalaraja, A.S. Kumar, P. Manohar, F.D. Gnanam. J. Magn. Magn. Mater., *25*3
(2002) 56.
34. P. Donta, V.K. Katrapally, V.R. Pendyala, NanoWorld J., 2 (2016) 27.
35. B. V. Bhise, A. K. Ghatage, B. M. Kulkarni, S. D. Lotke, S. D. Patil, Bull. Mater. Sci., 19 (1996) 527.
36. E. J.W. Verwey and J.M. De Boer, Rec. Trav. Chim. Phys. Bas, 55 (1936) 531.
37. D. Kothari, S. Phanjoubam and J.S. Baijal, J. Mater. Sci., 25 (1990) 5142.
38. L.R. Devi, S. Phanjoubam, H.N.K. Sarma and C. Prakash, Mater. Lett., 44 (2000) 65.
39. R. Satyanarayan, S.R. Murthy and T.S. Rao, J. Less Common Met., 86 (1982) 115.

40. N. Rezelescu, E. Rezelescu, C. Doroftei and P.D. Popa, J. Phys. Conf. Ser., 15 (2005) 296.
41. C. Cantalini, M. Faccio, G. Ferri and M. Pelino, Sens. Actuators B, 18 (1994) 437.
42. S. A. Saafan, T. M. Meaz, E. H. El-Ghazzawy, M. K. El-Nimr, M. M. Ayad, M. Bakr, J. Magn. Magn. Mater., 322 (2010) 2369.
43. P. P. Sarangi, S.R. Vadera, M. K. Patra, N.N. Ghosh, Powder Tech., 203 (2010) 348.
44. K.S. Rane, Y.M.S. Verenkar, R.M. Pednekar and P.Y. Sawant, J. Mater. Sci.: Mater. Elect., 10 (1999) 121.
45. A. Verma, T.C. Goel, R.G. Mendiratta and R.G. Gupta, J. Magn. Magn. Mater., 192 (1999) 271.
46. Gutiérrez-López, J. Masó, N. Levenfeld, B.A. Várez, A.R. West, J. Am. Ceram. Soc., 99(2016) 2327.
47. M. Maisnam, S. Phanjoubam, Bull. Mater. Sci., 37 (2014) 1227.
48. A. Verma, T.C. Goel, R.G. Mendiratta, R.G. Gupta, J. Magn. Magn. Mater., 192 (1999) 271.
49. A. K. Singh, A. Verma, O.P. Thakur, C. Prakash, T.C. Goel, R.G. Mendiratta, Jpn. J. Appl. Phys., 41 (2002) 5142.
50. Z. V. Mocanu, M. Airimioaei, C. E. Ciomaga, L. Curecheriu, F. Tudorache, S. Tascu, A. R. Iordan, N.M. Palamaru, L. Mitoseriu, J. Mater. Sci., 49 (2014) 3276.
51. M.A. Gabal, Y.M.A. Angari, F.A. Al-Agel, J. Magn. Magn. Mater., 391 (2015) 108.
52. L. Neel, Ann. Phys. (1948) 3137.
53. Y. Yafet, C. Kittel, Phys. Rev., 87 (1952) 290.
54. R. Topkaya, A. Baykal, A. Demir, J. Nanopart. Res., 15 (2013) 1359.
55. R. Topkaya, Ö. Akman, S. Kazan, B. Aktaş, Z. Durmus, A. Baykal, J. Nanopart.Res., 14 (2012) 1156.
56. P. Shirsath, B. G. Toksha, R. H. Kadam, S. M. Patange, D. R. Mane, G. S. Jangam, A. Ghasemi, J. Phys. Chem. Solids, 71 (2010)1669.
57. A.R. Bueno, M.L. Gregori, M.C.S. Nóbrega, Mater. Chem. Phys., 105 (2007) 229.
58. K. Jalaiah, K.V. Babu, J. Magn. Magn. Mater., 423 (2017) 275.
59. G. Xi, Y. Xi, H. Xu, L. Wang, J. Magn. Magn. Mater., 398 (2016) 196.

60. H. Mohseni, H. Shokrollahi, I. Sharifi, K. Gheisari, J. Magn. Magn. Mater., 324 (2012) 3741.
61. A. K. Singh, A. Verma, O.P. Thakur, C. Prakash, T.C. Goel, R.G. Mendiratta, Mater. Lett., 57 (2003) 1040.
62. M. A. Dar, J. Shah, W.A. Siddiqui, R.K. Kotnala, Appl. Nanosci., 4 (2014) 675.
63. C. Srinivas, B.V. Tirupanyam, A. Satish, V. Seshubai, D.L. Sastry, O.F. Caltun, J. Magn. Magn. Mater., 382 (2015) 15.
64. S.G. Gawas, S.S. Meena, P. Bhat, V.M.S. Verenkar, Mater. Chem. Front., 2 (2018) 300.
65. M. Li, X. Liu, T. Xu, Y. Nie, H. Li, C. Zhang, J. Magn. Magn. Mater., 439 (2017) 228.
66. M. Zhang, Z. Zi, Q. Liu, P. Zhang, X. Tang, J. Yang, X. Zhu, Y. Sun, J. Dai, Adv. Mater. Sci. Eng., 2013 (2013) 1.
67. Z. Beji, T.B. Chaabane, L.S. Smiri, S. Ammar, F. Fievet, N. Jouini, J.M. Greneche, Phys. Stat. Sol. (a), 203 (2006) 504.
68. B. Issa, I.M. Obaidat, B.A. Albiss, Y. Haik, Int. J. Mol. Sci., 14 (2013) 21266.
69. D.M. Coutinho, V.M.S. Verenkar, J. Alloys Compd., 782 (2019) 392.
70. I. Szczygieł, K. Winiarska, A. Bieńko, K. Suracka, D. Gaworska- Koniarek, J. Alloys Compd., 604 (2014) 1.
71. L. R. Gonsalves, S. C. Mojumdar, V. M. S. Verenkar, J. Therm. Anal. Calorim., 100 (2010) 789.
72. V.G. Harris; N.C. Koon; C.M. Williams; Q. Zhang; M. Abe; J.P. Kirkland, IEEE Trans. Magn., 31 (1995) 3473.
73. R. Jaina, S. Gulati, Vib. Spec.,126 (2023)103540.
74. S. Ahmad, S. Ali, I. Ullah, M. S. Zobaer, A. Albakri, Sci. Rep., 11 (2021)16190.
75. F. K. Lotegering, J. Phys. Chem. Solid., 25 (1964) 95.
76. W. D. Kingery, H.K. Bowen, P.R. Uhlmann, Introduction to Ceramics, Wiley, New York, (1975) 904.
77. S. Ramesh, B. Dhanalakshmi, B. Chandra Sekhar, P.S.V. Subba Rao, B. Parvatheeswara Rao, Ceram. Int., 42 (2016) 9591.
78. K. Iwauchi, Jpn. J. Appl. Phys., 10 (1971) 1520.
79. A.K. Singh, T.C. Goel, R.G. Mendiratta, O.P. Thakur, C. Prakash, J. Appl. Phys., 92 (2002) 3872.

80. T. Tsutaoka, M. Ueshima, T. Tokunaga, T. Nakamura, K. Hatakeyama, J. Appl. Phys., 78 (1995) 3983.
81. A.K.M.A. Hossain, K.K. Kabir, M. Seki, T. Kawai, H. Tabata, J. Phys. Chem. Solids, 68 (2007) 1933.
82. M.P. Reddy, W. Madhuri, N.R. Reddy, K.V.S. Kumar, V.R.K. Murthy, R.R. Reddy, J. Electroceram., 28 (2012) 1.
83. X. N. X. Liu, X. Huang, K. Huang, Y. Ma, F. Huang, F. Lv, High Temp. Mater. Proc., 35 (2016) 417.
84. N. D. Chaudhari, U.R. Ghodake, S.S. Suryavanshi, Int. J. Adv. Res. Sci. Eng. Technol., 3 (2016) 2940.
85. J. Hwang, M. Choi, H.-S. Shin, B.-K. Ju, M. Chun, Appl. Sci., 10 (2020) 6279.
86. U.B. Gawas, V.M.S. Verenkar, V.T. Vader, A. Jain, S.S. Meena, Mater. Chem. Phys., 275 (2022) 125250.
87. A.A. Sattar, H.M. El-Sayed, K.M. El-Shokrofy, M.M. El-Tabey, J. Mater. Eng. Perform., 14 (2005) 99.
88. U.B. Gawas, V.M.S. Verenkar, V.T. Vader, A. Jain, S.S. Meena, Mater. Chem. Phys., 275 (2022) 1.
89. M. D. S. Rana, R.C. Sinha, D.K. Saha, J. Bangladesh Acad. Sci., 35 (2011) 171.
90. I. N. Esha, Md. Al-Amin, F.T.Z. Toma, Enayet Hossain, M.N.I. Khand, K.H. Maria, J. Ceram. Process. Res., 20 (2019) 530.
91. K. H. Maria, U. S. Akther, I. N. Esha, M. S. Hossain, M. Khan, J. Supercond. Nov. Magn., 33 (2020) 2133.
92. J. S. Ghodake, R. C. Kambale, S. D. Kulkarni, S. R. Sawant, S. S. Suryavanshi, Smart Mater. Struct., 18 (2009) 125009.
93. M. N. Islam, A. Hossain, J. Mater. Res. Technol., 8 (2019) 208.
94. A. M. Sankpal, S.V. Kakatkar, N.D. Chaudhari, R.S. Patil, S.R. Sawant, S.S. Suryavanshi, J. Mater. Sci. Mater. Electron., 9 (1998) 173.
95. S. Kumar, V. Singh, S. Aggarwal, U. K. Mandal, R. K. Kotnala, Mater. Sci. Eng. B, 16 (2010) 76.
96. V. D. Kapse, Research J. Chem. Sci., 7 (2015).

97. R. M. Shedam, P. P. Kashid, S. N. Mathad, R. B. Deshmukh, M. R. Shedam, A.B. Gadkari, Phy. Chem. Solid State, 23 (2022) 626.
98. A. B. Gadkari, T. J. Shinde, P. N. Vasambekar, IEEE Sens. J., 11 (2010) 849.
99. S. Joshi, V. B Kamble, M. Kumar, A. M. Umarji, G. Srivastava, J. Alloys Compd., 654 (2016) 460.
100. A. K. Yadav, R. K. Singh, P. Singh, Sen. Actuators B: Chem., 229 (2016) 25.
101. X. Yang, S. Zhang, Q. Yu, P. Sun, F. Liu, H. Lu, X. Yan, X. Zhou, X. Liang, Y. Gao, G. Lu, Sen. Actuators B: Chem., 270 (2018) 538.
102. J. Wu, D. Gao, T. Sun, J. Bi, Y. Zhao, Z. Ning, G. Fan, Z. Xie, Sens. Actuators, B: Chem.,235 (2016) 258.
103. C. V. G. Reddy, S. V. Manorma, V. J. Rao, Sci. Lett., 19 775 (2000).
104. L. Satyanarayana, K. M.Reddy, & S. V. Manorama, Mater. Chem. Phys., 82 (2003) 21.
105. K. M. Reddy, L. Satyanarayana, S. V. Manorama, R. D. K. Misra, Mater. Res. Bull., 39 (2004) 1491.
106. I. Sandu, L. Presmanes, P. Alphonse, P. Tailhades, Thin Solid Films, 495 (2006) 130.
107. G. M. Shweta, L. R. Naik, R. B. Pujar, S. N. Mathad, Int. J. Self-Propagating High-Temp. Synt., 29 (2020) 157.
108. A. Dey, Mater. Sci. Eng. B, 229 (2018) 206.
109. B. D. Cullity, Elements of X-Ray Diffraction. Reading, MA: Addison Wesley, (1956).
110. J. Wu, D. Gao, T. Sun, J. Bi, Y. Zhao, Z. Ning, G. Fan, Z. Xie, Sens. Actuators, B: Chem., 235 (2016) 258.
111. N. Rezlescu, C. Doroftei, E. Rezlescu, P. D. Popa, Phys. Status Solidi (A) Appl. Mater. Sci., 203 (2006) 306.
112. E. Manova, B. Kunev, D. Paneva, I. Mitov, L. Petrov, C. Estournès, C. D'Orléan, J. L. Eh springer, M. Kurmoo, Chem. Mater., 16 (2004) 5689.
113. R. S. Morrison, Sens. Actuators, 12 (1987) 425.
114. Z. Tianshu, P. Hing, Z. Jiancheng, K. Lingbing, Mater. Chem. Phys., 61, (1999) 192.
115. X. Q. Liu, S. W. Tao, Y. S. Shen, Sens. Actuators B: Chem., 40 (1997) 161.
116. M. Sugimoto, J. American Ceram. Soc., 82 (1999) 269.
117. S. Tao, F. Gao, X. Liu, & O. T. Sørensen, Mater. Sci. Eng. B, 77 (2000) 172.

118. V. Lantto, P. Romppainen, Surf. Sci., 192 (1987) 243.
119. S. Masti, Comp. Appl. Sci., 2 (2013).
120. N. Rezlescu, E. Rezlescu, F. Tudorache, and P. D. Popa, Sens. Transd. J., 78 (2007) 1134
121. L. Liao, T. Fang, G. Yin, D. Zhang, B. Li, Int. J. Electrochem. Sci., 12 (2017) 10211.
122. D.K. Pawar, J.S. Shaikh, B.S. Pawar, S.M. Pawar, P.S. Patil, S.S. Kolekar, J. Porous Mater., 19 (2012) 649.
123. V. Vignesh, K. Subramani, M. Sathish, R. Navamathavan, Colloids Surf. A: Physicochem. Eng. Asp., 538 (2018) 668.
124. S. Tajik, D.P. Dubal, P. Gomez-Romero, A. Yadegari, A. Rashidi, B. Nasernejad, Inamuddin, A.M. Asiri, Int. J. Hydrog. Energy, 42 (2017) 12384.
125. W.G. Pell, B.E. Conway, J. Electroanal. Chem., 500 (2001) 121.
126. M.A.S. Amulya, H.P. Nagaswarupa, M.R.A. Kumar, C.R. Ravikumar, S.C. Prashantha, K.B. Kusuma, Appl. Surf. Sci. Adv., 1 (2020) 100023.
127. M. K. Zate, V. V. Jadhav, S. K. Gore, J. H. Shendkar, S. U. Ekar, A. Al-Osta, M. Naushad, R.S. Mane, J. Anal. Appl. Pyrolysis,122 (2016) 224.
128. E. Elkholy, F.E.-T. Heakal, N.K. Allam, RSC adv., 7 (2017) 51888.
129. Y. Lin, J. Wang, H. Yang, L. Wang, M. Cao, Mater. Sci. Eng. B, 228 (2018) 103.
130. F.M. Ismail, M. Ramadan, A. M. Abdellah, I. Ismail, N.K. Allam, J. Electroanal. Chem., 817 (2018) 111.
131. Zha, P. Xiong, X. Wang, Electrochim. Acta, 185 (2015) 218.
132. L.S. Ferreira, T.R. Silva, V.D. Silva, T.A. Sim˜oes, A.J.M. Araújo, M.A. Morales, D. A. Macedo, Adv. Powder Technol. 31 (2020) 604.
133. E. Elanthamilan, S. Rajkumar, J.P. Merlin, D.S. Jona, K. Monisha, B.C. Meena, , Electrochim. Acta, 359 (2020) 136953.
134. B. Mordina, R. Kumar, N.S. Neeraj, A.K. Srivastava, D.K. Setua, A. Sharma, J. Energy Storage 31 (2020) 101677
135. A. D. Jagadale, V. S. Kumbhar, D.S. Dhawale, C. D. Lokhande, Electrochim. Acta, 98 (2013) 32.
136. A. Rai, A.L. Sharma, A.K. Thakur, Solid State Ion., 262 (2014) 230.

137. B. Bhujun, M.T.T. Tan, A.S. Shanmugam, Results Phys., 7 (2017) 345.
138. S.M. Nikam, A. Sharma, M. Rahaman, A.M. Teli, S.H. Mujawar, D.R.T. Zahn, P. S. Patil, S.C. Sahoo, G. Salvan, P.B. Patil, RSC Adv., 10 (2020) 19353.
139. P. Sen, A. De, Electrochimica Acta, 55(2010) 4677.
140. J. S. Sagu, K. G. U. Wijayantha, A. A. Tahir, Electrochim. Acta, 246 (2017) 870.
141. H. Kennaz, A. Harat, O. Guellati, D.Y. Momodu, F. Barzegar F, J.K. Dangbegnon, N. Manyala, M. Guerioune, J. Solid State Electrochem., 22 (2018) 835.
142. P. Liu, H. Chen, X. Chang, Y. Xue, J. Zhou, Z. Zhao, H. Lin, S. Han, Electrochim. Acta, 231 (2017) 565.
143. Y. Bi, A. Nautiyal, H. Zhang, J. Luo, X. Zhang, Electrochim. Acta, 260 (2018) 952.
144. Meng, M. Yang, L. Zhao, Y. Zhang, X. Shang, P. Jin, W. Zhang, Ceram. Int., 43 (2017) 15959.
145. K. Ishaq, A. Ambali Saka, A. O. Kamardeen, A. Ahmed, M. Is'haq Alhassan, H. Abdullahi, Eng. Sci. Technol. Int. J., 20 (2017) 563.
146. H. Yun, J. D. Kim, H. C. Choi, C. W. Lee, Bull. Korean Chem. Soc., 34 (2013) 11.
147. S. H. Khoreem, A. H. AL-Hammadi, Al-Razi Univ. J. Med. Sci., 6 (2022) 11.
148. M. Satish, V. Sathana, A. Venkatesan, S. David Amalraj, A. Gaspar, M. Maria Julie, J. Jayaprakash, Asian J. Chem., 36 (2024) 377.
149. S. Panicker, I. Ahmady, C. Han, M. Chehimi, A. Mohamed, Mater. Today Chem., 16 (2020)100237.
150. M. A. Zakria, A. A. Menazea, A. M. Mostafa, E. A. Al-Ashkar, Surf. Interfaces 19 (2020) 100438.
151. N.G. Yadav, L. Chaudhary, P. A. Sakhare, T. D. Dongale, P. S. Patil, A. D. Sheikh, J. Colloid Interface Sci., 527 (2018) 289.
152. Hajipour P, Bahrami A, Eslami A, Hosseini-Abari A, Hagh Ranjbar Hr., J. Alloys Compd., 821 (2020) 153456.

Chapter 5

Summary & Conclusion

5.1 Summary of the Thesis

The chapter includes a thesis summary entitled 'Synthesis, Characterisation, and Solid-State Properties of Substituted Ni-Co and Ni-Mn Ferrites and Their Applications'. The precursor combustion technique was used to synthesize zinc-doped Ni-Co ferrite series, while the zinc-doped Ni-Mn ferrite series was produced by the combustion method using hexamine as the fuel. In both cases, non-magnetic zinc was incorporated as the dopant, and its impact on the 'as-prepared' samples' structural, microstructural, morphological, and solid-state properties was understood. In addition, the samples were also sintered at high temperatures, and their effect on sample properties was also included in the present study.

Chapter 1: This chapter includes the introduction to ferrites, their origin, different types of ferrites, and their classification based on their properties, followed by the literature review on samples synthesized using the precursor-combustion method, and the literature on samples produced by the combustion technique. Further, a thorough literature review on Ni-Zn-Co ferrite, followed by literature on Ni-Zn-Mn ferrite, is discussed. A literature survey on applications such as gas sensing, electrochemical performance/ supercapacitance, and anti-microbial studies has also been included.

Chapter 2: This chapter includes the methods and preparation techniques utilized to synthesise the two series with different preparation techniques, namely the combustion and precursor-combustion methods. The precursor-combustion method was used to synthesize the Zn-doped Ni-Co ferrite series, while the protocol followed for the Zn-doped Ni-Mn series was the combustion method, which is discussed in detail. The calcination, pre-sintering, and sintering temperature and their purpose are also discussed here. The characterization techniques, such as IR, TG-DTA, C, H, N, S analyser, isothermal loss, and hydrazine estimation, are discussed in detail.

A brief theory about instrumental techniques used to characterize the ferrite samples is also discussed: XRD, IR, SEM/EDX, TEM/SAED, Raman spectroscopy, XPS, and BET. The solid-state properties were studied as further investigation of the 'as-prepared' and 'sintered' ferrites. Hence, a brief on all the techniques used, such as magnetic studies, including VSM and AC susceptibility, dielectric studies via LCQR meter, DC resistivity, and initial

permeability, is also noted. The setup and protocol followed during gas sensing, electrochemical, and anti-microbial studies are also reported.

Chapter 3 includes synthesizing and characterising zinc-doped nickel cobalt ferrites and their application, along with a comparative study between the a's-prepared' and 'sintered' ferrites. The synthesis of $Ni_{0.6}Co_{0.4}Zn_xFe_2O_4$(x=0.0-0.6) ferrites was done by the precursor combustion method, wherein stoichiometric precursor $Ni_{0.6-x}Co_{0.4}Zn_xFe_2(C_4H_2O_4)_3.6N_2H_4$ (x=0.0,0.1,0.2,0.3,0.4,0.5,0.6) was synthesized in the first step.

The precursor was characterized as soon as it was formed due to its rapid decomposition in moist conditions. The yellow-coloured precursor was estimated by C, H, N, S analyser for its C, H, N, content, while hydrazine content in the samples was verified by titrimetric hydrazine estimation. The weight loss data were collected from TG-DTA-DTG experimental studies, which gave the decomposition temperature and stepwise mass losses. The isothermal weight loss was also obtained via decomposing the samples at set temperatures, which supported the data obtained from TG. The IR data also backed the isothermal and TG data very well. All the reports, when cumulated, successfully confirmed the formation of the precursor through this method.

The 'as-prepared' $Ni_{0.6}Co_{0.4}Zn_xFe_2O_4$(x=0.0-0.6) ferrites calcined at 500 °C was first characterized by XRD, revealing a slight impurity of hematite in the sample x=0.6. The peaks were sharp owing to crystallinity in the materials. When a comparison was made against the samples sintered at 1100 °C for 10h, a noticeable change occurred in peak intensity. The impurity in the x=0.6 sample vanished, giving it a clear single phase. The X-ray data generated parameters such as lattice constant, particle size, density, and porosity. The data revealed that 'sintered' ferrite samples had greater lattice constant values with higher crystallite size, while the porosity was lower due to increased density. With the addition of zinc in the system, the lattice values increased, whereas crystallite size and porosity were random. the chemical analysis revealed the exact stoichiometry of the compounds. The SEM and TEM analysis gave the shape, size, and crystallinity of the compounds. The chemical analysis showed accurate experimental percentages of elemental content owing to a perfect stoichiometry of the compounds. The SEM images revealed nano-sized spherical images, and the EDX measurement done along showed the presence of the elements in appropriate amounts. TEM micrographs showed the exact shape at the nanocrystalline ferrites, and the

crystallinity of the samples was verified via SAED patterns. Both methods employed resulted in agglomerated particles. Inner surface morphology was determined via the BET technique, and the nitrogen isotherm proceeded through multilayer capillary condensation, evolving into a type IV isotherm for mesoporous materials. The ferrite sample x=0.5 achieved the highest area of $39m^2/g$. Further characterisation of ferrites was conducted using Raman spectroscopy. The spectra displaced the peaks, indicating the Raman active modes. No extra peaks were observed, confirming the clear and pure phase. The Raman peaks shift with changes in intensity with the addition of zinc content. The lattice values rise with zinc, where the frequency lowers, as obtained from the spectra, which very well agrees with the reported data. The Raman data were evaluated for both 'as-prepared' and 'sintered' ferrites, wherein 'sintered' ferrite samples showed clear spectra. The XPS measurements were performed, and the valence states of elements present in the ferrite samples were verified. The 2+ oxidation states of Ni, Co, and Zn and the 3+ oxidation state of Fe were confirmed. The presence of satellite peaks alongside the main peaks at specific binding energies is found, which is a characteristic feature for recognizing the respective oxidation states.

The solid-state properties of both 'as-prepared' and 'sintered' ferrites were also compared. The DC resistivity studies were conducted in temperatures between RT and 500 °C for both type of ferrites. The heating and cooling events showed a decrease in resistivity with elevation in thermal heat. At very low temperatures, the resistivity started increasing with temperature for a few ferrite samples, while for the most of the others it remained constant, and after a while, a decrease was observed till 500 °C. The cooling event showed a lower resistivity as the addition of zinc increased for 'as-prepared' and 'sintered' ferrites, though not all the samples showed a proper trend.

The DC magnetization studies of the 'as prepared' and 'sintered' ferrites were performed on a VSM instrument. The M-H analysis at RT and 60K, and M-T studies at variable fields (250, 500, 1000 Oe) in temperatures between 350-60K were conducted. The M_s increased with the addition of zinc, and the increase is attributed to Neel's two-layer model, while the decrease is explained by the Yaket-Kittel model. The highest value of Ms was 76 emu/g for sample x=0.3 among 'as-prepared' ferrite and 87emu/g for the 'sintered' ferrite. The increase in M_s was continuous till x=0.5 and decreased at x=0.6. The M_s values were found to be slightly higher in the case of 'sintered' ferrites. The coercivity and remanence performed at RT for the 'as

prepared' ferrites were larger than those of the thermally 'sintered' material. The M-H studies at 60K showcased a similar performance and trends. Their Ms values, Hc, and Mr values were larger than the RT studies data owing to the freezing of the spins at 60K.

The temperature-dependent FC and ZFC studies revealed that in the case of 'as prepared' ferrites, as the field increases, the blocking temperature lowers, and with zinc addition, the blocking temperature increases except for sample x=0.6. In the case of 'sintered' ferrites, the determination of blocking temperature was difficult as it lay beyond 350K.

The AC susceptibility studies of 'as prepared' and 'sintered' ferrites were carried out from RT to 500 °C. As the heat elevated, the susceptibility was seen to increase, forming a Hopkinson peak. Further, the drop in susceptibility was established until T_c. The Curie temperature (T_c) is the temperature up to which the sample is stable. The plots showed a single Tc proving the purity of the 'as prepared' and 'sintered' ferrite samples. The peak formation indicated the single-domain particles in the ferrite material. As the zinc content rises, this peak formation diminishes, concluding the superparamagnetic nature with the addition of zinc. The doping of zinc leads to a decline in the T_c due to the inclusion of a larger non-magnetic ion. The T_c of 'sintered' ferrites was lower than that of the 'as-prepared' ferrites. This is explained by the lattice constant values, which are larger for 'sintered' samples; thus, the spacing between the ions is larger, so the T_c is smaller.

Dielectric studies were performed at RT at variable frequencies, and studies were also conducted while heating the samples between RT and 500 °C at 1kHz and 1MHz. For the RT studies, the zinc-doped nickel cobalt ferrite showed a usual trend of increase. At lower frequencies, the values are quite high and remain unchanged at higher frequencies. The dielectric loss versus frequency plots showed a similar trend, which is a decrease with an increase in frequency for samples x=0.0 and x=0.3, while the rest of the samples illustrated a peaking behaviour. The sample x=0.1 had the highest dielectric constant as well as the loss. In a similar fashion, the 'sintered' ferrites also had the same trend, with x=0.1 having the highest values. With the addition of zinc, one proper trend was obtained in both cases. When samples were studied against temperature, the 'as-prepared' and 'sintered' ferrite samples both showed a constant dielectric constant for a certain temperature range. The start of the rise in dielectric constant varied for the samples, but was not in order of increasing zinc content. The 'as-prepared' samples showed a hump like peak at 1kHz frequency, while the 'sintered' ferrite

samples did not. Also, no humps were observed for 'as prepared' and 'sintered samples' at1MHz frequency. The sintering of ferrites lowered the dielectric parameters compared to the 'as prepared' ferrites.

The permeability studies of $Ni_{0.6-x}Co_{0.4}Zn_xFe_2O_4$ (x=0.0-0.6) ferrites were done on toroids. The permeability increased to a certain frequency, after which the permeability remained unchanged until a very high frequency was reached, which broke the stability, and again, a rise in permeability was observed. The zone in which the initial permeability remained constant is referred to as the zone of utility, making it commercially useful. The temperature-based studies showed an increase and then a sharp decrease at the Curie temperature. The 'sintered' toroids of ferrites measurements also served as a technique to support PXRD and AC susceptibility studies in proving purity in the samples, as only one Tc was observed. The Tc declined as the zinc was added, just as in AC susceptibility studies. The decline in Tc was due to a larger zinc size in the lattice, increasing the A-B interactions.

The 'as prepared' ferrites were also studied for their applications, such as gas sensing, electrochemical performance, and antimicrobial properties. The gas sensing was performed on several gases: LPG, NH_3, Cl_2, and NO_x. First, the optimum temperature was decided for each gas by measuring the response performance of sample x=0.3 over all the gases at RT, 50, 100, 150, and 200 °C. The results displayed responses against all the temperatures, but their response and recovery time differed, which helped in selecting the best temperature. NO_x studies were therefore conducted at 100 °C for the rest of the samples, while for chlorine, the temperature chosen was room temperature. The reducing gases, such as NH_3 and LPG, were sensed at 100 °C. The highest response obtained for NO_x was 8%, while for Cl_2 was ~60%, LPG gave a good response of 65% and NH_3 was around 9%.

The CV plots of the calcined $Ni_{0.6-x}Co_{0.4}Zn_xFe_2O_4$ (x=0.0, 0.1, 0.2, 0.3, 0.4, 0.5,0.6) ferrites are illustrated, showing electrochemical performance, and the measurements of specific capacitance values were done when the analysis was done at variable scan rates (3, 5, 10, 20, 30, 50, and 80 mV). A three-electrode system was used to carry out the studies in the potential range of 0- 0.5V. The plots indicated a pseudocapacitive behavior with oxidation and reduction peaks. The peaks shifted as the scanning rate changed. The specific capacitance was highest for a 3mV scan rate for all the compositions. The largest specific capacitance was acquired for sample x=0.2 with C_{sp} of 78.9 F/g.

The antibacterial effect was investigated against *Staphylococcus aureus* bacteria at two different dose concentrations (500 and 1000µg/mL). The results were compared with a control, which had 100% survival. For a 1000µg/mL dosage, three samples showed excellent results; they are given as follows: x=0.4>x=0.0> x=0.6, while at 500µg/mL, x=0.0 proved the best material for the efficacy, followed by x=0.4, x=0.6. The other sample did show antibacterial ability, but to a lesser extent.

Chapter 4: Deals with zinc-doped nickel manganese series $Ni_{0.6-x}Zn_xMn_{0.4}Fe_2O_4$ (x=0.0, 0.1, 0.2, 0.3, 0.4, 0.5,0.6) ferrites developed by redox combustion process wherein the fuel utilized was hexamine, the samples were calcined at 500 °C for five hours and sintered at 1100 °C. Several metal nitrate: fuel ratios were optimized to select the appropriate one for further synthesis. Several key characterizations were introduced to evaluate the most suitable ratio. The selected ratio was (1:0.625), using which 'as-prepared' ferrite samples were obtained. The 'as-prepared' ferrites were characterized by PXRD, from which the nano-scale material with a very small size was identified. The phase obtained was pure, with six spinel peaks in the diffractogram. The peaks were broad with lower intensity. A clear peak of spinel was obtained for 'sintered' ferrites, except for sample x=0.6, which showed a hematite phase. The peaks were crystalline and highly intense, proving crystallinity in the samples. The lattice constant was calculated for the 'as prepared' and 'sintered' ferrites, showing a linear trend with the addition of zinc. The values of 'sintered' ferrites were higher than those of the 'as-prepared' ferrites. The 2 theta values shifted towards the lower value with zinc doping. The porosity decreased while the density increased.

The chemical analysis was performed on an ICP-AES instrument, which detected the elements in stoichiometric amounts. The theoretically calculated percentages of elements matched exactly with experimental data. The infrared spectroscopy study was conducted of the 'as prepared' and 'sintered' $Ni_{0.6-x}Zn_xMn_{0.4}Fe_2O_4$ (x=0.0, 0.1, 0.2, 0.3, 0.4, 0.5, 0.6) ferrites at RT. The plots illustrated two bands of M-O bonding belonging to the tetrahedral site and the octahedral site, which lay between 400- 600 cm^{-1}. In the case of the 'sintered' plot, it is clearly demonstrated that the υ_1 peaks gradually shift towards the lower frequency with the addition of larger zinc ions.

The morphological features were determined by SEM-EDX, which showed that synthesized particles possessed predominantly spherical morphology, with sizes falling in the nanometer range, confirming successful formation of nanoparticles. However, significant agglomeration was observed, suggesting that particles tend to cluster together. This agglomeration is caused by high surface energy or high magnetic material. The TEM-SAED identified agglomeration of the nanoparticles, which affected image clarity due to extremely small particle size. The particles were so small that clear individual structures were difficult to distinguish. A particle size distribution histogram indicated sizes between 4 and 30 nm, confirming the nanoscale material. Additionally, SAED patterns displayed some bright spots, suggesting partial crystallinity within the samples. Thus, the two surface techniques contributed to identifying the nanoparticles and supported the data obtained from PXRD.

The BET surface area was measured of the 'as prepared' ferrite samples using a multipoint BET system. The N_2 adsorption-desorption isotherms are type IV with H3-type hysteresis loop, mesopore structures of the samples with slit-like pores were identified. The calculated surface area peaked at 128.64m^2/g for x=0.1, following a drop in surface area, with the rise in zinc content, reaching 56.671m^2/g at x=0.6. This trend suggests that Zn doping affects porosity and particle aggregation. The inverse relation between size and area is evident, with increased zinc content leading to larger crystallites as confirmed by XRD and BET analysis.

The Raman analysis study was conducted at RT, and the results were analyzed of 'as prepared' and 'sintered' $Ni_{0.6-x}Mn_{0.4}Zn_xFe_2O_4$ (x=0.0, 0.1, 0.2, 0.3, 0.4, 0.5,0.6) ferrites. The samples showed four peaks for the 'as prepared' ferrite samples, while clear peaks were shown for the 'sintered' samples. The A_{1g} (1) peak is found to be highest in the sample without Zn due to equal distribution of Fe^{3+} in octahedral and tetrahedral sites. The small size and strong bonding of Fe^{3+} and O^{2-} in tetrahedral sites result in a high force constant. With Zn doping, the Fe^{3+} ion shifts to the octahedral site, reducing the force constant and thus lowering the Raman shift. The photoelectron peaks of Ni 2p, Mn 2p, Zn 2p, Fe 2p, and O1s, along with their satellite peak, confirmed the Ni, Mn, and Zn to be in their respective 2+ oxidation state, while Fe was in the 3+ oxidation state.

The DC resistivity studies for 'as prepared' and 'sintered' $Ni_{0.6-x}Mn_{0.4}Zn_xFe_2O_4$ (x=0.0, 0.1, 0.2, 0.3, 0.4, 0, 5, 0.6) ferrites were measured with increased temperature. The plots showed semiconducting behaviour during the heating and cooling sessions. The resistivity was

between 10^3–10^5ohm cm. The 'as prepared' ferrite had no proper trend with the doping of zinc. Thus, other factors like porosity, particle size, and entrapped moisture play a role in showing the resistivity trend. The sintered also showed a similar trend with temperature increase. The cooling plots of the 'sintered' ferrites were clear and showed lower values than the 'as prepared' ferrites. This trend was related to grain size. When zinc content rose, there was a continuous decrease in resistivity.

The AC susceptibility measurements of the 'as prepared' as well as the 'sintered' $Ni_{0.6-x}Mn_{0.4}Zn_xFe_2O_4$ (x=0.0, 0.1, 0.2, 0.3, 0.4, 0.5, 0.6) ferrites were measured between room temperature and 850 K. The susceptibility rose with temperature, indicating domain formation, followed by a drop at the Curie temperature, where magnetic ordering vanished. A slow fall occurred for 'as prepared' ferrites, while 'sintered' ferrites showed a sharp decline. The T_c was found to decrease with zinc content up to x=0.5, then slightly increases for x=0.6, except for an anomaly for x=0.3. the higher T_c for the 'as prepared' is linked to a smaller lattice parameter. As zinc substitution expands the lattice, it weakens the magnetic field.

At RT, the 'as prepared' ferrite samples showed unsaturation magnetization up to 30,000 Oe, with lower values (9-19 emu/g) because of size and spin disorder. The saturation magnetization increased with zinc content up to x=0.3 (with a drop at x=0.2), then further declined with further doping. This trend follows Neel's two-sublattice model. The excess zinc causes magnetic dilution and spin canting as explained by the Yafet-Kittel model. At 60K, higher values of magnetization were obtained. The trend with zinc content remained constant but shifted to a peak at x=0.5 (as-prepared) and x=0.4 (sintered). The coercivity lowered with the addition of zinc content due to grain growth and reduced magnetic anisotropy. The 'ss-prepared' ferrites exhibited higher coercivity than 'sintered' ferrites due to smaller grain size and higher porosity, which hinders domain wall motion. In 'sintered' ferrites, larger grain size and reduced porosity lead to lower coercivity, consistent with easier domain wall movement and lower magnetic field resistance. The ZFC and FC magnetization studies of the synthesized series were performed between 60-350K at 250, 500, and 1000Oe. In FC mode, magnetization decreased with rising temperature due to thermal disruption of aligned spins. The ZFC curves showed a peak at the blocking temperature, above which superparamagnetic behaviour emerged. Increasing Zn led to lower T_B and reduced anisotropy. The ZFC and FC curves remained apart, indicating particle size variation and clustering. In 'sintered' ferrite samples,

magnetic behaviour shifted from ferrimagnetic to superparamagnetic and paramagnetic with more zinc. A stronger field narrowed the ZFC-FC separation.

The dielectric behaviour was examined for both 'as prepared' and 'sintered' ferrite samples. The dielectric constant showed a rapid drop at low frequencies and gradually leveled off at higher frequencies, a pattern typical of spinel ferrites. This behaviour was explained by the Maxwell-Wagner model, where polarization occurs due to charge buildup at insulating grain boundaries. The dielectric loss followed a similar frequency-dependent trend, decreasing with frequency after a slight initial rise, forming a peak most noticeable in the 'as prepared' ferrites, caused by the matching of electron hopping and applied field frequency. Among all samples, x=0.2 (as-prepared) and x=0.4 (sintered) showed optimal dielectric performance. The temperature-dependent measurements of 'as-prepared' and 'sintered' ferrite samples at fixed frequencies of 1 kHz and 1 MHz were performed. At low temperatures, the dielectric constant remained nearly stable, but increased noticeably at higher temperatures. For 1 kHz, the onset of this rise was established sooner with higher zinc content. The dielectric loss followed a similar pattern, rising with temperature and showing a distinct hump at 1kHz, which was less prominent at 1MHz. An unusual rise in dielectric constant was measured, x=0.3 at 1 kHz, deviating from the general trend.

The initial permeability of zinc-doped Ni-Mn ferrites increased at low frequency due to domain wall motion, remained stable over the mid-frequency range, and rose again at higher frequency due to magnetic resonance. The stable reason is ideal for the device applications, with resonance around 1MHz linked to spin rotation. The permeability increases due to Zn content up to x=0.4, then declines, following the trend of saturation magnetization and anisotropy. The sample x=0.4 showed the highest permeability. The loss tangent was high at low frequency and decreased with frequency, attributed to a lag in domain wall motion caused by lattice imperfections.

The temperature-dependent loss tangent plot shows that the losses remain nearly constant initially, followed by a sharp rise at a specific temperature for each sample. This rise aligns with the temperature where initial permeability begins to drop, just before the Curie temperature. At high temperatures, a gradual increase in loss occurs, marked by a change in slope, indicating the onset of the Curie temperature. This behaviour is attributed to increased

damping of domain wall motion. Additionally, the overall loss tangent decreases with increasing zinc, suggesting improved magnetic stability with Zn substitution.

The study evaluated the gas-sensing capabilities of the materials against both oxidizing gases (Cl_2, NO_x) and reducing gases (LPG, NH_3). The different operating temperatures (RT, 50, 100, 150, 200 °C) were tested to determine the optimal sensing conditions. Each gas was studied across the temperature range using x=0.3 composition to determine its best performance point. NOx: best response (20%) was seen at 100°C; performance dropped above this temperature. Cl_2: 50°C showed the highest response (60%) but with slower recovery; responses declined with higher temperature. NH_3: good responses at lower temperatures (RT and 50°C), with a peak at 100°C using x=0.3; performance dropped at higher temperatures. LPG: displayed the strongest sensing at room temperature, with a peak response of 40%. However, the response decreased with increasing temperature. Further, the gas responses were measured for all compositions (x=0.0 to 0.6) under their respective optimum temperature. For NO_x at 100°C, x=0.3 showed the best response (20.6%). For Cl_2 at 50°C, x=0.3 showed the highest response (61.5%). For NH_3 at 100°C, x=0.3 was the optimal composition with a peak response of 48%. For LPG at RT, x=0.0 had the highest response (76%), followed by x=0.2 and x=0.1.

The supercapacitance activity of the synthesized ‘as prepared’ ferrites was investigated using cyclic voltammetry across a scanning voltage ranging from 3 to 80mV/s in a three-electrode system, with 3M KOH as the electrolyte and between 0 and 0.5 V. The voltammogram displayed distinct cathodic and anodic peaks, confirming the pseudocapacitive nature of the material. With the rise in scan rate, the current density also rose, and the anode peak shifted positively while the cathodic peak shifted negatively. A smaller scan rate resulted in reduced area under the curve, indicating a direct correlation between scan rate and electrochemical performance.

The synthesized nanoparticles were evaluated for antibacterial efficiency against *Staphylococcus aureus* at two different concentrations: 500 and 1000µg/mL. The enhanced bacterial inhibition was observed at higher doses, with the x=0.5 sample exhibiting the highest effectiveness, nearly eliminating bacterial survival at 1000µg/mL. The antibacterial mechanism is linked to nanoparticle-induced membrane damage, reactive oxygen species

formation, and the release of zinc ions, which collectively impair bacterial function. The amorphous structure, fine particle size, and synthesis method contribute to this behaviour. These results highlight the potential of zinc-substituted ferrites, particularly x=0.5, as a strong antibacterial material for water purification.

5.2 Conclusion

Some of the salient features of 'as prepared' and 'sintered' zinc-doped Ni-Co and Ni-Mn ferrites are listed in this section.

- The effect of the addition of non-magnetic zinc ions in $Ni_{0.6}Co_{0.4}Zn_xFe_2O_4$(x=0.0-0.6) ferrite series
    - Rise in lattice parameter.
    - No proper trend with zinc substitution was seen in the case of resistivity, except that x=0.6 sintered samples showed the lowest resistivity, as per the reports.
    - Saturation magnetization for 'as prepared' ferrite samples increases up to x=0.3 for RT measurements, while for 60K measurements, the saturation magnetization continuously rises, with the exception of sample x=0.5.
    - For 'sintered' ferrite, the saturation magnetization rises till x=0.3 for RT study, while at 60K, the magnetization increases up to x=0.5 and then drops for x=0.6.
    - Blocking temperature increases.
    - The dielectric constant and dielectric loss for the 'as prepared' at RT did not show a peculiar trend with zinc doping, while when studied with respect to temperature, the values decreased with zinc content, with a few samples showing out-of-trend behaviour, while for 'sintered' ferrites, when studied with respect to temperature at fixed frequencies, the values increased.
    - With an increase in zinc, initial permeability at RT increased with anomalous behaviour for sample x=0.5. The Tc dropped as the addition of zinc increased, just like the AC susceptibility behaviour.

❖ Comparative study between the 'as prepared' and 'sintered' $Ni_{0.6}Co_{0.4}Zn_xFe_2O_4$(x=0.0-0.6) ferrites

- The lattice parameters of the 'as prepared' ferrites were lower than those of the 'sintered' ones.
- The porosity for 'sintered' ferrites was lower, while the density and crystallite size were higher.
- The resistivity for 'sintered' ferrites at increased temperature was less than that of the 'as prepared' ferrite samples, while at lower temperatures, the resistivity was high.
- The magnetic saturation was higher for 'sintered' ferrites in the case of RT and 60 K studies. The coercivity and residual magnetization were lower in the case of 'sintered' ferrites.
- The blocking temperatures (T_B) for 'as prepared' ferrites were obtained for all the fields, while only the lower field T_B was obtained in the case of 'sintered' ferrites. The T_B was higher for 'sintered' ferrites in a particular field than for 'as prepared' ferrites.
- The T_c for 'sintered' ferrites was lower than that of the 'as prepared' ferrites. The 'as-prepared' ferrites showcased single-domain characteristics, while the plots obtained for the 'sintered' ferrites were of a multi-domain particle type.
- The high values of dielectric constant and dielectric losses were obtained for the 'as prepared' ferrites at RT. When the studies were conducted at varying temperatures from RT to 500 °C at fixed frequencies, the values of dielectric constant and dielectric loss were higher in the case of 'as prepared' ferrites.

❖ Applications of $Ni_{0.6}Co_{0.4}Zn_xFe_2O_4$(x=0.0-0.6) ferrites

1. Gas sensing studies showed a good response towards the gases, making it a useful material
   - ✓ The optimum temperature for NO_x was 100 °C; sample x=0.0 was found to give a high response with quick recovery.
   - ✓ RT was selected to study chlorine gas; sample x=0.5 yielded the highest response of 63%.
   - ✓ At 100^{o}C the LPG response were optimal, with sample x=0.3 showing great performance of 65%.

- ✓ NH_3 gas at 100°C showed a response of 9% for x=0.3 which was highest in the entire series.

2. Electrochemical performance of the samples yields good capacitive properties.
   - ✓ Highest supercapacitance was measured for the lowest scan rate of 3mV.
   - ✓ As the zinc content increased, the supercapacitance also increased, with a few exceptions in between.
   - ✓ The sample x=0.6 showed the highest C_{sp} for all the scan rates except for 3Mv, where the highest was observed for x=0.2.

3. Antibacterial performance of ferrite was measured against *S. aureus* bacterial culture.
   - ✓ At 500 µg/mL, the order of activity was as follows: x=0.0>0.4>0.6>0.3>0.1>0.2>0.5.
   - ✓ At 1000µg/mL, the order of activity was as follows: x=0.4>0.0>0.6>0.3>0.2>0.1>0.5.

- The effect of doping large zinc ions in $Ni_{0.6-x}Mn_{0.4}Zn_xFe_2O_4$ (x=0.0, 0.1, 0.2, 0.3, 0.4, 0.5, 0.6) ferrites.
  - Lowering of lattice parameter with lowering of zinc content, and shifting of the 2theta value to a lower value with an increase in zinc.
  - The IR band observed at ~600 cm^{-1} shifted towards a lesser wavenumber with zinc as seen in sintered data.
  - The A_{1g} (1) band diminished as the zinc content rose.
  - The resistivity decreased with the addition of zinc, as per the heating curves of sintered samples.
  - The M-H study concluded that saturation magnetization in the case of 'as prepared' and 'sintered' increased up to x=0.3, with further lowering, except x=0.2 (as-prepared) showed an anomaly.
  - In the case of the 60K M-H study, the 'as prepared' ferrite samples showed an increase till x=0.5 and then a decrease, while for the 'sintered' ferrite samples, the increase was up to x=0.4, following a decrease.
  - The blocking temperature decreased with the addition of zinc.
  - The Curie temperature decreased with zinc up to x=0.5.

- The dielectric curves were not in order with the doping of zinc in the case of the dielectric study.
- The initial permeability increased till x=0.4, further decreased just as magnetization.
- The Tc obtained from initial permeability decreased with zinc content.

❖ Comparative study between the 'as prepared' and 'sintered' $Ni_{0.6-x}Mn_{0.4}Zn_xFe_2O_4$ (x=0.0, 0.1, 0.2, 0.3, 0.4, 0.5, 0.6) ferrites.

- Lattice constants, x-ray density, and crystallite size were greater for 'sintered' ferrite samples, and the porosity was smaller.
- The intensity of peaks in the case of 'sintered' ferrites was high and sharp.
- At minimum temperature, the resistivity of 'sintered' ferrites was higher, while at maximum temperature, the resistivity was lower, with some exceptions.
- The saturation magnetization values for the RT and 60K studies were higher for 'sintered' ferrites.
- Sharp falls at T_c were seen in 'sintered' ferrites susceptibility plots, indicating a multi-domain nature of the samples, while the plots for 'as-prepared' ferrites indicated a single-domain nature.
- The Tc for 'sintered' ferrites was lower than that of 'as prepared' materials.
- The dielectric constant and dielectric loss for 'as prepared' ferrites were higher than those of 'sintered' ferrites.
- When the dielectric study was conducted at 1kHz, the 'sintered' ferrite samples showed higher values, while at 1MHz, the 'as prepared' ferrites showed higher values.

❖ Application of $Ni_{0.6-x}Mn_{0.4}Zn_xFe_2O_4$ (x=0.0, 0.1, 0.2, 0.3, 0.4, 0.5, 0.6) ferrites.

1. The gas-sensing properties of the ferrites against oxidizing and reducing gases were tested.
   - ✓ The sample x=0.3 showed the best response towards NOx gas at 100^{o}C with 20.6% response.
   - ✓ At 50 °C, Cl_2 was detected with a high response of 61.5%.
   - ✓ NH_3 was detected at optimal temperature of 100^{o}C with response of 31% for sample x=0.0.

- ✓ LPG detection by the samples in the series showed an excellent outcome at RT, with the highest being 76% for sample x=0.0.

2. Cyclic voltammetry evaluated the supercapacitance ability of the ferrites under study.
    - ✓ The lowest scan rate yielded the highest supercapacitance value for all the compositions.
    - ✓ The sample x=0.5 showed the 99F/g specific capacitance.
    - ✓ The anodic and cathodic peaks indicated the pseudocapacitive nature of the samples.
    - ✓ The peaks shifted as the scan rate changed, and the area under the curve reduced with a lower scan rate.
3. The activity of the ferrites against the pathogen was evaluated thoroughly.
    - ✓ At 500 µg/mL, the order of activity was as follows: x=0.5>0.1>0.2>0.6>0.3>0.0>0.4
    - ✓ At 1000 µg/mL, the order of activity was as follows: x=0.5>0.1>0.2>0.6>0.3>0.0>0.4.

Appendix I

List of Publications

Sanjali Navelkar, K. Salkar, L. Charya, V.M.S. Verenkar, Effect of Zn Substitution on Properties of $Ni_{0.6-x}Zn_xMn_{0.4}Fe_2O_4$(x= 0.0,0.2,0.4,0.6) and to Study its Antibacterial Activity as a Potential Antibacterial Agent, Journal of Cluster Science, 36 (1) (2024).DOI:10.1007/s10876-024-02745-3

Appendix II

List of Symposiums, Workshops, and Conferences Attended

1. Participated in the three-day workshop "X-ray Crystallography" held on 21st – 23rd July 2022, organized by the School of Chemical Sciences and School of Physical & Applied Sciences, Goa University, Goa.

2. Participated in an oral presentation at the 23rd DAE-BRNS symposium on Thermal Analysis (THERMANS 2022) held at Khalsa College, Amritsar, Punjab from November 3rd-5th, 2022.

3. International Conference on Nanotechnology: Opportunities & Challenges (ICNOC-2022) online, organized by the Department of Applied Sciences & Humanities, Faculty of Engineering & Technology, Jamia Millia Islamia, New Delhi, India, on November 28-30, 2022.

4. Participated in DAE-BRNS 9th Interdisciplinary Symposium on Material Chemistry (ISMC 2022) held at Bhabha Atomic Research Centre, Mumbai, during 7-10 December 2022.

5. Participated in the oral International Conference on Functional Materials in Advanced Technologies-1 organized by the Department of Physics, Central University of Kerala, from 2-4 January 2023.

6. International Conference on Advanced Materials: Properties and Applications 20-24 February 2023 Organized by the School of Physical and Applied Sciences and the School of Chemical Sciences, Goa University.

7. Participated in National seminar, Theme: Trends in Techniques of Preparation & Characterization of Smart Material at Ravindra Bhavan, Margao, Goa, Day 3-4 March 2023.

8. Participated in ICDD workshop on 'Material Characterizations using Powder X-ray Diffraction' under the Goa University Crystallography workshop 2023-GUCW-I.

9. Participated in the Goa University Crystallography workshop 2024-GUCW-II held on 23rd-24th October 2024.

10. Participated in ‘‘Igniting Curiosity: a one-day symposium on Advanced Science for Young Researchers’’ held on 8th November 2024.

11. International Conference on Functional Nanomaterials and their Applications in Sustainability, Environment, Energy, and Biotechnology (ICFNA-2024).

Journal of Cluster Science (2025) 36:23
https://doi.org/10.1007/s10876-024-02745-3

ORIGINAL PAPER

Effect of Zn Substitution on Properties of $Ni_{0.6-x}Zn_xMn_{0.4}Fe_2O_4$(x = 0.0,0.2,0.4,0.6) and to Study its Antibacterial Activity as a Potential Antibacterial Agent

Sanjali Navelkar[1] · Komal Salkar[2] · Lakshangy Charya[2] · V. M. S. Verenkar[1]

Received: 23 July 2024 / Accepted: 28 November 2024 / Published online: 16 December 2024
© The Author(s), under exclusive licence to Springer Science+Business Media, LLC, part of Springer Nature 2024

Abstract

$Ni_{0.6-x}Zn_xMn_{0.4}Fe_2O_4$ (x = 0.0,0.2,0.4,0.6) were prepared by the combustion method using hexamine as the fuel. Zinc replacement in place of Ni and its effect on various structural, electric, magnetic, and dielectric properties was studied using several instrumental techniques. X-ray diffraction revealed a monophasic cubic spinel structure for the samples. Scherrer's formula determined that the crystallite size (D) was in the nano range from 8 to 15 nm. The lattice constant values showed an increment with zinc content while porosity was seen to drop. The scanning electron microscopy images showcased agglomerated particles due to magnetic interaction between them and were found to have spherical morphology. TEM provided the average particle size obtained from the histogram, while the SAED pattern revealed the semicrystalline nature of the samples. Infrared spectra showed two metal-oxygen peaks peculiar to spinel ferrite in the range of ~400–600 cm^{-1}. Confirmation of the spinel phase was made using room temperature Raman analysis, and the change in Raman peaks was observed with an increase in zinc content. XPS studies revealed Ni^{+2}, Mn^{+2}, Zn^{+2}, and Fe^{+3} to be in their respective valence states. A resistivity study was conducted from RT- 500 °C, which showed a decrease in resistivity with an increase in temperature, a typical trend of semiconduction. Dielectric studies performed at RT showed the highest dielectric constant with the minimum dielectric loss for sample x = 0.2, while variable temperatures studied at different frequencies showed x = 0.6 with the highest dielectric constant. Saturation magnetization values increased up to x = 0.4, which Neel's two sublattices model explained, and a further decrease in magnetization was explained by the Yafet- Kittle model. AC susceptibility revealed Curie temperature up to the point where the sample behaved as ferrimagnetic material. The main aim and objective were to explore the suitability of synthesized materials for their applications and to study zinc's influence on various properties and antibacterial activity. The antibacterial activity of the samples was investigated as a potential candidate against highly resistant and infectious *Staphylococcus aureus*, and sample x = 0.2 showed the best results.

Keywords Combustion synthesis · Spinel ferrites · Nanomaterials · X-ray diffraction · Antibacterial studies

Introduction

The spinel nanoparticles are an essential class of compounds possessing several applications, which range from biomedical [1], antimicrobial agent [2–4], antenna core [5], catalyst/photocatalyst [6–10], microwave absorbing materials [11], gas sensors [12–16], etc. Synthesis of these ferrites involves several methods, including some very commonly exploited methods such as the ceramic method [17–19], co-precipitation [20–22], combustion [23, 24], citrate-precursor method [25], solvothermal [26, 27], hydrothermal [28, 29], sol-gel method [30–32], microemulsion [33], sonochemical method

✉ V. M. S. Verenkar
vmsv@rediffmail.com

[1] School of Chemical Sciences, Goa University, Taleigao Plateau, Goa 403206, India

[2] School of Biological Sciences & Biotechnology, Goa University, Taleigao Plateau, Goa, India

[34], polyol method [35], mechanical milling [36], spray pyrolysis [37] etc. Methods like solution combustion permit control over size, homogeneity, composition, and stoichiometry, yielding high-purity quality products [38]. Ni-Mn ferrites have attracted researchers due to their tremendous properties. This soft magnetic material has excellent magnetic, electrical, and optical properties. These materials possess high electrical resistivity, permeability, permittivity, coercivity, saturation magnetization, and low power losses. These characteristic features make this material very useful in various fields. Ni-Mn ferrites are utilized in multiple applications: transducers, electronic appliances, transformers, and inductors. They are also valuable for biomedical applications and as sensors and biosensors [39, 40]. E. R. Kumar et al. [41] synthesized Mn-substituted nickel ferrites under different fuel ratios of (50%, 75%, and 100%). The study was based on the effect of fuel concentration on various properties of the compounds. The structural properties like lattice parameter, interplanar distance, and size were obtained from the XRD data, and the calculated size was found to be well in the nanoscale region from 25 to 75 nm for as-prepared samples. The saturation magnetization values increased with the rise in fuel percent and sintering temperature. Manganese zinc ferrites have good magnetic and dielectric properties; their permeability and magnetization make them technologically essential as transformers, recording heads, and coils. However, these ferrites possess low resistivity, so high eddy current losses exist at higher frequencies [42–45]. Nickel-zinc ferrites are known for low and high-frequency applications but have limitations. Ni-Zn ferrites have high resistivity but low permeability at high frequency. They can be used as inductors, transformers, phase shifters, etc. [46–51]. The properties of these ferrites are studied individually. To overcome the limitations, a combination of these elements has been studied; A. A. Sattar et al. [52] synthesized nickel manganese zinc ferrites where manganese was doped into the Ni-Zn system, and its influence on the properties was studied. With increased manganese concentration, the grain size increased, increasing the magnetization and permeability. They also learned their electrical properties, such as resistivity and thermoelectric power. The increase in dopant enhanced resistivity, thus proving a suitable material for high-frequency application. They also reported the dielectric properties, which agreed with other reported data. Various other authors have performed similar studies, obtaining comparable results as the manganese concentration increased [53–56].

S. Thota and co-workers [57] have studied nickel-substituted manganese zinc ferrite and their structural, vibrational, and electronic structure in detail. The Raman spectroscopy in their studies revealed the presence of Fe and Zn ions in the tetrahedral interstitial sites in the FCC anion lattice in equal fractions. The Mossbauer spectra showed that Fe^{+3} was present in tetrahedral and octahedral interstitial sites, whereas Ni^{+2} was in the octahedral site. XPS also confirmed the Fe^{+3} ions in both sites. The X-ray diffraction technique helped to calculate the intensity ratio and compared it with the observed ratio, which provided information about cation distribution. F.A. Ahmed et al. [58] studied the nickel substitution on manganese zinc ferrite. The X-ray studies of their samples confirmed the formation of a single phase. They determined the resonance line width and Lande's splitting factor using EPR spectroscopy. EPR revealed super-paramagnetism in the compounds. The saturation magnetization of $x = 0.1$ was found to be the highest. The SEM images of the samples revealed porous agglomerates. Many reports on Ni substitution in the Mn-Zn system are available where characterization, solid-state properties, and applications like sensing have been reported [46, 59, 60]. Our main aim is to focus on zinc-doped Ni-Mn ferrite and to study the effect of dopant on various properties and the application under study. Zinc, being non-magnetic in nature, alters or enhances the properties of the nanomaterials. The structural and magnetic properties are seen to improve with an increase in the content of the dopant (zinc) concentration [61, 62]. In the literature, very few reports are available on the zinc-doped series, and therefore, we aim to study the zinc-doped Ni-Mn ferrite series. Ferrites are known to show antibacterial activities; however, no reports are available in the literature sharing the antibacterial activity of the present ferrite series against *Staphylococcus aureus* bacteria. *Staphylococcus aureus* is a Gram-positive, opportunistic pathogen known to cause nosocomial infections. *Staphylococcus aureus* is the cause of several skin infections, bacteremia, nosocomial pneumonia, surgical wound infections, and endocarditis [63]. The tendency of the bacteria to cause cross infections and to colonize the individual persistently makes it even more problematic. Unchecked usage of antibiotics to curb the spread of this bacteria has resulted in resistance to several antibiotics, particularly cephalosporins. This has also led to the emergence of numerous resistant varieties of Staphylococcus aureus, such as Methicillin-resistant Staphylococcus aureus (MRSA), Vancomycin intermediate Staphylococcus aureus (VISA), and Vancomycin-resistant *Staphylococcus aureus* (VRSA) [64]. Life-threatening diseases caused by *Staphylococcus aureus* and its ability to resist many antibiotics have made it a concerning issue in the medical field. Consequently, an urgent need for new antimicrobial agents has surfaced. In the present study, we have used zinc-doped nickel manganese ferrite as an antibacterial agent. The oxide materials can be scaled down and altered depending on the metals they contain, the method of preparation used, the crystallinity of the sample, etc., which changes its structural, mechanical, electrical, and

optical properties. The changes in the properties, especially size, increase the surface area of the samples, enhancing the interactions between the cell molecules, thus enabling better activity. Studies on zinc oxide nanomaterials and their activity against various pathogens have been reported [65]. Zinc oxides have been reported to enter the pathogen's cells, interact with the surface and nucleus, and exhibit antibacterial activity [66]. Various food industries have adopted nanomaterials as antimicrobial agents, such as oxides of metals like zinc and nickel, which are harmful to pathogens but not to human cells. This is due to the large surface area to volume ratio of the nanomaterials possessed [67]. Due to their biocompatibility with humans using nanomaterials as antimicrobial agents, they can be considered good candidates in the field. Due to various reports on zinc activity as an antimicrobial agent, zinc was selected as a dopant with increasing concentration to study the effect of zinc at different concentration levels. In a recent study, NiO/ZnO nanohybrid materials have been tested against various bacterial and fungal pathogens. The study tested 25% and 50% NiO/ZnO ratios and pure NiO and ZnO as antimicrobial agents. The study was conducted via the agar-well diffusion method to understand and study the antibacterial activity of the nanohybrid. 100 µL of nanohybrid material was utilized to study the effect on gram-positive and gram-negative bacteria and fungal pathogens by measuring its inhibition zones. Results showcased activity against all pathogens with good results for hybrid compounds compared to pure NiO or ZnO compounds [65]. CuO@BaO/CaO was synthesized using a simple co-precipitation method to study its antibacterial activity against gram-positive and gram-negative bacteria. The disk diffusion method was adopted to study the E. coli and S. aureus specimens. Ba/Ca doped CuO showed results against both pathogens at various doses. The S. aureus gram-positive bacteria microorganism development was reduced more than E. coli when exposed to a (0.5:0:3:0.2) ratio. Activity improved with decreased barium concentration and increased calcium concentration [68].

We are reporting here zinc-doped Ni-Mn ferrite with composition $Ni_{0.6-x}Zn_xMn_{0.4}Fe_2O_4$ (x = 0.0, 0.2, 0.4, 0.6) for the first time. It was also observed that very little literature is available for similar ferrite series where zinc is being doped in Ni-Mn ferrite and whose antibacterial properties are studied for gram-positive bacteria via the viable count method. Secondly, using hexamine as fuel in the present combustion synthesis results in nano-range (below 20 nm) particles, which is relatively small compared to most of the literature data reported, making it a good candidate for various applications.

Experimental Procedures

Synthesis and Characterisation

$Ni_{0.6-x}Zn_xMn_{0.4}Fe_2O_4$ (x = 0.0, 0.2, 0.4, 0.6) zinc-doped nickel manganese ferrites were synthesized via the combustion technique. The analytical grade nitrate salts, namely nickel nitrate hexahydrate (99% Thomas Baker), zinc nitrate hexahydrate (97% Thomas Baker), manganese nitrate tetrahydrate (99% SRL), and ferric nitrate nonahydrate (99% Thomas Baker) were taken into the beaker. They were kept on a hot plate for the solid to melt. Once the melt was obtained, it was cooled, and an appropriate amount of hexamine (99% Thomas Baker) as fuel was added. Further, heating continued until combustion occurred, yielding ferrite powder, which was ground for an hour and calcined at 500°C for five hours to remove unburned carbon, if any. The obtained 'as-prepared' ferrite was again ground for two hours to homogenize the compound. Instrumental techniques then characterized the $Ni_{0.6-x}Zn_xMn_{0.4}Fe_2O_4$ (x = 0.0, 0.2, 0.4, 0.6) ferrites. The phase identification study used a Rigaku Smart Lab X-ray diffractometer. The morphology and elemental analysis were studied using Carl Zeiss SEM model no. EVO18, along with the EDX facility. The average particle size was confirmed by HR-TEM images, which were done using the FEI Tecnai G2, F30 make and model instrument. Shimadzu FTIR prestige-21 spectrophotometer was used to get IR spectra. The studies done using the Horiba Lab-Ram HR Evolution Raman spectrometer gave the active modes of samples. Surface characterization was performed using (XPS) X-ray photoelectron microscopy using model/Supplier: PHI 5000 Versa Probe II, FEI Inc. Electrical studies by the two-probe resistivity set-up. Wayne Kerr 6500P LCR meter helped in studying dielectric properties. Quantum design Versa Lab Vibrating Sample Magnetometer was utilized to measure hysteresis. AC susceptibility, ADEC Embedded Technology, and Solution Pvt. Ltd. evaluated Curie temperature and domain structure.

Antibacterial Study of Zn Doped Nickel Manganese Ferrites

A series of four $Ni_{0.6-x}Zn_xMn_{0.4}Fe_2O_4$ (where x = 0.0, 0.2, 0.4, 0.6) were tested against gram-positive strain of *Staphylococcus aureus* at different concentrations. An 18-hour-old culture of *Staphylococcus aureus* was inoculated in a nutrient broth medium supplemented with two different concentrations (500 µg/mL and 1000 µg/mL) of chemical compound prepared in saline. Nutrient broth medium without the chemical compound acted as control. The flasks were incubated at 37°C, 110 rpm for 18 h. After incubation, the growth of *Staphylococcus aureus* was checked by examining optical

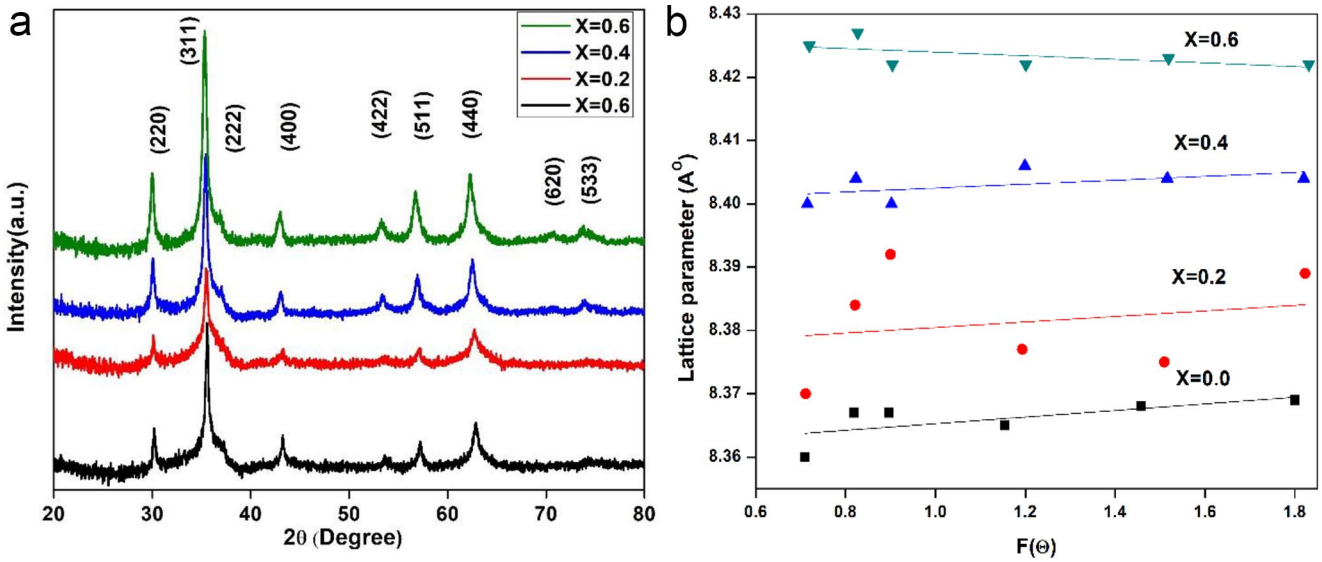


Fig. 1 (**a**) X-ray diffraction patterns of 'as prepared' $Ni_{0.6-x}Zn_xMn_{0.4}Fe_2O_4$ (x = 0.0,0.2,0.4,0.6). (**b**) Plot of lattice constant vs. F(θ) of 'as prepared' $Ni_{0.6-x}Zn_xMn_{0.4}Fe_2O_4$ (x = 0.0,0.2,0.4,0.6)

density at 600 nm. Serial dilution of the culture broth was carried out using 0.85% saline, and the required dilutions were spread plated on nutrient agar plates. The viable count was thus determined, and the percentage survival of the bacteria in the presence of $Ni_{0.6-x}Zn_xMn_{0.4}Fe_2O_4$ (x = 0.0, 0.2, 0.4, 0.6) nanoparticles was calculated using the formula.

$$\text{Survival } (\%) \frac{\text{Number of colonies forming units in presence of nanoferrite}}{\text{Number of colonies forming units in absence of nanoferrite}} \times 100$$

Results and Discussions

Structural Study

X-ray Diffraction

X-ray diffractograms of all samples calcined at 500°C for five hours showcased the pure phase of cubic spinel structure with no extra impurity peak, which can be seen from Fig. 1a. Bragg's equation helped to calculate interplanar distance. Hence, the lattice constant was also obtained. The d spacing was determined by the formula in Eq. (1) reported by [69].

$$n\lambda = 2d\sin\theta \tag{1}$$

Where n is an integer, λ is the wavelength, d is the interplanar distance, and θ is the glancing angle.

Table 1 Lattice constant, crystallite size, X-ray density, porosity

Sample	Avg. lattice constant (α)	True lattice constant (α_0)	ρ_{X-ray} (g/c.c.)	Porosity (%)	Crystallite size (nm)
X = 0.0	8.366	8.362	5.290	56.17	15.2
X = 0.2	8.381	8.376	5.294	59.84	8.8
X = 0.4	8.403	8.399	5.280	58.40	13.0
X = 0.6	8.423	8.426	5.260	53.50	12.3

Nelson Riley function F(θ) vs. lattice constant (α) was plotted, whose calculation was done using the following Eq. (2) and Eq. (3)

$$F(\theta) = \frac{1}{2}\left(\frac{cos^2\theta}{sin\theta} + \frac{cos^2\theta}{\theta}\right) \tag{2}$$

$$\alpha_{XRD} = \frac{\lambda}{2}\frac{\sqrt{h^{2+}k^{2+}l^2}}{sin\theta} \tag{3}$$

Where 'α' is the lattice constant, θ is the glancing angle, and (h, k, l) is the miller indices. These equations measured the true lattice constant (α_0) [70]. The Fig. 1b illustrates the plot of lattice parameter vs. *F(θ)*. The true lattice constant was obtained by extrapolating the lattice parameter vs. *F(θ)* graph, while the average lattice constant was obtained from the equation, α=d $\sqrt{h^2+l^2+k^2}$and the values of both are presented in Table 1. Table 1 shows little difference in the average and true lattice constants; average lattice constant values are slightly higher than the true ones. Still, both show the same trend with an increase in dopant content.

The lattice constant in the studied samples appears to increase with the increase in zinc content, which obeys

Vegard's law, and a similar trend is also reported in the literature [71–73]. This increase in lattice parameter with an increase in zinc concentration is explained based on ionic radii. Zn^{2+} ions tend to occupy tetrahedral voids, whereas Ni^{2+} ions prefer octahedral voids. Also, the ionic radii of zinc are 0.82 Å, and that of nickel is 0.78 Å, so when larger zinc ions are added by replacing smaller nickel ions, there is an expansion in the crystal lattice, which increases unit cell volume and lattice constant [74–76]. The lattice constant values obtained in the present study are 8.360–8.426 Å, which closely matches the reported value [76–78].

The crystallite size '*D*' was measured using the Scherrer's formula stated in Eq. (4) [69, 79, 80]

$$D = \frac{0.9 * \lambda}{\beta \ Cos\,\theta} \tag{4}$$

where '*D*' is the crystallite size, λ is the wavelength and β is full width at half maxima of highest intensity peak.

The FWHM of the diffraction peak is a combined effect of instrumental and sample broadening. To subtract the instrumental broadening from the FWHM value, the FWHM of crystalline silicon standard was considered, and the correct value was calculated using the following Eq. 5 [79]

$$\beta_{corrected} = \left(\beta^{2}_{observed} - \beta^{2}_{instrumental}\right)^{1/2} \tag{5}$$

where $\beta\, observed$ is FWHM observed for the sample, and $\beta\, instrumental$ is FWHMobserved for crystalline silicon standard. On substituting Eq. 5 in Eq. 4, a modified Eq. 6 is obtained, which gives the most accurate crystallite size value.

$$D_{crystallite} = \frac{k\lambda}{\beta corrected\, Cos\theta} \tag{6}$$

The crystallite size of zinc-doped nickel-manganese ferrites obtained was 7–20 nm [Table 1]. The values are well within the nanoscale range and confirm nanoparticle formation. The crystallite size obtained for the composition with x = 0.4 is 13 nm, which is relatively smaller than that of a similar composition with a crystallite size of 26 nm [77].

The dislocation density (δ), which denoted dislocation lines per unit volume, is calculated using the following Eq. 7 [81, 82].

$$\delta = \frac{1}{D^2} \tag{7}$$

The dislocation lines were 5–12 $*10^{15}$ lines/m^2. The dislocation density illustrated the degree of crystallinity of the nanoparticles.

The X-ray density of the ferrite samples was calculated using the equation given in Eq. 8 [83]

$$\rho_{X-ray} = \frac{Z\ M}{Na^3} \tag{8}$$

where Z denotes molecules per unit cell, and its value is 8, M is the molecular weight, N is Avogadro's number, which is 6.023×10^{23}, and the lattice constant is denoted as '*a*'. The obtained X-ray density of ferrites ranges from 5.260 to 5.294 g/cm^3. The X-ray density decreases with the addition of zinc content and is in tune with the literature report [78].

The bulk density of the cylindrical ferrite pellet was measured using the relation given below in Eq. (9).

$$\rho_{bulk} = \frac{m}{\pi\ r^2 h} \tag{9}$$

where m is the mass of the pellet, while $\pi r^2 h$ is the volume of the pellet. The porosity of the ferrites was calculated using the formula given below in Eq. 10. The pore sizes were reduced with an increase in zinc.

$$P\,\% = \left(1 - \frac{\rho_{bulk}}{\rho_{X-ray}}\right) \times 100 \tag{10}$$

The porosity obtained in the present ferrite series is relatively high and is found to decrease with increasing zinc content.

The specific surface area was calculated using the Eq. (11) [84]

$$S = \frac{6}{\rho_{x-ray\ Dcryt}} \tag{11}$$

It was observed that as the grain size decreased, the surface area increased. This trend follows the reported data [85, 86].

The hopping lengths between tetrahedral (L_A) and octahedral sites (L_B) have been calculated using Eq. (12) and Eq. (13) [83], respectively

$$L_A = \frac{a\sqrt{3}}{4} \tag{12}$$

$$L_B = \frac{a\sqrt{2}}{4} \tag{13}$$

Where, '*a*' is a lattice constant. It was observed from Table 2 that hopping length increases with zinc concentration and lattice constant, which suggests an increase in the jumping probability of ions [78].

Table 2 Dislocation lines, surface area, tetrahedral hopping length, octahedral hopping length, and IR data

Sample	δ(Lines/m^2x10^{15}) Dislocation lines	Surface area (m^2/g)	L_A	L_B	Wavenumber (cm^{-1})	
					ν_1	ν_2
X = 0.0	4.300	89.45	3.620	2.956	586	392
X = 0.2	12.00	151.1	3.626	2.961	575	395
X = 0.4	5.900	81.17	3.636	2.969	572	403
X = 0.6	6.600	85.13	3.705	2.979	569	406

Table 3 Theoretical and experimental percentages of 'as prepared' $Ni_{0.6-x}Zn_xMn_{0.4}Fe_2O_4$ (x = 0.0,0.2,0.4,0.6)

X	(%) Fe		(%) Ni		(%) Mn		(%) Zn	
	Theoretical	Experimental	Theoretical	Experimental	Theoretical	Experimental	Theoretical	Experimental
0.0	47.90	47.17	15.12	15.74	9.40	8.50	-	-
0.2	47.82	47.70	10.02	10.22	9.37	8.93	5.58	4.70
0.4	47.40	48.10	4.98	4.63	9.32	9.33	11.10	11.30
0.6	47.10	47.17	-	-	9.27	9.10	16.50	18.00

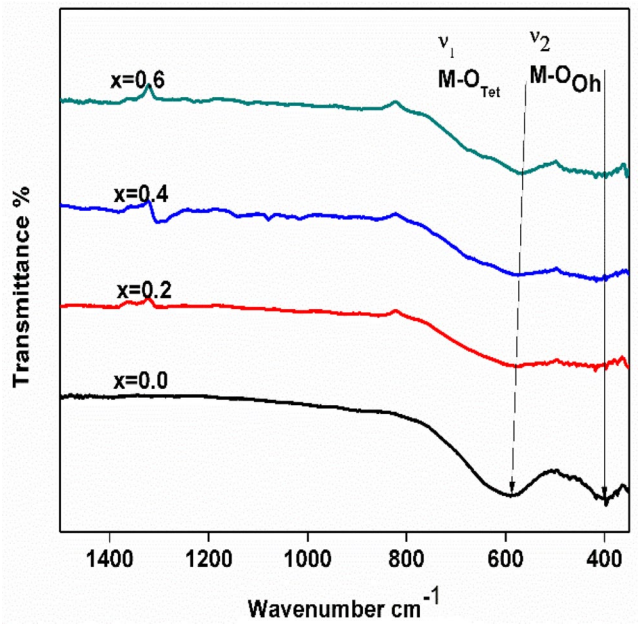


Fig. 2 Infrared spectra of 'as prepared' $Ni_{0.6-x}Zn_xMn_{0.4}Fe_2O_4$ (x = 0.0,0.2,0.4,0.6)

Chemical Analysis

The elemental composition was evaluated by chemical analysis of 'as-prepared' $Ni_{0.6-x}Zn_xMn_{0.4}Fe_2O_4$ (x = 0.0,0.2,0.4,0.6) ferrite. The observed percentages of metals are displayed in Table 3, which closely matches the theoretically calculated percentages and confirms the formation of ferrite samples.

Infrared Spectroscopy

The IR spectrum for $Ni_{0.6-x}Zn_xMn_{0.4}Fe_2O_4$ (x = 0.0,0.2,0.4,0.6) has been depicted in Fig. 2, and the data obtained from the same is given in Table 2. Two prominent IR bands were seen in a range of 300–600 cm^{-1}, which are characteristic of spinel ferrites and provide the environment of oxygen coordination in tetrahedral (A site) and octahedral (B sites) in the ferrites [87]. The higher value band ν_1 shows the tetrahedral metal-oxygen bond, whereas the lower value band ν_2 is because of vibrations in metal-oxygen at the octahedral site [86]. The band ν_1 shifts to a lower frequency with an increment in zinc content while the band ν_2 values increase. Many factors, such as synthesis conditions and chemical composition, cause the change in band position. The shift of the ν_1 peaks suggests a structural change in the tetrahedral (A site) as the x value varies in the series [31]. So also, changes are occurring in the octahedral (B site), shown by the shift in wavenumber. The difference in metal and oxygen bond lengths in the A and B sites results in differences in frequency values. The tetrahedral site has a shorter bond length between the ions, thus leading to a more covalent nature than octahedral site ions. This results in higher frequency values for the A site and low values for the B site. As zinc ion prefers tetrahedral sites over iron, the transition is expected to happen by increasing the zinc content. The Fe^{3+} ions from the tetrahedral site are pushed towards the octahedral site, thereby weakening the metal-oxygen bond in the tetrahedral sites due to large ionic radii and atomic weight of Zn^{2+} [88]. When Fe^{3+} enters the octahedral site, it replaces the larger Ni^{2+} ions, which leads to a higher frequency value at the octahedral site. Therefore, with an increase in zinc content, the ν_2 value increases [89, 90].

Raman Spectroscopy

The vibrational and structural properties, as well as lattice effects, were investigated by Raman spectroscopy [91]. The Raman spectra of $Ni_{0.6-x}Zn_xMn_{0.4}Fe_2O_4$ (x = 0.0,0.2,0.4,0.6) are depicted in Fig. 3 and are characteristic of spinel space

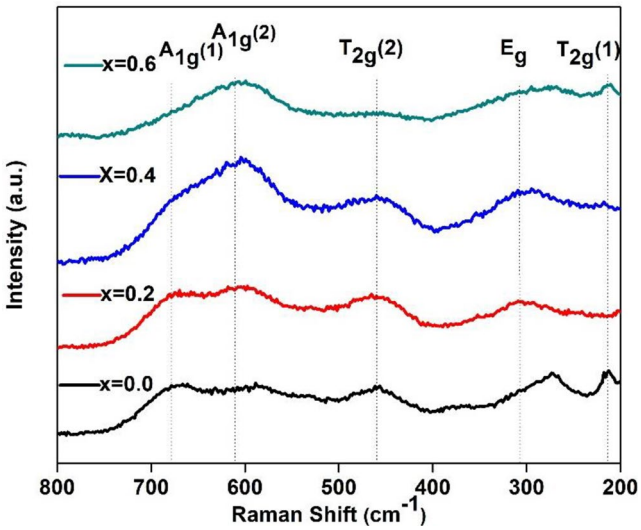


Fig. 3 Raman spectrum of 'as prepared' $Ni_{0.6-x}Zn_xMn_{0.4}Fe_2O_4$ (x = 0.0,0.2,0.4,0.6)

Table 4 Raman vibration modes of 'as-prepared' $Ni_{0.6-x}Zn_xMn_{0.4}Fe_2O_4$ (x = 0.0,0.2,0.4,0.6)

Sample	Eg	T_{2g} (2)	A_{1g} (2)	A_{1g} (1)
0.0	273	459	588	675
0.2	310	463	599	675
0.4	295	460	601	678
0.6	274	460	607	-

group Fd3M. All the spectra indicate the formation of a spinel structure. The Raman vibrational mode frequencies are tabulated in Table 4. The most prominent band in the spectrum is the A_{1g} mode. The A_{1g} mode is observed above 600 cm^{-1} due to the symmetric stretching of oxygen atoms along the metal-oxygen bond at the tetrahedral site. The peaks below 600 cm^{-1} are of symmetric bending of an oxygen atom, asymmetric stretching of M-O, and asymmetric bending of oxygen at the octahedral site, confirming the formation of spinel ferrite [91, 92]. As the spectra show, incorporating zinc into the system changes peak height and position. It is reported that the Raman spectra for normal spinel structure appear at 600–620 cm^{-1} for $ZnFe_2O_4$ while the other A_{1g} mode of inverse spinel $NiFe_2O_4$ appears around 670–710 cm^{-1} while Fe-O mode also appears at 660–700 cm^{-1} [92, 93]. In the present study, the A_{1g} peak was observed at ~675 cm^{-1}, denoted as A_{1g} (1), which ascribes to the Ni-O bond in the tetrahedral site, while the second peak, referred to as A_{1g} (2) at 588–607 cm^{-1} is assigned to the Zn-O bond. It is visible from the data that as the zinc content increases, the A_{1g} (1) band intensity decreases, which is associated with Ni-O, while the A_{1g} (2) band intensity increases associated with Zn-O. The peaks show a shift with the increase in zinc content. In this case, the peak shows a blue shift, i.e., the shift to a higher wavenumber with an increase in zinc. The force constant of a bond is involved in positioning the peak; the higher the force constant, the higher the band appearing in the Raman spectra. It is important to note that other authors have also obtained similar results [94]. The three T_{2g} bands usually occurring in spinel ferrite are T_{2g} (3), T_{2g} (2) and T_{2g} (1). The T_{2g} (3) usually occurs at 500–590 cm^{-1} and is assigned to the antisymmetric bending of M-O. The T_{2g} (2) is due to antisymmetric stretching of M and O and observed around 450–520 cm^{-1}. The T_{2g} (2) band observed in our case is in the range of 455–460 cm^{-1}. The intensity of the T_{2g} (2) mode decreases with zinc content, which suggests that some of the Fe is still present in the A-site. These results indicate that the asymmetric stretching vibration is stronger for Ni-O than Zn-O in the A-site [92]. The T_{2g} (1) is usually observed near 180–220 cm^{-1} due to M-O translational motion [95]. In our case, only sample x = 0.0 and x = 0.6 shows a tiny peak. The peaks observed from 273 to 309 cm^{-1} are assigned to symmetric bending of oxygen with respective metals and are assigned as E_g. The vibrational motion frequencies depend on factors like bond length and covalency, which affect the bond strength. The vibrational frequencies also are dependent on reduced mass [93].

Microstructural Studies: Scanning Electron Microscopy

SEM/EDX microscopy was employed to study the microstructure of $Ni_{0.6-x}Zn_xMn_{0.4}Fe_2O_4$ (x = 0.0,0.2,0.4,0.6). The SEM micrograph in Fig. 4a showcases ferrite with irregularly shaped particles with a diameter of less than 100 nm. Ferrite shows a tendency for cohesion or agglomeration. The magnetic ferrite samples show such coalescence, which can be due to dipole-dipole interaction between magnetic particles [30, 96–98]. The auto-combustion process curtails the particle growth in the proper orientation. The ignition process initially results in the formation of the porous structure due to multiple evolutions of gases during the burning process, which leads to nano-porous structures. The morphologies of the sample upon zinc doping did not change significantly, but it is observed that size decreases slightly with zinc as zinc inhibits grain growth, as also seen from XRD data. The second reason could be that the soft ferrimagnetic nature of the samples has high magnetostatic interactions, which lead to increased agglomeration in the samples. The energy dispersion X-ray (EDX) spectra gave qualitative data of the ferrites seen in Fig. 4b, indicated by the peaks of all the desired elements, i.e., Ni, Mn, Zn, and Fe in the sample material.

Transmission Electron Microscopy

TEM analysis confirmed the nano-size nature of the 'as-prepared' ferrite. The analysis of particle size was found to be almost similar to that calculated from XRD data. Figure 5

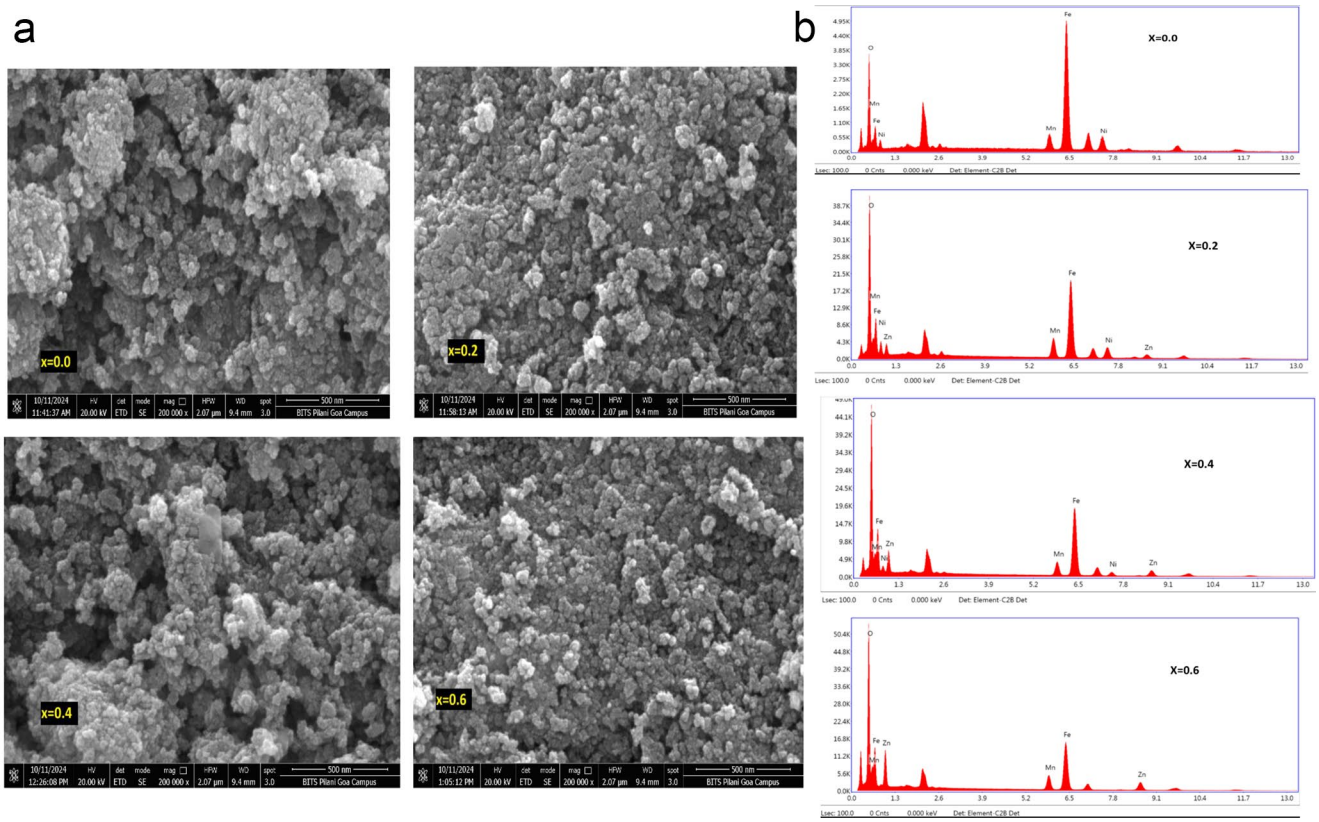


Fig. 4 (**a**)SEM micrograph of 'as prepared' $Ni_{0.6-x}Zn_xMn_{0.4}Fe_2O_4$ (x = 0.0,0.2,0.4,0.6). (**b**)EDX plot of 'as prepared' $Ni_{0.6-x}Zn_xMn_{0.4}Fe_2O_4$ (x = 0.0,0.2,0.4,0.6)

shows the TEM micrograph of $Ni_{0.6-x}Zn_xMn_{0.4}Fe_2O_4$ (x = 0.0,0.2,0.4,0.6), histogram plot, and SAED images. Although the particles are agglomerated, they are semi-uniform and range between 4 and 30 nm, as seen from histogram plots. The aggregation is due to magnetic interaction and weak Van der Waals contact [46, 49, 83]. The diffraction ring pattern showcased in SAED images confirms the crystallinity of ferrite samples.

XPS

The full scan spectrum and individual deconvoluted spectra of all the elements in samples x = 0.2 have been portrayed in Fig. 6a and b. The data obtained from XPS analysis for $Ni_{0.6-x}Zn_xMn_{0.4}Fe_2O_4$ (x = 0.0,0.2,0.4,0.6) is given as supplementary data in Table S1 a-d, and the deconvoluted spectra of all the elements of remaining samples of $Ni_{0.6-x}Zn_xMn_{0.4}Fe_2O_4$ (x = 0.0,0.4,0.6) are presented in Fig S1-S3. The XPS spectrum of Fe shows that binding energy around ~710 eV corresponds to $2p_{3/2}$. This $2p_{3/2}$ peak splits into two peaks, i.e., one ~710 eV, which confirms the presence of Fe^{+3} cations at the octahedral site, while the peak at ~713 eV corresponds to Fe^{+3} ions at the tetrahedral site. A satellite peak at around ~718 eV indicates that Fe is in the Fe^{+3}oxidation state only [99, 100], thereby ruling out the presence of Fe^{+2}. A peak observed at around ~725 eV corresponds to $2p_{1/2}$, and a corresponding satellite peak is obtained around ~732 eV, further confirming the Fe in the Fe^{+3} oxidation state. The Ni spectra of XPS showcase two prominent peaks corresponding to Ni $2p_{3/2}$ and Ni $2p_{1/2}$, obtained at a binding energy of ~854 eV and ~872 eV. Apart from prominent peaks, other peaks at binding energies of ~860 eV and ~878 eV are also observed [101, 102]. The prominent peaks have a difference in the value of ~17 eV, which proves that Ni is present in the Ni^{+2} oxidation state [103]. The XPS spectra of Mn show two peaks with a binding energy of ~641 eV and ~653 eV, which belong to Mn $2p_{3/2}$ and Mn $2p_{1/2}$, respectively, proving the Mn^{+2} state. The satellite peak confirms the presence of no Mn^{+3} or Mn^{+4} states in ferrite samples [104, 105]. The satellite peak of Mn^{2+} is observed around ~645 eV in the ferrite series. The XPS spectra of zinc in the samples have been depicted clearly in the figures, and the peaks are seen at ~1022 eV and ~1044 eV for $Zn^{+2,}$ corresponding to $2p_{3/2}$ and $2p_{1/2,}$ respectively. This proves that zinc is in a Zn^{+2} oxidation state and the zinc ions are at a tetrahedral site [105]. The XPS spectra for oxygen 1s show a precise splitting of peaks at ~529 eV and ~531 eV. The peak at 529 eV is of lattice

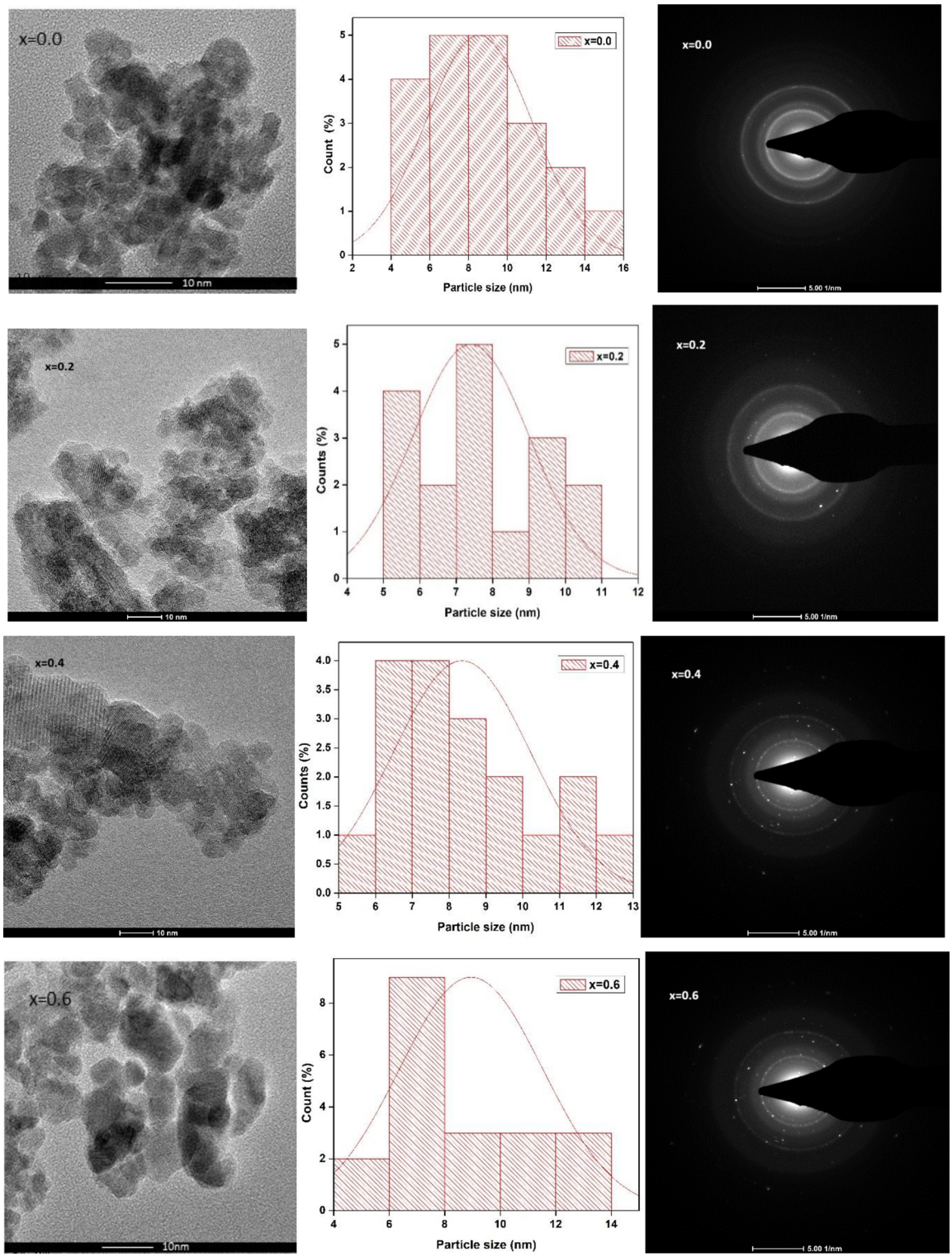


Fig. 5 TEM micrograph, histogram plot, and SAED IMAGES of 'as prepared' $Ni_{0.6-x}Zn_xMn_{0.4}Fe_2O_4$ (x = 0.0,0.2,0.4,0.6)

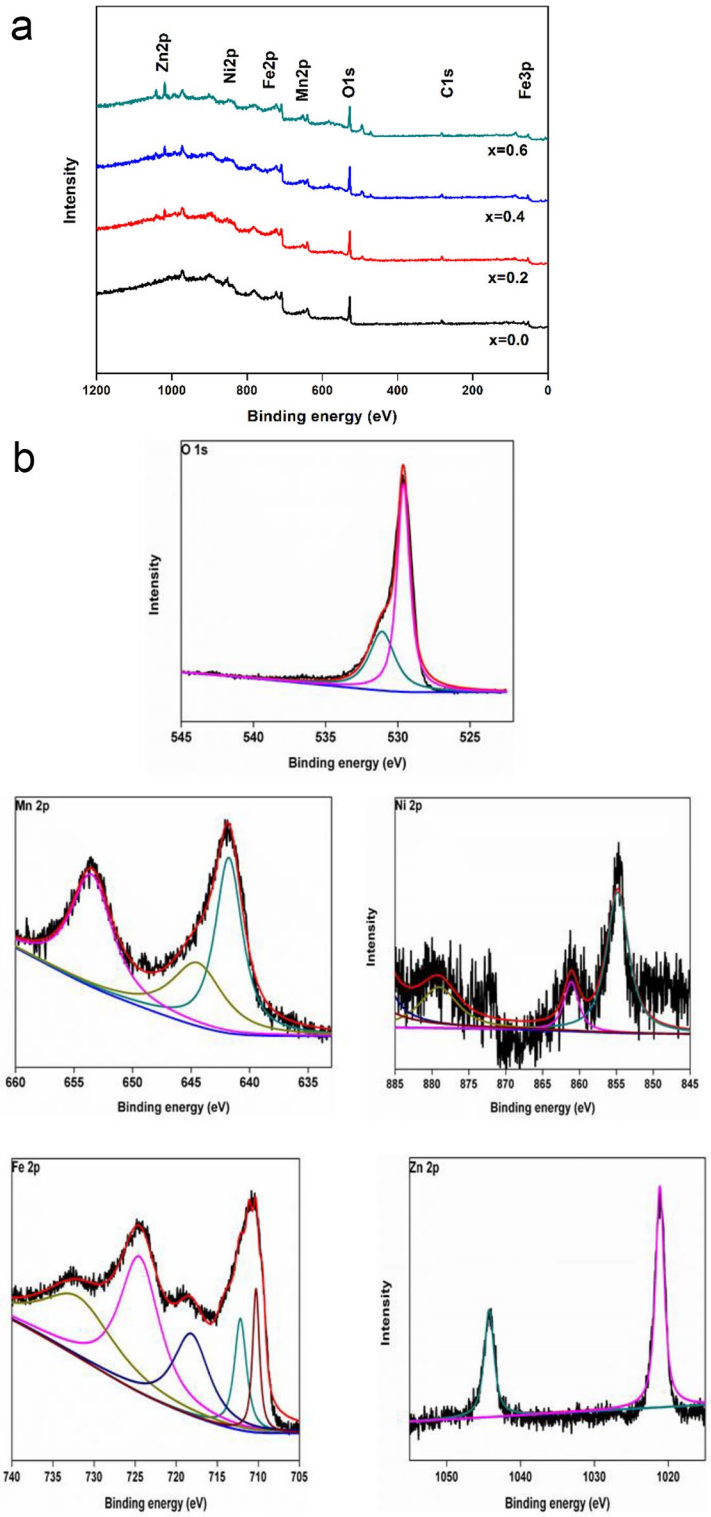


Fig. 6 (**a**) The survey scan of 'as prepared' $Ni_{0.6-x}Zn_xMn_{0.4}Fe_2O_4$ (x = 0.0,0.2,0.4,0.6). (**b**) The deconvoluted peaks of Fe 2p, Ni 2p, Mn 2p, Zn 2p, O 1s $Ni_{0.2}Zn_{0.4}Mn_{0.4}Fe_2O_4$

oxygen, and the one present at ~531 eV is due to defects in the oxide or surface-adsorbed oxygen [106].

Resistivity Studies

Figure 7 represents the log resistivity versus 1/T*1000 plot of $Ni_{0.6-x}Zn_xMn_{0.4}Fe_2O_4$ (x = 0.0,0.2,0.4,0.6). The relation with which the resistivity is measured is given by Arrhenius equation Eq. 14 [107]

$$\rho = \rho_O e^{-\frac{\Delta E}{KT}} \quad (14)$$

Where ρ denotes resistivity at any temperature while ρ_O is resistivity at absolute temperature, K and ΔE are Boltzmann's constant and activation energy, respectively. The resistivity measurement of $Ni_{0.6-x}Zn_xMn_{0.4}Fe_2O_4$ (x = 0.0,0.2,0.4,0.6) was performed from 333 K to 773 K. The resistivity studies suggested that with an increment in temperature, resistivity decreases due to drift in mobility carriers. This trend observed in resistivity plots confirms the semiconducting nature of ferrites [17]. Verwey-Boer's mechanism can explain the resistivity variation. Figure 7 showcases two regions; in the first region, from 333 K to around 393 K, the resistivity increases initially and reaches maximum temperature. This trend can be attributed to open pores, loose agglomeration, and adsorbed moisture due to porosity in the ferrite samples [108]. Also, the higher resistivity at low temperatures could be because of phonon vibrations that disperse the charges and curtail the free path [109]. The total moisture evaporation also occurs in this region; therefore, the highest resistivity is reached. The resistivity increases with a decrease in the size of particles [110]. In the present studies, a similar pattern is observed, i.e., x = 0.2 ferrite, which shows the smallest size, has the highest resistivity value. The resistivity values are in the range of 10^7-$10^8\Omega$ cm and are close to values in literature reports [77]. The resistivity is found to increase up to x = 0.2 and then decrease. Adding Zn ion in x = 0.2 decreases Ni^{+2} concentration at (B site), resulting in a decrease of hopping between the same ions at that site; thus, the resistivity increases. Also, as shown in this equation, $Ni^{+2}+Fe^{+3}\Diamond$, $Ni^{+3}+Fe^{+2}$, the decrease in Ni^{+2} decreases the formation of Fe^{+2} and Ni^{+3} ion formation, increasing resistivity. For very high zinc concentrations, the Fe^{+3} converts to Fe^{+2} by following the reaction $Fe^{+3}+Mn^{+2}\Diamond Fe^{+2}+Mn^{+3}$. The hopping between ions of the same element increases at the octahedral (B site), ultimately lowering resistivity [111].

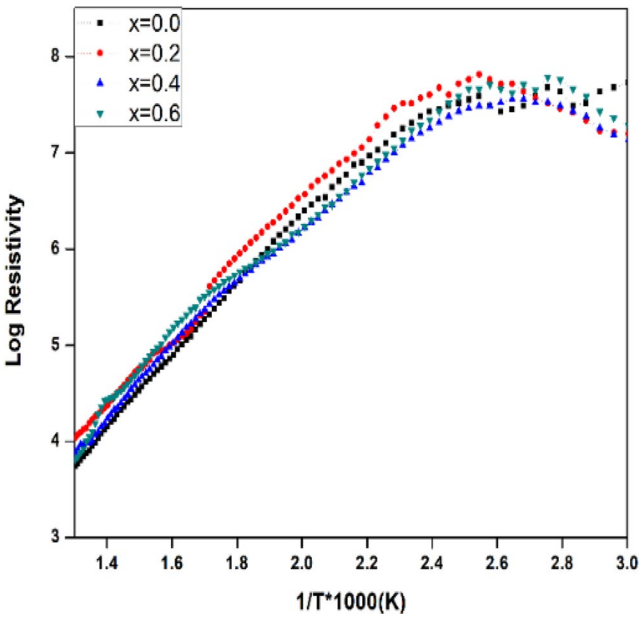


Fig. 7 Plot of resistivity vs. 1/T*1000 of 'as prepared' $Ni_{0.6-x}Zn_xMn_{0.4}Fe_2O_4$ (x = 0.0,0.2,0.4,0.6)

Dielectric Studies

Dielectric Study w.r.t Frequency

The dielectric study of $Ni_{0.6-x}Zn_xMn_{0.4}Fe_2O_4$ (x = 0.0,0.2,0.4,0.6) was conducted at RT from 20 Hz to 1 MHz, and the plot of dielectric constant versus log frequency and dielectric loss versus log of frequency are shown plotted in Fig. 8a and b respectively. As expected, the dielectric constant values lower as the frequency increases. The values are much higher at lower frequencies, and with a further rise in frequency, the value decreases rapidly and becomes constant. This kind of conduct is always observed in spinel ferrites. To understand this response, one needs to understand the composition of the ferrites. Ferrites are made up of highly conducting grains and are separated by grain boundaries which are insulating. The charges accumulate under the applied electric field, leading to space charge polarisation, which is explained based on Maxwell Wagner's two-layer model [75, 112]. As the applied frequency increases, the probability of the electrons reaching the boundary decreases due to the reverse motion of the electrons; thus, the dielectric constant decreases. In the dielectric loss versus frequency plot, a decrease was seen with the increase in frequency, with a peak generally observed when an electron hopping frequency becomes equal to the applied field [113, 114]. Koop's model very well explains the higher values of dielectric loss at a lower frequency, which states that at the lower frequencies, the resistance is relatively high, which requires higher energy for electrons to hop at the grain boundary, and therefore, higher energy losses are observed [114].

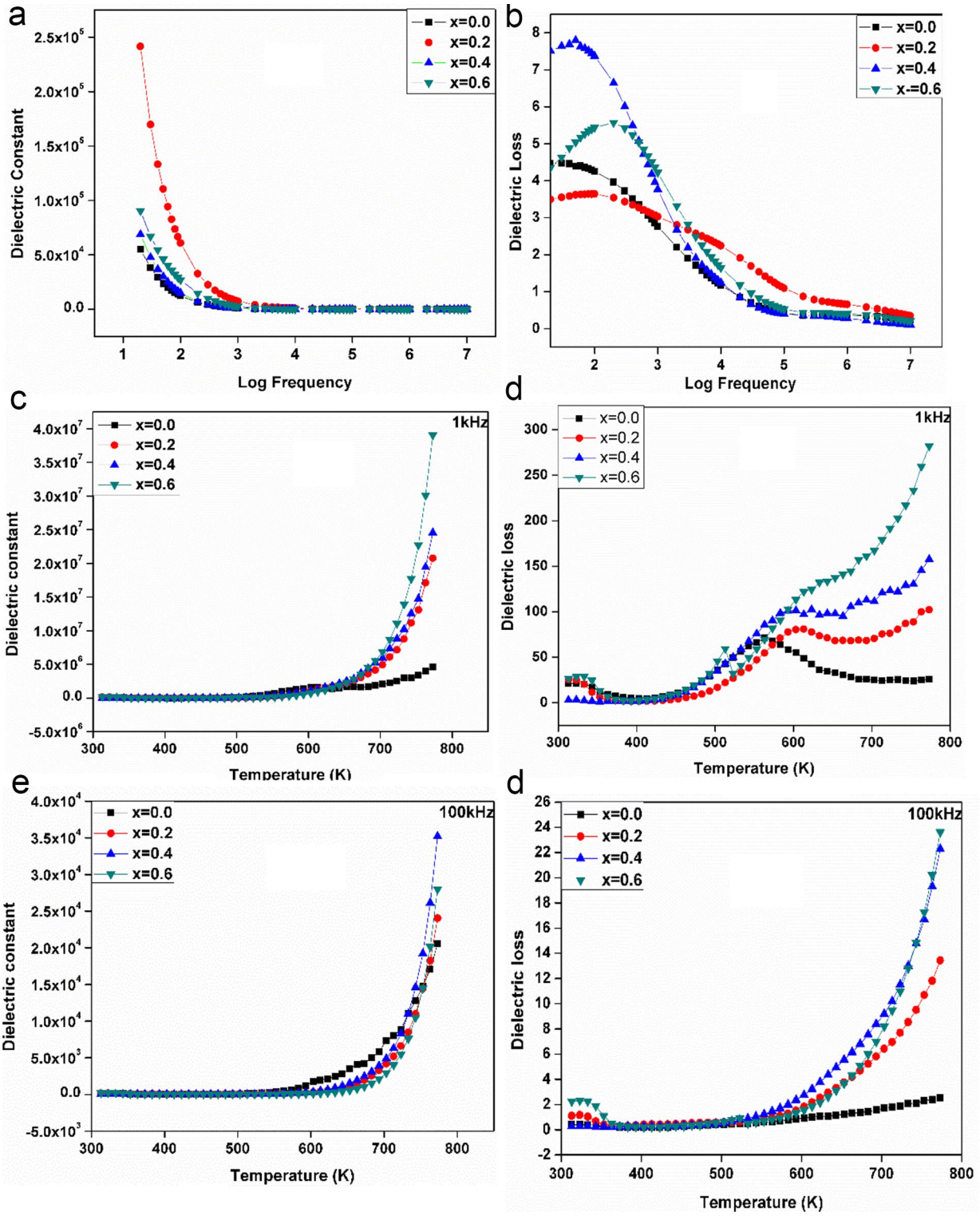


Fig. 8 (**a** & **b**) Frequency variation of dielectric constant and dielectric loss of 'as prepared' $Ni_{0.6-x}Zn_xMn_{0.4}Fe_2O_4$ (x = 0.0,0.2,0.4,0.6). (**c** & $Ni_{0.6-x}Zn_xMn_{0.4}Fe_2O_4$ (x = 0.0,0.2,0.4,0.6) at a constant frequency of 1 kHz. **d**) Dielectric constant and dielectric loss as the function of the temperature of 'as prepared'. (**e** & **f**) Dielectric constant and dielectric loss as the function of the temperature of 'as prepared' $Ni_{0.6-x}Zn_xMn_{0.4}Fe_2O_4$ (x = 0.0,0.2,0.4,0.6) at a constant frequency of 100 kHz

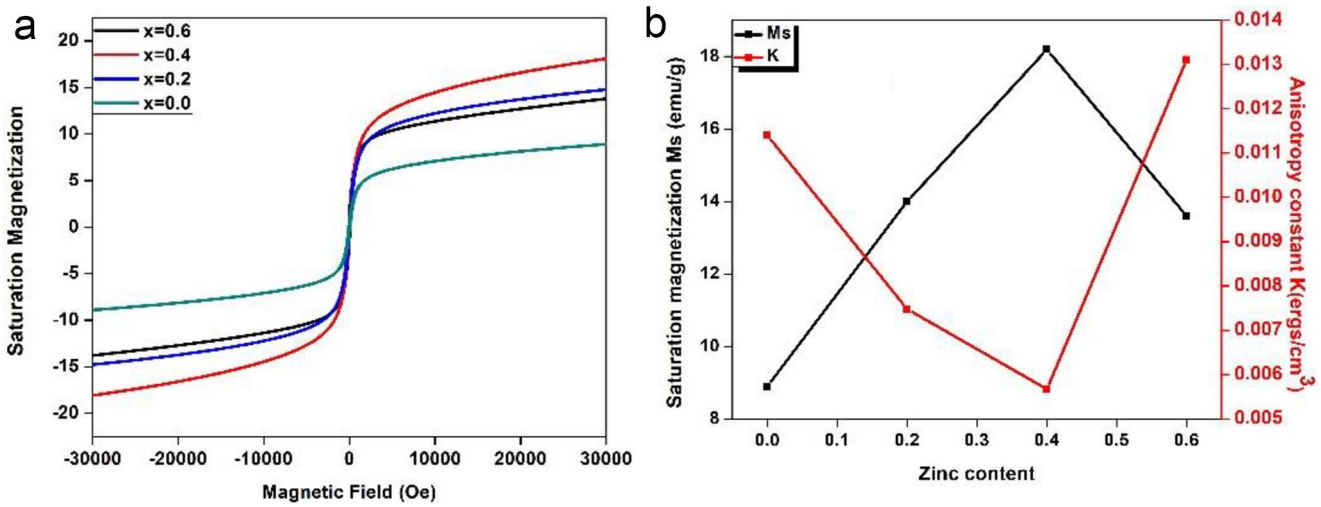


Fig. 9 (**a**) Plot of saturation magnetization vs. magnetic field of 'as prepared' $Ni_{0.6-x}Zn_xMn_{0.4}Fe_2O_4$ (x = 0.0,0.2,0.4,0.6). (**b**) Plot of saturation magnetization and anisotropy constant as a function of the zinc content of 'as prepared' $Ni_{0.6-x}Zn_xMn_{0.4}Fe_2O_4$ (x = 0.0,0.2,0.4,0.6)

Table 5 Magnetic parameters for the $Ni_{0.6-x}Zn_xMn_{0.4}Fe_2O_4$ (x = 0.0,0.2,0.4,0.6)

X	Ms	Mr	*R* = Mr/Ms	Hc	η_B	y-kα	K(x10^{5}ergs/cm^3)	Tc(K)
X = 0.0	8.900	0.663	0.074	82.01	0.377	39.81	0.1140	823
X = 0.2	14.00	0.334	0.023	34.20	0.583	56.93	0.0748	809
X = 0.4	18.197	0.277	0.015	19.97	0.763	67.41	0.0567	807
X = 0.6	13.605	0.520	0.038	61.76	0.577	76.69	0.1311	825

Dielectric Study w.r.t Temperature

The dielectric study versus temperature at constant frequencies for all the as-prepared ferrite samples ranging from x = 0.0 to x = 0.6 has been carried out. Two frequencies, 1 kHz and 100 kHz, were chosen for the study. The plots of dielectric constant and dielectric loss versus temperature for 1 kHz frequency and 100 kHz frequency have been showcased in Fig. 8c, d and e, and 8f, respectively. The dielectric constant at 1 kHz and 100 kHz frequencies have risen at elevated temperatures, whereas it is independent for lower temperatures. The onset of the plot is seen to decrease with increased zinc content; however, with an increase in the x value, the dielectric constant has increased. A similar trend is observed in the dielectric loss versus temperature studies, i.e., the dielectric loss increases with increased zinc content and temperature. A slight dispersion can be seen in the case of a 1 kHz frequency plot. The sample imperfections and grain boundary result in dielectric loss, which is caused when polarisation falls back to the applied field. The hump observed at ~340 K in both frequency plots is due to the relaxation effect and is caused when the rate of hopping between ions of the same valence state becomes equal to the applied frequency [114]. With increased zinc content, the onset of relaxation peak shifts to a higher temperature and is attributed to the increased rate of hopping of charge carriers. The dielectric loss is relatively high in the 1 kHz frequency compared to the 100 kHz frequency.

Magnetic Study

Vibrating Sample Magnetometer

A magnetic study of $Ni_{0.6-x}Zn_xMn_{0.4}Fe_2O_4$ (x = 0.0,0.2,0.4,0.6) was done at RT in the 30000Oe magnetic field. The plots of the same are shown in Fig. 9a, along with plotted data of saturation magnetization and anisotropy constant in Fig. 9b. The saturation magnetization, remanence, coercivity, reduced remanent magnetization, y-k angle, and anisotropy constant have been tabulated in Table 5. The narrow hysteresis loop indicated the soft ferrimagnetic nature of the samples. The saturation magnetization (M_s) values rise with zinc content up to x = 0.4 and then decrease at x = 0.6 composition. This trend is also seen in literature reports for other ferrites [115]. Neel's two-sublattice model can explain this trend in the magnetization values [31, 116, 117]. As the zinc concentration increases, the zinc ion (Zn^{2+}) prefers the tetrahedral position (A site), which leads to the iron (Fe^{3+}) shifting to the (B site), i.e., the octahedral position, which leads to increased magnetization. According to the two sublattice model, an antiparallel arrangement between the magnetic ions in the A-site and the B-site with collinear spins is present. Due to the

occupation of non-magnetic zinc in the A-site, the magnetic moment decreases. At the same time, the magnetic moment of B-sites increases due to the occupancy of Fe^{3+} ions, and hence, the net magnetization increases (M_B-M_A) [46, 49, 75]. As a result, the M_s values increase. However, the values of saturation magnetization for $Ni_{0.6-x}Zn_xMn_{0.4}Fe_2O_4$ (x = 0.0,0.2,0.4,0.6) are relatively low [118]. The low values of M_s can be either due to the random distribution of cations or the random canting of surface spin in addition to the small particle size. The non-saturation behavior indicated the presence of ordered core spin and bent or canted surface spin in the samples. Smaller values of M_s can also be due to Fe^{2+} ions in the samples. Still, this possibility is ruled out, as confirmed by XPS results. As the zinc content increases more than x = 0.4, the magnetization decreases, and Neel's two-sublattice model becomes inefficient in explaining the decrease. The magnetization in the A site becomes very weak, and therefore, A-B interactions become feeble, and B-B interaction starts to dominate; alteration of parallel arrangements of spin results in spin canting. Splitting the B sub-lattice into B_1 and B_2 increases the Yafet-Kittle angle, thus decreasing the magnetization. The data in Table 5 shows that the Y-K angle enlarges with the rise in the dopant concentration (x). This explains the decrease in M_s values at higher zinc content [116, 117, 119]. The remanent magnetization (M_r) values decreased up to x = 0.4 and rose at x = 0.6 concentration; coercivity is impacted by various factors such as the morphology of samples, microstrain, magneto crystalline anisotropy, and oxygen vacancies. Coercivity (H_c) also showed a similar trend as the zinc concentration increased; both M_r and H_C showed an inverse trend to M_s; the coercivity decreased to x = 0.4 and then increased. This can be attributed to the porosity of the samples. The pores present in the sample create the demagnetizing field.

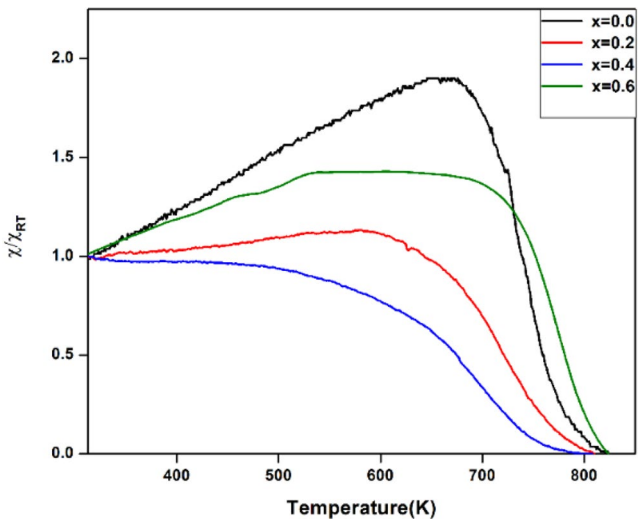


Fig. 10 Plot of normalized susceptibility vs. temperature of 'as prepared' $Ni_{0.6-x}Zn_xMn_{0.4}Fe_2O_4$ (x = 0.0,0.2,0.4,0.6)

When the porosity is decreased, a high magnetic field is required to initiate the domain wall, decreasing coercivity [120]. The more zinc content, the less coercivity there is. The data tabulated in Table 5 indicates lower coercivity values pointing towards the soft ferrimagnetic nature; such samples can be utilized in devices requiring soft ferrimagnets [30]. The reduced remnant magnetization [Table 5] was less than 0.5, suggesting uniaxial anisotropy, given by the Stoner-Wohlfarth model [118]. The uniaxial anisotropy is measured using the equation $H_c = 0.64\ K/M_s$, where K is the anisotropic constant. The reduced remanent magnetization decreased due to decreased magnetic anisotropy with the rise in zinc content. The magnetic moment was measured using Eq. 15 [106], Where M_s and M_w are saturation magnetization values and formula weights. With increased zinc content, magnetic moment increases to x = 0.4 while a decrease is obtained at x = 0.6, which follows the trend of M_s.

$$\eta_B = \frac{M_w M_S}{5585} \tag{15}$$

AC Susceptibility

The AC susceptibility analysis of all the 'as-prepared' ferrite samples ranging from x = 0.0-0.6 was done to determine their domain structure and Curie temperature. The plots of normalized susceptibility versus temperature in Kelvin of all the 'as-prepared' ferrites are depicted in Fig. 10. This plot gives information about the domain structure, whether it is superparamagnetic, single domain, or multi-domain, which in turn provides an idea about the size of the particles. Besides this, the plot also offers the ferrites Curie temperature (T_c). It is observed that with an increase in zinc content, the T_c decreases until x = 0.4, whereas, for x = 0.6, T_c increases. The T_c is the point at which the ferromagnetic ion changes to a paramagnetic one. The cumulative doping of zinc ions is expected to increase lattice parameters due to their larger size than other ions. Consequently, the distance between the ions increases, and therefore, the strength between the ions decreases [74, 121]. The reduced exchange interaction between the Fe-O-Fe ions leads to a fall of the Tc. Also, introducing non-magnetic zinc in nickel reduces the magnetic interaction and, hence, the trend.

Antibacterial Studies

The antibacterial performance of a series of four zinc-doped nickel manganese ferrites $Ni_{0.6-x}Zn_xMn_{0.4}Fe_2O_4$ (where x = 0.0, 0.2, 0.4, 0.6) was tested against gram-positive *Staphylococcus aureus* at different ferrite concentration. The Fig. 11a depicts the survival percentage of the bacteria

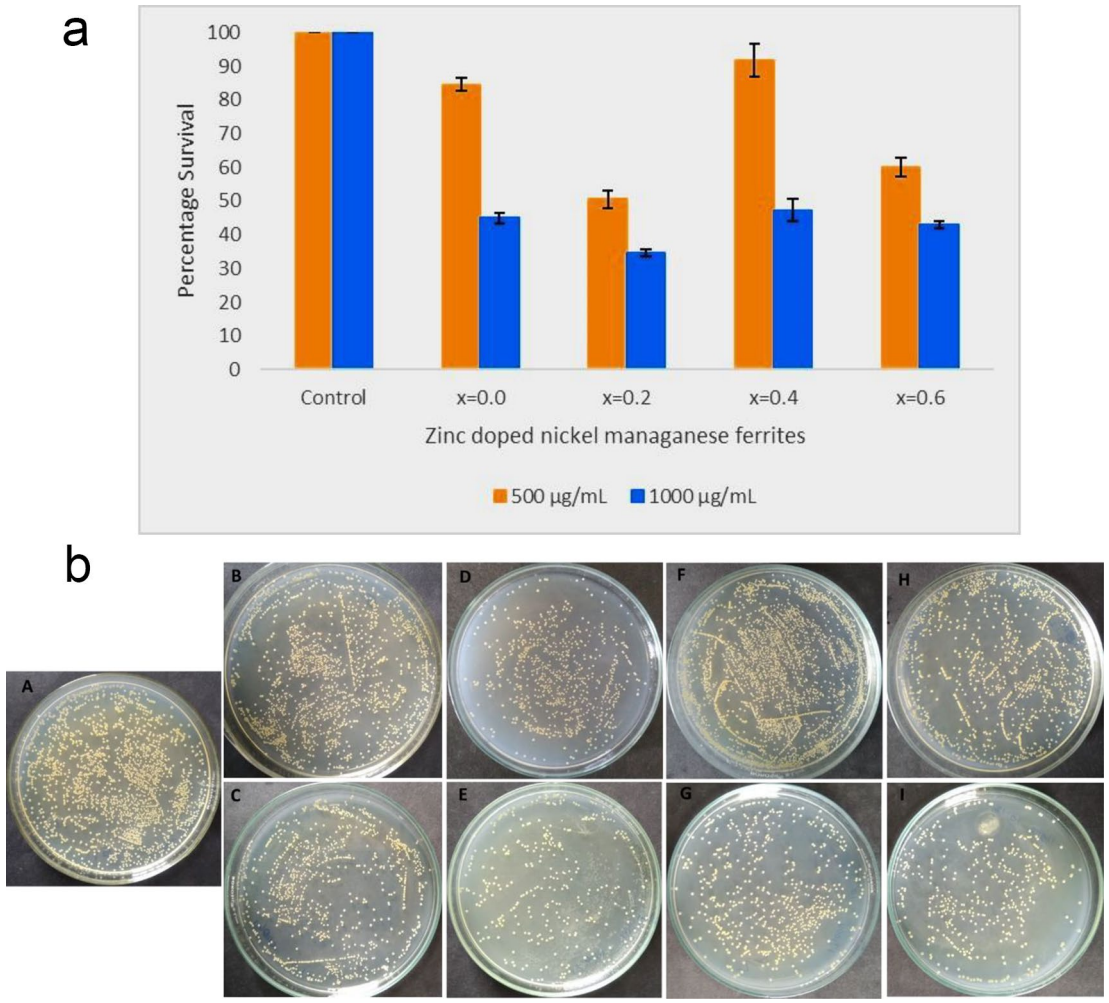


Fig. 11 (**a**) Graph showing the effect of 2 different concentrations of Zn doped nickel manganese ferrites $Ni_{0.6-x}Zn_xMn_{0.4}Fe_2O_4$ on percentage survival of *Staphylococcus aureus.* x = 0.0: $Ni_{0.6}Mn_{0.4}Fe_2O_4$; x = 0.2: $Ni_{0.4}Zn_{0.2}Mn_{0.4}Fe_2O_4$; x = 0.4: $Ni_{0.2}Zn_{0.4}Mn_{0.4}Fe_2O_4$; x = 0.6: $Zn_{0.6}Mn_{0.4}Fe_2O_4$. (**b**) Antibacterial activity of Zn doped nickel manganese ferrites. Effect of different concentrations of Zn doped nickel manganese ferrites on percentage survival of *Staphylococcus aureus.* A: Control; B: $Ni_{0.6}Mn_{0.4}Fe_2O_4$ (Conc: 500 µg/mL); C: $Ni_{0.6}Mn_{0.4}Fe_2O_4$ (Conc: 1000 µg/mL); D: $Ni_{0.4}Zn_{0.2}Mn_{0.4}Fe_2O_4$ (Conc: 500 µg/mL); E: $Ni_{0.4}Zn_{0.2}Mn_{0.4}Fe_2O_4$ (Conc: 1000 µg/mL); F: $Ni_{0.2}Zn_{0.4}Mn_{0.4}Fe_2O_4$ (Conc: 500 µg/mL); G: $Ni_{0.2}Zn_{0.4}Mn_{0.4}Fe_2O_4$ (Conc: 1000 µg/mL); H: $Zn_{0.6}Mn_{0.4}Fe_2O_4$ (Conc: 500 µg/mL); I: $Zn_{0.6}Mn_{0.4}Fe_2O_4$ (Conc: 1000 µg/mL)

at 500 µg/mL and 1000 µg/mL doses. Zinc-doped nickel manganese ferrites showed promising results against a gram-positive human pathogen, *Staphylococcus aureus*, in a concentration-dependent manner. The antibacterial results of the compounds were in the order: x = 0.2 > x = 0.6 > x = 0 .0 > x = 0.4, where the highest activity against Staphylococcus aureus was shown by the compound having x value of 0.2, and the lowest by x = 0.4. One can note from Tables 1 and 2 that the crystallite size and surface area significantly increase the activity against the pathogens. The inference can be drawn that the compound with a smaller size and larger surface area shows better activity than the one with a larger size. Literature reports also suggest the same. Hashim et al. [122] reported that size is significant in the efficient antibacterial activity of the compounds; due to the large surface area of the particles, better contact was developed with a microorganism which ruptures the cell by producing a reactive oxygen species and release of toxic metal from the core of the ferrite nanoparticles. A similar explanation based on size and its antibacterial activity is reported [123, 124]. Several authors have studied the effect of metal oxides on gram-positive *S. aureus* bacteria using various techniques and found good results [2, 3, 65, 68]. On comparing the percentage survival of bacteria with control, considered as 100%, it was observed that compound x = 0.2 showed an impressive antibacterial activity with the lowest percentage survival, followed by compound x = 0.6. The percentage survival of bacteria in the presence of compound x = 0.2 was 50.57% at 500 µg/mL and 34.57% at 1000 µg/mL, and in the presence of compound x = 0.6, the percentage survival

was 60.1% at 500 µg/mL and 42.99% at 1000 µg/mL dose. However, notable antibacterial activity in *Staphylococcus aureus*, as shown by compounds x = 0.0 and x = 0.4, was comparatively less. The percentage survival in the presence of compound x = 0.0 was 84.63% at 500 µg/mL and 44.90% at 1000 µg/mL, whereas in the presence of compound x = 0.4, the percentage survival was 91.78% at 500 µg/mL and 47.31% at 1000 µg/mL dose. Thus, compounds x = 0.2 and x = 0.6 had superior antibacterial activity and could be exploited as antimicrobial agents.

Conclusion

The $Ni_{0.6-x}Zn_xMn_{0.4}Fe_2O_4$(x = 0.0,0.2,0.4,0.6) ferrite series was synthesized by the combustion method. And characterized by various techniques. The X-ray diffraction confirms that the synthesized ferrites crystallize in a cubic spinel structure and are in the nano-size range. The IR and Raman spectroscopy validated the formation of cubic spinel single phase. The appearance of two bands between 350 and 600 cm^{-1} in IR and five active phonon modes in Raman validate the same. The morphology and particle size were corroborated using SEM and TEM as spherical nanosized agglomerates ranging from 4 to 30 nm. The XPS confirmed the 2 + and 3 + oxidation state of the respective metal ions. The resistivity values lowered as the temperature increased, proving the semi-conducting nature of ferrite samples. The dielectric constant at ambient temperature decreased with frequency, whereas the temperature studies showcased an elevation in a curve as the temperature reached maximum. The M_s values reached maximum till x = 0.4 and dropped as the x value increased. The AC susceptibility studies gave information about Curie temperature, which lessened with increased zinc content. The compound with x = 0.2, having the smallest size, showed the best antibacterial activity in the entire series.

Supplementary Information The online version contains supplementary material available at https://doi.org/10.1007/s10876-024-02745-3.

Acknowledgements One of the authors, Ms. Sanjali Navelkar, would like to thank DST for providing a fellowship under DST-PURSE. All authors thank DST-FIST, DST-Nano-Mission, DST-PURSE, and UGC-SAP for the infrastructural support. We would also like to thank SAIF- IIT Bombay for the HR-TEM facility, Mr. D. Pal, ACMS, IIT Kanpur, for the XPS facility, and CSIF- BITS Pilani, Goa for FE-SEM analysis.

Author Contributions All authors have contributed to the research paper. The material preparation, data collection, analysis, and original manuscript writing were performed by S N. and Prof. V. M. S. Verenkar, who conceptualized data, editing, manuscript correction, validation, and supervision. K. S and Dr. L. Charya analyzed and collected data and script writing on antibacterial studies.

Funding No funds.

Data Availability No datasets were generated or analysed during the current study.

Declarations

Ethical Approval This declaration is "not applicable".

Competing Interests The authors declare no competing interests.

References

1. S. Nasrin, F.-U.-Z. Chowdhury, S.M. Hoque, J. Magn. Magn. Mater. 479, 126–134 (2019)
2. M. M. Naik, H. S. B. Naik, G. Nagaraju, M. Vinuth, K. Vinu, R. Viswanath, Nano-Struc. Nano-Objects 19, 100322 (2019)
3. A. Al Mahmood, S. Bin Syeda, Z. Hasana, M. Bodiul Islama, R. Hossainb, S. Rahman, Results Surf. Interfaces 17, 100303 (2024)
4. S. Jamal Salih, Heliyon 10, e31428 (2024)
5. J. K. Ji, W. K. Ahn, J. S. Kum, S. H. Park, G. H. Kim, W. M. Seong, IEEE Magn. Lett. 1, 5000104 (2010)
6. J. C. Navarro, C. Hurtado, M. Gonzalez-Castaño, L.F. Bobadilla, S.Ivanova, F. L. Cumbrera, M.A. Centeno, J. A. Odriozola, J. CO2 Util. 68, 102356 (2023)
7. B. Shia, Z. Zhanga, B. Zhaa, D. Liua, Mol. Catal. 456, 31–37 (2018)
8. R. Dou, H. Cheng, J. Ma, S. Komarneni, Mater. Chem. Phys. 240, 122181 (2020)
9. A. R. Liandia, A. H.Cahyanab, A. J. F. Kusumaha, A. Lupitasaria, D. N. Alfarizaa, R. Nurainia, R. W. Saria, F. C. Kusumasaric, Case Stud. Chem. Environ. 7, 100303 (2023)
10. Y. Mohammed, H. Y. H. C. E. Ndikilar, J. Mohammed, A. B. Suleiman, M. G. Idris. Next Energy 4, 100145 (2024)
11. M. Gharagozlou, B. Ramezanzadeh, Z. Baradaran, Appl. Surf. Sci. 377, 86–98 (2016)
12. P. D. Prasad, J. Hemalatha, J. Magn. Magn. Mater. 484, 225–233 (2019)
13. S. Dlamini, S. Nkosi, T. Moyo, A. Nhlapo, Mater. Sci. Eng. B 294, 116554 (2023)
14. A. Pathaniaa, P. Thakurb, A. V. Trukhanovc, S. V. Trukhanovc, L.V. Paninac, U. Luderse, A. Thakur, Results Phys. 15, 1025–31(2019)
15. T. Ravikumar, L. Thirumalaisamy, S. Madanagurusamy, K. Sivaperuman, J. Alloys Compd. 959, (2023) 170568
16. P. Lata Mahapatra, S. Das N. Ann Keasberry, S. B. Ibrahim, D. Saha, J. Alloys Compd. 960, 170792 (2023)
17. G. Kogias, S. Zaspalis, D. Holz, V. Zaspalis, J. Magn. Magn. Mater. 604, 172297 (2024)
18. B.V. Bhise, M.B. Dongare, S.A. Patil, S.R. Sawant, J. Mater. Sci. Lett. 10, 922–924 (1991)
19. B.V. Bhise, A.K. Ghatage, B.M. Kulkarni, S.D. Lotke, S.A. Patil, Bull. Mater. Sci. 19, 527–531(1996)
20. S. S. Thomas, I. H. Joe, P. Aswathy, E. Mathew, A. A. Noble, Mater. Sci. Eng. B 297, 116696 (2023)
21. C. Venkataraju, G. Sathishkumar, K. Sivakumar, J. Alloys Compd. 498, 203–206 (2010)
22. Durgadsimi S. U., Kattimani V.R., Maruti N.S., Kulkarni A.B., Mathad S. N, Eurasian Phys. Tech. J. 18, 14–19 (2021)
23. T. Prabhakaran, R.V. Mangalaraja, J. C. Denardin, J. A. Jiméne, Ceram. Int. 42, 14113–14120 (2016)
24. M.M. Naik, H.S.B. Naik, G. Nagaraju, M. Vinuth, K. Vinu, S.K. Rashmi, J. Mater. Sci.: Mater. Electron. 29, 20395–20414 (2018)

25. L. A. Garcıa Cerda, Sagrario M., J. Magn. Magn. Mater. 294, e43–e46 (2005)
26. T. Zhou, S. Cao, N. Sui, J. Tu, T. Zhang, Sens. Actuators: B. Chem. 344, 130152 (2021)
27. K. Sarkar, R. Mondal, S. Dey, S. Kumar, Phys. B Condens. Matter 583, 412015 (2020)
28. R. S. Melo, P. Banerjee, A. Franco Jr., J. Mater. Sci. Mater. Electron. 29, 14657–14667 (2018)
29. C-L. Chiang, K-S. Lin, P-J. Hsu, Y-G. Lin, Int. J. Hydrog. Energy 42, 22123–22137 (2017)
30. K. Kogulakrishnan, S. Nithiyanantham, R. Mohan, N.V. Giridharan, S. Silambarasan, A. Venkadesh, V. Latha, B. Gunasekaran, L. Palaniappan, J. Mol. Struct. 1321, 140026 (2025)
31. X. Zhoua, J. Wanga, L. Zhoua, Y. Wanga, D. Yao, J. Magn. Magn. Mater. 534, 168043 (2021)
32. S. A. Jadhav, M.V. Khedkar, D.D. Andhare, S.B. Gopale, K.M. Jadhav, Ceram. Int. 47, 13980–13993 (2021)
33. G. Murtaza, R. Ahmad, T. Hussain, R. Ayub, I. Ali, M. A. Khan, M. N. Akhtar, J. Alloys Compd. 602, 122–129 (2014)
34. P. P. Goswami, H. A. Choudhury, S. Chakma, V. S. Moholkar, Ind. Eng. Chem. Res. 52, 17848–17855 (2013)
35. A. l M. Ibrahima, M. M. Abd El-Latif b, Morsi M. Mahmoud, J. Alloys Compd. 506, 201–204 (2010)
36. A. Narayanswami, N. Sivakumar, Bull. Mater. Sci. 31, 373–380 (2008)
37. A. Sutka, G. Strikis, G. Mezinskis, A. Lusis, J. Zavickis, J. Kleperis, D. Jakovlevs, Thin Solid Films 526, 65–69 (2012)
38. Singanahally T. A., in Solution Combustion Synthesis, Concise Encyclopedia of Self-Propagating High-Temperature Synthesis History, Theory, Technology, and Products, ed by I. Borovinskaya, A. Gromov, E. A. Levachov, Y. Maksimov, A. Mukasyan, A. S. Rogachev, (Elsevier Publications, 2017), 344–346,
39. A. C. Juglan, A. Jain, AIP Conf. Proc. 2986, 030127 (2024)
40. Köseoğlu, Yüksel, Ceram. Int. 39, 4221–4230 (2013)
41. E. Ranjith Kumar, Aleksandr S. Kamzin, T. Prakash, J. Magn. Magn. Mater. 378, 389–396 (2015)
42. G. Padmapriya, A. Manikandan, V. Krishnasamy, S.K. Jaganathan, S.A. Antony, J. Supercond. Nov. Magn. 29, 2141–2149 (2016)
43. K. Winiarska, R. Klimkiewicz, J. Winiarski, I. Szczygieł, React. Kinet. Mech. Catal. 120, 261–278 (2017)
44. A. H. Farha, M. S. Shams, H.A. Alalia, Z. H. Alhashema, S. A. Mansour, S. H. Aleithan, R. A. Elsad, Arab. J. Chem 17, 105459 (2024)
45. M. Deepty, Ch. Srinivas, E.R. Kumar, P.N. Ramesh, N.K. Mohan, S.S. Meena, C.L. Prajapat, A. Verma, D.L. Sastry, Sens. Actuators B Chem. 316, 128127 (2020)
46. T. L. Thokoane, T.A. Nhlapo, V. N. Adoons, L. Kotsedi, T.P. Mokoena, T.S. Mahule, T. C. Mokhena, T. Moyo, J. Mol. Struct. 1315, 138906 (2024)
47. G. Padmapriya, A. Manikandan, V. Krishnasamy, S.K. Jaganathan, S.A. Antony, J. Mol. Struct. 1119, 39–47 (2016)
48. R. Thejas, T. L. Soundarya, G. Nagaraju, K. Swaroop, S.C. Prashantha, M. Veena, E. Melagiriyappa, C.S. Naveen, Mater. Lett.: X 15, 100156 (2022)
49. T. A. Wania, G. Suresha, R. Masrourb, K. M. Batooc, A. Rasool, Mater. Chem. Phys. 307, 128169 (2023)
50. E. A. Alghamdi, R. Sai, Results Phys. 59, 107549 (2024)
51. D.S. Nair, M. Kurian, J. Water Process Eng. 16, 69–80 (2017)
52. A. A. Sattar, H. M. El-Sayed, K. M. El-Shokrofy, M. M. El-Tabey, J. Mater. Sci. 42, 149–155 (2007)
53. S. Ramesh, L. N. Patro, B. Dhanalakshmi, B. Chandrasekhar, T. Anil Babu, K. Chandra Babu Naidu, B. Parvatheeswara Rao, Mater. Chem. Phys. 306, 128055 (2023)
54. A. K. Singha, A. Vermaa, O.P. Thakurb, Chandra Prakashb, T.C. Goela, R.G. Mendirattaa, Mater. Lett. 57, 1040–1044 (2003)
55. P. P. Gauns Dessai, A. K. Singh,V.M.S. Verenkar, Mater. Res. Bull. 149, 111699 (2022)
56. B. Parvatheeswara Rao, B. Dhanalakshmi, S. Ramesh, P.S.V. Subba Rao, J. Magn. Magn. Mater. 456, 444–450 (2018)
57. S. Thota, Subhash C. Kashyap, S. K. Sharma, V. R. Reddy, Mater. Sci. Eng. B 206, 69–78 (2016)
58. F. A. Ahmed, L. N. Singh, ISSN J. Mater. Sci. & Sur. Engg. 6, 825–830 (2018)
59. A. K. Singha, A.K. Singha, T.C. Goelb, R.G. Mendiratta, J. Magn. Magn. Mater. 281, 276–280 (2004)
60. U.B. Gawas, V.M.S. Verenkar, D.R. Patil, Sens. Transducers 134, 45–55 (2011)
61. Amarendra K. Singh, T.C. Goel, R.G. Mendiratta, Solid State Commun. 125, (2003) 121–125
62. M. I. M Ismail, Mater. Res. Express 5, 095004 (2018)
63. X. Zheng, R. Fang, C. Wang, X. Tian, J. Lin, W. Zeng, T. Zhou, C. Xu, Infect. Drug Resist. 14, 1527–1536 (2021)
64. P. S. Loomba, J. Taneja, B. Mishra, J. Global Infect. Dis. 2, 275–283 (2010)
65. R. Kaliyaperumal, S. Paramsivam, S. Boonyuen, V. K. Poovan, Bull. Mater. Sci. 46, 147(2023)
66. E. Indrajith Naik, H.S.Bhojya Naik, R. Viswanath, B.R. Kirthan, M.C. Prabhakara Chem. Data Collect. 29 100505 (2020)
67. B. Lallo da Silva, M.P. Abuçafy, E. B. Manaia, J. A. Oshiro Junior, B. G.Chiari-Andréo, R. CL R Pietro, L. A. Chiavacci, Int. J. Nanomedicine 14, 9395–9410 (2019)
68. R. Kaliyaperumal, V. K. Poovan, P. Shanmugam, J. Indian Chem. Soc. 100, 100842 (2023)
69. Durgadsimi S. U., Kattimani V. R., Maruti N. S., Kulkarni A. B, Mathad S.N, 14 ISSN Eurasian Phys. Tech. J. 18, 2413–2179 (2021)
70. S. Rather, U. Saeed, A. A.Al-Zahrani, H. S. Bamufleh, H. A. Alhumade, A. A. Taimoor, O. M. Lemine, A. M. Ali, B. Al Zaitone, M. M. Alam, J. Nanomater. 2021, 12 pages (2021)
71. K. Rama Krishna, D. Ravinder, K. Vijaya Kumar, C. A. Lincon, Synthesis, J. Condens. Matter Phys. 2, 153–159 (2012)
72. S.B. Khan, S. Irfan, S-L. Lee, Nanomaterials 9, 1–17 (2019)
73. H. J. Kim, S. W. Hyun, S. H. Kim, H. Choi, J. Radioanal. Nucl. Chem. 330, 445–454 (2021)
74. R. B. Sathe, C. U. Narayankar, N. Abderrahim, P. Kumar, J. S. Ghodake, R. H. Patil, S. H. Khoreem, A. Dinesh, M. Ayyar, H. Elhouichet, R. P. Patil, S. B. Patil, Inorg. Chem. Commun. 113408 (2024) https://doi.org/10.1016/j.inoche.2024.113408
75. A. Sharma, N. Aggarwal, N. Kumar, P. Patial, S. Kumar, Shilpi Jindal, Physica B: Condens. Matter 668, 415237 (2023)
76. P. P. G. Dessai, V. M. S. Verenkar, J. Therm. Anal. Calorim. 142, 1399–1411 (2020)
77. U. B. Gawas, M. M. Kothawale, R. Pednekar, S. S. Meena, N. K. Prasad, S. K. Alla, J Supercond. Nov. Magn. 30, 1287–1292 (2017)
78. D. R. Mane, D. D. Birajdar, S. E. Shirsath, R. A. Telugu, R. H. Kadam, Phys. Status Solidi A 207, 2355–2363 (2010)
79. J. Bennet, R. Tholkappiyan, K. Vishista, N. Victor Jaya, F. Hamed, Appl. Surf. Sci. 383, 113–125 (2016)
80. M. Masuku, J. F. Nure I. Nkambule, J. Water Process Eng. 64, 105587 (2024)
81. M. M. El-Nahassa, Z. El-Goharyb, H. S. Soliman, Opt. Laser Technol. 35, 523–531 (2003)
82. M. Dongol, A. El-Denglawey, A.F. Elhady, A.A. Abuelwafa, Curr. Appl. Phys. 12, 1334 (2012)
83. F. Naaz, P. Lahiri, V. K. Mishra, H. K. Dubey, P. K.Tripathi, E. Shakerzadeh, Inorg. Chem. Commun. 162, 112185 (2024)
84. R. Tholkappiyan, K. Vishista, Mater. Sci. Semicond. Process. 40, 631–642 (2015)

85. M. Aadil, A. Ghanim Taki, S. Zulfiqar, A. Rahman, M. Shahid M. F. Warsi, Z. Ahmad, A. A. Alothman, S. Mohammad, RSC Adv 13,28063–28075 (2023)
86. S. Aradea, P. Agalea, S. Balgudeb, S. Patangec, D. Hinganed, P. More, Inorg. Chem. Commun. 170, 113170 (2024)
87. R. D. Waldron, Physical Review 99, 1727–1735 (1955)
88. A. T. Raghavender, N. Biliskov, Z. Skoko, Mater. Lett. 65, 1727–1735 (2011)
89. R. Sharma, S. Singhal, Physica B 414, 83–90 (2013)
90. A.M. El-Sayed, Ceram. Int. 28, 363–367 (2002)
91. P. Kashida, S.N. Mathada, M. R. Shedamb, A. Somyac, A. Ansarid, M. Hashemi, M. M. Alsaranie, O. Alageel, Ain Shams Eng. J. 15, 10254 (2024)
92. C. A. P. Gomez, C. A. Barrero Meneses, J. A. Jaen, J. Magn. Magn. Mater. 505, 166710 (2020)
93. S. Thota, S. C. Kashyap, S. K. Sharma, V.R. Reddy, J. Phys. Chem. Solids 91, 136–144 (2016)
94. F. Bibi, A. Ahmed, Y. Ajaj, A. Abd Al-Sattar Dawood, M. Usman, A. Alodhayb, S. Mohammad, Zubair Ahmad, A. Kalsoom, Shahid Iqbal, Polyhedron 250, 116826 (2024)
95. W. Li, B. Dai, Z. Li, H. Yang, G. Liu, F. Xu, J. Mater. Sci.: Mater. Electron 541, (2024)
96. D. Andhare, S. R. Patade, J. S. Kounsalye, K. M. Jadhav, Physica B: Condens. Matter 583, 412051 (2020)
97. Aamir Mahmood, Asghari Maqsood, Mater. Sci. Eng. B 296, 116615 (2023)
98. E. A. Alghamdi, Refka Sai, Results in Phys. 59, 107549 (2024)
99. A. A. Alakshar, M. E. Goher, M. G. Abd El-Moghny, M. S. El-Deab, Desalination and Water Treat. 320, 100676 (2024)
100. Y. Lin, J. Dong, J. Dai, J. Wang, H. Yang, H. Zong, Inorg. Chem. 56, 14960–1496 (2017)
101. S. Vadivelan, S. Sowmiya, Physics Open 9, 100094 (2021).
102. A. Abu El-Fadl, A. M. Hassan, M. A. Kassem Results Phys. 28, 104622 (2021)
103. Y. Bi, A. Nautiyal, H. Zhang, J. Luo, X. Zhang, Electrochim. Acta 260, 952–958 (2018)
104. R. Grissa, H. Martinez, S. Cotte, J. Galipaud, B. Pecquenard, F. Le Cras, Appl. Surf. Sci. 411, 449–456 (2017)
105. M. Li, H. Fang, H. Li, Y. Zhao, T. Li, H. Pang, J. Tang, X. Liu, J. Supercond. Nov. Magn. 30, 2275–2281 (2017)
106. C. C. Naik, S. K. Gaonkar, I. Furtado, A. V. Salker, J. Mater. Sci.: Mater. Electron. 29, 14746–14761 (2018)
107. D. Parajuli, P. Taddesse, N. Murali, K. Samatha, J. Indian Chem. Soc. 99, 100380 (2022)
108. N. Jahani, F.Z. Chowdhury, A.K.M. Zakaria, Mater. Sci.-Pol. 34, 185–191 (2016)
109. K. Y. Salkar, R. B. Tangsali, R. S. Gad, A. Gangwar, N. K. Prasad, J. Mater. Sci.: Mater. Electron. 30, 18374–18383 (2019)
110. A. K. Singh, T. C. Goel R. G. Mendiratta, Jpn. J. Appl. Phys. 42, 2690–2691 (2003)
111. A. K. Singh, T.C. Goel, R.G. Mendiratta, Solid State Commun. 125, 121–1 25 (2003)
112. A. K. Singh, T. C. Goel, R. G. Mendiratta, O. P. Thakur, C. Prakash, J. Appl. Phys. 91, 6626–6629 (2002)
113. S. Ramesh, B. Dhanalakshmi, B. Chandra Sekhar, P. S. V. Subba Rao, B. Parvatheeswara Rao, Ceram. Int. 42, 9591–9598 (2016)
114. J. Parashar, V. K. Saxena, Jyoti, D. Bhatnagar, K. B. Sharma, J. Magn. Magn. Mater. 394, 105–110 (2015)
115. G. Vaidyanathan, S. Sendhilnathan, Phys. B: Condens. Matter 403, 2157–2167 (2008)
116. D. M. Coutinho, V. M. S. Verenkar, J. Alloys Compd. 782, 392–403 (2019)
117. D. V. Kurmude, C. M. Kale, P. S. Aghav, D. R. Shengule, K. M. Jadhav, J. Supercond. Nov. Magn. 27, 1889–1897 (2014)
118. C. Venkataraju, G. Sathishkumar, K. Sivakumar, J. Magn. Magn. Mater. 322, 230–233 (2010)
119. R. Topkaya, A. Baykal, A. Demir, J. Nanopart. Res. 15, 359 (2013)
120. Abdul Ahad, A.K.M. Akther Hossain, Heliyon 10 (2024) e26050
121. S. Mazena, N. I. Abu-Elsaada, A. S. Nawara, Phys. Solid State 62, 1183–1194 (2020)
122. M. Hashim, Alimuddin, S. E. Shirsath, S. S. Meena, R. K. Kotnala, A. Parveen, A. S. Roy, S. Kumar, P. Bhatt, R. Kumar, J. Magn. Magn. Mater. 341, (2013)148–157
123. S. J. Soenena, P. R. Gilb, J. M. Montenegro, W. J. Parak, S. C. De Smedt, K. Braeckmans, Nano Today 6, 446–465 (2011)
124. S.K. Rajabi, Sh. Sohrabnezhad, J. Fluor. 206, 36–42 (2018)

Publisher's Note Springer Nature remains neutral with regard to jurisdictional claims in published maps and institutional affiliations.

Springer Nature or its licensor (e.g. a society or other partner) holds exclusive rights to this article under a publishing agreement with the author(s) or other rightsholder(s); author self-archiving of the accepted manuscript version of this article is solely governed by the terms of such publishing agreement and applicable law.